Exploring TGF-β superfamily-dependent regulation of smooth muscle cell phenotypes in the context of saphenous vein graft disease

Julian Tristan Schwartze

MD

Submitted in fulfilment of the requirements for the degree of Doctor of Philosophy to the Institute of Cardiovascular and Medical Sciences, University of Glasgow.

Research conducted at the British Heart Foundation Glasgow Cardiovascular Research Centre, Institute of Cardiovascular and Medical Sciences, College of Medical, Veterinary and Life Sciences, University of Glasgow, UK

March 2021

Author's declarations

I herewith declare that I, Julian Tristan Schwartze, have written this thesis myself and that this thesis is a record of my own work except for:

- IHC staining of human pre-implantation saphenous vein cross sections for contractile smooth muscle cell markers was partially carried out by Daniel Kelly (University of Glasgow, UK).

- The murine carotid artery wire injury study was performed by Dr Sammy El-Mansi (University of Glasgow, UK).

- The first murine carotid artery ligation study and partial H&E staining of carotid arteries were performed by Daria Boyd (University of Glasgow, UK).

- The BMP-9 cross-linking experiment was performed by Dr Emma Low (University of Glasgow, UK) and Midory Thorikay from Peter ten Dijke's group (University Medical Center, Leiden, Netherlands).

- Single cell library preparation and next-generation sequencing were carried out at the Glasgow Polyomics Insitute (University of Glasgow, Glasgow, UK)

- Adam Kurkiewicz and Marcell Pék (Biomage Ltd, UK and University of Glasgow, UK) generated the computational scRNAseq pipeline and used this pipeline to analyse data from the scRNAseq study.

This thesis has not previously been submitted for a higher degree. I carried out this research at the BHF Glasgow Cardiovascular Research Centre, Institute of Cardiovascular and Medical Sciences, College of Medical, Veterinary and Life Sciences, University of Glasgow, UK under the supervision of Dr Angela Bradshaw and Professor Stuart Nicklin.

Acknowledgements

Firstly, I want to thank both my supervisors, Dr Angela Bradshaw and Professor Stuart Nicklin for their scientific insights, guidance and fantastic support during my time at ICAMs. I want to thank Ange for enabling me to carry out a PhD at the University of Glasgow and for her continuous and relentless effort to support me through emotionally rough times during my PhD. Her appreciation for my work, her unique scientific insights into TGF-β biology as well as her continuous motivation, positivity and passion for science have motivated and inspired me throughout my time at the University of Glasgow. I want to thank Medical Research Scotland and Batavia Sciences B.D. (Leiden, Netherlands) for their financial support and funding of this project. I also want to thank Dr Wilfried Bakker and Dr Menzo Havenga (Batavia Biosciences, B.D.) for organising a company visit, enabling me to complete a GMP course and giving me the opportunity to write a review on adenoviral gene therapy applications for cardiovascular diseases. Working with Batavia has given me great insights into how biopharmaceutical companies function and how collaboration between academia and industry drives drug development and innovation.

Secondly, I want to thank all members of the BHF GCRC Level 3 and 4. I want to thank Dr Rheure Lopes who provided invaluable advice on analysing Ca^{2+} transients in vascular smooth muscle cells. I want to thank Elaine Friel for her assistance in processing pre-implantation saphenous vein graft tissue. I want to thank Nicola Britton who taught me how to propagate and purify adenoviruses. I want to thank Adam Kurkiewicz and Marcell Pék who provided a computational scRNAseq pipeline and assisted with scRNAseq data analysis. I want to thank Dr Martin McBride, Dr John McClure and Simon Fisher who provided great advice on scRNAseq and statistical analyses.

I have made great friends during my PhD and all of them deserve a special thanks for making my time in Glasgow. Thank you especially to Aisling, Laura, Sonya, Tuuli, Ahmad, Arun, Ashton, Antoniya, Eleni Simon and Sammy. I also want to thank my entire family who have always supported and encouraged me throughout my PhD.

Finally, and most importantly, I want to thank my loving wife Natalia who I first met at the University of Glasgow and who has always stood by my side. Without her continuous, tremendous and loving support throughout my entire PhD and beyond, all of this would not have been possible. My time at the University of Glasgow has been remarkable and unique. Glasgow will forever remain in my heart.

Table of contents

Author's declarations ii
Acknowledgements iii
Table of contents v
List of figures xi
List of tables xv
List of abbreviations and definitions xvii
List of presentations, awards and publications xxii
Summary xxiii
Chapter 1 Introduction 27
1.1 Coronary artery disease 28
1.2 Coronary artery bypass graft surgery 29
1.2.1 Saphenous vein graft versus internal mammary artery graft 30
1.3 Saphenous vein graft disease 32
1.3.1 Neointima formation 35
1.3.2 vSMC heterogeneity 46
1.4 Vascular TGF-ß superfamily signalling 48
1.4.1 The TGF-ß superfamily 48
1.4.2 TGF-$ß_1$ production, storage and activation 48
1.4.3 BMP-9 production and secretion 49
1.4.4 Canonical and non-canonical signalling pathways in the vasculature 50
1.4.5 Vascular development and hereditary vascular disorders 54
1.5 Adenoviral vector-based gene therapy in saphenous vein graft disease 58
1.5.1 Adenovirus structure and genome organisation 58
1.5.2 Distinct AdV vector generations 60
1.5.3 HAdV-5-dependent transgene delivery 63
1.5.4 HAdV-5-based gene therapy advantages and clinical challenges ... 65
1.5.5 Recent and current HAdV-5-based cardiovascular gene therapy trials in humans 66
1.5.6 Pre-clinical evidence for efficacy of HAdV-5-based gene therapy in preventing vein graft NF 68
1.6 Aims of the study 69
1.6.1 Aims 69
Chapter 2 Materials and Methods 70
2.1 Preparation of saphenous vein samples from CABG patients 71
2.1.1 Human saphenous vein sample fixation 71
2.2 Cell culture 72
2.2.1 Primary HSVSMC isolation and outgrowth 72

2.2.2 Primary HSVSMC expansion and cryopreservation 73
2.2.3 Primary HCASMC expansion 74
2.2.4 SMDS-induced contractile differentiation protocol for primary human SMCs 74
2.2.5 Ligand stimulation in primary HSVSMCs 77
2.2.6 HAdV-5-mediated *ACVR2A* delivery to primary HSVSMCs 79
2.2.7 HEK293 cell expansion 80
2.3 Gene expression analysis 80
2.3.1 RNA extraction, purification and quantification 80
2.3.2 Reverse transcription reaction 82
2.3.3 TaqMan™ quantitative real-time polymerase chain reaction 83
2.4 Protein expression analysis 86
2.4.1 Cell lysis 86
2.4.2 Determining protein sample concentration 87
2.4.3 Protein sample preparation for SDS-PAGE and immunoblotting 88
2.4.4 Immunoblot analysis 88
2.5 Scratch assay 92
2.6 BrdU proliferation assay 93
2.6.1 BrdU incorporation and cell fixation/denaturation 93
2.6.2 BrdU ELISA analysis 93
2.7 Calcium handling studies 94
2.7.1 Whole region of interest analysis 96
2.7.2 Single cell region of interest analysis 96
2.8 Crosslinking of ^{125}I-BMP-9 to HSVSMC cell surface receptors 97
2.9 Cloning methods using the pAdEasy-1 system for generation of a recombinant HAdV-5 98
2.9.1 Construct design and plasmid preparation 98
2.9.2 Transformation and propagation of XL10-Gold Ultracompetent Cells® 98
2.9.3 MINI plasmid purification 100
2.9.4 MAXI plasmid purification 101
2.9.5 Restriction digests 102
2.9.6 Agarose gel electrophoresis 105
2.9.7 Gel DNA extraction 106
2.9.8 Phenol/chloroform purification (PCP) 106
2.9.9 pSHUTTLE-CMV de-phosphorylation 107
2.9.10 DNA ligation 107
2.9.11 Plasmid sequencing 108
2.9.12 Homologous recombination 108
2.9.13 HEK293 transfection with pAdEasy-1::pSHUTTLE-CMV::*ACVR2A*s 109

2.9.14 Crude virus isolation 110
2.9.15 First plaque purification 111
2.9.16 Second plaque purification 112
2.9.17 Seed stock generation 112
2.9.18 Scale up and virus isolation 113
2.9.19 CsCl gradient preparation and centrifugation 113
2.9.20 Dialysis 116
2.9.21 Virus aliquot preparation 117
2.9.22 Viral particle quantification 117
2.9.23 Generation of recombinant E1/E3-deficient HAdV-5 ACVR2A 118
2.10 Single cell RNA sequencing 124
2.10.1 Sample preparation 124
2.10.2 The principle of 3'-end 10x Chromium microfluidics-based single cell RNA sequencing 125
2.10.3 cDNA library preparation and next-generation sequencing 127
2.10.4 Raw data processing 127
2.11 Carotid artery ligation study in mice 128
2.11.1 Experimental mice and housing conditions 128
2.11.2 Study design 128
2.11.3 The carotid artery ligation procedure 130
2.11.4 Schedule 1 procedure (termination) 133
2.11.5 Organ/Blood harvest 133
2.12 EdU staining 133
2.13 Haematoxylin and Eosin staining 137
2.14 Tissue processing for histology 140
2.15 Immunohistochemistry 140
2.16 Statistical analysis 144
Chapter 3 Investigating BMP-9 in human saphenous veins and murine arterial vasculature 145
3.1 Introduction 146
3.1.1 SMC phenotype switching during NF in murine vascular injury models 146
3.1.2 BMP-9 in vascular health and disease 151
3.2 Aims 155
3.3 Results 156
3.3.1 BMP-9 is present in all layers of pre-implantation SVs from CABG patients 156
3.3.2 Pre-implantation SVs from CABG patients display SMC phenotype switching 158
3.3.3 BMP-9 antibody optimisation in mouse lung tissue 163

3.3.4 Carotid artery wire injury triggers an increase in vascular BMP-9 immunoreactivity and SMC phenotype switching 165
3.3.5 Carotid artery ligation triggers neointima formation and media hypertrophy in mice 169
3.3.6 Carotid artery ligation triggers early peripheral vascular cell proliferation in mice 174
3.3.7 Preliminary IHC αSMA staining indicates *in vivo* SMC phenotype switching following carotid ligation injury 178
3.4 Discussion 182
3.5 Summary 190
Chapter 4 Exploring TGF-β superfamily signalling-driven HSVSMC phenotype responses 191
4.1 Introduction 192
4.1.1 TGF-β-dependent regulation of contractile gene expression in vSMCs 192
4.1.2 Conflicting role of TGF-β signalling in vascular injury-driven NF 194
4.1.3 Activin A receptor type 2A/B signalling in vSMCs and vascular disease 196
4.1.4 Venous versus arterial SMCs 196
4.2 Aims 198
4.3 Results 199
4.3.1 Generation of a contractile differentiation protocol for primary HSVSMCs 199
4.3.2 Contractile HSVSMCs display a decrease in proliferation 203
4.3.3 Activin A receptor type 2a mRNA expression levels increase during contractile differentiation of HSVSMCs 207
4.3.4 Contractile differentiation is paralleled by a reduction in *ID1* mRNA expression levels in HSVSMCs 210
4.3.5 Generation of an undirected contractile differentiation protocol for primary HCASMCs 212
4.3.6 Contractile differentiation is paralleled by an increase in TGF-β superfamily receptor mRNA expression levels in HCASMCs 215
4.3.7 Pharmacological ALK5 inhibition prevents contractile differentiation of primary HSVSMCs 218
4.3.8 HAdV-5-mediated ACVR2A delivery to HSVSMCs increases *ACVR2A* mRNA expression levels 223
4.3.9 BMP-9 binds to type I and type II TGF-β superfamily receptors on HSVSMCs 228
4.3.10 BMP-9 treatment drives SMAD1 phosphorylation in primary HSVSMCs 230
4.3.11 BMP-9 and TGF-β_1 treatment induce target gene expression in primary HSVSMCs 232
4.3.12 Pharmacological ALK5 inhibition prevents TGF-β_1-induced increase in contractile gene expression in HSVSMCs 234

4.3.13 TGF-β_1 demonstrates anti-proliferative effects in primary HSVSMCs. 238

4.3.14 TGF-β_1 stimulation indicates inhibition of serum-induced migration in primary HSVSMCs 240

4.3.15 TGF-β_1 suppresses osteoblast and macrophage-like gene expression via ALK5 in primary HSVSMCs 243

4.4 Discussion 246

4.5 Summary 259

Chapter 5 Evaluating TGF-β superfamily-dependent regulation of intracellular Ca^{2+} mobilisation in HSVSMCs 260

5.1 Introduction 261

5.1.1 Regulation of vSMC contraction and relaxation 261

5.1.2 TGF-β_1-dependent regulation of Ca^{2+} handling in vSMCs 264

5.2 Aims 265

5.3 Results 266

5.3.1 Development and validation of a protocol for assessing AngII-driven intracellular Ca^{2+} release in primary human vascular SMCs 266

5.3.2 BMP-9 attenuates TGF-β_1/ALK5 pathway-driven contractile responses in primary HSVSMCs 270

5.3.3 Evidence for distinct Ca^{2+} handling in primary HCASMCs 272

5.3.4 Single cell resolution uncovers HSVSMC population heterogeneity 274

5.3.5 AngII-induced intracellular Ca^{2+} mobilisation is mediated via AT_1R in primary HSVSMCs 279

5.3.6 Pharmacological ROCK blockade does not prevent AngII-mediated intracellular Ca^{2+} mobilisation in primary HSVSMCs 281

5.3.7 TGF-β_1 represses *MAS1* mRNA expression levels in HSVSMCs..... 283

5.4 Discussion 285

5.5 Summary 297

Chapter 6 Characterising primary HSVSMC transcriptome heterogeneity using single cell RNA sequencing 299

6.1 Introduction 300

6.1.1 Single cell RNA sequencing as a technique to investigate vSMC heterogeneity 300

6.2 Aims 302

6.3 Results 303

6.3.1 Quality control filtering reveals high percentage of mitochondrial genes in primary HSVSMCs 303

6.3.2 Initial principal component analysis reveals distinct transcriptomes for each treatment group 306

6.3.3 Combined UMAP and Louvain clustering reveals transcriptome heterogeneity in primary HSVSMCs 309

6.3.4 Serum-starved HSVSMC control population displays 7 distinct clusters 311
6.3.5 ScRNA-seq analysis reveals a potentially osteogenic HSVSMC lineage following BMP-9 treatment 317
6.3.6 TGF-β_1-treated primary HSVSMC lineages express contractile, fibrotic and chemotactic genes 324
6.3.7 Single cell transcriptomics uncover potential mechanisms for negative regulation of contractility in BMP-9/TGF-β_1-co-treated primary HSVSMCs 334
6.4 Discussion 346
6.5 Summary 354
Chapter 7 General discussion 355
7.1 Overall Summary 356
7.2 Future perspectives 363
List of references 366

List of figures

Figure 1-1 Schematic cross-sectional representation of a narrowed coronary artery 28
Figure 1-2 Schematic representation of coronary artery bypass graft surgery using the great saphenous vein 29
Figure 1-3 Cross-sectional schematic representation of Internal mammary artery versus great saphenous vein histology 30
Figure 1-4 Saphenous vein graft disease pathology following CABG surgery..... 33
Figure 1-5 Schematic representation of contractile gene expression regulation in vSMCs..... 38
Figure 1-6 Schematic representation of the cell cycle..... 40
Figure 1-7 Schematic representation of vSMC migration..... 42
Figure 1-8 Basic schematic representation of canonical TGF-β superfamily signalling 52
Figure 1-9 Schematic representation of ACVR2A/B signalling..... 53
Figure 1-10 Schematic representation of AdV structure and genome organisation 59
Figure 1-11 Schematic representation of HAdV-5-dependent transgene delivery and its clinical challenges 64
Figure 2-1 Workflow for SMDS-induced contractile differentiation of primary HSVSMCs 75
Figure 2-2 Workflow for SMDS-induced contractile differentiation of primary HCASMCs..... 76
Figure 2-3 Workflow for ligand stimulation experiments in primary HSVSMCs ... 78
Figure 2-4 Workflow for HAdV-5-mediated *ACVR2A* transgene delivery..... 79
Figure 2-5 Scratch closure quantification 92
Figure 2-6 Workflow diagram for generation of pSHUTTLE-CMV::*ACVR2A* 119
Figure 2-7 *Pme*I linearisation and *Pac*I linearisation following homologous recombination 121
Figure 2-8 Generation of recombinant HAdV-5 ACVR2A..... 123
Figure 2-9 Schematic representation of 3′-end 10x Chromium single cell RNA sequencing 126
Figure 2-10 Carotid artery ligation study design 129
Figure 2-11 Schematic representation of carotid artery ligation procedure and target tissue processing..... 132
Figure 2-12 Workflow for quantifying EdU-stained murine carotid artery sections. 136
Figure 2-13 Workflow for quantifying intimal and medial areas of H&E-stained ligation injured murine carotid arteries..... 139
Figure 3-1 BMP-9 is present in all layers of pre-implantation SVGs from CABG patients..... 157
Figure 3-2 Decreased intimal calponin presence hints at *in vivo* SMC phenotype switching 159
Figure 3-3 SM22-α co-localises with αSMA$^+$ cells in all layers of pre-implantation SVs from CABG patients..... 160
Figure 3-4 Decreased intimal MYH11 presence indicates SMC phenotype switching 161
Figure 3-5 Decreased intima/media ratios of mature SMC markers suggest SMC phenotype switching in pre-implantation SVGs from CABG patients..... 162
Figure 3-6 Mouse lung tissue displays BMP-9 immunoreactivity..... 164

Figure 3-7 Carotid artery wire injury triggers an increase in vascular BMP-9 immunoreactivity in mice 166
Figure 3-8 Wire injured murine carotid arteries display BMP-9 immunoreactivity at 21 days following injury 167
Figure 3-9 Carotid wire injury triggers an increase in vascular BMP-9 immunoreactivity and SMC phenotype switching in mice 168
Figure 3-10 Carotid artery ligation triggers NF in mice (part 1) 171
Figure 3-11 Carotid artery ligation triggers NF in mice (part 2) 172
Figure 3-12 Carotid artery ligation triggers NF and medial hypertrophy 173
Figure 3-13 Carotid artery ligation triggers early peripheral vascular cell proliferation 175
Figure 3-14 Carotid artery ligation triggers intimal and medial cell proliferation at day 7 176
Figure 3-15 28-day old neointimal lesions do not display proliferating cells in mice 177
Figure 3-16 Carotid artery ligation triggers a decrease in medial αSMA immunoreactivity in mice 179
Figure 3-17 Carotid artery ligation triggers a decrease in medial αSMA immunoreactivity in mice 180
Figure 3-18 28-day old neointimal lesions display αSMA immunoreactivity in mice 181
Figure 4-1 SMDS treatment drives accumulation of contractile gene expression levels in primary HSVSMCs 201
Figure 4-2 SMDS treatment drives accumulation of contractile protein expression levels in primary HSVSMCs 202
Figure 4-3 Contractile HSVSMCs demonstrate reduced levels of pro-proliferative gene expression levels 205
Figure 4-4 SMDS-treated primary HSVSMCs display decreased proliferation 206
Figure 4-5 TGF-β type I receptor gene expression levels remain unchanged during contractile differentiation of primary HSVSMCs 208
Figure 4-6 Contractile differentiation is paralleled by an increase in *ACVR2A* mRNA expression levels in primary HSVSMCs 209
Figure 4-7 Contractile primary HSVSMCs display a reduction in relative *ID1* mRNA expression levels 211
Figure 4-8 SMDS-cultured primary HCASMCs accumulate contractile gene expression levels 213
Figure 4-9 SMDS-cultured primary HCASMCs accumulate contractile protein expression levels 214
Figure 4-10 Increased contractile protein expression levels are paralleled by an increase in *ALK5*, *ALK1* and *ACVR2A* mRNA expression levels in primary HCASMCs 216
Figure 4-11 Contractile primary HCASMCs demonstrate a reduction in relative *ID1* mRNA expression levels 217
Figure 4-12 Pharmacological ALK5 inhibition prevents SMDS-triggered increase in αSMA gene expression levels in primary HSVSMCs 220
Figure 4-13 Pharmacological ALK5 inhibition prevents SMDS-driven contractile protein expression levels in primary HSVSMCs 221
Figure 4-14 Pharmacological ALK5 inhibition inhibits SMDS-induced phosphorylation of MLC9 and increase in total-MLC9 protein expression levels in primary HSVSMCs 222
Figure 4-15 HAdV-5 GFP transduction efficiency 225

Figure 4-16 HAdV-5 ACVR2A successfully delivers the *ACVR2A* transgene to primary HSVSMCs 226
Figure 4-17 HAd-5 GFP dose-dependently potentiates SMDS-driven α*SMA* expression levels in primary HSVSMCs 227
Figure 4-18 ^{125}I-BMP-9 crosslinking assay in primary HSVSMCs 229
Figure 4-19 BMP-9 time-dependently drives SMAD1 phosphorylation in primary HSVSMCs 231
Figure 4-20 BMP-9 and TGF-β_1 induce target gene expression in primary HSVSMCs 233
Figure 4-21 TGF-β_1 drives contractile gene expression levels in primary HSVSMCs via the ALK5 pathway 236
Figure 4-22 72-h starved HSVSMCs demonstrate an increase in contractile protein expression levels 237
Figure 4-23 TGF-β_1 prevents serum-induced primary HSVSMC proliferation 239
Figure 4-24 TGF-β_1 prevents serum-induced primary HSVSMC-driven scratch closure 241
Figure 4-25 TGF-β_1 demonstrates anti-migratory effects on serum-induced primary HSVSMC-driven scratch closure 242
Figure 4-26 TGF-β_1 ALK5-dependently suppresses osteoblastic and macrophage-like gene expression levels in primary HSVSMCs 245
Figure 5-1 Regulation of vascular SMC contraction and relaxation..... 263
Figure 5-2 Protocol for assessing AngII mediated intracellular Ca^{2+} release in primary HSVSMCs 268
Figure 5-3 15% serum suppresses AngII-mediated intracellular Ca^{2+} release in primary HSVSMC 269
Figure 5-4 BMP-9 and pharmacological ALK5 inhibition prevent TGF-β_1-driven enhanced intracellular Ca^{2+} release in primary HSVSMCs 271
Figure 5-5 Evidence for distinct Ca^{2+} handling in primary HCASMCs 273
Figure 5-6 Protocol for assessing intracellular Ca^{2+} release in single primary HSVSMCs 276
Figure 5-7 Single cell resolution reveals HSVSMC population heterogeneity (A) 277
Figure 5-8 Single cell resolution reveals HSVSMC population heterogeneity (B) 278
Figure 5-9 AngII triggers intracellular Ca^{2+} release via AT_1R in primary HSVSMCs 280
Figure 5-10 Pharmacological Rho-kinase blockade does not prevent AngII-induced intracellular Ca^{2+} release in primary HSVSMCs 282
Figure 5-11 TGF-β_1 suppresses *MAS1* gene expression via ALK5 284
Figure 6-1 Preliminary quality control filtering identifies high percentage of mitochondrial genes in primary HSVSMCs 304
Figure 6-2 Final quality control filtering confirms high percentage of mitochondrial gene percentage..... 305
Figure 6-3 Principal component analysis reveals distinct transcriptomes within each treatment group 307
Figure 6-4 BMP-9 and TGF-β_1 drive target gene expression in primary HSVSMCs 308
Figure 6-5 ScRNAseq uncovers transcriptional heterogeneity in each treatment group 310
Figure 6-6 UMAP/Louvain clustering and RNA velocity in untreated control primary HSVSMCs 313
Figure 6-7 Top 30 most differentially regulated genes (DEGs) per cluster in untreated control primary HSVSMCs 314

Figure 6-8 GO identifies enrichment for regulation of high voltage-gated calcium channel activity in cluster 0 in untreated control primary HSVSMCs 316
Figure 6-9 UMAP/Louvain clustering and RNA velocity in BMP-9-treated primary HSVSMCs 320
Figure 6-10 Top 30 most differentially regulated genes per cluster in BMP-9-treated primary HSVSMCs 321
Figure 6-11 GO analysis identifies a potential osteogenic sub-lineage in BMP-9-treated primary HSVSMCs 323
Figure 6-12 UMAP/Louvain clustering and RNA velocity in TGF-β_1-treated primary HSVSMCs 327
Figure 6-13 Top 30 most DEGs per cluster in TGF-β_1-treated primary HSVSMCs 328
Figure 6-14 Cluster 1 displays enrichment for genes associated with stress fibre formation in primary HSVSMCs following TGF-β_1 treatment 330
Figure 6-15 Cluster 2 displays enrichment for pro-fibrotic genes in primary HSVSMCs following TGF-β_1 treatment 331
Figure 6-16 Cluster 3 demonstrates overlap of genes associated with induction of positive chemotaxis in primary HSVSMCs following TGF-β_1 treatment..... 332
Figure 6-17 Cluster 5 displays overlap of genes associated with negative regulation of pathway-restricted SMAD protein phosphorylation in primary HSVSMCs following TGF-β_1 treatment 333
Figure 6-18 UMAP/Louvain clustering and RNA velocity in BMP-9/TGF-β_1-co-treated primary HSVSMCs 338
Figure 6-19 Top 30 most differentially regulated genes per cluster in BMP-9 and TGF-β_1 co-treated primary HSVSMCs (part 1) 339
Figure 6-20 Top 30 most differentially regulated genes per cluster in BMP-9 and TGF-β_1 co-treated primary HSVSMCs (part 2) 340
Figure 6-21 GO analysis reveals a sub-lineage in cluster 0 enriching for genes associated with negative regulation of vascular calcification and contraction in BMP-9/TGF-β_1-co-treated primary HSVSMCs 343
Figure 6-22 Cluster 1 displays overlap of pro-fibrotic genes in BMP-9/TGF-β_1-co-treated primary HSVSMCs. 344
Figure 6-23 Cluster 2 demonstrates overlap of genes associated with regulation of the citrulline/NO cycle in BMP-9/TGF-β_1-co-treated primary HSVSMCs..... 345
Figure 7-1 Proposed model of BMP-9/ALK1/2- and TGF-β_1/ALK5-driven regulation of HSVSMC phenotypes 362

List of tables

Table 1-1 List of histological differences between the internal mammary artery and great saphenous vein 31
Table 1-2 Summary of key pathophysiological features of SVG disease following CABG surgery 34
Table 1-3 List of murine homozygous knockout models and their cardiovascular phenotypes 56
Table 1-4 List of known genetic defects culminating in HVDs in humans 57
Table 1-5 List of current AdV vector-based vaccine development programmes . 62
Table 1-6 List of current cardiovascular gene therapy trials employing recombinant HAdV-5 vectors 67
Table 2-1 Summary of anthropometric donor characteristics 71
Table 2-2 Recipe for 1 L of 4% (w/v) PFA solution 71
Table 2-3 Wash medium composition 72
Table 2-4 15% (v/v) FCS media smooth muscle cell growth medium composition 73
Table 2-5 SMGS medium composition 74
Table 2-6 SMDS medium composition 75
Table 2-7 SMC starvation medium composition (without L-glutamine) (MEDIA1). 77
Table 2-8 HEK293 medium composition 80
Table 2-9 RNA sample preparation for reverse transcription reaction 82
Table 2-10 Reverse transcription master mix 83
Table 2-11 TaqMan™ qRT-PCR reaction mix 84
Table 2-12 List of Thermo Fisher Scientific TaqMan™ gene expression assays (part 1) 85
Table 2-13 List of Thermo Fisher Scientific TaqMan™ gene expression assays (part 2) 86
Table 2-14 Recipe for 100 mL RIPA buffer (pH 8.8) 87
Table 2-15 Recipe for 1× transfer buffer 88
Table 2-16 Recipe for Ponceau stain 89
Table 2-17 List of primary antibodies for immunoblot analysis 90
Table 2-18 Recipe for stripping buffer 91
Table 2-19 SMC starvation medium composition (with L-glutamine) (MEDIA2) ... 93
Table 2-20 HEPES medium composition for Ca^{2+} handling studies 95
Table 2-21 Recipe for 1× Ca^{2+}-free 0.1 mM EGTA-containing HEPES solution 96
Table 2-22 Recipe for AGAR 100
Table 2-23 Recipe for Luria Broth medium 100
Table 2-24 Large scale double restriction digest for pEX-A2::*ACVR2A* and pSHUTTLE-CMV 102
Table 2-25 Single restriction digest for pSHUTTLE-CMV 103
Table 2-26 Set-up for double-cut diagnostic digest 103
Table 2-27 Set-up for *Pme*I linearisation 104
Table 2-28 Set-up for *Pac*I diagnostic digest 104
Table 2-29 Set-up for large scale *Pac*I linearisation 105
Table 2-30 Recipe for 0.7% (w/v) agarose gel 106
Table 2-31 De-phosphorylation of double-cut pSHUTTLE-CMV backbone 107
Table 2-32 Set-up for ligation reaction 108
Table 2-33 Virus dilution table 111
Table 2-34 Recipe for 10× TD buffer 115
Table 2-35 Recipe for 10× Tris-EDTA (TE) buffer 115
Table 2-36 1.25 g/mL CsCl solution 115

Table 2-37 1.34 g/mL CsCl solution 115
Table 2-38 1.40 g/mL CsCl solution 116
Table 2-39 scRNAseq medium composition 124
Table 2-40 Processing sequence for dewaxing and rehydrating sections for EdU Click-iT staining 134
Table 2-41 Recipe for 500 mL of 1× citric saline antigen retrieval buffer (pH 6) 134
Table 2-42 Composition of Click-iT reaction cocktail for approximately 50 slides. 135
Table 2-43 Processing sequence for dewaxing and rehydrating sections prior to H&E staining 137
Table 2-44 Processing sequence for staining sections with H&E..... 138
Table 2-45 Processing sequence for dewaxing and rehydrating sections prior to IHC staining 141
Table 2-46 Recipe for 1 L of 10× TBS buffer (pH 7.5) 141
Table 2-47 Recipe for 1 L of 10× TBS 0.5% (v/v) Tween buffer (pH 7.5) 142
Table 2-48 List of primary antibodies used for IHC. 143
Table 3-1 Murine vascular injury models 150
Table 6-1 GO enrichment terms for top 100 most DEGs within each cluster in untreated control primary HSVSMCs 315
Table 6-2 GO enrichment terms for top 100 most DEGs within each cluster in BMP-9-treated primary HSVSMCs..... 322
Table 6-3 GO enrichment terms for top 100 most DEGs within each cluster in TGF-β_1-treated primary HSVSMCs..... 329
Table 6-4 GO enrichment terms for top 100 most DEGs for clusters 0 to 5 in BMP-9 and TGF-β_1-co-treated primary HSVSMCs 341
Table 6-5 GO enrichment terms for top 100 most DEGs for clusters 6-8 in BMP-9 and TGF-β_1 co-treated primary HSVSMCs..... 342

List of abbreviations and definitions

α-SMA	alpha smooth muscle actin
ACVR2A	gene encoding activin A receptor type IIa
ACVR2B	gene encoding activin A receptor type IIb
ACVRL1	gene encoding activin receptor-like kinase 1
ADP	adenosine di-phosphate
AGTR1	gene encoding angiotensin II receptor type 1
AGTR2	gene encoding angiotensin II receptor type 2
ALK1	activin receptor-like kinase 1
ALPL	gene encoding alkaline phosphatase
AMP	adenosine monophosphate
AngII	angiotensin II
AT_1R	angiotensin II receptor type 1
AT_2R	angiotensin II receptor type 2
ATP	adenosine triphosphate
AVM	arteriovenous malformation
BCA	bicinchoninic acid
BHF	British Heart Foundation
BMI	body mass index
BMP-9	bone morphogenetic protein-9
BMPR2	gene encoding bone morphogenetic protein receptor 2
BMPR2	bone morphogenetic protein receptor 2
BRE	BMP responsive element
BSA	bovine serum albumin
CABG	coronary artery bypass grafting
CACNB2	calcium voltage-gated channel auxiliary subunit beta 2
CAD	coronary artery disease
CAR	coxsackie and adenovirus receptor
CCN2	gene encoding connective tissue growth factor
CCND1	gene encoding cyclin D1
CD	cluster of differentiation
CDK	cyclin-dependent kinase
CDKN1A	gene encoding cyclin-dependent kinase inhibitor 1a
CEPI	Coalition for Epidemic Preparedness Innovation
CHF	chronic heart failure
CKD	chronic kidney disease
CMV	cytomegalyvirus
CNN1	gene encoding calponin 1
COL	collagen
COMP	gene encoding cartilage oligomeric matrix protein
COVID	coronavirus disease
CPE	cytopathic effect

CT	cycle threshold
CTGF	connective tissue growth factor
DAG	diacylglycerol
DAMP	damage associated molecular pattern
DAPI	4′,6-diamidino-2-phenylindole
DEG	differentially regulated genes
DMEM	Dulbecco's modified Eagle Medium
DMSO	dimethyl sulfoxide
DNA	deoxyribonucleic acid
DPP4	gene encoding dipeptidyl peptidase-4
EC	endothelial cell
ECM	extracellular matrix
EDTA	ethylenediamine tetra acetic acid
EEL	external elastic lamina
EGF	epidermal growth factor
EGTA	ethylene glycol tetra acetic acid
ELK	ternary complex factor (transcription factor)
EMT	endothelial-to-mesenchymal transition
ENG	endoglin
ER	endoplasmic reticulum
ERK	extracellular signal-regulated kinase
ERS	European Respiratory Society
FCS	fetal calf serum
FDR	false discovery rate
FGF	fibroblast growth factor
GAPDH	Glyceraldehyde 3-phosphate dehydrogenase
GDF2	gene encoding growth differentiation factor-2 (BMP-9)
GFP	green fluorescent protein
GMP	good manufacturing practice
GO	gene ontology
GPCR	G protein-coupled receptor
GREM1	gene encoding gremlin-1
GTP	guanine tri-phosphate
HAdV-5	human adenovirus-5
HASMC	human aortic smooth muscle cell
HCASMC	human coronary artery smooth muscle cell
HEK293	human embryonic kidney cell 293
HELA	Henrietta Lacks cell
HEPES	N-2-hydroxyethylpiperazine-N-ethanesulfonic acid
HGF	hepatocyte growth factor
HHT	haemorrhagic telangiectasia
HIF1A	gene encoding hypoxia inducible factor 1-alpha
HIV	human immunodeficiency virus
HPAH	hereditary pulmonary arterial hypertension

HSV	human saphenous vein
HSVSMC	human saphenous vein smooth muscle cell
HVD	hereditary vascular disorder
ICAM	intercellular adhesion molecule
ID1	gene encoding inhibitor of differentiation-1
IEL	internal elastic lamina
IGF1	insulin-like growth factor-1
IHC	immunohistochemistry
IL	interleukin
IMA	internal mammary artery
IMAG	internal mammary artery graft
IMASMC	internal mammary artery smooth muscle cell
INHBA	inhihin A
IP3	inositol trisphosphate
IP3R	inositol trisphosphate receptor
ISR	in-stent restenosis
ITR	inverted terminal repeat
KAN	kanamycin
KLF	kruppel-like factor
LAD	left anterior descending coronary artery
LAP	latency-associated protein
LCAR	left carotid artery
LCX	left circumflex coronary artery
LDL	low density lipoprotein
LGALS3	gene encoding galectin-3
LLC	large latent complex
LPS	lipopolysaccharide
LTBP1	gene encoding latent transforming growth factor beta-binding protein 1
MADH1	gene encoding s-mothers against decapentaplegic 1
MAPK	mitogen-activated protein kinase
MAS1	gene encoding MAS proto-oncogen
MEK	mitogen-activated protein/extracellular signal-regulated kinase kinase
MERS	Middle Eastern Respiratory Syndrome
MHC	major histocompatibility complex
MI	myocardial infarction
MLC	myosin light chain
MLCK	myosin light chain kinase
MLCP	myosin light chain phosphate
MMP	matrix metalloprotein
MRTF	myocardin-related transcription factor
MYH11	gene encoding myosin heavy chain-11
MYOCD	myocardin
NADPH	Nicotinamide adenine dinucleotide phosphate
NF	neointima formation

NFAT	nuclear factor of activated T-cells
NICOR	The National Institute for Cardiovascular Outcomes Research
NO	nitric oxide
PAH	pulmonary arterial hypertension
PAI-1	plasminogen activator inhibitor-1
PASMC	pulmonary artery smooth muscle cell
PBS	phosphate-buffered saline
PCA	principal component analysis
PCI	percutaneous coronary intervention
PCNA	gene encoding proliferating cell nuclear antigen
PCR	polymerase chain reaction
PDGF	platelet-derived growth factor
PFA	paraformaldehyde
PFU	plaque forming unit
PIP2	phosphatidylinositol 4,5-bisphosphate
PKC	protein kinase C
PLC	phospholipase C
PPARG	gene encoding peroxisome proliferator-activated receptor gamma
QC	quality control
RASMC	rat aortic smooth muscle cell
RCAR	right carotid artery
RGD	Arg-Gly-Asp tri-peptide sequence
RIPA	radioimmunoprecipitation assay
RNA	ribonucleic acid
ROCK	RhoA/Rho kinase
ROS	reactive oxygen species
RQ	relative quantification
SARS	Severe Acute Respiratory Syndrome
SBE	SMAD-binding element
SCX	gene encoding scleraxis
SERCA2A	sarco/endoplasmic reticulum Ca^{2+}-ATPase
SERPINE1	gene encoding plasminogen activator inhibitor-1
SIRS	Severe Inflammatory Response Syndrome
SHRSP	Spontaneously Hypertensive Stroke-prone rat
SM22- α	smooth muscle cell protein 22-alpha
SMAD	s-mothers against decapentaplegic
SMC	smooth muscle cell
SMDS	smooth muscle differentiation supplement
SMGS	smooth muscle growth supplement
SNAI2	gene encoding snail family transcriptional repressor 2
SP7	gene encoding osterix
SRF	serum response factor
SVG	saphenous vein graft

SVM	starvation medium
T2DM	type 2 diabetes mellitus
TAGLN	gene encoding smooth muscle protein 22-alpha
TBE	tris-borate EDTA
TBS	tris-buffered saline
TCE	transforming growth factor-beta control element
TF	transcription factor
TGF-β_1	transforming growth factor-beta-1
TGFB1	gene encoding transforming growth factor beta-1
TGFBR1	gene encoding activin receptor-like kinase 5
TIMP	tissue inhibitor of metalloproteinases
TLR4	toll-like receptor 4
TNF-α	tumour necrosis factor-alpha
TPM1	gene encoding tropomyosin-1
UBC	gene encoding polyubiquitin-c
UMAP	uniform manifold approximation and projection
UMI	unique molecular identifier
VCAM	vascular adhesion molecule
VEGF	vascular endothelial growth factor
VGF	vein graft failure
VP	viral particle
vSMC	vascular smooth muscle
WKY	Wistar Kyoto rat

List of presentations, awards and publications

- Presentations:
    - Poster presentation at the Scottish Cardiovascular Forum 2017 in Glasgow (UK).
    - Poster presentation at the International Vascular Biology Meeting 2018 in Helsinki (Finland).
    - Planned poster presentation at the Single Cell Biology Meeting 2020 in Cambridge (UK) (meeting was cancelled due to the COVID-19 pandemic).
- Awards:
    - Graham Wilson Travelling Scholarship 2019 (University of Glasgow, UK).
- Publications:
    - J.T. Schwartze, E.L. Low, and A.C. Bradshaw, 2019, TGF-β in vascular pathobiology, in R. M. Touyz, and C. Delles, eds., Textbook of Vascular Medicine, Springer, p. 137-148, doi:10.1007/978-3-030-16481-2_13
    - E.L. Low, J. Schwartze, A. Kurkiewicz, M. Pek, D. Kelly, A. Shaw, M. Thorikay, J. McClure, M. McBride, S. Arias-Rivas, S. Francis, N. Morrell, C. Delles, P. Herzyk, M. Havenga, S. Nicklin, P.T. Dijke, A. Baker, and A.C. Bradshaw, 2019, Transforming growth factor-beta signaling via ALK1 and ALK5 regulates distinct functional pathways in vein graft intimal hyperplasia, biorxiv, doi: https://doi.org/10.1101/860320

Summary

Coronary artery bypass grafting (CABG) is a surgical technique utilised to bypass one or more stenosed coronary arteries to re-establish blood supply to cardiac tissue. The great saphenous vein of the leg remains the most used conduit for all non-left anterior descending (LAD) territories. Despite advances in surgical technique and optimised pharmacological treatment, approximately 50% of all saphenous vein grafts (SVGs) fail at 10 years following coronary implantation often requiring potentially life-threatening and costly re-interventions. Pathogenic drivers of SVG disease include early thrombosis, neointima formation (NF) and accelerated atherosclerosis. Together, these pathologies culminate in SVG obstruction, thromboembolism, aneurysm formation and haemorrhaging. The key driver of SVG disease is occluding NF which is defined as a continuous thickening of the inner most layer of the venous conduit which culminates in lumenal obstruction. Pre-clinical and clinical studies have demonstrated that de-differentiated smooth muscle cells (SMCs) are the main contributor to NF. This process is termed SMC phenotype switching which entails a loss in contractile properties and instead a gain in migratory and proliferative capacity. Targeting SMC phenotype switch-driven NF with specific pharmacological compounds and gene therapy remain important therapeutic strategies to prolong SVG patency following CABG surgery.

Transforming growth factor (TGF)-β_1 and bone morphogenetic protein (BMP)-9 are both pleiotropic growth factors which are members of TGF-β superfamily. Whereas TGF-β_1 may signal via the activin receptor-like kinase (ALK)5 or ALK1 receptors, BMP-9 mainly signals via the ALK1 receptor. Studies in small and large animal models have shown that TGF-β_1 is up-regulated following vein grafting. In contrast, BMP-9 has not yet been investigated in the context of vascular injury-driven NF. To date, the role of TGF-β_1 signalling in NF remains controversial. Our group has shown that TGF-β_1/ALK1 signalling drives SMC migration and that NF in ligation-injured carotid arteries is blunted in heterozygous *Smad1* knockout mice. Since BMP-9 signals via the ALK1 receptor, it may be speculated that this ligand acts as a pathogenic mediator of NF. Hence, the main aims of this PhD were to (i) determine the presence of BMP-9 and SMC phenotype switching in pre-implantation SVGs and murine vascular injury models, (ii) to evaluate ALK1

and ALK5-driven regulation of primary human saphenous vein (HSV) SMC phenotypes, (iii) to characterise single HSVSMC transcriptomes following BMP-9 and/or TGF-β_1 treatment and to (iv) develop a replication-deficient human adenovirus serotype 5 vector (HAdV-5) expressing the activin/BMP receptor activin A receptor type IIa (ACVR2A).

Immunohistochemistry (IHC) demonstrated that BMP-9 was present in human pre-implantation SVGs and murine carotid arteries. Moreover, intimal SVG SMCs displayed a decrease in myosin heavy chain (MYH)11 and a trend towards a decrease in calponin expression compared to medial SMCs, suggesting *in vivo* SMC phenotype switching. In addition, carotid artery wire injury in mice triggered a trend towards an increase in total vascular BMP-9 levels, which was paralleled by SMC phenotype switching, indicating a potential role for BMP-9 in NF. Together, these results prompted an observational multiple timepoint carotid artery ligation study in mice which aimed to link BMP-9 presence with vascular injury responses. Carotid ligation triggered intimal and medial SMC proliferation which was paralleled by a loss of SMC α-smooth muscle actin (SMA) indicating SMC phenotype switching. Due to the COVID-19 pandemic and subsequent lab closure, BMP-9 staining could not be completed. A crosslinking study revealed that recombinant human (rh) BMP-9 bound to ALK1, ALK2, bone morphogenetic protein receptor (BMPR)2, ACVR2A/B and endoglin on primary HSVSMCs. Functionally, BMP-9-treated HSVSMCs displayed a time-dependent increase in s-mothers against decapentaplegic (SMAD)1 phosphorylation paralleled by an increase in *ID1* (encodes inhibitor of differentiation-1) mRNA expression levels indicating that BMP-9 activates the SMAD1 pathway in this cell type.

The observation of *in vivo* SMC phenotype switching in pre-implantation SVGs prompted development and generation of a ligand-independent contractile differentiation protocol for primary HSVSMCs and primary human coronary artery (HCA) SMCs. This enabled investigation of functional ALK1 and ALK5 signalling during contractile SMC differentiation. In parallel, the direct, ligand-mediated effect of TGF-β_1 and BMP-9 on primary HSVSMCs was studied. Immunoblot, quantitative real-time polymerase chain reaction (qRT-PCR) and BrdU proliferation assays demonstrated that smooth muscle differentiation

supplement (SMDS)-treated HSVSMCs displayed an accumulation of contractile SMC markers which was paralleled by a decrease in proliferation. These observations indicated the presence of a contractile HSVSMC phenotype. ALK1 target gene *ID1* mRNA expression levels were suppressed in SMDS-treated HSVSMCs indicating dampened ALK1 pathway activity during contractile differentiation. Moreover, SMDS treatment induced the expression of mRNA for the activin/BMP receptor *ACVR2A* in HSVSMCs suggesting a potential role for *ACVR2A* during contractile differentiation. Similar observations were made in HCASMCs. This prompted development and generation of a replication-deficient HAdV-5 expressing the *ACVR2A* transgene. HAdV-5-mediated delivery of *ACVR2A* to primary HSVSMCs was successful. However, increased *ACVR2A* expression had no effect on α*SMA* mRNA levels in 15% fetal calf serum (FCS)- or SMDS-treated HSVSMCs. Pharmacological ALK5 inhibition prevented contractile differentiation in SMDS-treated HSVSMCs. In contrast, pharmacological ALK1 inhibition had no effect on the induction of contractile gene expression. In line with these findings, TGF-β_1 drove contractile gene expression in an ALK5-dependent manner and suppressed serum-induced HSVSMC proliferation and migration. BMP-9 had no effect on TGF-β_1/ALK5-driven contractile gene expression.

These findings led to an investigation into the impact of BMP-9 and/or TGF-β_1 stimulation on angiotensin (Ang)II-dependent intracellular Ca^{2+} mobilisation, which served as an upstream surrogate marker of SMC contraction. Following development of a robust fluorescence-based Ca^{2+} handling protocol, it was observed that TGF-β_1-treated HSVSMCs displayed an increase in AngII-driven intracellular Ca^{2+} mobilisation in an ALK5-dependent manner, indicating an increase in contractile potential. In contrast, BMP-9 blunted this effect indicating ALK5 antagonism and/or differential utilisation of intracellular Ca^{2+}. Opposed to findings in primary HSVSMCs, TGF-β_1 had no effect on AngII-dependent Ca^{2+} release in primary HCASMCs indicating differential regulation of Ca^{2+} handling in this cell type. Single cell (sc) region of interest (ROI) analysis revealed heterogeneous Ca^{2+} transient responses in HSVSMC populations independent of ligand treatment. However, TGF-β_1-treated HSVSMC populations demonstrated a trend towards a reduction in non-responding cells and instead an increase in cells responding with higher fluorescence intensities indicating a more homogeneous intracellular Ca^{2+} release response. TGF-β_1-induced

homogeneity was reversed in the presence of BMP-9 paralleling whole ROI findings.

Since primary HSVSMCs displayed heterogeneous Ca^{2+} transient responses, influenced by TGF-β_1 and BMP-9, the next aim was to evaluate potential transcriptome heterogeneity in BMP-9 and/or TGF-β_1-treated HSVSMCs using the 10x Chromium microfluidics-based scRNA sequencing (seq) platform. Combined uniform manifold approximation and projection (UMAP)/Louvain clustering uncovered transcriptional heterogeneity in untreated and ligand treated HSVSMCs potentially reflecting a heterogeneous composition of SMC sub-lineages within pre-implantation SVG media. Both BMP-9 and TGF-β_1 drove target gene expression demonstrating functional ALK5 and ALK1/ALK2 pathway activation. Principal component analysis (PCA) showed greater spatial distances between TGF-β_1 and BMP-9-treated HSVSMCs suggesting that TGF-β_1 triggered greater transcriptional activation compared to BMP-9. Within BMP-9 treated HSVSMCs, combined RNA velocity and gene ontology (GO) analysis revealed a potential osteogenic HSVSMC sub-lineage. Finally, GO identified potentially contractile and pro-fibrotic sub-lineages within TGF-β_1-treated HSVSMCs.

In conclusion, the TGF-β_1/ALK5 pathway positively regulates the contractile HSVSMC phenotype. In contrast, BMP-9 drives *ID1* expression and blunts TGF-β_1/ALK5-driven AngII-dependent Ca^{2+} responses via ALK1 and/or ALK2 indicating partial ALK5 antagonism. Together, these data suggest that ALK5 agonism/ALK1 antagonism may protect HSVSMCs from phenotype switching and dampen NF in the context of SVG disease.

Chapter 1 Introduction

1.1 Coronary artery disease

Coronary artery disease (CAD) is caused by thickening of the innermost vessel layer (intima) or neointima formation (NF), intimal lipid deposition/plaque formation and stiffening of the middle vessel layer (media) which culminates in lumenal narrowing and/or thrombosis (Kumar et al., 2007) (Figure 1-1). This results in reduced blood flow and insufficient oxygen/nutrient supply of cardiac tissue. Clinical complications include angina pectoralis, myocardial infarction (MI), cardiac arrhythmias and chronic heart failure (CHF) (Cassar et al., 2009). Classic risk factors for developing CAD include age, obesity, type 2 diabetes (T2DM), systemic hypertension, dyslipidaemias and chronic kidney disease (CKD) (Kumar et al., 2007). To date, CAD is the leading cause of death worldwide, entails substantial personal/socioeconomic burden and affects approximately 3.5% of the UK population (Bhatnagar et al., 2015; Collaborators, 2015). CAD management includes life-style modification, drug treatment and revascularisation therapies including non-invasive percutaneous coronary intervention (PCI) and invasive coronary artery bypass graft (CABG) surgery (Neumann et al., 2019).

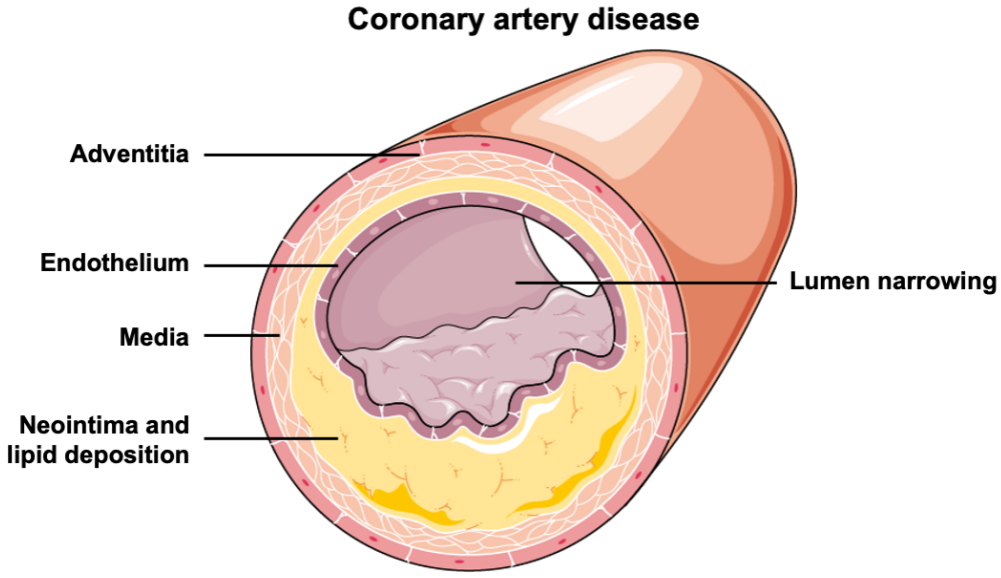

Figure 1-1 Schematic cross-sectional representation of a narrowed coronary artery. The coronary artery wall is made up of three distinct layers (starting from the inner most layer: intima, media and adventitia). Continuous intimal thickening drives lipid deposition and plaque formation in CAD (Nakashima et al., 2007). This results in lumenal obstruction and impedes coronary blood flow to cardiac tissue. Image taken and adapted from Servier Medical Art (CREATIVE COMMONS LICENCE).

1.2 Coronary artery bypass graft surgery

CABG is a surgical technique which utilises the internal mammary artery (IMA), the radial artery (RA) or the great saphenous vein (SV) of the leg to bypass one or more critically occluded coronary arteries (Harris et al., 2013) (Figure 1-2). Following European and US guidelines CABG surgery is the gold standard for the treatment of patients with multivessel CAD and left anterior descending (LAD) CAD (Fihn et al., 2014; Neumann et al., 2019). Overall, 14,527 CABG surgeries were performed in the UK between 2017 and 2018 highlighting the medical and socioeconomic importance of this operation (NICOR, 2019).

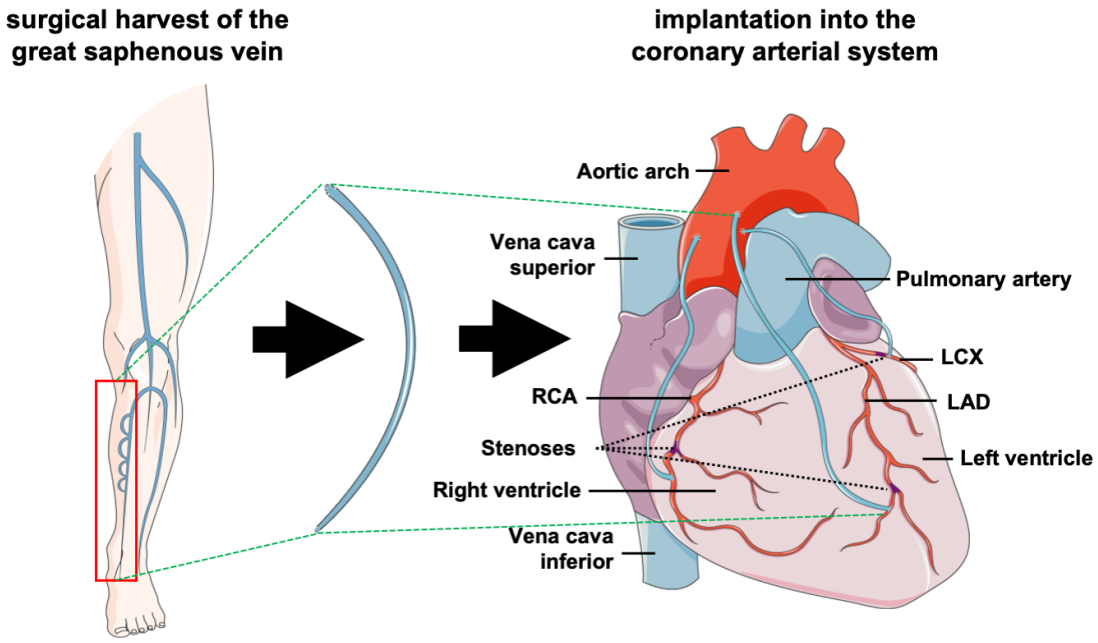

Figure 1-2 Schematic representation of coronary artery bypass graft surgery using the great saphenous vein. In brief, CABG involves performing sternotomy to gain access to the heart (Harris et al., 2013). The great SV, IMA or RA are harvested and placed into a sterile preservation solution. These conduits are engrafted to bypass critically stenosed coronary arteries thereby restoring cardiac blood supply. Abbreviations: RCA, right coronary artery; LCX, left circumflex artery; LAD, left anterior descending artery. Images taken and adapted from Servier Medical Art (CREATIVE COMMONS LICENCE).

1.2.1 Saphenous vein graft versus internal mammary artery graft

The IMA and great SV are both composed of three distinct layers: the intima, media and adventitia (Canham et al., 1997). Cross-sectional schematic representations are presented in Figure 1-3. Despite the same basic structure, the two vessels display substantial histological differences due to distinct functions within the cardiovascular system (Canham et al., 1997) (Table 1-1).

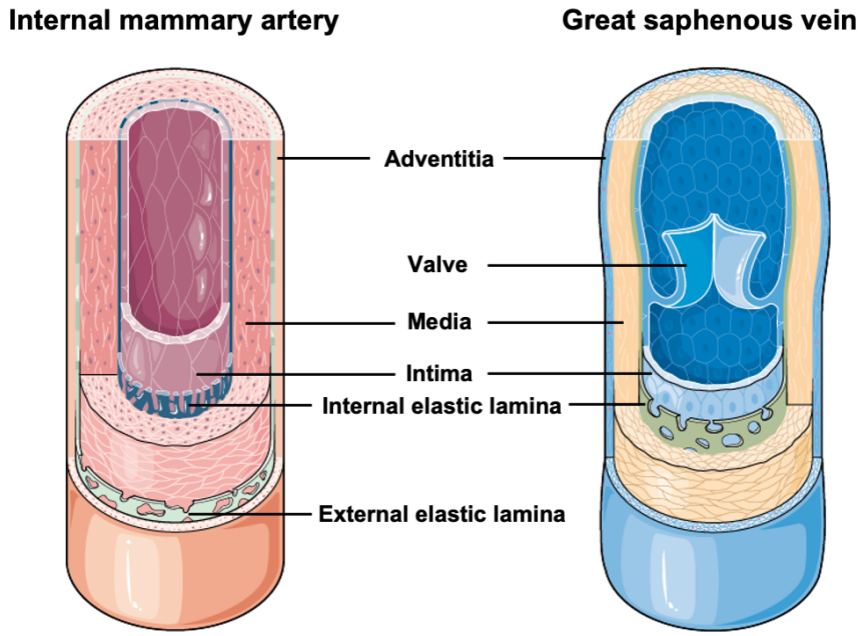

Figure 1-3 Cross-sectional schematic representation of Internal mammary artery versus great saphenous vein histology. (Left image) IMA: the intima consists of a single ellipsoidal EC layer and thin sub-endothelium. The intima separates the vessel lumen from the vessel wall. Continuous and well-defined internal elastic lamina (IEL) separates intima from media. Depending on anatomic location, IMA media is composed of several distinguishable elastic laminae and interspersed SMCs (proximal and distal segments) or mainly elastic laminae (middle segment). A well-defined continuous external elastic lamina (EEL) separates media from adventitia. IMA adventitia contains few vasa vasorum. (Right image) Great SV. The intima consists of a single layer of short and wide ECs and sub-endothelium. Valves project into the SV lumen guiding blood flow towards the upper torso. A poorly developed IEL separates the intima from the media. The media is thinner compared to IMA media and contains an inner layer of longitudinally orientated SMCs and an outer layer of circumferentially orientated SMCs. The EEL is absent. The adventitia contains longitudinally orientated collagen fibres, fibroblasts, few longitudinally orientated SMCs and vasa vasorum. Compared to the IMA, SV adventitia constitutes most of the wall thickness. Images taken and adapted from Servier Medical Art (CREATIVE COMMONS LICENCE).

Table 1-1 List of histological differences between the internal mammary artery and great saphenous vein.

Parameter	Internal mammary artery	Great saphenous vein
Anatomy	• Chest • Originates from subclavian artery • Guides blood towards musculophrenic and superior epigastric arteries	• Lower limb • Guides blood flow towards torso
Intravascular flow and pressure	• High	• Low
Intima	• Single lumenal endothelial layer and sub-endothelium • Ellipsoidal ECs, alignment in direction of blood flow • Continuous and well-defined IEL and EEL • Distinguishable elastic lamellae	• Single lumenal endothelial layer and sub-endothelium • Valves projecting into lumen, guide blood flow towards torso • Short and wide ECs • Poorly developed IEL • Undistinguishable elastic lamellae
Media	• Thin, thicker compared to SV • Proximal: elasto-muscular (elastic laminae and SMCs) • Transitions to predominantly elastic in nature with few SMCs • Distal: elasto-muscular	• Thinner compared to IMA • Inner media: longitudinally orientated SMCs • Outer media: circumferentially orientated SMCs
Adventitia	• Longitudinally orientated collagen fibres • Few vasa vasorum • Constitutes approximately half of wall thickness	• Longitudinally orientated collagen fibres with interspersed longitudinally orientated SMCs • Fibroblasts and vasa vasorum • Constitutes majority of wall thickness
References: (Canham et al., 1997; dela Paz and D'Amore, 2009; Elsharawy et al., 2007; Galili et al., 2004; Sisto et al., 1990; van Son et al., 1993; van Son et al., 1990)		

Due to its elasto-muscular nature, long-standing adaptation to the arterial high pressure/high flow environment and relative protection from developing atherosclerosis the IMA graft (IMAG) displays a higher patency rate compared to the SVG (Gaudino et al., 2019).

However, the SVG remains the most utilised graft for all non-LAD territories (80-90% of all patients) (Caliskan et al., 2020). SVGs display several advantages when compared to arterial grafts. They are easily harvested, readily available in most patients, easier to handle when performing anastomoses, display absence of vasospasm following coronary implantation and reduce the risk of sternal infection following the CABG procedure (De Vries et al., 2016). SVGs are preferable for patients with poor distal targets, for patients who may benefit from higher initial blood flow in SVGs and for patients who require redo surgery following failure of an arterial conduit (Anyanwu and Adams, 2018). Furthermore, SVGs harvested with "no-touch technique" demonstrated improved patency rates compared to SVGs harvested with the conventional technique (Samano et al., 2015). The same study revealed that patency rates achieved in SVGs harvested with the "no-touch technique" were comparable to IMAG patency rates at 16 years follow up. Taken together, SVGs are and will remain a crucial repertoire for CABG surgery.

1.3 Saphenous vein graft disease

Early thrombosis (Grondin et al., 1974), occlusive intimal thickening or NF (Kockx et al., 1996) and accelerated atherosclerosis (Bulkley and Hutchins, 1977) drive SVG disease and contribute to SVG failure. To date, 10-15% of SVGs fail within the first year rising to approximately 50% at 10 years following CABG surgery (Harskamp et al., 2013). A schematic representation of SVG disease pathology is shown in Figure 1-4 and a chronological order of key pathophysiological features is provided in Table 1-2.

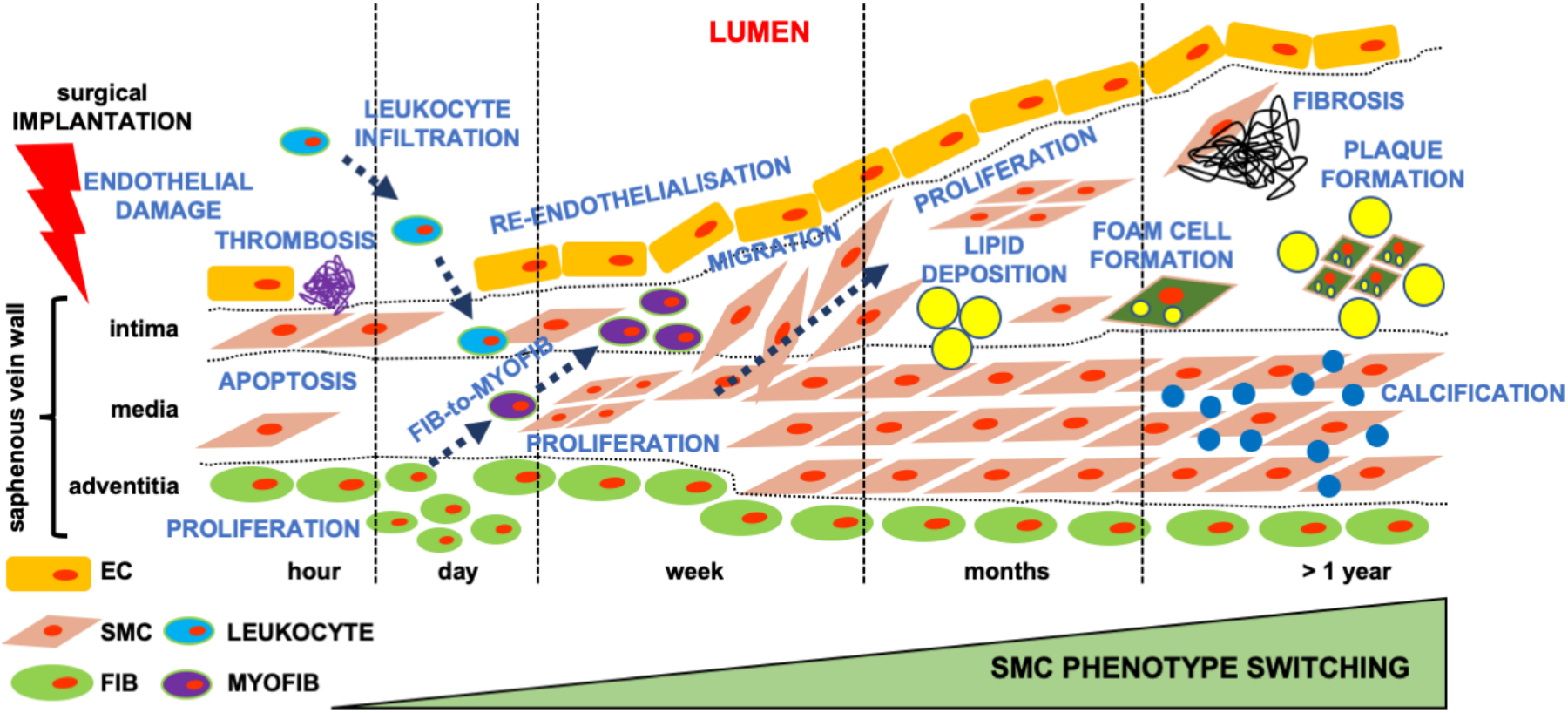

Figure 1-4 Saphenous vein graft disease pathology following CABG surgery. Following implantation into the coronary arterial system, SVG endothelium is subjected to increased blood flow and pressure culminating in endothelial denudation, local thrombus formation and leukocyte infiltration into the SVG wall (Sasaki et al., 2000). In addition to triggering re-endothelialisation (Shiokawa et al., 1989), SVG injury drives early medial SMC apoptosis (Rodriguez et al., 2000), medial SMC phenotype switching (Kockx et al., 1992) and fibroblast-to-myofibroblast differentiation (Kalra and Miller, 2000; Shi et al., 1997) orchestrating occlusive NF and medial thickening. Together, these biological changes drive accelerated neointimal atherosclerosis (Bulkley and Hutchins, 1977), neointimal fibrosis (Unni et al., 1974; Vlodaver and Edwards, 1971) and medial calcification (Pedigo et al., 2017). Late complications of SVG disease include NF-driven lumenal narrowing (Kockx et al., 1996), plaque rupture/thrombosis (Walts et al., 1982) and aneurysm formation/haemorrhaging (Neitzel et al., 1986). Abbreviations: EC, endothelial cell; SMC, smooth muscle cell; FIB, fibroblast; MYOFIB, myofibroblast.

Table 1-2 Summary of key pathophysiological features of SVG disease following CABG surgery.

Stages	Key pathophysiological features	Key molecular and cellular responses	Clinical therapies
Saphenous vein harvest	• Surgical handling during harvest • Dilatation during leakage check • Ischaemia	• EC apoptosis/necrosis	• No-touch harvesting technique
Saphenous vein engraftment	• Reperfusion → longitudinal and circumferential shear stress	• EC apoptosis/necrosis • Local thrombosis • Inflammatory cell infiltration and initiation of inflammatory signalling	• Single and dual anti-platelet drug therapy
Early stage (<1 month)	• Thrombus formation • Initiation of NF	• Platelet aggregation • SMC phenotype switching	• Single (Aspirin) and dual anti-platelet (Aspirin + Clopidogrel) drug therapy
Intermediate stage (1 month to 1 year)	• Continuous neointimal expansion • Outward remodelling → media thickening	• EndMT • Fibroblast-to-myofibroblast differentiation • Fibrotic remodelling of neointima • Neointimal lipid retention and foam cell formation	• LDL lowering drug therapy
Late stage (>1 year)	• Calcification • Accelerated atherosclerosis and lumenal occlusion • Necrotic core formation, intraplaque haemorrhage, plaque rupture and thromboembolism • Aneurysm formation	• Osteoblastic SMC de-differentiation • Neointimal foam cell and SMC apoptosis	• Thrombectomy • Repeat CABG surgery • PCI with or without balloon angioplasty

Surgical and pharmacological strategies for tackling SVG disease focus on preserving endothelial function, early/late thrombosis and accelerated atherosclerosis. The surgical “no-touch technique” preserves SVG endothelium during harvesting (Souza et al., 1999), improves SVG tension development and contractility (Vestergaard et al., 2017) and improves overall SVG patency at 16-years follow up (Samano et al., 2015). Single anti-platelet therapy (aspirin) (Goldman et al., 1989), dual anti-platelet therapy (aspirin and clopidogrel) following off-pump CABG surgery (Deo et al., 2013) and lipid-lowering (Kulik et al., 2011) drug therapies reduce SVG thrombosis and atherosclerosis rates, respectively.

Leading complications of late SVG disease culminating in graft failure include NF-driven lumenal obstruction (Kockx et al., 1996), atherosclerotic plaque rupture resulting in thromboembolism (Walts et al., 1982) and aneurysm formation pre-disposing to haemorrhaging (Neitzel et al., 1986). Treatment strategies for late SVG complications are potentially life-threatening and include thrombectomy (Kuntz et al., 2002), repeat CABG surgery (Locker et al., 2019) and percutaneous stent implantation with or without balloon angioplasty (Latif et al., 2020).

1.3.1 Neointima formation

Occlusive intimal thickening or NF is a key pathological feature of SVG disease (Kockx et al., 1996) (Figure 1-4). Evidence obtained from human SVGs (Kockx et al., 1992) and experimental murine vein graft injury studies (Wu et al., 2020; Zou et al., 1998) demonstrated that SMCs were the main contributors of SVG NF. In large vessels, quiescent SMCs within the media provide structural support and regulate vascular tone, pressure and blood flow via contraction and relaxation (Rensen et al., 2007). Quiescent or contractile vascular (v)SMCs express high levels of contractile proteins such as α-smooth muscle actin (SMA), calponin, smooth muscle protein (SM)22-α and myosin heavy chain (MYH)11 (Chen et al., 2016b; Han et al., 2009). Following vascular injury, vSMCs de-differentiate triggering vascular repair and NF. This process is known as ‘phenotype switching’ and entails loss of contractile protein expression, a universally accepted indicator of SMC de-differentiation (Frismantiene et al., 2018) and instead a gain in proliferative, migratory and extracellular matrix (ECM) synthesis capabilities

(Chen et al., 2016b; Kumar and Lindner, 1997; Liao et al., 2016; Yu et al., 2011) (Figure 1-4).

1.3.1.1 Local thrombosis and Inflammation

Surgical handling as well as an increase in blood pressure and blood flow within the coronary arterial system damage the inner lining of SVGs following implantation and culminate in EC denudation. SVG endothelium breakdown triggers local platelet aggregation/thrombus formation and allows leukocytes and erythrocytes to infiltrate SVG intima (Hoch et al., 1994; Sasaki et al., 2000) (Figure 1-4). Pre-clinical *in vivo* vein graft models have shown that these two pathophysiological processes result in the local production and release of growth factors and pro-inflammatory cytokines (Francis et al., 1994; Li et al., 2014; Sterpetti et al., 1998). These factors include but are not limited to transforming growth factor (TGF)-β_1, platelet-derived growth factor (PDGF), fibroblast growth factor (FGF), interleukin (IL)-1 and tumor necrosis factor (TNF)-α. These powerful factors orchestrate complex downstream cellular signalling events which trigger initiation of SVG wall remodelling following coronary implantation. Although these events are important for adaptive SVG remodelling, pre-clinical studies have demonstrated that TGF-β_1 (Wolff et al., 2006), PDGF (Hu et al., 1999), FGF (Dol-Gleizes et al., 2013), IL-1β (Li et al., 2014) and TNF-α (Zhang et al., 2004) drive 'SMC phenotype switching' and vein graft NF.

1.3.1.2 Regulation of vSMC quiescence

Experimental *in vivo* studies and histological evidence from occluded human SVGs demonstrates that vascular injury triggers SMC phenotype switching which in turn drives NF (Chappell et al., 2016; Chen et al., 2016b; Kockx et al., 1992) (Figure 1-4). In uninjured vessels, vSMCs maintain a quiescent state which enables regulation of vascular tone and blood flow. Transitioning of vSMCs from a quiescent/differentiated state to a de-differentiated state is a tightly regulated molecular process and forms the basis for 'SMC phenotype switching'.

The transcription factors serum response factor (SRF) and myocardin (MYOCD) jointly regulate contractile gene expression in vSMCs (Du et al., 2003; Rensen et al., 2006; Yoshida et al., 2003) (Figure 1-5). SRF binds to a 10-base pair CArG-

box sequence (CC[A/T]6CC) which is predominantly found in muscle and cytoskeletal genes (McDonald et al., 2006; Minty and Kedes, 1986; Strobeck et al., 2001). In contractile vSMCs the transcription factor MYOCD forms a complex with SRF and the CArG sequence thereby selectively driving *αSMA*, *SM22-α*, *CNN1* and *MYH11* gene expression subsequently maintaining the contractile phenotype (Du et al., 2003; Rensen et al., 2006; Yoshida et al., 2003) (Figure 1-5 left panel). In experimental vascular injury in mice, adenoviral (AdV)-mediated delivery of *myocd* reduced NF by dampening SMC migration and proliferation (Talasila et al., 2013). The same study demonstrated that heterozygous *Myocd*-deficient mice displayed enhanced NF and SMC de-differentiation following vascular injury, highlighting the ability of Myocd to prevent SMC de-differentiation and NF.

Several transcription factors may act as downstream regulators of vSMC de-differentiation (Frismantiene et al., 2018) (Figure 1-5 right panel). Upon activation, Krüppel-like factor (KLF)4 translocates to the nucleus where it disrupts the CArG-SRF-MYOCD complex and binds to G/C repressor elements which results in loss of contractile gene expression in vSMCs (McDonald et al., 2006; Salmon et al., 2012). Importantly, PDGF-BB, a strong regulator of SMC de-differentiation and proliferation, drives KLF4 expression in SMCs thereby preventing CArG-SRF-MYOCD complex formation and repressing contractile gene expression (Liu et al., 2005a). Furthermore, experimental vascular injury triggers up-regulation and nuclear translocation of forkhead box protein (FOX)O4 in SMCs enabling binding to MYOCD thereby disrupting the CArG-SRF-MYOCD complex and promoting SMC proliferation (Liu et al., 2005b). In line with these findings, genetic ablation of *Foxo4* in mice prevented NF following vascular injury (Li et al., 2007). The same study demonstrated that siRNA-mediated inhibition of *foxo4* prevented SMC migration highlighting this transcription factor as a driver of SMC de-differentiation. Moreover, ETS-like protein (ELK)-1 is a negative regulator of the CArG-SRF-MYOCD complex (Wang et al., 2004).

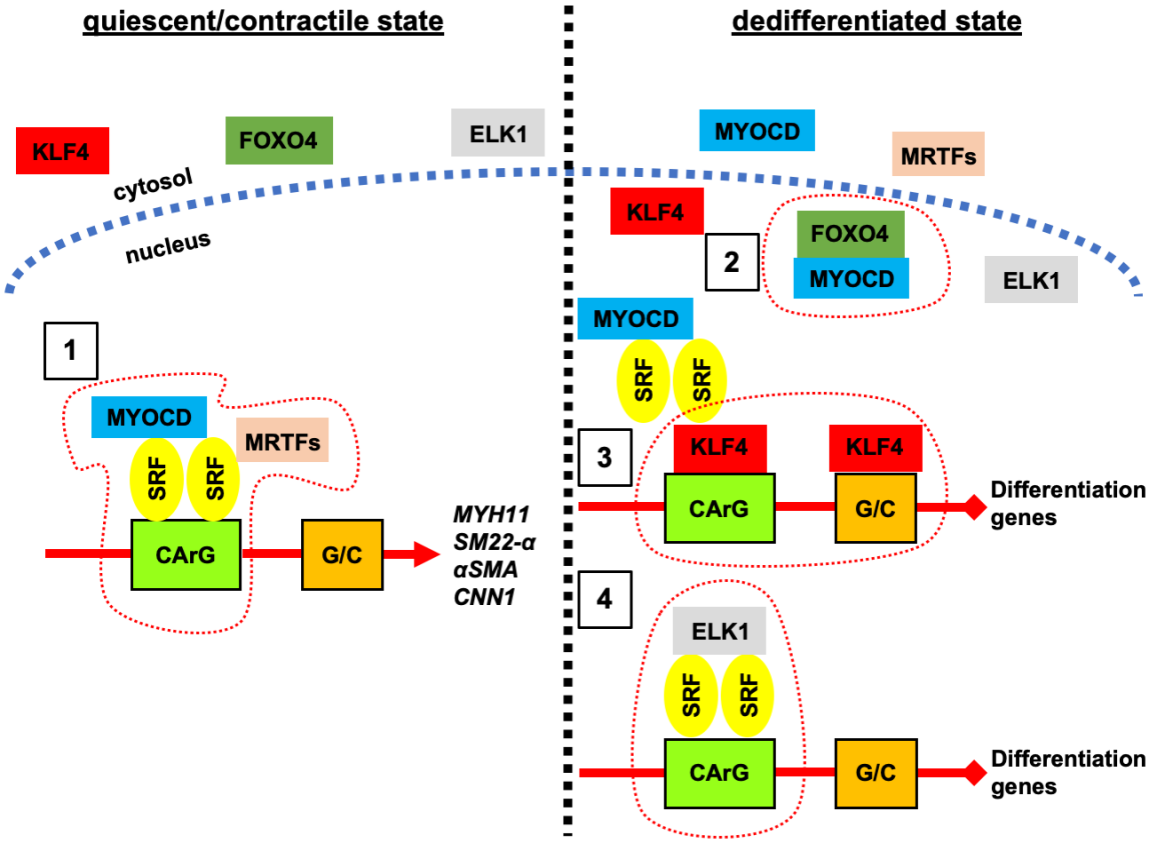

Figure 1-5 Schematic representation of contractile gene expression regulation in vSMCs. (**1**) Myocardin (MYOCD) and/or myocardin-related transcription factors (MRTFs) together with serum response factor (SRF) form a complex with the CArG box sequence positively regulating the contractile SMC phenotype. (**2**) The forkhead box protein (FOX)O4 translocates to the nucleus and binds MYOCD disrupting the MYOCD-SRF-CArG complex. (**3**) Krüppel-like factor (KLF)4 translocates to the nucleus and binds to the CArG box sequence and G/C repressor elements thereby negatively regulating contractile gene expression. (**4**) ETS-like protein (ELK)-1 competes with MYOCD for complex formation with SRF-CArG negatively regulating contractile gene expression. Image taken and modified from Frismantiene *et al.* (Frismantiene et al., 2018).

1.3.1.3 Regulation of vSMC proliferation

Upon vascular injury, pro-proliferative pathways suppress CArG-SRF-MYOCD complex formation in vSMCs which culminates in a reduction of contractile gene expression and enables SMCs to enter the cell cycle and proliferate (Liu et al., 2005b) (Figure 1-6). Experimental murine vascular injury models which recapitulate vSMC de-differentiation and NF are presented and discussed in more detail in section 3.1.1.

Cyclins, cyclin-dependent kinases (CDKs) and cyclin-dependent inhibitors (CKIs) regulate the different phases of the cell cycle (Lim and Kaldis, 2013) (Figure 1-6). Whereas cyclins activate a partner CDK (Andrews and Measday, 1998), CKIs deactivate CDKs (Dai and Grant, 2003). Cyclin/CDK complexes drive vSMC proliferation (Qin et al., 2014) and CKIs inhibit vSMC proliferation (Lee and Kang, 2019). Moreover, upstream growth factor signalling pathways regulate downstream cyclin, CDK and CKI activity and subsequent vSMC proliferation (Weber et al., 1997). Cyclin A, cyclin B, cyclin C, cyclin D and cyclin E form the cyclin family (reviewed in) (Ding et al., 2020). Levels of cyclins D, E, A and B differ substantially during the different cell cycle stages and are associated with specific sets of CDKs (Figure 1-6).

PDGF is a potent inducer of vSMC proliferation (Mii et al., 1993) which is locally released following vascular injury (Caplice et al., 1997) and promotes NF (Ferns et al., 1991). As well as disrupting the CArG-SRF-MYOCD complex by triggering p-ELK1-SRF-CArG complex formation (Wang et al., 2004) (Figure 1-5 right panel), PDGF-BB drives vSMC proliferation via mitogen activated protein kinase kinase (MEK)/extracellular regulatory kinase (ERK)1 and MAPK14 activation (Wu et al., 2019; Zhao et al., 2011). Weber and colleagues demonstrated that sustained PDGF-induced ERK1 activation in fibroblasts drove continued cyclin D1 (CCND1) expression thereby supporting G1 progression and cell proliferation (Weber et al., 1997). Similar observations were made in rat aortic SMCs (Izzard et al., 2002) revealing a clear PDGF-driven proliferative signalling axis. This has led to the development of treatment strategies to inhibit vSMC proliferation in SVGs, aiming to dampen NF following coronary implantation.

The transcription factor (TF) E2F activates pro-proliferative factors including but not limited to CDK2 (Furukawa et al., 1994) and PCNA (proliferating cell nuclear antigen) (Yamaguchi et al., 1995). Edifoligide is an oligodeoxynucleotide decoy which binds the E2F-binding protein and, hence, blocks E2F-mediated activation of pro-proliferative factors (Morishita et al., 1995). Moreover, edifoligide prevented vSMC proliferation and NF following experimental vein graft inter-positioning in rabbits (Ehsan et al., 2001). However, despite promising pre-clinical results the Project of Ex-Vivo Vein Graft Engineering via Transfection (PREVENT)IV trial which included 3014 CABG patients did not show a beneficial effect of *ex vivo* SVG edifoligide treatment on restenosis rates at early time points (12 to 18 months) (Alexander et al., 2005) and at 5 years (Lopes et al., 2012).

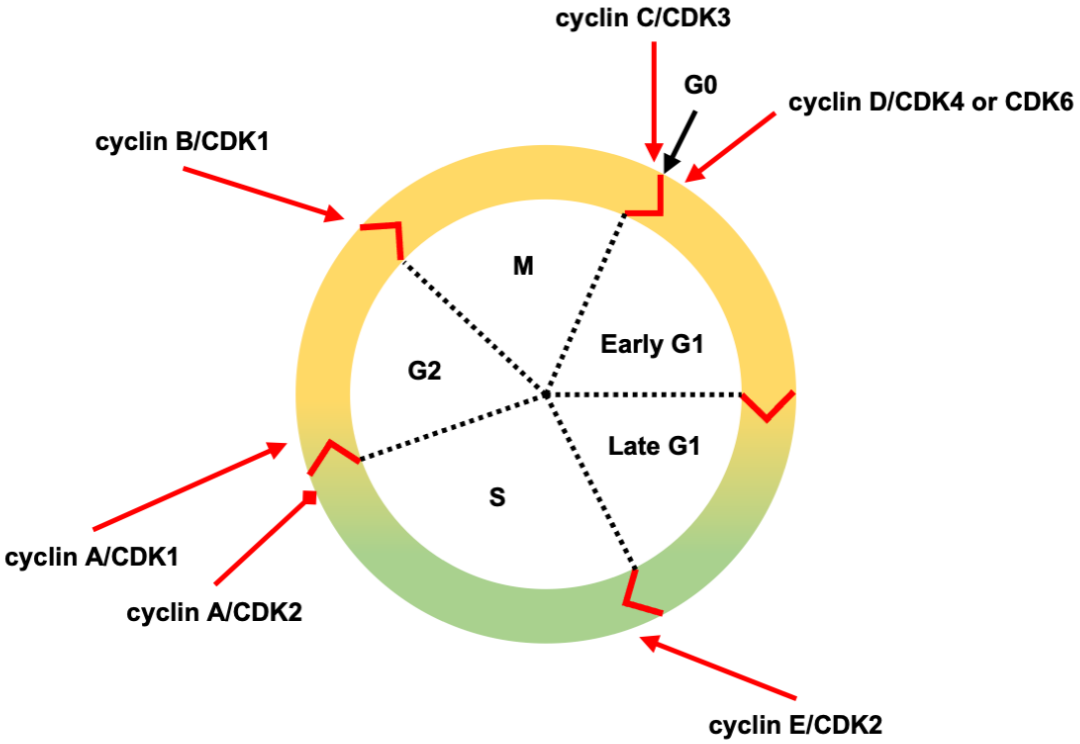

Figure 1-6 Schematic representation of the cell cycle. The cyclin C/CDK3 complex regulates the quiescent state or gap (G)0 phase. Pro-mitogenic pathways drive cyclin D/CDK4/6 complex formation which promotes entry into the G1 phase (Chung et al., 2004; Ding et al., 2020). During the G1 phase the cell commits to cell division (reviewed in) (Tan et al., 2017). The cyclin E/CDK2 complex progresses the cell into the synthesis (S) phase which is characterised by DNA replication. The cyclin A/CDK2 complex terminates the S phase. Cyclin A then forms a complex with CDK1 which allows the cell to enter the G2 phase which enables the cell to check for any DNA damage prior to cell division. During the mitosis (M) phase, CDK1 activity is maintained by forming a complex with cyclin B allowing the cell to divide into two daughter cells. Together, the G1, S and G2 phases form the interphase.

1.3.1.4 Regulation of SMC migration

Extensive SMC migration from the media to the intima is observed in SVGs within the first 24-h following CABG surgery (Kockx et al., 1992). The same study demonstrated a reduction in αSMA expression by medial SMCs within SVGs revealing the presence of non-quiescent SMC phenotypes. This indicates that vSMCs must enter the cell cycle (Figure 1-6) to migrate. Indeed, Fukui *et al*. showed that vSMCs achieved maximum migration capacity during the late G1 phase following PDGF-BB stimulation (Fukui et al., 2000). In line with these *in vitro* findings, Chappell and colleagues demonstrated that medial SMC proliferation precedes medial SMC migration towards the intima following arterial injury in mice (Chappell et al., 2016) (Figure 1-4). A vein graft study in rats demonstrated that vein graft IEL degrades rapidly as a consequence of haemodynamic changes (Chang et al., 2009) potentially enabling an increase of SMC migration from the media to the intima.

Mitogen-dependent stimulation of cell surface receptors and intracellular signal transduction initiate vSMC migration (Fukui et al., 2000; Grosskreutz et al., 1999). Activation of upstream pro-migratory signalling pathways orchestrates remodelling events which alter the structure of the cytoskeleton (reviewed in) (Gerthoffer, 2007) (Figure 1-7). Together, these remodelling events enable protrusion of the leading edge of the cell followed by detachment of focal contacts at the trailing edge propelling the cell towards a chemotactic stimulus.

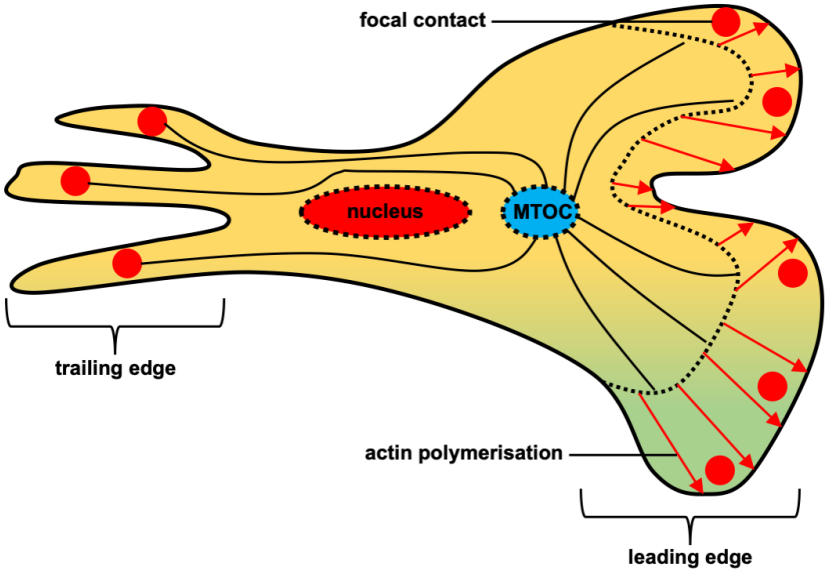

Figure 1-7 Schematic representation of vSMC migration. Mitogen-dependent activation of pro-migratory signalling pathways trigger vSMC migration (Fukui et al., 2000; Grosskreutz et al., 1999; Pickering et al., 1997). Activation of pro-migratory pathways initiates filopodial formation at the leading edge of the migrating cell (Wang et al., 2009). Actin polymerisation at the leading edge of the cell enables lamellipodial formation (protrusion) (Cleary et al., 2014) followed by generation of focal adhesion contacts between the vSMC and ECM (Kohno et al., 2013). This is followed by disassembly of focal adhesion contacts at the trailing edge of the cell (Palecek et al., 1998). Actomyosin-driven contraction exceeds adhesiveness at the trailing edge pulling the cell forward (reviewed in) (Afewerki et al., 2019). Microtubules radiate from the microtubule-organising centre (MTOC) towards the leading and trailing edge of the cell. Image taken and modified from Gerthoffer (Gerthoffer, 2007).

1.3.1.5 Neointimal fibrosis

Histopathological analysis of occluded human SVGs demonstrated marked intimal thickening and fibrosis (Vlodaver and Edwards, 1971). Importantly, electron microscopic examination by Unni and colleagues revealed the presence of SMCs, collagen fibres and ground substance within the thickened neointima (Unni et al., 1974). In line with histopathological findings in human SVGs, a vein graft study in rabbits demonstrated that late neointimal thickening was characterised by a conversion from a pro-proliferative to a pro-fibrotic morphology (Jiang et al., 2009). Taken together, it is speculated that de-differentiated SMCs may be the source of fibrotic neointimal remodelling in SVGs.

In general, vascular fibrosis is characterised by a reduction in lumenal diameter accompanied by wall thickening/stiffening which culminates in vessel dysfunction (reviewed in) (Lan et al., 2013). Vascular SMC proliferation, ECM accumulation and inhibition of ECM degradation are key underlying pathological drivers of vascular fibrosis. Neointimal ECM accumulation in vein grafts is characterised by an increase in pro-fibrotic protein deposition including but not limited to proteoglycans (Jiang et al., 2009), connective tissue growth factor (CTGF) (Jiang et al., 2009), plasminogen activator inhibitor (PAI)-1 (Kauhanen et al., 1997) and collagens (Wolff et al., 2006). The TGF-β signalling pathway is a positive regulator of pro-fibrotic gene expression in pre-implantation SVG SMCs (unpublished data) (Low et al., 2019). In depth characterisation of TGF-β signalling is presented in section 1.4.4.

1.3.1.6 Endothelial-to-mesenchymal transition

The term endothelial-to-mesenchymal transition (EndMT) describes the phenotypic conversion of endothelial to mesenchymal cells (reviewed in) (Choi et al., 2020). EndMT entails a loss of EC-specific cluster of differentiation (CD)31, vascular endothelial (VE) cadherin, angiopoietin-1 receptor and von Willebrand factor expression and instead a gain in fibroblast-specific protein (FSP)-1, αSMA and type I/III collagen expression. In arterial and venous vessels, a single EC layer lines the lumenal side of the intima which forms an anatomic barrier between the lumen and the vascular wall (Figure 1-3 and Figure 1-4). In healthy vessels, the intact EC monolayer regulates vascular tone (contraction

and relaxation), suppresses vSMC de-differentiation and exerts anti-inflammatory and anti-thrombotic properties (reviewed in) (Davignon and Ganz, 2004). Endothelial cell dysfunction underlies NF and subsequent vascular obstruction in pulmonary arterial hypertension (PAH) (Long et al., 2015). Reduced endothelial bone morphogenetic protein receptor (BMPR)2 (Evans et al., 2016)/activin receptor-like kinase (ALK)1 (Trembath et al., 2001) signalling is a key pathological process in PAH development and progression. The pleiotropic growth factor bone morphogenetic protein (BMP)-9 (section 1.4.3) activates ALK1/BMPR2 signalling (Figure 1-8) (Salmon et al., 2020; Scharpfenecker et al., 2007), restores defective ALK1/BMPR2 signalling and, hence, reverses experimental PAH in mice (Long et al., 2015). In contrast, Tu *et al*. implicated BMP-9 as a pathogenic driver of PAH development and progression (Tu et al., 2019). Taken together, these two studies found conflicting results warranting further research into physiological/pathophysiological actions of BMP-9 in the context of PAH and vascular disease.

In the context of SVG disease, altered haemodynamic forces within the coronary arterial system trigger endothelial denudation within the venous conduit which culminates in local thrombus formation and infiltration of inflammatory cells (Sasaki et al., 2000). A pre-clinical vein graft study found that endothelial coverage ranged between 81.3% and 95.5% at 4 weeks post-implantation (Ishikawa et al., 1996). Whether or not, or to what extent, EndMT contributes to NF in SVGs following CABG surgery is a matter of ongoing scientific debate. Whereas Cooley *et al*. demonstrated that pharmacological EndMT inhibition prevented NF (Cooley et al., 2014), Wu and colleagues revealed that EndMT only marginally contributed to NF in a murine vein graft model (Wu et al., 2020). In addition, Cooley's study revealed that TGF-β signalling was a driver of EndMT (Cooley et al., 2014).

1.3.1.7 Fibroblast-to-myofibroblast differentiation

In fibroblast-to-myofibroblast differentiation, fibroblasts acquire a SMC-like phenotype, termed myofibroblast (reviewed in) (Zent and Guo, 2018). In the context of vascular injury, this entails a loss of adventitial fibroblast-specific vimentin expression and instead a gain in SMC-specific αSMA expression (Shi et al., 1996b). Shi *et al*. demonstrated that adventitial fibroblasts invaded the

media, underwent fibroblast-to-myofibroblast transition and contributed to NF in a porcine vein graft model (Shi et al., 1997) (Figure 1-4). Next to driving pro-fibrotic gene expression and EndMT, the TGF-β signalling pathway also positively regulates fibroblast-to-myofibroblast transition (Schwartze et al., 2014).

1.3.1.8 Accelerated atherosclerosis

Atherosclerosis is a progressive and inflammation-driven disease which primarily affects large arteries of the vascular system and is characterised by progressive intimal lipid deposition followed by fibroatheroma formation (reviewed in) (Lusis, 2000). Diffuse intimal thickening (Nakashima et al., 2007), subendothelial low-density lipoprotein (LDL) retention (Saxena et al., 1993; Saxena et al., 1992; Skålén et al., 2002), blood flow disturbance-driven endothelial dysfunction (Chang et al., 2017; Dai et al., 2004; Ku et al., 1985), inflammatory cell recruitment (Babaev et al., 1993), LDL modification (Heinecke et al., 1984; Steinbrecher et al., 1984) and macrophage foam cell formation (Kruth et al., 2002) drive arterial atherosclerosis development and progression. Arterial fatty streak lesion/intimal xanthoma development occurs early in the life course, with studies showing that fatty streaks are already present in teenagers (Strong et al., 1999). Some neointimal fatty streak lesions gradually remodel into early fibroatheroma which are characterised by an accumulation of lipids, macrophage foam cells, inflammatory cells and vessel resident cells (reviewed in) (Insull, 2009). In time, SMC and macrophage foam cell necrosis occur within the fibroatheroma triggering necrotic core formation. Together, these changes disrupt the normal architecture of the intima. A fibrous cap which mainly consists of SMCs, connective tissue and macrophages develops to cover the lipid-rich necrotic core (reviewed in) (Virmani et al., 2000). A thin-cap fibroatheroma (TCFA) is characterised by a thin overlying fibrous cap (<65 μm) which contains a high degree of macrophage infiltration (Virmani et al., 2002). TCFAs are precursor lesions of plaque rupture (Virmani et al., 2002). Following TCFA rupture the highly thrombogenic core is exposed to the circulation which triggers thrombosis, a potentially life-threatening event (Moreno et al., 1996). Furthermore, advanced atherosclerosis pre-disposes to arterial aneurysm formation (Albini et al., 2014) which upon dissection may result in fatal haemorrhaging.

Histopathological analysis of SVGs demonstrated that atherosclerosis also presented within SVG neointima following CABG surgery and contributed to late SVG occlusion (Bulkley and Hutchins, 1977; Neitzel et al., 1986) (Figure 1-4). Moreover, SVG neointimal atherosclerotic remodelling may similarly culminate in fibroatheroma rupture/thrombosis (Walts et al., 1982) and aneurysm formation (Neitzel et al., 1986) contributing to late SVG failure. Kockx and colleagues found that neointimal thickening correlated with lumenal accumulation of foam cells and mural thrombi in sub-occluded SVGs (mean SVG age 9.9 ± 2.4 years) (Kockx et al., 1994). These findings demonstrated that atherosclerotic remodelling of SVGs progressed more rapidly compared to arteries, highlighting atherosclerotic susceptibility of SVGs. Next to monocyte-derived macrophage foam cell formation, pre-clinical data suggests that cholesterol uptake into intimal vSMCs induces a macrophage-like SMC phenotype (Allahverdian et al., 2014; Vengrenyuk et al., 2015). Hence, cholesterol-driven SMC de-differentiation may contribute to atherosclerotic lesion formation in SVGs.

1.3.2 vSMC heterogeneity

Vascular SMCs derive from at least 8 distinct origins during embryonic development giving rise to inter-regional SMC phenotypic diversity (reviewed in) (Majesky, 2007). Inter-regional SMC phenotypic diversity may partially explain why arterial and venous SMCs respond differently to the same external stimuli, which in turn may explain why SVGs display enhanced susceptibility to NF and atherosclerosis (Shi et al., 2001; Turner et al., 2007).

In addition to inter-regional SMC phenotypic diversity, *in vitro* studies identified two major SMC phenotypes which resided in arterial media within the same area (Hao et al., 2002; Li et al., 2001a). Li *et al*. reported cloning of 12 distinct primary human SMC lines from a single fragment of distal internal thoracic artery (Li et al., 2001a). Of these 12 SMC lines, 3 lines were spindle-shaped, and 9 lines were epithelioid-shaped. Spindle-shaped SMCs were larger in size, grew slower and showed more robust Ca^{2+} transients in response to AngII stimulation. In contrast, epithelioid-shaped SMCs displayed greater proliferation and migration in response to PDGF-BB treatment. In line with these findings, a study by Hao *et al*. revealed spindle- and rhomboid-shaped SMC phenotypes in porcine coronary artery media (Hao et al., 2002). This study went on to show that neointimal

lesions from stented porcine coronary arteries revealed a large proportion of rhomboid-shaped SMCs which demonstrated higher proliferative and migratory activities compared to spindle-shaped SMCs. Furthermore, Frid *et al*. showed that based on immunobiochemical characteristics, cell morphology and elastic lamellae arrangement pattern at least four distinct vSMC phenotypes resided in mature bovine pulmonary arterial media (Frid et al., 1994). More recently, single cell (sc) RNA transcriptomic analysis has investigated vSMC heterogeneity in the context of vascular disease and injury (Dobnikar et al., 2018). Key findings are presented in section 6.1.1.

Taken together, these studies strongly suggest that distinct SMC sub-populations reside within healthy vascular media in different vascular beds. It may be speculated that these distinct phenotypes exert different functions regarding vessel homeostasis and react differently in response to vascular injury.

1.4 Vascular TGF-β superfamily signalling

1.4.1 The TGF-β superfamily

TGF-β_1 and BMP-9 are pleiotropic growth factors which belong to the TGF-β superfamily (reviewed in) (David and Massagué, 2018). The TGF-β superfamily comprises 32 growth factors widely conserved across species and is mainly subdivided into TGF-β, BMP and Activin/Inhibin subfamilies except for some outliers (for example, Mullerian Inhibiting Substance). The TGF-β subfamily includes three TGF-β isoforms (TGF-β_1, TGF-β_2 and TGF-β_3), two activin isoforms (activin A and activin B), Nodal, myostatin and several related growth differentiation factors (GDF). In contrast, the BMP subfamily includes twelve BMP isoforms, the anti-Muellerian hormone and several related GDFs. Together, TGF-β superfamily members orchestrate normal embryonic development and maintenance of whole-body homeostasis.

1.4.2 TGF-β_1 production, storage and activation

TGF-β_1 is synthesised as a 390 amino acid pre-pro-TGF-β_1 monomer which is formed of the N-terminal signal peptide (29 amino acids), the latency associated protein (LAP) (249 amino acids) and C-terminal mature TGF-β_1 (112 amino acids) (Gentry and Nash, 1990). The pre-pro-TGF-β_1 monomer enters the rough endoplasmic reticulum (ER) where the N-terminal signal peptide is enzymatically removed yielding pro-TGF-β_1 (Gentry et al., 1988). In addition, two pro-TGF-β_1 monomers dimerise via three disulphide bonds (two within the LAP and one within mature TGF-β_1) within the rough ER (Gentry et al., 1988) forming the pro-TGF-β_1 homodimer. Furin convertase cleaves the pro-TGF-β_1 homodimer which culminates in LAP homodimer and mature TGF-β_1 homodimer separation (Dubois et al., 1995). Despite cleavage, both monomers remain non-covalently bound forming the small latent complex (SLC) (Wakefield et al., 1988). The SLC binds covalently binds to the larger latent TGF-β_1-binding protein (LTPB) forming the large latent complex (LLC) (Saharinen et al., 1996). This step is critical for efficient LLC secretion from the cell (Miyazono et al., 1991). Following secretion, the inactive LLC complex is anchored to the ECM (Unsöld et al., 2001). Microenvironmental changes such as acidification (Jullien et al., 1989) and reactive oxygen species (ROS) generation (Barcellos-Hoff and Dix, 1996) as

well as matrix metalloproteinases (MMPs) (Yu and Stamenkovic, 2000) and integrins (Munger et al., 1999) enable the release of mature TGF-β_1 from the ECM-anchored LLC.

The spleen, placenta, bone marrow, lymph nodes and the lung demonstrate the highest *TGFB1* mRNA expression levels within the human body (The Human Protein Atlas). In relation to the spleen, relative smooth muscle *TGFB1* mRNA expression levels are approximately 4-fold times lower. Next to ECM storage, latent TGF-β_1 circulates in blood plasma (Areström et al., 2012; Hering et al., 2002) or is stored in circulating platelet cells (Blakytny et al., 2004) in humans. Immunohistochemical analysis revealed that TGF-β_1 and LTBP were present in human SVG intima and media (Friedl et al., 2004). The same study showed that SVGs with NF demonstrated an increase in TGF-β_1 and LTBP staining compared to SVGs without NF. Dr Emma Low (previous PhD student) demonstrated that SMCs isolated from pre-implantation SVGs expressed *TGFB1* suggesting SMCs as a TGF-β_1 source within the SVG wall.

1.4.3 BMP-9 production and secretion

In contrast to *TGFB1*, *GDF2* (gene encoding BMP-9) is almost exclusively expressed in the liver in humans (The Human Protein Atlas) (Bidart et al., 2012). BMP-9 is synthesised as a 429 amino acid precursor peptide monomer which comprises an N-terminal signal peptide (22 amino acids), a pro-domain (297 amino acids) and C-terminal mature BMP-9 (109 amino acids) (Tillet and Bailly, 2014). Following N-terminal signal peptide cleavage, two precursor BMP-9 monomers form a precursor BMP-9 homodimer via a disulfide bridge within the mature domain. A furin convertase cleaves both BMP-9 monomers between the pro- and mature domain (Bidart et al., 2012). Despite cleavage, both pro-domains remain non-covalently bound to the mature BMP-9 homodimer. Bidart and colleagues demonstrated that human BMP-9 circulates in its inactive (40%, unprocessed precursor BMP-9 homodimer) and its active form (60%, mature BMP-9 homodimer). Next to BMP-9 homodimers, Tillet *et al*. went on to show that a BMP-9 monomer could also associate with a BMP-10 monomer to form a biologically active heterodimer (Tillet et al., 2018). The same study demonstrated that BMP-9/BMP-10 heterodimers circulated in human plasma.

1.4.4 Canonical and non-canonical signalling pathways in the vasculature

TGF-β superfamily members signal via transmembrane serine/threonine kinase TGF-β type I (TβRI) and TGF-β type II receptors (TβRII) (reviewed in) (David and Massagué, 2018). There are seven TβRI (ALKs) and five TβRIIs. TGF-β superfamily ligands bind to the extracellular domain of TβRI and/or TβRIIs which culminates in complex formation with a second TβRI or TβRII. Next to TβRI and TβRIIs, the transmembrane TGF-β type III co-receptors (TβRIII) endoglin and betaglycan also bind TGF-β superfamily ligands (Barbara et al., 1999; López-Casillas et al., 1994) and may complex with TβRI and/or TβRIIs (Blanco et al., 2005; López-Casillas et al., 1993). Both endoglin and betaglycan may modulate TβRI/TβRII-dependent downstream pathway activation (Lebrin et al., 2004; Schwartze et al., 2014).

Ligand-dependent complex formation between a TβRI and TβRII results in activation of kinase sites within the TβRI or TβRII's cytoplasmic domain (Figure 1-8 and Figure 1-9). Activated cytoplasmic domains drive phosphorylation of receptor-regulated (R)-s-mothers against decapentaplegic (SMAD)s which function as intracellular signalling messengers. TβRIs are internalised via endocytosis following activation, another important component of R-SMAD phosphorylation (Di Guglielmo et al., 2003; Tao et al., 2020). Following internalisation, receptors may be recycled to the cell surface where they may signal again (Di Guglielmo et al., 2003). In addition, the TβRII bone morphogenetic protein receptor (BMPR)2 may be degraded via the lysosomal pathway, a mechanism which enables a stable equilibrium of cell surface BMPR2 presence (Gomez-Puerto et al., 2019).

R-SMAD phosphorylation triggers canonical TGF-β signalling pathway activation. Upon phosphorylation, R-SMADs complex with the common (co)-SMAD4 which enables the heteromeric complex to enter the nucleus where it acts as a TF for target genes. Depending on complex composition, R-SMAD/co-SMAD4 complexes interact with distinct DNA elements. These elements include but are not limited to the 8-base pair (bp) palindromic 5'-GTCTAGAC-3' sequence (SMAD-binding element or SBE) (Zawel et al., 1998), the 5'-AG(C/A)CAGACA-3' sequence (CAGA

motif) (Dennler et al., 1998), 5'-AGACAAGGTTGT-3' (Song et al., 1998) and GC rich BMP responsive elements (BREs) (Katagiri et al., 2002).

The inhibitory (I)-SMADs, SMAD6 and SMAD7, disrupt R-SMAD activation thereby forming a negative feedback loop mechanism (Hata et al., 1998; Yan et al., 2016). Furthermore, the SMAD specific E3 ubiquitin protein ligase (SMURF)1 and SMURF2 mediate ubiquitination-proteasome-dependent degradation of R-SMADs, thereby contributing to negative regulation of TGF-β signalling (Lin et al., 2000; Zhu et al., 1999). In addition, SMURF2 may also associate with SMAD7 which induces direct degradation of the TβRI ALK5 and the TβRII transforming growth factor-β receptor (TGFBR)2 via proteasome and lysosomal pathways (Kavsak et al., 2000). Moreover, protein phosphatases including but not limited to protein phosphatase (PP)1 and the Bδ subunit of PP2A dephosphorylate activated ALK5, thereby forming an additional negative feedback mechanism (Batut et al., 2008; Shi et al., 2004).

Next to activation of canonical SMAD signalling, active ALK5 may also drive major non-canonical cell signalling pathways including but not limited to phosphatidylinositol 3-kinase (Yi et al., 2005), extracellular regulatory kinase (ERK) (Lee et al., 2007), p38 MAPK (Yu et al., 2002) and c-Jun N-terminal kinase signalling (Shi-Wen et al., 2006).

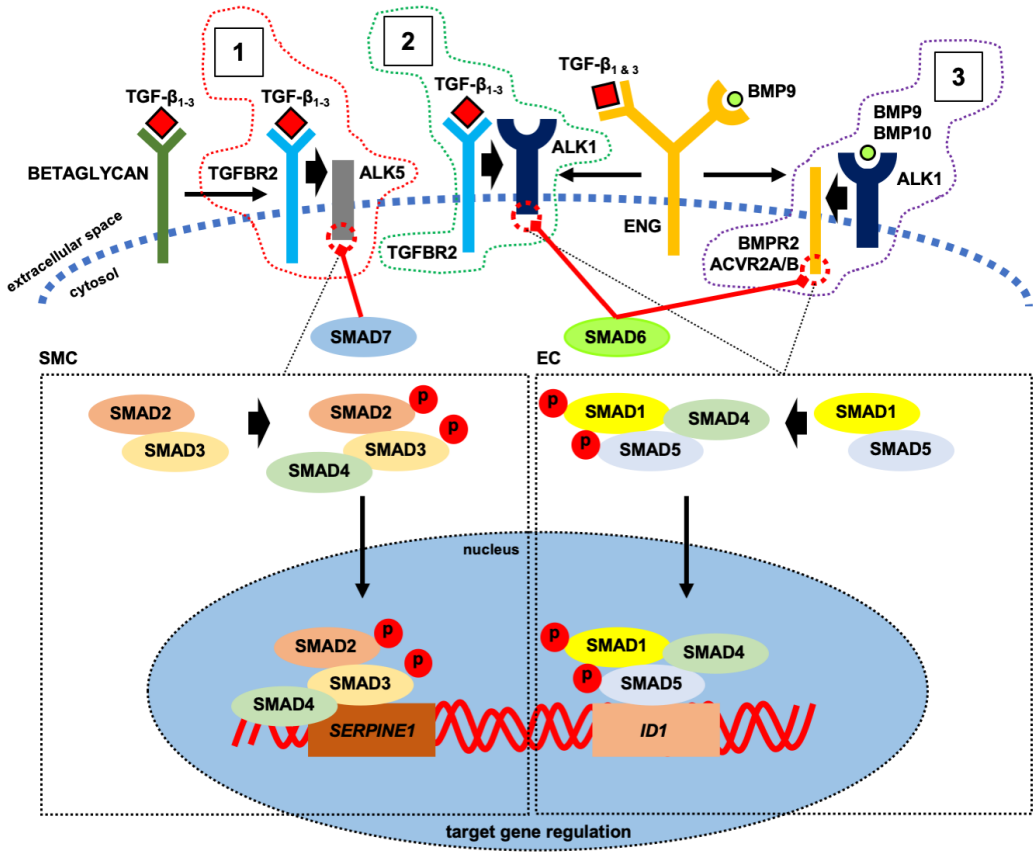

Figure 1-8 Basic schematic representation of canonical TGF-β superfamily signalling. (**1**) The TGF-β_1/TGFBR2/ALK5 signalling axis: activated TGF-β_1 binds to the extracellular domain of the type II TGF-β receptor (TGFBR)2 (Wrana et al., 1992). Following activation, TGF-β_1/TGFBR2 complexes with the TβRI ALK5. Complex formation activates kinase sites within the ALK5 cytoplasmic domain which drive phosphorylation (p) of the R-SMADs SMAD2 (Macías-Silva et al., 1996) and SMAD3 (Liu et al., 1997). Phosphorylated SMAD2 and SMAD3 form a heteromeric complex with co-SMAD4 which enables the complex to translocate to the nucleus (Zhang et al., 1997) and function as a TF (Dennler et al., 1998). This complex interacts with CAGA boxes on the DNA within promoter or repressor regions of target genes (Dennler et al., 1998). The *SERPINE1* gene (encodes the protein PAI-1) is a target gene of the TGF-β_1/TGFBR2/ALK5 signalling axis (Dennler et al., 1998). (**2**) The TGF-β_1/TGFBR1/ALK5 signalling axis: TGF-β_1/TGFBR2 interaction may also trigger ALK5-dependent complex formation with the TβRI ALK1 (Goumans et al., 2003; ten Dijke et al., 1994). Activated ALK1 phosphorylates the R-SMADs SMAD1 and SMAD5 (Goumans et al., 2003). (**3**) The BMP-9/ALK1/BMPR2 signalling axis: BMP-9 binds to the extracellular domain of the ALK1 receptor (Salmon et al., 2020; Scharpfenecker et al., 2007). Following activation, BMP-9/ALK1 complexes with either the TβRII bone morphogenetic protein receptor (BMPR)2 or the TβRIIs activin a receptor type IIa/IIb (ACVR2A/B) (Upton et al., 2009). Complex formation activates cytoplasmic kinase domains of BMPR2 and/or ACVR2A/B which drives SMAD1 and SMAD5 phosphorylation. Phosphorylated SMAD1 and SMAD5 recruit the co-SMAD4 to form a heteromeric complex which enables nuclear translocation (Ramachandran et al., 2018; Zhang et al., 1997). This complex acts as a TF by interacting with GC rich BREs on the DNA within promoter and repressor regions of target genes (Chai et al., 2015; Katagiri et al., 2002). The *ID1* gene (encodes the protein inhibitor of differentiation-1) is a target gene of the TGF-β_1/TGFBR2/ALK1 (Lebrin et al., 2004) and the BMP-9/ALK1/BMPR2 signalling axes (Upton et al., 2009). I-SMADs SMAD6/SMAD7 and TβRIII co-receptors modulate ALK5 and ALK1-dependent downstream pathway activation. SMAD7 pre-dominantly disrupts ALK5-driven SMAD2/3 phosphorylation (Yan et al., 2016), SMAD6 inhibits ALK1/BMPR2-driven SMAD1/5 phosphorylation (Hata et al., 1998). Betaglycan binds all three TGF-β isoforms (Cheifetz et al., 1990). Upon ligand binding, betaglycan forms a complex with TGFBR2 (López-Casillas et al., 1993). Endoglin (ENG) binds TGF-β_1, TGF-β_3 (Cheifetz et al., 1992) and BMP-9 (Scharpfenecker et al., 2007) and may complex with ALK1 (Blanco et al., 2005). Although ALK5 signalling outweighs ALK1 signalling in vSMCs and vice versa in ECs, both pathways are present in vSMCs and ECs and maintain a continuous physiological balance.

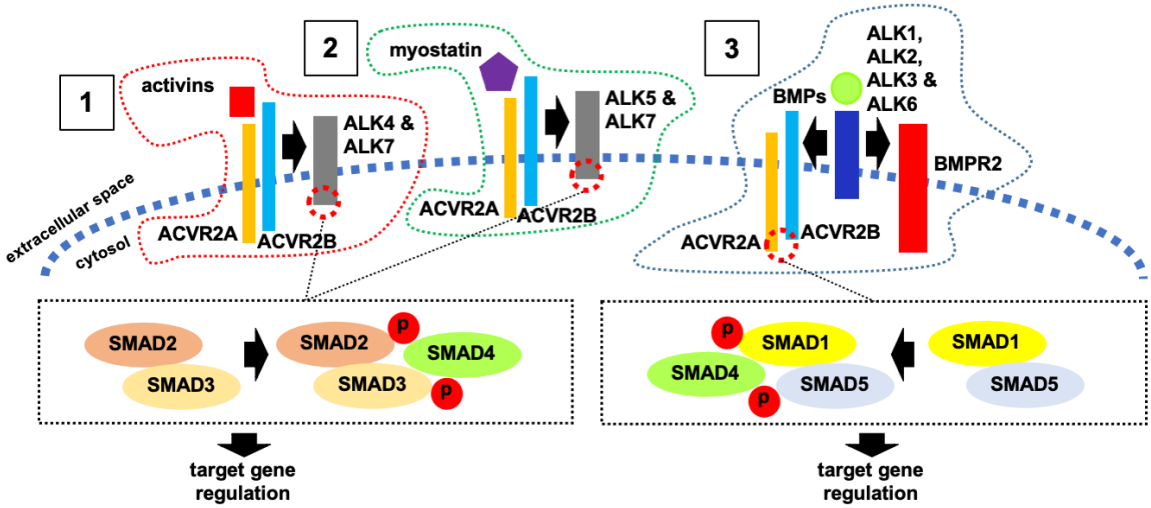

Figure 1-9 Schematic representation of ACVR2A/B signalling. ACVR2A and ACVR2B are transmembrane serine/threonine TβRIIs (Attisano et al., 1992; Mathews and Vale, 1991). (**1**) Activins bind to the extracellular domain of ACVR2A (Mathews and Vale, 1991) and/or ACVR2B (Attisano et al., 1992). Upon activation ACVR2A/B complex with the TβRIs ALK4 (ten Dijke et al., 1994) or ALK7 (Tsuchida et al., 2008) and induce SMAD2/3 phosphorylation (Bernard, 2004). (**2**) Myostatin binds to the extracellular domains of ACVR2A or B (Lee et al., 2005; Rebbapragada et al., 2003). This triggers complex formation with either ALK5 or ALK7 and subsequent SMAD2/3 phosphorylation. (**3**) In contrast, BMP/ALK1,2,3 and 6 complexes may recruit ACVR2A/B or BMPR2 which culminates in SMAD1/5 phosphorylation (Ebisawa et al., 1999; Salmon et al., 2020; Yamashita et al., 1995). Phosphorylated SMAD2/3 and SMAD1/5 complexes recruit the common SMAD4 to translocate to the nucleus (Ramachandran et al., 2018; Zhang et al., 1997).

1.4.5 Vascular development and hereditary vascular disorders

Vascular TGF-β superfamily signalling mediators are in continuous physiological balance and maintain vascular homeostasis.

Defective global ALK1 signalling culminates in embryonic lethality as a result of major vascular defects including arteriovenous malformation (AVMs) in *Acvrl1* (encodes ALK1) knockout mice (Urness et al., 2000). In humans, genetic defects within the *ACVRL1* gene are linked to hereditary haemorrhagic telangiectasia (HHT) type 2 (Bossler et al., 2006), a hereditary vascular disorder (HVD) characterised by organ telangiectasias and AVMs prone to potentially life-threatening haemorrhaging. Similarly, defective ALK5 signalling in *Tgfbr1* (encodes ALK5) knockout mice also culminates in embryonic lethality because of defective vasculogenesis (Larsson et al., 2001). In humans, defects within the *TGFBR1* gene are linked to the Loeys-Dietz Syndrome (LDS) type I (Loeys et al., 2005), a complex syndrome characterised by defects in cardiovascular, craniofacial, neurodegenerative and skeletal development. LDS type I patients typically display arterial tortuosity and aneurysms prone to potentially life-threatening haemorrhaging.

Many more murine knock out studies have revealed that intact TGF-β superfamily signalling is crucial for normal cardiovascular development and homeostasis (reviewed in) (Pardali et al., 2010) (Table 1-3). Furthermore, many more genetic defects within genes encoding for TGF-β superfamily proteins have been linked to HVDs in humans highlighting the importance of intact vascular TGF-β superfamily signalling (reviewed in) (Schwartze et al., 2019) (

Table 1-4). Involvement of vascular BMP-9, TGF-β_1 and ACVR2A signalling in the pathophysiological context of vascular injury/SVG disease is presented in sections 3.1.2, 4.1.2 and 4.1.3 respectively.

Table 1-3 List of murine homozygous knockout models and their cardiovascular phenotypes.

Gene name	Protein name	Cardiovascular phenotype	Reference
Tgfb1	Tgf-β_1	Defective vascular development	(Dickson et al., 1995)
Tgfb2	Tgf-β_2	Aortic arch malformation	(Molin et al., 2002)
Tgfb3	Tgf-β_3	Cardiac outflow tract and atrioventricular canal defects	(Chakrabarti et al., 2020)
Gdf2	Bmp-9	No overt defects in vascular development	(Ricard et al., 2012)
Tgfbr1	Alk5	Embryonic lethality, severe angiogenesis defects	(Larsson et al., 2001)
Acvrl1	Alk1	Embryonic lethality, vascular defects, AVM	(Urness et al., 2000)
Tgfbr2	Tgfr2	Embryonic lethality, defective vascular development	(Oshima et al., 1996)
Bmpr2	Bmpr2	Embryonic lethality, impaired mesoderm development	(Beppu et al., 2000)
Acvr2a	Acvr2A	No overt defects in vascular development	(Matzuk et al., 1995)
Acvr2b	Acvr2B	Randomised heart position, malposition of the great arteries, and ventricular and atrial septal defects	(Oh and Li, 1997)
Tgfbr3	Betaglycan	Embryonic lethality, impaired coronary vessel development	(Compton et al., 2007)
Eng	Endoglin	Embryonic lethality, defective vascular development, cardiac defects	(Arthur et al., 2000)
Madh1	Smad1	Embryonic lethality, impaired allantois formation	(Tremblay et al., 2001)
Madh2	Smad2	Embryonic lethality, impaired visceral endoderm function and deficiency of mesoderm formation	(Hamamoto et al., 2002)
Madh3	Smad3	Premature death due to aortic aneurysm	(van der Pluijm et al., 2016)
Madh4	Smad4	Embryonic lethality	(Takaku et al., 1998)
Madh5	Smad5	Embryonic lethality, lack of well-organised vasculature	(Chang et al., 1999)
Madh6	Smad6	Embryonic and post-natal lethality, hyperplastic cardiac valve thickening, outflow tract septation defects, hypertension, embryonic vessel haemorrhaging	(Wylie et al., 2018)
Madh7	Smad7	Embryonic and post-natal lethality, ventricular septal defect, outflow tract malformation, impaired cardiac function, cardiac arrhythmias	(Chen et al., 2009)

Table 1-4 List of known genetic defects culminating in HVDs in humans.

Gene name	Protein name	Syndrome;loss or gain of gene/protein function; disease and vascular phenotype	Reference
FBN1	Fibrillin 1	Marfan's syndrome; loss of function; aortic root dilatation, dysfunctional fibrillin 1 fails to sequester LLC to ECM culminating in excessive vascular wall TGF-β_1 signalling	(Matt et al., 2009)
TGFB2	TGF-β_2	LDS type 4; loss of function; familial thoracic aneurysms and dissections	(Boileau et al., 2012; Lindsay et al., 2012)
TGFB3	TGF-β_3	LDS type 5; loss of function; aortic aneurysms and dissections	(Bertoli-Avella et al., 2015)
GDF2	BMP-9	HHT5; loss of function; AVMs, dermal telangiectasia	(Wooderchak-Donahue et al., 2013)
BMP10	BMP-10	PAH; predicted loss of function	(Eyries et al., 2019)
ENG	Endoglin	HHT1 and HHT-associated PAH; loss of function; AVMs, telangiectasia, PAH	(Bossler et al., 2006; Mache et al., 2008)
TGFBR1	ALK5	LDS type; loss of function; arterial aneurysms/tortuosity	(Loeys et al., 2005)
ACVRL1	ALK1	HHT2 and HHT-associated PAH, loss of function; AVMs, telangiectasia, PAH	(Trembath et al., 2001)
TGFBR2	TGFBR2	LDS type 2; gain of function; aortic aneurysm/dissection	(Loeys et al., 2005)
BMPR2	BMPR2	HPAH; loss of function	(Evans et al., 2016)
BMPR1B	ALK6	HPAH; gain of function	(Chida et al., 2012)
MADH1	SMAD1	HPAH; loss of function	(Nasim et al., 2011)
MADH3	SMAD3	LDS type 3; gain of function; arterial aneurysms/tortuosity	(van de Laar et al., 2012)
MADH4	SMAD4	JP-HHT Syndrome; loss of function; AVMs, telangiectasia, aortic root dilatation	(Jelsig et al., 2016)
MADH5	SMAD5	HPAH; loss of function	(Nasim et al., 2011)
MADH9	SMAD9	HPAH; loss of function	(Nasim et al., 2011)
SKI	v-ski avian sarcoma viral oncogene homologue	SGS; loss of function; aortic aneurysm	(Doyle et al., 2012)

Abbreviations: JP, juvenile polyposis; SGS, Sphrintzen-Goldberg Syndrome.

1.5 Adenoviral vector-based gene therapy in saphenous vein graft disease

Identification of causative defects in genes encoding for TGF-β superfamily members culminating in HVDs in humans opens the door for therapeutic genetic targeting. Gene therapy is defined as the treatment of a disease by transfer of engineered genetic material into human cells, often achieved by viral transduction (Scheller and Krebsbach, 2009). SVG occlusion rates following CABG surgery remain high despite optimal pharmacological treatment (Harskamp et al., 2013) and, hence, there remains an unmet clinical need to improve long-term SVG outcomes. Gene therapy has been proposed as one novel approach to tackle SVG occlusion, particularly via the use of adenoviral-mediated gene transfer.

1.5.1 Adenovirus structure and genome organisation

Adenoviruses are classified under the family of adenoviridae which is subdivided into 5 distinct generations: mastadenovirus, aviadenovirus, siadenovirus, atadenovirus, and ichtadenovirus (reviewed in) (Harrach et al., 2011). HAdVs belong to the generation of mastadenoviridae which are subdivided into 7 subgroups (A-G) with a total number of 67 known serotypes (reviewed in) (Singh et al., 2018). A schematic representation of AdV structure and genome organisation is presented in Figure 1-10.

In humans, wild-type HAdVs typically cause conjunctivitis, keratoconjunctivitis, upper and lower respiratory infections, pneumonia, gastroenteritis, hepatitis and cystitis (Borkenhagen et al., 2019). AdVs infect a broad range of species and include, simian, bovine, porcine, ovine, canine, murine, fowl, bat, snake, reptile and fish AdVs (Harrach et al., 2019; Mittal et al., 2016).

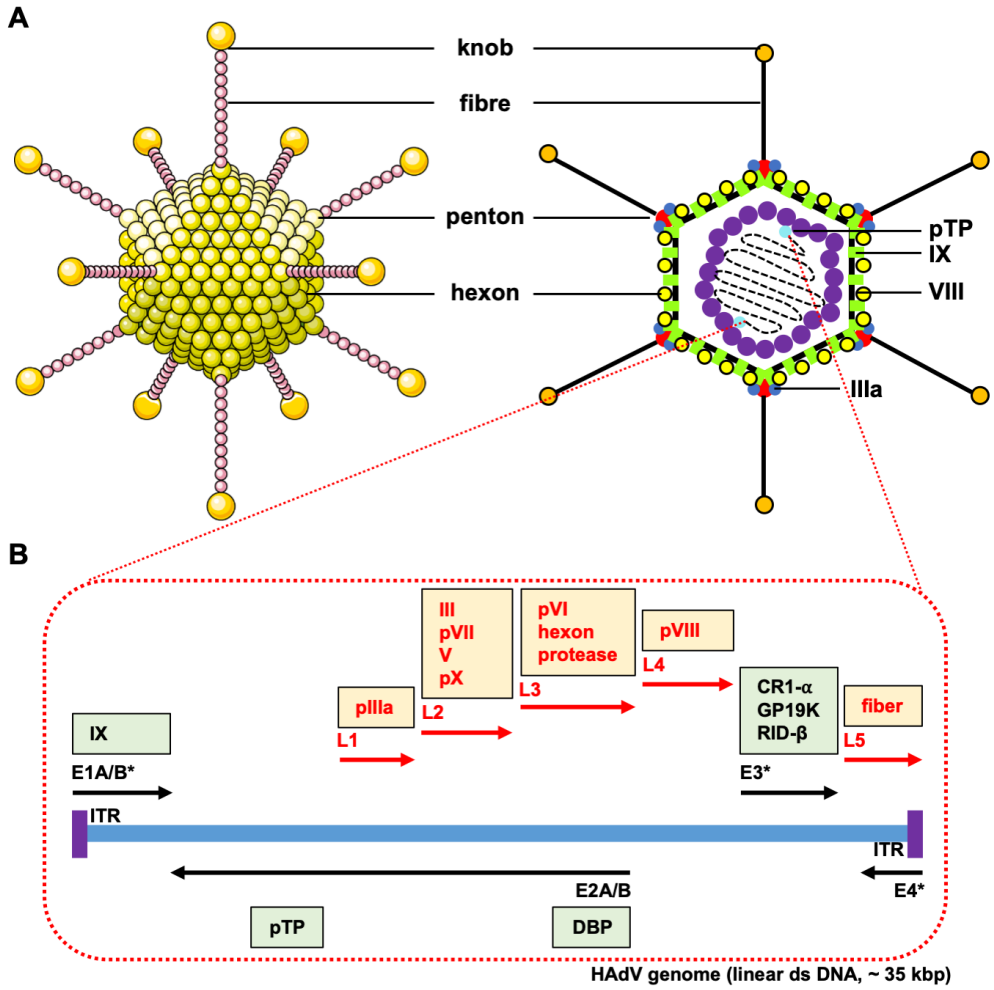

Figure 1-10 Schematic representation of AdV structure and genome organisation. (**A**) AdV virions are non-enveloped and are made up of icosahedral-shaped capsids ranging from 70 to 90 nm in diameter (Robinson et al., 2011). Each capsid encompasses a total of 252 proteins classified into 240 trimeric hexons, 12 penton bases and 12 trimeric proteins (reviewed in) (Lee et al., 2017). The capsid contains linear double-stranded (ds) DNA ranging from 26-46 kb. (**B**) The AdV genome is divided into 4 early (E) and 5 late (L) transcriptional units. Early transcriptional units encode non-structural proteins which regulate AdV DNA replication and host cell metabolism (Russell, 2000). Late transcriptional units encode structural proteins which form the AdV virion. *Indicates regions which are often manipulated/deleted to generate HAdV-5 gene therapy vectors. Abbreviations: IX, gene encoding capsid protein IX; pIIIa, gene encoding capsid protein precursor pIIIa; III, gene encoding penton base; pVII, gene encoding core protein precursor VII; V, gene encoding core protein V; pVI, gene encoding capsid protein precursor VI; pVIII, gene encoding capsid protein precursor VIII; CR1-α, gene encoding membrane glycoprotein E3 CR1-α; GP19K, gene encoding membrane glycoprotein E3 gp19K; RID-β, membrane protein E3 RID-β; ITR, inverted terminal repeat; pTP, gene encoding pre-terminal protein; DBP, gene encoding DNA-binding protein.

1.5.2 Distinct AdV vector generations

Distinct genetic modifications of the AdV genome enabled the development of a variety of replication-deficient Ads capable of delivering transgenes to target cells/tissues. Based on specific viral gene deletion, replication deficient AdVs are classified into first, second and third generation vectors. In addition, conditionally replicating or oncolytic AdVs were designed to target and destroy tumour cells.

In first generation AdV vectors the E1 and often E3 regions are substituted for an expression cassette with an insert capacity of 8.2 kb (reviewed in) (Capasso et al., 2014; Danthinne and Imperiale, 2000) (Figure 1-10 B). Genes within the E1 region encode proteins which orchestrate viral replication and promote host cell proliferation (reviewed in) (Danthinne and Imperiale, 2000; Steegenga et al., 1999; Zamanian and La Thangue, 1992). The development of the HEK293 cell line which is integrated with adenoviral DNA encoding the E1 region provided a crucial helper cell line able to provide the key replicative functions of the virus in trans to enable laboratory amplification and production of replication deficient vectors (Graham et al., 1977). In contrast, the E3 region contains genes encoding proteins which modulate the immune response (Fu et al., 2011) functions which are only activated when E1 is functional, and E3 is therefore dispensable for the function of adenovirus as a gene therapy vector. Owing to the nature of triggering strong immunogenic responses AdV-based vectors are widely employed for vaccine development (reviewed in) (Tatsis and Ertl, 2004). Recent non-replicating human and non-human AdV-based vectors for vaccine development include but are not limited to Ad26.COV2.S and simian ChAdOx1 nCoV-19 for SARS-CoV-2 (Folegatti et al., 2020; Mercado et al., 2020), Ad26.ZEBOV/MVA-BN®-Filo for Ebola (Anywaine et al., 2019) and Ad26.Mos4.HIV for HIV (Baden et al., 2020). A list of current AdV-based vaccine development programmes is presented in Table 1-5.

Conditionally replicating or oncolytic AdVs have the ability to directly target and terminate cancer cells due to the lytic nature of replicating AVs (reviewed in) (Fernandes et al., 2016). Intact E1A and E1B regions are crucial for AdV replication in healthy host cells to enable the virus to block host cell defence mechanisms mediated through p53 and Retinblastoma (Rb) signalling. In

contrast, these regions are dispensable in tumour cells with defective Rb or p53 tumour suppressor signalling. Hence, manipulation/deletion of specific E1A or E1B genes enables targeted AdV replication in cancerous cells and subsequent termination (Bischoff et al., 1996; Lamfers et al., 2002). Targeted tumour cell lysis may also be achieved by tissue-specific promoter-driven transcriptional control of the E1 region (Cheng et al., 2006; Li et al., 2001b). Oncolytic HAdV-5-based products approved by the China Food and Drug Administration include Oncorine (rAd5-H101) and Gendicine (rAd-p53) (Liang, 2018; Pearson et al., 2004).

Second generation AdV vectors feature a combination of E1/E3 with E2 and/or E4 deletions and are less immunogenic compared to first generation vectors (reviewed in) (Fernandes et al., 2016) (Figure 1-10 B). However, their use has largely been surpassed using third generation adenoviral vectors.

Third generation or helper-dependent (HD) AdV vectors lack all viral genes except two ITRs and the packaging signal, thereby allowing a maximal insert size of 36 kb (Alemany et al., 1997; Fisher et al., 1996). HD-AdV propagation requires an additional E1-deleted helper virus (HV) which provides all viral proteins crucial for the rescue of the HD-AdV. To reduce HV contamination in the final product, HD-AdVs are upscaled in a 293-derived cell line which stably expresses Cre recombinase (Parks et al., 1996). The packaging site of the HV is flanked by two *lox*P sites and, hence, Cre recombinase excises the HV's packaging site rendering the HV genome unpackageable. In order to eliminate HV contaminants from the final product, Lee *et al.* successfully upscaled a HD-AdV with a helper plasmid instead of a HV (Lee et al., 2019).

Table 1-5 List of current AdV vector-based vaccine development programmes.

Start and finish date	Indication	Product Name	Viral vector and delivery route	Number of patients	Phase	Clinical trial number	Company/university
09/2020 until 03/2023	SARS-CoV-2		Ad26.COV2.S	60000	III	NCT04505722	Janssen (Belgium)
05/2020 until 08/2021	SARS-CoV-2		ChAdOx1	10260	II and III	NCT04400838	Jenner Institute (Oxford, UK), AstraZeneca (UK)
03/2020 until 12/2022	SARS-CoV-2		Ad5 vectored COVID-19 vaccine	108	I	NCT04313127	CanSino Biologics Inc. (China)
06/2020 until 08/2020	SARS-CoV-2	Gam-COVID-Vac Lyo	1st dose: rAd26.S 2nd dose: rAd5.S	38	I and II	NCT04436471 and NCT04437875	Gamaleya Research Institute of Epidemiology and Microbiology, Health Ministry of the Russian Federation (Russia)
12/2019 until 01/2021	MERS-CoV		ChAdOx1 MERS	24	Ib	NCT04170829	King Abdulaziz Medical City, National Guard Health Affairs (Riyadh, Saudi Arabia)
08/2019 until 12/2021	Ebola	Ad26.ZEBOV/MVA-BN®-Filo	Ad26	800	II	NCT04028349	Janssen, CEPI
10/2019 until 09/2023	HIV	Ad26.Mos4.HIV	Ad26	3800	III	NCT03964415	Janssen

Abbreviations: SARS-CoV-2, severe acute respiratory syndrome coronavirus 2; MERS-CoV, Middle Eastern respiratory syndrome-related coronavirus; HIV, human immunodeficiency virus; CEPI, Coalition for Epidemic Preparedness Innovations.

1.5.3 HAdV-5-dependent transgene delivery

The HAdV serotype 5 (HAdV-5) belongs to the HAdV subgroup C (Sharma et al., 2009) and many viral vectors employed in current cardiovascular gene therapy trials are based on HAdV-5 (Table 1-6). HAdV-5 utilises a range of cell surface receptors for cell attachment and internalisation. These include the coxsackie and adenovirus receptor (CAR) (Tomko et al., 1997), heparan sulphate proteoglycans (HSPG) (Shayakhmetov et al., 2005), major histocompatibility complex (MHC)-I (Hong et al., 1997), vascular cell adhesion molecule (VCAM)-1 (Chu et al., 2001) and integrins (Wickham et al., 1993) (Figure 1-11). Following receptor-mediated endocytosis (Wickham et al., 1993), the viral capsid gradually disassembles allowing binding to the nuclear pore complex, and viral DNA import into the nucleus (Greber et al., 1993). Nuclear uptake of viral DNA initiates transcription of early units followed by transcription of late units (reviewed in) (Russell, 2000). In wild-type AdVs replicated viral genomes are packaged into fully functional viral capsids culminating in virus-induced cell lysis which is followed by viral release (Fernandes et al., 2016). E1 and/or E3 deletions in HAdV-5 render the viral genome unpackageable and, hence, the genetically modified HAdV-5 cannot replicate in healthy wild-type host cells. The E1 and/or E3 regions are often substituted for an expression cassette which contains a transgene of interest. Following delivery to a target cardiovascular cell the transgene is expressed in the nucleus, remains extrachromosomal and produces a therapeutic protein (Lai et al., 2000).

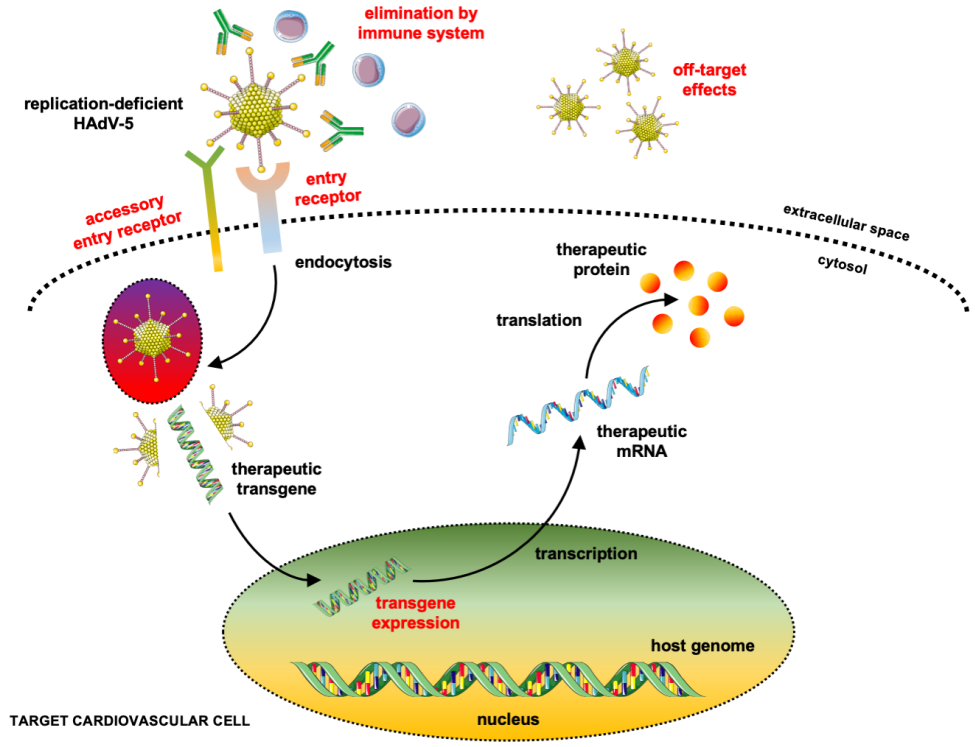

Figure 1-11 Schematic representation of HAdV-5-dependent transgene delivery and its clinical challenges. Replication-deficient HAdV-5 enters a target cardiovascular cell via an entry ± accessory entry receptor. Following receptor-mediated endocytosis, HAdV-5 is broken down and the viral DNA is imported into the nucleus via nuclear core complexes. The transgene remains extrachromosomal and produces a therapeutic protein. Clinical limitations following HAdV-5 delivery include viral elimination by the immune system, off target effects and hepatotoxicity, reduced transduction efficiency based on tissue-dependent entry/accessory entry receptor density, transient/loss of transgene expression because of episomal degradation.

1.5.4 HAdV-5-based gene therapy advantages and clinical challenges

The continued use of HAdV-5-based gene therapy vectors for *in vitro* and *in vivo* applications is based on several advantages. The HAdV-5 genome has been extensively researched which has thus facilitated genetic engineering enabling reproducible HAdV-5 genome manipulation and/or therapeutic transgene insertion (reviewed in) (Alonso-Padilla et al., 2016). Furthermore, HAdV-5 demonstrates wide tropism for quiescent and non-quiescent cells and its genome does not integrate into the host cell genome which reduces the risk of mutagenesis (Benihoud et al., 1999; Dormond et al., 2009). From an industry perspective, replication-deficient HAdV-5 gene therapy vectors can be upscaled achieving high titers of up to 10^{13} viral particles (VPs)/ml following good manufacturing practices. In contrast, HAdV-5-based gene therapy products also carry a range of clinical challenges.

Elimination of replication-deficient HAdV-5 by the immune system poses a major challenge for clinical gene therapy trials. Based on the geographical setting, the seroprevalence of neutralising antibodies (nAbs) for HAdV-5 in humans ranges between 72-85.2% (Mast et al., 2010; Yu et al., 2012). Clinical trials have demonstrated that these nAbs suppress immunogenicity of HAdV-5-based vaccine vectors, thereby hampering vaccine efficiency (Priddy et al., 2008; Zhu et al., 2020). Murine *in vivo* studies showed that systemic recombinant AdV delivery activated innate immune mechanisms which resulted in rapid AdV clearance and, hence, inefficient transgene delivery/expression (Worgall et al., 1997; Zhang et al., 2001). Yang *et al.* demonstrated that retrograde biliary E1-deleted HAdV-5 delivery in mice not only resulted in desired hepatocyte transgene expression but also in low-grade viral gene expression (Yang et al., 1994). This triggered a virus-specific cellular immune response culminating in the destruction of genetically modified hepatocytes highlighting the role of the adaptive immune system in eliminating recombinant HAdV-5.

Targeted cardiovascular transgene delivery via the vascular route is further complicated by sequestration of replication-deficient HAdV-5 to the liver combined with reduced viral transduction efficiency in the vasculature and aged cardiomyocytes (Communal et al., 2003; Fechner et al., 1999; Nicklin et al.,

2001; Work et al., 2004). More importantly, intra-portal vein delivery of E1-deleted HAdV-5 to non-human primates led to hepatotoxicity and features of potentially life-threatening systemic inflammatory response syndrome (SIRS) (Schnell et al., 2001). In the human context, intra-hepatic artery delivery of E1-/E4-deleted HAdV-5 harbouring the human *OTC* gene (encoding ornithine transcarbamylase) to an OTC-deficient patient triggered a fatal SIRS resulting in the termination of one of the first gene therapy trials in humans (Raper et al., 2003). Finally, pre-clinical *in vivo* studies have demonstrated transient loss of transgene expression due to episomal degradation following first generation HAdV-5-dependent delivery (Ehrhardt and Kay, 2002; Vassalli et al., 1999).

1.5.5 Recent and current HAdV-5-based cardiovascular gene therapy trials in humans

Despite significant clinical obstacles, substantial progress has been made around improving HAdV-5 vector safety and efficacy enabling cardiovascular gene therapy trials in humans. Current strategies to circumvent potential deleterious side effects of recombinant HAdV-5 administration in the context of cardiovascular disease include optimised local delivery strategies and dose adjustments. Current cardiovascular gene therapy trials focus on improving cardiac angiogenesis and function. A list of recent and current trials is provided in Table 1-6.

Table 1-6 List of current cardiovascular gene therapy trials employing recombinant HAdV-5 vectors.

Trial name	Start and finish date	Indication	Product Name	Viral vector and delivery route	Number of patients	Phase	Clinical trial number	Company/university
AdeLE	06/2018 until 12/2024	Secondary lymphoedema	Lymfactin®	AdAptVEGF-C *ex vivo* perinodal injection	39	II	NCT03658967	Herantis Pharma Plc.
n/a	06/2016 until 02/2024	Secondary lymphoedema	Lymfactin®	AdAptVEGF-C *ex vivo* perinodal injection	15	I	NCT02994771	Herantis Pharma Plc.
EXACT	01/2020 until 09/2021	Drug-refractory CAD	XC001	AdVEGFXC1 Transthoracic epicardial intramyocardial injection	29	I and II	NCT04125732	XyloCor Therapeutics Inc.
n/a	12/2020 until 10/2030	Drug-refractory CAD		AdVEGF-AII6A+ Transthoracic epicardial intramyocardial injection	41	I and II	NCT01757223	Weill Medical College of Cornell University
FLOURISH	06/2019 until 06/2023	Heart failure with reserved ejection fraction	RT-100	Ad5.hAC6 Intracoronary injection	0	III	NCT03360448	Renova Therapeutics
n/a	07/2010 until 11/2017	Congestive heart failure	RT-100	Ad5.hAC6 Intracoronary injection	56	I and II	NCT00787059	Renova Therapeutics
AFFIRM	06/2021 until 12/2022	Refractory angina due to myocardial ischaemia[2]	Generx® (Alferminogene tadenovec)	Ad5FGF-4 Intracoronary infusion under transient ischaemia	160	III	NCT02928094	Angionetics Inc., Huapont Life Sciences
n/a	04/2018	Ischaemic heart disease		Ad-HGF Trans-endocardial injections	30	IIa	n/a	The First Affiliated Hospital with Nanjing Medical University
n/a	07/2017 (3-year study)	Severe CAD		Ad-HGF Intracoronary infusion	22	I	n/a	The First Affiliated Hospital with Nanjing Medical University
n/a	07/2008 (35-day and 11-14 month follow ups)	3-vessel CAD		Ad-HGF Intracoronary infusion	18	I	n/a	The First Affiliated Hospital with Nanjing Medical University

Abbreviations: VEGF-C, vascular endothelial growth factor-C; hAC6, human adenylyl cyclase 6; HGF, hepatocyte growth factor.

1.5.6 Pre-clinical evidence for efficacy of HAdV-5-based gene therapy in preventing vein graft NF

Although HAdV-5 vectors have been used in the clinical context of CAD and/or CHF, they have only been employed in pre-clinical studies of vein graft occlusion trials to date. These studies have shown that gene therapy is an attractive strategy to prevent experimental NF in rodent vascular injury models (Deguchi et al., 1999; Engelse et al., 2002; Kloppenburg et al., 2009; Wolff et al., 2006).

From a translational point of view, lumenal AdV-mediated transgene delivery to human SVGs may be achieved (Dakin et al., 2015) while the graft remains outside of the patient's body thereby eliminating off target effects. George *et al*. showed that RAdTIMP-3 (E1-deleted HAdV-5 expressing tissue inhibitor of metalloproteinase-3 from a CMV promoter) inhibited NF in *ex vivo* human pre-implantation SVG organ cultures and in porcine SVGs 28 days following carotid artery inter-position grafting, a translationally relevant large animal model of vein graft occlusion (George et al., 2000). A subsequent study by George *et al*. confirmed that *ex vivo* RAdTIMP-3 delivery to porcine SVGs reduced NF 3 months after carotid artery inter-positioning (George et al., 2011). This is a significant observation with the knowledge that transgene expression following first generation HAdV-5 delivery is typically lost by 21 days due to the host immune response (Yang et al., 1994) and suggests that early and acute intervention to prevent NF might be sustained. A Phase I/II clinical trial in CABG patients is planned.

1.6 Aims of the study

Systemic pharmacological and genetic ablation of ALK1-mediated SMAD1/5 signalling retards NF following experimental carotid artery injury in mice, indicating that ALK1 is pathogenic driver of NF. BMP-9 circulates in the blood and binds strongly to ALK1 thereby activating SMAD1/5 signalling in vascular ECs. Furthermore, de-regulation of BMP-9/ALK1 signalling is implicated in endothelial-driven vascular diseases such as HPAH or HHT. To date, the role of BMP-9 in SVG disease has not been investigated. TGF-β_1 induces ALK5/SMAD2/3 and lateral ALK1/SMAD1/5 signalling in vascular cells. To date, the role of TGF-β_1 in vascular injury-driven NF has been controversial with many studies demonstrating opposing results. Vascular SMC de-differentiation predominantly drives NF following vascular injury and, hence, this study aimed to explore BMP-9 and/or TGF-β_1-driven ALK1/ALK5 crosstalk and dependent downstream regulation of HSVSMC phenotypes in the context of SVG disease.

1.6.1 Aims

- To determine the presence of BMP-9 and SMC phenotype switching in human pre-implantation saphenous vein grafts and murine vascular injury models.

- To evaluate ALK1 and ALK5 driven regulation of HSVSMC phenotypes.

- To characterise single HSVSMC transcriptomes following BMP-9 and/or TGF-β_1 stimulation.

- To determine HAdV-5-mediated *ACVR2A* transgene delivery to primary HSVSMCs.

Chapter 2 Materials and Methods

2.1 Preparation of saphenous vein samples from CABG patients

Surplus pre-implantation saphenous veins from patients undergoing CABG surgery at the Golden Jubilee National Hospital in Glasgow (UK) were collected after ethical approval in collaboration with the NHS Greater Glasgow & Clyde Biorepository (REC reference 16/WS/0207; Bio-repository project reference 107). The study was authorised by the West of Scotland Research Ethics Committee 4 (reference number: 10/S0704/60) and conformed to the Declaration of Helsinki. Informed consent was obtained from each donor prior to surgery. Anthropometric donor characteristics of samples utilised for *ex vivo*/*in vitro* experiments are presented in Table 2-1.

Table 2-1 Summary of anthropometric donor characteristics

Anthropometric parameters	mean ± S.E.M (N=34)[1]	range
Male/female	17/8	
Age [years]	56.96 ± 2.75	31-82
[1] unable to establish authorisation for sharing characteristics for N=4 CABG patients, N=5 CABG patients withdrew consent for sharing donor characteristics.		

2.1.1 Human saphenous vein sample fixation

A section of surplus human saphenous vein (HSV) sample was placed in a 15 mL Universal tube (cat. no.: PF-SL-155254, Starlab, Germany) and fixed in 4% (w/v) PFA (cat. no.: 76240, Fluka, NJ, USA) at 4°C overnight (Table 2-2). The following day, samples were washed twice in sterile 1× PBS, placed in a 15 mL Universal tube with 70% (v/v) ethanol (cat. no.: E/0600DF/17, UN1170 Fisher Scientific, PA, USA) and stored at 4°C.

Table 2-2 Recipe for 1 L of 4% (w/v) PFA solution.

Reagent	Amount
PFA powder	40 g
sterile 1× PBS	1 L
Note: prepare on heat stirrer underneath sterile hood.	

2.2 Cell culture

2.2.1 Primary HSVSMC isolation and outgrowth

The remaining surplus HSV sample was placed in a sterile plastic petri dish in a cell culture hood. Superfluous tissue and surgical sutures were carefully removed using a pair of sterile scissors. Sample veins were cut open longitudinally and the EC layer was removed by gently rubbing down the vessel with a plunger from a 5 mL syringe (Injekt®-F Solo, B. Braun, Germany). The media was carefully pulled off the vessel by using a pair of sterile forceps and placed in a new sterile plastic petri dish containing wash medium Table 2-3.

Table 2-3 Wash medium composition.

Reagent	Volume
Minimal Essential Medium (cat. no.: 11090081, Thermo Fisher Scientific, MA, USA)	500 mL
HEPES (cat. no.: 75277-39-3, VWR International, PA, USA)	25 mM
L-glutamine (cat. no.: 25030081, Thermo Fisher Scientific, MA, USA)	2 mM
Sodium pyruvate (cat. no.: 11360070, Thermo Fisher, MA, USA)	100 nM
Penicillin/streptomycin (cat. no.: 15070063, Thermo Fisher Scientific, MA, USA)	5 mL (100 I.U/mL and 100 µg/mL)

Saphenous vein media was homogenised using a McIlwain tissue chopper (Ted Pella Inc., CA, USA) and transferred to a sterile 50 mL centrifuge tube (cat. no.: 430828, Corning Life Sciences, NY, USA) containing 40 mL wash medium. Floating tissue debris was removed by gently discarding the supernatant. Homogenised tissue was washed twice with wash medium and then covered in 15% (v/v) fetal calf serum (FCS) SMC growth medium (15% FCS media) (Table 2-4) for 5 min. Homogenised tissue was smeared onto the bottom of a T25 flask (cat. no.: CLS430639, Merck, Germany) using a 1 mL syringe. Excess 15% (v/v) FCS media was carefully removed and the T25 flask was placed in an incubator (37°C and 5% CO_2) overnight. The next day, 5 mL 15% (v/v) FCS media were added to the T25 flask. Upon achieving 90-100% confluence, primary HSVSMCs were transferred to a fresh T75 flask (cat. no.: CLS430641U, Merck, Germany).

Table 2-4 15% (v/v) FCS media smooth muscle cell growth medium composition.

Reagent	Volume
Smooth Muscle Cell Growth Medium 2 (cat. no. C-22262, PromoCell GmbH, Germany)	500 mL
Smooth Muscle Cell Growth Medium 2 SupplementMix (cat. no.: C-39267, PromoCell GmbH, Germany)	25 mL
L-glutamine	2 mM
FCS (cat. no.: 10500064, Thermo Fisher Scientific, MA, USA)	50 mL
Penicillin/streptomycin	5 mL (100 I.U/mL and 100 µg/mL)

2.2.2 Primary HSVSMC expansion and cryopreservation

Upon achieving 90-100% confluence, cells were expanded 1:3 until passage (P)4. 15% (v/v) FCS media was removed from the T75 flask and primary HSVSMCs were gently washed in 1× sterile Ca^{2+}-free phosphate buffered saline (PBS; NaCl 0.137 M, KCl 0.0027 M, Na_2HPO_4 0.01 M, KH_2PO_4 0.0018 M; cat. no.: 10010023, Thermo Fisher Scientific, MA, USA). 1× PBS was removed, 5 mL 1× sterile trypsin (cat. no.: 59427C, MilliporeSigma, MO, USA) were added and the T75 flask was placed in an incubator (37°C and 5% CO_2) for 5 min. 7 mL 15% (v/v) FCS media were added to the flask. The cell suspension was transferred to a sterile 50 mL centrifugation tube and subjected to centrifugation at 500 g and room temperature for 5 min. Supernatant was discarded and cells were re-suspended in 9 mL 15% (v/v) FCS media. 12 mL 15% (v/v) FCS media were added to each of 3 fresh T75 flasks. 3 mL cell suspension were added to each T75 flask (15 mL 15% (v/v) FCS media/flask). Flasks were gently swirled and placed in an incubator (37°C and 5% CO_2). All primary HSVSMC experiments were initiated at P5.

Whenever possible, early passaged primary HSVSMCs were subjected to cryopreservation (1 confluent T75 flask/2 mL cryopreservation vial). Early passaged primary HSVSMCs were detached from 1 T75 flask and pelleted as described above. Cells were re-suspended in 1 mL 15% (v/v) FCS media containing 10% (v/v) dimethyl sulfoxide (DMSO; cat. no.: D/4120/PB08, Thermo Fisher Scientific, MA, USA). The cell suspension was transferred to a sterile 2 mL cryopreservation tube (cat. no.: BCS-2502, Brooks Life Sciences, UK). Cells were gradually frozen down by submerging the cell suspension-containing cryopreservation vial in 100% (v/v) isopropanol (cat. no.: 24137, Honeywell

International Inc., NC, USA) and placing the submerged vial in a -80°C freezer for 24-h. The following day, the cryopreservation vial was transferred to a liquid nitrogen tank. Cryopreserved HSVSMCs were revived by rapid thawing in a 37°C water bath. 12 mL 15% (v/v) FCS media were added to a T75 flask. Upon thawing, 1 mL cell suspension from 3 cryopreservation vials (same passage, same donor) were added to the T75 flask. The following day, media was replaced with fresh 15% (v/v) FCS media and cells were cultured as described above.

2.2.3 Primary HCASMC expansion

Primary HCASMCs were obtained from Thermo Fisher Scientific (cat. no.: C0175C, MA, USA). One vial of cryopreserved primary HCASMCs was revived as described in section 2.2.2 and was added into 15 mL smooth muscle growth supplement (SMGS) medium (Table 2-5) in a T75 flask. Upon achieving 90-100% confluency, primary HCASMCs were expanded 1:3 as described in section 2.2.2. All experiments were performed between P5 and P8.

Table 2-5 SMGS medium composition.

Reagent	Volume
Medium 231 (cat. no.: M231500, Thermo Fisher Scientific, MA, USA)	500 mL
Smooth muscle growth supplement (cat. no.: S00725, Thermo Fisher Scientific, MA, USA), final concentration of components: 4.9% (v/v) FCS, human basic fibroblast growth factor (FGF) 2 ng/mL, human epidermal growth factor 0.5 ng/mL, heparin 5 ng/mL, recombinant human insulin-like growth factor-I 0.01 µg/mL, bovine serum albumin (BSA) 0.2 µg/mL	25 mL
Penicillin/streptomycin	5 mL (100 I.U/mL and 100 µg/mL)

2.2.4 SMDS-induced contractile differentiation protocol for primary human SMCs

This protocol was partially based on a study by Chen *et al.* (Chen et al., 2016b). Confluent primary HSVSMCs and HCASMCs intended for mRNA expression analysis were seeded into 12-well plates (cat. no.: 3513, Corning Life Sciences, NY, USA) (1×10^5/well, technical n=3/condition) and cells intended for protein expression analysis were seeded into 6-well plates (cat. no.: 3516, Corning Life Sciences, NY, USA) (1.5×10^5/well, technical n=3/condition).

Primary HSVSMCs were cultured in 15% (v/v) FCS media and upon achieving 80% confluence, cells were divided into 3 groups (Figure 2-1). To maintain proliferation, the first group was cultured in 15% (v/v) FCS media (Table 2-4). To induce contractile differentiation, the second group was cultured in smooth muscle differentiation supplement (SMDS) 231 medium (Table 2-6). The third group was cultured in SMGS 231 medium (Table 2-5). Primary HSVSMCs were lysed for RNA and/or protein extraction at indicated time points.

Table 2-6 SMDS medium composition.

Reagent	Volume
Medium 231	500 mL
Smooth muscle differentiation supplement (cat. no. S0085, Thermo Fisher Scientific, MA, USA), final concentration of components: 1% (v/v) FCS, heparin 30 µg/mL.	5 mL
Penicillin/streptomycin	5 mL (100 I.U/mL and 100 µg/mL)

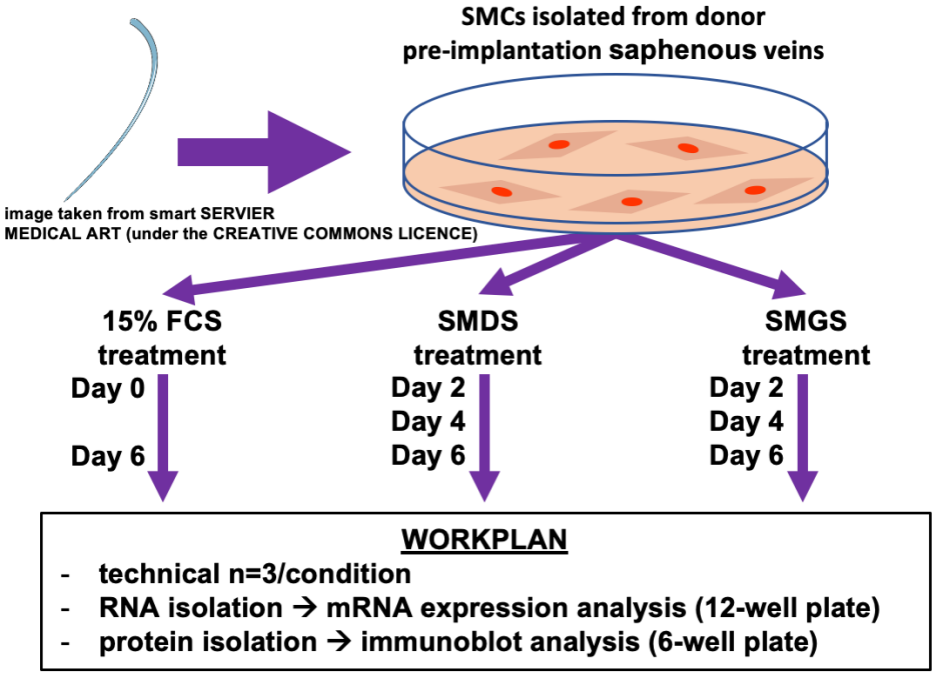

Figure 2-1 Workflow for SMDS-induced contractile differentiation of primary HSVSMCs. Primary SMCs were isolated from pre-implantation SVs from CABG patients and subjected to outgrowth. Upon achieving confluency, cells were seeded into 12-(mRNA expression) or 6-well plates (protein expression) and split into 3 treatment groups (group 1 → 15% (v/v) FCS media, group 2 → SMDS, group 3 → SMGS). Cells were lysed for RNA and/or protein extraction at indicated time points.

Primary HCASMCs were cultured in SMGS medium and upon achieving 80% confluency, cells were divided into 2 groups (Figure 2-2). To induce contractile SMC differentiation, the first group was cultured in SMDS medium (Table 2-6) and the second group was cultured in SMGS medium (Table 2-5). Primary HCASMCs were lysed for RNA and/or protein extraction at indicated time points.

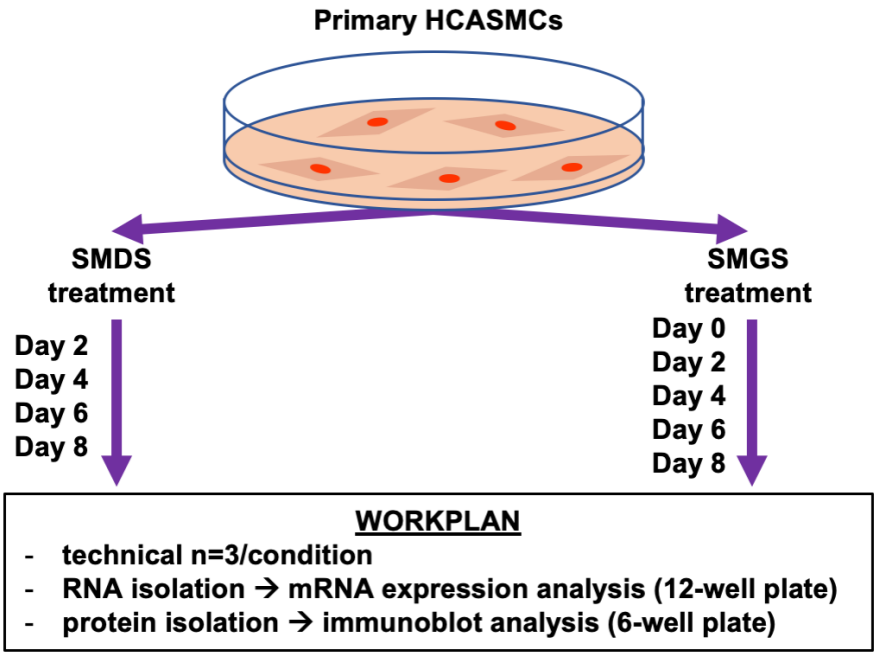

Figure 2-2 Workflow for SMDS-induced contractile differentiation of primary HCASMCs. Confluent primary HCASMCs were seeded into 12-(mRNA expression) or 6-well plates (protein expression) and split into 2 treatment groups (group 1 → SMDS, group 2 → SMGS). Cells were lysed for RNA and/or protein extraction at indicated time points.

2.2.5 Ligand stimulation in primary HSVSMCs

Confluent primary HSVSMCs intended for mRNA expression analysis were seeded into 12-well plates (1×10^5/well, technical n=3/condition) and cells intended for protein expression analysis were seeded into 6-well plates (1.5×10^5/well, technical n=3/condition). Upon achieving 80% confluence, 15% (v/v) FCS media was removed, and cells were starved in L-glutamine-free 0.2% (v/v) FCS starvation medium (SVM) (MEDIA1) for 72-h (Table 2-7) to achieve quiescence.

Cells intended for experiments including the pharmacological ALK5 inhibitor SB525334 (cat. no.: S8822, MilliporeSigma, MO, USA) were split into two groups of four (Figure 2-3). To achieve pharmacological ALK5 inhibition prior to ligand stimulation, the first 4 groups were incubated in MEDIA1 containing 10 μM SB525334 (dissolved in DMSO) vehicle) for 30 min. In parallel, the second 4 groups were incubated in MEDIA1 containing DMSO vehicle (1:1000) for 30 mins. Following this incubation step, medium was replaced with fresh MEDIA1 containing recombinant human (rh) BMP-9 (10 ng/mL) (dissolved in 4 mM HCl containing 1% (w/v) BSA, cat. no.: 3209-BP-010, R&D Systems, MN, USA), rh TGF-β_1 (10 ng/mL) (dissolved in 4 mM HCl containing 1% (w/v) BSA, cat. no.: 240-B-010, R&D Systems, MN, USA), both ligands and vehicle control (4 mM HCl/1% (w/v) BSA) ± DMSO (1:1000) or SB525334 (10 μM). After 24-h stimulation, primary HSVSMCs were either lysed and subjected to RNA and/or protein extraction or utilised for Ca^{2+} handling studies.

Table 2-7 SMC starvation medium composition (without L-glutamine) (MEDIA1).

Reagent	Volume
DMEM (cat. no.: 21969035, Thermo Fisher Scientific, MA, USA)	500 mL
FCS	1 mL
Penicillin/streptomycin	5 mL (100 I.U/mL and 100 μg/mL)

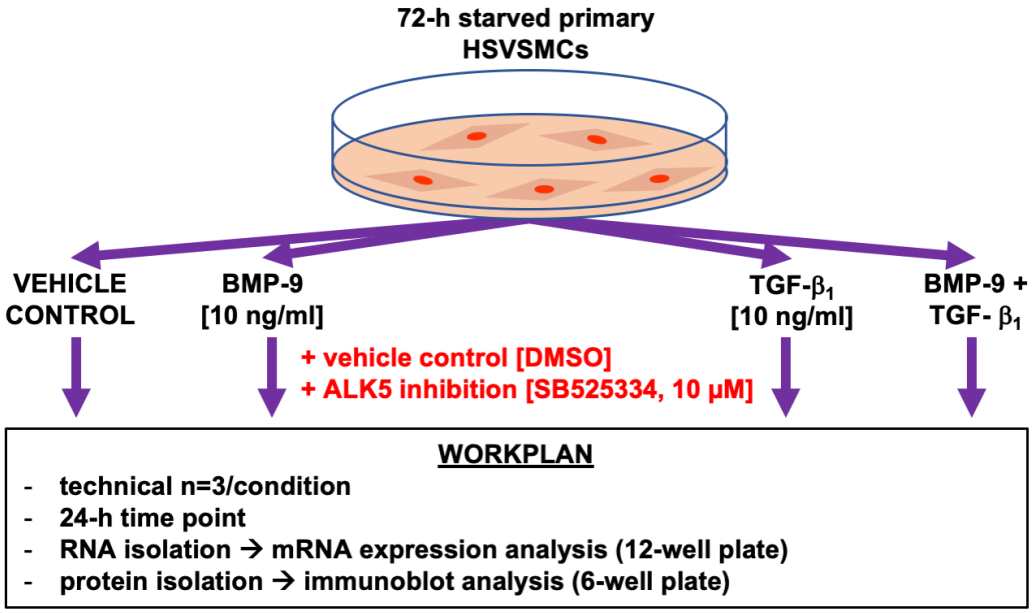

Figure 2-3 Workflow for ligand stimulation experiments in primary HSVSMCs. Confluent primary HSVSMCs were seeded into 12-(mRNA expression) or 6-well plates (protein expression). Upon achieving 80% confluence, cells were quiesced for 72-h. Cells were subsequently incubated in medium containing BMP-9, TGF-β_1, both ligands or vehicle control (4 mM HCl/1% (w/v) BSA) ± 30-min pre-incubation in SB525334 or vehicle control (DMSO). Cells were lysed for RNA and/or protein extraction following 24-h stimulation.

2.2.6 HAdV-5-mediated *ACVR2A* delivery to primary HSVSMCs

Confluent primary HSVSMCs (P4) were seeded into 12-well plates (1×10^5/well, technical n=3/condition) and cultured in 15% (v/v) FCS media. Upon achieving 80% confluence, cells were divided into 2 main groups (Figure 2-4). Cells intended for virus-mediated transgene delivery were transduced with an increasing amount of HAdV-5 GFP and HAdV-5 ACVR2A (2.9) (1,000 viral particles (VP), 5,000 VP and 10,000 VP/cell) in 15% (v/v) FCS media overnight. Cells intended for mock control treatment were also cultured in 15% (v/v) FCS media overnight. The next day, one set of mock 15% (v/v) FCS media-treated cells were lysed and subjected to RNA extraction. Non-virus and virus-containing 15% (v/v) FCS media was replaced with fresh non-virus containing 15% (v/v) FCS media and SMDS media. Following 24-h incubation, HAdV-5 GFP-transduced HSVSMCs were imaged on a fluorescence/brightfield microscope at 10× magnification to determine the efficiency of virus-mediated transgene delivery. Following 48-h incubation, cells were lysed and subjected to RNA extraction.

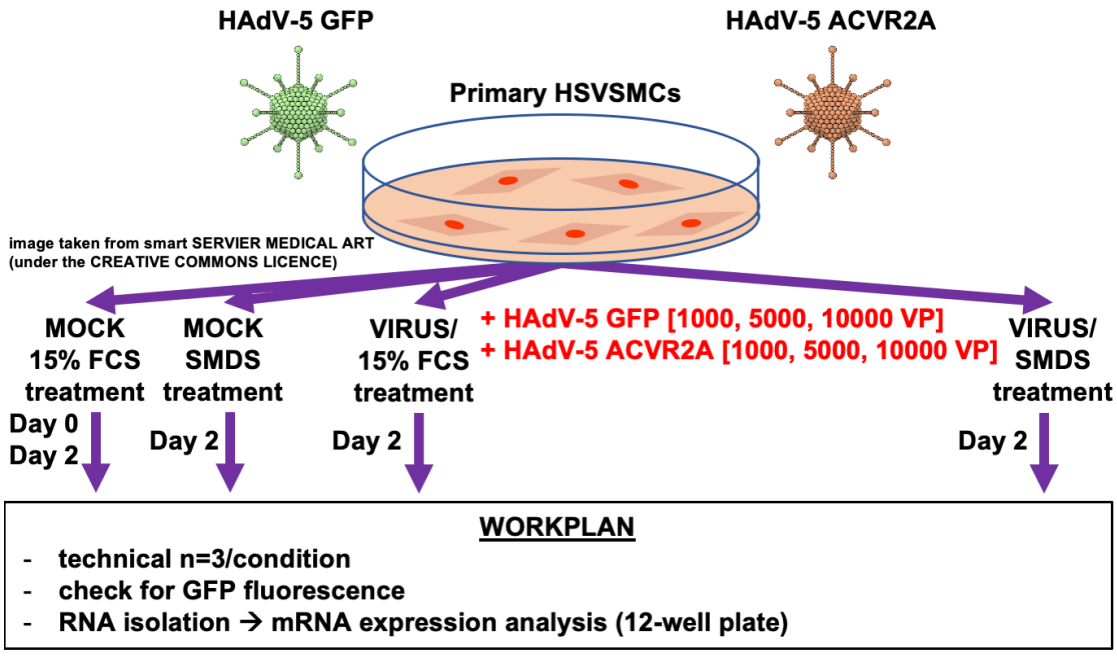

Figure 2-4 Workflow for HAdV-5-mediated *ACVR2A* transgene delivery. Confluent primary HSVSMCs were seeded into 12-well plates. Upon achieving 80% confluence, cells were divided into 2 main groups (mock/no virus vs virus transduction). The virus group was transduced with indicated HAdV-5 GFP or HAdV-5 ACVR2A VPs in 15% (v/v) FCS media overnight. The mock group remained in fresh 15% (v/v) FCS media overnight. The next day, virus- and non-virus containing medium was replaced with fresh non-virus containing 15% (v/v) FCS media or SMDS medium. GFP fluorescence was determined at 24-h. 48-h post transduction, cells were lysed for RNA extraction.

2.2.7 HEK293 cell expansion

HEK293 cells were already available and cultured in T150 flasks (cat. no.: CLS430825, Merck, Germany) containing 25 mL of HEK293 medium (Table 2-8) in an incubator (37°C and 5% CO_2). 1 vial of cryopreserved HEK293 cells was revived as described in section 2.2.2 and added to a T150 flask containing 25 mL HEK293 medium. Upon achieving 90% confluence, 1 T150 flask was expanded 1:5. Growth medium was removed, and cells were washed in 1× sterile Ca^{2+}-free PBS. PBS was removed, and 5 mL 1× sterile citric saline was added to the T150 flask to induce cell detachment. The flask was placed in an incubator (37°C and 5% CO_2) for 5 minutes. 7 mL HEK293 medium were added to the T150 flask. The cell suspension was transferred to a sterile 50 mL centrifugation tube and subjected to centrifugation at 500 g for 5 min. The supernatant was discarded, and cells were re-suspended in fresh 15 mL HEK293 medium. 22 mL HEK293 medium was added to each of 5 fresh T150 flasks and 3 mL cell suspension was added to each T150 flask. Flasks were placed in an incubator (37°C and 5% CO_2).

Table 2-8 HEK293 medium composition.

Reagent	Volume
Minimal Essential Medium	500 mL
FCS	50 mL
Sodium pyruvate	100 nM
L-Glutamine	2 mM
Penicillin/streptomycin	5 mL (100 I.U/mL and 100 µg/mL)

2.3 Gene expression analysis

2.3.1 RNA extraction, purification and quantification

RNA extraction was performed using the miRNeasy Mini Kit (cat. no.: 217004, Qiagen, Netherlands) following the manufacturer's instructions.

In brief, culture medium was removed, and cells were washed once in ice cold sterile 1× PBS. PBS was discarded and 700 µL Qiazol Lysis reagent were added to

each well underneath a hood. Each well was scratched with the top of a sterile 1,000 μL pipette tip to ensure efficient cell lysis. Lysis reagent containing lysed cells was transferred to a sterile RNase-free 1.5 mL microcentrifuge tube and 140 μL chloroform (cat. no.: C/4960/17, Thermo Fisher Scientific, MA, USA) were added to each sample. Microcentrifuge tubes were shaken for 15 s and left to incubate at room temperature for 3 min. Centrifugation was performed at 12,000 g and 4°C for 15 min. The RNA-containing upper aqueous phase was transferred to a fresh 1.5 mL sterile RNase-free microcentrifuge tube and 525 μL 100% (v/v) ethanol were added to each sample. The solution was gently mixed by pipetting up and down several times and transferred onto a fresh RNeasy Mini-spin column. Centrifugation was performed at 8,000 g and room temperature for 15 s. The flow-through was discarded and 350 μL RWT buffer were added onto the column. Centrifugation was performed at 8,000 g and room temperature for 15 s. The flow-through was discarded and 80 μL DNase/buffer solution (10 μL DNase + 70 μL Buffer RDD per sample) were added onto the column and left to incubate at room temperature for 15 min. 350 μL RWT buffer were added onto the column. Centrifugation of the column was performed at 8,000 g and room temperature for 15 s and the flow-through was discarded. 500 μL RPE buffer were added onto the column, centrifugation of the column was performed at 8,000 g and room temperature for 15 s and the flow-through was discarded. 500 μL RPE buffer were added onto the column and centrifugation was performed at 8,000 g and room temperature for 2 min and the flow-through was discarded. The RNeasy column was placed on a fresh sterile RNase-free 2 mL collection tube. Centrifugation was performed at full speed and room temperature for 1 min. The RNeasy column was placed on a fresh sterile RNase-free 1.5 mL microcentrifuge tube and 30 μL RNase-free H_2O were added onto the column to elute the RNA. Centrifugation of the column was performed at 8,000 g and room temperature for 1 min.

RNA concentrations for each sample were determined using the NanoDrop™ 1000 spectrophotometer (Thermo Fisher Scientific, MA, USA). The RNA concentration for each sample was calculated utilising Beer's Law.

$c = A/(E*b)$

A = absorbance (represented in absorbance units), E = wavelength-dependent molar absorptivity (extinction co-efficient in L/(mol-cm)), b = path length in cm, c = sample concentration in moles/L. The 260/280 nm and the 260/230 nm ratios were calculated to determine RNA purity. A 260/280 ratio of $\geq$ 2.0 and a 260/230 ratio between 1.8-2.2 generally reflect pure RNA. RNA samples were either directly subjected to complementary c(DNA) synthesis or stored at -80°C.

2.3.2 Reverse transcription reaction

The reverse transcription reaction was performed for each RNA sample to generate cDNA. RNA samples were diluted in RNase-free H_2O to a final concentration of 100 ng/10 µL in a sterile RNase-free 96-well plate (cat. no.: E1403-5200, Starlab, Germany) on ice as outlined in Table 2-9.

Table 2-9 RNA sample preparation for reverse transcription reaction.

Reagent	Volume
RNA sample (diluted in RNase-free H_2O)	x µL (equals 100 ng)
RNase-free H_2O	x µL
Note: total volume **10 µL**/sample, add 2 negative controls for each 96-well plate → 1 RNase-free H_2O control with reverse transcriptase and 1 RNA sample control without reverse transcriptase.	

The reverse transcription master mix was prepared as outlined in Table 2-10.

Table 2-10 Reverse transcription master mix.

Reagent	Volume
SuperScript™ II Reverse Transcriptase 10 U/μL (cat. no.: 18064022, Thermo Fisher Scientific, MA, USA)	1 μL
5× SuperScript™ II buffer (supplied with SuperScript™ II Reverse Transcriptase, Thermo Fisher Scientific, MA, USA)	4 μL
Deoxynucleotides (dNTPs; cat. no.: N0447S, New England BioLabs® Inc. (NEB), MA, USA)	1 μL
Random hexamers (cat. no.: SO142, Thermo Fisher Scientific, MA, USA)	1 μL
Dithiothreitol 5 mM (DTT; (supplied with SuperScript™ II Reverse Transcriptase, Thermo Fisher Scientific, MA, USA)	1 μL
RNase inhibitor (cat. no.: N8080119, Thermo Fisher Scientific, MA, USA)	0.5 μL
RNase-free H_2O	1.5 μL
Note: total volume **10 μL**/sample	

The 96-well plate was sealed (cat. no.: ZLAB0558, Thermo Fisher Scientific, MA, USA), placed on the MJ Research Tetrad PTC-225 Thermal Cycler (Global Medical Instrumentation Inc, MN, USA) and the outlined thermal cycling programme was initiated (denaturation: 10 min at 70°C; add reverse transcription master mix: 10 min at 4°C; primer binding: 10 min at 25°C; elongation: 60 min at 42°C; enzyme inactivation: 15 min at 72°C). Following the denaturation step, the 96-well plate was briefly removed and 10 μL reverse transcription master mix were added to each sample bringing the total volume up to 20 μL per sample. Each sample was mixed by gently pipetting up and down several times. The 96-well plate was sealed and placed back into the thermal cycler.

Following completion of the reverse transcription programme, the 96-well plate was removed, and each cDNA sample was diluted by adding 80 μL RNase-free H_2O. Samples were either directly subjected to quantitative real-time polymerase chain reaction (qRT-PCR) analysis or stored at -20°C.

2.3.3 TaqMan™ quantitative real-time polymerase chain reaction

Relative mRNA expression levels of target genes were determined by TaqMan™qRT-PCR analysis utilising custom-made TaqMan™ gene expression assays

(Table 2-12 and Table 2-13). Each TaqMan™ gene expression assay consists of a forward primer, a reverse primer and a complementary probe which contains a fluorophore (FAM® or VIC®) attached to the 5'-end and a quencher attached to the 3'-end. Each qRT-PCR reaction was prepared in duplicate in a sterile RNase-free 384-well plate (cat. no.: 4309849, Thermo Fisher Scientific, MA, USA) on ice as outlined in Table 2-11. The RNase-free H_2O control (+ reverse transcriptase) and the RNA control (- reverse transcriptase) served as negative controls for each TaqMan™ qRT-PCR experiment.

Table 2-11 TaqMan™ qRT-PCR reaction mix.

Reagent	Volume
TaqMan™ Universal MasterMix II (cat. no.: 4440040, Thermo Fisher Scientific, MA, USA)	5 μL
Respective Thermo Fisher Scientific TaqMan™ probe (MA, USA)	0.5 μL
cDNA sample	2.5 μL
RNase-free H_2O	2 μL
Note: total volume **10 μL**/sample	

The 384-well plate was sealed and placed in the QuantStudio™ 12K Flex Real-Time PCR System (Thermo Fisher Scientific, MA, USA). Each Taqman™ qRT-PCR experiment was performed utilising the following thermal cycling programme: hold: 2 min at 50°C; hold: 10 min at 95°C, 40 cycles: 15 s at 95°C followed by 1 min at 60°C.

The threshold cycle (Ct) was utilised to determine relative mRNA expression levels of target genes in each sample. The Ct is the number of cycles necessary for probe-mediated fluorescent signals to cross the background level. Whereas low Ct values are indicative of high relative mRNA expression levels, high Ct values reflect low relative mRNA expression levels. Normalisation was performed by subtracting housekeeping gene polyubiquitin-c (*UBC*) Ct values from respective target gene Ct values thereby generating delta Ct (ΔCt) values. ΔCt values were subjected to fold change/relative quantification (RQ) transformation ($RQ = 2^{-\Delta\Delta Ct}$, ΔΔCt = target ΔCt – control ΔCt).

Table 2-12 List of Thermo Fisher Scientific TaqMan™ gene expression assays (part 1).

Gene abbreviation	Gene name	cat. no.
UBC	Polyubiquitin-C	Hs01871556_s1
aSMA	α-smooth muscle actin	Hs00426835_g1
CNN1	Calponin	Hs200959434_m1
MYH11	Myosin heavy chain 11	Hs00975796_m1
SM22-a	Smooth muscle protein 22-α	Hs1038777_g1
SERPINE1	Plasminogen activator inhibitor-1	Hs00167155_m1
ID1	Inhibitor of differentiation-1	Hs03676575_s1
AGTR1	Angiotensin II type 1 receptor	Hs00258938_m1
AGTR2	Angiotensin II type 2 receptor	Hs03987590_g1
MAS1	Mas proto-oncogene	Hs00267157_s1
SP7	Osterix	Hs01866874_s1
ALPL	Alkaline phosphatase	Hs01029144_m1
LGALS3	Galectin-3	Hs00173587_m1
CD68	Cluster of differentiation 68	Hs02836816_g1
PCNA	Proliferating cell nuclear antigen	Hs00427214_g1
CCND1	Cyclin D1	Hs00765553_m1
CDKN1A	Cyclin-dependent kinase inhibitor 1	Hs00355782_m1

Table 2-13 List of Thermo Fisher Scientific TaqMan™ gene expression assays (part 2).

Gene abbreviation	Gene name	cat. no.
ALK5	Activin receptor-like kinase 5	Hs00610320_m1
ALK1	Activin receptor-like kinase 1	Hs00953798_m1
ALK2	Activin receptor-like kinase 2	Hs00153836_m1
TGFBR2	TGF-β receptor 2	Hs00234253_m1
BMPR2	BMP receptor type 2	Hs00176148_m1
ACVR2A	Activin A receptor type 2A	Hs00155658_m1
ACVR2B	Activin A receptor type 2B	Hs00609603_m1

2.4 Protein expression analysis

2.4.1 Cell lysis

Cell lysis was performed on ice. Culture medium was removed, and cells were washed once in ice cold sterile 1× PBS. PBS was discarded and 70 µL of ice cold radioimmunoprecipitation assay (RIPA) buffer (Table 2-14) supplemented with protease and phosphatase inhibitors were added to each well. Each well was scratched with the base of a 1,000 µL pipette tip to ensure cell lysis. Protein lysates from 3 wells (technical n=3) were pooled, transferred to a sterile 1.5 mL microcentrifuge tube and centrifuged at maximum speed and 4°C for 1 min. The supernatant was transferred to a fresh sterile 1.5 mL microcentrifuge tube and placed on ice. Protein samples were either directly subjected to BCA reactions or stored at -20°C.

Table 2-14 Recipe for 100 mL RIPA buffer (pH 8.8).

Reagent	Amount
Tris-HCl (cat. no.: 15506017, Thermo Fisher Scientific, MA, USA)	50 mM
NaCl (cat. no.: X190, VWR International, PA, USA)	150 mM
Ethylenediaminetetraacetic acid (EDTA; cat. no.: 15576-028, Thermo Fisher Scientific, MA, USA)	1 mM
Triton™ X-100 (cat. no.: 9002-93-1, MilliporeSigma, MO, USA)	1 mL
Sodium dodecyl sulfate (cat. no.: BP166-500, Thermo Fisher Scientific, MA, USA)	0.1 g
Sodium deoxycholate (cat. no.: D6750, MilliporeSigma, MO, USA)	0.5 g
ddH_2O	100 mL
Note: pH to 8.8. For each use, add ½ tablet cOMPLETE protease inhibitor (cat. no.: 11873580001, Roche, Switzerland) and 50 µL phosphatase inhibitor (cat. no.: P0044, MilliporeSigma, MO, USA) to 5 mL RIPA buffer.	

2.4.2 Determining protein sample concentration

Sample protein concentration was determined utilising the Pierce™ BCA Protein Assay kit (cat. no.: 23227, Thermo Fisher Scientific, MA, USA) following the manufacturer's instructions.

In brief, BSA standards were prepared via serial dilution in sterile 1× PBS (range: 25 – 2000 µg/mL). Sterile 1× PBS was used as a blank control (0 µg/mL). Next, 10 µL of each respective standard were pipetted into duplicate wells of a clear, flat-bottomed 96-well plate. Next, 10 µL of each respective protein sample were pipetted into remaining wells (one well per sample). The working BCA solution was made up by mixing 1 part of Reagent B with 50 parts of Reagent A in a 15 mL centrifuge tube (cat. no.: 430790, Corning Life Sciences, NY, USA). 150 µL working BCA solution were gently added to each well. The 96-well plate was gently tapped to ensure mixing and left to incubate in the dark at 37°C for 30 min. Following 30-min incubation, the 96-well plate was placed into the Wallac 1420 Victor2 Microplate Reader (LabMakelaar Benelux B.V., Netherlands) and absorbance was determined at 562 nm. Blank control absorbance was subtracted from each sample to adjust for background and duplicate readings for each standard were averaged to generate a standard curve. Unknown protein sample

concentrations were calculated using the linear equations based on this standard curve.

2.4.3 Protein sample preparation for SDS-PAGE and immunoblotting

Protein samples (total volume: 45 µL) were prepared in a sterile 96-well plate (protein sample: x (equals 20 µg); sterile 1× PBS: x µL; 4× NuPAGE™ LDS Sample Buffer (cat. no.: NP0007, Thermo Fisher Scientific, MA, USA): 9 µL). Following preparation, the 96-well plate was sealed and placed on the MJ Research Tetrad PTC-225 Thermal Cycler to enable denaturation at 95°C for 5 min.

2.4.4 Immunoblot analysis

First, 45 µL denatured protein sample were gently loaded into one well of a 12-well NuPAGE™ 4-12% Bis-Tris resolving gel (cat. no.: WG1401BOX, Thermo Fisher Scientific, MA, USA) and separated in 1× NuPAGE™ MES SDS running buffer (cat. no.: NP002, Thermo Fisher Scientific, MA, USA) at room temperature and 120 V for approximately 2 h. 2.5 µL Chameleon Duo protein ladder (cat. no.: 928-60000, LI-COR Biosciences, NE, USA) were added to each gel as a protein size reference. Following separation, protein transfer from the pre-cast gel onto Amersham™ Protran™ 0.2 µm nitrocellulose membrane (cat. no.: GE10600001, Merck, Germany) was achieved via electroelution in 1× transfer buffer (Table 2-15) at 4°C and 100 V for 90 min.

Table 2-15 Recipe for 1× transfer buffer.

Reagent	Amount
Tris-base (cat. no.: BP152-1, Thermo Fisher Scientific, MA, USA)	6.06 g
Glycine (cat. no.: BP381-1, Thermo Fisher Scientific, MA, USA)	28.8 g
ddH_2O	1,600 mL
Methanol (cat. no.: M/4056/17, Thermo Fisher Scientific, MA, USA)	400 mL

Following protein transfer, each nitrocellulose membrane was subjected to Ponceau staining (Table 2-16) to ascertain successful transfer.

Table 2-16 Recipe for Ponceau stain.

Reagent	Amount
Ponceau S tetrasodium salt (cat. no.: 14330, Cayman Chemical, MI, USA)	0.5 g
Acetic acid (cat. no.: 20104.323, VWR International, PA, USA)	25 mL
ddH_2O	475 mL
Note: add 25 mL acetic acid to 400 mL ddH_2O, add 0.5 g ponceau S tetrasodium salt to acetic acid/ddH_2O solution, top up to 500 mL with ddH_2O.	

Following Ponceau staining, each nitrocellulose membrane was placed into a plastic trough and washed in sterile 1× PBS on a shaker at room temperature for 5 min. PBS was discarded and depending on the primary antibodies (Table 2-17), membranes were either blocked in 1× TBS 0.05% (v/v) Tween (Table 2-47)/SEA BLOCK (cat. no.: 37527, Thermo Fisher Scientific, MA, USA) 1:1 or 1× TBS 0.05% (v/v) Tween/3% (w/v) BSA on a shaker at room temperature for 1 h. Membranes were incubated with respective primary antibodies diluted in respective blocking buffer in sealed plastic bags on a shaker at 4°C overnight. The next day, membranes were subjected to 3 5-min washes in 1× TBS 0.05% (v/v) Tween on a shaker at room temperature. Membranes intended for αSMA, calponin and SM22-α protein expression analysis were incubated with a secondary fluorescently conjugated goat anti-rabbit IgG antibodies (IgG Alexa Fluor® 680, 2 mg/mL, 1:15,000, cat. no.: A-21109, Thermo Fisher Scientific, MA, USA) in 1× TBS 0.05% (v/v) Tween/SEA BLOCK 1:1 on a shaker protected from light at room temperature for 1 h. Membranes intended for pMLC9 and tMLC9 protein expression analysis were incubated with the same secondary antibodies (1:5,000) in 1× TBS 0.05% (v/v) Tween on a shaker protected from light at room temperature for 1 h. Membranes were subjected to 3 5-min washes in 1× TBS 0.05% (v/v) Tween on a shaker protected from light at room temperature. Membranes were visualised utilising the LI-COR system (model: ODYSSEY CLx, LI-COR Biosciences, NE, USA).

Table 2-17 List of primary antibodies for immunoblot analysis.

Protein	Source	Clonality	Conc [mg/mL]	Working dilution, blocking buffer	cat. no. / company
αSMA	Rabbit	Polyclonal	0.2	1:500, 1× TBS 0.05% (v/v) Tween/SEA BLOCK	ab5694, abcam®, UK
Calponin	Rabbit	Monoclonal	0.063	1:2,000, 1× TBS 0.05% (v/v) Tween/SEA BLOCK	ab46794, abcam®, UK
SM22-α	Rabbit	Polyclonal	1	1:1,000, 1× TBS 0.05% (v/v) Tween/SEA BLOCK	ab14106, abcam®, UK
pMLC9	Rabbit	Polyclonal	1	1:1,000, 1× TBS 0.05% (v/v) Tween/3% (w/v) BSA	ab2480, abcam®, UK
tMLC9	Rabbit	Polyclonal	unknown	1:1,000, 1× TBS 0.05% (v/v) Tween/3% (w/v) BSA	PA5-17624, Thermo Fisher Scientific, MA, USA
GAPDH	Rabbit	Polyclonal	unknown	1:3,000, 1× TBS 0.05% (v/v) Tween/SEA BLOCK	STJ97090, St John's Laboratory Ltd,, UK

Following visualisation, membranes were placed in plastic troughs on a shaker and stripped in 200 mM sodium hydroxide solution (Table 2-18) at room temperature for 20 min. Membranes were re-blocked in 1× TBS 0.05% (v/v) Tween/SEA BLOCK 1:1 at room temperature for 1 h and subsequently incubated with an anti-glyceraldehyde 3-phosphate dehydrogenase (GAPDH) antibodies in 1× TBS 0.05% (v/v) Tween/SEA BLOCK 1:1 in sealed plastic bags on a shaker at 4°C overnight. The next day, membranes were subjected to 3 5-min washes in 1× TBS 0.05% (v/v) Tween on a shaker at room temperature and subsequently incubated with the secondary fluorescently conjugated goat anti-rabbit IgG antibodies (1:15,000) in 1× TBS 0.05% (v/v) Tween/SEA BLOCK 1:1 on a shaker protected from light at room temperature for 1 h. Membranes were subjected to 3 5-min washes in 1× TBS 0.05% (v/v) Tween on a shaker at room temperature protected from light and subsequently visualised. Band intensities were quantified by densitometry using the Image Studio Lite Ver 5.2 software (LI-COR Biosciences, NE, USA). Target protein expression was normalised to housekeeper

GAPDH expression ([target protein]/[GAPDH]). The constant 1 was added to each value prior to $\log_{10}$ transformation. Log_{10}-transformed values were subjected to statistical analyses.

Table 2-18 Recipe for stripping buffer.

Reagent	Amount
Sodium hydroxide (cat. no.: 1310-73-2, Thermo Fisher Scientific, MA, USA)	2 pellets
ddH_2O	50 mL

2.5 Scratch assay

Prior to seeding primary HSVSMCs into 12-well plates (1×10^5 cells/well, technical n=3/condition) in 15% FCS media, 3 equally distanced lines were drawn with a marker pen on the back of each plate (Figure 2-5).

Upon achieving 80% confluence, cells were quiesced in L-glutamine-free SVM for 72-h. Following quiescence, a scratch was performed down the middle of each well using the tip of a sterile 200 µL pipette tip (cat. no.: Z365688, MilliporeSigma, MO, USA). Next, L-glutamine-free SVM was gently replaced with stimulation medium. Scratches were imaged at 3 locations on the EVOS microscope (Thermo Fisher Scientific, MA, USA) at 10× magnification (0-h time point). Following a 20-h stimulation period, the same 3 locations were imaged again. For each image, distances between 10 points along both edges were measured using the ImageJ software. Values were expressed as % closure of the scratch compared to the 0-h baseline distance.

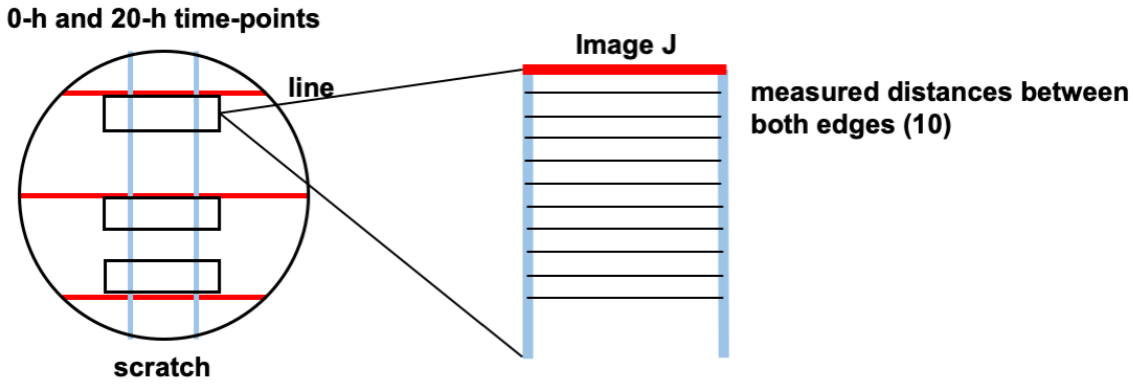

Figure 2-5 Scratch closure quantification. Scratches were imaged at 10× magnification at the same 3 locations at 0 and 20 h (left image → pre-drawn equally distanced lines on back of 12-well plate). Distances between scratches were measured between 10 pre-defined points at each of the 3 locations using the ImageJ software (right image). Values were averaged (30 points/scratch) for each treatment group and time point. Scratch closure at 20 h was expressed as % closure compared to 0-h baseline.

2.6 BrdU proliferation assay

5-bromo-2'-deoxyuridine (BrdU) proliferation assays (cat.no.: 2750, Merck, Germany) were performed following the manufacturer's instructions. Primary HSVSMCs were seeded into 96-well plates (1×10^4 cells/well, technical n=5/condition) and cultured in 100 µL 15% (v/v) FCS media. Upon achieving 80% confluence, respective experiments were initiated. For ligand stimulation experiments, cells were cultured in SMC starvation medium containing L-glutamine (Table 2-19).

Table 2-19 SMC starvation medium composition (with L-glutamine) (MEDIA2).

Reagent	Volume
DMEM (cat. no. 21969035, Thermo Fisher Scientific, MA, USA)	500 mL
FCS	1 mL
L-glutamine	2 mM
Penicillin/streptomycin	5 mL (100 I.U/mL and 100 µg/mL)

2.6.1 BrdU incorporation and cell fixation/denaturation

Depending on the experimental set-up, BrdU was incorporated (1:2,000, **final volume 100 µL**/well) either 24 or 48-h prior to termination of the experiment. At least one set of cells was not loaded with BrdU, and 5 wells remained without cells filled with medium only for background correction. Following each respective period, stimulation medium was removed, and cells were fixed in 70 µL ready-made fixing/denaturing solution at room temperature for 30 min. The fixing/denaturing solution was aspirated, and 96-well plates were patted dry. Plates were either directly subjected to BrdU ELISA analysis or stored in a heat-sealed plastic bag protected from light at 4°C for up to a week.

2.6.2 BrdU ELISA analysis

The required amount of 1× washing buffer (1:50 dilution in ddH_2O) was made up prior to performing BrdU ELISA analyses. 96-well plates were subjected to 3 washes with 1× washing buffer (200 µL/well). 50 µL ready-made BrdU detection antibodies were added to each well and plates were left to incubate on a shaker

at room temperature protected from light for 1-h. Plates were again subjected to 3 washes with 1× washing buffer (200 µL/well). The secondary antibodies were made up in ready-made conjugate diluent (1:2,000 solution) and sterile filtered. 50 µL secondary antibody solution were added to each well and plates were left to incubate on a shaker at room temperature protected from light for 30 min. Plates were again subjected to 3 washes with 1× washing buffer (200 µL/well) and 1 final wash with ddH_2O (flood the plate). Plates were patted dry prior to incubation with ready-made substrate solution (50 µL/well) at room temperature protected from light for 30 min and 50 µL ready-made stop solution were added to each well. The 96-well plate was placed into a Wallac 1420 Victor2 Microplate Reader and absorbance was determined at 450 nm. All absorbance values were corrected for background intensity by subtracting the mean background values derived from unloaded cells from target values.

2.7 Calcium handling studies

Primary human SMCs were seeded into 12-well plates (1×10^5 cells/well, technical n=3/condition). Primary HSVSMCs were cultured in 15% (v/v) FCS media medium and primary HCASMCs were cultured in SMGS medium. Upon achieving 80% confluence, HSVSMCs were quiesced in MEDIA1 (Table 2-7) and HCASMCs were quiesced in MEDIA2 (Table 2-19). Quiescence media was removed, and SMCs were stimulated with respective ligands/pharmacological inhibitors (see section 2.2.5) in respective quiescence media.

Following 24-h, stimulation medium was replaced with 400 µL 0.5% (v/v) FCS HEPES medium (Table 2-20) containing 2 µM single wave Ca^{2+} indicator Cal-520 (dissolved in DMSO, cat. no.: ab171868, abcam®, UK). Cells were left to incubate at 37°C and 5% CO_2 protected from light for 75 min. Cal-520-containing medium was removed and cells were gently washed once with Ca^{2+}-free 0.1 mM ethylene glycol-bis(β-aminoethyl ether)-N,N,N',N'-tetraacetic acid (EGTA) HEPES solution (Table 2-21). Cells were incubated in 800 µL Ca^{2+}-free 0.1 mM EGTA HEPES solution and left to equilibrate at room temperature protected from light for 25 min. For pharmacological inhibitor studies, cells were incubated with 800 µL Ca^{2+}-free 0.1 mM EGTA HEPES solution containing 10 µM losartan (dissolved in sterile ddH_2O, cat. no.: 61188, MilliporeSigma, MO, USA), 10 µM fasudil (dissolved in sterile ddH_2O, cat. no.: CDS021620, MilliporeSigma, MO, USA) or

vehicle control (sterile ddH_2O) at room temperature protected from light for 25 min.

Following equilibration, 12-well plates were imaged (Excitation/Emission (Ex/Em) 490/525 nm) on a live-cell microscope (Zeiss, Germany) at 10× magnification. Each well was imaged for 6 min. Cells were left to equilibrate for 2 min. At 2 min, 100 µL Ca^{2+}-free 0.1 mM EGTA HEPES solution containing AngII (cat. no.: A9525, MilliporeSigma, MO, USA) were added into respective wells (final concentration → **1 µM** AngII) to induce intracellular Ca^{2+} release and a subsequent increase in fluorescence intensity mediated by Cal-520/Ca^{2+} ion interaction. At 4 min, 100 µL Ca^{2+}-free 0.1 mM EGTA HEPES solution containing ionomycin (IM, cat. no.: I0634, MilliporeSigma, MO, USA) were added into respective wells (final concentration → **1 µM** IM) to induce maximum intracellular Ca^{2+} release by puncturing all cellular membranes (Beeler et al., 1979). At 6 min, the trace was terminated.

Table 2-20 HEPES medium composition for Ca^{2+} handling studies.

Reagent	Volume
DMEM, low glucose, pyruvate, HEPES medium (cat. no.: 22320-022, Thermo Fisher Scientific, MA, USA)	500 mL
FCS	2.5 mL
Penicillin/streptomycin	5 mL (100 I.U/mL and 100 µg/mL)

Table 2-21 Recipe for 1× Ca^{2+}-free 0.1 mM EGTA-containing HEPES solution.

Reagent	Amount [g]
NaCl	7.6 (130 mM)
KCl (cat. no.: 26752.366, VWR International, PA, USA)	0.373 (5 mM)
$MgCl_2$ hexahydrate (cat. no.: 0288, VWR International, PA, USA)	0.203 (1 mM)
HEPES	4.77 (20 mM)
D-glucose (cat. no.: 15023021, Thermo Fisher Scientific, MA, USA)	1.8 (10 mM)
EGTA (cat.no.: 324626, MilliporeSigma, MO, USA)	0.38 (0.1 mM)
Note: add 900 mL of ddH_2O, pH to 7.4, top up with ddH_2O to 1 L (store at 4°C).	

2.7.1 Whole region of interest analysis

Following live-cell recordings, all whole frame fluorescent traces were background corrected using the Zeiss Zen software (Zeiss; Germany) and plotted using the GraphPad Prism 4.0 software (GraphPad Software, Inc., CA, USA). Trace normalisation to background fluorescence enabled calculation of AngII-(AngII$_{max}$ fluorescence – baseline fluorescence$_{average}$) and IM-induced fluorescence amplitudes (IM$_{max}$ - baseline fluorescence$_{average}$).

2.7.2 Single cell region of interest analysis

Live-cell video recordings were imported into the ImageJ software. Each recording was duplicated, set to the correct scale and brightened using the same settings for each recording. The recording was played and paused shortly after IM-induced fluorescence intensity facilitating identification of single cells. Single regions of interest were drawn around each cell within one frame and 5 individual background regions were defined. A screenshot was taken for each frame prior to using the multi measure tool to assess time-dependent fluorescence intensity changes within each cell. The generated data matrix was then exported into an excel file. Background fluorescence changes were calculated for each timepoint averaging values from the 5 pre-defined background regions. Cell fluorescence values for each timepoint were then normalised to respective background fluorescence values. This enabled

calculation of AngII-induced amplitudes ($AngII_{max}$ – $baseline_{average}$) for each cell. AngII-induced amplitudes for each treatment group were plotted as a histogram using the GraphPad Prism 4.0 software enabling visualisation of distribution.

2.8 Crosslinking of ^{125}I-BMP-9 to HSVSMC cell surface receptors

This experiment was based on a protocol developed by Professor P. ten Dijk's group (University Medical Center, Leiden, Netherlands) and performed by Dr Emma Low (University of Glasgow, Glasgow, UK) and Midory Thorikay (University Medical Center, Leiden, Netherlands). In brief, primary HSVSMCs were cultured in 15% (v/v) FCS media in T75 flasks and upon achieving confluence, cells were washed twice in ice cold 1× PBS containing 1% (w/v) BSA. Cells were incubated with ^{125}I-BMP-9 (100 μg/mL) and gently rocked at 4°C for 3-h. Following 3-h incubation, radiolabelled BMP-9 was removed, and cells were washed twice in ice cold 1× PBS containing 1% (w/v) BSA to remove unbound ^{125}I-BMP-9. Crosslinking was performed by subjecting cells to 54 nM disuccinimidyl suberate and 3 mM bis(sulfosuccinimidyl)suberate at 4°C for 15 min. Cells were washed twice with 4 mL detachment buffer (10 mM Tris-HCl, 1 mM EDTA, 10% (v/v) glycerol, 1 mM phenylmethylsulfonylfluoride (PMSF), pH 7.4) and detached using a cell scraper. Cell suspensions were transferred to 1.5 mL microcentrifuge tubes and subjected to centrifugation at 10,000 g for 2 min. Supernatants were removed, and cell pellets were re-suspended in 500 μL solubilisation buffer (125 mM NaCl, 10 mM Tris-HCl pH 7.4, 1 mM EDTA pH 7.4, 1% (v/v) Triton X-100, PMSF (10 μL/mL), aprotinin (1 μL/mL) and leupeptin (1 μL/mL)) and left to incubate on ice for 30 min. Lysates were subjected to centrifugation at maximum speed for 10 min and transferred to fresh 15 mL centrifugation tubes. Lysates were incubated with primary antibodies against ALK1, ALK2, BMPR2, ENG and ACVR2A/B at 4°C overnight. The next day, immune complexes were precipitated by incubation with protein A beads on a rotating wheel at 4°C for 45 min. Following incubation, beads were washed 4 times with solubilisation buffer containing 1× Complete Protease Inhibitor Cocktail to remove any non-specific binding. Samples were boiled in SDS sample buffer (50 mM Tris-HCl, 2% (w/v) SDS, 10% (v/v) glycerol, 1% (v/v) β-mercaptoethanol, 12 mM EDTA and 0.02% (w/v) bromophenol blue) and subjected to SDS-PAGE. Gels were fixed in fixation

buffer (25% (v/v) methanol and 7.5% (v/v) acetic acid) for 30 min. Next, gels were washed in drying buffer (25% (v/v) methanol and 10% (v/v) glycerol) and analysed on an autoradiograph.

2.9 Cloning methods using the pAdEasy-1 system for generation of a recombinant HAdV-5

The pAdEasy-1/pSHUTTLE-CMV system (Agilent Technologies, CA, USA) was used to generate HAdV-5 ACVR2A (Alba et al., 2012). In brief, the pAdEASY-1 plasmid contains DNA for an E1/E3-deficient HAdV-5. The pSHUTTLE-CMV system contains a CMV promoter which drives expression of an inserted transgene of interest. The CMV/transgene section is inserted into the pAdEasy-1 plasmid via homologous recombination.

2.9.1 Construct design and plasmid preparation

The full human *ACVR2A* exon protein-coding sequence (name: ACVR2A-201, transcript ID: ENST00000241416.12) excluding the untranslated region was downloaded from the Ensembl genome browser (https://www.ensembl.org/index.htmL). Using the translated region as a template a *Sal*I endonuclease restriction site (ERS) was designed at the 5' and a *Xho*I ERS was designed at the 3' end (total construct length: 1,605 base pairs (bp)). This sequence was artificially synthesised into the commercially available pEX-A2 carrier plasmid (Eurofins Scientific, Luxembourg). The lyophilised pEX-A2::*ACVR2A* plasmid was diluted in sterile ddH_2O to approximately 100 ng/mL prior to transformation.

2.9.2 Transformation and propagation of XL10-Gold Ultracompetent Cells®

XL10-Gold Ultracompetent Cells® (cat. no.: #200317, Agilent Technologies, CA, USA) were transformed with respective plasmids (pEX::*ACVR2A*, pSHUTTLE-CMV::*ACVR2A*, pAdEasy-1::pSHUTTLE-CMV::*ACVR2A*). Depending on the plasmid's antibiotic resistance open reading frame, transformed XL10-Gold cells were incubated/plated on either ampicillin (AMP)- or kanamycin (KAN)-containing AGAR (Formedium™). One 50 µL aliquot of XL10-Gold cells was thawed on ice for 30 min while an ampicillin/kanamycin containing AGAR plate (Table 2-22) was

brought to room temperature. One round-bottom polypropylene 14 mL BD centrifuge tube (cat. no.: 352059, Becton Dickinson, NJ, USA) was pre-chilled on ice and SOC outgrowth medium (cat. no.: B9020S, NEB, MA, USA) was pre-warmed to 42°C. The XL10-Gold aliquot was transferred to pre-chilled centrifuge tube and 4 µL β-mercaptoethanol (part of cat. no.: 200317, Agilent Technologies, CA, USA) were added to competent cells to increase transformation efficiency. The centrifuge tube was gently swirled and incubated on ice for 10 min swirling the centrifuge tube every 2 min. Respective plasmid (pEX-A2::*ACVR2A* → 1 µL; pSHUTTLE-CMV::*ACVR2A* → 2 µL; pAdEasy::pSHUTTLE-CMV::*ACVR2A* → 2 µL) was added to XL10-Gold cell suspension and the Centrifuge tube was gently swirled and placed on ice for 30 min. For transformation with pSHUTTLE-CMV::*ACVR2A* an additional set of competent cells was transformed with de-phosphorylated double cut pSHUTTLE-CMV to control for background bacterial growth.

Heat shock was performed at 42°C for 30 s to facilitate plasmid uptake by permeabilising the bacterial membrane. Following heat shock, the centrifuge tube was placed on ice for 2 min. Following heat shock, centrifuge tubes were placed on ice for 2 min. 900 µL pre-warmed SOC medium were added to respective centrifuge tube which was placed on a shaker at 5.7 g and 37°C for 1-h. 100 µL SOC medium/competent cell suspension (**low density** group) were pipetted and spread onto pre-warmed AMP- or KAN-containing AGAR plate. Remaining 900 µL cell suspension were subjected to centrifugation at 13,000 g and 37°C for 1 min. Pellets were re-suspended in 100 µL pre-warmed SOC medium (**high density** group). Suspensions were pipetted and spread onto pre-warmed AMP- or KAN-containing AGAR plates. AGAR plates were placed in an incubator at 37°C overnight.

The next day, 12 colonies were picked with sterile 200 µL pipette tips. Each tip was placed in 5 mL liquid AMP- or KAN-containing Luria broth (LB) medium (Table 2-23) in a 15 mL centrifuge tube which was placed in a shaker at 5.7 g and 37°C overnight (**MINI culture**). pSHUTTLE-CMV::*ACVR2A* and pAdEasy-1::pSHUTTLE-CMV::*ACVR2A* MINI-cultures were subjected to MINI plasmid purification and subsequent diagnostic restriction digest. The next day, 5 mL of respective MINI culture were added to 400 mL AMP- or KAN-containing LB

medium in a 2 L Erlenmeyer flask. The flask was placed in a shaker at 3.6 g and 37°C overnight (**MAXI culture**). 1 mL of respective MINI culture was frozen at -80°C in 500 µL glycerol (cat. no.: G5516, MilliporeSigma, MO, USA) (total volume **1.5 mL**) in a cryovial. The next day, the MAXI culture was transferred to a large bug pot which was subjected to centrifugation at 6,000 g and 4°C for 15 min. The MAXI culture was either frozen at -20°C or subjected to plasmid purification.

Table 2-22 Recipe for AGAR.

Reagent	Amount
AGAR (cat. no.: AGA03, Formedium, UK)	7.5 g
Luria broth Miller's (cat. no.: 12795027, Thermo Fisher Scientific, MA, USA)	7.75 g
Ampicillin (cat. no.: A5354, MilliporeSigma, MO, USA) or kanamycin (cat. no.: K0254, MilliporeSigma, MO, USA)	100 mg/mL
Note: add 500 mL of ddH_2O, mix well and autoclave. [1]Add respective antibiotic after autoclave step, leave to cool down and then poor into respective petri dishes.	

Table 2-23 Recipe for Luria Broth medium.

Reagent	Amount
Luria broth Miller's	15 g
Ampicillin or kanamycin[1]	100 mg/mL
Note: add 1 L of ddH_2O, mix well and autoclave. [1]Add respective antibiotic after autoclave step, leave to cool down and then poor into petri dishes.	

2.9.3 MINI plasmid purification

MINI plasmid purifications were performed using the PureYield™ Plasmid Miniprep System (cat. no.: A1223, Promega, Wis, USA).

Ready-made Neutralisation Solution was pre-chilled at 4°C. 1 mL LB medium/competent cell suspension was retained in a 4°C fridge. 4 mL LB medium/competent cell suspension were transferred into 2 sterile 2 mL microcentrifuge tubes. Tubes were subjected to centrifugation at maximum speed and 4°C for 30 s. Supernatants were discarded. The bacterial pellet was re-suspended in 600 µL sterile ddH_2O. 100 µL ready-made Cell Lysis Buffer were

added and each tube was gently inverted 6 times. 350 µL pre-chilled Neutralising Solution were added and each tube was inverted 6 times. Tubes were subjected to centrifugation at maximum speed and room temperature for 3 min. PureYield™ Minicolumns were placed into Collection Tubes. 900 µL plasmid-containing supernatant were transferred onto a PureYield™ Minicolumn without disturbing the cell debris pellet. Columns were subjected to centrifugation at maximum speed and room temperature for 15 s. The flow-through was discarded. 200 µL ready-made Endotoxin Removal Wash (ERB) were added onto each column which were centrifuged at maximum speed at room temperature for 15 s. The flow-through was discarded. 400 µL ready-made Column Wash Solution (CWC) were added to each column which were subjected to centrifugation at maximum speed at room temperature for 30 s. Each column was transferred onto a fresh sterile 1.5 mL microcentrifuge tube and 30 µL sterile ddH_2O were added to elute plasmid DNA. The columns were left to incubate at room temperature for 1 min and then subjected to centrifugation at maximum speed and room temperature for 15 s. The plasmid DNA concentration for each sample was determined using a NanoDrop™ 1000 spectrophotometer.

2.9.4 MAXI plasmid purification

MAXI plasmid preparations were performed using the Qiagen Plasmid Maxi Kit (cat. no.: 12162, Qiagen, Netherlands).

The ready-made P3 buffer was pre-chilled at 4°C while the bacterial pellet thawed. The pellet was re-suspended in 10 mL ready-made P1 buffer. 10 mL ready-made P2 buffer was added, and the bug pot was inverted 6 times and left to incubate at room temperature for 5 min. 10 mL pre-chilled P3 buffer was added and inverted 6 times. The lysate was poured into a fresh bug pot and subjected to centrifugation at 12,000 g at 4°C for 10 min. The supernatant was gently poured into a Qiagen Cartridge barrel and left to incubate at room temperature for 10 min. The Qiagen tip was placed on a rack and equilibrated with 10 mL QBT buffer. The barrel was allowed to empty by gravity. A plunger was gently inserted into the Qiagen Cartridge and the plasmid-containing lysate was filtered onto the equilibrated Qiagen tip which was allowed to empty by gravity. The Qiagen tip was washed twice with 30 mL ready-made QC buffer. A

50 mL collection centrifuge tube was placed underneath the Qiagen tip and plasmid DNA was eluted with 15 mL ready-made QF buffer.

10.5 mL isopropanol was added to the centrifuge tube. The solution was transferred to a fresh small container. The container was inverted 6 times to ensure mixing and was subjected to centrifugation at 15,000 g and 4°C for 30 min. The supernatant was decanted. The plasmid DNA pellet was re-suspended with 1.5 mL 70% (v/v) ethanol and transferred to a fresh sterile 1.5 mL microcentrifuge tube. The tube was subjected to centrifugation at 15,000 g and room temperature for 10 min. The supernatant was decanted, and the plasmid DNA pellet was re-suspended in 200 µL sterile ddH_2O. The plasmid DNA concentration was determined using the NanoDrop™ 1000 spectrophotometer.

2.9.5 Restriction digests

Large scale double restriction digest of pEX-A2::*ACVR2A* and pSHUTTLE-CMV (cat. no.: 16403, Addgene, MA, USA) was performed with the *Sal*I (cat. no.: R0138T, NEB, MA, USA) and *Xho*I (cat. no.: R0146S, NEB, MA, USA) restriction enzymes as outlined in Table 2-24.

Table 2-24 Large scale double restriction digest for pEX-A2::*ACVR2A* and pSHUTTLE-CMV.

Reagent	Amount
Plasmid DNA	x µL (equals 10 µg)
*Sal*I	2.5 µL
*Xho*I	2.5 µL
10× CutSmart® buffer (cat. no.: B7204S, NEB, MA, USA)	5.5 µL
Sterile ddH_2O	x µL
Note: total volume **55 µL**/reaction, mix well in a sterile 1.5 mL microcentrifuge tube and incubate at 37°C for 2-h.	

In addition, pSHUTTLE-CMV plasmid DNA was subjected to single restriction digests with *Sal*I and *Xho*I as outlined in Table 2-25.

Table 2-25 Single restriction digest for pSHUTTLE-CMV.

Reagent	Amount
Plasmid DNA	x μL (equals 1 μg)
*Sal*I or *Xho*I	1 μL
10× CutSmart® buffer	2 μL
Sterile ddH_2O	x μL
Note: total volume **20 μL**/reaction, mix well in a sterile 1.5 mL microcentrifuge tube and incubate at 37°C for 2-h.	

Diagnostic restriction digests were performed as outlined in Table 2-26.

Table 2-26 Set-up for double-cut diagnostic digest.

Reagent	Amount
Plasmid DNA	x μL (equals 1 μg)
*Sal*I	0.5 μL
*Xho*I	0.5 μL
10× CutSmart® buffer	2 μL
Sterile ddH_2O	x μL
Note: total volume **20 μL**/reaction, mix well in a sterile 1.5 mL microcentrifuge tube and incubate at 37°C for 2-h.	

*Pme*I linearisation was performed on pSHUTTLE-CMV::*ACVR2A* as outlined in Table 2-27. pSHUTTLE-CMV::*ACVR2A* linearisation is required for homologous recombination with pAdEasy-1.

Table 2-27 Set-up for *Pme*I linearisation.

Reagent	Amount
pSHUTTLE-CMV::*ACVR2A* plasmid DNA	x μL (equals 10 μg)
*Pme*I (cat. no.: R0560S, NEB, MA, USA)	2.5 μL
10× CutSmart® buffer	5.5 μL
ddH_2O	x μL
Note: total volume **55 μL**/reaction, mix well in a sterile 1.5 mL microcentrifuge tube and incubate at 37°C for 2-h.	

*Pac*I diagnostic digests were performed for pAdEasy-1::pSHUTTLE-CMV::*ACVR2A* as outlined in Table 2-28.

Table 2-28 Set-up for *Pac*I diagnostic digest.

Reagent	Amount
Plasmid DNA	x μL (equals 1 μg)
*Pac*I (cat. no.: R0547S, NEB, MA, USA)	1 μL
10× CutSmart® buffer	2 μL
Sterile ddH_2O	x μL
Note: total volume **20 μL**/reaction, mix well in a sterile 1.5 mL microcentrifuge tube and incubate at 37°C for 2-h.	

A large scale *Pac*I linearisation for pAdEasy-1::pSHUTTLE-CMV::*ACVR2A* was performed as outlined in Table 2-29.

Table 2-29 Set-up for large scale *Pac*I linearisation.

Reagent	Amount
pAdEasy-1::pSHUTTLE-CMV::*ACVR2A*	x μL (equals 20 μg)
*Pac*I	2 μL
10× CutSmart® buffer	5 μL
Sterile ddH_2O	x μL
Note: total volume **50 μL**/reaction, mix well in a sterile 1.5 mL microcentrifuge tube and incubate at 37°C for 2-h.	

Successful restriction digests were confirmed by agarose gel electrophoresis.

2.9.6 Agarose gel electrophoresis

11 μL 6× loading dye (cat. no.: B7024S, NEB, MA, USA) were added to 55 μL double cut pEX-A2::*ACVR2A*. This sample was loaded into two combined wells of a 0.7% (w/v) agarose gel (Table 2-30). 5 μL uncut, single and double cut pSHUTTLE-CMV were made up to 20 μL using ddH_2O. 4 μL 6× loading dye were added to each sample prior to gel loading. 4 μL 6× loading dye were added to each single/double cut plasmid DNA sample. 10 μL 1 kbp DNA ladder (cat. no.: 10787018, Thermo Fisher Scientific, MA, USA) were loaded into one pocket of each 0.7% (w/v) agarose gel for DNA size reference. Samples were run out at 130 V for 45 min in 1× TBE buffer and subsequently imaged (ChemiDoc™ XRS+, Bio-Rad, CA, USA). When required, respective DNA bands were cut out on a UV light table and gel DNA extraction was performed.

Table 2-30 Recipe for 0.7% (w/v) agarose gel.

Reagent	Amount
Agarose (cat. no.: 16500100, Thermo Fisher Scientific, MA, USA)	1.4 g
1× TBE buffer (cat. no.: 15581044, Thermo Fisher Scientific, MA, USA)	200 mL
Ethidium bromide (cat. no.: E1510, MilliporeSigma, MO, USA)	4 μL
Note: add agarose powder to 1× TBE buffer in an Erlenmeyer flask and swirl gently, place flask in microwave and bring solution to boiling, prepare gel mould under hood while agarose/TBE solution is heating in the microwave, remove flask from microwave and place under hood, add 4 μL ethidium bromide to flask and swirl gently, pour solution into gel mould and leave to solidify (approximately 30 min).	

2.9.7 Gel DNA extraction

DNA purification following gel extraction was performed using QIAquick Gel Extraction Kit (cat. no.: 28115, Qiagen, Netherlands). The gel slice containing the respective DNA band was weighed in a fresh sterile 1.5 mL microcentrifuge tube. 3 volumes ready-made QG buffer were added to 1 volume gel (100 µL QG buffer equals 100 mg gel). The tube was incubated at 50°C for 10 min and then vortexed for 3 min. 1 gel volume isopropanol was added to the tube. A QIAquick spin column was placed onto a provided 2 mL collection tube. The DNA sample was pipetted onto the QIAquick spin column which was subjected to centrifugation at 13,000 g for 1 min. The flow-through was discarded. 750 µL ready-made PE buffer were added to the column which was subjected to centrifugation at 13,000 g for 1 min. The flow through was discarded. The column was left to incubate at room temperature for 5 min and was subjected to centrifugation at 13,000 g for 1 min to remove residual wash buffer. The column was placed onto a fresh sterile 1.5 mL microcentrifuge tube. 30 µL sterile ddH_2O were added to the column which was subjected to centrifugation at 13,000 g for 1 min to elute the DNA.

2.9.8 Phenol/chloroform purification (PCP)

150 µL sterile ddH_2O were added to each respective sample. An equal volume of phenol/chloroform/isoamyl alcohol (cat. no.: P3803, MilliporeSigma, MO, USA) was added to each sample. The tube was vortexed for 30 s and was subjected to centrifugation at 13,000 g and room temperature for 2 min. The upper aqueous

phase containing the DNA was carefully removed and transferred to a fresh sterile 1.5 mL microcentrifuge tube. An equal volume of chloroform was added to remove phenol residue. The tube was vortexed for 30 s and was subjected to centrifugation at 13,000 g and room temperature for 2 min. The upper phase was carefully transferred to a fresh sterile 1.5 mL microcentrifuge tube. 1/10 volume 3 M sodium acetate (pH 5.2) and 2 volumes 100% (v/v) ethanol were added to the DNA sample. The sample was placed in a -80°C freezer for 30 min. The tube was subjected to centrifugation at 13,000 g and 4°C for 10 min. The supernatant was gently discarded, and the DNA pellet was re-suspended in 100 µL 70% (v/v) ethanol. The tube was subjected to centrifugation at 13,000 g and 4°C for 2 min. The supernatant was carefully removed. The DNA pellet was left to air dry for 10 min and was re-suspended with the original ddH_2O volume. The DNA concentration was determined using the NanoDrop™ 1000 spectrophotometer.

2.9.9 pSHUTTLE-CMV de-phosphorylation

Following PCP, 1 µg double-cut pSHUTTLE-CMV was de-phosphorylated as outlined in Table 2-31 to reduce background bacterial growth following ligation/transformation.

Table 2-31 De-phosphorylation of double-cut pSHUTTLE-CMV backbone.

Reagent	Amount
Double-cut pSHUTTLE-CMV plasmid DNA	x µL (equals 1 µg)
Antarctic phosphatase (cat. no.: M0289S, NEB, MA, USA)	1 µL
Antarctic phosphatase buffer (cat. no.: B0289S, NEB, MA, USA)	2 µL
Sterile ddH_2O	x µL
Note: total volume **20 µL**/de-phosphorylation reaction, mix well in a sterile 1.5 mL microcentrifuge tube and incubate at 37°C for 30 min, heat inactivation at 80°C for 2 min.	

2.9.10 DNA ligation

Ligation between de-phosphorylated double cut pSHUTTLE-CMV and the *ACVR2A* DNA fragment was performed as outlined in Table 2-32.

Table 2-32 Set-up for ligation reaction.

Reagent	Amount
De-phosphorylated double-cut pSHUTTLE-CMV plasmid DNA	2 μL (equals 100 ng, 7.5 kbp)
ACVR2A DNA fragment	x μL (1,605 bp equals 1 (pSHUTTLE-CMV):5 (*ACVR2A* cDNA insert) molar equivalent
DNA ligase T4 (cat. no.: M0202S, NEB, MA, USA)	1 μL
DNA ligase buffer (cat. no.: B0202S, NEB, MA, USA)	2 μL
Sterile ddH_2O	x μL
Note: total volume **20 μL**/ligation reaction, mix well in a sterile 1.5 mL microcentrifuge tube and incubate at 16°C overnight, heat inactivation at 65°C for 10 min.	

2.9.11 Plasmid sequencing

The *ACVR2A* insertion site was sequenced (Eurofins Scientific, Luxembourg) to confirm DNA identity and integrity using respective primers: forward (fw)1 primer: 5'-CGCAAATGGGCGGTAGGC-3', fw2 primer: 5'-TGTTCCAACTCAAGACC-3'; fw3 primer: 5'-CTATGGGAACTGGCTTC-3'.

2.9.12 Homologous recombination

Homologous recombination between pAdEasy-1 and *Pme*I-linearised pSHUTTLE-CMV::*ACVR2A* was performed in BJ5183-AD-1 Electroporation Competent Cells (cat. no.: #200157, Agilent, CA, USA). BJ5183-AD-1 cells already contain pAdEasy-1.

BJ5183-AD-1 cells were thawed on ice. SOC medium and electroporation cuvettes (cat. no.: ECU105, Geneflow Ltd., UK) were pre-chilled on ice. 1 μg *Pme*I-linearised pSHUTTLE-CMV::*ACVR2A* was added to sterile ddH_2O (**total volume 6 μL**) in a sterile 1.5 mL microcentrifuge tube which was placed on ice. Linearised plasmid/ddH_2O suspension was added to 50 μL thawed BJ5183-AD-1 cell suspension and mixed by gently pipetting up and down several times. The entire sample was transferred to a pre-chilled electroporation cuvette and left to incubate on ice for 3 min. The cuvette was placed into an electroporator (MicroPulser, Bio-Rad, CA, USA) and pulsed for 1 s (Ec2 mode, 200 Ω, 2.5 kV, 25

μF). The cuvette was immediately removed and 500 μL of pre-chilled SOC medium were added. The cell/plasmid/SOC medium suspension was mixed by gently pipetting up and down several times and then transferred to a fresh sterile 1.5 mL microcentrifuge tube. The tube was placed in a shaker at 5.7 g and 37°C for 1-h. The tube was subjected to centrifugation at 2,000 g for 1 min. The pellet was re-suspended in 100 μL SOC medium. The suspension was plated and spread onto a kanamycin-containing AGAR plate which was placed in an incubator at 37°C overnight. The next day, 12 smallest colonies were subjected to MINI-culture and MINI plasmid purification.

2.9.13 HEK293 transfection with pAdEasy-1::pSHUTTLE-CMV::*ACVR2A*s

Plasmid transfection into HEK293 cells was performed using the Xfect™ transfection Reagent (cat.no.: 631317, TaKaRa Bio, Japan). HEK293 cell DNA contains the HAdV-5 packaging signal and E1 region which are necessary for viral replication.

HEK293 cells were seeded into one 6-well plate (6×10^5 cells/in **1 mL** medium). Upon achieving 50-70% confluence, plasmid transfection was performed. Precipitated *Pac*I-linearised AdEasy-1::pSHUTTLE-CMV::*ACVR2A* and the control GFP plasmid were thawed on ice. Just prior to use, Xfect™ Polymers and Xfect™ Reaction Buffer were brought to room temperature. Both reagents were vortexed prior to use. 5 μg plasmid DNA (equals 1 well) were diluted in Xfect™ Reaction Buffer to a final volume of 100 μL in a sterile 1.5 mL microcentrifuge tube. The tube was vortexed for 5 s. 1.5 μL Xfect™ Polymer was added to diluted plasmid solution. The tube was vortexed for 10 s (**RATIO**: 0.3 μL of Xfect™ Polymer equals 1 μg of plasmid DNA) and left to incubate at room temperature for 10 min to allow nanoparticle complex formation. The entire volume was added dropwise to respective well. The 6-well plate was rocked gently for 10 s and incubated at 37°C and 5% CO_2 for 4-h. Nanoparticle-containing medium was replaced with 2 mL fresh HEK293 growth medium and the 6-well plate was placed back in an incubator at 37°C and 5% CO_2.

Following 48-h, GFP plasmid-transfected cells were imaged on a microscope at 10× magnification to confirm successful plasmid transfection. HEK293 growth

medium was replaced with fresh medium every 2-3 days. Medium replacement was stopped once plaque formation became evident. Plaque-containing wells were marked, and the 6-well plate was left to incubate until the cytopathic effect (CPE) was complete (approximately 2 additional days).

2.9.14 Crude virus isolation

Once CPE had spread throughout the entire well, HEK293 cells gradually started to lift off the bottom of the well. Each well was carefully washed with medium from the same well and HEK293 cell suspensions containing crude HAdV-5 ACVR2A (HEK293 cells contain crude virus) were transferred to separate sterile 1.5 mL microcentrifuge tubes (1 mL/tube, 2 tubes for 1 well). Tubes were subjected to centrifugation at 250 g and room temperature for 10 min. Supernatants were gently discarded. Cell pellets were gently re-suspended in 250 µL sterile 1× PBS and 250 µL 1,1,2-Trichloro-1,2,2-trifluoro-ethane (cat. no.: 34874, MilliporeSigma, MO, USA) were added to the suspension. Tubes were gently inverted 6 times, gently shaken and subjected to centrifugation at 750 g and room temperature for 10 min. The crude virus-containing top liquid layer was carefully transferred to fresh sterile 1.5 mL microcentrifuge tubes (50 µL/tube). Crude virus aliquots were either directly subjected to the first round of plaque purification or stored in a -80°C freezer.

2.9.15 First plaque purification

HEK293 cells were seeded into a 96-well plate (12 medium + 8 mL HEK293 suspension from one T150 flask → 200 µL/well). The first and last column were filled with 1× sterile PBS. The next day, a serial virus dilution was performed in HEK293 growth medium (Table 2-33).

Table 2-33 Virus dilution table

Dilution	Virus [µL]	Medium [µL]
10^{-2}	50 (crude virus)	4,950
10^{-3}	500 of 10^{-2}	4,500
10^{-4}	500 of 10^{-3}	4,500
10^{-5}	500 of 10^{-4}	4,500
10^{-6}	500 of 10^{-5}	4,500
10^{-7}	500 of 10^{-6}	4,500
10^{-8}	500 of 10^{-7}	4,500
Control	0	5,000

HEK293 growth medium was very carefully replaced with 100 µL respective virus suspension or non-virus containing control medium. The next day, respective virus suspension was very carefully replaced with 200 µL fresh HEK293 growth medium. Growth medium was replaced with fresh medium every 2 days. Medium replacement was stopped once CPE became evident and wells containing plaque were marked. The aim was to isolate HAdV-5 ACVR2A from the lowest possible virus suspension treatment group to exclude crude virus contamination. Once CPE had spread throughout an entire well of a low virus suspension treatment group, mature virus isolation was performed. Respective well was gently washed with 200 µL growth medium from the same well to detach the plaque and the HEK293 cell suspension was gently transferred to a fresh sterile 1.5 mL microcentrifuge tube. The tube was subjected to centrifugation at 250 g and room temperature for 10 min. The supernatant was gently discarded. The cell pellet was carefully re-suspended in 200 µL sterile 1× PBS and 200 µL 1,1,2-

Trichloro-1,2,2-trifluoro-ethane were added. The tube was gently inverted 6 times, shaken and subjected to centrifugation at 750 g and room temperature for 10 min. The virus-containing top liquid layer was carefully transferred to fresh sterile 1.5 mL microcentrifuge tubes (50 µL/tube). Virus aliquots were either directly subjected to a second round of plaque purification or stored in a -80°C freezer.

2.9.16 Second plaque purification

The second plaque purification was performed as outlined in section 2.9.15. The aim was to isolate HAdV-5 ACVR2A from the lowest possible virus suspension treatment group to further exclude crude virus contamination during subsequent seed stock generation. Mature virus aliquots were either directly subjected to seed stock generation or stored at -80°C.

2.9.17 Seed stock generation

HEK293 cells were seeded into two T150 flasks (25 mL growth medium/T150 flask). Upon achieving 80-90% confluency, one T150 flask was infected with one HAdV-5 ACVR2A 50 µL aliquot derived from the 2nd plaque purification. The second T150 flask remained as an uninfected control. The next day, virus- and non-virus-containing medium was replaced with 25 mL fresh growth medium. Once CPE was complete (approximately 3-4 days), the HEK293 cell layer was gently detached in 25 mL growth medium from the same flask. The cell suspension was transferred to a fresh sterile 50 mL centrifuge tube. The centrifuge tube was subjected to centrifugation at 250 g and room temperature for 10 min. The supernatant was gently discarded, and the pellet was gently re-suspended in 1.2 mL sterile 1× PBS. The suspension was transferred to a fresh sterile 15mL centrifuge tube. 1.2 mL 1,1,2-Trichloro-1,2,2-trifluoro-ethane were added, and the centrifuge tube was gently inverted 6 times, shaken and subjected to centrifugation at 750 g and room temperature for 10 min. The top liquid layer containing HAdV-5 ACVR2A was transferred to fresh sterile 1.5 mL microcentrifuge tubes (20× 50 µL aliquots). Aliquots were stored at -80°C.

2.9.18 Scale up and virus isolation

HEK293 cells were seeded into one T150 flask (25 mL growth medium/T150 flask). Upon achieving 90% cell confluence, the flask was split 1:5. Upon achieving 90% cell confluence, the 5 flasks were again split 1:5 generating a total number of 25× T150 flasks. Upon achieving approximately 70% confluence, 24× T150 flasks were infected with purified HAdV-5 ACVR2A (1× 50 µL HAdV-5 ACVR2A aliquot was added to 1× bottle HEK293 growth medium, 25 mL infected growth medium/T150 flask). 1× T150 flask remained as an uninfected control. The next day, virus- and non-virus-containing medium was replaced with 25 mL fresh growth medium. Once CPE was complete (approximately 2-3 days), the HEK293 cell layer was gently detached in 25 mL growth medium from the same flask. Cell suspensions were transferred to fresh sterile 50 mL centrifuge tubes. Centrifuge tube were subjected to centrifugation at 2,000 g and room temperature for 10 min. Supernatant was discarded and cell pellets were gently re-suspended in 6 mL sterile 1× PBS. 6 mL 1,1,2-Trichloro-1,2,2-trifluoro-ethane were added to each Centrifuge tube. Centrifuge tubes were inverted 5 times and subjected to centrifugation at 3,000 g and room temperature for 15 min. Upper aqueous layers containing HAdV-5 ACVR2A were transferred to a fresh sterile 50 mL centrifuge tube. The virus suspension was either directly subjected CsCl gradient purification or stored at -80°C.

2.9.19 CsCl gradient preparation and centrifugation

HAdV-5 ACVR2A suspension was subjected to two sequential CsCl gradients to separate all viral particles from debris. Gradient preparation was performed underneath a cell culture hood.

The required number of SW40 ultracentrifuge tubes (cat. no.: 344060, Beckman Coulter Life Sciences, IN, USA) were rinsed in 70% (v/v) ethanol and sterile 1× PBS prior to gradient preparation. 2.5 mL 1.40 g/mL CsCl (

Table 2-38)/1× TD buffer (Table 2-34) were carefully added to the bottom of an ultracentrifuge tube. 2.5 mL 1.25 g/mL CsCl (Table 2-36)/1× TD buffer were gently dripped on top. The virus suspension was carefully dripped on top. Sterile 1× PBS was carefully dripped on top to completely fill the ultracentrifuge tube. The ultracentrifuge tube was carefully placed in a SW40 rotor and subjected to centrifugation in an ultracentrifuge (cat. no.: Optima™ L-80 XP Ultracentrifuge, Beckman Coulter Life Sciences, IN, USA) at 218,000 g and 18°C for 90 min (acceleration → maximum, no brake). The ultracentrifuge tube was carefully removed from the spin column and placed in a tube holder underneath a cell culture hood. A plastic waste beaker was placed underneath the tube holder. The virus band was identified between both CsCl layers.

The side of the ultracentrifuge tube was pierced with a 5 mL syringe (Injekt®-F Solo, B. Braun, Germany) + 21 G sterile green needle (Becton Dickinson, NJ, USA) (needle opening facing downwards) on the level of the 1.25 g/mL CsCl gradient above the virus band. Debris was carefully aspirated. The syringe + needle remained inside the ultracentrifuge tube, and the ultracentrifuge tube was rotated so the syringe faced the back of the hood. The side of the ultracentrifuge tube was pierced again with a fresh 5 mL syringe + 21 G green needle (needle opening facing downwards) just below the virus band. The needle opening was gently rotated upwards and with a sweeping motion the virus band was aspirated. The syringe was pulled out of the ultracentrifuge tube and the virus suspension was transferred to a fresh sterile 5 mL bijoux vial (cat. no.: E1412-0710, Starlab, Germany).

HAdV-5 ACVR2A suspension was subjected to a second CsCl gradient purification to separate mature from immature viruses. Gradient preparation was performed in a SW40 ultracentrifuge tube. 5 mL 1.34 g/mL CsCl/1× TD buffer (Table 2-37) were carefully added to the bottom of an ultracentrifuge tube. The virus suspension was carefully dripped on top. Sterile 1× PBS was carefully dripped on top to completely fill the ultracentrifuge tube. The ultracentrifuge tube was then subjected to the same steps as described above. The virus suspension was transferred to a fresh sterile 5 mL bijoux.

Table 2-34 Recipe for 10× TD buffer.

Reagent	Amount
NaCl	80 g
KCl	3.8 g
Na_2HPO_4 12 H_2O (cat. no.: 71649, MilliporeSigma, MO, USA)	2.5 g
Tris-base	30 g
Note: add 900 mL ddH_2O, adjust pH to 7.4 with HCl, top up with ddH_2O to 1 L. Autoclave and store at 4°C.	

Table 2-35 Recipe for 10× Tris-EDTA (TE) buffer.

Reagent	Amount
Tris-HCl	12.1 g
EDTA	3.72 g
Note: add 900 mL ddH_2O, adjust pH to 8 with NaOH, top up with ddH_2O to 1 L. Autoclave and store at room temperature.	

Table 2-36 1.25 g/mL CsCl solution.

Reagent	Amount
CsCl (cat. no.: 289329, MilliporeSigma, MO, USA)	36.16 g
1× TD buffer	100 mL
Note: check by weighing, filter sterilise underneath hood before use (0.22 µm filter) and store at room temperature for up 1 year.	

Table 2-37 1.34 g/mL CsCl solution.

Reagent	Amount
CsCl	51.2 g
1× TD buffer	100 mL
Note: check by weighing, filter sterilise underneath hood before use (0.22 µm filter) and store at room temperature for up 1 year.	

Table 2-38 1.40 g/mL CsCl solution.

Reagent	Amount
CsCl	62.2 g
1× TD buffer	100 mL
Note: check by weighing, filter sterilise underneath hood before use (0.22 µm filter) and store at room temperature for up 1 year.	

2.9.20 Dialysis

CsCl is removed from the virus suspension during this step. A 2 L plastic beaker was sprayed down with 70% (v/v) ethanol underneath a cell culture hood. The beaker was carefully washed with 200 mL autoclaved ddH_2O. 2 L 1× TE buffer (200 mL 10× TE buffer (Table 2-35) + 1,800 mL autoclaved ddH_2O) was added to the beaker. The beaker was placed on a magnetic stirrer plate underneath the cell culture hood. One injection port of a dialysis cassette (10,000 MWCO, cat. no.: 66380, Thermo Fisher Scientific, MA, USA) was circled to label the virus injection site.

The virus suspension was aspirated with a 5 mL syringe + 21 G needle. Approximately 0.5 mL air were additionally aspirated into the syringe. The syringe needle was gently advanced into the pre-labelled injection port of the dialysis cassette until the opening just became visible inside the cassette. Air followed by virus sample were gently injected into the cassette without piercing the membrane. Once the sample was injected, as much air as possible was aspirated allowing the liquid sample level to rise to the top of the membrane. The dialysis cassette was placed in a floater and was floated upside down (cassette submerged in 1× TE buffer) in the pre-filled plastic beaker. The stirrer was switched on and the dialysis cassette was stirred for 2-h. 1× TE buffer was replaced with 2 L of fresh 1× TE buffer and the dialysis cassette was stirred for another 2-h. 1× TE buffer was replaced with glycerol-containing 1× TE buffer (200 mL 10× TE buffer + 200 mL autoclaved glycerol + 1600 mL autoclaved ddH_2O) and the dialysis cassette was stirred overnight.

2.9.21 Virus aliquot preparation

The next day, virus aliquot preparation was performed. 1.5 mL air were aspirated into a 5 mL syringe + 21 G needle and the needle was gently advanced along a different injection port of the dialysis cassette until the needle opening became fully visible. Air was then gently injected, and the virus solution was gently aspirated and transferred to a fresh sterile 5 mL bijoux. 50 µL aliquots were prepared in fresh sterile 1.5 mL microcentrifuge tubes and stored at -80°C. In addition, 1× 30 µL aliquot was also stored at -80°C and was later used for setting up the plaque-forming unit (PFU) titre plate.

2.9.22 Viral particle quantification

The Micro BCA™ Protein Assay Kit (cat. no.: 23235, Thermo Fisher Scientific, MA, USA) was utilised to determine the number of VPs/mL.

BSA standards were prepared via serial dilution in sterile 1× PBS (range: 0.5 - 200 µg/mL). Sterile 1× PBS was used as a blank control (0 µg/mL). 150 µL of each respective standard were pipetted into duplicate wells of a clear, flat-bottomed 96-well plate. Next, 1, 3 and 5 µL purified HAdV-5 ACVR2A stock were added in duplicate to empty wells on the same 96-well plate. Volumes were adjusted to 150 µL with sterile 1× PBS. The working Micro BCA solution was made up by mixing 25 parts of Reagent MA and 24 parts Reagent MB with 1 part of Reagent MC in a sterile 15 mL centrifuge tube. 150 µL working Micro BCA solution were gently added to each well. The 96-well plate was gently tapped to ensure mixing and left to incubate in the dark at 37°C for 2-h. Following 2-h incubation, the 96-well plate was placed into the Wallac 1420 Victor2 Microplate Reader and absorbance was determined at 562 nm. Blank control absorbance was subtracted from each sample to adjust for background and duplicate readings for each standard were averaged to generate a standard curve. Unknown protein sample concentrations were calculated using the linear equation based on this standard curve. Protein sample concentrations were converted to respective VP titer (VP/mL) according to the following formula (1 µg viral protein equals 1×10^9 VP) (Von Seggern et al., 1998).

2.9.23 Generation of recombinant E1/E3-deficient HAdV-5 ACVR2A

XL10-Gold Ultracompetent cells were transformed with pEX-A2::*ACVR2A* and subjected to propagation (2.9.2) (Figure 2-6). Transformed/propagated XL10 Gold cells were subjected to MAXI plasmid isolation/purification (2.9.4). Propagated pEX-A2::*ACVR2A* and already available pSHUTTLE-CMV were subjected to *Sal*I/*Xho*I restriction digests (2.9.5). Successful restrictions were confirmed by agarose gel electrophoresis (2.9.6). The *ACVR2A* DNA band was cut out on a UV table and subjected to gel extraction (2.9.7) and PCP (2.9.8). In addition, double cut pSHUTTLE-CMV was also subjected to PCP.

S2.9.10uccessful ligation between purified *ACVR2A* and double cut pSHUTTLE-CMV was achieved (2.9.10) (colony 10, Figure 2-6). Following overnight ligation, XL10-Gold cells were transformed with ligated pSHUTTLE-CMV::*ACVR2A* and subjected to propagation, MINI plasmid purification (2.9.3), *Sal*I/*Xho*I diagnostic digests (2.9.5) and subsequent gel electrophoresis (2.9.6). pSHUTTLE-CMV::*ACVR*2A deriving from colony was subjected to sequencing using respective primers (2.9.11). Following confirmation of DNA integrity, XL10-Gold cells were transformed with pSHUTTLE-CMV::*ACVR2A* and subjected to MAXI propagation (2.9.2). MAXI-prepped (2.9.4) pSHUTTLE-CMV::*ACVR2A* was subjected to a diagnostic *Sal*I/*Xho*I restriction digest (2.9.5) and subsequent gel electrophoresis (2.9.6) to confirm plasmid integrity.

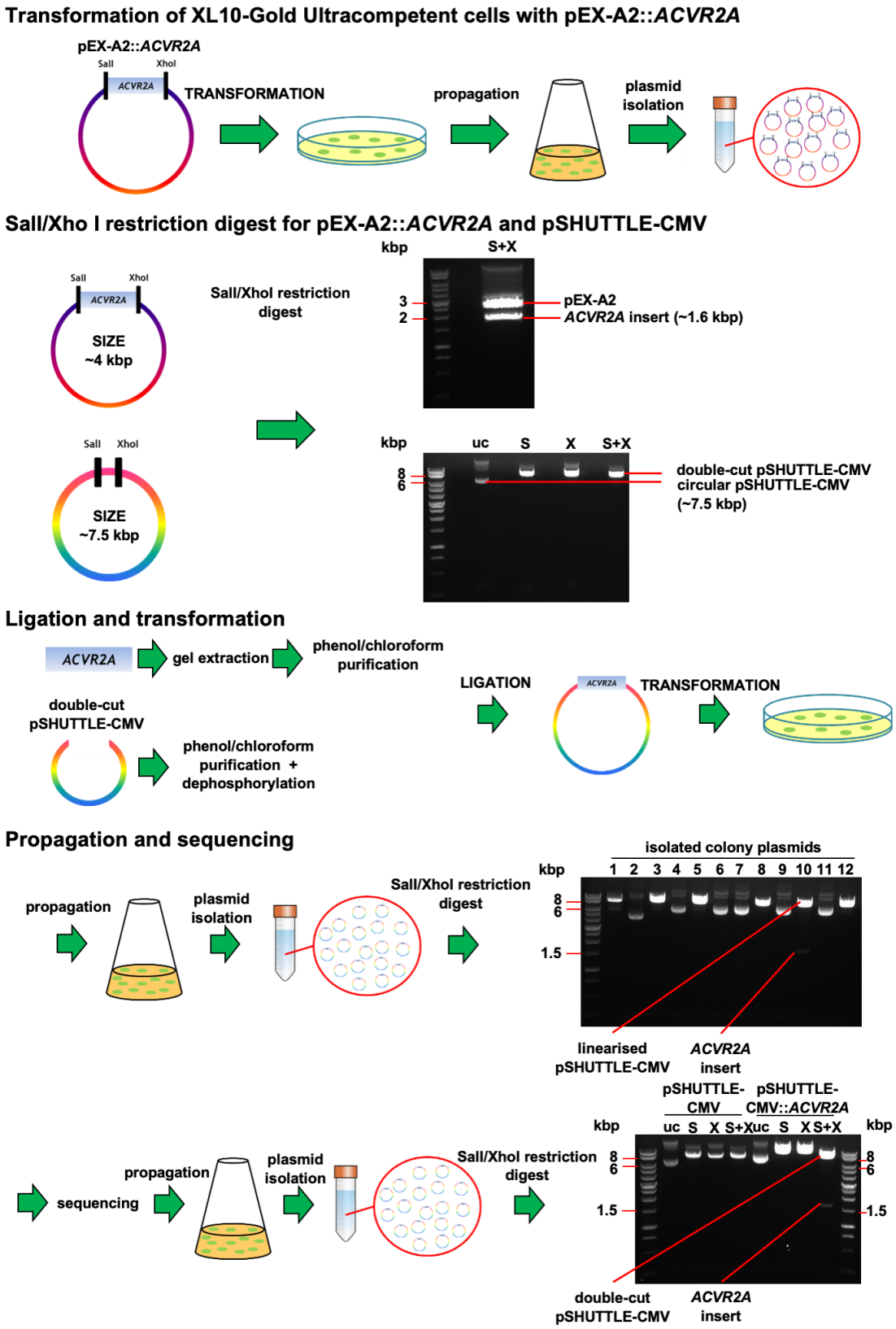

Figure 2-6 Workflow diagram for generation of pSHUTTLE-CMV::*ACVR2A*. The *ACVR2A* protein-coding exon sequence was inserted into pSHUTTLE-CMV downstream of the CMV promoter which drives gene expression. Sequencing confirmed that plasmids isolated from colony 10 contained the *ACVR2A* insert. Colony 10 was subsequently propagated.

MAXI prepped pSHUTTLE-CMV::*ACVR2A* was subjected to *PmeI* linearisation (2.9.5) which is necessary for homologous recombination with pAdEasy-1 (Figure 2-7). *PmeI*-linearised pSHUTTLE-CMV::*ACVR2A* was subjected to gel electrophoresis. The linearised DNA band was cut out on a UV table and subjected to gel extraction (2.9.7).

Homologous recombination between gel extracted/*Pme*I-linearised pSHUTTLE-CMV::*ACVR2A* and pAdEasy-1 was performed in BJ5183-AD-1 cells (2.9.12). Transformed BJ5183-AD-1 cells were subjected to MINI culture propagation (2.9.2). MINI cultures were subjected to MINI plasmid purification (2.9.3) and *Pac*I diagnostic digests (2.9.5). Subsequent gel electrophoresis (2.9.6) confirmed successful recombination between *Pme*I-linearised pSHUTTLE-CMV::*ACVR2A* and pAdEasy-1 (Figure 2-7). XL10-Gold cells were transformed with pAdEasy-1::pSHUTTLE-CMV::*ACVR2A* deriving from colonies 1 and 2 and subjected to MAXI culture propagation (2.9.2). Cultures were subjected to MAXI plasmid purification (2.9.4) and sequencing (2.9.11).

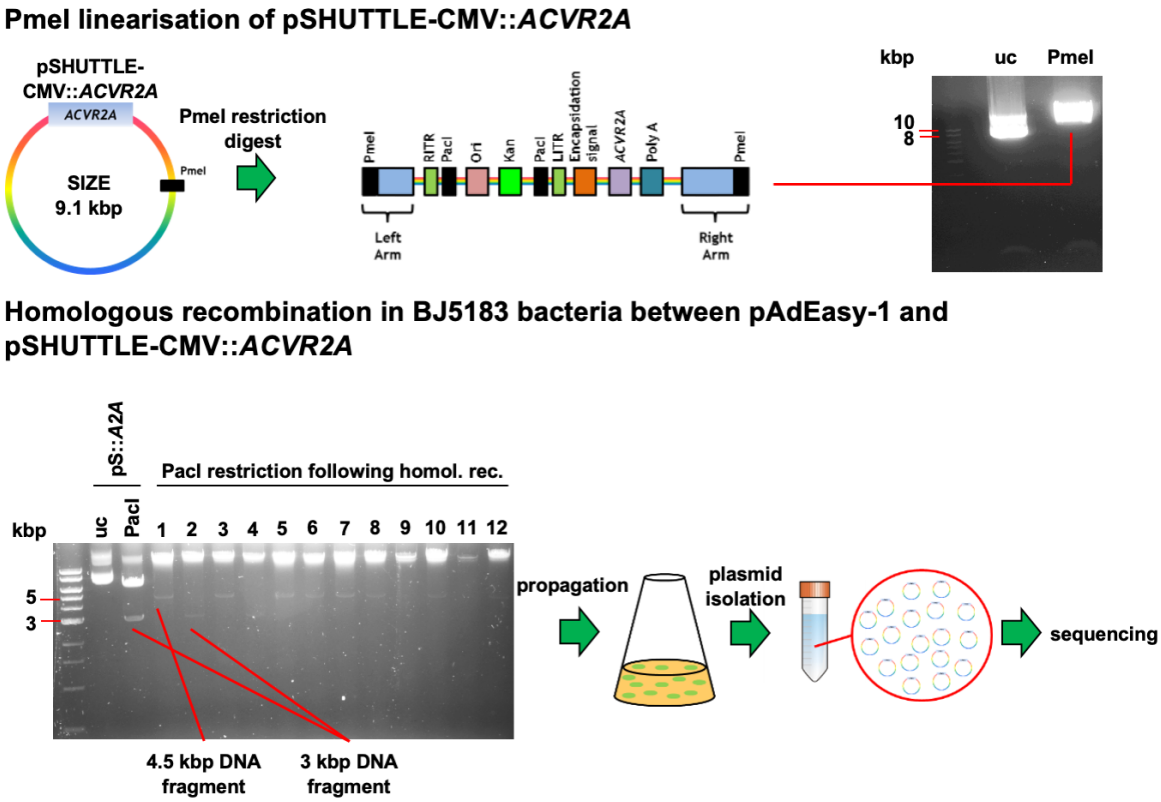

Figure 2-7 *Pme*I linearisation and *Pac*I linearisation following homologous recombination. (Top panel) Image on the right shows respective DNA bands of uncut and *Pme*I-linearised pSHUTTLE-CMV::*ACVR2A* following separation in a 0.7% (w/v) agarose gel. (Bottom panel) Image on the left shows respective DNA bands of uncut and *Pac*I-linearised pSHUTTLE-CMV::*ACVR2A* and *Pac*I-linearised pAdEasy-1::pSHUTTLE-CMV::*ACVR2A* following separation in a 0.7% (w/v) agarose gel.

MAXI-prepped pAdEasy-1::pSHUTTLE-CMV::*ACVR2A* deriving from colonies 1 and 2 were subjected to diagnostic PacI linearisation (2.9.5) (Figure 2-8 A). Gel electrophoresis (2.9.6) confirmed successful cleavage of respective 3.0 kbp and 4.5 kbp fragments which contain the KAN resistance frame. Following confirmation of DNA integrity, pAdEasy-1::pSHUTTLE-CMV::*ACVR2A* was subjected to a large scale restriction digest with *Pac*I (2.9.5) prior to HEK293 transformation. This step is necessary to hinder transcription of the DNA sequence which contains the KAN resistance frame which counters transcription of the viral genome. Successful *Pac*I linearisation was confirmed by gel electrophoresis (2.9.6) (Figure 2-8 B).

HEK293 cells were transfected with *Pac*I-linearised pAdEasy-1::pSHUTTLE-CMV::*ACVR2A* to generate HAdV-5 ACVR2A (2.9.13). Control HEK293 cells which were transfected with a GFP plasmid displayed GFP-mediated fluorescence at 48-h confirming successful transfection (Figure 2-8 C). Once CPE was complete, crude HAdV-5 ACVR2A isolation was performed (2.9.14). Crude HAdV-5 ACVR2A was subjected to two rounds of plaque purification (2.9.15,2.9.16) prior to seed stock generation (2.9.17) and scale up (2.9.18). Propagated HAdV-5 ACVR2A was isolated and subjected to CsCl gradient purification, ultracentrifugation (2.9.19) (Figure 2-8 D and E) and dialysis (2.9.20). Purified HAdV-5 ACVR2A was subjected to VP quantification (2.9.22) prior to usage in *in vitro* experiments.

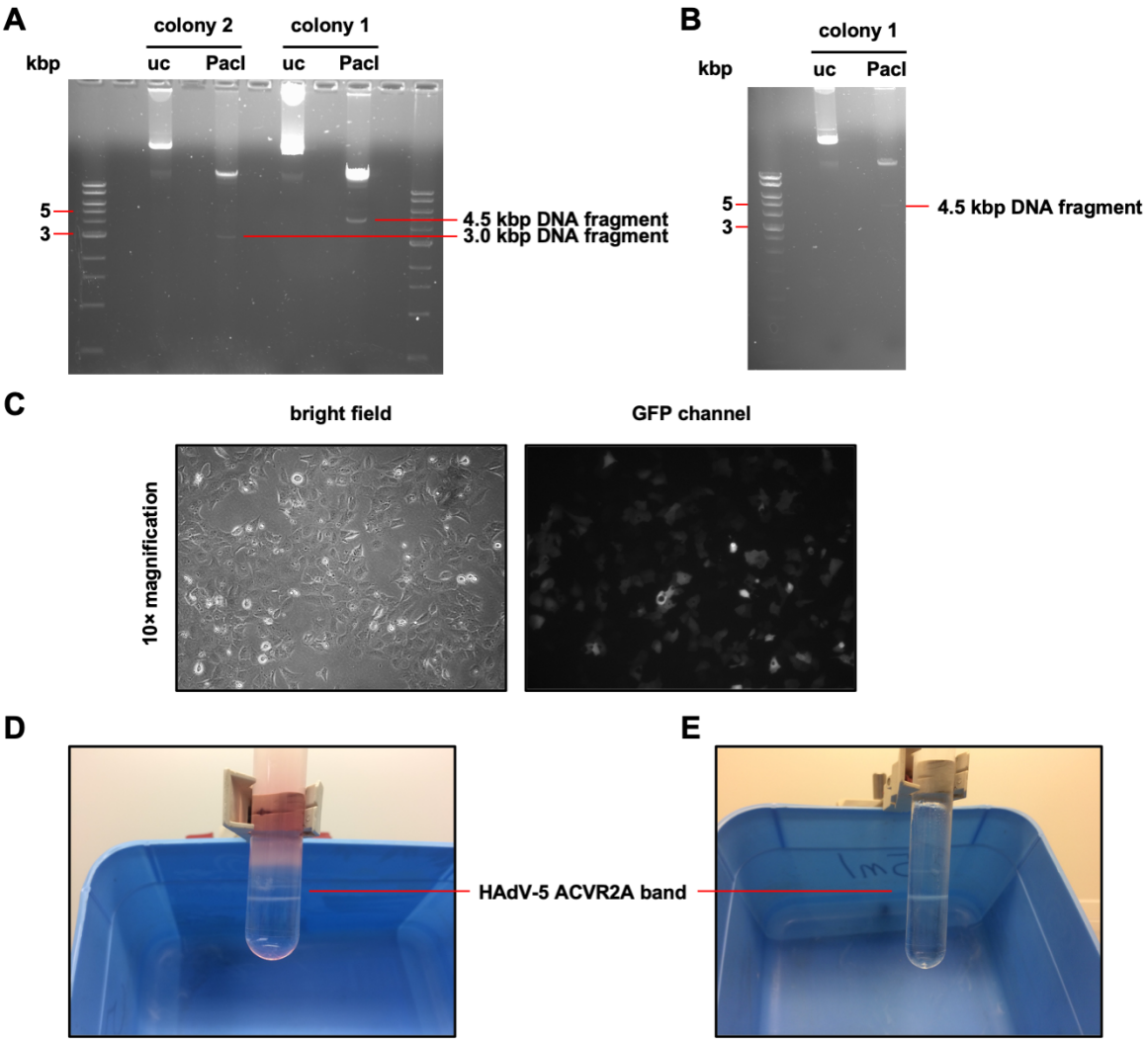

Figure 2-8 Generation of recombinant HAdV-5 ACVR2A. (**A**) pAdEasy-1::pSHUTTLE-CMV::*ACVR2A* plasmids deriving from colonies 1 and 2 were propagated and subjected to diagnostic *Pac*I restriction digest. Image shows respective DNA bands following separation of uncut and *Pac*I-linearised pAdEasy-1::pSHUTTLE-CMV::*ACVR2A* in a 0.7% (w/v) agarose gel. (**B**) pAdEasy-1::pSHUTTLE-CMV::*ACVR2A* deriving from colony 1 was subjected to a large scale *Pac*I restriction digest. Image shows respective DNA bands following separation of uncut and *Pac*I-linearised pAdEasy-1::pSHUTTLE-CMV::*ACVR2A* in a 0.7% (w/v) agarose gel. (C) Control GFP plasmid was transfected into HEK293 cells. 48-h following transfection, HEK293 cells were imaged at 10× magnification to determine GFP expression. Left image shows cells under bright field. Right image shows cells under GFP fluorescence. (**D**) First ultracentrifugation: image shows purified HAdV-5 ACVR2A band between both CsCl layers (layer above virus band → CsCl 1.25 g/mL, layer below virus band → CsCl 1.25 g/mL) following ultracentrifugation. Top CsCl layer contains debris. (**E**) Second ultracentrifugation: image shows purified HAdV-5 ACVR2A band between CsCl 1.34 g/mL and PBS layers (layer above virus band → PBS, layer below virus band → CsCl 1.34 g/mL) following ultracentrifugation.

2.10 Single cell RNA sequencing

All experiments leading up to generation of single cell suspensions for each treatment group were performed by Julian Schwartze.

2.10.1 Sample preparation

Confluent primary HSVSMCs were seeded into 2× 6-well plates (1.5×10^5 cells/well, 3× technical repeats for each treatment group) in 15% FCS media. Upon achieving 80% confluence, 15% (v/v) FCS media was replaced with MEDIA1 for 72-h (Table 2-7). Medium was replaced with fresh MEDIA1 containing BMP-9 (10 ng/mL), TGF-β_1 (10 ng/mL), both ligands and vehicle control (4 mM HCl/1% (w/v) BSA). Following 24-h, stimulation medium was removed, and cells were washed once with sterile 1× PBS (2 mL/well). PBS was discarded and 1 mL 1× sterile trypsin was added to each well to detach cells from well bottoms. 6-well plates were placed in an incubator at 37°C and 5% CO_2 for 5 min. Successful cell detachment was determined by imaging cells under a microscope. 1 mL L-glutamine-free 0.2% (v/v) SVM was added to each well and suspensions were gently mixed to stop the trypsin reaction. Technical repeats (2 mL/well) were pooled in fresh sterile 15 mL universal tubes (total volume: **6 mL** per treatment group). Tubes were subjected to centrifugation at 500 g and room temperature for 5 min. Supernatants were gently removed and cell pellets were re-suspended in 500 µL scRNAseq medium (Table 2-39).

Table 2-39 scRNAseq medium composition.

Reagent	Volume
DMEM (cat. no. 21969035, Thermo Fisher Scientific, MA, USA)	500 mL
Penicillin/streptomycin	5 mL (100 I.U/mL and 100 µg/mL)

Cell strainers (pore size 70 µm, cat. no.: 542070, Greiner, Germany) were placed on respective fresh sterile 50 mL centrifuge tubes underneath a cell culture hood. 500 µL cell suspensions were pipetted onto respective cell strainers/50 mL centrifuge tubes. Cell count and viability were assessed by performing trypan blue (cat. no.: T18154, MilliporeSigma, MO, USA) staining (in a sterile 1.5 mL microcentrifuge tube → mix 50 µL cell suspension + 50 µL trypan blue). 50 µL

cell/trypan blue suspensions were pipetted onto a prepared haemocytometer (cat. no.: BS 748, Hawksley, UK). The haemocytometer was imaged on a microscope and viable cells (unstained) were counted (4 squares; top right, top left, bottom right and bottom left → each square measuring 4×4 squares). The total number of cells per volume was calculated using the following formula: (total number of counted cells/4) × 10,000 × 0.5 mL. Cell suspensions were then delivered on ice to the Glasgow Polyomics Institute.

2.10.2 The principle of 3′-end 10x Chromium microfluidics-based single cell RNA sequencing

The 3′-end 10x Chromium microfluidics-based scRNAseq platform allows high throughput single cell transcriptome analysis. Our group successfully utilised this technology to analyse transcriptomes from TGF-β_1-treated and untreated control primary HSVSMCs (unpublished data) (Low et al., 2019). Gel Bead-in-Emulsion (GEM)s are generated by combining barcoded Single Cell 3′ v3 Gel Beads, a master mix containing HSVSMCs and partitioning oil on an 8-channel microfluidic chip (Figure 2-9 A) (Zheng et al., 2017). Each Gel Bead is made up of oligo(dT)VN primers which contain a unique 16 bp 10x barcode which allows mapping of each amplified RNA molecule to the original cell following next-generation sequencing (Figure 2-9 B). In addition, each primer contains an Illumina Read 1 sequence and a unique molecular identifier (UMI) sequence. Cells are delivered at a limiting dilution to minimise the chance of co-occurrence of more than one cell in the same GEM thereby achieving single cell resolution. Within each generated GEM, oligo(dT)VN primers prime mature mRNAs at the 3′ poly-A tail for reverse transcription. GEMs are then collected in the GEM outlet and subjected to cDNA library generation which forms the basis for next-generation sequencing. In summary, this technology enables individual transcriptome profiling of a defined number of primary HSVSMCs following 24-h BMP-9 and/or TGF-β_1-treatment.

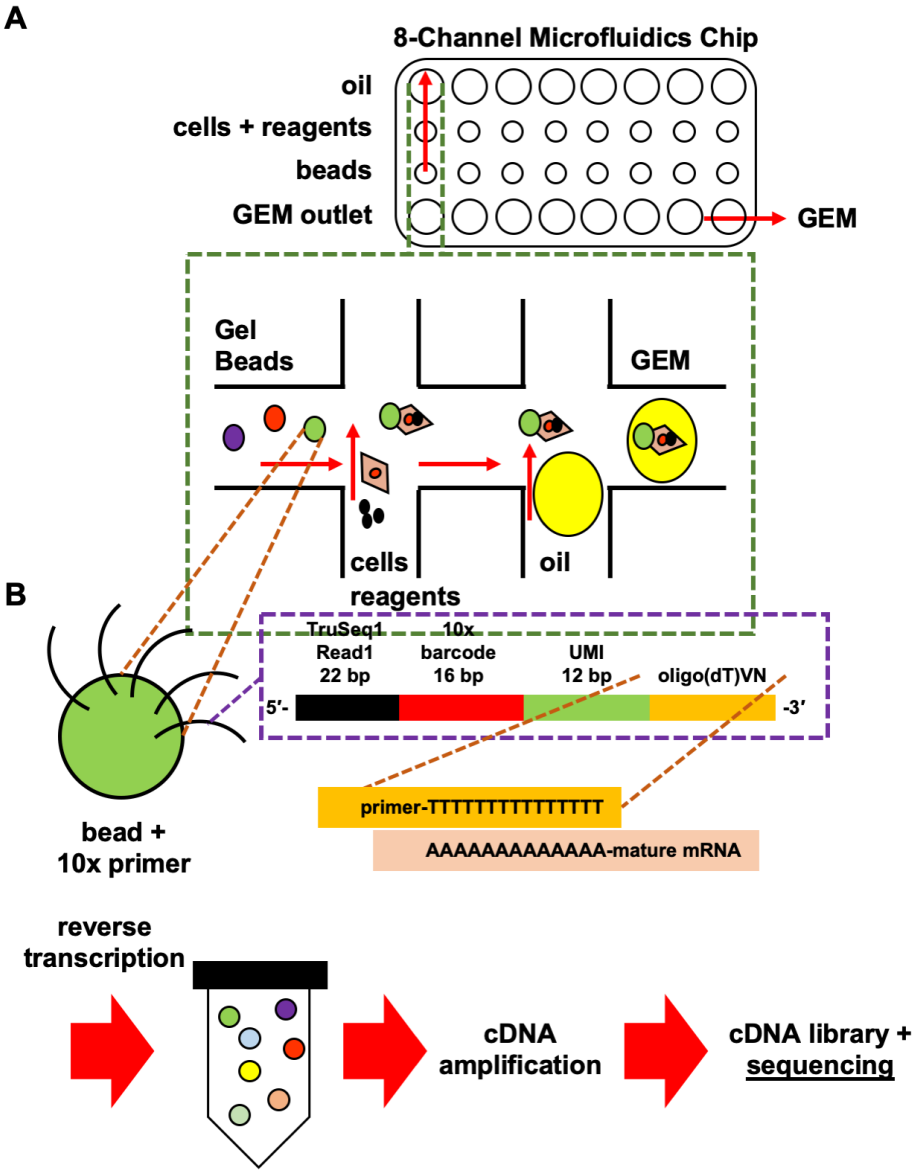

Figure 2-9 Schematic representation of 3′-end 10x Chromium single cell RNA sequencing. (**A**) GEM generation by mixing of single cell/master mix suspension, Gel Beads and partitioning oil on an 8-channel microfluidic chip. (**B**) Single Cell 3′ v3 Gel Bead is a bead loaded with primers which contain an oligo(dT)VN, a 12 bp UMI, a unique 16 bp 10x barcode and a 22 bp Illumina Read 1 sequence (TrueSeq1 Read1). Each GEM is subjected to reverse transcription, cDNA amplification/library preparation and NextGeneration sequencing. Taken and modified from Zheng *et al.* (Zheng et al., 2017).

2.10.3 cDNA library preparation and next-generation sequencing

Single cell cDNA library preparation and next-generation sequencing were performed at the Glasgow Polyomics Institute. The 10x v3 chemistry kit (cat. no.: PN-1000092, 10x Genomics, CA, USA) was used to generate Illumina compatible cDNA libraries following the manufacturer's instructions. Libraries were then sequenced on an Illumina NextSeq500 sequencer.

2.10.4 Raw data processing

Biomage Ltd (Adam Kurkiewicz and Marcell Pék) adapted an existing computational Python pipeline for single cell (sc) RNA sequencing (seq) analysis and performed biostatistical analyses. Julian Schwartze participated in biostatistical analyses.

In brief, the CellRanger v3.1.0 software (10x Genomics, CA, USA) was used to process FASTQ files obtained from the NextSeq500 sequencer, to perform nucleotide sequence alignment against the GRCh38 reference genome and to generate BAM files (Zheng et al., 2017). The aligner utilised by the CellRanger software is the spliced transcripts alignment to a reference (STAR) aligner (Dobin et al., 2013). BAM files entailed position-sorted/aligned reads and error-corrected cellular/molecular barcodes. The dropEst pipeline was utilised to process BAM files (Petukhov et al., 2018). This included estimating molecular counts per cell and creating a primary count matrix. To perform RNA velocity analysis, dropEst was utilised to separate count matrices which only accounted for UMIs classified as intronic, exonic or exon/intron spanning. Resulting R matrices were exported in the MatrixMarket format. Generated matrices containing cellular barcodes identified by CellRanger were loaded into the existing computational Python pipeline for scRNAseq. An aggregated AnnData matrix was generated for further data processing. Detailed notebooks are freely available on GitHub (https://nbviewer.jupyter.org/github/picrin/vascular_TGFB1/tree/master/analysis/). Quality control and data analyses are presented in section 6.3.

2.11 Carotid artery ligation study in mice

All animal procedures were approved by the Home Office under the Animals Scientific Procedures Act 1986. This study was performed as authorised by the Home Office under the project license number 70/8572, procedure 3 (PPL holder: Prof. Simon Kennedy, ICAMs).

2.11.1 Experimental mice and housing conditions

Male C57BL/6 mice (8-10 weeks old) were ordered from Charles River Laboratories (MA, USA). Mice were housed in 12-h light/dark conditions at a constant temperature of 21°C with free access to water and standard mouse chow. Following arrival, mice were allowed to adjust to their new housing conditions for 2 weeks prior to being subjected to the carotid artery ligation procedure. Following the surgical procedure, mice were separated and housed in individual cages until termination (Schedule 1 procedure) at indicated time points.

2.11.2 Study design

Following the carotid artery ligation procedure (section 2.11.3), mice were divided into 6 groups (n=6-8 per group) and terminated at indicated time points (Figure 2-10). 5-ethynyl-2′-deoxyuridine (EdU) (cat. no.: C10337, Thermo Fisher Scientific, MA, USA) was made up in sterile 1× phosphate-buffered saline (PBS; cat. no.: 14190144, Thermo Fisher Scientific, MA, USA) to achieve a concentration of 25 mg/mL. 100 μL of 25 mg/mL EdU/1× PBS solution (effective dose 2.5 mg/animal) was injected intraperitoneally (i.p.) to each animal with a 30G insulin syringe (cat. no.: 324826, Becton Dickinson, NJ, USA) 3-5 h prior to termination to label proliferating vascular cells. Following termination (section 2.11.4), target tissues and blood were harvested for analysis.

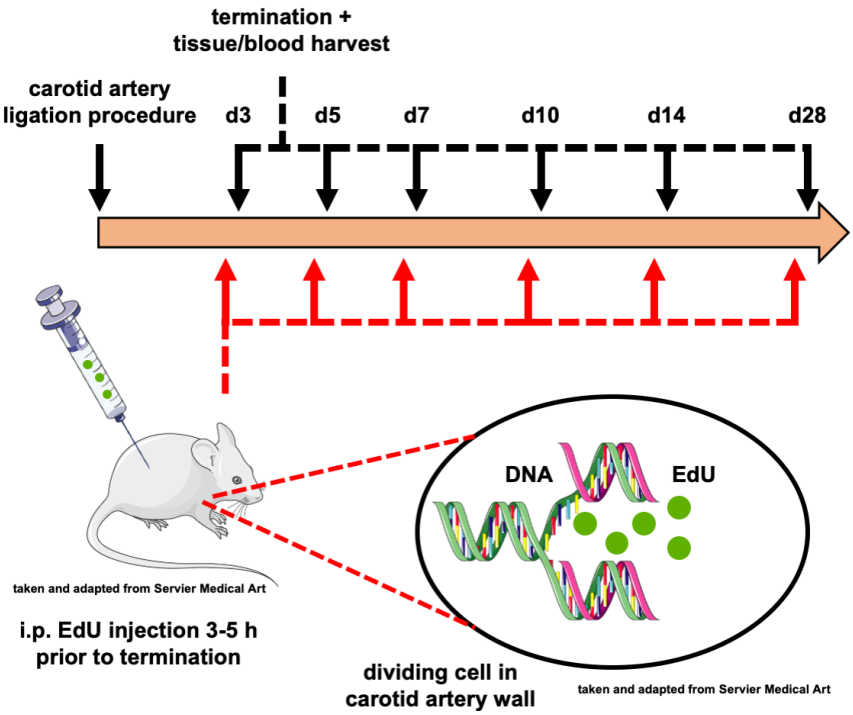

Figure 2-10 Carotid artery ligation study design. Following carotid artery ligation surgery, mice (aim → n=8 per group) were terminated at indicated time points. EdU/1× PBS solution (effective dose 2.5 mg/animal) was injected i.p. 3-5 h prior to termination and subsequent organ/blood harvest. EdU labels proliferating cells thereby enabling quantification of dividing vascular cells at indicated time points.

2.11.3 The carotid artery ligation procedure

The carotid artery ligation procedure induces NF, and was performed as described by Kumar and colleagues (Kumar and Lindner, 1997) (Figure 2-11A). All operating instruments and equipment were sterilised prior to surgery.

Prior to surgery, each animal received a subcutaneous (s.c.) 0.5 mL saline/glucose solution injection (0.9% (w/v) sodium chloride/5% (w/v) glucose, cat. no.: FKE1064, Baxter, IL, USA) to prevent dehydration during surgery. Each animal received a s.c. 0.03 mL buprenorphine injection for peri- and post-operative pain relief (Vetergesic®, Ceva Animal Health Ltd., UK). Sedation was initiated with isoflurane (IsoFlo®, Zoetis, NJ, USA) at a flow rate of 2 L/min. Each animal's neck incision site was shaved and pre-warmed chlorhexidine (Hydrex™, Ecolab, MI, USA) was applied to sterilise the skin. A lubricant creme was applied to the eyes to prevent drying out during surgery. The sedated mouse was gently positioned on its back below the operating microscope and above a pre-warmed heat pad, located below a sterile surgical field. The mouse's back neck was placed on a small cushion to achieve neck extension thereby facilitating ventral neck incision. Both front paws were gently extended and loosely fixated with sterile autoclave tape. The mouse's nose was placed inside an anaesthetic cone used to deliver isoflurane (flow rate 2 L/min) and 100% O_2 (flow rate 2 L/min) to achieve peri-operative sedation. The absence of paw reflexes indicated sedation prior to incision. A sterile surgical drape was placed over the anaesthetic cone prior to making the first incision. The operative assistant continuously monitored the mouse's breathing throughout the surgical procedure.

The initial incision was made below the chin towards the top of the sternum by using a sterile pair of scissors. Saline solution was injected onto the incision site with a 1 mL syringe (Injekt®-F Solo, B. Braun, Germany) to keep tissues hydrated. The left and right salivary glands were separated by blunt dissection using two pairs of fine sterile forceps. Following gland separation, the left salivary gland was liberated by creating a pocket between the gland and the skin. Some saline solution was added to the skin left of the incision site and a small swab was placed on top. The left salivary gland was everted onto the hydrated swab and the remaining piece of the swab was folded onto the gland.

Saline solution was added to protect the gland from dehydration. The left common carotid artery (LCAR) was exposed by blunt dissection and carefully liberated from the left vagal nerve and surrounding tissues. A sterile non-absorbable suture was cut to a length of approximately 7 cm, carefully passed underneath the left carotid artery and a single knot was made just caudal of the carotid bifurcation to achieve complete common carotid artery ligation. Surplus suture ends were cut off and the left salivary gland was placed back into its original position. The incision was closed with non-absorbable 6-0 Vicryl suture (Ethicon Inc., NJ, USA) using the uninterrupted suturing technique. Instrument sterilisation was performed prior to operating on the next mouse using an autoclave.

Following surgery, each mouse was placed in a separate pre-labelled recovery cage with access to water, water-soaked chow and baby food (Cow & Gate, UK). Cages were placed in the recovery room and mice were monitored daily. EdU was administered via i.p. injection 2- to 3-h prior to termination.

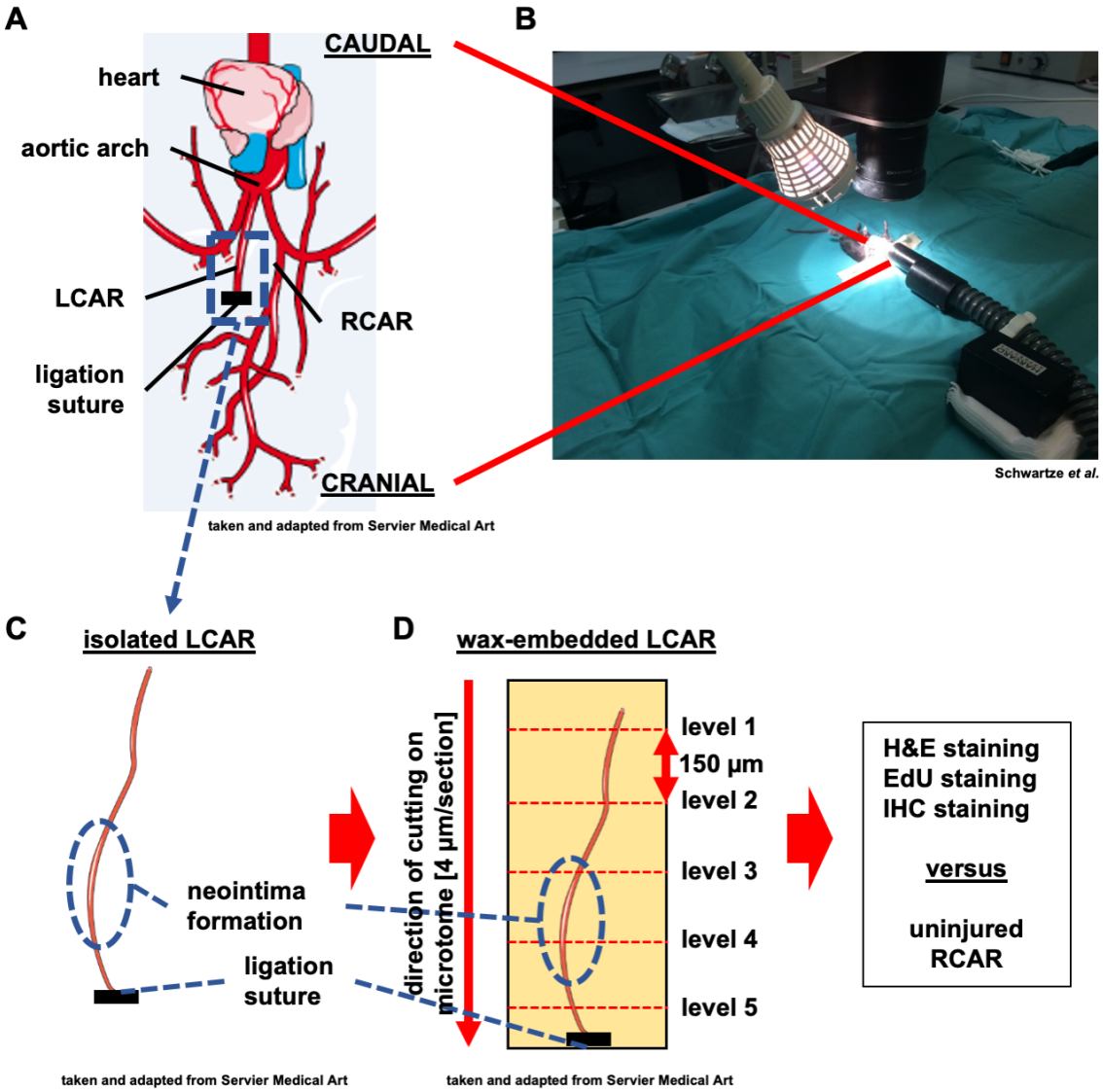

Figure 2-11 Schematic representation of carotid artery ligation procedure and target tissue processing. (**A**) The LCAR is exposed and ligated just caudal of the carotid bifurcation. The RCAR serves as an uninjured control. (**B**) Image shows surgical setup for cadaver practice. (**C**) Following termination, the LCAR (reaching from aortic arch to suture knot) is dissected. (**D**) Following tissue processing, the LCAR is wax embeded and sections are cut at 4 µm on a microtome (5-6 sections/slide, 5-6 slides/level, at least 5 levels/LCAR with each level being 150 µm apart). LCAR sections are then subjected to haematoxylin and eosin (H&E), EdU and immunohistochemistry (IHC) staining.

2.11.4 Schedule 1 procedure (termination)

Mice were separately terminated at indicated time points following the schedule 1 procedure. The mouse was placed into a CO_2 chamber using the non-aversive tunnelling technique. The chamber was sealed, and CO_2 flow rate was turned to 2 L/min until the mouse was unconscious (approximately 2 min). The flow rate was turned up to 80% of the maximum flow rate for another 2 min. The CO_2 supply was turned off and the mouse remained in the sealed chamber for another 2 min. The terminated mouse was taken out of the chamber and checked for signs of life which included assessing breathing, paw reflexes and palpating for a heartbeat. The chamber was tipped over to allow CO_2 to flow out. Death was confirmed by cervical dislocation prior to proceeding to organ/blood harvest.

2.11.5 Organ/Blood harvest

Following termination, the LCAR, the RCAR, the heart and the thoracic aorta were carefully removed, and a blood sample was taken. All dissected tissues were carefully placed in 4% (w/v) PFA (Table 2-2) in individual 1.5 mL microcentrifuge tubes and kept in a +4-°C fridge overnight. The next day, each tissue sample was washed twice in sterile 1× PBS, placed in 70% (v/v) ethanol in a fresh sterile 1.5 mL microcentrifuge tube and stored in a 4°C fridge prior to tissue processing. Serum containers (cat. no.: 367959, Becton Dickinson, NJ, USA) were subjected to centrifugation at 8,000 g and room temperature for 1 min enabling blood phase separation. The upper phase/blood serum was carefully transferred to a sterile 1.5 mL microcentrifuge tube which was stored in a -80°C freezer.

2.12 EdU staining

EdU staining was performed following the manufacturer's instructions (cat. no.: C10337, Thermo Fisher Scientific, MA, USA). One slide per mouse was stained. This slide contained the level demonstrating the most pronounced lesion following ligation surgery (Figure 2-11 D). Respective slides were put in a slide rack and placed in a glass trough for dewaxing and rehydration described in Table 2-40.

Table 2-40 Processing sequence for dewaxing and rehydrating sections for EdU Click-iT staining.

Stage	Reagent	Time [min]
Dewaxing	Histoclear (cat. no.: HS 200, national diagnostics, GA, USA)	5
	Histoclear	5
Rehydration	100% (v/v) ethanol	5
	95% (v/v) ethanol	5
	70% (v/v) ethanol	5
	50% (v/v) ethanol	5
	Running tap water	5

During the last step, 1× citric saline antigen retrieval buffer (pH 6) was prepared (Table 2-41).

Table 2-41 Recipe for 500 mL of 1× citric saline antigen retrieval buffer (pH 6).

Reagent	Amount
Tri-sodium citrate (cat. no.: 71402, MilliporeSigma, MO, USA)	1.47 g
ddH_2O	500 mL
Note: adjust pH to 6.	

The buffer was poured into a plastic trough, covered with saran wrap containing punched holes and was pre-heated on high power in a microwave for 4 min. The slide rack containing respective slides was placed in the plastic trough containing pre-heated antigen retrieval buffer. The plastic trough was covered with saran wrap containing punched holes and was microwaved on low power for 15 min. The slide rack was placed under running tap water for 10 min to cool down the slides. Slides were gently patted dry on absorbent paper and wax circles were drawn around each individual section on each slide using a wax pen (cat. no.: NC9545623, CA, USA). Sections were then permeabilised with 70 μL 0.1% (v/v) triton-X-100 (cat. no.: X100, MilliporeSigma, MO, USA)/1× PBS solution in a humidifying chamber at room temperature for 10 min. During this

step, the Click-iT reaction cocktail was made up allowing a final volume of 60 μL per section (Table 2-42).

Table 2-42 Composition of Click-iT reaction cocktail for approximately 50 slides.

Component	Volume
1× Click-iT reaction buffer	10.7 mL
$CuSO_4$ (component E)	500 μL
Alexa Fluor azide	31 μL
Reaction buffer additive	1.25 mL
Note: total volume **12.5 mL**, add ingredients in the order listed in the table (all ingredients part of EdU staining kit).	

The permeabilisation buffer was removed and sections were washed twice in 60 μL 3% (w/v) BSA (cat. no.: A3311, MilliporeSigma, MO, USA)/1× PBS solution. Following these washing steps, 60 μL Click-iT reaction cocktail was added to each section and slides were left to incubate in a humidifying chamber (protected from light) at room temperature for 30 min. The reaction cocktail was discarded, and sections were washed twice in 60 μL 3% (w/v) BSA/1× PBS solution. Slides were washed once in 1× PBS in a plastic trough covered with tin foil. During this step, a 1:1,000 Hoechst solution (part of the Click-iT kit) was prepared in 1× PBS. Slides were gently tapped on absorbent paper to remove excess PBS. 1:1,000 Hoechst/1× PBS solution was added to each section and slides were incubated in in a humidifying chamber (protected from light) at room temperature for 10 min. Slides were washed twice in 1× PBS in a plastic trough covered with tin foil. Following these washing steps, slides were gently tapped on absorbent paper to remove excess 1× PBS. Next, 4′,6-diamidino-2-phenylindole (DAPI) Pro-long GOLD mounting medium (cat. no.: ab104139, abcam®, UK) was added to each section and a cover slip was carefully placed on each slide and left to set overnight. The next day, slides were sealed with nail varnish prior to imaging on the LSM880 confocal microscope (Zeiss, Germany). All visualisation and quantification steps are outlined in Figure 2-12.

A

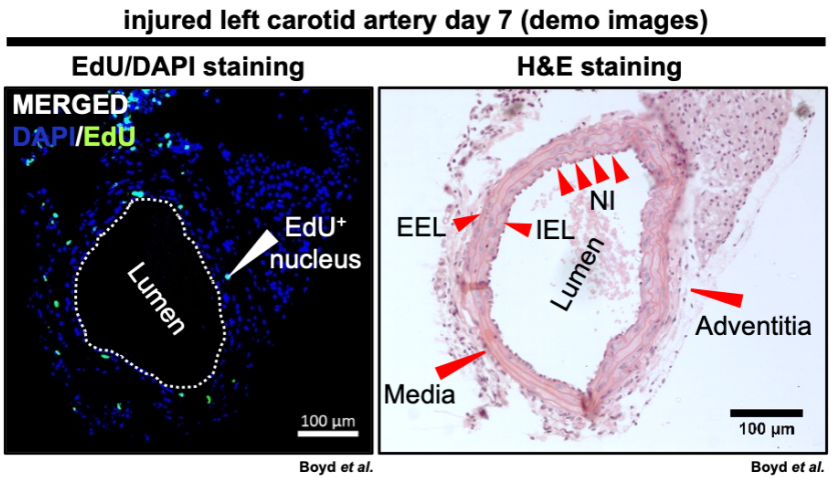

B

Take images on confocal microscope (LSM880, Zeiss)

→ 20× magnification, GaAsP-T1 channel (DAPI & 488)
→ obtain images using the Zen system software (Zeiss)
→ export image as jpeg. file without scale bar

Area fluorescence analysis using the Image J software

→ open jpeg. file in picture viewer and increase magnification (if possible, analyse 3 sections/animal)
→ For **488** (green) channel → EdU staining analysis:
  → upload jpeg. file without the scale bar into the Image J software
  → Image → Type → 8-bit (convert to grey scale)
  → Image → Adjust Threshold (increase background to cancel out DAPI staining) → Apply
  → Analyze → Measure (black background %)
→ For **DAPI** (blue) channel → DAPI staining analysis
  → upload jpeg. file without the scale bar into the Image J software
  → Image → Color → Split Channels (continue with blue channel)
  → Image → Adjust Threshold → Apply
  → Analyze → Measure (black background %)

calculations in Microsoft Excel

→ EdU staining % = 100% - black background %
→ DAPI staining % = 100% - black background %
→ EdU/DAPI ratio = EdU staining % / DAPI staining %

Figure 2-12 Workflow for quantifying EdU-stained murine carotid artery sections. (**A**) Corresponding DAPI/EdU- (left) and H&E-stained (right) demo images of a ligation injured murine carotid artery. Left image → green dots indicate EdU$^+$-positive nuclei, blue dots indicate DAPI-stained nuclei. Right image → EEL, external elastic lamina; IEL, internal elastic lamina; NI, neointima. (**B**) Workflow for imaging of DAPI/EdU co-stained murine carotid artery sections and quantifying vascular cell proliferation.

2.13 Haematoxylin and Eosin staining

Sections from ligation injured murine carotid arteries were subjected to H&E staining to determine changes in intimal area, medial area and intima/media ratio. Morphometric analysis for one ligation injured murine carotid artery entailed one slide (3-4 sections) for each level (Figure 2-11 D). Respective slides were put in a slide rack which was placed in a glass trough for dewaxing and rehydrating described in Table 2-43.

Table 2-43 Processing sequence for dewaxing and rehydrating sections prior to H&E staining.

Stage	Reagent	Time [min]
Dewaxing	Histoclear	7
	Histoclear	7
Rehydration	100% (v/v) ethanol	7
	95% (v/v) ethanol	7
	70% (v/v) ethanol	7
	ddH_2O	7

Following dewaxing and rehydrating, slides were subjected to H&E staining outlined in Table 2-44.

Table 2-44 Processing sequence for staining sections with H&E.

Stage	Reagent	Time
H&E staining	Harris modified Haematoxylin (cat. no.: HHS16, MilliporeSigma, MO, USA)	2 min
	Running tap water	5 min
	70% (v/v) ethanol	30 s (10 dips → 5 min)
	Eosin Y solution (cat. no.: 318906, MilliporeSigma, MO, USA)	2 min
Dehydration	95% (v/v) ethanol	30 s
	95% (v/v) ethanol	30 s
	100% (v/v) ethanol	1 min
	100% (v/v) ethanol	7 min
	100% (v/v) ethanol	5 min
	Histoclear	5 min
	Histoclear	5 min

Following the last step, slides were gently tapped on absorbent paper to remove excess Histoclear solution. 1 drop of DPX (mixture of distyrene, a plasticiser, and xylene; (cat. no.: 05622, MilliporeSigma, MO, USA) was carefully added to each section with a Pasteur pipette to preserve the H&E stain and a cover slip was placed on each slide. Slides were left to dry in the histology hood overnight and were sealed with nail varnish the next day. All visualisation and quantification steps are outlined in Figure 2-13.

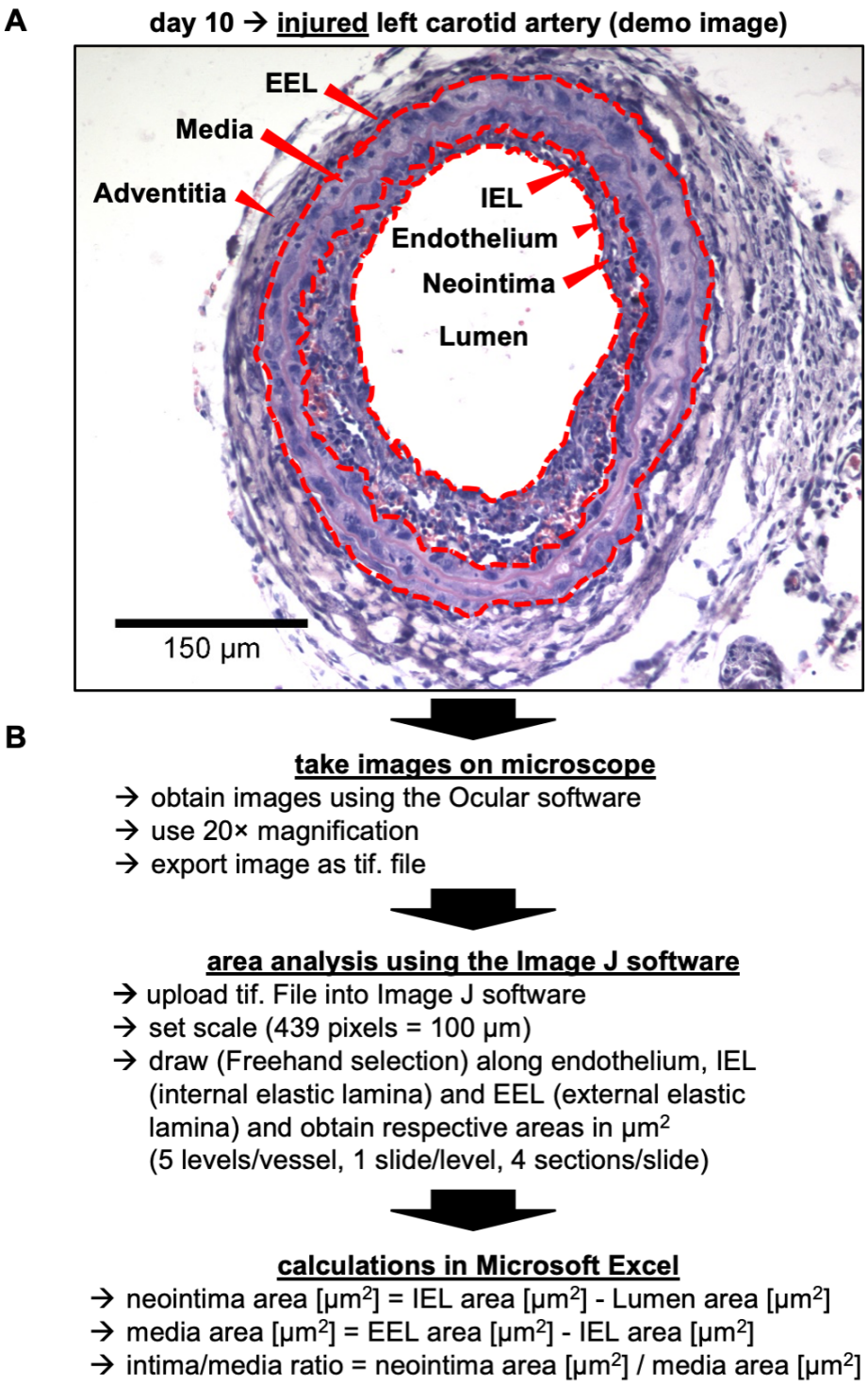

Figure 2-13 Workflow for quantifying intimal and medial areas of H&E-stained ligation injured murine carotid arteries. (**A**) Demo image (20× magnification) showing H&E-stained section of murine carotid artery 10 days following ligation injury (haematoxylin staining → dark purple, indicates nuclei; eosin staining → light purple → indicates cytoplasm/ECM; dotted red lines indicate respective borders between vascular compartments. (**B**) Workflow for imaging H&E-stained murine carotid artery sections and quantifying intimal area, medial area and intima/media ratio.

2.14 Tissue processing for histology

Murine and human tissue samples were placed in labelled tissue cassettes and soaked in 70% (v/v) ethanol. Tissue cassettes were placed in a tissue cassette holder which was placed in a tissue processor for dehydration and paraffin wax embedding (cat. no.: 12505356, Shandon Excelsior™, Fisher Scientific, PA, USA). The next day, tissues were paraffin wax embedded using the Shandon Histocentre 3 embedder (Thermo Fisher Scientific, MA, USA). Human and murine vessels (Figure 2-11 D) were embedded in the upright position. The wax mould containing target tissue/tissue cassette were left to cool for 30 min prior to removing the mould. Embedded tissues were stored at room temperature and placed at -20°C for 1-h prior to sectioning. Embedded HSV samples were sectioned at 5 μm and murine vessels were sectioned at 4 μm on a microtome. Wax ribbons were carefully transferred to a 40°C water bath and left to float. Wax ribbons were mounted on pre-labelled silane-treated glass slides (cat.no.: N/C360G, Dixon Science, UK), placed in a 60°C oven to melt the paraffin wax overnight and stored in a slide box at room temperature the next day.

2.15 Immunohistochemistry

HSV and murine carotid artery sections were subjected to IHC staining to determine target protein presence. Respective slides were put in a slide rack which was placed in a glass trough for dewaxing and rehydrating described in Table 2-45.

Table 2-45 Processing sequence for dewaxing and rehydrating sections prior to IHC staining.

Stage	Reagent	Time [min]
Dewaxing	Histoclear	5
	Histoclear	5
Rehydration	100% (v/v) ethanol	5
	100% (v/v) ethanol	5
	90% (v/v) ethanol	5
	70% (v/v) ethanol	5
	50% (v/v) ethanol	5
	Running tap water	5

During the last step, 1× citric saline antigen retrieval buffer (Table 2-41) was prepared and pre-heated in a plastic trough in a microwave. The slide rack was placed in the plastic trough containing pre-heated antigen retrieval buffer. The plastic trough was covered with saran wrap containing punched holes and was microwaved on low power for 15 min. The slide rack was placed under running tap water for 10 min to cool down the slides. Slides were gently patted dry on absorbent paper and wax circles were drawn around each individual section on each slide using a wax pen. Slides were washed 3 times for 3 min in 1× tris-buffered saline (TBS) buffer (Table 2-46).

Table 2-46 Recipe for 1 L of 10× TBS buffer (pH 7.5).

Reagent	Amount
Tris-base	24.2 g
NaCl (cat. no.: X190, VWR International, PA, USA)	87.7 g
Note: add 900 mL of ddH_2O, pH to 7.5 using HCl (cat. no.: 320331, MilliporeSigma, MO, USA), top up with ddH_2O to 1 L. For 1 L of 1× TBS buffer, dilute 100 mL 10× TBS buffer in 900 mL ddH_2O.	

Following these washing steps, each section was incubated in 1× TBS + 0.05% (v/v) Tween 20 (TBST, (Table 2-47)/15% (v/v) goat serum (cat.no.: S-1000-20,

Vector Laboratories, UK) in a humidified chamber at room temperature for 30 min.

Table 2-47 Recipe for 1 L of 10× TBS 0.5% (v/v) Tween buffer (pH 7.5).

Reagent	Amount
Tris-base	24.2 g
NaCl	87.7 g
Tween 20	5 mL
Note: add 900 mL of ddH_2O, add 5 mL Tween 20, pH to 7.5 using HCl, top up with ddH_2O to 1 L. For 1 L of 1× TBST buffer, dilute 100 mL 10× TBST buffer in 900 mL ddH_2O.	

Following the blocking and permeabilisation steps, sections were incubated with respective primary antibodies (Table 2-48) diluted to required concentrations in 1× TBST/10% (v/v) goat serum at 4°C overnight. Appropriate IgG controls (normal rabbit IgG, 3 mg/mL, cat.no.: 10500C, Thermo Fisher Scientific, MA, USA; normal mouse IgG, 3 mg/mL, cat.no.: 10400C, Thermo Fisher Scientific, MA, USA) were diluted to corresponding concentrations in 1× TBST/10% (v/v) goat serum to control for non-specific staining.

Table 2-48 List of primary antibodies used for IHC.

Protein	Source	Clonality	Concentration [mg/mL]	Working dilution	Cat. no., company
αSMA	Mouse	Monoclonal	0.071	1:100	GA61161-2, Agilent Technologies, CA, USA
Calponin	Rabbit	Monoclonal	0.063	1:100	ab46794, abcam®, UK
SM22-α	Rabbit	Polyclonal	1	1:100	ab14106, abcam®, UK
MYH11	Rabbit	Polyclonal	2	1:100	ab53219, abcam®, UK
BMP-9	Rabbit	Polyclonal	1	1:100	ab35088, abcam®, UK

The next day, slides were gently tapped on absorbent paper to remove the primary antibody solution and washed 3 times for 5 min in 1× TBS buffer. Following these washing steps, sections were incubated with the respective fluorescent secondary antibodies (goat anti-rabbit IgG Alexa Fluor® 546, 2 mg/mL, 1:500, cat. no.: A-11035, Thermo Fisher Scientific, MA, USA; goat anti-mouse IgG Alexa Fluor® 488, 2 mg/mL, 1:500, cat. no.: A-11001, Thermo Fisher Scientific, MA, USA) diluted in 1× TBST at room temperature for 2-h protected from light. Following this incubation step, slides were gently tapped on absorbent paper to remove the secondary antibody solution and washed 3 times for 5 min in 1× TBS buffer protected from light. Each section was incubated with Sudan Black B (cat. no.: 199664, MilliporeSigma, MO, USA) in 70% (v/v) ethanol at room temperature for 10 min (protected from light) to quench lipofuscin-mediated fluorescence. Following this step, slides were gently tapped on absorbent paper to remove Sudan Black B solution and washed 3 times for 5 min in 1× TBS buffer protected from light. Sections were stained with 10 μg/mL DAPI diluted in 1× TBS buffer at room temperature for 10 min (protected from light). DAPI Pro-long GOLD mounting medium was added to each section and a cover slip was carefully placed on each slide. Mounting medium was allowed to set overnight. The next day, slides were sealed with nail varnish prior to imaging on the LSM510 confocal microscope (Zeiss, Germany).

For each related set of slides confocal microscope settings were guided by imaging IgG controls first to control for non-specific background fluorescence. Microscope settings were kept constant to allow unbiased comparisons between

slides. Fluorescence intensity analysis was performed using the ImageJ software. Each set of related images was corrected for IgG background fluorescence and the total fluorescence area % was calculated.

2.16 Statistical analysis

Group sizes for carotid artery ligation studies in mice were calculated following the 3Rs guidelines (http://www.3rs-reduction.co.uk/html/6__power_and_sample_size.html). The significance level was set at 5% and the power was set at 80%. Mean sham, mean injury and standard deviation (S.D.) injury were based on a previous carotid ligation study (Daria Boyd) in mice which investigated the effect of a pharmacological inhibitor on vascular proliferation and NF (I/M ratio uninjured carotid artery day 3 mean: 0.04; I/M ratio injured carotid artery day 7 mean ± S.D.: 0.15 ± 0.11). The standard effect size (signal/noise ratio) was calculated following the formula (0.15-0.04)/0.11=1.0. Based on a power of 80% the sample size per group was calculated to be n=17. However, this was refined to group sizes of n=6-8 assuming an approximate standard effect size of 1.6.

Statistical analyses were performed using the GraphPad Prism 4.0 software package. Unless otherwise stated, data are presented as mean ± standard error of the mean (S.E.M.). Comparisons between multiple groups were made using a repeated measures one-way ANOVA test with Tukey's post-hoc correction. Each *in vitro* experiment was carried out in triplicate and was repeated at least three independent times unless otherwise stated. Where indicated, a paired Student's t-test was performed to determine significance. P-values <0.05 were considered statistically significant. N numbers and statistical tests are presented in each figure legend.

Chapter 3 Investigating BMP-9 in human saphenous veins and murine arterial vasculature

3.1 Introduction

Coronary artery disease frequently entails partial or complete stenosis of one or more major coronary arteries limiting blood flow to cardiac tissue and causing common complications such as angina pectoralis, MI, CHF and cardiac arrhythmias (Cassar et al., 2009). Percutaneous coronary intervention or CABG revascularisation therapies may be indicated to re-establish blood flow to cardiac tissue by widening or bypassing stenosed coronary arteries (Neumann et al., 2019). However, re-stenosis is a common complication following these procedures (Campeau et al., 1983; Komatsu et al., 1998). Smooth muscle cell (SMC) phenotype switch-driven NF is a key pathological feature in in-stent re-stenosis (ISR) and coronary SVG disease which results in lumenal obstruction and leads to a decrease in blood flow and subsequent cardiac ischaemia (Farb et al., 1999; Grewe et al., 2000; Kockx et al., 1992; Kockx et al., 1996).

3.1.1 SMC phenotype switching during NF in murine vascular injury models

Several murine vascular injury models display SMC phenotype switch-driven NF, a key pathogenic feature of occlusive SVG disease and ISR (Table 3-1).

Kumar *et al.* first described the murine carotid artery ligation model in which the common LCAR is exposed and ligated just proximal of the carotid bifurcation while the common RCAR serves as an uninjured control.(Kumar and Lindner, 1997). Following total LCAR ligation and abrupt cessation of blood flow, the authors observed an early increase in medial and intimal SMC proliferation which was paralleled by a decrease in medial αSMA expression demonstrating SMC phenotype switching. In addition, leukocytes were detected within the adventitia and forming neointima indicating an inflammatory component during the injury response. Alongside medial hypertrophy 28-day old ligation-injured LCARs displayed an 80% reduction in lumenal area caused by external elastic lamina (EEL) shrinkage and NF. Transgenic mouse studies have since utilised this injury model to identify the origin of the neointimal cells. Yu *et al.* showed that diphteria toxin (DT)-mediated SMC depletion in transgenic SM22-α human DT receptor mice prior to carotid artery ligation blunted NF revealing vSMCs as the source of neointimal cells (Yu et al., 2011). Moreover, a carotid artery ligation

study in SMC lineage-tracing mice demonstrated that approximately 80% of cells within neointimal lesions derived from differentiated mature SMCs indicating SMC phenotype switching as a key pathogenic driver of NF (Herring et al., 2014). Although both studies identified vSMCs as the main source of neointimal cells following carotid artery ligation injury, it was unclear whether medial SMC proliferation preceded proliferation-independent SMC migration to the intima or not. More recently, the transgenic lineage tracing Myh11-CreERt2/Rosa26-Confetti mouse has been utilised to address this question (Chappell et al., 2016). In these mice, vSMCs randomly express 1 of 4 fluorescent proteins (green, yellow, red and cyan) which enables more accurate tracing of neointimal cells following carotid artery ligation injury. Chappell *et al.* found that 28-day old vSMC-derived neointimal patches were connected to medial patches that expressed the identical fluorescent colour. This means that medial SMC proliferation precedes SMC migration to the intima and subsequent intimal SMC proliferation. The authors estimated that <0.1% of medial vSMCs contributed to NF highlighting extensive SMC plasticity. In addition to SMC phenotype switching, the murine carotid artery ligation model triggers endothelial dysfunction and inflammation thereby recapitulating additional pathogenic drivers of coronary SVG disease and ISR (Costa and Simon, 2005; de Vries et al., 2016; Squadrito et al., 2003; Yahagi et al., 2016; Yamashita et al., 2001). However, the presence of intact endothelium and absence of platelet aggregation limit this model's ability to accurately mimic human pathology, since endothelial denudation along with platelet aggregation occur upon coronary SVG and/or stent implantation (Grewe et al., 2000; Sasaki et al., 2000).

Lindner *et al.* introduced the murine carotid wire injury model in which a flexible wire (0.35 mm diameter) is inserted into the LCAR under rotation causing endothelial denudation (Lindner et al., 1993). The uninjured RCAR serves as a control. In contrast to ligation injury, wire injury enables the study of vascular injury responses in the absence of endothelium while blood flow is maintained. Hence, it more accurately mimics mechanical endothelial damage and platelet aggregation which occur upon coronary SVG and/or stent implantation. Like ligation injury, carotid artery wire injury induces early medial and intimal SMC proliferation accompanied by a loss of SMC αSMA expression demonstrating SMC phenotype switching. In contrast to ligation injury, SMC

proliferation only occurs in endothelium-denuded segments. 14-day old injured LCARs display mild NF alongside leukocyte infiltration and re-endothelialisation is fully achieved by day 21. Transgenic mouse studies have also been successful in identifying novel regulators of NF. Yoshida *et al.* showed that SMC-specific inhibition of pro-inflammatory nuclear factor (NF)κB signalling in transgenic SM22-α-Cre/IκBDeltaN mice attenuated repression of SMC contractile proteins and NF following carotid artery wire injury indicating SMCs as a major source of NF in this injury model (Yoshida et al., 2013).

Although wild-type mice do not spontaneously develop atherosclerotic lesions following vascular injury, carotid artery ligation and wire injury in transgenic hyperlipidaemic ApoE-deficient mice fed an atherogenic diet triggers accelerated neointimal atherosclerotic plaque development compared to wild-type controls (Chang et al., 2017; Schober et al., 2004). Hence, these injury models also enable the study of accelerated atherosclerosis, an important pathogenic feature in late stages of SVG disease and ISR (Hasegawa et al., 2006; Kern et al., 1981). From a technical point of view the carotid artery ligation surgery is less challenging compared to the carotid artery wire injury surgery and more reproducibly triggers NF. In terms of pathophysiological relevance for SVG disease and ISR, carotid artery wire injury more closely mimics human disease.

In addition to ligation injury and carotid artery wire injury, the femoral artery wire injury and venous bypass graft atherosclerosis models were developed in mice to recapitulate human disease (Sata et al., 2000; Zou et al., 1998). In femoral artery wire injury, a guide wire is inserted into the right or left femoral artery causing endothelial denudation and vessel dilatation. Like carotid artery wire injury, femoral artery wire injury causes SMC phenotype switching. However, NF is greater, probably because of utilisation of a larger guide wire in a smaller vessel causing greater damage. Hence, this model more accurately mimics mechanical dilatation and endothelial denudation as seen in SVGs during checking for graft leakage and following implantation as well as in coronary balloon angioplasty and/or stent inflation (de Vries et al., 2016; Grewe et al., 2000; Morinaga et al., 1985; Steele et al., 1985). In the murine venous bypass graft atherosclerosis model, either the autologous right external jugular vein (REJV) or isogenic REJV or inferior vena cava are inter-positioned into the

common carotid artery via end-to-end anastomosis triggering vein graft SMC phenotype switching and NF (Zou et al., 1998). In addition, it is valuable tool for studying *ex vivo* gene transfer or drug treatment. Furthermore, this model may be used to inter-position vein grafts from genetically modified mice into carotid arteries from wild-type litter mates. Although this model most closely resembles human SVG disease compared to arterial injury models, high technical skills are required to reproducibly employ this technique.

Table 3-1 Murine vascular injury models

Model	Procedure	Key pathogenic features of SVG disease and/or ISR	Advantages/disadvantages
Carotid ligation (Kumar and Lindner, 1997)	Complete CA ligation proximal to carotid bifurcation	• Endothelial activation • Inflammation • SMC phenotype switching • Medial hypertrophy and NF	• Non-thrombogenic surface, endothelium remains mechanically intact • Reproducible neointimal lesions • Simple procedure
Carotid wire injury (Lindner et al., 1993)	Wire insertion via external CA into communal CA	• ED • Inflammation • SMC phenotype switching • NF	• ED in the presence of blood flow mimic early SVG disease • SMC proliferation stops once re-endothelialisation has occurred • Neointima does not exceed 2-3 layers
Femoral artery wire injury (Sata et al., 2000)	Wire insertion via muscular FA branch into main FA	• ED and early SMC apoptosis • Vessel dilatation • Inflammation • SMC phenotype switching • NF	• ED in the presence of blood flow mimic early SVG disease • Reproducible neointimal lesions
Perivascular collar (Moroi et al., 1998)	Cuff loosely tied in place around FA	• Compromised vasa vasorum in adventitia • Inflammation • SMC phenotype switching • NF (male > female)	• Non-thrombogenic surface, endothelium remains intact • Compromised vasa vasorum mimic initial loss of vasa vasorum in vein graft • Reproducible neointimal lesions
Perivascular electric stimulation (Carmeliet et al., 1997)	Single perivascular FA electric shock	• ED and non-occlusive TF • Inflammation • SMC phenotype switching • NF	• Non-occlusive TF mimics early SVG disease • Reproducible neointimal lesions • Great level of trauma to vessel
Venous bypass graft atherosclerosis (Zou et al., 1998)	Inter-positioning of autologous external JV or isogenic JV/VC	• Ischaemia, ED and dilatation • Vessel wall degeneration • Inflammation • SMC phenotype switching • NF	• Closely mimics early and intermediate SVG disease • Vein graft can derive from genetically modified mouse • *Ex vivo* gene transfer or drug treatment

Abbreviations. CA, carotid artery; FA, femoral artery; JV, jugular vein; VC, vena cava; SVG DISEASE, vein graft disease; ISR, in-stent restenosis; CD45, cluster of differentiation 45; SMC, smooth muscle cell; NF, neointima formation; ED, endothelial denudation; TF, thrombus formation.

3.1.2 BMP-9 in vascular health and disease

BMP-9 is a member of the TGF-β superfamily and regulates osteogenesis and glucose and lipid metabolism (Liao et al., 2017; Song et al., 1995; Yang et al., 2019). Two murine studies found that the liver and lung predominantly expressed BMP-9, which is encoded by the *Gdf2* (growth differentiation factor 2) gene (Liu et al., 2020b; Miller et al., 2000). In healthy adult humans, circulating BMP-9 serum/plasma concentrations were found to range between 2 and 12 ng/mL (David et al., 2008). For this study, the authors utilised an activity assay to determine BMP-9 serum and plasma levels. In contrast, *Olsen et al*. utilised an ELISA assay to determine circulating BMP-9 serum levels in healthy humans (Olsen et al., 2014). The study revealed a median of 110 pg/mL for circulating BMP-9 serum levels in healthy humans and, hence, much lower circulating BMP-9 levels than previously reported. Importantly, Wang *et al*. found that circulating BMP-9 plasma levels, determined by ELISA assay, ranged between 20.8 and 60.7 pg/mL in healthy humans (Wang et al., 2019). This indicates that circulating BMP-9 plasma levels were lower than serum levels as previously shown by *Olsen et al*. and, hence, BMP-9 plasma and serum levels are not equivocal.

Functionally, BMP-9 binds to ALK1 triggering complex formation with BMPR2 and/or ACVR2A/B and subsequent SMAD1/5 phosphorylation (David et al., 2007; Mitrofan et al., 2017). Pre-clinical and clinical studies have implicated de-regulation of BMP-9/ALK1 signalling in endothelial-driven pathologies including cancer neo-angiogenesis, HHT and PAH (Brand et al., 2016; David et al., 2008; Hodgson et al., 2020; Levet et al., 2013; Long et al., 2015; Wang et al., 2019; Wooderchak-Donahue et al., 2013; Zhu et al., 2015). The involvement of BMP-9/ALK1 signalling in angiogenesis has shown opposing results in different disease settings. Suzuki *et al*. found that BMP-9 treatment promoted *in vivo* angiogenesis in a Matrigel-plug assay and in a murine xenograft model of human pancreatic cancer indicating BMP-9/ALK1 signalling as a driver a cancer angiogenesis (Suzuki et al., 2010). In contrast, David *et al*. demonstrated that BMP-9 inhibited FGF-driven angiogenesis suggesting that BMP-9 mediates vascular quiescence in healthy vessels (David et al., 2008). In line with these findings, a 2013 study showed that 4 distinct *GDF2* mutations were linked with vascular activation and anomalies associated with HHT (Wooderchak-Donahue et al., 2013).

More recently, causal *GDF2* mutations have also been identified in idiopathic (I)PAH patients (Wang et al., 2019). In addition, PAH patients carrying *GDF2* mutations also demonstrated reduced BMP-9 serum levels. Systemic administration of recombinant BMP-9 to mice carrying a heterozygous human *BMPR2* mutation, known to cause PAH, reversed PAH suggesting a protective effect in the pulmonary vasculature (Long et al., 2015). Contrasting these findings, Tu *et al*. showed that loss of BMP-9 by genetic deletion or pharmacological inhibition partially protected mice and rats from experimental pulmonary hypertension indicating BMP-9 as a pathogenic driver of PAH (Tu et al., 2019).

More recent studies investigating the role of BMP-9 in metabolic disease reported reduced circulating BMP-9 levels in newly diagnosed T2DM patients (Luo et al., 2017). In parallel to these findings, a further study demonstrated a negative association of circulating BMP-9 levels with BMI, hepatic insulin resistance (IR) and fasting glucose levels (Liu et al., 2019). The same study revealed reduced BMP-9 levels in CAD and systemic hypertension patients suggesting that lower BMP-9 levels may be linked to increased cardiovascular risk. Opposing these results, Zhu *et al*. found that paediatric CKD patients demonstrated increased circulating BMP-9 serum levels (Zhu et al., 2015). This study also showed that BMP-9/ALK1 signalling mediated osteoblastic differentiation of isolated primary murine aortic SMCs suggesting a role for BMP-9 in arterial calcification. Furthermore, BMP-9/ALK1 signalling potentiated lipopolysaccharide (LPS)-induced monocyte recruitment to bovine ECs via up-regulation of toll-like receptor (TLR)4, vascular adhesion molecule (VCAM)-1 and E-selectin expression (Appleby et al., 2016). The same study revealed that i.p. injection of BMP-9 increased leukocyte recruitment to pulmonary endothelium in LPS-challenged mice compared to LPS-challenged mice only, suggesting a role for BMP-9 in mediating vascular inflammatory responses.

The pleiotropic cytokine TGF-β_1 may also activate ALK1 signalling (Schwartze et al., 2014). TGF-β_1 binds to TGFBR2 which either forms a complex with ALK5 or ALK1 (Bobik, 2006). Whereas ALK5 activation triggers SMAD2/3 phosphorylation, ALK1 activation induces SMAD1/5 phosphorylation (Schwartze et al., 2014). The ability of TGF-β_1 to signal via the ALK5 and/or the ALK1 signalling axis poses a

challenge when investigating this pleiotropic cytokine in NF. SMC-specific depletion of ALK5 in transgenic mice attenuated NF following femoral artery wire injury indicating that ALK5 signalling drives phenotype switching (Liao et al., 2016). Less research has focussed on lateral opposing ALK1/SMAD1/5 signalling in SMC phenotype-switch driven NF. Traditionally, vascular ALK1 signalling predominates in ECs (Goumans et al., 2002; Lebrin et al., 2004). More recently, Low *et al.* demonstrated that ALK1 was also expressed on intimal αSMA$^+$ SMCs and co-localised with TGFBR2 in pre-implantation SVGs from CABG patients (unpublished data) (Low et al., 2019). Furthermore, small interfering (si) RNA-mediated knockdown and pharmacological inhibition of ALK1 prevented TGF-β_1-driven SMAD1/5 phosphorylation in primary HSVSMCs demonstrating TGF-β_1-dependent ALK1/SMAD1/5 pathway activity in HSVSMCs. The same study demonstrated that carotid artery wire injury-induced NF was reduced in heterozygous *Smad1* knockout mice and in mice treated with the pharmacological inhibitor LDN-193189 potentially implicating ALK1/SMAD1/5 signalling as a contributor to NF. Whereas Sanvitale *et al.* demonstrated ALK1 inhibition with LDN-193189 *in vitro* (Sanvitale et al., 2013), Upton and colleagues showed that LDN-193189 did not prevent BMP-9-dependent ALK1 signalling in ECs (Upton et al., 2020). Furthermore, LDN-193189 has also been shown to inhibit ALK2, ALK3, ALK6 and ActRIIa as well as other kinases including receptor-interacting serine/threonine-protein kinase (RIPK)2, fibroblast growth factor receptor (FGFR)2, calcium/calmodulin-dependent protein kinase kinase (CAMKK)-beta and vascular endothelial growth factor receptor (VEGF-R) (Horbelt et al., 2015; Vogt et al., 2011; Yu et al., 2008). Given the fact that LDN-193189 inhibits a multitude of kinases, it is important to point out that observed inhibition of NF following systemic administration of LDN-193189 is likely not a result of sole ALK1 inhibition.

In the context of atherosclerosis, human aortic atherosclerotic lesions display ALK1 presence (Yao et al., 2007). Kraehling *et al.* demonstrated that ALK1 mediated low density lipoprotein (LDL)-cholesterol uptake into endothelial cells and promoted LDL transcytosis (Kraehling et al., 2016). The same study demonstrated that endothelium-specific ablation of ALK1 in hyperlipidaemic LDL receptor-deficient mice resulted in reduced endothelial LDL uptake, indicating a role for ALK1 in lipoprotein metabolism and potentially in atherosclerotic lesion

formation. Opposing the potentially pathogenic role of ALK1 in atherosclerosis, Kim *et al*. reported decreased BMPR2 presence in advanced human coronary atherosclerotic lesions (Kim et al., 2013). The authors demonstrated that BMPR2 knockdown in ECs induced inflammatory signalling. Paralleling these findings hyperlipidaemic heterozygous BMPR2-deficient/apolipoprotein (Apo)E-deficient mice developed accelerated atherosclerosis indicating that BMPR2 exerts anti-inflammatory and athero-protective actions.

Taken together, the BMP-9/ALK1/BMPR2 pathway can either drive or attenuate vascular disease depending on disease setting, distinct vascular compartments and cell types as well as other signalling pathways. ALK1 signalling predominates in vascular ECs, however, vSMC ALK1 signalling may also partially contribute to vascular injury-driven NF. Since BMP-9 acts as an ALK1 ligand, it may be speculated that BMP-9 may regulate vSMC-driven NF in vascular injury via the ALK1 pathway to some extent. To date, no study has directly investigated BMP-9 in vSMC-driven NF in SVG disease or ISR.

3.2 Aims

The aims of this chapter were:

- To determine the presence of BMP-9 and mature SMC markers in pre-implantation SVGs from CABG patients.
- To evaluate BMP-9 expression during *in vivo* SMC phenotype switch-driven NF in murine carotid artery injury models.
- To assess changes in vascular structure and vascular cell proliferation at defined time-points following carotid artery ligation in mice.

3.3 Results

3.3.1 BMP-9 is present in all layers of pre-implantation SVs from CABG patients

Previous findings from our laboratory localised the BMP-9 receptor ALK1 to SMCs in pre-implantation SVGs from CABG patients (unpublished data) (Low et al., 2019). This prompted evaluation of BMP-9 presence/expression in pre-implantation SVG conduits. Surplus SVG samples were obtained from patients undergoing the CABG procedure at a hospital in Glasgow. BMP-9 IHC analysis was performed on SVG sections from 3 CABG patients.

IHC analysis localised αSMA^+ cells (green) and BMP-9 (red) to all pre-implantation SVG layers from CABG patients (Figure 3-1 A-C). BMP-9 directly co-localised (yellow) with αSMA^+ cells within the intima and media indicating BMP-9 expression in SVG SMCs (Figure 3-1 A and B). In addition, BMP-9 co-localised with nuclei (purple) in all SVG compartments (Figure 3-1 A-C). Furthermore, extracellular space within all SVG layers also stained positive for BMP-9. Taken together, these data demonstrate that BMP-9 is present in all pre-implantation SVG layers from CABG patients.

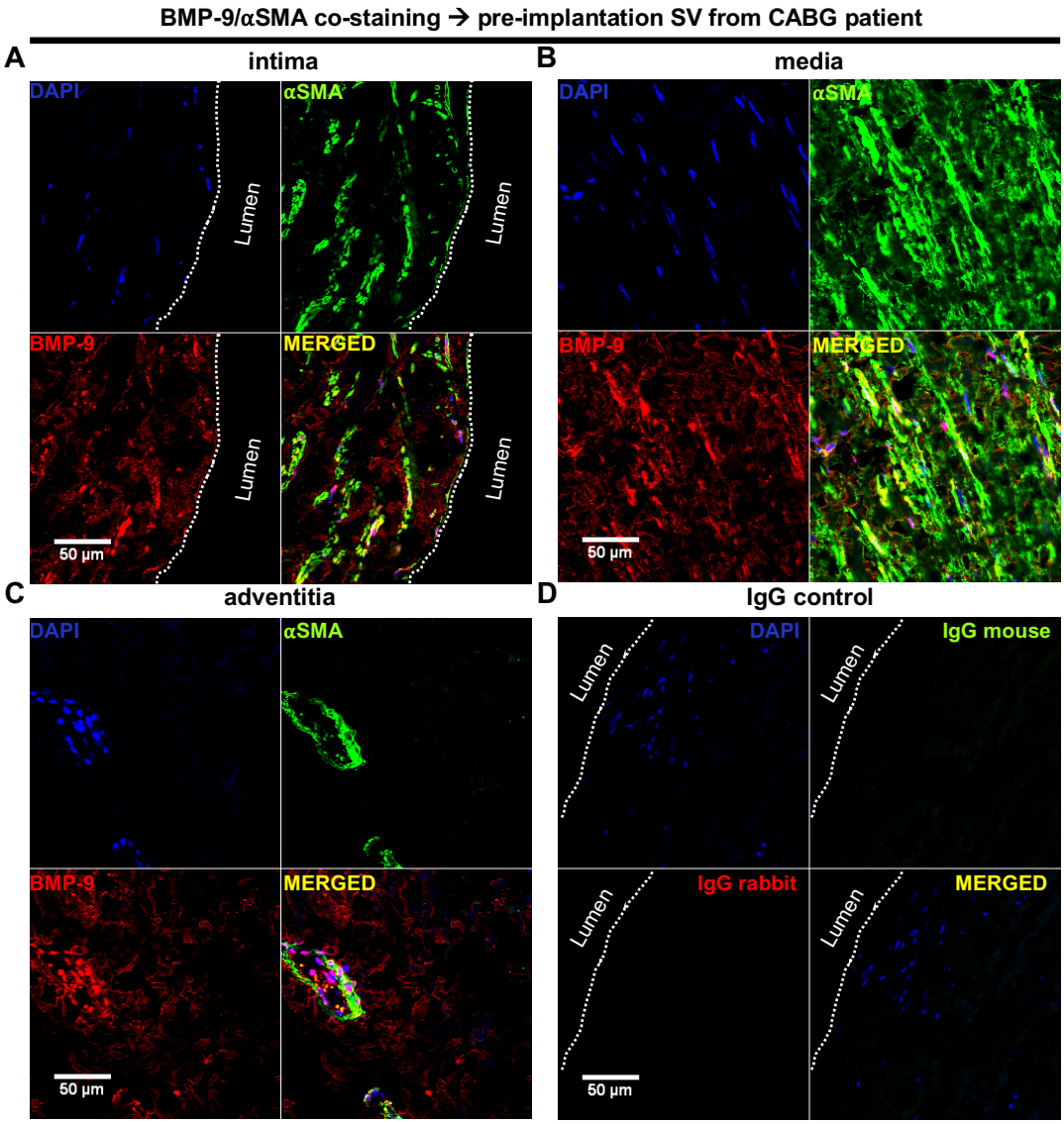

Figure 3-1 BMP-9 is present in all layers of pre-implantation SVGs from CABG patients. Surplus SVG samples from CABG patients were fixed in paraformaldehyde, embedded in paraffin and sectioned on a microtome. IHC staining was performed to determine the presence of αSMA (green) and BMP-9 (red). 4′,6-diamidino-2-phenylindole (DAPI) staining (blue) was used to detect nuclei. Respective IgG controls were added to adjust for unspecific binding (**D**). Images of the intima (**A**), media (**B**) and adventitia (**C**) were taken on a confocal microscope at 40× magnification. One representative image is shown for each vascular layer (n=3 CABG patients).

3.3.2 Pre-implantation SVs from CABG patients display SMC phenotype switching

SMC phenotype switching is an early event following coronary SVG implantation forming the basis for neointimal lesion development (Kockx et al., 1992). Previous work from our group showed that intimal calponin and *MYH11* mRNA expression levels in SVGs were lower compared to the media hinting at pre-implantation *in vivo* SMC de-differentiation (Daniel Kelly, personal communication). To substantiate these observations IHC analysis was performed on pre-implantation SVGs from CABG patients to determine intimal and medial calponin, SM22-α and MYH11 expression.

IHC localised calponin (red) to αSMA$^+$ cells (green) within the intima and media of pre-implantation SVG conduits (Figure 3-1 A and B). Although not reaching statistical significance (p=0.08), intimal calponin immunoreactivity appeared visually decreased compared to the media (mean calponin area % ± S.E.M., intima: 1.12 ± 0.34, media: 5.8 ± 2.34) (Figure 3-2 E). Calponin$^+$ cells were absent in the adventitia (Figure 3-2 C). SM22-α^+ cells (red) co-localised with αSMA$^+$ cells (green) within all layers of pre-implantation SVGs (Figure 3-3 A-C). Intimal SM22-α immunoreactivity appeared visually reduced compared to the media (mean SM22-α area % ± S.E.M., intima: 4.14 ± 1.1, media: 7.45 ± 1.01). However, this difference was not statistically significant (p=0.27) and was not as pronounced as changes observed for calponin and MYH11 (Figure 3-3 E). Paralleling SM22-α findings, MYH11$^+$ cells (red) localised to αSMA$^+$ cells (green) within all SVG layers (Figure 3-4 A-C). Furthermore, intimal MYH11 immunoreactivity was significantly decreased compared to the media (mean MYH11 area % ± S.E.M., intima: 0.4 ± 0.09, media: 3.0 ± 0.38, p=0.01) (Figure 3-4 D). Taken together, these findings suggest an overall trend towards a decrease of mature SMC marker expression within intimal SMCs compared to medial SMCs. This points towards an *in vivo* shift of quiescent SMCs to a de-differentiated phenotype.

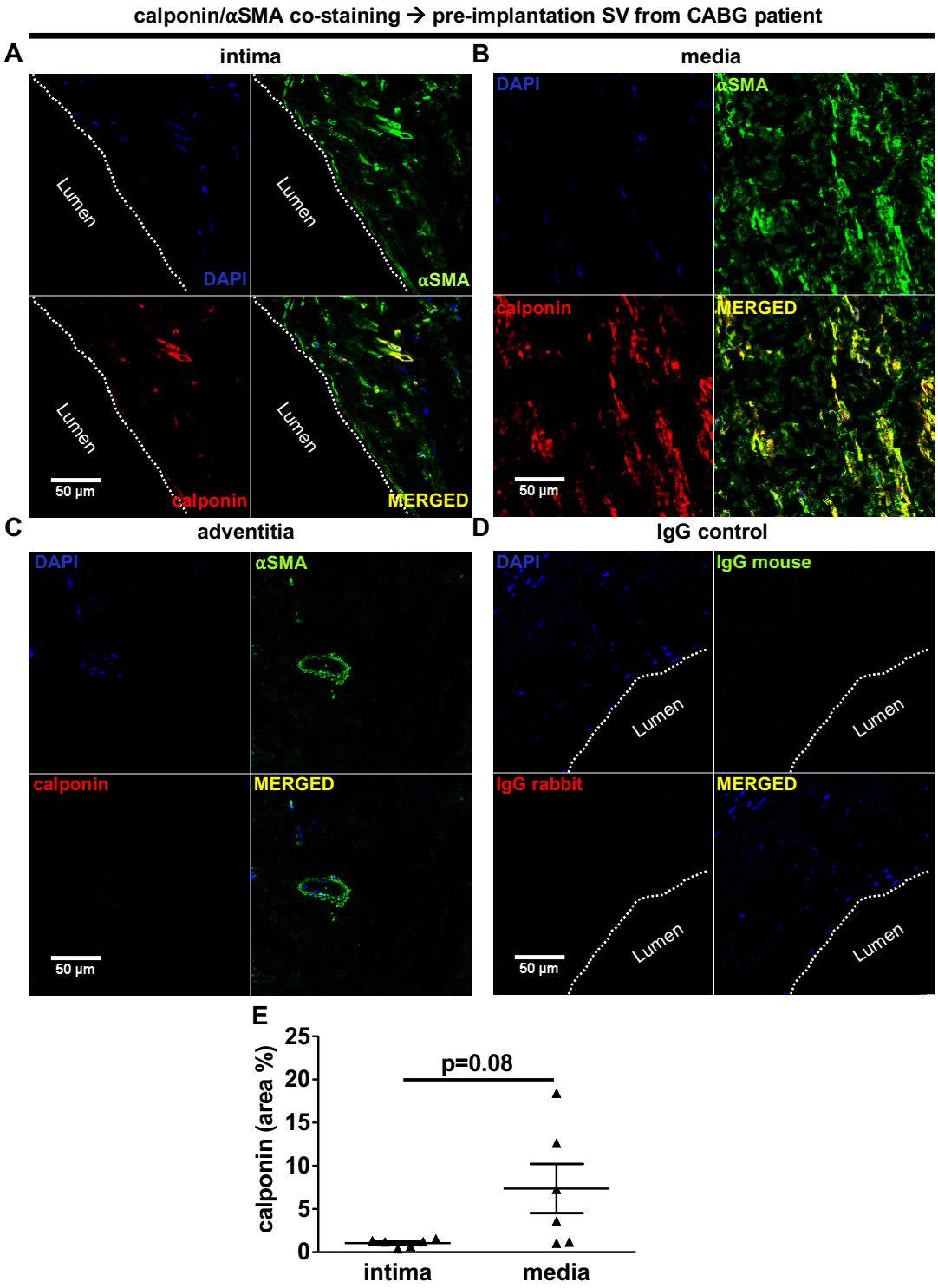

Figure 3-2 Decreased intimal calponin presence hints at *in vivo* SMC phenotype switching. Surplus SVG samples from CABG patients were fixed in paraformaldehyde, embedded in paraffin and sectioned on a microtome. IHC staining was performed to determine the presence of αSMA (green) and calponin (red). DAPI staining (blue) was used to detect nuclei. Respective IgG controls were added to adjust for unspecific binding (**D**). Images of the intima (**A**), media (**B**) and adventitia (**C**) were taken on a confocal microscope at 40× magnification. (**E**) The ImageJ software was used to quantify calponin pixel intensity (area %). Data are presented as mean ± S.E.M. (n=6 CABG patients). A paired Student's t-test was used to compare groups (p-value<0.05 was considered significant). One representative image is shown for each vascular layer. Daniel Kelly generously gifted calponin/αSMA-stained sections from 3 CABG patients.

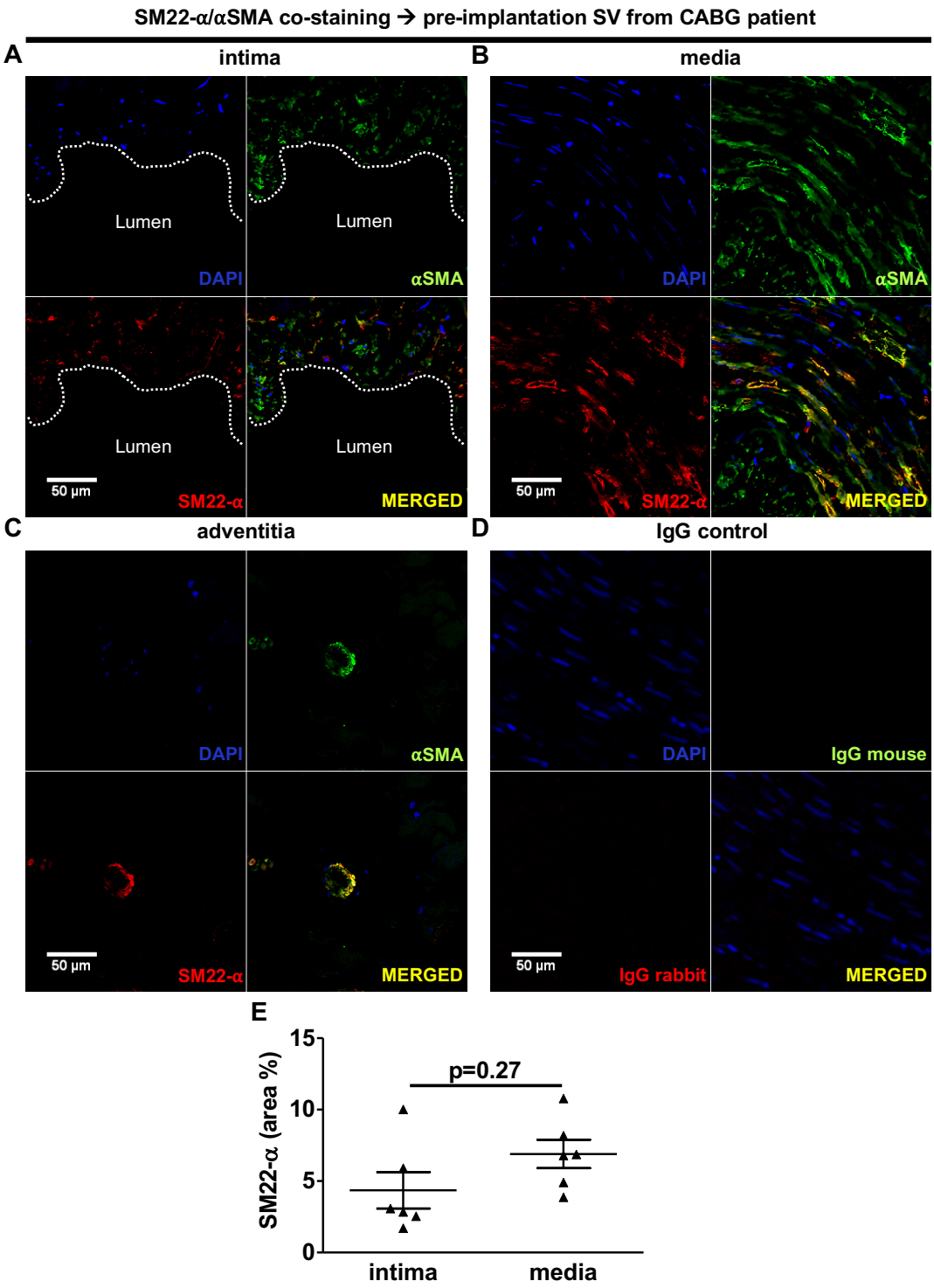

Figure 3-3 SM22-α co-localises with αSMA⁺ cells in all layers of pre-implantation SVs from CABG patients. Surplus SVG samples from CABG patients were fixed in paraformaldehyde, embedded in paraffin and sectioned on a microtome. IHC staining was performed to determine the presence of αSMA (green) and SM22-α (red). DAPI staining (blue) was used to detect nuclei. Respective IgG controls were added to adjust for unspecific binding (**D**). Images of the intima (**A**), media (**B**) and adventitia (**C**) were taken on a confocal microscope at 40× magnification. (**E**) The ImageJ software was used to quantify SM22-α pixel intensity (area %). Data are presented as mean ± S.E.M. (n=6 CABG patients). A paired Student's t-test was used to compare groups (p-value<0.05 was considered significant). One representative image is shown for each vascular layer (Daniel Kelly). Daniel Kelly generously gifted SM22-α/αSMA-stained sections from 3 CABG patients.

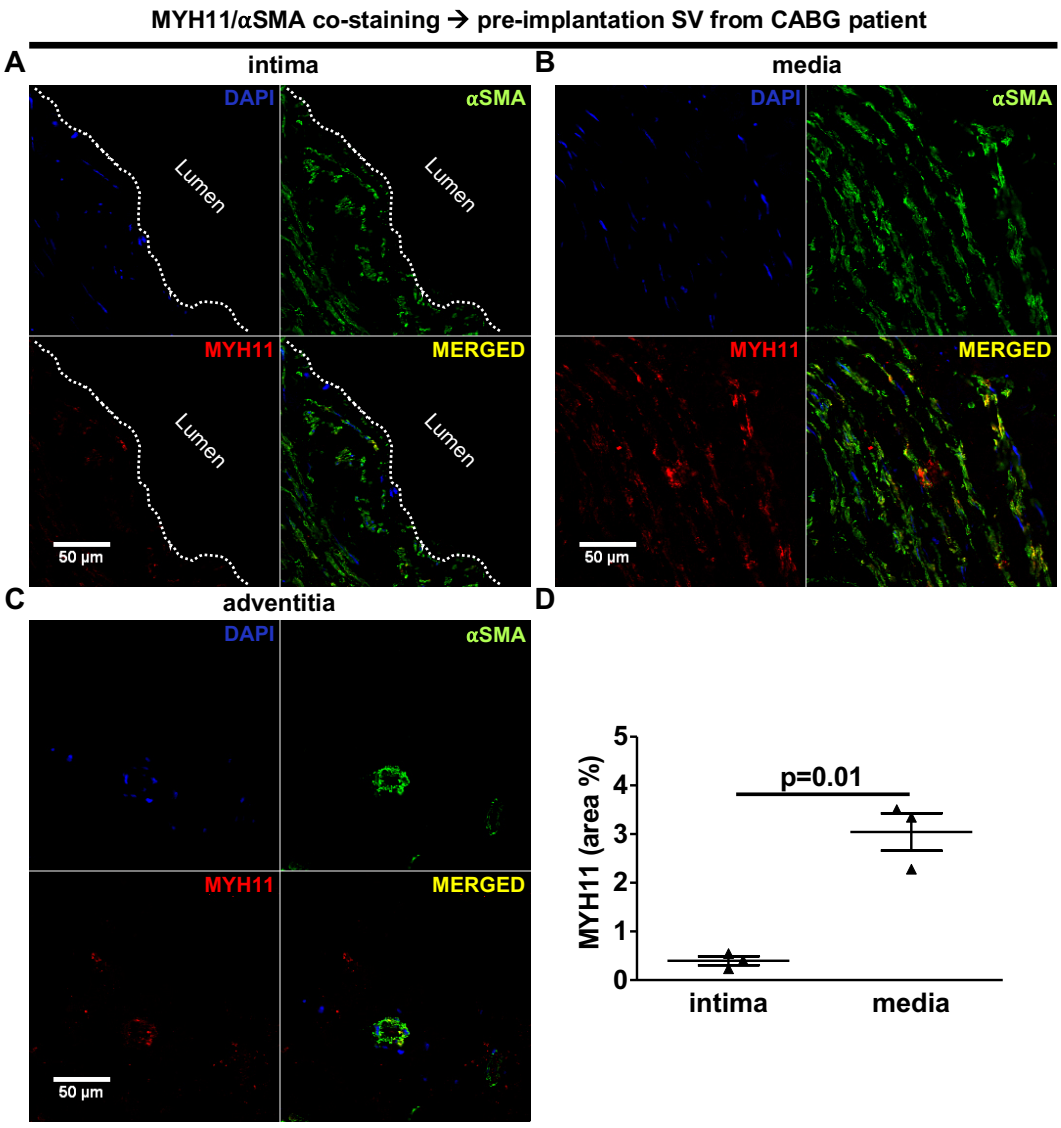

Figure 3-4 Decreased intimal MYH11 presence indicates SMC phenotype switching. Surplus SVG samples from CABG patients were fixed in paraformaldehyde, embedded in paraffin and sectioned on a microtome. IHC staining was performed to determine the presence of αSMA (green) and MYH11 (red). DAPI staining (blue) was used to detect nuclei. Images of the intima (**A**), media (**B**) and adventitia (**C**) were taken on a confocal microscope at 40× magnification. (**E**) The ImageJ software was used to quantify MYH11 pixel intensity (area %). Data are presented as mean ± S.E.M. (n=3 CABG patients). A paired Student's t-test was used to compare groups (p-value<0.05 was considered significant). One representative image is shown for each vascular layer. Daniel Kelly generously gifted MYH11/αSMA-stained sections from 3 CABG patients.

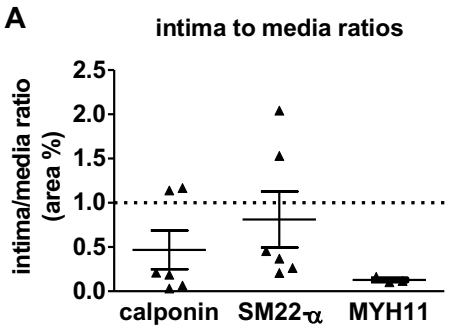

Figure 3-5 Decreased intima/media ratios of mature SMC markers suggest SMC phenotype switching in pre-implantation SVGs from CABG patients. Surplus SVG samples from CABG patients were fixed in paraformaldehyde, embedded in paraffin and sectioned on a microtome. IHC staining was performed to determine the presence of calponin, SM22α and MYH11. Images of the intima and media were taken on a confocal microscope at 40× magnification. (**A**) The ImageJ software was used to quantify intimal and medial calponin, SM22α and MYH11 intensity (area %). One field per vascular compartment and section was assessed. Respective intima area % was divided by respective media area % (intima/media ratio). Data are presented as mean ± S.E.M. (calponin and SM22-α n=6 CABG patients; MYH11 n=3 CABG patients).

3.3.3 BMP-9 antibody optimisation in mouse lung tissue

IHC analysis revealed BMP-9 presence in all layers of pre-implantation SVGs. In addition, SVG conduits displayed reduced mature SMC marker expression within the intima compared to the media hinting at pre-implantation *in vivo* SMC phenotype switching. The next aim was to study vascular BMP-9 expression during SMC phenotype switch-driven NF following carotid artery wire and ligation injury in mice. This required BMP-9 antibody optimisation in murine tissue. Since the lung expresses BMP-9, murine lung tissue served as a positive control to determine optimal BMP-9 antibody concentrations (Liu et al., 2020b; Miller et al., 2000).

Lung parenchyma displayed an increase in BMP-9 immunoreactivity (red) with higher concentrations of antibodies (Figure 3-6 A-C). At the highest concentration (1:50 dilution), BMP-9 localised to nuclei potentially indicating unspecific nuclear staining (Figure 3-6 A). Since BMP-9/DAPI co-localisation was less pronounced at the 1:100 dilution (compare Figure 3-6 B and C with A), this working dilution was chosen for subsequent IHC experiments.

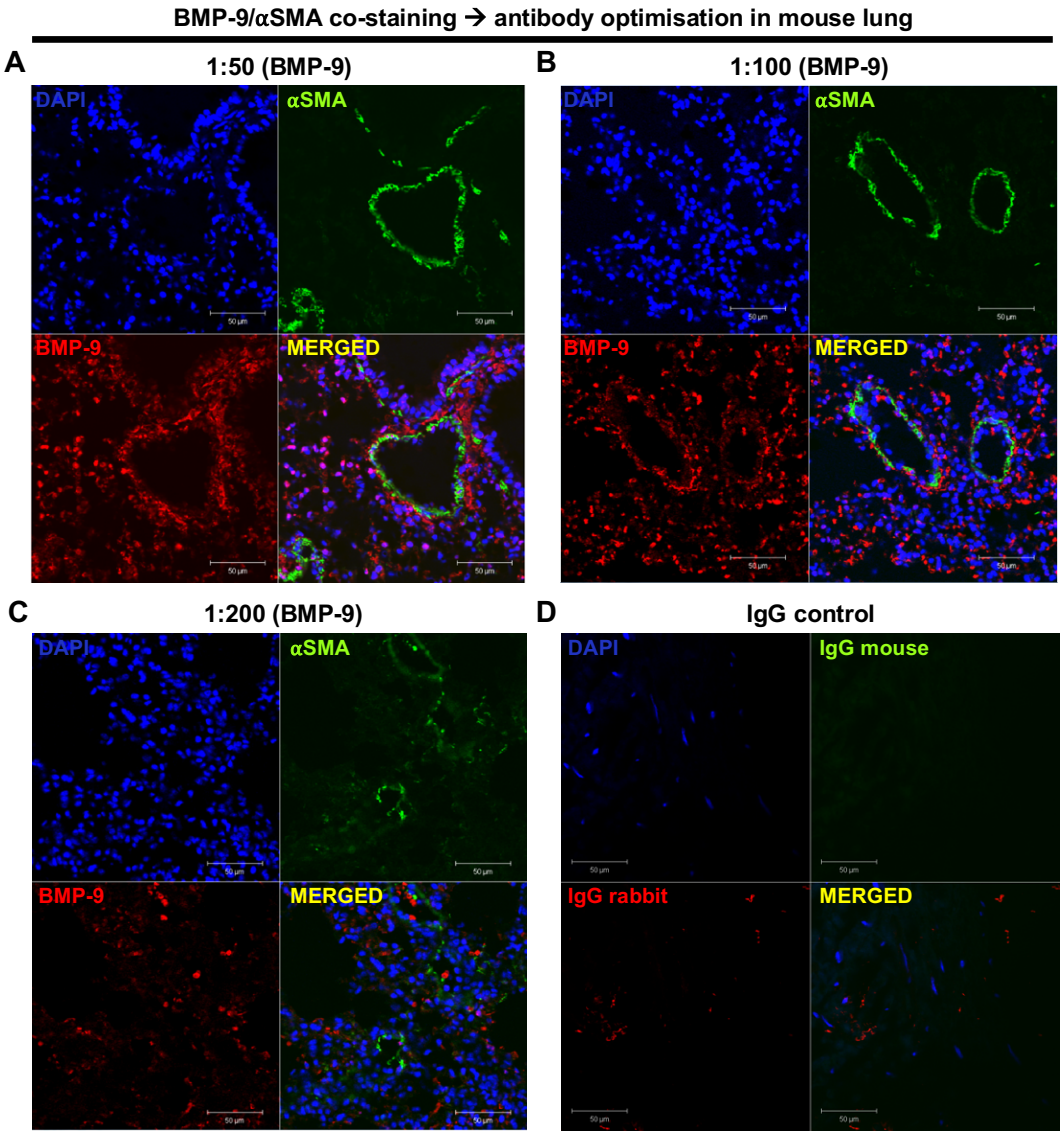

Figure 3-6 Mouse lung tissue displays BMP-9 immunoreactivity. Control adult mice were terminated. Harvested lungs were fixed in paraformaldehyde, embedded in paraffin and sectioned on a microtome. IHC staining was performed to determine the presence of αSMA (green, 1:100 dilution) and BMP-9 (red). BMP-9 antibodies (1 mg/ml) were used at three different concentrations (**A** → 1:50 dilution, **B** → 1:100 dilution, **C** → 1:200 dilution, **D** → respective IgG controls). DAPI staining (blue) was used to detect nuclei. Images were taken on a confocal microscope at 40× magnification. One representative image is shown for each group.

3.3.4 Carotid artery wire injury triggers an increase in vascular BMP-9 immunoreactivity and SMC phenotype switching

Pre-implantation SVGs from CABG patients display BMP-9 presence and SMC phenotype switching. This prompted analysis of BMP-9 presence in uninjured (day 0, n=2) and wire injured (day 14, n=3; day 21, n=3) murine carotid arteries. Unstained sections from a previous carotid artery wire injury study by Dr Sammy El-Mansi were utilised for this IHC analysis.

In uninjured day 0 controls BMP-9 (red) mainly localised to the adventitia (Figure 3-7 A). Light punctate BMP-9 staining was also visible in the media. αSMA$^+$ cells (green) localised to the media. 14-day old wire injured lesions displayed a reduction in total SMC αSMA expression suggesting SMC phenotype switching (mean total vessel staining % ± S.E.M., day 0 uninjured control: 6.8 ± 0.58, day 14 injured: 1.51 ± 0.49, [$p<0.05$]) (Figure 3-7, compare B with A; Figure 3-9 B). Paralleling loss of vSMC αSMA expression, punctate BMP-9 staining was visible along the IEL and neointima (Figure 3-7 B). Furthermore, total vessel BMP-9 immunoreactivity demonstrated a trend towards an increase compared to uninjured day 0 controls (day 0 uninjured control: 2.71 ± 0.43, day 14 injured: 5.43 ± 0.92) (Figure 3-7, compare B with A; Figure 3-9 A). Although total vessel vSMC αSMA expression remained significantly suppressed in injured day 21 vessels (day 0 uninjured control: 6.8 ± 0.58, day 21 injured: 3.2 ± 0.93, [$p<0.05$]), there was a visible trend towards restoration of αSMA expression within the intima and media suggesting the presence of a more quiescent SMC phenotype (compare Figure 3-8 A with Figure 3-7 A and B, Figure 3-9 B). Total vessel BMP-9 immunoreactivity demonstrated a trend towards a decrease compared to injured day 14 vessels reaching similar levels compared to uninjured day 0 controls (day 21 injured: 3.12 ± 0.52, day 14 injured: 5.43 ± 0.92, $p>0.05$) (compare Figure 3-8 A with Figure 3-7 A and B, Figure 3-9 A).

Taken together, these data suggest a dynamic increase in total BMP-9 vessel immunoreactivity following carotid artery wire injury which is paralleled by SMC de-differentiation. This prompted the initiation of a murine carotid artery ligation study aimed at evaluating BMP-9 presence at multiple time points and correlating IHC findings with vascular morphological changes, SMC phenotype switching and downstream ALK1 pathway activation.

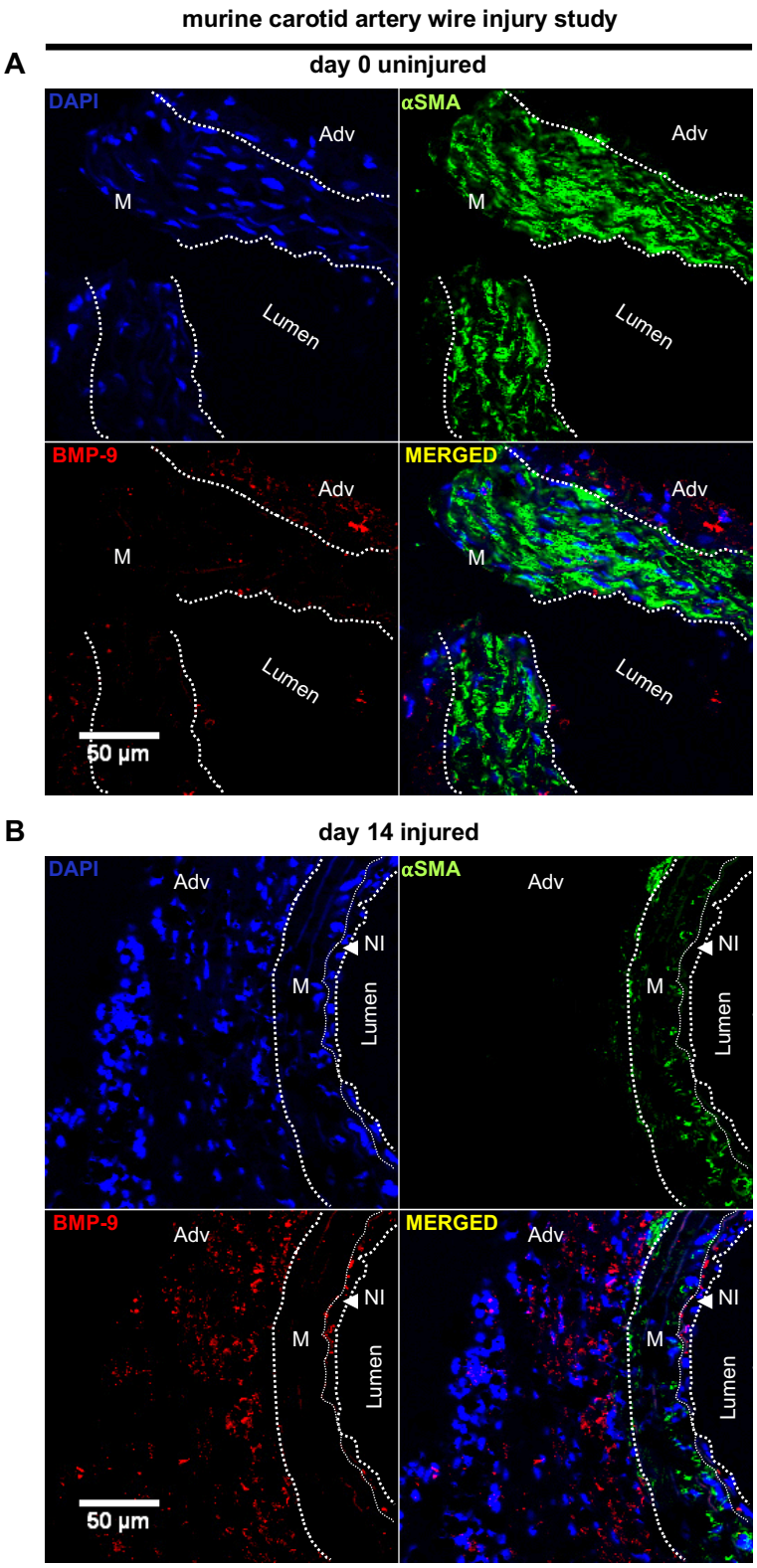

Figure 3-7 Carotid artery wire injury triggers an increase in vascular BMP-9 immunoreactivity in mice. The carotid artery wire injury procedure was performed as described by (Lindner et al., 1993). C57BL/6J mice were terminated at indicated time points. Injured left carotid arteries and uninjured right carotid arteries were fixed in paraformaldehyde, embedded in paraffin and sectioned on a microtome. Unstained day 0 uninjured and day 14 injured sections were a generous gift from Dr Sammy El-Mansi (**A** and **B**). IHC staining was performed to determine the presence of αSMA (green) and BMP-9 (red). DAPI staining (blue) was used to detect nuclei. Images were taken on a confocal microscope at 40× magnification. One representative image is shown for each group (day 0 uninjured, n=2; day 14 injured, n=3). Adv, adventitia; M, media; NI, neointima.

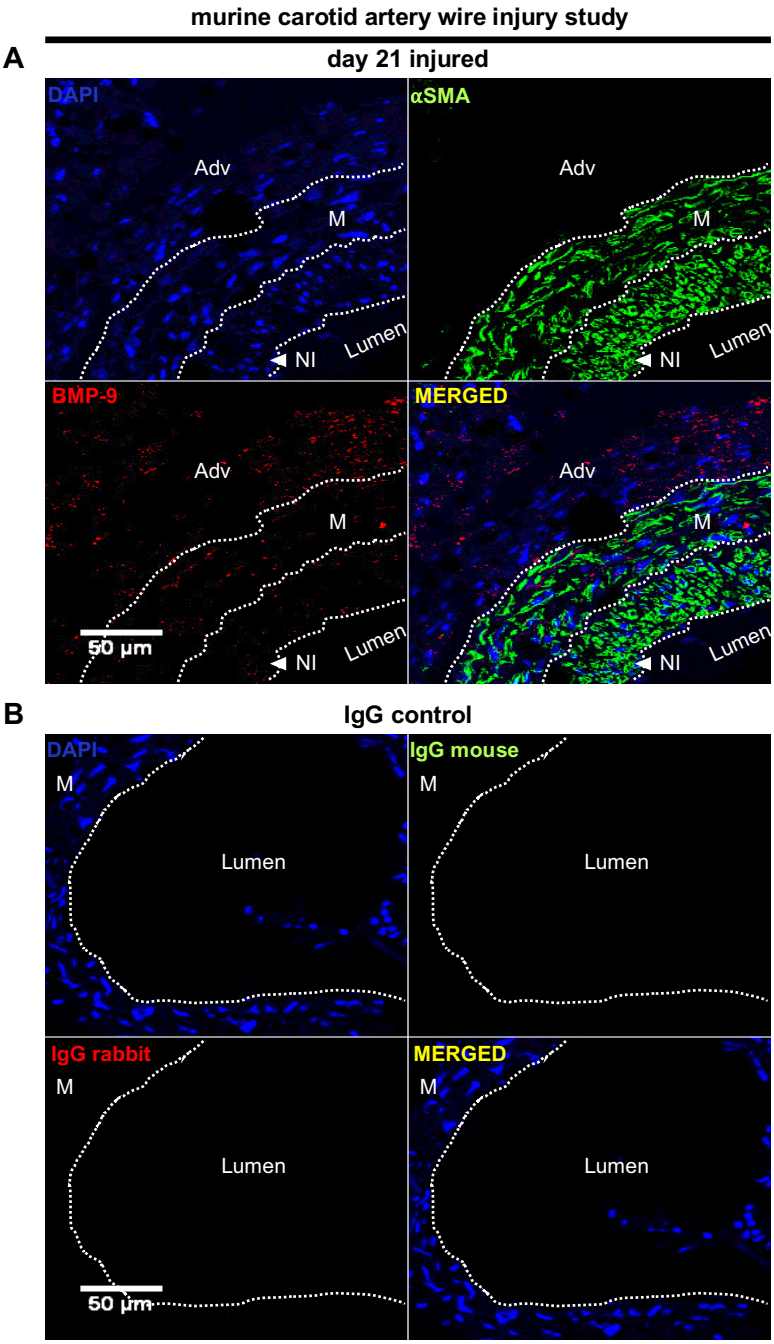

Figure 3-8 Wire injured murine carotid arteries display BMP-9 immunoreactivity at 21 days following injury. Unstained day 21 injured sections were a generous gift from Dr Sammy El-Mansi (**A**). IHC staining was performed to determine the presence of αSMA (green) and BMP-9 (red). DAPI staining (blue) was used to detect nuclei. (**B**) Respective IgG controls were added to adjust for unspecific binding. Images were taken on a confocal microscope at 40× magnification. One representative image is shown for each group (day 21 injured, n=3). Adv, adventitia; M, media; NI, neointima.

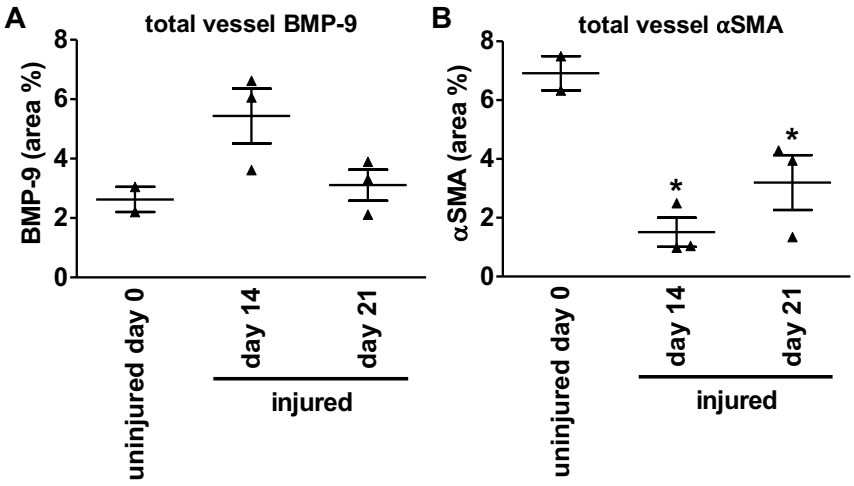

Figure 3-9 Carotid wire injury triggers an increase in vascular BMP-9 immunoreactivity and SMC phenotype switching in mice. Uninjured and ligation-injured murine carotid arteries were fixed in paraformaldehyde, embedded in paraffin and sectioned on a microtome. IHC staining was performed to determine the presence of BMP-9 and αSMA. Images were taken on a confocal microscope at 40× magnification. The ImageJ software was used to determine total vessel BMP-9 (**A**) and αSMA (**B**) pixel intensity (area %). Data are presented as mean ± S.E.M. (uninjured day 0, n=2; injured day 14, n=3; injured day 21, n=3). A One-way ANOVA with a Tukey's correction was performed to compare groups. * p-value<0.05 (respective group versus uninjured day 0 control, p-value<0.05 was considered significant).

3.3.5 Carotid artery ligation triggers neointima formation and media hypertrophy in mice

These findings together with previous results demonstrating a dynamic increase in total vessel BMP-9 immunoreactivity following carotid artery wire injury prompted a multiple timepoint murine carotid artery ligation study to link BMP-9 with early and late vascular changes following ligation injury. The first aim was to analyse morphometric changes in injured carotid arteries at day 3 (Daria Boyd), day 5, day 7 (Daria Boyd), day 10, day 14 and day 28 following carotid artery ligation injury. Injured and uninjured control carotid artery sections were stained with H&E to determine intimal area, medial area and the intima to media (I/M) ratio which served as an indicator of NF (Figure 3-10, Figure 3-11 and Figure 3-12).

It is important to point out that morphometric data obtained from these 2 *in vivo* studies requires careful interpretation due to the amount of intra-group variability which may explain the absence of significant changes between different time points. The potential underlying reasons for this are discussed in 3.4. Despite increased variability, presented findings demonstrate that structural changes occur in ligation injured carotid arteries. Elastic laminae stretching in 3- and 5-day old, injured vessels was evident suggesting onset of lesion formation (Figure 3-10 B and C). Reduced medial haematoxylin staining in day 3, 5 and 7 injured carotid arteries indicated SMC loss (Figure 3-10 B and C). At day 7, 3 injured vessels displayed NF indicated by an increase in intimal nuclear haematoxylin staining and an increase in I/M ratio (Figure 3-10 D and Figure 3-11 D). At day 10, intimal lesions were detected in 5 out of 6 injured carotid arteries (Figure 3-11 A and D). This was paralleled by a trend towards an increase in I/M ratio indicating neointimal expansion (mean $\log_{10}$-transformed I/M ratio ± S.E.M., day 10 injured: 0.09 ± 0.03, day 3 uninjured control: 0.02 ± 0.003, $p>0.05$) (Figure 3-11 D). Furthermore, the media surface area significantly increased compared to that of the day 5 injury group indicating medial hypertrophy (mean media surface area [μm^2] ± S.E.M., day 10 injured: 37,448.1 ± 3,567.4, day 5 injured: 22,942 ± 1394,4, [$p<0.05$]) (Figure 3-11 A and Figure 3-12 B). Only 4 out of 7 injured vessels displayed neointimal lesions at day 14 (Figure 3-11 B and D). Visually, these lesions demonstrated less intimal nuclear haematoxylin staining and an increase in ECM/cytoplasm eosin staining

compared to day 7 and 10 timepoints indicating neointimal remodelling. All 3 day 28-old, injured vessels showed neointimal lesions (Figure 3-11 C and D).

Taken together, the I/M ratio in injured vessels increases between the day 5 and 10 timepoint and peaks at day 10 suggesting that maximal intimal thickening is achieved between these 2 timepoints. Furthermore, intimal remodelling occurs in two phases. Enhanced intimal nuclear haematoxylin staining at day 7 and 10 indicates cell hyperplasia within the developing neointima. Between the day 10 and 28 timepoint, intimal nuclear haematoxylin staining visually decreases and eosin staining increases pointing towards neointimal remodelling. Finally, the media surface area peaks at day 10 indicating medial hypertrophy.

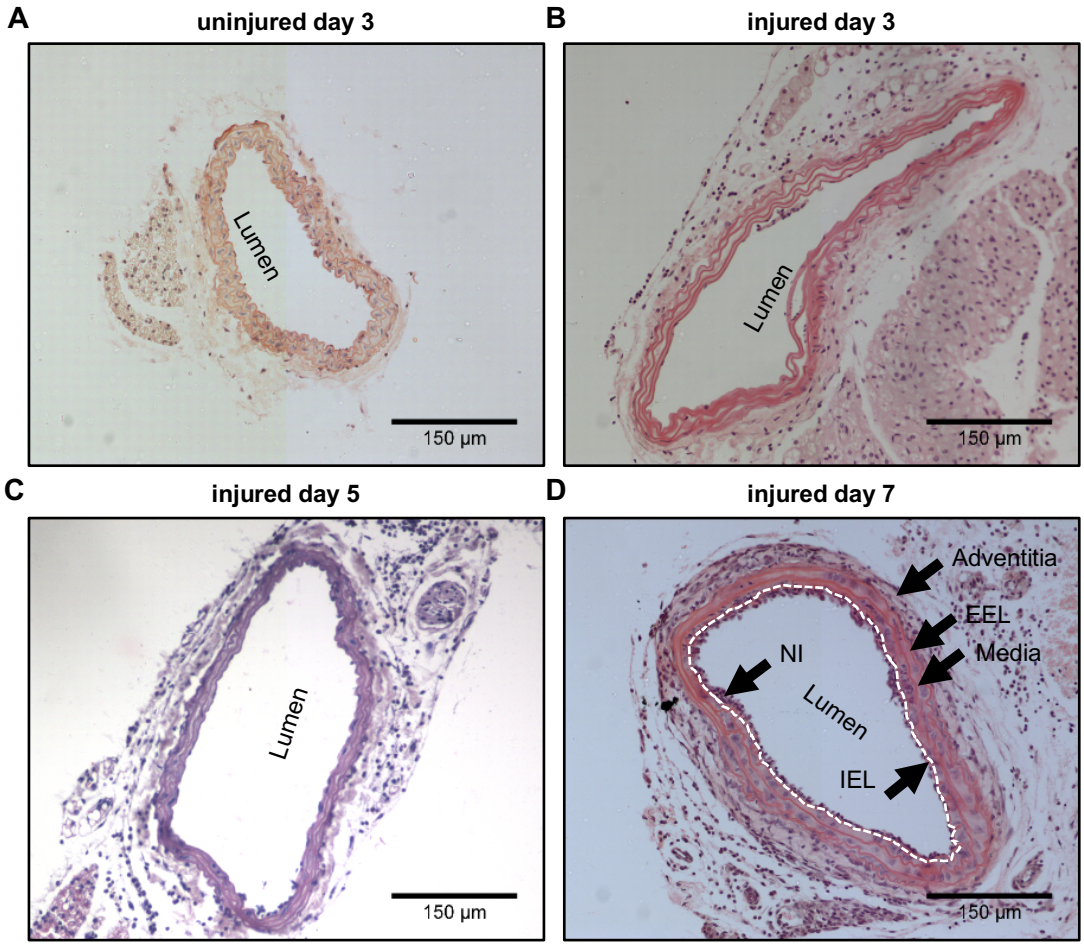

Figure 3-10 Carotid artery ligation triggers NF in mice (part 1). The carotid artery ligation procedure was performed as described by Kumar *et al.* (Kumar and Lindner, 1997). C57BL/6J mice were terminated at indicated time points. Injured left carotid arteries and uninjured right carotid arteries were fixed in paraformaldehyde, embedded in paraffin and sectioned on a microtome. H&E staining was performed to determine morphometric changes. H&E-stained day 3 and 7 sections were a generous gift from Daria Boyd. This figure displays representative images of H&E-stained uninjured day 3 (**A**, n=3), injured day 3 (**B**, n=8), injured day 5 (**C**, n=6) and injured day 7 (**D**, n=8) carotid arteries. H&E-stained sections were imaged on a microscope at 20× magnification. EEL, external elastic lamina; IEL, internal elastic lamina; NI, neointima. Haematoxylin → purple = nuclei, eosin → pink = cytoplasm.

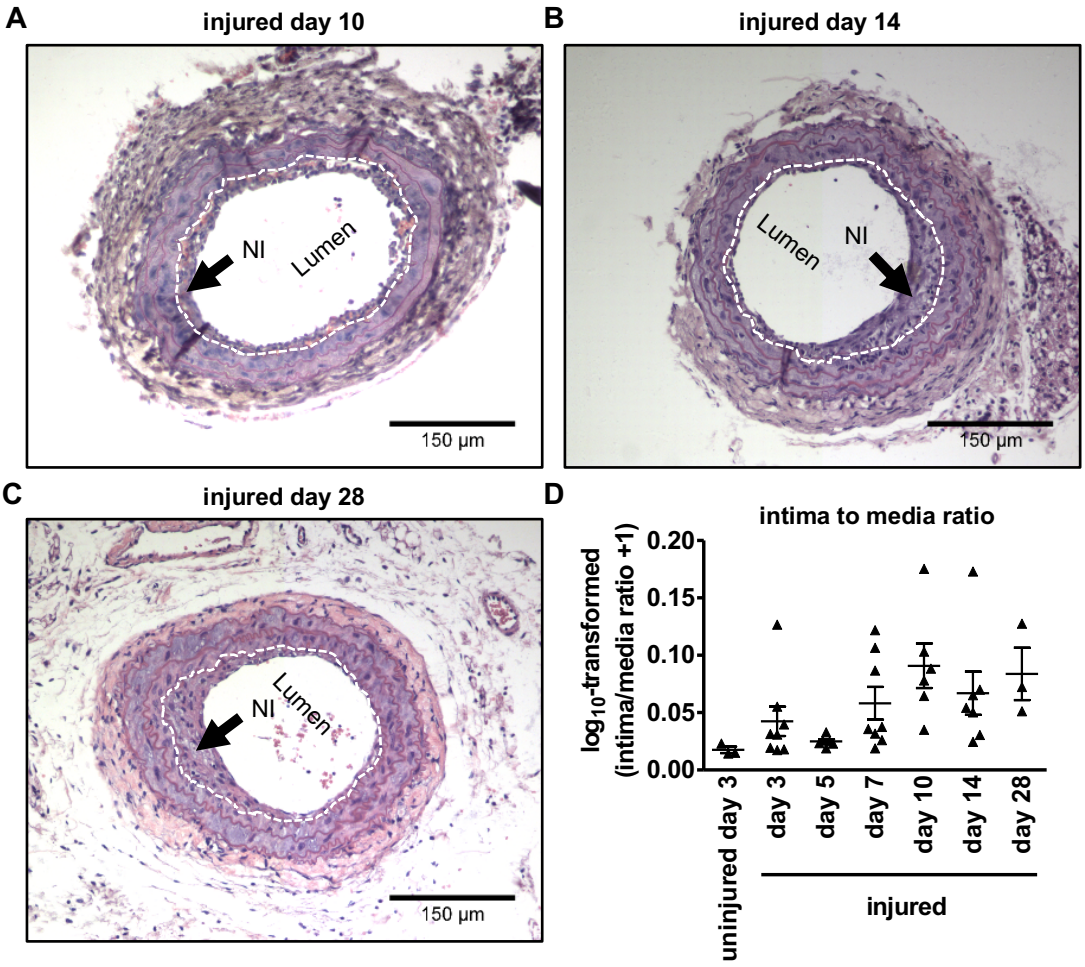

Figure 3-11 Carotid artery ligation triggers NF in mice (part 2). The carotid artery ligation procedure was performed as described by Kumar *et al.* (Kumar and Lindner, 1997). C57BL/6J mice were terminated at indicated time points. Injured left carotid arteries were fixed in paraformaldehyde, embedded in paraffin and sectioned on a microtome. H&E staining was performed to determine morphometric changes. H&E-stained sections were imaged on a microscope at 20× magnification. This figure displays representative images of H&E-stained injured day 10 (**A**, n=6), injured day 14 (**B**, n=7) and injured day 28 (**C**, n=3) carotid arteries. (**D**) The ImageJ software was used to determine intimal and medial areas (μm^2). Log_{10}-transformed intima/media ratios (log_{10}(intima/media + 1)) are displayed as mean ± S.E.M. (one data point represents one animal). A One-way ANOVA with Tukey's correction was performed to compare groups. One representative image is shown for each group. Haematoxylin → purple = nuclei, eosin → pink = cytoplasm NI, neointima.

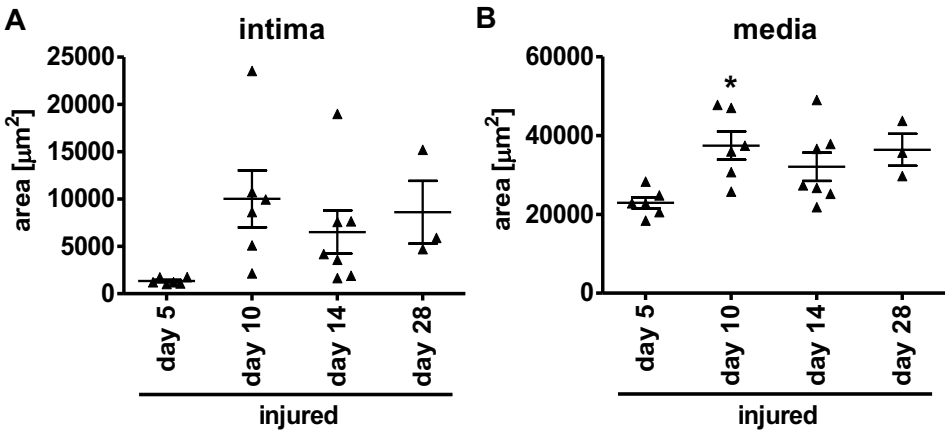

Figure 3-12 Carotid artery ligation triggers NF and medial hypertrophy. The carotid artery ligation procedure was performed as described by Kumar *et al.* (Kumar and Lindner, 1997). C57BL/6J mice were terminated at indicated time points. Injured left carotid arteries were fixed in paraformaldehyde, embedded in paraffin and sectioned on a microtome. H&E staining was performed to determine morphometric changes. H&E-stained sections were imaged on a microscope at 20× magnification. Intima (**A**) and media (**B**) surface areas of H&E-stained injured day 5 (n=6), day 10 (n=6), day 14 (n=7) and day 28 (n=3) left carotid artery sections were quantified using the ImageJ software and are displayed in μm^2 as mean ± S.E.M. (one data point represents one animal). A One-way ANOVA with a Dunnett's correction was performed to compare respective groups versus the injured day 5 group (* p-value<0.05, $p<0.05$ was considered statistically significant). Data from Daria Boyd's *in vivo* trial was excluded in this analysis since images of uninjured and injured carotid artery sections were taken on a different microscope with different settings.

3.3.6 Carotid artery ligation triggers early peripheral vascular cell proliferation in mice

The second aim was to investigate time- and area-dependent vascular cell proliferation in injured versus uninjured carotid arteries following ligation injury and to link these findings to onset and progression of NF. As outlined in section 3.3.5, two studies were merged to interrogate this aim. The EdU to DAPI ratio served as a surrogate marker for proliferating vascular cells.

In similarity to previously presented findings, this EdU analysis requires careful interpretation due to increased intra-group variability which may explain the absence of statistical significance between groups. The potential underlying reasons for this are discussed in section 3.4. In uninjured day 3 controls, some nuclei in peripheral vascular cells stained positive for EdU (Figure 3-13 A). 3-day old, injured vessels displayed increased EdU^+ nuclei within cells in the adventitia and perivascular tissue indicating increased cell proliferation (Figure 3-13, compare A with B; Figure 3-15 B). Although EdU staining was less pronounced in injured day 5 vessels, EdU^+ nuclei were still detected in the adventitia and peripheral vascular tissue indicating ongoing proliferation in these vascular compartments (Figure 3-13, compare C with A and B). At day 7, EdU^+ nuclei were detected in 6 out of 8 injured carotid arteries (Figure 3-14 A, Figure 3-15 B). The EdU/DAPI ratio peaked at this timepoint with proliferating cells localising to perivascular tissue, the adventitia, the media and the intima (mean log_{10}-transformed $EdU^+/DAPI^+$ ± S.E.M., day 7 injured: 0.015 ± 0.003, day 3 uninjured control: 0.004 ± 0.002, $p>0.05$). 10-, 14- and 28-day old neointimal lesions did not display any EdU^+ nuclei potentially indicating absence of vascular cell proliferation (Figure 3-14 B and C, Figure 3-15 A and B).

Overall, these findings show that carotid artery ligation triggers peripheral, medial and intimal vascular cell proliferation at early time points following vascular injury (day 3-7). SMC proliferation within the media and intima reflects SMC phenotype switching. Later time points (day 10-28) did not show any proliferation potentially suggesting suppressed vascular cell proliferation.

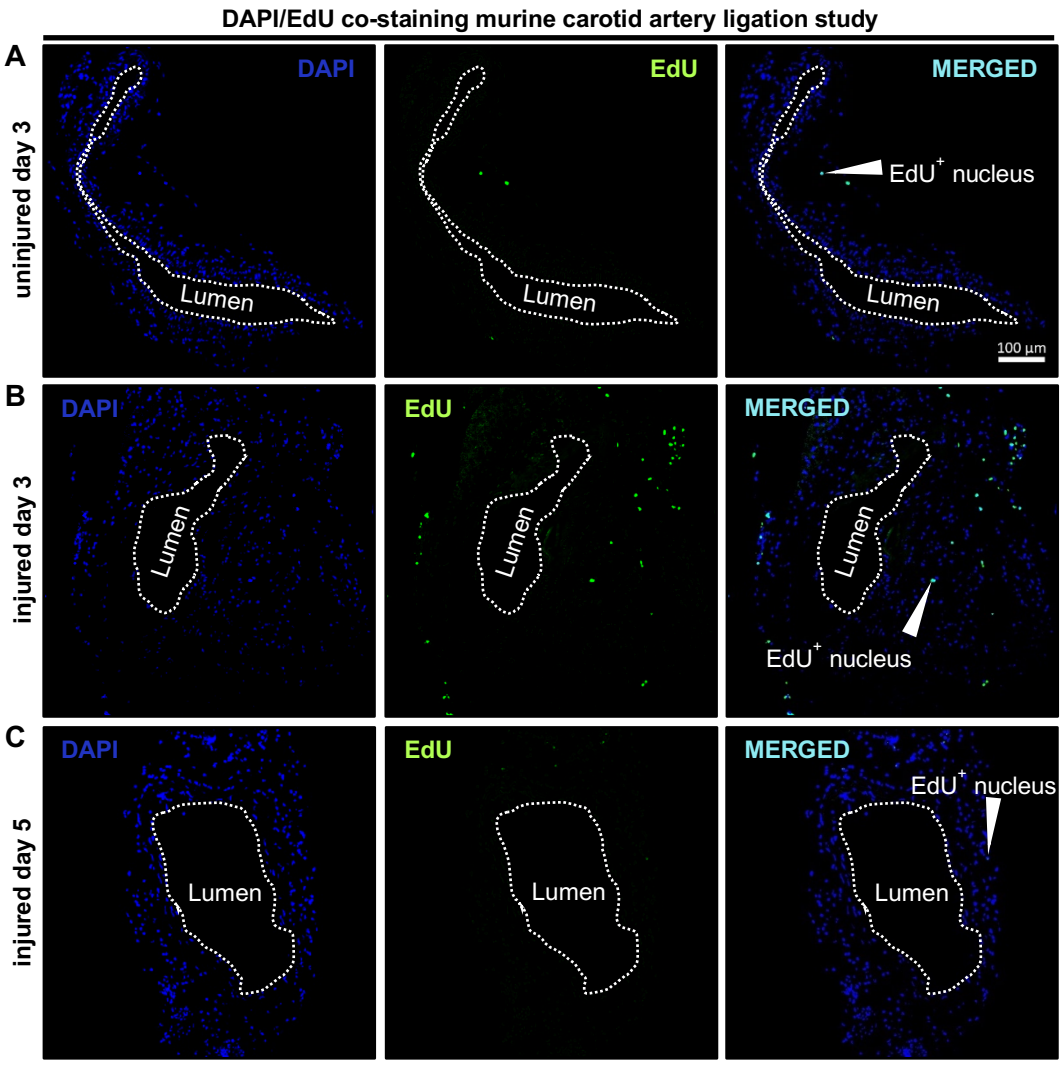

Figure 3-13 Carotid artery ligation triggers early peripheral vascular cell proliferation. The carotid artery ligation surgery was performed as described by Kumar *et al.* (Kumar and Lindner, 1997). EdU in 1× sterile PBS (dose: 100 mg/kg body weight) was injected intraperitoneally 3-h prior to termination at indicated time points. Injured left carotid arteries and uninjured right carotid arteries were fixed in paraformaldehyde, embedded in paraffin and sectioned on a microtome. EdU (green)/DAPI (blue) co-staining was performed to assess the number of proliferating vascular cells. Unstained day 3 sections were a generous gift from Daria Boyd. This figure displays representative images of DAPI/EdU-stained uninjured day 3 (**A**, n=3), injured day 3 (**B**, n=7) and injured day 5 (**C**, n=6) carotid arteries. EdU-stained sections were imaged on a confocal microscope at 20× magnification.

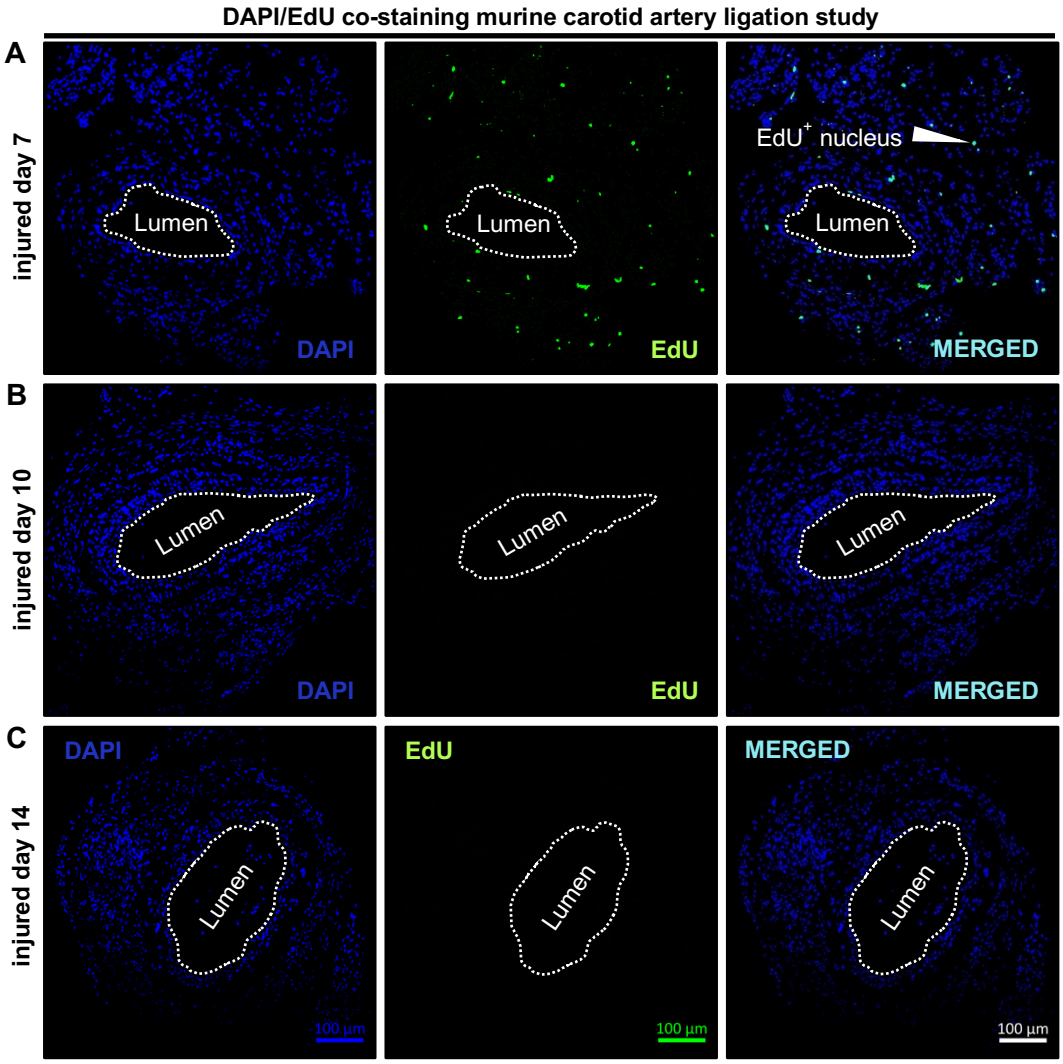

Figure 3-14 Carotid artery ligation triggers intimal and medial cell proliferation at day 7. The carotid artery ligation surgery was performed as described by Kumar *et al.* (Kumar and Lindner, 1997). EdU in 1× sterile PBS (dose: 100 mg/kg body weight) was injected intraperitoneally 3-h prior to termination at indicated time points. Injured left carotid arteries and uninjured right carotid arteries were fixed in paraformaldehyde, embedded in paraffin and sectioned on a microtome. EdU (green)/DAPI (blue) co-staining was performed to assess the number of proliferating vascular cells. Unstained day 7 sections were a generous gift from Daria Boyd. This figure displays representative images of DAPI/EdU-stained injured day 7 (**A**, n=8), injured day 10 (**B**, n=6) and injured day 14 (**C**, n=7) carotid arteries. EdU-stained sections were imaged on a confocal microscope at 20× magnification.

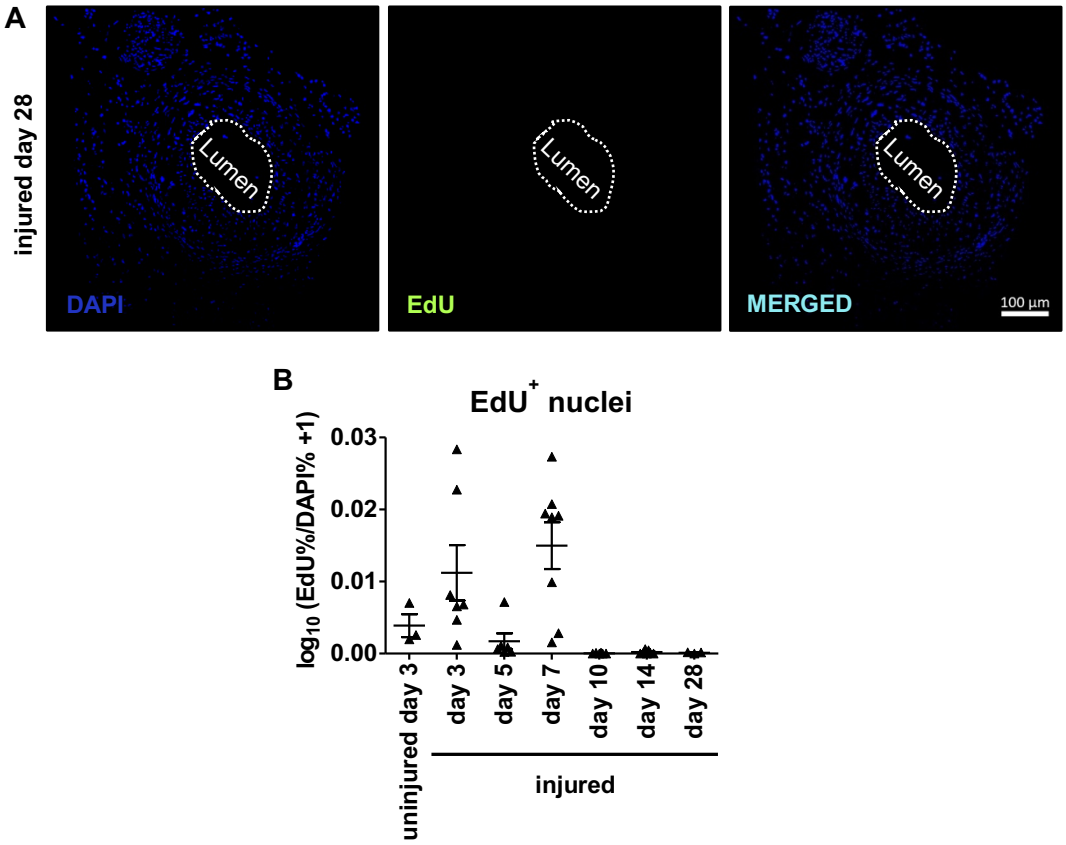

Figure 3-15 28-day old neointimal lesions do not display proliferating cells in mice. The carotid artery ligation surgery was performed as described by Kumar *et al.* (Kumar and Lindner, 1997). EdU in 1× sterile PBS (dose: 100 mg/kg body weight) was injected intraperitoneally 3-h prior to termination at indicated time points. Injured left carotid arteries and uninjured right carotid arteries were fixed in paraformaldehyde, embedded in paraffin and sectioned on a microtome. EdU (green)/DAPI (blue) co-staining was performed to assess the number of proliferating vascular cells. This figure displays representative images of a DAPI/EdU-stained injured day 28 carotid artery (**A**, n=3). (**B**) The ImageJ software was used to determine EdU- and DAPI-positive area percentages following threshold normalisation. Log_{10}-transformed EdU/DAPI ratios ($(log_{10}$(EdU %/DAPI % + 1)) are displayed as mean ± S.E.M. (one data point represents one animal). A One-way ANOVA with Tukey's correction was performed to compare groups.

3.3.7 Preliminary IHC αSMA staining indicates *in vivo* SMC phenotype switching following carotid ligation injury

Previously presented findings demonstrate that carotid artery ligation triggers early vascular cell proliferation which precedes NF and media hypertrophy. Intimal and medial SMC proliferation indicated SMC phenotype switching. To characterise the SMC phenotype in more detail following carotid artery ligation injury, IHC analysis was performed to evaluate SMC αSMA expression in uninjured and injured carotid arteries. Due to the 2020 COVID-19 pandemic and subsequent lab closure αSMA IHC analyses could only be performed on few n numbers. Moreover, BMP-9 and phospho-SMAD1 staining could not be performed. Hence, presented data requires careful interpretation due to small n numbers.

IHC localised αSMA^+ cells to the media of uninjured day 3 carotid arteries (Figure 3-16 A Figure 3-18 C). 3- and 5-day old, lesioned vessels displayed reduced medial αSMA immunoreactivity compared to uninjured controls (Figure 3-16, compare B and C with A; Figure 3-18 C). At day 7, injured vessels showed close to 0 αSMA^+ cells indicating loss of SMC αSMA expression (Figure 3-17 A). αSMA immunoreactivity in injured vessels remained suppressed at day 10 and 14 (Figure 3-17 B and C). At day 28, IHC localised αSMA^+ cells to the neointima and media suggesting a recovery of αSMA expression in vSMCs (Figure 3-18 A and C). Overall, this data set points towards a loss of SMC αSMA expression following carotid artery ligation injury. Taken together with previous proliferation data, suppression of SMC αSMA expression at day 7 is paralleled by an increase in medial and intimal SMC proliferation indicating SMC phenotype switching.

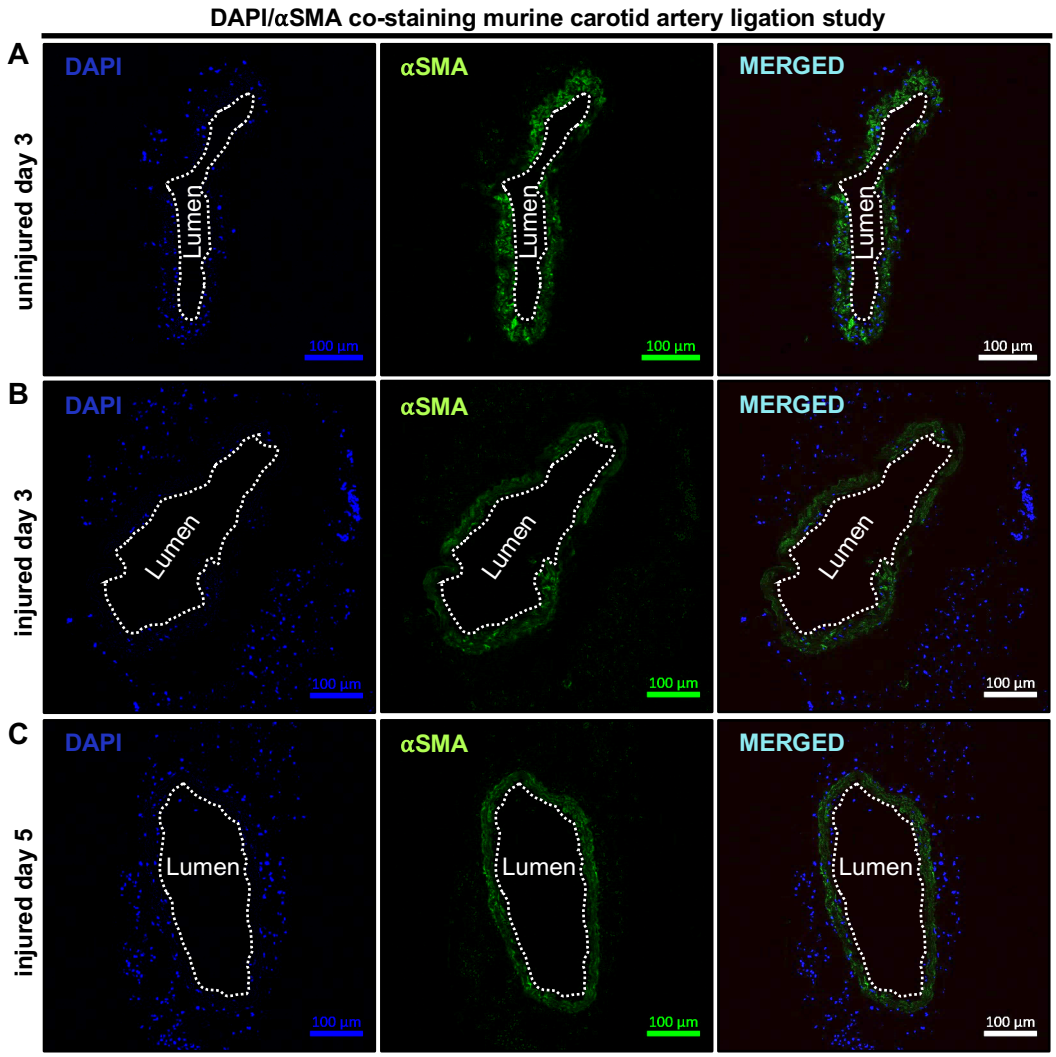

Figure 3-16 Carotid artery ligation triggers a decrease in medial αSMA immunoreactivity in mice. The carotid artery ligation procedure was performed as described by Kumar *et al.* (Kumar and Lindner, 1997). C57BL/6J mice were terminated at indicated time points. Injured left carotid arteries and uninjured right carotid arteries were fixed in paraformaldehyde, embedded in paraffin and sectioned on a microtome. Unstained day 3 sections were s generous gift from Daria Boyd. IHC staining was performed to determine the presence of αSMA (green). DAPI staining (blue) was used to detect nuclei. This figure displays representative images of αSMA /DAPI-stained uninjured day 3 (**A**, n=2), injured day 3 (**B**, n=1) and injured day 5 (**C**, n=1) carotid arteries.

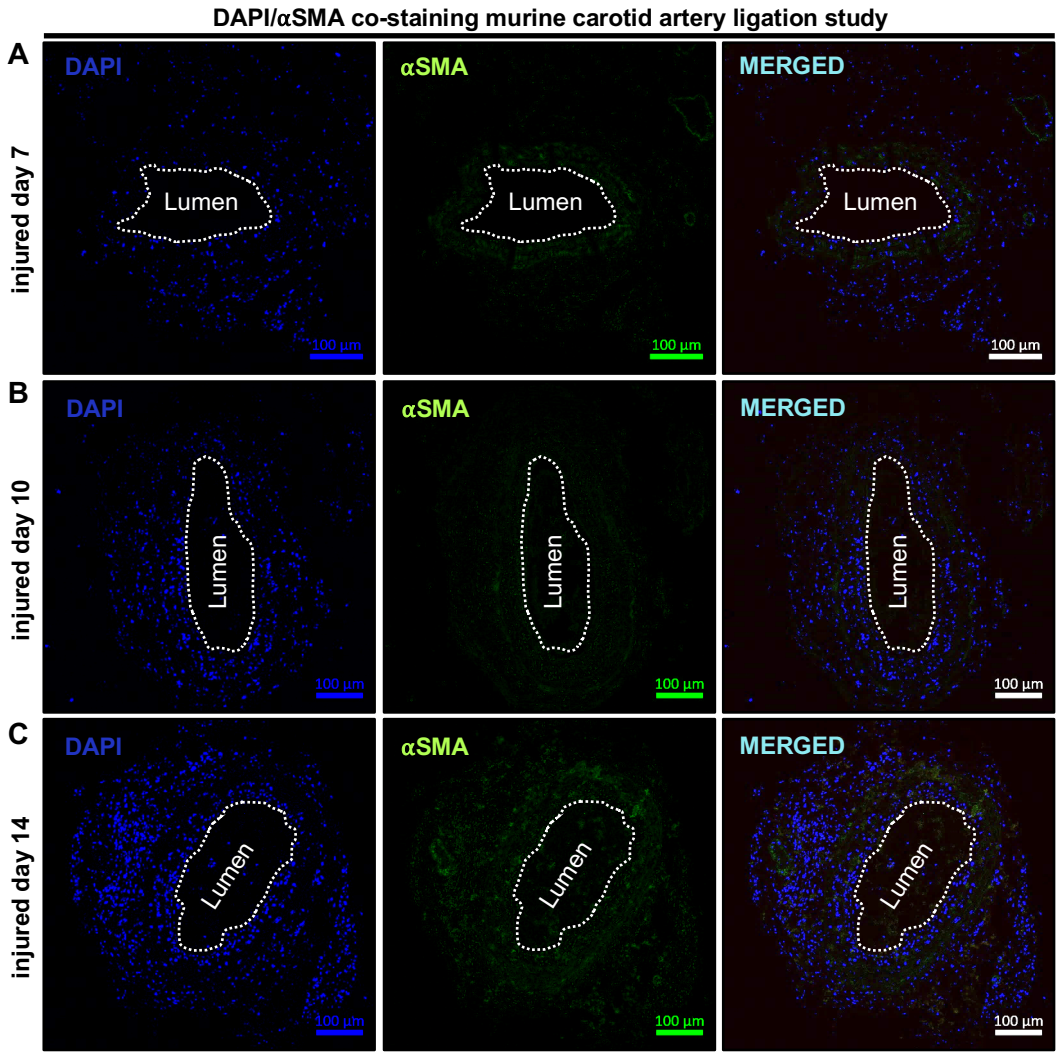

Figure 3-17 Carotid artery ligation triggers a decrease in medial αSMA immunoreactivity in mice. The carotid artery ligation procedure was performed as described by Kumar *et al.* (Kumar and Lindner, 1997). C57BL/6J mice were terminated at indicated time points. Injured left carotid arteries were fixed in paraformaldehyde, embedded in paraffin and sectioned on a microtome. IHC staining was performed to determine the presence of αSMA (green). DAPI staining (blue) was used to detect nuclei. Unstained day 7 sections were a generous gift from Daria Boyd. This figure displays representative images of αSMA /DAPI-stained injured day 3 (**A**, n=2), injured day 10 (**B**, n=2) and injured day 14 (**C**, n=1) carotid arteries.

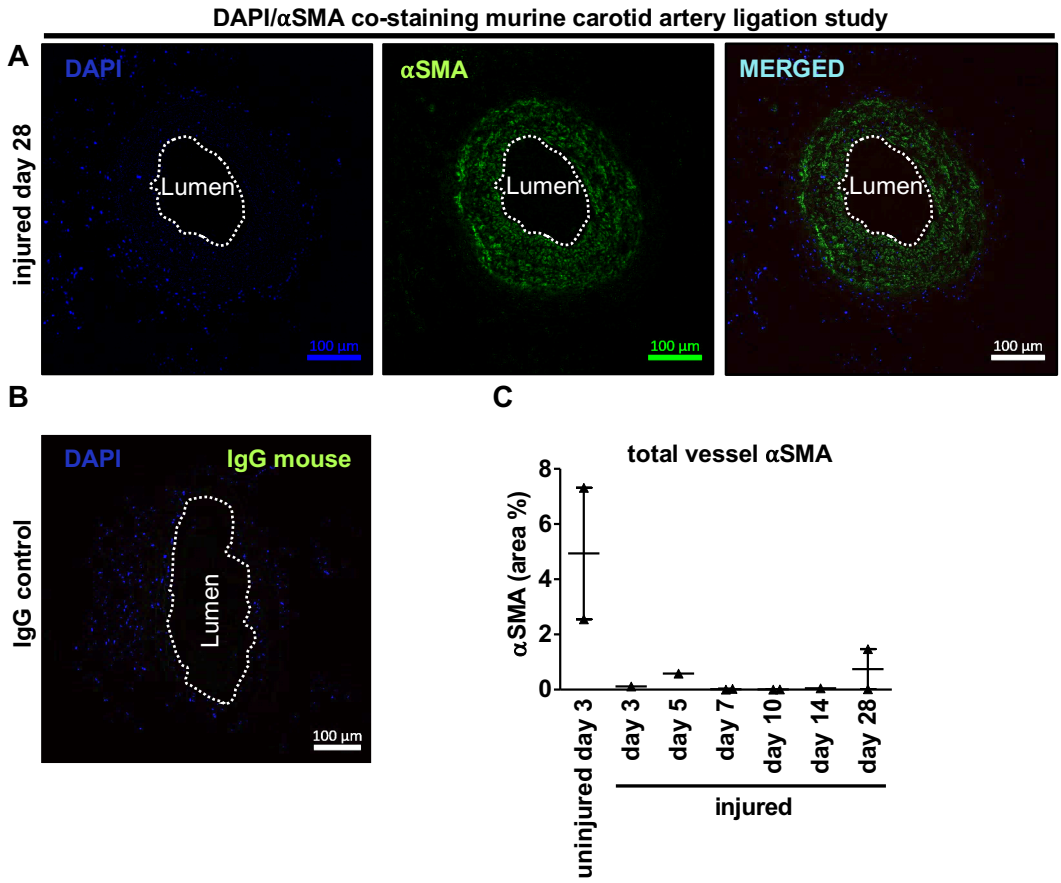

Figure 3-18 28-day old neointimal lesions display αSMA immunoreactivity in mice. The carotid artery ligation procedure was performed as described by Kumar *et al.* (Kumar and Lindner, 1997). C57BL/6J mice were terminated at indicated time points. Injured left carotid arteries were fixed in paraformaldehyde, embedded in paraffin and sectioned on a microtome. IHC staining was performed to determine the presence of αSMA (green). DAPI staining (blue) was used to detect nuclei. (**A**) One representative image is displayed for injured day 28 timepoint (n=2). (**B**) Respective IgG control was added to adjust for unspecific binding. (**C**) The ImageJ software was used to determine total vessel αSMA pixel intensity (area %) following threshold normalisation. Data are presented as mean ± S.E.M..

3.4 Discussion

The aims of this chapter were to evaluate BMP-9 and SMC phenotype switching in pre-implantation SVGs from CABG patients and injured murine carotid arteries, and to characterise vascular remodelling and cell proliferation at multiple time points following carotid artery ligation injury in mice.

Abundant BMP-9 immunoreactivity was detected in all SVG layers and co-localised with αSMA$^+$ cells suggesting SMC *GDF2* expression. Some BMP-9 staining was also detected within the extracellular space. These data confirm the presence of BMP-9 in pre-implantation SVGs from patients undergoing CABG surgery. However, it is not clear whether SVG SMCs are also the source of BMP-9. Since BMP-9 circulates in the bloodstream in humans, it maybe speculated that BMP-9 penetrates the saphenous vein wall via the lumen or vasa vasorum and is then stored extracellularly or taken up into vSMCs (David et al., 2008). In line with this speculation, Miller *et al*. demonstrated that radioactively labelled [^{125}]BMP-9 was taken up into liver ECs and Kupffer cells via an unknown receptor (Miller et al., 2000). Surprisingly, qRT-PCR analysis did not detect any BMP-9 (*GDF2*) mRNA expression levels in isolated primary HSVSMCs (data not shown). Outgrowth in 15% FCS SMC growth media may suppress BMP-9 mRNA expression levels which may then become undetectable, or primer insufficiency may have generated false negative results. Moreover, BMP-9 may be produced by other vascular cell types such as ECs, fibroblasts or inflammatory cells. In addition, BMP-9 antibody specificity may not be accurate. It should be noted that liver tissue, rather than lung tissue (as shown in Figure 3-6) would have been more appropriate for confirming BMP-9 antibody specificity. For example, Owen *et al*. confirmed BMP-9 antibody specificity in livers of wild-type and homozygous *Bmp-9* knockout mice (Owen et al., 2020). Moreover, co-incubation of BMP-9 antibodies with rising concentrations of rh BMP-9 should be undertaken to confirm antibody specificity for IHC in the future. Furthermore, *in situ* hybridisation should be used in future experiments aimed at localising potential BMP-9 mRNA expression in pre-implantation SVG sections.

IHC analysis demonstrated that SVGs displayed SMC phenotype switching indicated by reduced intimal SMC calponin and MYH11 expression compared to the media. In line with these findings Low *et al*. demonstrated reduced intimal

pre-implantation SVG *CNN1* (encodes calponin) and *MYH11* mRNA expression levels compared to the media (unpublished data) (Low et al., 2019). Furthermore, a study by Panettea *et al.* demonstrated that pre-implantation SVGs from CABG patients displayed marked pre-existing neointimal thickening, a known risk factor for early and late vein graft failure (VGF) (Panetta et al., 1992). In addition, decreased medial calponin expression is an independent risk factor for VGF following CABG surgery (Perek et al., 2013). A post-mortem study investigating SMC phenotype switching in SVGs following CABG surgery demonstrated early SMC de-differentiation towards a synthetic phenotype with reduced αSMA expression (Kockx et al., 1992). Taken together, pre-existing SMC phenotype switching may contribute to neointimal thickening in pre-implantation SVGs which then may exacerbate acute SMC phenotype switching following coronary implantation.

Pre-implantation SVGs from CABG patients displayed BMP-9 and SMC phenotype switching. To determine the potential pathophysiological relevance of BMP-9 in SMC de-differentiation-driven NF, wire-injured and uninjured murine carotid arteries were stained for BMP-9 and αSMA. Uninjured control carotid arteries demonstrated punctate medial and adventitial BMP-9 immunoreactivity. 14-day old wire-injured carotids displayed a trend towards an increase in total BMP-9 presence compared to uninjured controls, indicating a potential dynamic increase in vascular BMP-9 levels. In line with previous findings by Lindner *et al.*, 14-day old injured carotid arteries displayed reduced SMC αSMA expression indicating SMC phenotype switching following wire injury (Lindner et al., 1993). Alongside adventitial immunoreactivity, punctate BMP-9 staining was visible along the IEL and neointima at this time point. 21-day old, injured carotids displayed punctate BMP-9 staining within the neointima, media and adventitia. Total vascular BMP-9 levels had dropped to levels observed in uninjured control carotid arteries. This data set should be interpreted with caution. Firstly, BMP-9 staining was only performed in a small number of experimental animals. Secondly, only wire-injured day 14 and 21 carotid arteries were included in this study. Thirdly, morphometric and proliferation data were not readily available. Hence, more n numbers including corresponding uninjured controls, morphometric and proliferation analysis should be added to this study in the future.

Despite these limitations, this study, for the first time, suggests that the ALK1 ligand BMP-9 is present in the murine arterial vasculature. Moreover, a dynamic increase in total vascular BMP-9 immunoreactivity is accompanied by SMC phenotype switching and NF following wire injury. Furthermore, Garrido-Martín *et al.* found that ECs and vSMCs displayed an increase in ALK1 expression following femoral artery wire injury in mice (Garrido-Martín et al., 2013). BMP-9/ALK1 signalling drives endothelial TLR4, VCAM-1 and E-selectin expression thereby potentiating LPS-induced monocyte recruitment (Appleby et al., 2016). The same study showed that systemic BMP-9 delivery to LPS-challenged mice enhanced leukocyte recruitment to pulmonary endothelium indicating pro-inflammatory functions of BMP-9. In line with these findings, Cai *et al.* demonstrated that the damage associated molecular pattern (DAMP) protein high mobility group box (HMGB)1 was upregulated and interacted with TLR4 in wire injured murine carotid arteries (Cai et al., 2015). The same study showed that HMGB1 activated TLR4 signalling in macrophages and SMCs triggering macrophage chemotactic protein (MCP)-1 production and pro-inflammatory NF-κB signalling driving monocyte recruitment within the injured vessel. Furthermore, pharmacological inhibition of HMGB1/TLR4 interaction and genetic ablation of TLR4 prevented monocyte recruitment and NF in wire injured carotid arteries implicating the innate immune system as a pathogenic driver of intimal hyperplasia following vascular injury. In the context of SVG occlusion, Karper *et al.* showed that lesions in pre-implantation and failed SVGs displayed abundant TLR4 presence (Karper et al., 2011). The same study investigated the functional role of TLR4 in NF in a murine carotid artery venous inter-positioning model. The authors found that transgenic *Tlr4*-deficient and TLR4 gene silencing in hyperlipidaemic APOE* Leiden mice showed reduced NF following vein graft inter-positioning. This is in line with aforementioned study by Cai *et al.* demonstrating that TLR4 is a driver of NF following carotid artery wire injury in mice (Cai et al., 2015). Hence, it may be speculated that BMP-9 enhances TLR4 expression via ALK1 pathway activation thereby driving monocyte recruitment and NF following vascular injury. This hypothesis could be addressed in a future murine carotid artery ligation, wire injury or vein graft study evaluating the impact of neutralising BMP-9 antibodies or recombinant BMP-9 on vascular HMGB1/TLR4 signalling, leukocyte recruitment, SMC phenotype switching and NF.

BMP-9 findings from wire-injured carotid arteries prompted a multiple timepoint murine carotid artery ligation study aimed at correlating potential changes in vascular BMP-9 levels with SMC phenotype switching and NF. Although no statistically significant changes were found between groups due to increased intra-group variability, carotid artery ligation triggered early adventitial and peripheral vascular cell proliferation, SMC phenotype switching, NF and medial hypertrophy. The potential underlying reasons for the absence of statistical significances between groups will be explained in respective paragraphs. Furthermore, immunohistochemical BMP-9 staining could not be performed due to the COVID-19 pandemic and subsequent lab closure and should be performed in the future.

Three- and 5-day old injured carotid arteries demonstrated reduced medial cellularity indicating SMC loss. These findings are in line with a previous study investigating NF in *Enos* (encodes endothelial nitric oxide synthase)-deficient C57BL/6J mice following carotid artery ligation injury (Zhang et al., 2020). This is interesting, since early medial SMC loss has mainly been reported in the murine femoral artery wire injury and venous bypass graft atherosclerosis models (Sata et al., 2000; Zou et al., 1998). Together, these findings stand in contrast to Kumar's study, which reported medial cell proliferation in 5-day old injured carotid arteries following carotid artery ligation in FVB mice (Kumar and Lindner, 1997). This discrepancy may be explained by utilisation of C57BL/6J mice in the presented study. Indeed, Kelley *et al.* showed that mechanisms of lumen narrowing following carotid artery ligation differed substantially between several investigated inbred mouse strains (Harmon et al., 2000). Early medial SMC loss occurs upon coronary SVG and/or stent implantation and this is recapitulated in 3- and 5-day old ligation injured carotid arteries (Heldman et al., 2001; Kockx et al., 1992). Therefore, this model may prove useful for determining efficacy of novel experimental therapies aimed at preventing early SMC loss following ligation injury.

In addition to early medial SMC loss, 3-, 5- and 7-day old injured carotid arteries displayed visually enhanced EdU^+ nuclei compared to uninjured day 3 controls suggesting increased vascular cell proliferation. Whereas proliferating cells at day 3 and 5 were localised to the adventitia and perivascular tissue, replicating cells within the intima and media were detected at day 7 indicating SMC

phenotype switching. Very few to no proliferating cells were detected at later time points within ligation-injured carotid arteries. The absence of proliferating intimal cells beyond day 7 stands in contrast to Kumar's study, which demonstrated sustained intimal cell proliferation until 28 days following carotid artery ligation (Kumar and Lindner, 1997). Several reasons may explain this discrepancy. Firstly, as mentioned above, the authors utilised the FVB mouse strain in their study, which may affect vascular responses following injury. Secondly, mice received two BrdU injections at 12- and 1-h prior to termination, thereby potentially achieving enhanced incorporation into proliferating vascular cells. Thirdly, EdU staining in sections obtained from first ligation study (day 3 and 7 time points) appeared much brighter compared to sections obtained from the second ligation study (day 5, 10, 14 and 28 time points). Surgical procedures, EdU dosage/injections and tissue analyses for both studies were performed following the same established protocols. The fact that 5-day old injured carotid arteries displayed weak EdU staining, which co-localised with DAPI staining, confirmed that EdU incorporation had been achieved. However, the EdU batch utilised in the second ligation study differed from that utilised in the first study and this may explain the discrepancy. As an alternative to EdU staining, proliferating cellular nuclear antigen (PCNA) staining may be utilised to determine vascular cell proliferation in presented carotid artery ligation studies (Sata et al., 2000). Although EdU^+ nuclei were visually increased in day 3 and 7 ligation injured carotid arteries, no statistically significant differences were found when comparing these findings to uninjured day 3 controls. Enhanced inter-group variability may be explained by the low n number of experimental animals, the differences in EdU staining between the first and the second carotid artery ligation study and the fact that not all sections display cell proliferation.

Despite these limitations, interesting observations were made at day 3, 5 and 7 time points where ligation injured carotid arteries displayed enhanced adventitial and perivascular proliferation. Similar observations were made in a study by Zhang *et al.* in which 1-week old ligation injured murine carotid arteries demonstrated increased adventitial proliferation and thickness (Zhang et al., 2020). In line with these findings, 2- and 3-day old balloon injured porcine coronary arteries showed enhanced adventitial fibroblast proliferation (Shi et al., 1996a). The same study revealed adventitial fibroblast-to-myofibroblast

differentiation and subsequent myofibroblast migration to the forming neointima. Adventitial fibroblast-to-myofibroblast differentiation and myofibroblast migration contribute to SVG NF in pigs (Shi et al., 1997). Taken together, it may be speculated that carotid artery ligation injury triggers adventitial fibroblast proliferation and subsequent fibroblast-to-myofibroblast differentiation. In addition, both Kumar and Zhang reported the presence of adventitial $CD45^+$ leukocytes as well as $F4/80^+$ and $CD107b^+$ macrophages in ligation injured vessels indicating inflammatory cell infiltration (Kumar and Lindner, 1997; Zhang et al., 2020). In line with these findings, Okamoto *et al.* demonstrated up-regulation of perivascular adhesion molecule expression as well as adventitial neutrophil and macrophage infiltration in balloon injured coronary arteries in pigs (Okamoto et al., 2001). This indicates that inflammatory cells may enter the injured vessel wall via activated vasa vasorum. Hence, future experiments should be aimed at characterising proliferating adventitial and perivascular cells in more detail following carotid artery ligation in mice.

In line with previous findings by Zhang *et al.*, carotid arteries at the 7-day timepoint demonstrated intimal nuclear haematoxylin staining indicating onset of NF (Zhang et al., 2020). This was paralleled by a trend towards an increase in I/M ratio. Paralleling results from Kumar's study, IHC detected few to no medial SMCs displaying αSMA immunoreactivity compared to uninjured day 3 controls suggesting loss of SMC αSMA expression (Kumar and Lindner, 1997). Together with an increase in medial SMC proliferation these findings indicate *in vivo* SMC phenotype switching. Although these findings corroborate with previous murine carotid artery ligation studies, they require careful interpretation since IHC αSMA analysis was only performed on 1-2 animals/group. To overcome this limitation, more n numbers should be added to this IHC analysis in the future.

Alongside hyperplasia, 10-day old neointimal lesions demonstrated a visual increase in eosin staining, potentially indicating ECM expansion. The I/M ratio showed a trend towards an increase compared to 7-day old injured carotid arteries. Beyond day 10, the I/M ratio remained unchanged suggesting that maximal neointimal area expansion was achieved by this timepoint. In line with Kumar's findings, carotid arteries at the day 10 timepoint displayed an increase in medial area compared to the day 5 injury group indicating medial hypertrophy

(Kumar and Lindner, 1997). At the day 28 timepoint, neointimal lesions demonstrated reduced cellularity accompanied by ECM expansion compared to neointimal lesions at the 10-day timepoint. These findings corroborate with a study by Liao *et al*. which reported that SMC-specific *Tgfbr1* deficiency in C57BL/6J mice attenuated NF following femoral artery wire injury compared to wild-type controls (Liao et al., 2016). Attenuation of NF was characterised by enhanced intimal cell proliferation, apoptosis and a reduction in intimal collagen content. Whereas functional ALK5 receptor signalling dampened SMC proliferation and apoptosis this pathway also drove neointimal ECM expansion.

Interesting observations were made at day 10 and 14 time points. Although intimal lesions appeared to be covered by endothelium, they frequently appeared to detach from the IEL forming subendothelial spaces which were filled with erythrocytes. Kumar *et al*. reported similar findings in perfusion-fixed, ligation-injured carotid arteries at the 5 day timepoint (Kumar and Lindner, 1997). The authors speculated that this may be explained by persistent and fixed vessel contraction indicated by the presence of wavy elastic laminae. Hence, it may be speculated that persistent vessel contraction in this injury model may cause endothelial discontinuities allowing erythrocytes to enter the sub-endothelial space which may impact neointimal remodelling (Kumar and Lindner, 1997).

As previously outlined, morphometric findings from both presented carotid artery ligation studies should be interpreted with caution. Firstly, two 10- and three 14-old injured carotid arteries did not display neointimal lesions although injured carotid arteries had been evaluated at 5 points (150 µm apart) distal to the ligation. This may be explained by technical tissue handling errors during paraffin embedding. For example, it is possible that some carotid arteries were not embedded at a vertical angle which may hamper subsequent lesion detection when cutting sections on the microtome. Secondly, only injured carotid arteries were analysed for the second carotid artery ligation study. Uninjured controls were not added to this preliminary data set because that the main aims of the study were to primarily determine time-dependent NF and SMC phenotype switching in injured carotid arteries and to link these responses with the presence of BMP-9. To overcome this limitation uninjured control carotid

arteries should be added to complete morphometric and proliferation analysis of these two carotid artery ligation studies in the future.

3.5 Summary

Presented findings reveal BMP-9 presence in pre-implantation human SVGs and murine arterial vasculature. Moreover, SVGs display *in vivo* SMC phenotype switching which may drive pre-existing SV NF, a known risk factor for early and late vein graft disease. Carotid artery wire injury in mice triggered a trend towards an increase in total vascular BMP-9 levels which was paralleled by SMC phenotype switching indicating a potential role for BMP-9 in NF. These findings prompted initiation of an observational multiple timepoint murine carotid artery ligation study aimed at linking BMP-9 presence with vascular responses following injury. Carotid artery ligation injury in C57BL/6J mice triggered early adventitial and perivascular tissue cell proliferation paralleled medial SMC loss. 1-week old injured carotid arteries displayed onset of NF, intimal and medial cell proliferation and loss of SMC αSMA expression indicating SMC phenotype switching. Unfortunately, BMP-9 staining could not be performed for this study due to the COVID-19 pandemic and subsequent lab closure.

Chapter 4 Exploring TGF-β superfamily signalling-driven HSVSMC phenotype responses

4.1 Introduction

Quiescent contractile vSMCs express high levels of contractile markers including *αSMA*, *SM22-α*, *CNN1* and *MYH11*, important components of the SMC contraction machinery (Chen et al., 2016b; Han et al., 2009). SMC phenotype transition encompasses a decrease in contractile marker expression, a universally accepted indicator of SMC de-differentiation (Frismantiene et al., 2018). Depending on the vascular disease setting, this may be paralleled by a gain in proliferative, migratory or ECM production capacity or by transitioning to a macrophage-like, mesenchymal stem cell (MSC)-like or osteogenic phenotype (Chappell et al., 2016; Liao et al., 2016; Vengrenyuk et al., 2015; Zhu et al., 2015). Together, the transcription factors SRF and MYOCD jointly regulate contractile gene expression in vSMCs (Du et al., 2003; Rensen et al., 2006; Yoshida et al., 2003).

4.1.1 TGF-β-dependent regulation of contractile gene expression in vSMCs

Intact TGF-β superfamily signalling is crucial for normal vascular development and adult vascular homeostasis (reviewed in) (Schwartze et al., 2019). TGF-β_1 plays an important role in the regulation of vSMC development (Shah et al., 1996) and contractile gene expression (Hautmann et al., 1997).

Shah *et al.* demonstrated that TGF-β_1 induced vSMC differentiation in rodent neural crest stem cells (NCSCs) evidenced by an increase in αSMA and calponin expression along with an acquisition of SMC morphology (Shah et al., 1996). In line with these findings, TGF-β_1 induced vSMC differentiation in multi-lineage progenitor cells which originated from human umbilical cord blood (Yang et al., 2011). Furthermore, Grainger and colleagues showed that young heterozygous *Tgfb1* knockout mice displayed a decrease in aortic contractile protein expression levels compared to wild-type controls (Grainger et al., 1998). Taken together, these 3 studies demonstrated that TGF-β_1 can drive embryonic vSMC differentiation and positively regulate contractile gene/protein expression levels *in vitro* and *in vivo*. However, little was known about the underlying molecular mechanisms by which TGF-β_1 drove vSMC differentiation. To address this question, Hautmann *et al.* delivered several *SM22-α* promoter deletion mutants to quiescent rat aortic SMCs which were subjected to TGF-β_1 stimulation

(Hautmann et al., 1997). The authors showed that two CArG boxes and a TGF-β control element (TCE) conferred TGF-β_1 responsiveness driving *SM22-α* expression levels. Further analysis revealed enhanced binding of SRF to CArG elements and an unidentified factor to the TCE. In addition, this study showed that TGF-β_1 also drove *MYH11* and *CNN1* expression levels. Since this initial study, mechanistic studies have uncovered additional molecular mechanisms of TGF-β_1-dependent regulation of contractile gene expression.

In line with Hautmann *et al.*'s findings, Chen *et al.* demonstrated that the TGF-β_1-inducible SMAD3/SMAD4 complex directly bound to an SBE situated within the *SM22-α* promoter thereby also driving *SM22-α* expression (Chen et al., 2003). Nishimura and colleagues investigated the TF δEF1 in the context of TGF-β_1-dependent transcriptional control of *SM22-α* in rat aortic SMCs (Nishimura et al., 2006). The study showed that δEF1 TGF-β_1-dependently cooperated with SMAD3 and SRF thereby enhancing *SM22-α* promoter activity. Moreover, Qiu *et al.* found that the known CArG regulator MYOCD participated in TGF-β_1-dependent induction of *SM22-α, MYH11* and *αSMA* promoters (Qiu et al., 2005). The authors demonstrated direct interaction of activated SMAD3 and MYOCD *in vitro* and *in vivo* revealing functional synergy between these 2 TFs. In summary, these mechanistic studies showed that TGF-β_1-dependent regulation of contractile gene expression in vSMCs may be achieved by several molecular mechanisms.

Although these studies uncovered complex TGF-β_1-dependent transcriptional networks, they did not investigate via which signalling axis TGF-β_1 regulated the contractile vSMC phenotype. This is important since TGF-β_1 may transduce signals via the ALK5/SMAD2/3 or ALK1/SMAD1/5 signalling axis (Schwartze et al., 2014). Low *et al.* showed that pharmacological and siRNA-mediated inhibition of ALK5 and ALK1 in HSVSMCs attenuated TGF-β_1-dependent SMAD2/3 and SMAD1/5 phosphorylation respectively (unpublished data) (Low et al., 2019). Whereas TGF-β_1 drove contractile gene expression levels via the ALK5 signalling axis, pharmacological ALK1 inhibition had no impact on TGF-β_1-dependent induction of contractile gene expression. In line with these findings, combined pharmacological ALK4/5/7 with SB431542 inhibited TGF-β_1-driven contractile protein accumulation in primary HASMCs emphasising the role of TGF-

β_1/ALK5/SMAD2/3-driven contractile differentiation (Tang et al., 2010). Taken together, these studies showed that TGF-β_1 positively regulated contractile gene expression in venous and arterial vSMCs via the ALK5/SMAD2/3 pathway. Overall, presented *in vitro* and *in vivo* studies coherently identified TGF-β_1 as a driver of the contractile vSMC phenotype.

4.1.2 Conflicting role of TGF-β signalling in vascular injury-driven NF

Friedl *et al.* showed that SVGs with neointimal lesions displayed an increase in TGF-β_1 and LTBP compared to SVGs without NF (Friedl et al., 2004). Furthermore, Nikol and colleagues uncovered an increase in *TGFB1* mRNA expression levels within re-stenosed coronary arteries following balloon angioplasty (Nikol et al., 1992). Taken together, these two studies suggested the involvement of TGF-β_1 in NF following coronary SVG implantation and PCI. Subsequently, studies investigating the role of TGF-β signalling in *in vivo* vascular injury models generated conflicting results.

Tsai *et al.* revealed that balloon-injured rat carotid arteries displayed enhanced Smad3 expression compared to uninjured control (Tsai et al., 2009). Subsequent adenoviral-mediated Smad3 delivery to injured arteries triggered an increase in vSMC proliferation and worsened NF. Although TGF-β_1 treatment alone suppressed rat aortic SMC proliferation, TGF-β_1 potentiated adenoviral-mediated Smad3 overexpression-driven proliferation. A subsequent study by the same group found this effect was ERK/MAPK dependent (Suwanabol et al., 2012). This meant that TGF-β_1-driven cell responses might depend on intracellular signalling messenger expression levels. Although a study by Kobayashi *et al.* reported that TGF-β_1/SMAD3 signalling suppressed serum-induced SMC proliferation, Smad-3 depleted cells did not prevent TGF-β_1-driven chemotaxis indicating that this pro-migratory effect may be driven by the lateral TGFBR2/ALK1/SMAD1 signalling axis (Kobayashi et al., 2005). In the context of SVG disease, Cooley and colleagues demonstrated that TGF-β signalling antagonism by neutralising antibodies, short hairpin RNA-mediated Smad2 or Smad3 knockdown, Smad3 haploinsufficiency and EC-specific Smad2 knockdown prevented TGF-β_1-driven EndMT and subsequent vein graft NF in mice (Cooley et al., 2014). Moreover,

adenoviral-mediated TGF-β_1 antisense mRNA delivery to epigastric veins following inter-positional grafting into femoral arteries in rats significantly reduced NF (Wolff et al., 2006). These studies identified TGF-β_1 as a pathological driver of NF in murine arterial and venous vascular injury models. It was speculated that pharmacological inhibition of induction of *Tgfb1*, *Tgfb3* and *Alk5* mRNA expression levels in balloon-injured rat carotid arteries with tranilast would dampen NF following balloon angioplasty in humans (Ward et al., 1998). The Tranilast Restenosis Following Angioplasty Trial (TREAT-2) reported a marked reduction in restenosis rates in tranilast-treated patients receiving percutaneous transluminal coronary angioplasty compared to placebo-treated control trial participants (Tamai et al., 2002). However, the much larger Prevention of REStenosis with tranilast and its outcomes (PRESTO) Trial did not find a significant improvement of restenosis in patients receiving PCI treatment (Holmes et al., 2002). The fact, that anti-TGF-β_1 treatment did not yield a positive result means that human pathophysiology does not entirely reflect experimental *in vivo* findings.

Since vSMC de-differentiation largely contributes to NF following vascular injury and TGF-β_1-positively regulates the contractile vSMC phenotype, it appears conceivable that ALK5 agonism would protect vSMCs from phenotype switching and subsequent NF. Indeed, Nishimura's study clearly demonstrated positive TGF-β_1/δEF1-dependent regulation of *SM22-*α expression (Nishimura et al., 2006). The same study showed that adenoviral-mediated δEF1-overexpression promoted vSMC differentiation and prevented NF following experimental arterial injury in mice. Two *in vitro* studies found that TGF-β_1 attenuated PDGF- and/or serum-induced proliferation and migration of vSMCs (Martin-Garrido et al., 2013; Mii et al., 1993). In line with these findings *Smad3*-deficient mice displayed enhanced NF following femoral artery wire injury compared to wildtype controls (Kobayashi et al., 2005). The same study showed that TGF-β_1 suppressed serum-induced murine aortic SMC proliferation in a Smad3-depedendent manner. Moreover, Chen *et al.* found that enhanced ALK5/SMAD2 signalling by inhibition of antagonistic pro-proliferative FGF signalling, even in the presence of high serum levels, induced a contractile HASMC phenotype (Chen et al., 2016b). The same study demonstrated that SMC-specific FGF receptor adaptor substrate 2-α deletion in mice reduced NF following carotid artery ligation indicating that the

ALK5 receptor protects vSMCs from de-differentiation. In contrast to studies presented in the previous paragraph, these studies show that TGF-β_1 protects the contractile vSMC phenotype and attenuates SMC de-differentiation/NF following experimental vascular injury.

4.1.3 Activin A receptor type 2A/B signalling in vSMCs and vascular disease

In the context of contractile SMC phenotype regulation, Groenendijk *et al.* demonstrated the ACVR2A ligand activin A drove α*SMA*, *CNN1* and *SM22-*α mRNA expression levels in primary HSVSMCs (Groenendijk et al., 2011). In line with these findings, adenovirus-mediated activin A delivery inhibited NF in *ex vivo* human SVG organ cultures and following femoral artery cuff injury in mice (Engelse et al., 2002). Furthermore, Kloppenburg *et al.* demonstrated that adenovirus-mediated activin a delivery to epigastric vein dampened SMC proliferation and NF following inter-positioning into the femoral artery in rats (Kloppenburg et al., 2009). In contrast, Yndestad *et al.* found that PAH patients displayed elevated circulating activin A levels (Yndestad et al., 2009). The authors went on to demonstrate that hypoxia-induced experimental PAH in mice triggered an increase in pulmonary activin A mRNA expression levels and that activin a drove PASMC proliferation *in vitro*. In agreement with this study, Yung *et al.* showed that the myostatin/BMP11/activin ligand trap ActRIIa-FC attenuated PASMC and pulmonary microvascular EC proliferation. Moreover ActRIIa-FC administration improved pulmonary haemodynamics and attenuated right ventricular dysfunction and arteriolar remodelling in SUGEN5416/hypoxia-induced PAH in rats (Yung et al., 2020). Taken together, these studies suggest that activin A/ACVR2A/B signalling may either be protective or deleterious depending on the underlying vascular disease and potentially on distinct vascular beds.

4.1.4 Venous versus arterial SMCs

Owing to differences in blood flow and blood pressure pre-implantation SVGs and IMAGs differ substantially in histological structure (section 1.2.1) (Canham et al., 1997). Less well-defined histological structures such as the poorly developed IEL within the SVG wall may partially explain why venous conduits are more prone to

NF and atherosclerosis compared to IMAGs. In addition, it may be speculated that differences in differentiation status between SVG and IMAG SMCs differentially impact the injury response following CABG surgery.

Wong *et al*. demonstrated phenotypical differences between jugular vein and carotid artery SMCs in rabbits (Wong et al., 2005). The authors showed that venous SMCs demonstrated an increase in proliferative, migratory and collagen synthesis capacity compared to arterial SMCs suggesting that venous SMCs were more prone to de-differentiation. Deng and colleagues compared gene expression profiles and functional cell behaviour in response to oxidised (ox)-LDL and PDGF stimulation between HCASMCs and HSVSMCs (Deng et al., 2006). While ox-LDL inhibited HCASMC proliferation and migration, it promoted HSVSMC proliferation and simultaneously drove pro-inflammatory signalling pathways. Moreover, HSVSMCs elicited an increase in proliferation in response to PDGF treatment compared to HCASMCs paralleling findings from Wong's study. Shi *et al*. compared lipid retention and oxidative stress responses between SVGs and arterial grafts following graft inter-positioning in hyperlipidaemic pigs (Shi et al., 2001). In line with above-presented findings, the study revealed that SVG SMCs exhibited an increase in oxidative stress and LDL accumulation compared to arterial graft SMCs. Turner and colleagues went on to show that HSVSMCs displayed an increase in proliferative and migratory capacity in response to mitogenic stimuli compared to paired IMAG SMCs highlighting that HSVSMCs are more proliferative and invasive.

In conclusion, these studies comprehensively demonstrate that venous SMCs are more prone to de-differentiation compared to arterial SMCs which may in part explain why SVGs are more prone to NF and accelerated atherosclerosis compared to IMAGs.

4.2 Aims

- To develop and validate an undirected contractile differentiation protocol for primary human vSMCs.

- To determine TGF-β type I, II and III receptor expression levels and ALK1/ALK5 pathway activation during contractile differentiation of primary human vSMCs.

- To evaluate the impact of pharmacological ALK5 inhibition during contractile differentiation of primary HSVSMCs.

- To assess HAdV-5 *ACVR2A* transgene delivery to primary HSVSMCs.

- To determine BMP-9/TGF-β receptor complex formation on primary HSVSMCs.

- To characterise BMP-9 and/or TGF-β_1-driven phenotypical responses in primary HSVSMCs.

4.3 Results

4.3.1 Generation of a contractile differentiation protocol for primary HSVSMCs

Previous data shown in Chapter 3 demonstrated *in vivo* SMC phenotype switching in pre-implantation SVGs from CABG patients and injured murine carotid arteries. Pre-clinical and clinical studies have shown that SMC phenotype switching is a key contributor to NF in SVG disease and ISR (Chappell et al., 2016; Grewe et al., 2000; Kockx et al., 1992; Yu et al., 2011; Zou et al., 1998). Together, these findings prompted generation and validation of a low serum/heparin-induced contractile differentiation protocol (termed 'undirected') for primary human vSMCs enabling detailed investigation of ALK1 and ALK5 signalling during SMC phenotype switching in the context of SVG disease and ISR. This protocol was based on a study investigating cross-talk between FGF and TGF-β/ALK5 signalling during SMC phenotype-switch driven NF in vascular injury (Chen et al., 2016b).

Quantitative RT-PCR analysis demonstrated that relative *αSMA* (RQ_{mean} + max day 4 SMDS vs day 0 15% FCS: 26.3+5.1, $p<0.01$), *CNN1* (encodes calponin; day 4 SMDS vs day 0 15% FCS: 43.5+6.8, $p<0.001$), *MYH11* (day 4 SMDS vs day 0 15% FCS: 441.9+100.1, $p<0.001$) and *SM22-α* (day 4 SMDS vs day 0 15% FCS: 5.5+0.6, $p<0.05$) mRNA expression levels significantly increased in the SMDS and SMGS condition over a period of 6 days compared to 15% FCS-treated day 0 controls (Figure 4-1 A-D). 15% FCS-cultured HSVSMCs also demonstrated a significant increase in relative *CNN1* (day 6 15% FCS vs day 0 15% FCS: 16.8+2.9, $p<0.001$) and *MYH11* (day 6 15% FCS vs day 0 15% FCS: 158.2+34.2, $p<0.01$) mRNA expression levels compared to day 0 controls (Figure 4-1 B and C). Taken together, changes in contractile gene levels were most pronounced in the SMDS condition. The next aim was to establish whether increased relative contractile SMC marker mRNA expression levels were paralleled by increased protein expression levels. Whereas 15% FCS treatment suppressed mature SMC marker expression, SMDS-cultured HSVSMCs demonstrated a visual increase in αSMA ($densitometry_{mean}$ ± S.E.M. day 0 15% FCS: 0.03±0.02, day 6 SMDS: 0.3±0.17, $p>0.05$), calponin (day 0 15% FCS: 0.02±0.01, day 6 SMDS: 0.06±0.02, $p>0.05$) and SM22-α (day 0 15% FCS: 0.82±0.43, day 6 SMDS: 0.94±0.31, $p>0.05$) protein levels

compared to day 0 controls paralleling previous mRNA expression findings (Figure 4-2 A-D). In addition, day 6 SMDS-cultured HSVSMCs demonstrated a significant increase in calponin protein expression levels compared to day 6 15% controls (day 6 15% FCS: 0.01±0.002, day 6 SMDS: 0.06±0.02, $p<0.05$) (Figure 4-2 A and C). The absence of statistical significances for changes in αSMA and SM22-α protein levels following densitometric analysis may be explained by intra- and inter-patient variability and a low number of biological repeats (n=4 CABG patients). Nevertheless, immunoblot analysis paralleled mRNA expression findings consistently revealing higher levels of contractile SMC markers in SMDS-treated cells compared to control cells, particularly at the day 6 timepoint.

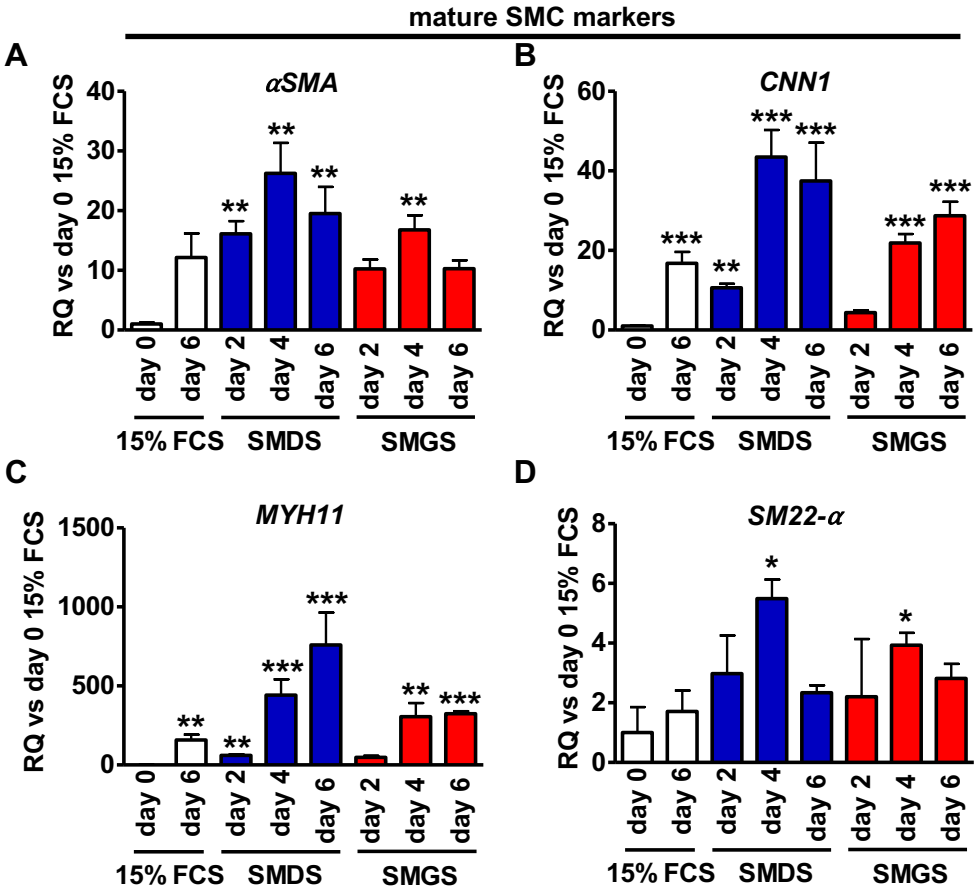

Figure 4-1 SMDS treatment drives accumulation of contractile gene expression levels in primary HSVSMCs. Cells were stimulated with 15% FCS (white bars), SMDS (blue bars) or SMGS (red bars). Cells were lysed for mRNA isolation and reverse transcription was performed to generate cDNA. Quantitative RT-PCR was performed to determine relative α*SMA* (**A**), *CNN1* (**B**), *MYH11* (**C**) and *SM22-*α (**D**) mRNA expression levels at indicated time points. Relative target gene expression was normalised to *UBC* expression to determine δCT values, which were used to calculate relative quantification (RQ) values (target group versus day 0 control). Data are presented as RQ_{mean} + error (biological n=3). A One-way repeated ANOVA with a Tukey's correction was performed to compare groups based on δCT values. P-value<0.05 was considered statistically significant (* p-value<0.05, ** p-value<0.01 and *** p-value <0.001, target group versus day 0 15% FCS control).

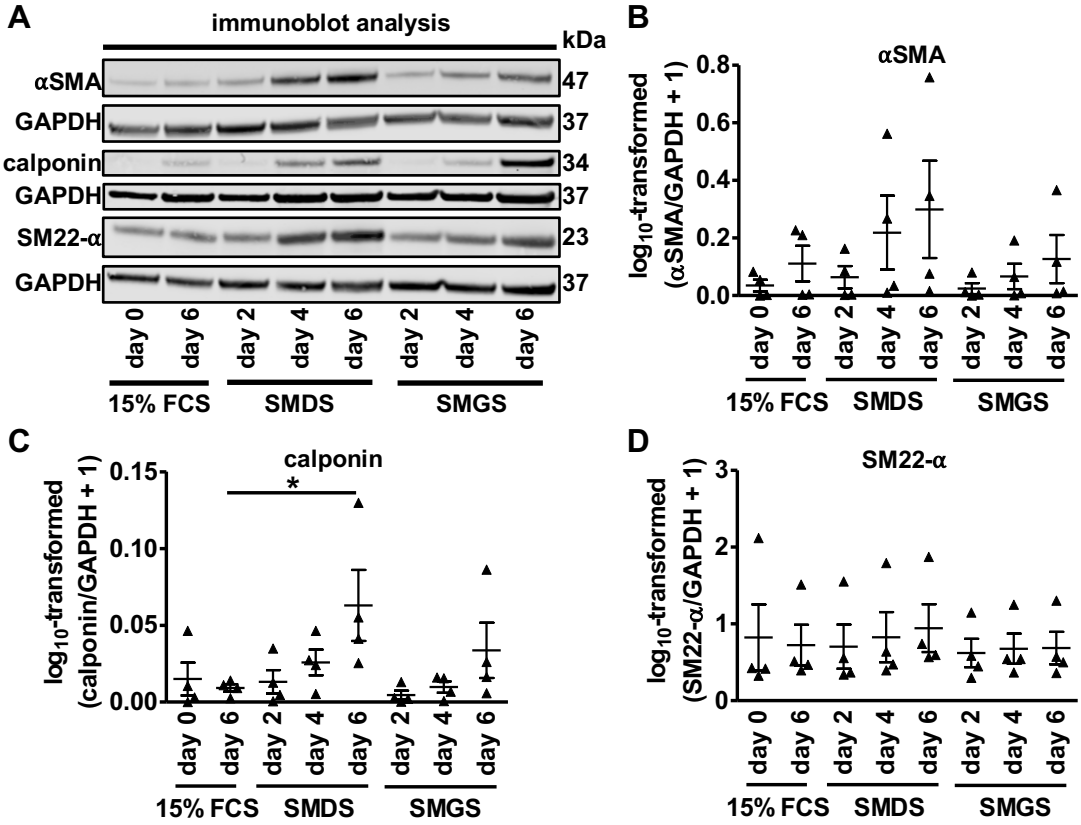

Figure 4-2 SMDS treatment drives accumulation of contractile protein expression levels in primary HSVSMCs. Cells were cultured in 15% FCS, SMDS or SMGS. Cells were lysed for protein isolation. (**A**) Immunoblot analysis (20 μg protein sample/lane) was performed to determine αSMA (**A** and **B**), calponin (**A** and **C**) and SM22-α (**A** and **D**) protein expression levels at indicated time points. GAPDH served as a housekeeper control. Densitometry (**B-D**) was performed to determine band intensities. Following normalisation to GAPDH (target protein/GAPDH) the constant 1 was added to each ratio value prior to $\log_{10}$-transformation. Data are presented as mean ± S.E.M. (biological n=4). A One-way repeated ANOVA with a Tukey's correction was performed to compare groups. P-value<0.05 was considered statistically significant (* p-value<0.05). kDa, kilo Dalton.

4.3.2 Contractile HSVSMCs display a decrease in proliferation

SMC phenotype switching entails loss of contractile protein expression and instead a gain in proliferative capacity following vascular injury (Chappell et al., 2016; Chen et al., 2016b; Kumar and Lindner, 1997; Liao et al., 2016; Yu et al., 2011). This prompted evaluation of changes in proliferation in 15% FCS- and SMDS-cultured HSVSMCs. Quantitative RT-PCR was performed to determine proliferation marker expression and 5-bromo-2'-deoxyuridine (BrdU) analysis was utilised as a surrogate marker of HSVSMC proliferation.

Pro-proliferative *CCND1* (encodes cyclin D1) (RQ_{mean} + error: day 6 SMDS vs day 0 15% FCS: 0.14+0.03, $p<0.001$) and *PCNA* mRNA expression levels (day 6 SMDS vs day 0 15% FCS: 0.27+0.05, $p<0.01$) time-dependently decreased in SMDS- and SMGS-treated HSVSMCs compared to day 0 15% FCS-treated controls (Figure 4-3 B and C). In addition, SMDS-treated cells demonstrated significantly reduced *CCND1* mRNA expression levels compared to 6-day 15% FCS-treated controls (day 6 SMDS: 0.14+0.03, RQ day 6 15% FCS: 0.56+0.1, $p<0.01$) (Figure 4-3 B). *PCNA* expression levels were substantially reduced in day 6 15% FCS-treated HSVSMCs compared to the day 0 15% FCS-treated controls (day 6 15% FCS vs day 0 15% FCS: 0.34+0.01, $p<0.05$) (Figure 4-3 C). Although comparisons between 6-day 15% FCS/SMDS treatment and day 0 15% FCS did not achieve statistical significance, there was a trend in up-regulation of anti-proliferative *CDKN1A* (encodes cyclin-dependent kinase inhibitor 1) expression levels (RQ day 6 SMDS: 2.4+0.4, RQ day 6 15% FCS: 5.1+0.9, RQ day 0 15% FCS: 1±0.3, $p>0.05$). (Figure 4-3 C). Functional assessment of HSVSMC proliferation utilising BrdU incorporation assays revealed that SMDS-cultured HSVSMCs were significantly less proliferative compared to 15% FCS-treated controls ($absorbance_{mean}$ ± S.E.M.; 15% FCS: 0.48±0.02, SMDS: 0.11±0.006, $p<0.01$) (Figure 4-4 A). Moreover, treatment of SMDS-cultured HSVSMCs with PDGF, demonstrated a trend towards an increase in BrdU incorporation, suggesting that contractile HSVSMCs could respond to a pro-proliferative stimulus (SMDS control: 0.11±0.006, SMDS + PDGF: 0.3±0.03, $p>0.05$) (Figure 4-4 A).

Taken together with previous data, SMDS-treated HSVSMCs displayed an accumulation of contractile proteins paralleled by a decrease in proliferation

compared to 15% FCS-treated controls indicating a quiescent contractile SMC phenotype.

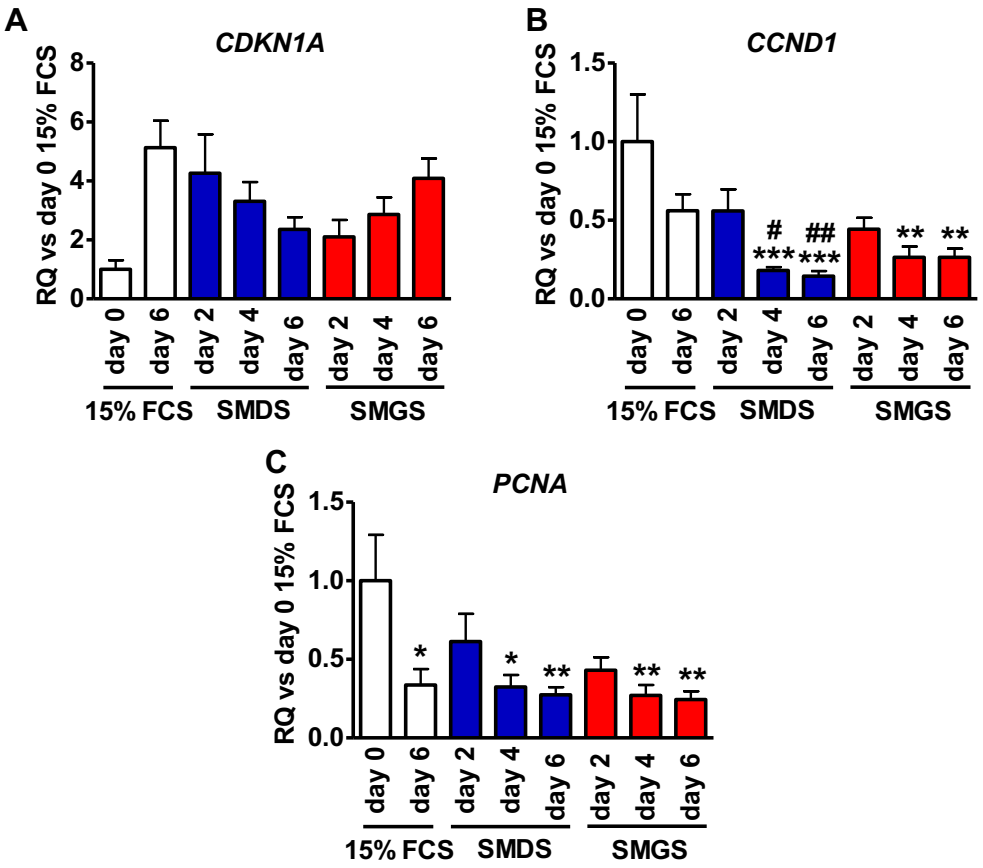

Figure 4-3 Contractile HSVSMCs demonstrate reduced levels of pro-proliferative gene expression levels. Cells were cultured in 15% FCS, SMDS or SMGS. Cells were lysed for mRNA isolation and reverse transcription was performed to generate cDNA. Quantitative RT-PCR was performed to determine relative *CDKN1A* (**A**), *CCND1* (**B**) and *PCNA* (**C**) mRNA expression levels at indicated time points. Relative target gene expression was normalised to *UBC* expression to determine δCT values, which were used to calculate relative quantification (RQ) values (target group versus day 0 control). Data are presented as RQ_{mean} + error (biological n=3). A One-way repeated ANOVA with a Tukey's correction was performed to compare groups based on δCT values. P-value<0.05 was considered statistically significant (* p-value<0.05, ** p-value<0.01 and *** p-value <0.001, target group versus day 0 15% FCS control; # p-value<0.05, ## p-value <0.01, target group versus day 6 15% FCS group).

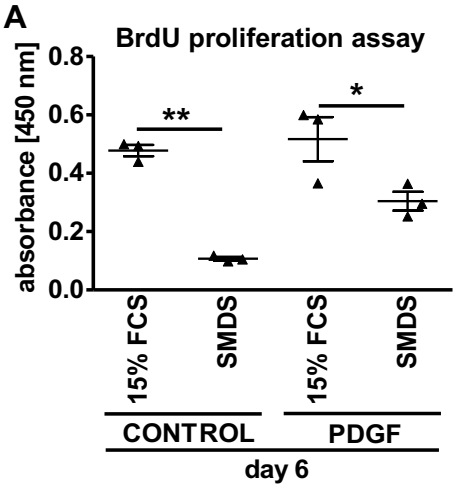

Figure 4-4 SMDS-treated primary HSVSMCs display decreased proliferation. (**A**) Cells were seeded into 96-well plates ($1*10^4$ cells/well) and cultured in 15% FCS (technical n=5/group). Upon achieving 80% confluence (day 0) media was removed and cells were either cultured in 15% FCS or SMDS. At day 5, one of the two groups within the 15% FCS or SMDS treatment group was stimulated with PDGF-BB (20 ng/ml) or vehicle control (ddH_20, 10 mM acetic acid, 0.2% BSA). BrdU (1:2000) was incorporated simultaneously and incorporation was assessed 24-h later. Scatter plot indicates mean ± S.E.M. (biological n=3). A One-way repeated ANOVA with a Tukey's correction was performed to compare groups. P-value<0.05 was considered statistically significant (* p-value<0.05, ** p-value<0.01).

4.3.3 Activin A receptor type 2a mRNA expression levels increase during contractile differentiation of HSVSMCs

Chen *et al*. demonstrated that *TGFBR1* expression increased during SMDS induced contractile differentiation of primary HASMCs (Chen et al., 2016b). This was paralleled by an increase in SMAD2 phosphorylation indicating an increase in ALK5 pathway activity. Hence, the next aim was to determine TGF-β type I and type II receptor mRNA expression levels during contractile differentiation of primary HSVSMCs.

15% FCS, SMDS and SMGS treatment did not significantly affect type I *ALK5*, *ALK1* or *ALK2* receptor mRNA expression levels (Figure 4-5 A-C). In contrast, day 4 SMDS and SMGS-treated HSVSMCs displayed increased type II *ACVR2A* receptor expression levels compared to 15% FCS-treated day 0 controls (RQ_{mean} + error, day 4 SMDS vs day 0 15% FCS: 7.56+1.25, $p<0.05$) (Figure 4-6 C). The type II receptors *TGFBR2*, *BMPR2* (n=2 CABG patients) and *ACVR2B* were not significantly affected by 15% FCS, SMDS or SMGS treatment (Figure 4-6 A, B and D).

In summary, *ACVR2A* mRNA expression levels were upregulated during contractile differentiation. It may be hypothesised that changes in *ACVR2A* expression regulate contractile differentiation of HSVSMCs.

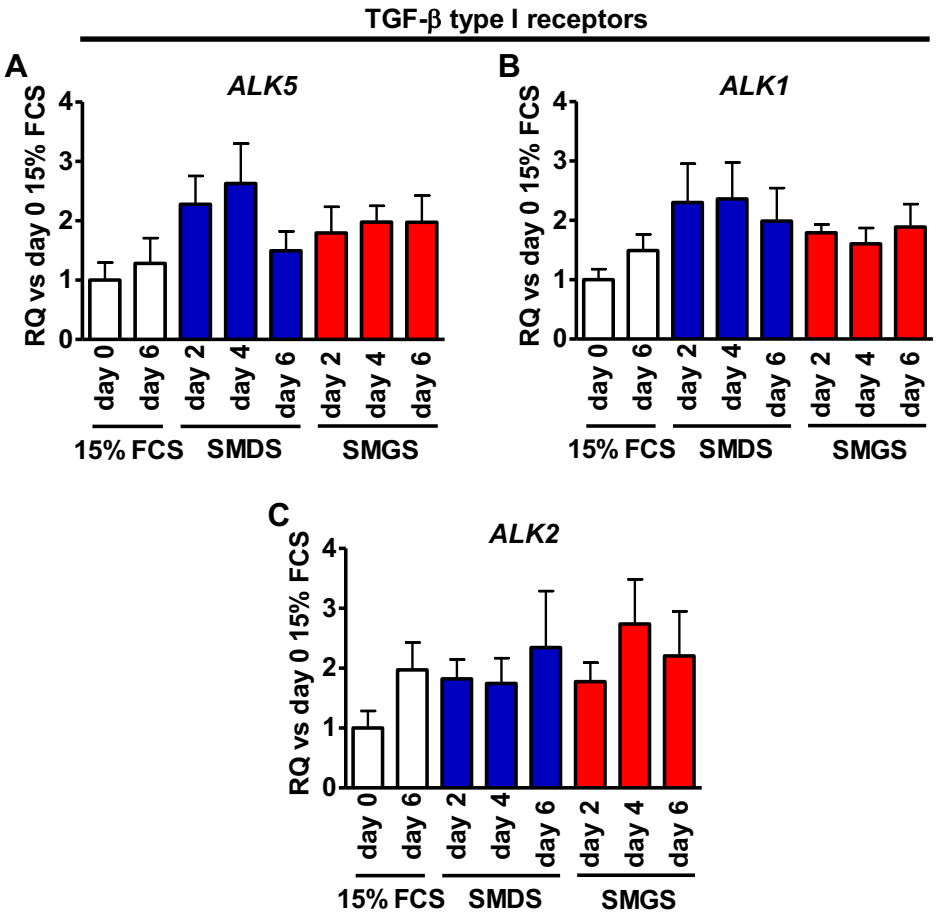

Figure 4-5 TGF-β type I receptor gene expression levels remain unchanged during contractile differentiation of primary HSVSMCs. Cells were cultured in 15% FCS, SMDS or SMGS. Cells were lysed for mRNA isolation and reverse transcription was performed to generate cDNA. Quantitative RT-PCR was performed to determine relative *ALK5* (**A**), *ALK1* (**B**) and *ALK2* (**C**) mRNA expression levels at indicated time points. Relative target gene expression was normalised to *UBC* expression to determine δCT values, which were used to calculate relative quantification (RQ) values (target group versus day 0 control). Data are presented as RQ_{mean} + error (biological n=3). A One-way repeated ANOVA with a Tukey's correction was performed to compare groups based on δCT values.

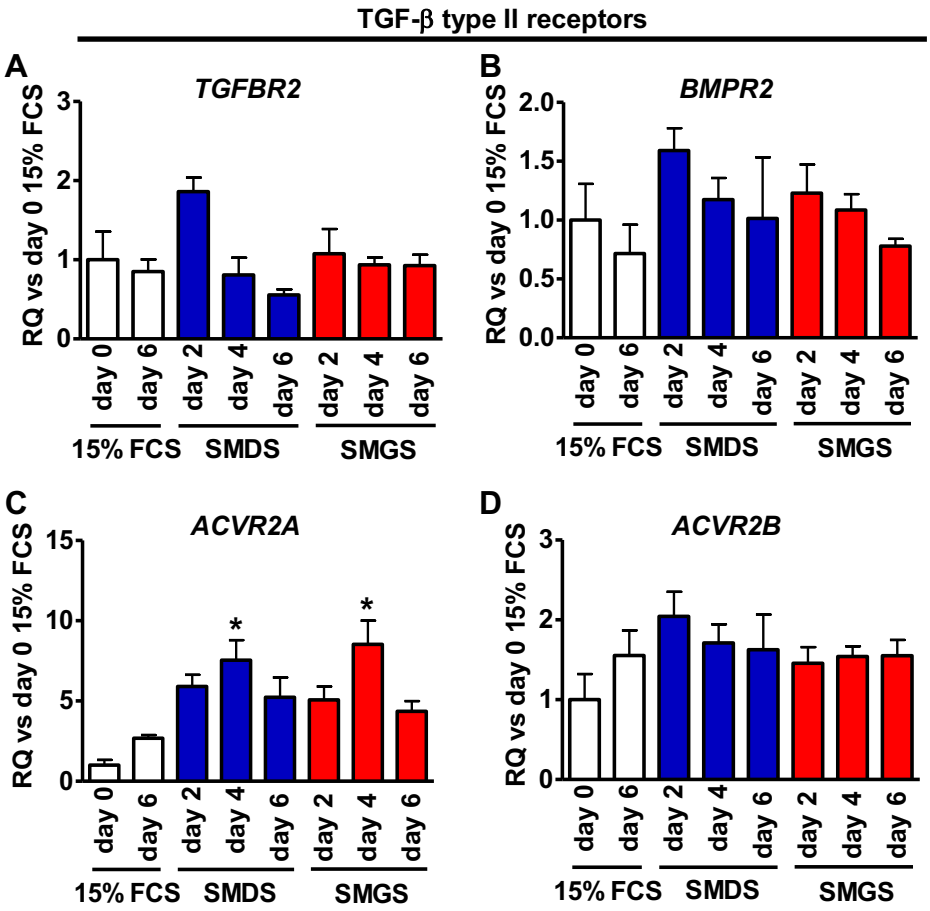

Figure 4-6 Contractile differentiation is paralleled by an increase in *ACVR2A* mRNA expression levels in primary HSVSMCs. Cells were cultured in 15% FCS, SMDS or SMGS. Cells were lysed for mRNA isolation and reverse transcription was performed to generate cDNA. Quantitative RT-PCR was performed to determine relative *TGFBR2* (**A**), *BMPR2* (**B** → biological n=2), *ACVR2A* (**C**) and *ACVR2B* (**D**) mRNA expression levels at indicated time points. Relative target gene expression was normalised to *UBC* expression to determine δCT values, which were used to calculate relative quantification (RQ) values (target group versus day 0 control). Data are presented as RQ_{mean} + error (biological n=3). A One-way repeated ANOVA with a Tukey's correction was performed to compare groups based on δCT values. P-value<0.05 was considered statistically significant (* p-value<0.05, target group versus day 0 15% FCS control).

4.3.4 Contractile differentiation is paralleled by a reduction in *ID1* mRNA expression levels in HSVSMCs

SMDS treatment robustly triggered contractile protein expression in HSVSMCs paralleling previous findings in primary human aortic (HA)SMCs by Chen *et al.* (Chen et al., 2016b). This enabled evaluation of the ALK5 target gene *SERPINE1* and the ALK1 target gene *ID1* serving as surrogate markers of respective pathway activation (unpublished data) (Low et al., 2019).

Whereas *SERPINE1* mRNA expression remained unchanged during contractile differentiation, SMDS- and SMGS-treated cells displayed a time-dependent decrease in *ID1* expression levels compared to 15% FCS-treated day 0 controls (RQ_{mean} + error, day 6 SMDS vs day 0 15% FCS: 0.04+0.02, $p<0.01$) (Figure 4-7 A and B). Although the 15% FCS-treated day 6 group demonstrated a trend towards reduced *ID1* expression levels compared to day 0 controls, the difference between groups was not statistically significant (day 6 15% FCS vs day 0 15% FCS: 0.23+0.07, $p>0.05$) (Figure 4-7 B). At this point, it must be noted that serum naturally contains active BMP-9 (David et al., 2008) and that serum drives relative *ID1* mRNA expression levels (Lewis and Prywes, 2013). Hence, higher relative *ID1* mRNA expression levels in HSVSMCs cultured in 15% FCS may solely reflect higher FCS and/or serum-derived BMP-9 concentrations rather than the cell differentiation state.

Overall, contractile HSVSMCs displayed reduced relative *ID1* mRNA expression levels, likely a reflection of reduced serum and/or serum-derived BMP-9 concentrations in SMDS media.

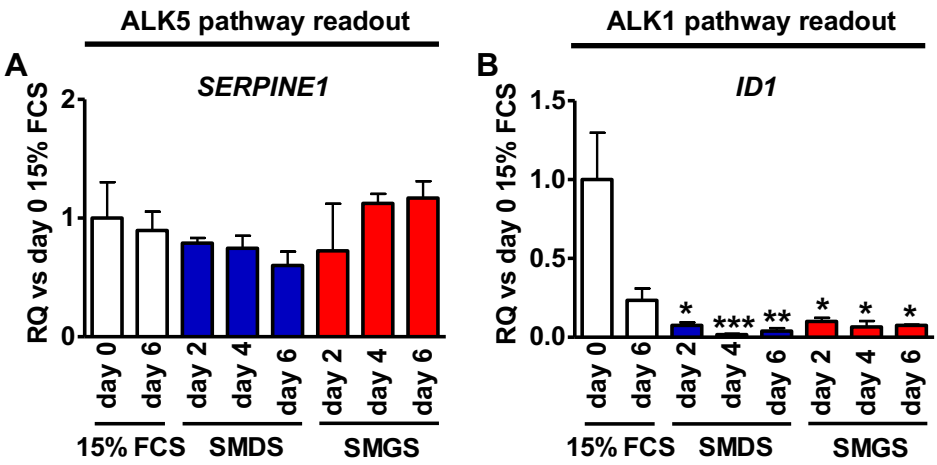

Figure 4-7 Contractile primary HSVSMCs display a reduction in relative *ID1* mRNA expression levels. Cells were cultured in 15% FCS, SMDS or SMGS. Cells were lysed for mRNA isolation and reverse transcription was performed to generate cDNA. Quantitative RT-PCR was performed to determine relative *SERPINE1* (**A**) and *ID1* (**B**) mRNA expression levels at indicated time points. Relative target gene expression was normalised to *UBC* expression to determine δCT values, which were used to calculate relative quantification (RQ) values (target group versus day 0 control). Data are presented as RQ_{mean} + error (biological n=3). A One-way repeated ANOVA with a Tukey's correction was performed to compare groups based on δCT values. P-value<0.05 was considered statistically significant (* p-value<0.05, ** p-value<0.01 and *** p-value <0.001, target group versus day 0 15% FCS control).

4.3.5 Generation of an undirected contractile differentiation protocol for primary HCASMCs

Previous findings demonstrated that SMDS treatment robustly induced a contractile HSVSMC phenotype suggesting that this approach is a valuable *in vitro* tool for studying cellular mechanisms that drive SMC de-differentiation in SVG disease. The next aim was to establish whether SMDS treatment also triggered contractile differentiation in primary HCASMCs using a similar protocol.

SMDS-treated HCASMCs demonstrated a time-dependent significant increase in relative α*SMA* (RQ_{mean} + error, day 4 SMDS vs day 0 SMGS: 17.9+2.51, $p<0.01$), *CNN1* (RQ_{mean} + error, day 4 SMDS vs day 0 SMGS: 8.8+0.24, $P<0.05$), *MYH11* (RQ_{mean} + error, day 4 SMDS vs day 0 SMGS: 75.1+16.2, $p<0.01$) and *SM22-*α (RQ_{mean} + error, day 4 SMDS vs day 0 SMGS: 2.4+0.57, $p<0.01$) mRNA expression levels compared to day 0 SMGS-treated controls paralleling findings in primary HASMCs from a previous study (Figure 4-8 A-D) (Chen et al., 2016b). In contrast, culture in SMGS had no effect on contractile gene expression indicating a proliferative SMC phenotype (Figure 4-8 A-D). Paralleling mRNA expression findings immunoblot revealed a time-dependent increase in αSMA ($densitometry_{mean}$ ± S.E.M.: day 8 SMDS: 0.11±0.008, day 0 SMGS: 0.003±0.001, $p<0.001$) and calponin (day 8 SMDS: 0.03±0.008, day 0 SMGS: 0.005±0.002, $p<0.001$) protein expression levels compared to day 0 SMGS-treated controls (Figure 4-9 A-C). Moreover, SMGS treatment had no effect on αSMA and calponin protein levels corroborating mRNA expression findings (Figure 4-9 A-C).

In conclusion, SMDS treatment robustly induced contractile differentiation in primary HCASMCs.

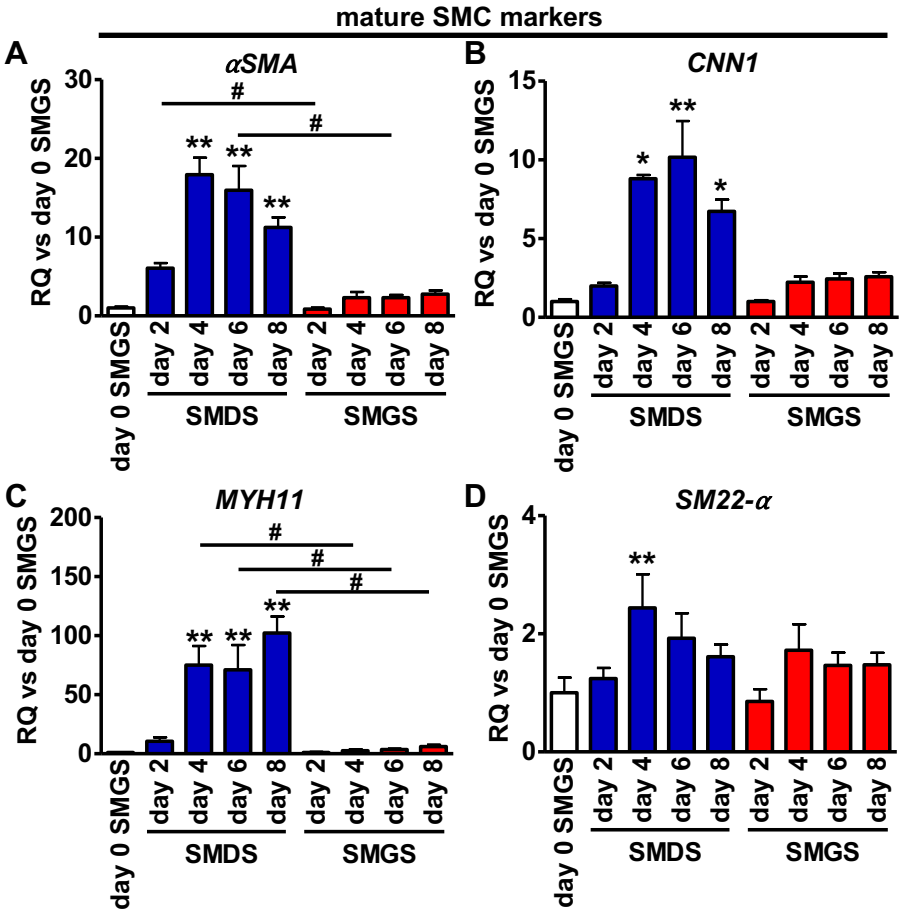

Figure 4-8 SMDS-cultured primary HCASMCs accumulate contractile gene expression levels. Cells were stimulated with SMDS (blue bars) or SMGS (red bars). Cells were lysed for mRNA isolation and reverse transcription was performed to generate cDNA. Quantitative RT-PCR was performed to determine relative *αSMA* (**A**), *CNN1* (**B**), *MYH11* (**C**) and *SM22-α* (**D**) mRNA expression levels at indicated time points. Relative target gene expression was normalised to *UBC* expression to determine δCT values, which were used to calculate relative quantification (RQ) values (target group versus day 0 control). Data are presented as RQ_{mean} ± error (1 patient, biological n=3). A One-way repeated ANOVA with a Tukey's correction was performed to compare groups based on δCT values. P-value<0.05 was considered statistically significant (* p-value<0.05, ** p-value<0.01, target group versus day 0 15% FCS control; # p-value<0.05).

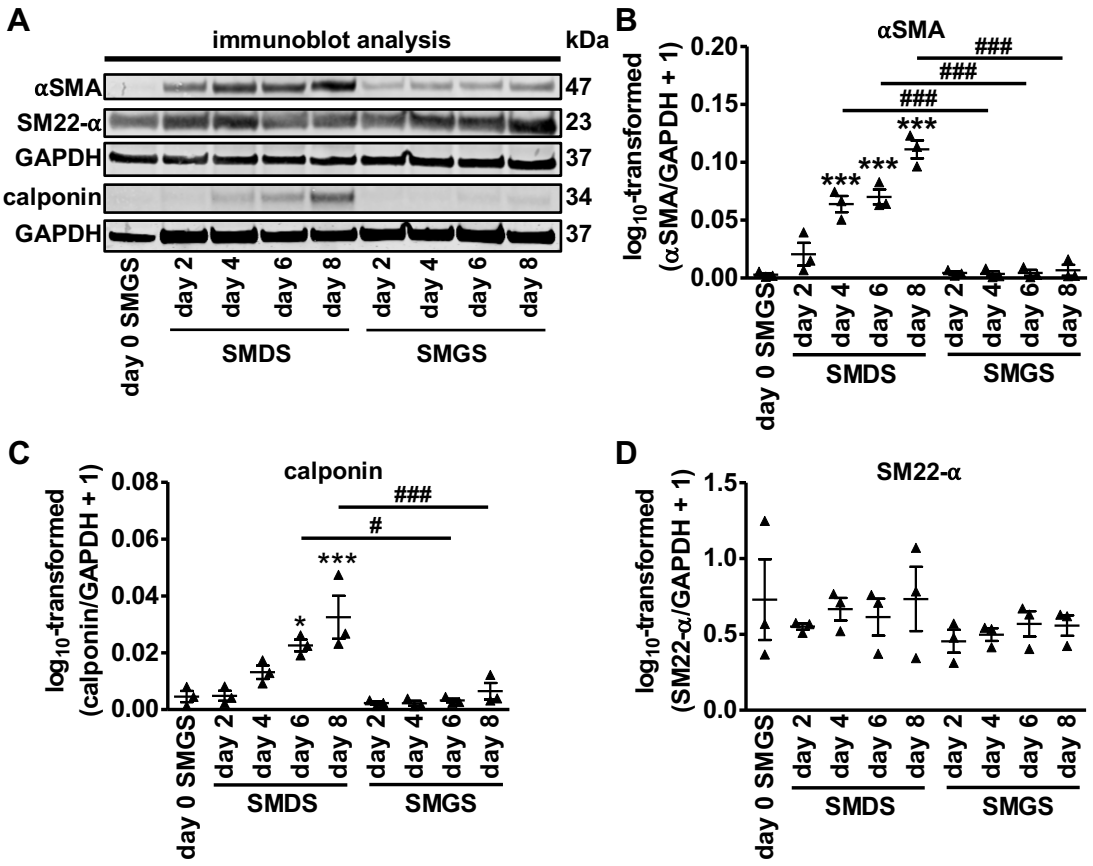

Figure 4-9 SMDS-cultured primary HCASMCs accumulate contractile protein expression levels. Cells were stimulated with SMDS (blue bars) or SMGS (red bars). Cells were lysed for protein isolation. (**A**) Immunoblot analysis (20 μg protein sample/lane) was performed to determine αSMA (**A** and **B**), calponin (**A** and **C**) and SM22-α (**A** and **D**) protein expression levels at indicated time points. GAPDH served as a housekeeper control. Densitometry (**B-D**) was performed to determine band intensities. Following normalisation to GAPDH (target protein/GAPDH) the constant 1 was added to each ratio value prior to $\log_{10}$-transformation. Data are presented as mean ± S.E.M. (1 patient, biological n=3). A One-way repeated ANOVA with a Tukey's correction was performed to compare groups. P-value<0.05 was considered statistically significant (*** p-value<0.001, target group versus day 0 15% FCS control; # p-value<0.05, ### p-value<0.001).

4.3.6 Contractile differentiation is paralleled by an increase in TGF-β superfamily receptor mRNA expression levels in HCASMCs

SMDS treatment robustly triggered accumulation of contractile markers in primary HCASMCs paralleling previous findings in HSVSMCs. The next aim was to evaluate TGF-β type I and II receptor mRNA expression levels in SMDS-cultured HCASMCs.

SMDS treatment induced a time-dependent increase in *ALK5* (RQ_{mean} + error, day 6 SMDS vs day 0 SMGS: 5.03+0.87, $p<0.001$), *ALK1* (day 6 SMDS vs day 0 SMGS: 2.5+0.86, $p<0.05$) and *ACVR2A* (day 6 SMDS vs day 0 SMGS: 3.67+1.69, $p<0.05$) mRNA expression levels compared to day 0 SMGS-treated controls (Figure 4-10 A, C and D). Although SMGS-cultured HCASMCs displayed a slight significant increase in ALK5 expression compared to day 0 control cells, these changes were not as pronounced as observed in SMDS-treated cells (Figure 4-10 A). *TGFBR2*, *ALK2* and *ACVR2B* expression levels remained unaffected by SMDS and SMGS treatment (Figure 4-10 B, E and F). SMDS-triggered accumulation of contractile proteins was paralleled by a reduction in *ID1* mRNA expression levels compared day 0 controls (RQ_{mean} + error, day 6 SMDS vs day 0 SMGS: 0.14+0.05, $p<0.05$) (Figure 4-11 A). As described in section 4.3.4, a reduction in *ID1* expression levels in primary HCASMCs cultured in SMDS media may solely reflect lower FCS and/or serum-derived BMP-9 concentrations rather than the cell differentiation state.

In summary, *ALK5*, *ACVR2A* and surprisingly *ALK1* mRNA expression levels dynamically increased during contractile differentiation of HCASMCs. In contrast, SMDS-cultured primary HCASMCs displayed a reduction in *ID1* mRNA expression levels, likely a reflection of lower FCS and/or serum-derived BMP-9 concentrations.

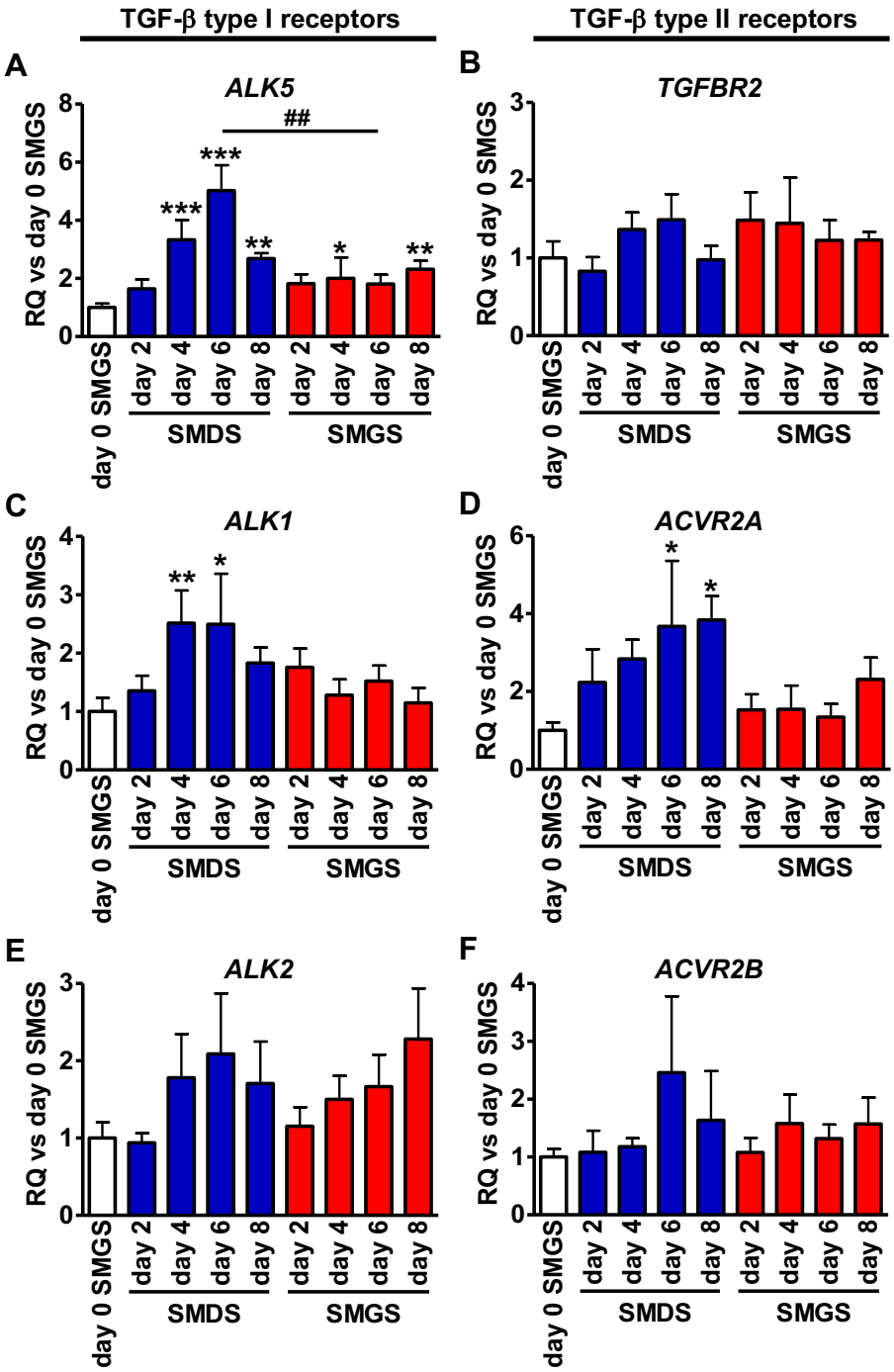

Figure 4-10 Increased contractile protein expression levels are paralleled by an increase in *ALK5*, *ALK1* and *ACVR2A* mRNA expression levels in primary HCASMCs. Cells were stimulated with SMDS (blue bars) or SMGS (red bars). Cells were lysed for mRNA isolation and reverse transcription was performed to generate cDNA. Quantitative RT-PCR was performed to determine relative *ALK5* (**A**), *TGFBR2* (**B**), *ALK1* (**C**), *ACVR2A* (**D**), *ALK2* (**E**) and *ACVR2B* (**F**) mRNA expression levels. Relative target gene expression was normalised to *UBC* expression to determine δCT values, which were used to calculate relative quantification (RQ) values (target group versus day 0 control). Data are presented as RQ_{mean} ± error (1 patient, biological n=3). A One-way repeated ANOVA with a Tukey's correction was performed to compare groups based on δCT values. P-value<0.05 was considered statistically significant (* p-value<0.05, ** p-value<0.01, *** p-value<0.001, target group versus day 0 15% FCS control; ## p-value<0.01).

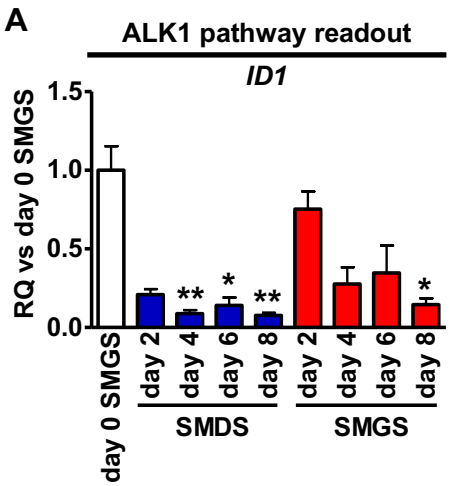

Figure 4-11 Contractile primary HCASMCs demonstrate a reduction in relative *ID1* mRNA expression levels. Cells were stimulated with SMDS (blue bars) or SMGS (red bars). Cells were lysed for mRNA isolation and reverse transcription was performed to generate cDNA. Quantitative RT-PCR was performed to determine relative *ID1* (**A**) mRNA expression levels. Relative target gene expression was normalised to *UBC* expression to determine δCT values, which were used to calculate relative quantification (RQ) values (target group versus day 0 control). Data are presented as RQ_{mean} ± error (1 patient, biological n=3). A One-way repeated ANOVA with a Tukey's correction was performed to compare groups based on δCT values. P-value<0.05 was considered statistically significant (* p-value<0.05, ** p-value<0.01, target group versus day 0 15% FCS control).

4.3.7 Pharmacological ALK5 inhibition prevents contractile differentiation of primary HSVSMCs

Chen *et al.* demonstrated that pharmacological ALK4/5/7 inhibition (SB431542) blunted SMDS-induced accumulation of contractile proteins in primary HASMCs indicating the ALK5 pathway as a regulator of contractile differentiation (Chen et al., 2016b).

Quantitative qRT-PCR analysis revealed a time-dependent increase in α*SMA* mRNA expression levels in SMDS/vehicle-treated primary HSVSMCs compared to day 0 15% FCS-treated controls (RQ_{mean} + error, day 6 SMDS vs day 0 15% FCS: 34.5+13.2, $p<0.001$) (Figure 4-12 A). 15% FCS treatment achieved full suppression of α*SMA* mRNA expression levels during the entire time course. Whereas ALK5 (SB525334, blue bars, day 6 SMDS/vehicle: 34.5+13.2, day 6 SMDS/SB525334: 11.3+4.1, $p>0.05$) and ALK4/5/7 inhibition (SB431542, red bars, day 6 SMDS/vehicle: 34.5+13.2, day SMDS/SB431542: 8.7+1.3, $p<0.01$) dampened accumulation of α*SMA* expression levels in SMDS-cultured HSVSMCs, ALK1 inhibition (K02288, purple bars, day 6 SMDS/vehicle: 34.5+13.2, day 6 SMDS/K02288: 42.6+11.8, $p>0.05$) had no effect on SMDS-induced increase in α*SMA* expression levels. Interestingly, SB525334 and SB431542 did not entirely prevent accumulation of α*SMA* expression levels in the presence of SMDS at day 2 and 4 potentially suggesting early ALK4/5/7-independent mechanisms driving contractile differentiation. Additional biological repeats confirmed that both SB525334 and SB431542 significantly blunted contractile gene expression in the presence of SMDS compared to vehicle-treated day 6 and 15% FCS-treated day 0 controls (unpublished data) (Low et al., 2019).

Taken together with findings from Low *et al.*'s study, singular pharmacological ALK5 and combined pharmacological ALK4/5/7 inhibition equally prevented accumulation of contractile gene expression levels indicating the ALK5 receptor as a driver of contractile differentiation in primary HSVSMCs (unpublished data) (Low et al., 2019). In contrast, singular pharmacological ALK1 inhibition did not affect SMDS-driven contractile gene expression levels. These findings prompted validation of contractile protein expression changes in the presence of SMDS and singular pharmacological ALK5 inhibition with SB525334 (biological n=5 CABG patients).

15% FCS treatment suppressed contractile protein expression levels in primary HSVSMCs at day 6 (Figure 4-13 A-D and Figure 4-14 A-C). The presence of SB525334 had no significant impact on target protein expression levels in 15% FCS-treated cells (Figure 4-13 A-D and Figure 4-14 A-C). At day 6, SMDS treatment significantly drove contractile protein expression levels compared to day 6 15% FCS/vehicle and day 0 15% FCS controls (mean log_{10}-transformed (αSMA/GAPDH)+1 ± S.E.M., day 6 SMDS/vehicle: 0.29±0.12, day 6 15%: 0.07±0.03, $p<0.05$) (Figure 4-13 A-D and Figure 4-14 A-C). At day 6, the presence of SB525334 significantly prevented SMDS-induced accumulation of αSMA (day 6 SMDS/SB525334: 0.15±0.07, day 0 15% control: 0.08±0.03, $p>0.05$), calponin (day 6 SMDS/SB525334: 0.01±0.004, day 0 15% control: 0.003±0.001, $p>0.05$) and total (t) myosin light chain (MLC)9 protein levels (day 6 SMDS/SB525334: 0.007±0.002, day 0 15% control: 0.004±0.001, $p>0.05$) compared to day 0 15% FCS-treated control cells (Figure 4-13 A-C, Figure 4-14 A and C). Although day 6 SMDS/SB525334-treated HSVSMCs did not demonstrate a significant reduction in αSMA, calponin, SM22-α and phospho (p)MLC9 protein levels compared to day 6 SMDS/vehicle-treated controls, there was a visible trend towards a decrease in expression levels (Figure 4-13 A-D, Figure 4-14 A and B). In contrast, SMDS-driven increase in tMLC9 protein levels was significantly blunted by SB525334 at day 6 (day 6 SMDS/vehicle: 0.02±0.009, day 6 SMDS/SB525334: 0.007±0.002, $p<0.05$) (Figure 4-14 A and C).

In summary, these two data sets coherently demonstrate that functional ALK5 signalling is necessary for SMDS-driven contractile differentiation. Hence, the ALK5 pathway plays an important role in the regulation of the contractile HSVSMC phenotype.

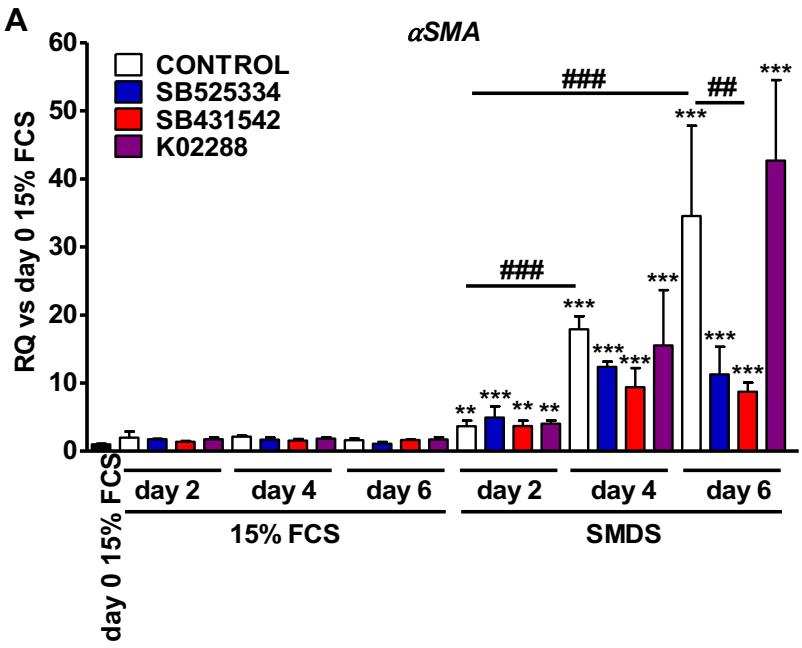

Figure 4-12 Pharmacological ALK5 inhibition prevents SMDS-triggered increase in αSMA gene expression levels in primary HSVSMCs. Upon achieving 80% confluence (day 0) one set of cells was lysed for RNA extraction and served as a reference control. Cells were stimulated with 15% FCS or SMDS in the presence of the ALK5 inhibitor SB525334 (10 μM, blue bars), the ALK4/5/7 inhibitor SB431542 (10 μM, red bars), the ALK1 inhibitor K02288 (0.1 μM, purple bars) and vehicle control (DMSO, white bars). Media was replaced with fresh respective media containing respective pharmacological inhibitors or vehicle control every 2 days. Respective groups were lysed on day 2, 4 and 6 for RNA extraction (technical n=3/group). Reverse transcription was performed to generate cDNA. Quantitative RT-PCR was performed to determine relative *αSMA* (**A**) mRNA expression levels. Relative target gene expression was normalised to *UBC* expression to determine δCT values, which were used to calculate relative quantification (RQ) values (target group versus day 0 control). Data are presented as RQ_{mean} ± error (biological n=1). A One-way repeated ANOVA with a Tukey's correction was performed to compare groups based on δCT values. P-value<0.05 was considered statistically significant (** p-value<0.01 and *** p-value <0.001, target group versus day 0 15% FCS control; ## p-value<0.01, ### p-value<0.001).

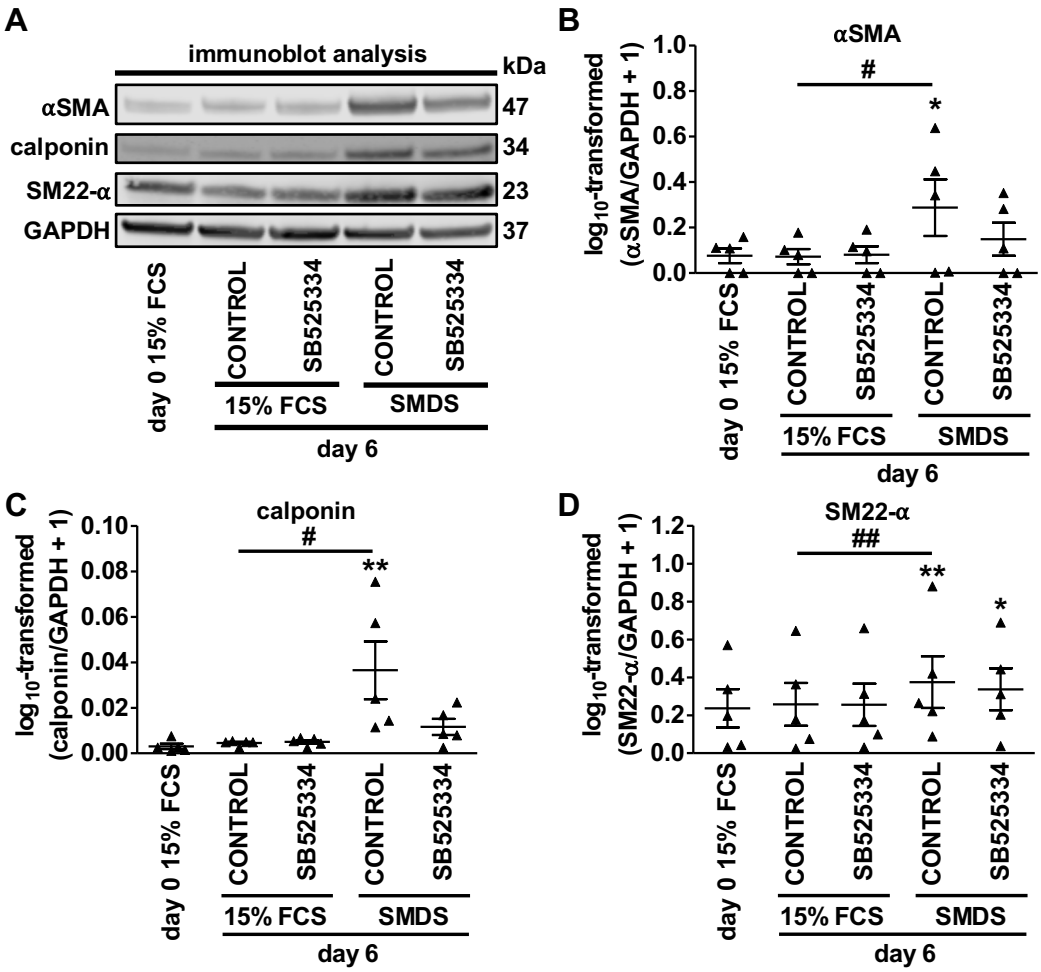

Figure 4-13 Pharmacological ALK5 inhibition prevents SMDS-driven contractile protein expression levels in primary HSVSMCs. Upon achieving 80% confluence (day 0) one set of cells was lysed for protein extraction and served as a reference control. Cells were stimulated with 15% FCS or SMDS in the presence of the ALK5 inhibitor SB525334 (10 μM) or vehicle control (DMSO, white bars). Media was replaced with fresh respective media containing SB525334 or vehicle control every 2 days. Respective groups were lysed on day 6 for protein extraction (technical n=3/group). Immunoblot analysis (20 μg protein sample/lane) was performed to determine αSMA (**A** and **B**), calponin (**A** and **C**) and SM22-α (**A** and **D**) protein expression levels. GAPDH served as a housekeeper control. Densitometry (**B-D**) was performed to determine band intensities. Following normalisation to GAPDH (target protein/GAPDH) the constant 1 was added to each ratio value prior to log_{10}-transformation. Data are presented as mean ± S.E.M. (biological n=5). A One-way repeated ANOVA with a Tukey's correction was performed to compare groups. P-value<0.05 was considered statistically significant (* p-value<0.05, ** p-value<0.01, target group versus day 0 15% FCS control; # p-value<0.05, ## p-value<0.01).

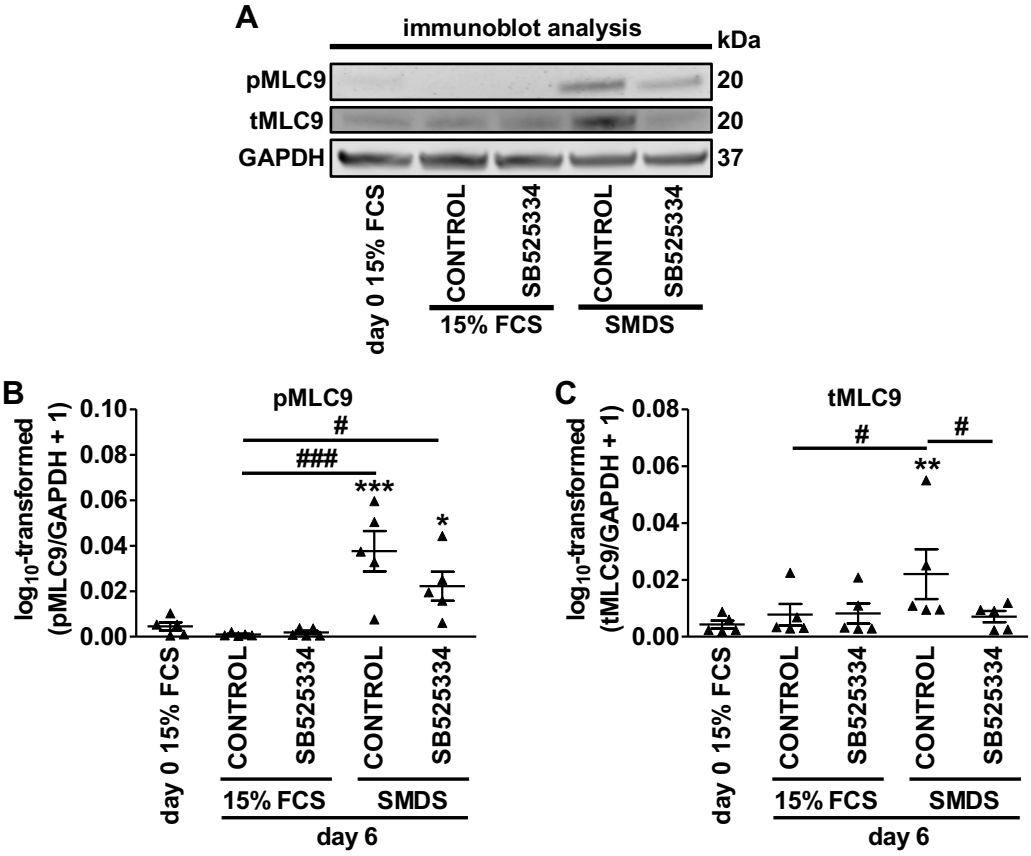

Figure 4-14 Pharmacological ALK5 inhibition inhibits SMDS-induced phosphorylation of MLC9 and increase in total-MLC9 protein expression levels in primary HSVSMCs. Upon achieving 80% confluence (day 0) one set of cells was lysed for protein extraction and served as a reference control. Cells were stimulated with 15% FCS or SMDS in the presence of the ALK5 inhibitor SB525334 (10 μM) or vehicle control (DMSO, white bars). Media was replaced with fresh respective media containing SB525334 or vehicle control every 2 days. Respective groups were lysed on day 6 for protein extraction (technical n=3/group). (**A**) Immunoblot analysis (20 μg protein sample/lane) was performed to determine pMLC9 (**A** and **B**) and tMLC9 (**A** and **C**) protein expression levels. GAPDH served as a housekeeper control. Densitometry (**B-D**) was performed to determine band intensities. Following normalisation to GAPDH (target protein/GAPDH) the constant 1 was added to each ratio value prior to log_{10}-transformation. Data are presented as mean ± S.E.M. (biological n=5). A One-way repeated ANOVA with a Tukey's correction was performed to compare groups. P-value<0.05 was considered statistically significant (* p-value<0.05, ** p-value<0.01, *** p-value<0.001, target group versus day 0 15% FCS control; # p-value<0.05, ### p-value<0.001).

4.3.8 HAdV-5-mediated ACVR2A delivery to HSVSMCs increases *ACVR2A* mRNA expression levels

Previous findings demonstrated a dynamic increase in *ACVR2A* mRNA expression during SMDS-induced contractile differentiation of primary HSVSMCs and HCASMCs. This prompted development of a replication-deficient HAdV-5 expressing the *ACVR2A* transgene (section 2.9.23). Following virus generation and propagation, the next aim was to test HAdV-5-mediated *ACVR2A* delivery to primary HSVSMCs and to assess the potential impact on SMDS-driven increase in and 15% FCS-driven suppression of α*SMA* mRNA expression levels.

HAdV-5 GFP-transduced HSVSMCs dose-dependently displayed an increase in GFP expression indicating successful transduction (Figure 4-15 A and B). However, transduction efficiency appeared low with 2.58% (10,000 VPs/cell) of cells displaying GFP expression (Figure 4-15 B). In line with previous findings SMDS treatment triggered a significant increase in *ACVR2A* mRNA expression levels in un-transduced mock HSVSMCs (RQ_{mean} + error, day 2 SMDS/MOCK versus day 0 15% FCS/MOCK: 8.47+0.56, $p<0.001$) (Figure 4-16 A, green bar). *ACVR2A* expression levels also significantly increased in 15% FCS media (Figure 4-16 A, purple bar). However, this increase was significantly less pronounced compared to SMDS-treated cells (Figure 4-16 A, compare green and purple bar) (day 2 SMDS/MOCK: 8.47±0.56, day 2 15% FCS/MOCK: 2.46±0.31, $p<0.001$). At day 2, HAdV-5 ACVR2A-transduced cells in 15% FCS demonstrated a significant dose-dependent increase in *ACVR2A* expression levels compared to 15% FCS-treated mock controls. At the lowest concentration (1,000 VP/cell), HAdV-5 ACVR2A transduction of 15% FCS-treated HSVSMCs did not result in increased *ACVR2A* expression levels compared to HAdV-5 GFP 15% FCS controls. However, at higher doses (5,000 and 10,000 VP/cell), HAdV-5 ACVR2A-transduced cells in 15% FCS displayed a significant increase in *ACVR2A* expression levels compared to HAdV-5 GFP 15% FCS controls (day 2 15% FCS/5,000 VP HAdV-5 ACVR2A: 13.9±1.53, day 2 15% FCS/5,000 VP HAdV-5 GFP 3.86±0.79, $p<0.001$; day 2 15% FCS/10,000 VP HAdV-5 ACVR2A: 22.5+0.56, day 2 15% FCS/10,000 VP HAdV-5 GFP: 3.61±1.07, $p<0.001$). In contrast, HAdV-5 ACVR2A-transduced cells in SMDS only demonstrated a significant increase in *ACVR2A* expression at the highest concentration (10,000 VP/cell) compared to un-transduced SMDS-treated mock controls (day 2 SMDS/10,000 VP HAdV-5 ACVR2A: 22.96±0.73, day 2 SMDS/MOCK:

8.47±0.56, p<0.001). Moreover, HAdV-5 ACVR2A-transduced cells in SMDS did not display increased *ACVR2A* expression compared to HAd-5 GFP/SMDS controls. Further analysis of the same data set showed that SMDS drove α*SMA* mRNA expression levels in un-transduced HSVSMCs compared to day 0 mock controls (Figure 4-17 A, green bar). In addition, 15% FCS-treated cells also demonstrated a significant increase in α*SMA* expression levels compared to day 0 controls (Figure 4-17 A, purple bar). However, this increase was significantly less pronounced compared to SMDS-treated cells (Figure 4-17 A, compare green and purple bar). Both HAdV-5 GFP- and HAdV-5 ACVR2A-transduced cells in SMDS demonstrated a dose-dependent increase in α*SMA* expression levels compared to day 2 SMDS mock controls.

In conclusion, HAdV-5 ACVR2A successfully delivered the *ACVR2A* transgene to HSVSMCs in 15% FCS at a concentration of 5,000 or 10,000 VP/cell. However, HAdV-5 ACVR2A transduction of HSVSMCs cultured in SMDS did not result in higher *ACVR2A* expression levels compared to HAdV-5 GFP or un-transduced SMDS-treated controls. Furthermore, HAdV-5 GFP transduction of HSVSMCs dose-dependently induced α*SMA* mRNA expression levels in the presence of SMDS indicating an unspecific potentiating effect of GFP expression and/or VP count per cell on α*SMA* gene expression. Hence, the dose-dependent increase in α*SMA* expression levels observed in SMDS-treated HAdV-5 ACVR2A-transduced cells most likely depends on the number of VPs per cell rather than an increase in *ACVR2A* expression levels.

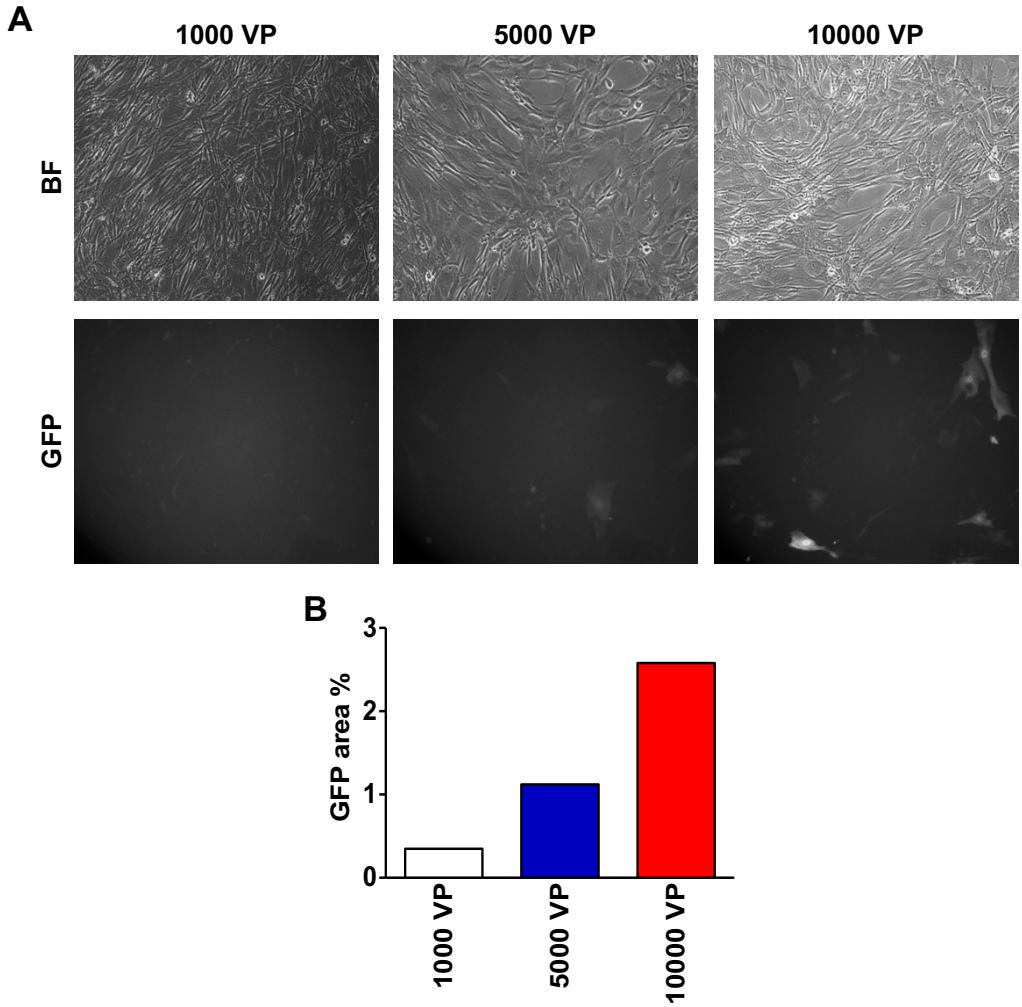

Figure 4-15 HAdV-5 GFP transduction efficiency. Primary HSVSMCs were transduced with increasing doses of HAdV-5 GFP in 15% FCS media and incubated overnight. (**A**) At 24-h post transduction cells were imaged on a brightfield (BF)/fluorescence microscope at 10× magnification. (**B**) The ImageJ software was utilised to determine GFP area %.

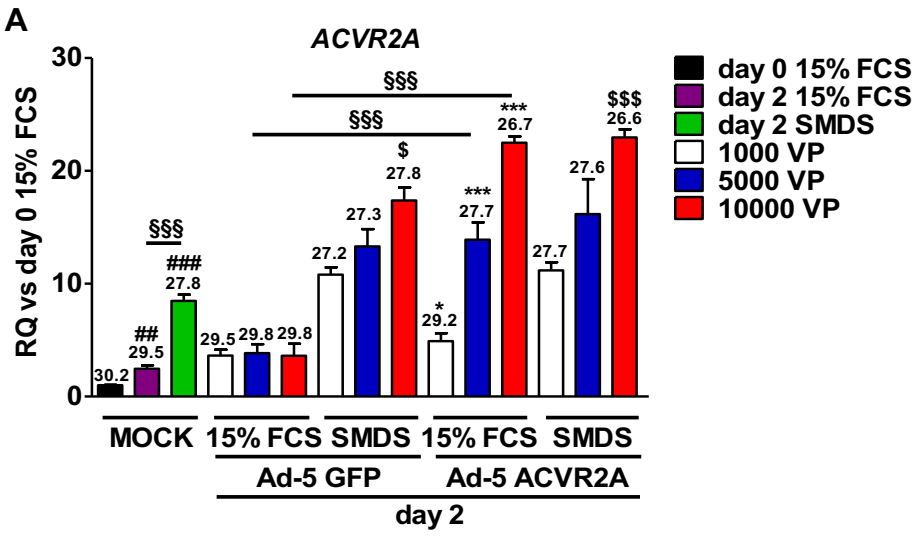

Figure 4-16 HAdV-5 ACVR2A successfully delivers the *ACVR2A* transgene to primary HSVSMCs. Upon achieving 80% confluence, cells were divided into 2 main groups. Cells intended for virus-mediated transgene delivery were transduced with an increasing amount of HAdV-5 GFP and HAdV-5 ACVR2A (1,000 viral particles (VP), 5,000 VP and 10,000 VP/cell) in 15% FCS media overnight. Cells intended for mock control treatment were also cultured in 15% FCS media overnight. The next day, one set of mock 15% FCS media-treated cells were lysed and subjected to RNA extraction. Non-virus and virus-containing 15% FCS media was replaced with fresh non-virus containing 15% FCS media and SMDS media. Following 48-h incubation, cells were lysed and subjected to RNA extraction. Reverse transcription was performed to generate cDNA. Quantitative RT-PCR was performed to determine relative *ACVR2A* (**A**) mRNA expression levels at indicated time points. Relative target gene expression was normalised to *UBC* expression to determine δCT values, which were used to calculate relative quantification (RQ) values (target group versus day 0 mock control, black bar). Data are presented as RQ_{mean} ± error (biological n=1). A One-way repeated ANOVA with a Tukey's correction was performed to compare groups based on δCT values. P-value<0.05 was considered statistically significant (## p-value<0.01, ### p-value<0.001, target group versus day 0 mock control; * p-value<0.05, *** p-value <0.001, target group versus day 2 15% FCS mock control; $ p-value<0.05, $$$ p-value<0.001, target group versus day 2 SMDS mock control; §§§ p-value<0.001).

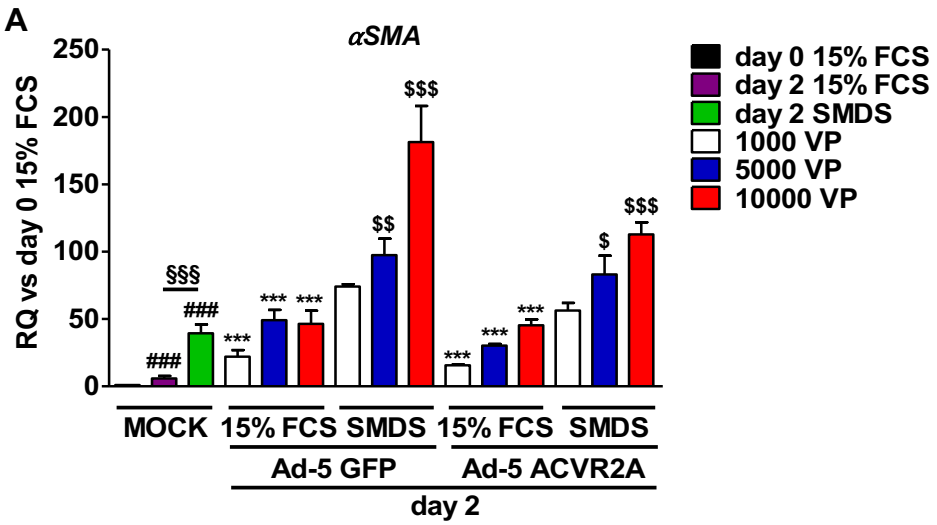

Figure 4-17 HAd-5 GFP dose-dependently potentiates SMDS-driven *αSMA* expression levels in primary HSVSMCs. Upon achieving 80% confluence, cells were divided into 2 main groups. Cells intended for virus-mediated transgene delivery were transduced with an increasing amount of HAdV-5 GFP and HAdV-5 ACVR2A (1,000 viral particles (VP), 5,000 VP and 10,000 VP/cell) in 15% FCS media overnight. Cells intended for mock control treatment were also cultured in 15% FCS media overnight. The next day, one set of mock 15% FCS media-treated cells were lysed and subjected to RNA extraction. Non-virus and virus-containing 15% FCS media was replaced with fresh non-virus containing 15% FCS media and SMDS media. Following 48-h incubation, cells were lysed and subjected to RNA extraction. Reverse transcription was performed to generate cDNA. Quantitative RT-PCR was performed to determine relative *αSMA* (**A**) mRNA expression levels at indicated time points. Relative target gene expression was normalised to *UBC* expression to determine δCT values, which were used to calculate relative quantification (RQ) values (target group versus day 0 mock control, black bar). Data are presented as RQ_{mean} ± error (biological n=1). A One-way repeated ANOVA with a Tukey's correction was performed to compare groups based on δCT values. P-value<0.05 was considered statistically significant (## p-value<0.01, ### p-value<0.001, target group versus day 0 mock control; * p-value<0.05, *** p-value <0.001, target group versus day 2 15% FCS mock control; $ p-value<0.05, $$$ p-value<0.001, target group versus day 2 SMDS mock control; §§§ p-value<0.001).

4.3.9 BMP-9 binds to type I and type II TGF-β superfamily receptors on HSVSMCs

Immunohistochemistry localised BMP-9 to αSMA$^+$ SMCs within all layers of pre-implantation SVGs from CABG patients. Furthermore, qRT-PCR analysis demonstrated that primary HSVSMCs expressed the type I TGF-β receptors *ALK1*, *ALK2* and *ALK5* as well as the type II TGF-β receptors *TGFBR2*, *BMPR2*, *ACVR2A* and *ACVR2B*. Moreover, our group has previously shown that TGF-β_1 binds to ALK1, ALK5, TGFBR2, ENG and betaglycan on primary HSVSMCs (unpublished data) (Low *et al.*, 2019). This prompted evaluation of BMP-9/TGF-β receptor interactions on primary HSVSMCs utilising a radioactive crosslinking assay.

Immunoprecipitation revealed that BMP-9 bound to the TGF-β type I receptors ALK1 and ALK2 (Figure 4-18 A and B, lane 2 and 3). The double band after ALK1 immunoprecipitation may be caused by monomeric or dimeric BMP-9 crosslinked to the receptor (Scharpfenecker et al., 2007). Furthermore, BMP-9 directly bound to the TGF-β type II receptors BMPR2 and ACVR2A/B (Figure 4-18 A and B, lane 4 and 6) and the TGF-β type III receptor endoglin (Figure 4-18 A and B, lane 5).

In summary, crosslinking analysis demonstrated that BMP-9 bound to respective TGF-β type I, II and III receptors on primary HSVSMCs suggesting biological activity.

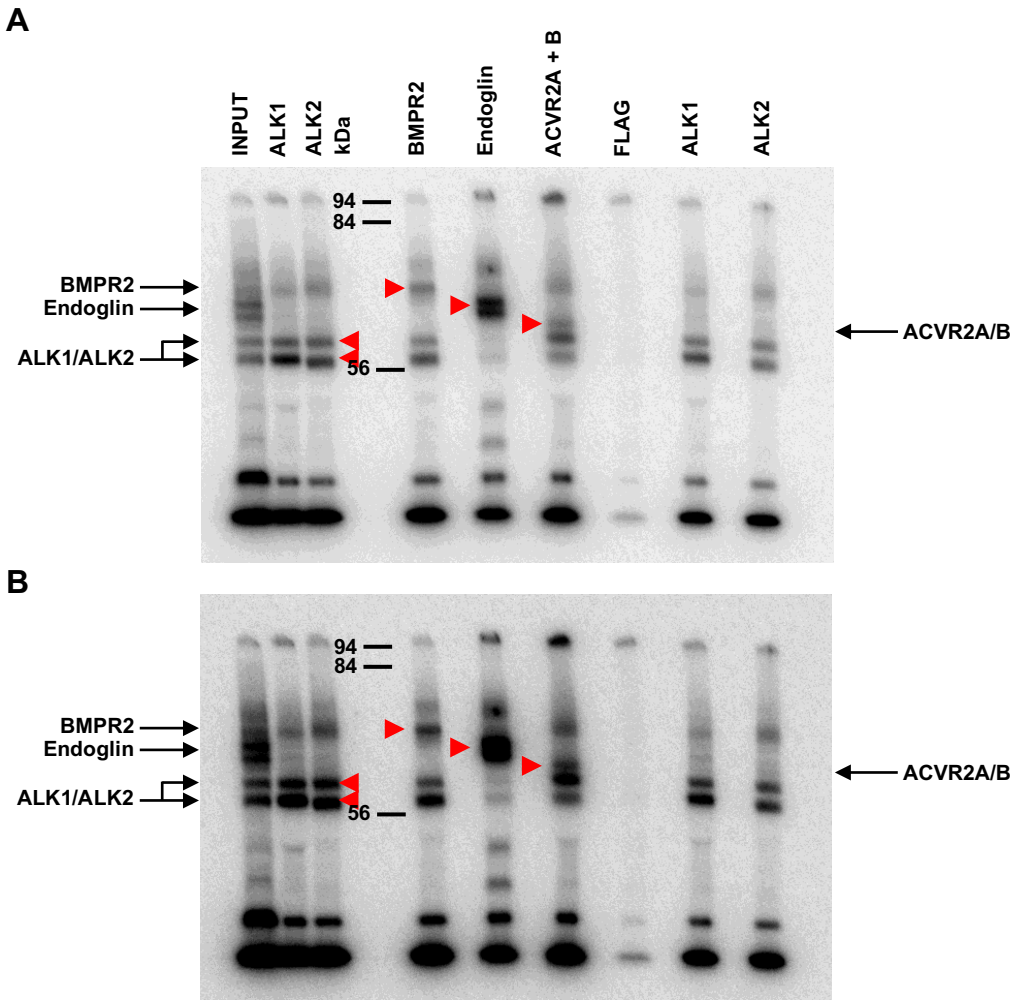

Figure 4-18 ^{125}I-BMP-9 crosslinking assay in primary HSVSMCs. Presented crosslinking analysis was performed by Dr Emma Low and Midori Thorikay in Prof. P. ten Dijk's laboratory (Leiden University Medical Centre, Leiden, Netherlands). Confluent cells were incubated with radioactively labelled ^{125}I-BMP-9 in T75 flasks for 3-h. Following incubation, cells were harvested for immunoprecipitation with TGF-β superfamily receptor antibodies (ALK1, ALK2, BMPR2, endoglin and ACVR2A and B). Anti-FLAG antibodies was utilised as a negative control. Autoradiography was performed to detect immunoprecipitated type I and type II TGF-β superfamily receptors crosslinked to ^{125}I-BMP-9. Autoradiography after 24-h exposure (**A**) and 48-h exposure (**B**). Red arrows indicate crosslinked BMP-9-receptor complexes (biological n=1 CABG patient).

4.3.10 BMP-9 treatment drives SMAD1 phosphorylation in primary HSVSMCs

The next aim was to evaluate whether BMP-9 activated SMAD1 phosphorylation in primary HSVSMCs and whether there was synergism in the presence of TGF-β_1.

BMP-9 significantly induced SMAD1 phosphorylation in a time-dependent manner indicating ALK1/ALK2 pathway activation (mean $\log_{10}$-transformed (pSMAD1/GAPDH)+1 ± S.E.M, 15-min BMP-9: 0.034±0.04, 15-min control: 0.004±0.001, [$p>0.05$], 30-min BMP-9: 0.063±0.02, 30-min control: 0.01±0.002, [$p<0.05$] (Figure 4-19 A and B). In addition, TGF-β_1 also triggered a visual increase in SMAD1 phosphorylation via ALK1. However, SMAD1 phosphorylation following TGF-β_1 stimulation occurred later and was less pronounced compared to BMP-9 treatment. No significant additive effect on SMAD1 phosphorylation was observed in the presence of both ligands compared to BMP-9 treatment alone.

These immunoblot analyses demonstrate that BMP-9 drives SMAD1 phosphorylation in primary HSVSMCs *in vitro* and, hence, this pathway may be biologically active in pre-implantation SVGs prior to implantation. Furthermore, BMP-9-driven SMAD1 phosphorylation appears to be stronger compared to TGF-β_1 stimulation.

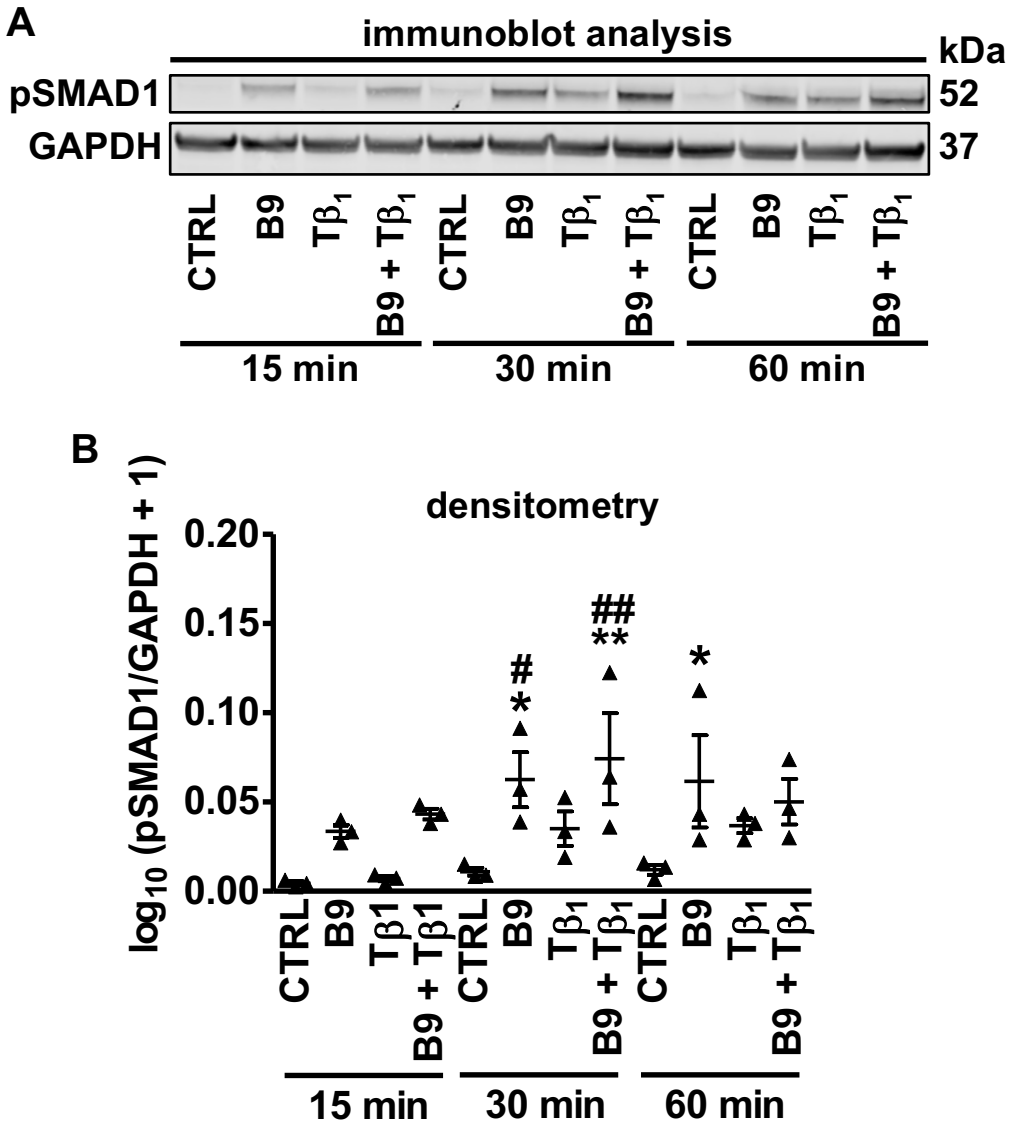

Figure 4-19 BMP-9 time-dependently drives SMAD1 phosphorylation in primary HSVSMCs. (**A**) Cells were seeded into 6-well plates ($1.5*10^6$ cells/well) and cultured in 15% FCS. Upon achieving 80% confluence cells were quiesced in 0.2% FCS media for 72-h. Quiesced cells were stimulated with BMP-9 (10 ng/ml, B9), TGF-β_1 (10 ng/ml, Tβ_1), both ligands and vehicle control (4 mM HCl, BSA 1 mg/ml, CTRL) for 15, 30 and 60 min respectively (technical n=3/group). Cells were lysed at respective timepoints and immunoblot analysis (20 μg protein sample/lane) was performed to determine pSMAD1 protein levels (**A**). Densitometry (**B**) was performed to determine band intensities. Following normalisation to GAPDH (target protein/GAPDH) the constant 1 was added to each ratio value prior to $\log_{10}$-transformation. Data are presented as mean ± S.E.M. (biological n=3). A One-way repeated ANOVA with a Tukey's correction was performed to compare groups. P-value<0.05 was considered statistically significant (* p-value<0.05, ** p-value<0.01, target group versus 15-min vehicle control; # p-value<0.05, ## p-value<0.01, target group versus 30-min vehicle control).

4.3.11 BMP-9 and TGF-β$_1$ treatment induce target gene expression in primary HSVSMCs

Both BMP-9 and TGF-β$_1$ and their respective type I receptors ALK1 and ALK5 are present in pre-implantation SVGs from CABG patients and co-localise with αSMA$^+$ SMCs (unpublished data) (Low et al., 2019). Furthermore, both ligands demonstrate biological activity in isolated primary HSVSMCs. Moreover, pharmacological ALK5 inhibition prevented undirected contractile differentiation in the same cell type indicating the ALK5 receptor as a regulator of the contractile phenotype. Hence, the next aim was to evaluate expression of the ALK1 target gene *ID1*, the ALK5 target gene *SERPINE1* and contractile genes in response to direct BMP-9 and/or TGF-β$_1$ treatment in the presence and absence of the ALK5 inhibitor SB525334.

Pharmacological ALK5 inhibition blunted TGF-β$_1$-induced *SERPINE1* expression levels indicating ALK5 pathway dependency (RQ_{mean} + error, TGF-β$_1$ + DMSO: 15.3+0.83, DMSO CTRL: 1+0.2, $p<0.001$; TGF-β$_1$ + DMSO: 15.3+0.83 vs TGF-β$_1$ + SB525334: 0.53+0.16, $p<0.001$) (Figure 4-20 A). In contrast, the presence of BMP-9 did not affect the ability of TGF-β$_1$ to drive *SERPINE1* expression. In line with previously presented pSMAD1 immunoblot findings, BMP-9 induced *ID1* mRNA expression levels compared to vehicle-treated controls indicating ALK1 and/or ALK2 pathway activation (BMP-9 + DMSO: 40.9+8.28, DMSO CTRL: 1+0.25, $p<0.05$) (Figure 4-20 B). The presence of TGF-β$_1$ blunted the ability of BMP-9 to induce *ID1* expression levels (BMP-9 + TGF-β$_1$: 8.4+1.64, DMSO CTRL: 1+0.25, $p>0.05$). Finally, pharmacological ALK5 inhibition did not prevent BMP-9-driven *ID1* expression (BMP-9 + SB525334: 24.16+8.58, SB525334 CTRL: 1.64+0.4, $p<0.05$) indicating that BMP-9-mediated ALK1/ALK2 pathway activation does not depend on functional ALK5 receptor signalling.

In conclusion, both ligands induced respective target gene expression in primary HSVSMCs. Whereas the presence of BMP-9 did not prevent TGF-β$_1$-driven *SERPINE1* expression, the presence of TGF-β$_1$-blunted the ability of BMP-9 to induce *ID1* expression indicating that TGF-β$_1$-driven ALK5/SMAD2/3 signalling promotes lateral inhibition of BMP-9-driven SMAD1 signalling.

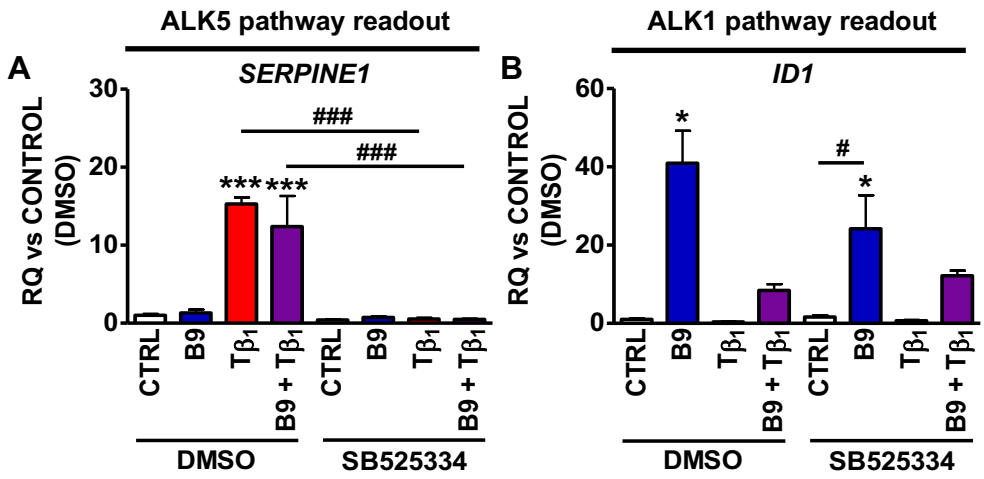

Figure 4-20 BMP-9 and TGF-β_1 induce target gene expression in primary HSVSMCs. 80% confluent primary HSVSMCs were quiesced in 0.2% FCS media (MEDIA1) for 72-h. To achieve pharmacological ALK5 inhibition prior to ligand stimulation, the first 4 groups were incubated in MEDIA1 containing 10 μM SB525334 for 30 min. In parallel, the second 4 groups were incubated in MEDIA1 containing DMSO vehicle (1:1,000) for 30 mins. Media was replaced with fresh MEDIA1 containing BMP-9 (10 ng/mL), TGF-β_1 (10 ng/mL) ± DMSO (1:1,000) or SB525334 (10 μM). After 24-h stimulation, primary HSVSMCs were lysed and subjected to RNA extraction. Reverse transcription was performed to generate cDNA. Quantitative RT-PCR was performed to determine relative *SERPINE1* (**A**) and *ID1* (**B**) mRNA expression levels. Relative target gene expression was normalised to *UBC* expression to determine δCT values, which were used to calculate relative quantification (RQ) values (target group versus DMSO vehicle control). Data are presented as RQ_{mean} ± error (biological n=3). A One-way repeated ANOVA with a Tukey's correction was performed to compare groups based on δCT values. P-value<0.05 was considered statistically significant (* p-value<0.05 and *** p-value <0.001, target group versus DMSO vehicle control, # p-value<0.05, ### p-value<0.001).

4.3.12 Pharmacological ALK5 inhibition prevents TGF-β$_1$-induced increase in contractile gene expression in HSVSMCs

Both BMP-9 and TGF-β$_1$ induced target pathway activity in primary HSVSMCs evidenced by up-regulation of target gene expression levels. TGF-β_1 drives contractile gene expression in arterial SMCs and thereby promotes a contractile SMC phenotype (Björkerud, 1991; Hautmann et al., 1997). In line with these findings Groenendijk *et al.* found that TGF-β_1 stimulated contractile gene expression in primary HSVSMCs paralleling findings in arterial SMCs (Groenendijk et al., 2011). However, this study did not investigate whether this effect was mediated via the ALK5 or ALK1 receptor. Furthermore, the potential effects of BMP-9 on contractile gene expression have not been investigated in this cell type so far. Together, this prompted investigation of contractile gene expression in primary HSVSMCs in response to BMP-9 and/or TGF-β_1 stimulation in the presence of pharmacological ALK5 inhibition with SB525334.

24-h TGF-β$_1$ treatment induced *αSMA* (RQ_{mean} + error, TGF-β$_1$: 19+3.39, DMSO CTRL: 1+0.3, $p<0.001$), *CNN1* (TGF-β$_1$: 27.84+9.16, DMSO CTRL: 1+0.2, $p<0.001$), *MYH11* (TGF-β$_1$: 38.63+20.4, DMSO CTRL: 1+0.41, $p<0.05$) and *SM22-α* (TGF-β$_1$: 4.21+1.05, DMSO CTRL: 1+0.12, $p<0.01$) mRNA expression levels in primary HSVSMCs compared to vehicle-treated controls (Figure 4-21 A-D). Pharmacological ALK5 inhibition with SB525334 blunted TGF-β$_1$-driven contractile gene expression indicating ALK5-dependent up-regulation of contractile gene expression (Figure 4-21 A-D). BMP-9 did not affect the ability of TGF-β$_1$ to induce *αSMA*, *CNN1* and *SM22-α* expression levels (Figure 4-21 A, B and D). Finally, BMP-9 stimulation mildly induced *αSMA* expression compared to vehicle-treated controls which was blunted by pharmacological ALK5 inhibition (BMP-9: 4.67+0.88, DMSO CTRL: 1+0.3, $p<0.05$) (Figure 4-21 A).

In line with previous findings, TGF-β$_1$ drives contractile gene expression. These findings prompted evaluation of contractile protein expression level changes in response to ligand treatment. Contrasting gene expression findings, 24-h ligand treatment had no impact on αSMA, calponin or SM22-α expression levels in quiesced primary HSVSMCs (Figure 4-22 A-D). Vehicle-treated, control quiesced HSVSMCs already demonstrated high contractile protein expression levels which

may explain the absence of an increase in protein expression following TGF-ß$_1$ treatment.

Taken together with previously presented data, these findings highlight functional TGF-ß$_1$/ALK5 signalling as a regulator of contractile gene expression in primary HSVSMCs. Moreover, BMP-9 induced *αSMA* expression levels in an ALK5-dependent manner. Vehicle-treated controls demonstrated high contractile protein levels. Target protein to GAPDH ratios were higher compared to those of 6-day SMDS/vehicle-treated cells indicating that 72-h quiescence in 0.2% FCS media may already induce a contractile phenotype.

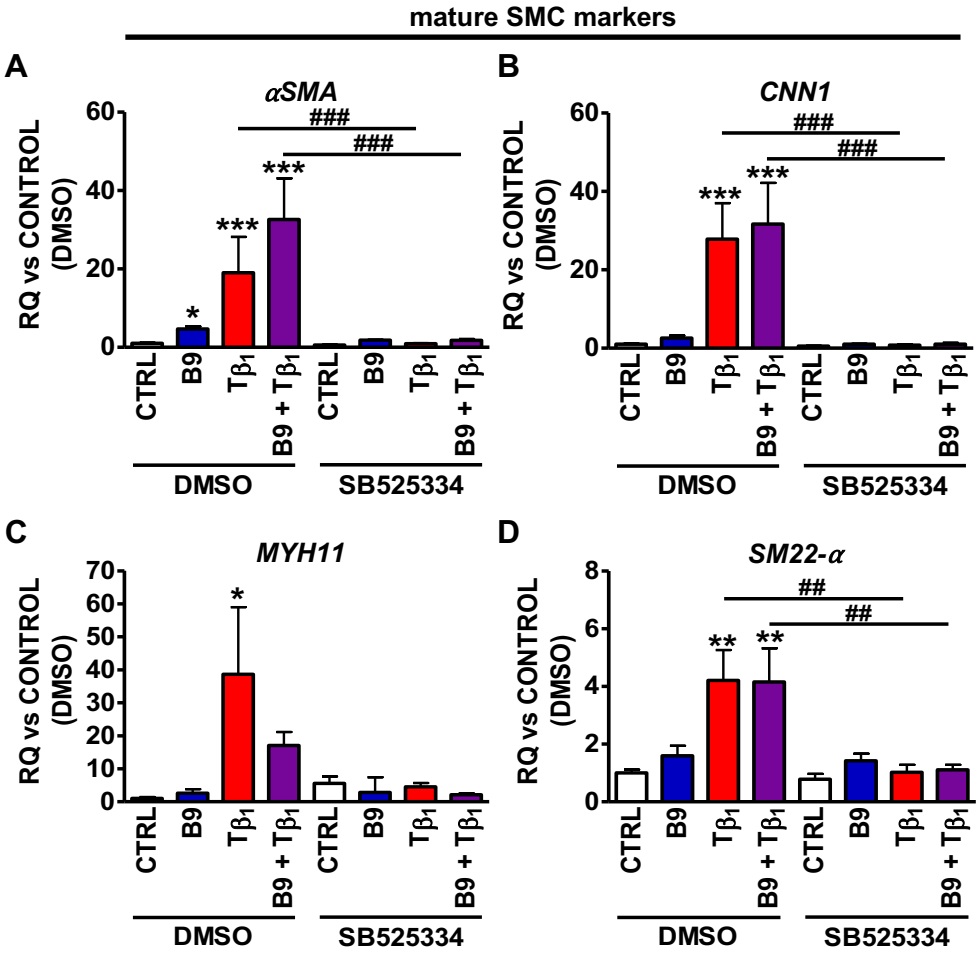

Figure 4-21 TGF-β_1 drives contractile gene expression levels in primary HSVSMCs via the ALK5 pathway. 80% confluent primary HSVSMCs were quiesced in 0.2% FCS media (MEDIA1) for 72-h. To achieve pharmacological ALK5 inhibition prior to ligand stimulation, the first 4 groups were incubated in MEDIA1 containing 10 μM SB525334 for 30 min. In parallel, the second 4 groups were incubated in MEDIA1 containing DMSO vehicle (1:1,000) for 30 mins. Media was replaced with fresh MEDIA1 containing recombinant BMP-9 (10 ng/mL), TGF-β_1 (10 ng/mL) ± DMSO (1:1,000) or SB525334 (10 μM). After 24-h stimulation, primary HSVSMCs were lysed and subjected to RNA extraction. Reverse transcription was performed to generate cDNA. Quantitative RT-PCR was performed to determine relative *αSMA* (**A**), *CNN1* (**B**), *MYH11* (**C**) and *SM22-α* (**D**) mRNA expression levels. Relative target gene expression was normalised to *UBC* expression to determine δCT values, which were used to calculate relative quantification (RQ) values (target group versus DMSO vehicle control). Data are presented as RQ_{mean} ± error (biological n=3). A One-way repeated ANOVA with a Tukey's correction was performed to compare groups based on δCT values. P-value<0.05 was considered statistically significant (* p-value<0.05, ** p-value<0.01 and *** p-value <0.001, target group versus DMSO vehicle control, ## p-value<0.01, ### p-value<0.001).

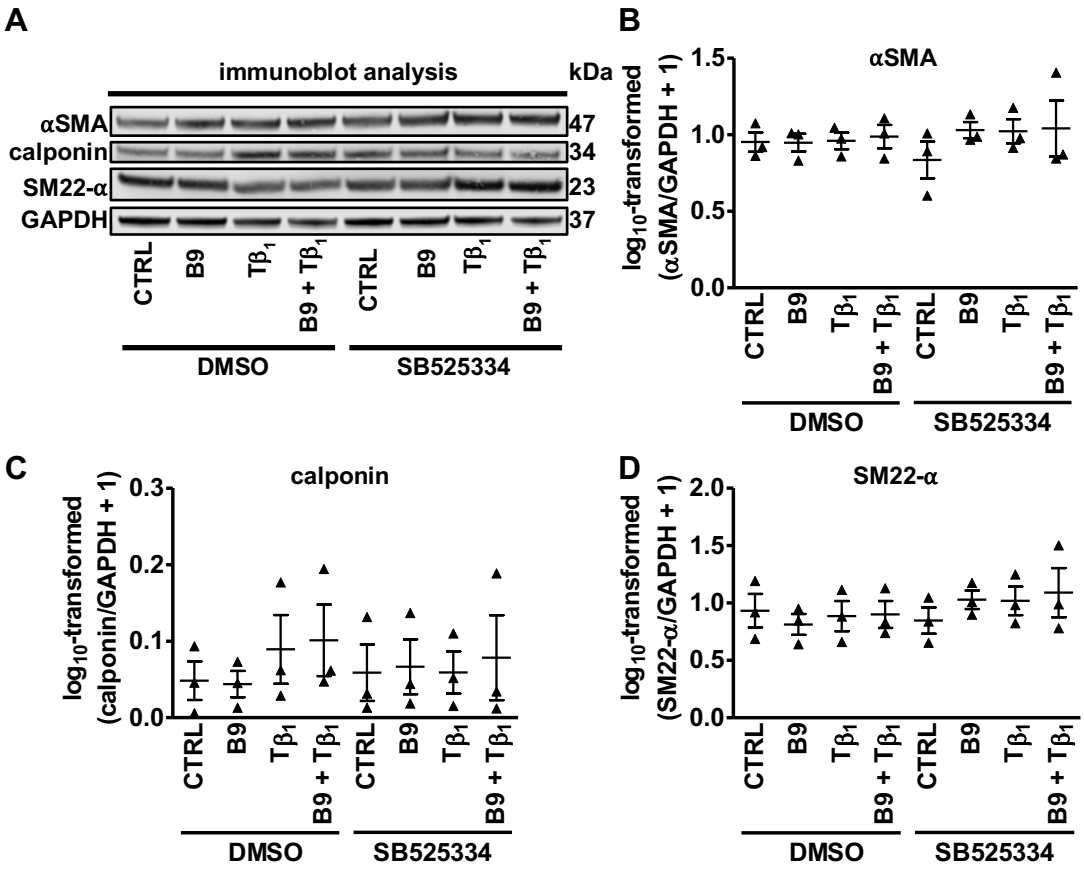

Figure 4-22 72-h starved HSVSMCs demonstrate an increase in contractile protein expression levels. 80% confluent primary HSVSMCs were quiesced in 0.2% FCS media (MEDIA1) for 72-h. To achieve pharmacological ALK5 inhibition prior to ligand stimulation, the first 4 groups were incubated in MEDIA1 containing 10 μM SB525334 for 30 min. In parallel, the second 4 groups were incubated in MEDIA1 containing DMSO vehicle (1:1,000) for 30 mins. Media was replaced with fresh MEDIA1 containing BMP-9 (10 ng/mL), TGF-β_1 (10 ng/mL) ± DMSO (1:1,000) or SB525334 (10 μM). After 24-h stimulation, primary HSVSMCs were lysed and subjected to protein extraction. (**A**) Immunoblot analysis (20 μg protein sample/lane) was performed to determine αSMA (**A** and **B**), calponin (**A** and **C**) and SM22-α (**A** and **D**) protein expression levels (**A**). Densitometry (**A**-**C**) was performed to determine band intensities. Following normalisation to GAPDH (target protein/GAPDH) the constant 1 was added to each ratio value prior to log_{10}-transformation. Data are presented as mean ± S.E.M. (biological n=3). A One-way repeated ANOVA with a Tukey's correction was performed to compare groups.

4.3.13 TGF-β_1 demonstrates anti-proliferative effects in primary HSVSMCs

TGF-β_1 ALK5-dependently drove contractile gene expression in primary HSVSMCs. SMC de-differentiation underlies NF following acute vascular injury (Chappell et al., 2016). Taken together, these findings prompted investigation of PDGF- and serum-induced primary HSVSMC proliferation in the presence of BMP-9 and/or TGF-β_1.

At 48-h, 15% FCS/vehicle- and 15% FCS/BMP-9-treated cells demonstrated a significant increase in BrdU incorporation compared to 0.2% FCS/vehicle-treated controls indicating enhanced cell proliferation ($absorbance_{mean}$ ± S.E.M.: 15% FCS CTRL: 0.48±0.13, 0.2% FCS CTRL: 0.07±0.02, $p<0.01$; 15% FCS + BMP-9: 0.43±0.09, 0.2% FCS CTRL: 0.07±0.02, $p<0.01$) (Figure 4-23 A). TGF-β_1 blunted the ability of 15% FCS to significantly induce cell proliferation (TGF-β_1: 0.28±0.07, 0.2% FCS CTRL:0.07±0.02, $p>0.05$). PDGF/vehicle-treated controls displayed a trend towards an increase in BrdU incorporation compared to 0.2% FCS vehicle-treated controls suggesting a trend towards an increase in cell proliferation (0.2% FCS + PDGF: 0.34±0.06, 0.2% FCS CTRL: 0.07±0.02, $p>0.05$). Although BMP-9 stimulation appeared to reduce PDGF-driven cell proliferation compared to the 0.2%/PDGF treatment group, the difference between these two groups was not statistically significant. Neither BMP-9 nor TGF-β_1 had an impact on BrdU incorporation in the presence of 0.2% FCS media. As outlined in sections 4.3.4 and 4.3.6, serum-derived BMP-9 may impact on the increase in proliferation observed in 15% FCS-cultured HSVSMCs.

Overall, TGF-β_1 stimulation prevented serum-induced HSVSMC proliferation thereby suggesting that early transient and selective ALK5 agonism may present a therapeutic strategy for preventing early medial SMC proliferation and subsequent migration and intimal monoclonal expansion following SVG injury.

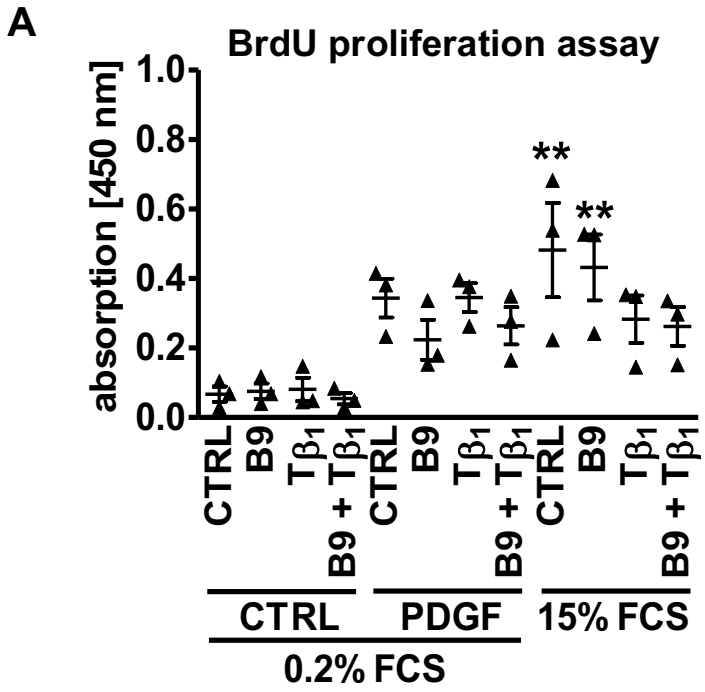

Figure 4-23 TGF-β_1 prevents serum-induced primary HSVSMC proliferation. Cells were seeded into 96-well plates ($1*10^4$ cells/well) and cultured in 15% FCS. Upon achieving 80% confluence cells were quiesced in 0.2% FCS media for 72-h. Quiesced cells were stimulated with BMP-9 (10 ng/ml, B9), TGF-β_1 (10 ng/ml, Tβ_1), both ligands and vehicle control in the presence of 0.2% FCS, PDGF-BB (20 ng/ml) or 15% FCS (technical n=5/group). BrdU (1:2,000) was incorporated simultaneously and incorporation was assessed 48-h later. Scatter plot indicates mean ± S.E.M. (biological n=3). A One-way repeated ANOVA with a Tukey's correction was performed to compare groups. P-value<0.05 was considered statistically significant (** p-value<0.01, target group versus 0.2% FCS control).

4.3.14 TGF-β_1 stimulation indicates inhibition of serum-induced migration in primary HSVSMCs

Medial SMC migration to the intima prompts the expansion of intimal monoclonal SMCs following vascular injury, driving NF (Chappell et al., 2016). The next aim was to establish whether BMP-9 and/or TGF-β_1 had an impact on serum-induced HSVSMC migration in wound healing/scratch assays.

Quiesced control HSVSMCs demonstrated 42.65% scratch closure in the absence of serum or extrinsic growth factors (Figure 4-24 A and Figure 4-25 A). In contrast,15% FCS controls demonstrated 64.82% scratch closure ($p<0.05$ versus 0.2% FCS). Moreover, TGF-β_1 significantly reduced serum-induced scratch closure to baseline levels (mean scratch closure % ± S.E.M., 15% FCS/vehicle: 64.82±0.25, 15% FCS/ TGF-β_1: 34.91±4.74, $p<0.05$). In contrast, BMP-9 had no effect on serum-induced scratch closure. As previously outlined in section 4.3.4, it is possible that serum-derived BMP-9 may impact on the increase in scratch closure observed in 15% FCS-cultured HSVSMCs.

In summary, TGF-β_1 prevented serum-induced scratch closure indicating an anti-migratory effect. However, it is not clear whether this effect occurs because of blunting serum-induced proliferation or direct inhibition of HSVSMC migration.

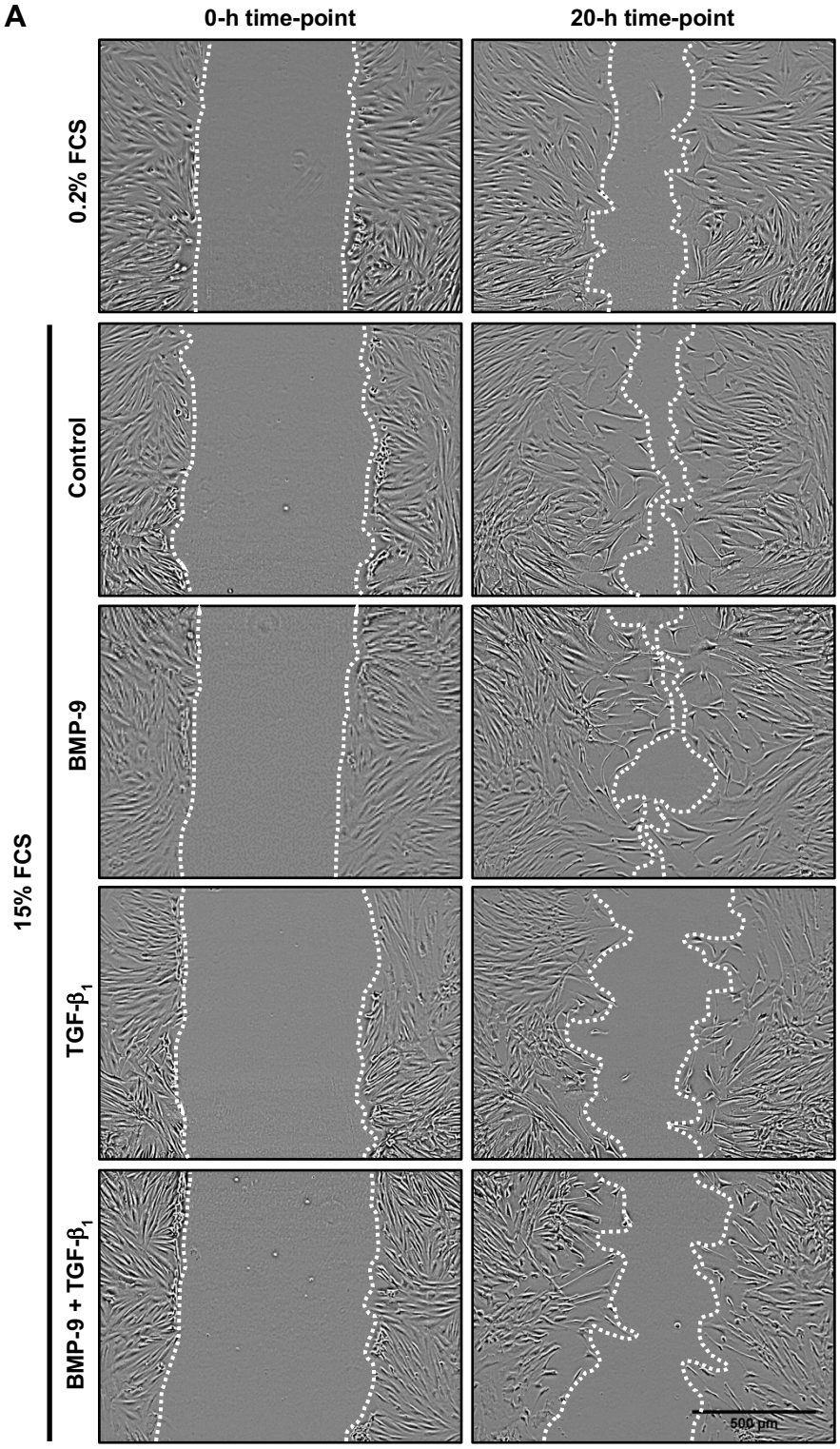

Figure 4-24 TGF-β_1 prevents serum-induced primary HSVSMC-driven scratch closure. Cells were seeded into 12-well plates (1*10^6 cells/well) and cultured in 15% FCS. Upon achieving 80% confluence cells were quiesced in 0.2% FCS media for 72-h. Wells were horizontally scratched with a sterile 200 μl pipette tip and imaged under a microscope at 10× magnification (left panel). Media was removed and replaced with fresh 0.2% FCS or 15% FCS containing vehicle control, BMP-9 (10 ng/ml), TGF-β_1 (10 ng/ml) or both ligands (technical n=3/group). Scratches were imaged again at 20 h at 10× magnification (right panel). White dotted lines indicate scratch edges.

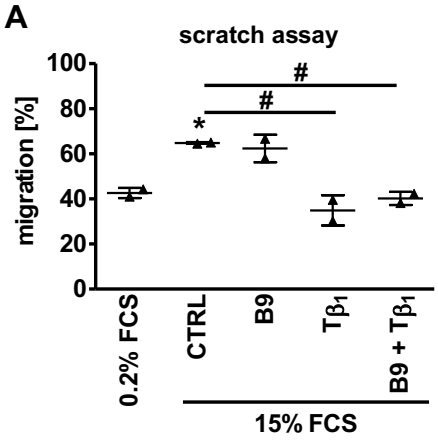

Figure 4-25 TGF-β_1 demonstrates anti-migratory effects on serum-induced primary HSVSMC-driven scratch closure. Cells were seeded into 12-well plates ($1*10^6$ cells/well) and cultured in 15% FCS. Upon achieving 80% confluence cells were quiesced in 0.2% FCS media for 72-h. Wells were horizontally scratched with a sterile 200 μl pipette tip and imaged under a microscope at 10× magnification (left panel). Media was removed and replaced with fresh 0.2% FCS or 15% FCS containing vehicle control, BMP-9 (10 ng/ml), TGF-β_1 (10 ng/ml) or both ligands (technical n=3/group). Scratches were imaged again at 20 h at 10× magnification (right panel). White dotted lines indicate scratch edges. (**A**) The ImageJ software was used to determine scratch closure percentage. Scatter plot indicates mean ± S.E.M. (biological n=2). A One-way repeated ANOVA with a Tukey's correction was performed to compare groups. P-value<0.05 was considered statistically significant (* p-value<0.05, target group versus 0.2% FCS control; # p-value<0.05).

4.3.15 TGF-β$_1$ suppresses osteoblast and macrophage-like gene expression via ALK5 in primary HSVSMCs

Depending on the underlying vascular disease, vSMCs may also de-differentiate into an osteoblast- and/or macrophage-like phenotype (Allahverdian et al., 2014; Zhu et al., 2015). Moreover, accelerated atherosclerotic lesion formation and calcification are key pathological features of SVG disease (Kern et al., 1981; Pedigo et al., 2017). These findings prompted evaluation of osteoblastic (*SP7* → encodes osterix; *ALPL* → encodes alkaline phosphatase) and macrophage marker mRNA expression levels (*LGALS3* → encodes galectin-3; *CD68* → encodes cluster of differentiation 68) in primary HSVSMCs in response to ligand stimulation.

24-h TGF-β$_1$ treatment suppressed *ALPL* mRNA expression levels in an ALK5-dependent manner (RQmean + error, TGF-β$_1$ + DMSO: 0.43+0.1, CTRL DMSO: 1+0.19, $p<0.05$; TGF-β$_1$ + DMSO: 1+0.19, TGF-β$_1$ + SB525334: 1.75+0.33, $p>0.05$) (Figure 4-26 C). Furthermore, BMP-9 blunted the ability of TGF-β$_1$ to significantly down-regulate *ALPL* expression levels. In addition, double BMP-9/TGF-β$_1$ stimulation restored *ALPL* expression levels in the presence of ALK5 inhibition. A similar trend was observed for *SP7* expression levels although TGF-β$_1$-induced suppression compared to vehicle-treated controls did not reach statistical significance (Figure 4-26 A). ALK5 inhibition and BMP-9 both blunted the ability of TGF-β$_1$ to significantly suppress *CD68* expression (TGF-β$_1$ + DMSO: 0.6+0.14 vs CTRL DMSO: 1+0.28, $p<0.01$; CTRL DMSO: 1+0.28 vs TGF-β$_1$/BMP-9 + DMSO: 0.78+0.22, $p>0.05$; TGF-β$_1$ + DMSO: 0.6+0.14vs TGF-β$_1$ + SB525334: 1.08+0.34, $p<0.01$ (Figure 4-26 D). In the presence of pharmacological ALK5 inhibition, BMP-9 mildly induced *CD68* expression compared to vehicle-treated DMSO controls.

TGF-β$_1$ stimulation demonstrated a trend towards a reduction in *LGALS3* expression levels (Figure 4-26 B). Pharmacological ALK5 inhibition in vehicle-treated controls drove *LGALS3* expression levels compared to vehicle-treated DMSO controls (CTRL + SB525334: 2.86+0.88 vs CTRL + DMSO: 1+0.36, $p<0.05$). Finally, combined BMP-9/TGF-β$_1$ treatment restored *LGALS3* expression levels in the presence of ALK5 inhibition (CTRL + SB525334: 2.86+0.88 vs BMP-9/TGF-β$_1$ + SB525334: 1.19+0.15, $p<0.05$). Singular BMP-9 stimulation had no impact on osteoblastic and macrophage marker expression levels in primary HSVSMCs.

In conclusion, TGF-β_1 stimulation significantly suppressed *ALPL* and *CD68* expression levels in an ALK5-dependent manner potentially indicating the ALK5 pathway as a negative regulator of osteoblastic and macrophage-like differentiation in primary HSVSMCs. Although BMP-9 treatment had no impact on osteoblastic or macrophage marker expression levels, it did prevent the ability of TGF-β_1 to significantly suppress osteoblastic and macrophage marker expression levels. Moreover, BMP-9 and TGF-β_1 synergised to restore suppression of osteoblastic and macrophage marker expression levels in the presence of ALK5 inhibition suggesting that ALK1/SMAD1 signalling may favour osteoblastic and macrophage-like differentiation in primary HSVSMCs, in opposition to ALK5/SMAD2/3 signalling, which favours contractile HSVSMC differentiation.

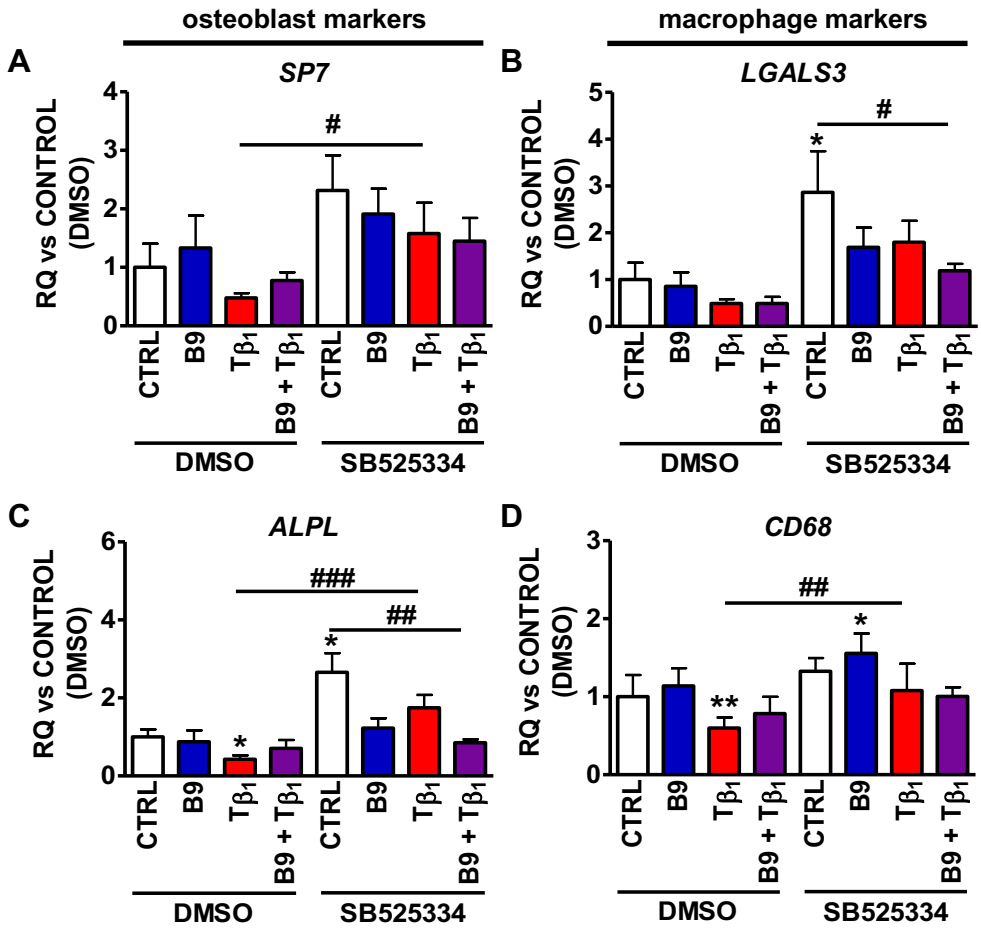

Figure 4-26 TGF-β_1 ALK5-dependently suppresses osteoblastic and macrophage-like gene expression levels in primary HSVSMCs. 80% confluent primary HSVSMCs were quiesced in 0.2% FCS media (MEDIA1) for 72-h. To achieve pharmacological ALK5 inhibition prior to ligand stimulation, the first 4 groups were incubated in MEDIA1 containing 10 μM SB525334 for 30 min. In parallel, the second 4 groups were incubated in MEDIA1 containing DMSO vehicle (1:1,000) for 30 mins. Media was replaced with fresh MEDIA1 containing recombinant human BMP-9 (10 ng/mL), TGF-β_1 (10 ng/mL) ± DMSO (1:1,000) or SB525334 (10 μM). After 24-h stimulation, primary HSVSMCs were lysed and subjected to RNA extraction. Reverse transcription was performed to generate cDNA. Quantitative RT-PCR was performed to determine relative *SP7* (**A**), *LGALS3* (**B**), *ALPL* (**C**) and *CD68* (**D**) mRNA expression levels. Relative target gene expression was normalised to *UBC* expression to determine δCT values, which were used to calculate relative quantification (RQ) values (target group versus DMSO vehicle control). Data are presented as RQ_{mean} ± error (biological n=3). A One-way repeated ANOVA with a Tukey's correction was performed to compare groups based on δCT values. P-value<0.05 was considered statistically significant (* p-value<0.05 and ** p-value<0.01, target group versus DMSO vehicle control, # p-value<0.05, ## p-value<0.01).

4.4 Discussion

The discovery of *in vivo* SMC phenotype switching in pre-implantation SVGs from CABG patients prompted development and validation of an *in vitro* contractile differentiation protocol for primary HSVSMCs and HCASMCs.

SMDS-cultured primary HSVSMCs time-dependently displayed an accumulation of α*SMA*, *CNN1*, *SM22-*α and *MYH11* mRNA expression levels versus day 0 15% FCS-treated controls indicating contractile differentiation. Although SMGS- and 15% FCS-cultured HSVSMCs also demonstrated a significant increase in contractile gene expression levels, fold changes were less pronounced compared to SMDS treatment. The increase in *CNN1* mRNA levels in SMDS-cultured HSVSMCs was paralleled by a significant accumulation of calponin protein expression. Interestingly, calponin protein expression levels remained suppressed in 15% FCS-treated HSVSMCs although the same cells displayed a significant increase in *CNN1* mRNA expression levels highlighting discrepancy between mRNA and protein expression levels. Although αSMA and SM22-α protein levels visually increased in the presence of SMDS, differences between groups did not reach statistical significance. This may be explained by increased inter-patient variability and low n-numbers (biological n=4 CABG patients). Indeed, isolated primary vSMCs are often pre-conditioned by their donors, which means that certain parameters such as age, gender and pharmacological treatment may affect SMC biology *in vitro* (Frismantiene et al., 2018). However, later studies investigating the effect of pharmacological ALK5 inhibition on SMDS-induced contractile HSVSMC differentiation revealed statistically significant differences between groups (biological n=5 CABG patients). Nevertheless, SMDS-induced accumulation of contractile gene and protein expression was paralleled by a significant decrease in pro-proliferative *CCND1* and *PCNA* mRNA expression levels compared to 15% FCS-treated controls. Moreover, 15% FCS-treated HSVSMCs displayed enhanced BrdU incorporation compared to the SMDS treatment group indicating a proliferative SMC phenotype.

SMDS-induced contractile differentiation of primary HSVSMCs prompted protocol validation for primary HCASMCs to assess potential differences between SMCs from distinct vascular beds. Indeed, SMDS-cultured HCASMCs demonstrated enhanced accumulation of α*SMA*, *CNN1*, *MYH11* and *SM22-*α mRNA expression

levels compared to SMGS-treated controls thereby displaying similar responses compared to primary HSVSMCs. Moreover, SMDS-cultured HCASMCs displayed a significant increase in αSMA and calponin protein expression levels matching mRNA level findings. Although *SM22-α* mRNA levels increased during SMDS treatment protein levels remained unchanged.

Similar SMDS-driven responses in HSVSMCs and HCASMCs may indicate shared conserved contractile differentiation mechanisms between these two distinct cell types. However, these pro-contractile responses differed in force. Whereas SMDS-driven increase in *αSMA* fold change expression was similar, HSVSMCs displayed higher increases in *CNN1* and *MYH11* fold change expression compared to HCASMCs. In contrast, immunoblot data in primary HCASMCs was more consistent and showed more significant changes between SMDS- and SMGS-treated groups. The reason for this may be explained by the fact that HCASMCs utilised for this experiment derived from one patient (biological n=3 repeats) whereas HSVSMCs derived from four individual CABG patients. This bias may be overcome by adding more experimental repeats utilising HCASMCs from different donor patients. Interestingly, SMGS media which contains the proliferative factors 4.9% FCS, hBFGF and hEGF more efficiently suppressed contractile gene expression in HCASMCs compared to SMGS-treated HSVSMCs potentially indicating less defined regulation of contractile differentiation in venous SMCs. Deng and colleagues demonstrated that primary HSVSMCs demonstrated an increase in proliferation in response to PDGF treatment compared to HCASMCs (Deng et al., 2006). Moreover, Turner and colleagues showed that primary HSVSMC were more proliferative and invasive than paired primary IMAG SMCs indicating functional differences between vSMCs from different vascular beds (Turner et al., 2007). Together, these two studies show that arterial SMCs possess more defined molecular mechanisms underlying regulation of cell behaviour which makes them less prone to de-differentiation compared to venous SMCs. Although SMDS-drives pro-contractile HSVSMC and HCASMC differentiation, HSVSMCs display higher contractile gene expression responses. Hence, it may be speculated that regulation of contractile differentiation is less defined in HSVSMCs compared to HCASMCs. Despite differences in pro-contractile responses, these findings in primary HSVSMCs and HCASMCs match previous findings in SMDS-cultured primary HASMCs (Chen et al., 2016b). SMDS-

induced accumulation of contractile protein levels paralleled by a decrease in pro-proliferative gene expression and proliferation strongly suggest the presence of a contractile SMC phenotype.

Protocol validation enabled investigation of TGF-β type I and II receptor and ALK1/ALK5 target gene mRNA expression levels during contractile differentiation of primary HSVSMCs and HCASMCs. SMDS-cultured HSVSMCs and HCASMCs displayed a dynamic increase in *ACVR2A* mRNA levels suggesting a potential role for this TGF-β type II receptor during contractile differentiation. Whereas *SERPINE1* mRNA levels remained un-changed, SMDS treatment resulted in a significant decrease in *ID1* mRNA levels in HSVSMCs. Moreover, SMDS-treated HCASMCs also displayed a dynamic decrease in *ID1* mRNA levels. It is possible that this reduction in relative *ID1* mRNA expression levels may indicate potential ALK1 pathway suppression during contractile differentiation in venous and arterial SMCs. However, it is more likely that this reduction reflects lower FCS and/or serum-derived BMP-9 concentrations rather than the cell differentiation state since serum naturally contains active BMP-9 (David et al., 2008) and serum drives relative *ID1* mRNA expression levels (Lewis and Prywes, 2013). Compared to HSVSMCs and in addition to *ACVR2A*, SMDS-cultured HCASMCs displayed a dynamic increase in *ALK5* and surprisingly *ALK1* mRNA levels during contractile differentiation. Chen's study also demonstrated that SMDS-cultured HASMCs displayed a dynamic increase in ALK5 protein expression levels along with increased SMAD2 phosphorylation (Chen et al., 2016b). The same study went on to show that combined pharmacological inhibition of ALK4/5/7 with SB431542 prevented SMDS-induced contractile marker accumulation highlighting ALK5/SMAD2 signalling as a regulator of contractile differentiation. Unfortunately, this study did not assess ALK1/SMAD1 pathway activity during contractile differentiation. Despite best efforts to optimise antibodies and the immunoblot protocol, it was not possible to detect pSMAD1, tSMAD1, pSMAD2 or tSMAD2 in protein lysates from 15% FCS-, SMDS and SMGS-treated primary HSVSMCs and/or HCASMCs. In the future, this limitation may be overcome by transfecting pSMAD3-(pCAGA) and/or pSMAD1/5/8 (BMP-responsive element, BRE)-responsive luciferase plasmids into primary human SMCs and perform luciferase assays to assess ALK5 and ALK1 pathway activation during contractile differentiation (Schwartze et al., 2014). In addition, pharmacological receptor

inhibition, adenoviral-mediated receptor overexpression or siRNA-mediated receptor knockdown studies may be employed to determine the functional contribution of ALK1 and ALK5 signalling during contractile differentiation.

The fact that pharmacological ALK4/5/7 inhibition with SB435142 prevented contractile differentiation of primary HASMCs evoked to test this approach in primary HSVSMCs. Indeed, combined pharmacological ALK4/5/7 and singular ALK5 inhibition prevented an increase in SMDS-induced *αSMA* mRNA expression levels compared to vehicle-treated controls. In contrast, pharmacological ALK1 inhibition had no effect on SMDS-mediated increase in *αSMA* mRNA levels. Although this experiment was only performed in one set of patient cells (biological n=1) subsequent repeats confirmed these findings (unpublished data) (Low et al., 2019). Interestingly, pharmacological ALK4/5/7 and/or ALK5 inhibition could not entirely prevent SMDS-induced accumulation of *αSMA* mRNA levels at day 4. Nonetheless, this initial experiment highlighted an important role for functional ALK5 signalling in driving contractile differentiation in primary HSVSMCs. This hypothesis was supported by subsequent immunoblot analyses demonstrating that pharmacological ALK5 inhibition with SB525334 blocked SMDS-mediated accumulation of αSMA, calponin and tMLC9 protein expression levels compared to 15% FCS-treated controls (biological n=5 CABG patients). Furthermore, SMDS-cultured HSVSMCs displayed a significant increase in αSMA, calponin, SM22-α, tMLC9 and pMLC9 protein levels compared to 15% FCS-treated controls underlying the importance of functional ALK5 receptor signalling during SMC maturation. Importantly, as observed for *αSMA* mRNA levels, ALK5 inhibition did not entirely attenuate the ability of SMDS to enhance MLC9 phosphorylation which implies that more pathways may be involved during contractile differentiation of HSVSMCs. Importantly, functional ALK5 receptor signalling is essential for maintaining vascular stability. Nonsense mutations in *TGFBR1* (encodes ALK5) causes type I LDS in humans, which, alongside widespread impaired organogenesis, is characterised by arterial aneurysms and tortuosity pre-disposing patients to potentially life-threatening bleeding events (Loeys et al., 2005). In the context of SVG disease, vein graft aneurysm formation on the basis of accelerated atherosclerosis pre-disposing to haemorrhaging events is observed in CABG patients (Neitzel et al., 1986). Hence, it may be speculated that maintaining ALK5 functionality may protect SVGs from

aneurysm formation. In the context of acute vascular injury SMC-specific *Tgfbr1* deletion in mice prevented NF following femoral artery wire injury (Liao et al., 2016). However, ALK5-depleted injured femoral arteries displayed persistent neointimal cell proliferation and apoptosis, fewer SMCs, enhanced neointimal inflammatory infiltrates, reduced collagen content and a thickened adventitial layer. This means, that on the one hand ALK5 is involved in neointimal thickening, most likely by driving ECM production in intimal SMCs. On the other hand, ALK5 deficiency most likely impairs long-term vascular performance following injury highlighting the importance of this receptor in maintaining vascular stability.

SMDS-cultured primary HSVSMCs and HCASMCs both displayed a dynamic increase in *ACVR2A* mRNA expression levels during contractile differentiation. This observation prompted development and validation of a HAdV-5 expressing *ACVR2A* and determining the effect of adenoviral-mediated *ACVR2A* delivery on proliferating and differentiating primary HSVSMCs (biological n=1 CABG patient). It was hypothesised that enhanced *ACVR2A* expression would potentiate SMDS-induced α*SMA* mRNA expression levels at day 2. In 15% FCS, HAdV-5 ACVR2A-transduced HSVSMCs demonstrated a dose-dependent increase in *ACVR2A* mRNA levels compared to HAdV-5 GFP-transduced controls indicating successful transgene delivery. In the presence of SMDS, only cells that were transduced with the highest dose (10^4 VP/cell) of HAdV-5 ACVR2A demonstrated a significant increase in *ACVR2A* mRNA levels versus mock controls. However, similar observations were made for SMDS-treated and HAdV-5 GFP-transduced cells (10^4 VP/cell) indicating that the increase in *ACVR2A* mRNA levels most likely occurred because of virus-related cytotoxicity. This effect was even more pronounced for α*SMA* mRNA levels which dose-dependently increased in HAdV-5 GFP-transduced cells in the presence of 15% FCS and SMDS compared to mock controls. In conclusion, HAdV-5-mediated *ACVR2A* transgene delivery was successful in the presence of 15% FCS. In contrast, adenoviral-mediated *ACVR2A* delivery did not induce or potentiate α*SMA* mRNA expression levels in the presence of 15% FCS or SMDS respectively since increasing concentrations of control HAdV-5 GFP positively impacted α*SMA* mRNA levels.

In general, it must be noted that these findings require careful interpretation since this experiment was only performed in one set of patient cells. More n numbers should be added to verify these observations in the future. Although qRT-PCR confirmed a dose-dependent increase in *ACVR2A* mRNA expression levels in primary HSVSMCs and HeLa cells, immunoblot analysis using two different antibodies from two different companies failed to detect ACVR2A protein levels in HeLa cell lysates (data not shown). In contrast, sequencing of the pAdEasy-1::pSHUTTLE-CMV::ACVR2A plasmid confirmed transgene integrity and identity suggesting that the utilised antibodies failed to detect ACVR2A. Hence, ACVR2A antibody optimisation for immunoblot and/or immunocytochemistry should be addressed in future experiments. Furthermore, viral transduction of HSVSMCs appeared inefficient since only 2.58% of HSVSMCs were GFP^+ following infection with HAdV-5 GFP at 10,000 VP/cell. This inefficiency may be explained by the fact that vSMCs display low CAR availability (Parker et al., 2013), the main entry mechanism for non-modified HAdV-5 (Nicklin et al., 2001). Work *et al.* demonstrated that genetic modification of HAdV-5 fibres by inserting the RGD-4C integrin targeting peptide into the HI loop significantly improved transduction of HSVSMC (Work et al., 2004). Hence, this limitation may be overcome by inserting the *ACVR2A* transgene into this genetically modified HAdV-5 vector in the future.

Since SMDS-treated, un-transduced cells already displayed high levels of *ACVR2A* mRNA levels it may be speculated that adenoviral-mediated *ACVR2A* delivery to SMDS-treated HSVSMCs was unable to induce an additional increase in receptor expression levels. Although 15% FCS-treated HAdV-5 ACVR2A-transduced cells failed to demonstrate an increase in α*SMA* mRNA levels it may be hypothesised that higher ACVR2A levels may impact on other cellular functions such as proliferation or migration. Hence, future experiments should address serum-induced BrdU incorporation and scratch closure in HAdV-5 ACVR2A-transduced HSVSMCs versus HAdV-5 GFP controls. Since SMDS-treated vSMCs demonstrated a dynamic increase in *ACVR2A* mRNA levels during contractile differentiation a future experiment should also determine the effect of siRNA-mediated *ACVR2A* knockdown in vSMCs in the presence of SMDS. In the context of acute vascular injury, a future *in vivo* study should assess NF following carotid artery ligation and/or carotid artery wire injury in *acvr2a* knockout mice versus wildtype

controls. A previous murine study investigating the impact of homozygous *Acvr2a* depletion on embryonic and post-natal development found that homozygous knockout mice were viable and only few demonstrated skeletal and facial abnormalities indicating that this transgenic mouse may be utilised for vascular injury studies. On the one hand, one may speculate that *Acvr2a* ablation may exacerbate NF following vascular injury since adenoviral-mediated activin A delivery to experimentally injured vessels prevented SMC proliferation and NF in rats and mice (Engelse et al., 2002; Kloppenburg et al., 2009). On the other hand, it is conceivable that *Acvr2a* depletion may ameliorate NF following vascular injury since administration of the ACVR2A-Fc ligand trap reversed experimental PAH in rats indicating a protective role for this signalling axis in the context of vascular injury (Yung et al., 2020). However, this discrepancy may also be explained by the fact that ACVR2A may exert different functions in distinct vascular beds.

Pre-implantation SVGs and wire-injured murine carotid arteries displayed BMP-9^{+} staining in addition to *in vivo* SMC phenotype switching. Hence, the next step was to investigate functional BMP-9 properties in more detail. A crosslinking study demonstrated that BMP-9 bound to ALK1, ALK2, BMPR2, ACVR2A/B and endoglin on primary HSVSMCs (biological n=1 CABG patient). These findings suggested that BMP-9 transduced signals into HSVSMCs. Indeed, immunoblot analyses revealed a time-dependent increase in SMAD1 phosphorylation in 0.2% FCS quiesced HSVSMCs demonstrating that BMP-9 activated downstream SMAD1 signalling. In addition, TGF-β_1 also induced SMAD1 phosphorylation paralleling previous findings from our group (unpublished data) (Low et al., 2019). Low *et al.*'s study demonstrated that TGF-β_1-induced SMAD1 activation was ALK1-dependent. No additive effect on SMAD1 phosphorylation was detected in the presence of both ligands compared to BMP-9 treatment alone suggesting absence of ligand interaction. Given that BMP-9 may also simultaneously drive SMAD5 phosphorylation (Upton et al., 2009), it must be noted that BMP-9/ALK1/ALK2-driven effects may also induce SMAD5 phosphorylation in primary HSVSMCs and, therefore, SMAD5 may also potentially contribute to downstream pathway effects. Hence, a future experiment should aim to investigate SMAD5 phosphorylation in response to BMP-9 stimulation in primary HSVSMCs. Despite best efforts to determine tSMAD1, pSMAD2 and tSMAD2 protein levels in response

to ligand treatment no reliable immunoblot nor in-cell western blot results could be achieved (data not shown). Hence, the potential impact of BMP-9 on lateral ALK5/SMAD2 signalling could not be assessed. Since Zhu *et al.* demonstrated that BMP-9 induced SMAD2 phosphorylation in addition to SMAD1 in primary mouse aortic SMCs, a continued effort should be undertaken to determine the potential impact on vSMC ALK5/SMAD2 signalling in the future (Zhu et al., 2015). Furthermore, at this stage it is unclear which receptors mediate BMP-9-dependent SMAD1 phosphorylation in HSVSMCs. The question remains by which means BMP-9 mediates SMAD phosphorylation. Based on previous findings many combinations are possible (Andersson et al., 2006; Appleby et al., 2016; David et al., 2007; Lee et al., 2005; Mitrofan et al., 2017; Olsen et al., 2015; Rebbapragada et al., 2003; Scharpfenecker et al., 2007). Firstly, BMP-9/ALK1 may recruit BMPR2 or ACVR2A/B triggering SMAD1 phosphorylation. Secondly, BMP-9/ALK2 may recruit the same TGF-β type II receptors. Thirdly, BMP-9 may bind to endoglin thereby potentiating ALK1 activation. Fourthly, BMP-9/ACVR2A/B may recruit ALK4 or ALK5 triggering SMAD2/3 phosphorylation. More siRNA-mediated receptor knockdown studies should be performed to elucidate the exact signalling mechanism in HSVSMCs in the future.

Both ligands induced proximal pathway activation in primary HSVSMCs. The next aim was to determine target ALK1/ALK5 and contractile gene expression in response to BMP-9 and/or TGF-β_1 treatment. Matching pSMAD1 findings, BMP-9 robustly induced *ID1* mRNA expression levels in an ALK5-independent manner. Although TGF-β_1 did not prevent BMP-9 driven SMAD1 activation, the presence of TGF-β_1 attenuated the ability of BMP-9 to drive *ID1* gene expression, a known downstream SMAD1 pathway target gene (Yang et al., 2013). Furthermore, TGF-β_1 induced SMAD1 phosphorylation did not translate into an increase in *ID1* mRNA levels. This discrepancy may be explained by ALK5-driven lateral downstream pathway inhibition (Goumans et al., 2002). TGF-β_1 ALK5-dependently drove *SERPINE1* mRNA levels, a known downstream ALK5/SMAD2/3 pathway target gene (Goumans et al., 2002). In contrast, BMP-9 had no direct effect on *SERPINE1* mRNA levels and did not prevent TGF-β_1-driven *SERPINE1* gene expression suggesting that ligand-dependent ALK5 activation outweighs ALK1 activation.

In the context of contractile genes, TGF-β_1-treated HSVSMCs displayed enhanced *αSMA, CNN1, SM22-α* and *MYH11* mRNA expression levels compared to vehicle treated controls. Singular pharmacological ALK5 inhibition with SB525334 attenuated TGF-β_1-driven increase in contractile gene expression highlighting the importance of ALK5 receptor signalling in the context of contractile HSVSMC differentiation. Interestingly, BMP-9 treatment triggered a moderate ALK5-dependent increase in *αSMA* mRNA levels. Taken together, these findings corroborate with previous findings demonstrating that singular pharmacological ALK5 inhibition attenuated ligand-independent accumulation of contractile vSMC markers. Furthermore, these findings are in line with a previous study which demonstrated increased contractile gene expression in primary HSVSMCs in response to TGF-β_1 treatment (Groenendijk et al., 2011). However, this study did not investigate whether this TGF-β_1-driven effect was mediated via ALK1 or ALK5. A further study showed that combined pharmacological ALK4/5/7 inhibition prevented contractile protein expression in primary HASMCs implicating that functional ALK4/5/7 receptor signalling is necessary for contractile differentiation of arterial SMCs (Tang et al., 2010). In contrast, TGF-β_1 stimulation had no effect on αSMA, calponin or SM22-α protein expression levels in quiesced HSVSMCs. Since target protein/GAPDH ratios in vehicle-treated cells were higher compared to day 6 SMDS/vehicle-treated cells 72-h quiescence in 0.2% FCS media prior to ligand stimulation may have already induced contractile differentiation. This speculation is supported by the fact that serum deprivation triggers contractile differentiation of primary human umbilical vein SMCs (Han et al., 2006).

Accelerated atherosclerosis and calcification are key pathological hallmarks of chronic SVG disease (Kern et al., 1981; Pedigo et al., 2017). Depending on external factors vSMCs may transdifferentiate into macrophage-like and/or osteoblastic phenotypes thereby promoting atherosclerotic lesion formation and medial calcification respectively (Allahverdian et al., 2014; Vengrenyuk et al., 2015; Zhu et al., 2015). These findings prompted evaluation of osteoblastic (*ALPL* and *SP7*) and macrophage (*LGALS3* and *CD68*) gene expression in HSVSMCs in response to ligand treatment. The presence of BMP-9 and SB525334 prevented TGF-β_1-driven *ALPL* suppression potentially indicating the ALK5 pathway as a negative regulator of osteoblastic differentiation. Although there was a trend

towards down-regulation of *SP7* in TGF-β_1-treated cells versus vehicle-treated controls this difference failed to achieve statistical significance. Singular BMP-9 treatment had no impact on *ALPL* or *SP7* mRNA levels. A previous study identified BMP-9 as a driver of osteoblastic vSMC differentiation and medial calcification (Zhu et al., 2015). This study demonstrated that 9-day BMP-9 stimulation potentiated high phosphate-induced vSMC calcification at a dose of 50 ng/ml. Moreover, 4-day BMP-9 treatment at 5 ng/ml enhanced *Sp7* and *Alpl* mRNA expression levels and induced alkaline phosphatase activity in the absence of high phosphate levels in murine vSMCs. Since HSVSMCs were only stimulated for 24-h it may be speculated that BMP-9 treatment was too short to induce a substantial change in osteoblastic gene expression. Longer BMP-9 exposure studies in absence and presence of high phosphate should be performed to evaluate HSVSMC calcification in the future. In line with the hypothesis that TGF-β_1/ALK5 signalling negatively regulates osteoblastic differentiation Guerrero *et al*. found that TGF-β_1 prevented high-phosphate-induced osteogenic differentiation of rat mesenchymal stem cells (Guerrero et al., 2014).

In the context of macrophage-like differentiation during atherosclerotic plaque progression, TGF-β_1-treated HSVSMCs displayed an ALK5-dependent reduction in *CD68* mRNA expression levels. Similar trends were observed for *LGALS3*, however, changes between groups did not achieve statistical significance. In contrast to *CD68* expression, pharmacological ALK5 inhibition triggered an increase in *LGALS3* mRNA levels compared to vehicle-treated controls. Like osteoblastic markers, BMP-9 did not impact *CD68* or *LGALS3* mRNA expression levels. These data suggest that TGF-β_1/ALK5 signalling may potentially act as a negative regulator of macrophage-like differentiation of HSVSMCs thereby exerting a protective role against atherosclerotic lesion formation in SVGs following CABG surgery. In line with these findings, it was shown that administration of TGF-β_1 neutralising antibodies to hyperlipidaemic ApoE-deficient mice accelerated atherosclerotic lesion formation and promoted plaque instability (Mallat et al., 2001). In the context of BMP-9, Kraehling *et al*. demonstrated that BMP-9 receptor ALK1 positively regulated LDL-cholesterol uptake into ECs and arterial wall lipid deposition (Kraehling et al., 2016). Hence, it is plausible that BMP-9-mediated ALK1/SMAD1 axis activation may synergise with cholesterol-loading triggering macrophage-like differentiation of HSVSMCs.

A future *in vitro* study should be performed to address this hypothesis in more detail.

Data consistently demonstrated that ALK5 pathway activation promoted the contractile HSVSMC phenotype. In experimental and acute SVG injury in humans vSMCs switch to a migratory and proliferative phenotype thereby initiating NF and expansion (Kockx et al., 1992; Zou et al., 1998). This prompted investigation of BMP-9 and/or TGF-β_1 stimulation on serum- and PDGF-induced HSVSMC proliferation as well as serum-induced scratch closure. Encouragingly, TGF-β_1 stimulation prevented a significant increase in serum-induced proliferation in HSVSMCs versus vehicle-treated 0.2% FCS controls. Opposed to TGF-β_1, BMP-9 had no impact on serum-induced cell proliferation. In addition, TGF-β_1 attenuated serum-induced HSVSMC-driven scratch closure potentially suggesting anti-migratory effects. Paralleling proliferation findings, BMP-9 had no effect on serum-induced scratch closure. It is important to point out that scratch assays were only performed for two sets of patient cells (biological n=2 CABG patients). Furthermore, the scratch assay cannot definitively distinguish between proliferation- and/or migration-driven scratch closure. Hence, more n numbers and Boyden chamber migration analysis should be added to this data set in the future. It must be noted that potential serum-derived BMP-9 impact on proliferation and migration in 15% FCS-cultured HSVSMCs was not accounted for in these experiments. Hence, a future experiment should investigate the effect of neutralising BMP-9 antibodies on serum-induced HSVSMC proliferation and migration to tease out any potential BMP-9-specific effects. Taken together, these data suggest that TGF-β_1 may exert potent anti-proliferative and -migratory effects in primary HSVSMCs. However, opposing studies have demonstrated that this pathway acts as a pathogenic driver of NF.

A study by Tsai *et al.* revealed that balloon-injured rat carotid arteries displayed enhanced Smad3 expression compared to uninjured control (Tsai et al., 2009). Subsequent adenoviral-mediated Smad3 delivery to injured arteries triggered an increase in vSMC proliferation and worsened NF. Although TGF-β_1 treatment alone suppressed rat aortic SMC proliferation, TGF-β_1 potentiated adenoviral-mediated Smad3 overexpression-driven proliferation. A subsequent study by the same group found this effect was ERK/MAPK dependent (Suwanabol et al.,

2012). This means that it is likely that TGF-β_1-driven cell responses depend on intracellular signalling messenger expression levels. Although a study by Kobayashi *et al.* reported that TGF-β_1/SMAD3 signalling suppressed serum-induced SMC proliferation, Smad-3 depleted cells did not prevent TGF-β_1-driven chemotaxis indicating that this pro-migratory effect may be driven by the lateral TGFBR2/ALK1/SMAD1 signalling axis (Kobayashi et al., 2005). Furthermore, adenoviral-mediated TGF-β_1 antisense mRNA delivery to epigastric veins following inter-positional grafting into femoral arteries in rats significantly reduced NF (Wolff et al., 2006). Tranilast is a drug which inhibits up-regulation of *Tgf-β_1*, *Tgf-β_3* and *Alk5* mRNA expression levels in balloon-injured rat carotid arteries (Ward et al., 1998). The Tranilast Restenosis Following Angioplasty Trial (TREAT-2) reported a marked reduction in restenosis rates in tranilast-treated patients receiving percutaneous translumenal coronary angioplasty compared to placebo-treated control trial participants (Tamai et al., 2002). However, the much larger Prevention of REStenosis with tranilast and its outcomes (PRESTO) Trial did not find a significant improvement of restenosis in patients receiving PCI treatment (Holmes et al., 2002).

In contrast and based on presented data in this chapter, it may be hypothesised that selective ALK5 agonism following acute SVG injury in humans may dampen SMC de-differentiation and NF. Indeed, previous *in vitro* studies found that TGF-β_1 attenuated PDGF- and/or serum-induced proliferation and migration of vSMCs (Martin-Garrido et al., 2013; Mii et al., 1993). In line with these findings *smad3*-deficient mice displayed enhanced NF following femoral artery wire injury compared to wildtype controls (Kobayashi et al., 2005). The same study showed that TGF-β_1 suppressed serum-induced murine aortic SMC proliferation in a Smad3-depedendent manner. Furthermore, Chen *et al.* found that enhanced ALK5/SMAD2 signalling by inhibition of antagonistic pro-proliferative FGF signalling induced a contractile HASMC phenotype in the presence of 10% FCS (Chen et al., 2016b). The same study demonstrated that SMC-specific FGF receptor adaptor substrate 2-α deletion in mice reduced NF following carotid artery ligation indicating that the ALK5 receptor protects vSMCs from de-differentiation. These studies show that the TGF-β_1/ALK5/SMAD2/3 signalling agonism induces a contractile SMC phenotype, attenuates SMC de-differentiation and NF following vascular injury.

In conclusion, many studies reported protective and pathogenic properties of TGF-β_1 in the context of vascular injury-driven SMC phenotype switching and NF. Discrepancies between opposing studies may be explained by utilisation of different vascular injury models in distinct rodent species, different methods and timing of interventional approaches and investigation of vSMCs from distinct species and vascular beds. Liao's study demonstrated that intact SMC ALK5 receptor signalling promoted NF (Liao et al., 2016). However, at the same time ALK5 also orchestrated physiological healing of injured vessels. On the one hand, TGF-β_1 attenuates vSMC proliferation and promotes a contractile SMC phenotype and on the other hand, this ligand exerts pro-chemotactic effects and triggers ECM production in vSMCs (Liao et al., 2016; unpublished data by Low et al., 2019; Martin-Garrido et al., 2013; Mii et al., 1993). Based on the pathophysiological ligation and wire injury response in mice several potential future intervention studies exploiting these effects of TGF-β_1 come to mind. (1) Since early medial proliferation most likely precedes SMC migration to the media, systemic administration of recombinant TGF-β_1 prior to and for the first 5 days following carotid artery ligation may protect the contractile SMC phenotype thereby preventing phenotype switching (Chappell et al., 2016). (2) Intimal hyperplasia usually becomes visible on day 7 following carotid artery ligation (Kumar and Lindner, 1997). Since migrated SMCs give rise to monoclonal expansion/proliferation systemic administration of SB525334 (ALK5 inhibitor) or neutralising TGF-β_1 antibodies on day 5 and 6 following carotid artery ligation may prevent pro-chemotactic TGF-β_1 effects on medial SMCs thereby attenuating SMC migration to the intima (Chappell et al., 2016). (3) SMC ALK5 receptor signalling plays an important role in vascular repair following injury at the same time driving neointimal ECM deposition and remodelling following femoral artery wire injury (Liao et al., 2016). It is conceivable that systemic administration of SB525334 or neutralising TGF-β_1 antibodies from day 7 until day 14 may dampen neointimal ECM deposition and thickening.

4.5 Summary

In conclusion, SMDS-supplemented media drove contractile marker expression in primary HSVSMCs which was paralleled by suppressed proliferation indicating a contractile phenotype. ALK1/SMAD1 target gene *ID1* mRNA expression levels were down-regulated in SMDS-treated HSVSMCs, likely a reflection of reduced serum and/or serum-derived BMP-9 concentrations rather than the cell differentiation state. Furthermore, SMDS treatment induced TGF-β type II receptor *ACVR2A* mRNA levels suggesting a potential regulatory function for this receptor during contractile differentiation. Similar observations were made in SMDS-treated primary HCASMCs. In addition, SMDS-treated primary HCASMCs demonstrated a dynamic increase in TGF-β type I receptor ALK5 and ALK1 mRNA levels during contractile differentiation paralleling previous findings in primary HASMCs (Chen et al., 2016b). HAdV-5-mediated *ACVR2A* transgene delivery to primary HSVSMCs was successful. However, increased *ACVR2A* expression had no effect on *αSMA* mRNA levels in serum- and SMDS-treated HSVSMCs.

Pharmacological ALK5 inhibition with SB525334 prevented SMDS-induced contractile differentiation of primary HSVSMCs. In line with this finding, TGF-β_1 drove contractile and suppressed osteoblastic/macrophage gene expression in an ALK5-dependent manner. Together, these two data sets comprehensively demonstrate that functional ALK5 receptor signalling plays an important role in contractile differentiation of primary HSVSMCs. Furthermore, TGF-β_1 dampened serum-induced proliferation and HSVSMC-driven scratch closure thereby demonstrating anti-proliferative and potentially anti-migratory properties in this cell type.

Finally, a crosslinking study revealed that BMP-9 bound to ALK1, ALK2, BMPR2, ACVR2A/B and endoglin on primary HSVSMCs. Subsequent BMP-9 stimulation of HSVSMCs demonstrated a time-dependent increase in SMAD1 phosphorylation, and potentially SMAD5, paralleled by an increase in *ID1* mRNA expression levels indicating that BMP-9 activates the ALK1/ALK2 pathway in this cell type.

Chapter 5 Evaluating TGF-β superfamily-dependent regulation of intracellular Ca^{2+} mobilisation in HSVSMCs

5.1 Introduction

Results presented in Chapter 4 consistently showed that the TGF-β_1/ALK5 pathway induced contractile gene and protein expression in primary HSVSMCs strongly suggesting that this pathway positively regulated the contractile SMC phenotype. Based on these findings the next aim was to evaluate the impact of BMP-9 and/or TGF-β_1 stimulation on AngII-dependent intracellular Ca^{2+} mobilisation serving as an upstream surrogate marker of SMC contraction.

5.1.1 Regulation of vSMC contraction and relaxation

Vascular SMC contraction is a finely regulated process involving both Ca^{2+}-dependent and Ca^{2+}-independent mechanisms (Figure 5-1) (reviewed in) (Touyz et al., 2018). The vasoactive peptide AngII binds to its G protein coupled receptor (GPCR) angiotensin II type 1 receptor (AT_1R) triggering phospholipase (PL)C activation and subsequent breakdown of phosphatidylinositol 4,5-bisphosphate (PIP2) into the second messengers, inositol trisphosphate (IP3) and diacylglycerol (DAG) (Alexander et al., 1985; Deraët et al., 2002; Miura and Karnik, 1999). IP3 binds to the IP3 receptor (IP3R) which serves as a Ca^{2+} channel on the membrane of the sarcoplasmic reticulum (SR). IP3R activation triggers SR Ca^{2+} release resulting in an increase in cytosolic [Ca^{2+}] and initiating Ca^{2+}-dependent cell contraction (Mignery and Südhof, 1990; Mikoshiba et al., 1993). Ca^{2+} ions bind to calmodulin which then activates the myosin light chain kinase (MLCK) (Adelstein et al., 1982; Hong et al., 2009). Activated MLCK phosphorylates the MLC S20 subunit triggering MLC/actin interaction generating force and shortening which subsequently results in vSMC contraction (Adelstein and Klee, 1981; Sellers and Pato, 1984). The DAG/protein kinase C (PKC) and RhoA/Rho kinase (ROCK) pathways regulate Ca^{2+}-independent SMC contraction by sensitising the contraction machinery (Touyz et al., 2018). DAG activates PKC triggering phosphorylation of PKC-potentiated protein phosphatase 1 inhibitor (CPI-17) which binds to myosin light chain phosphatase (MLCP) thereby inhibiting enzyme activity (Eto et al., 1995; Kishimoto et al., 1980; Mori et al., 1982). In its active state MLCP binds to MLC and de-phosphorylates the MLC S20 subunit (Pato and Kerc, 1985; Sellers and Pato, 1984). Hence, MLCP inhibition prevents de-phosphorylation of the MLC S20 subunit thereby supporting persistent SMC contraction (Touyz et al., 2018). In addition, AngII/AT_1R interaction directly

activates RhoA triggering downstream activation of ROCK which phosphorylates the myosin phosphatase target subunit (MYPT)1 (Bregeon et al., 2009; Feng et al., 1999). Furthermore, ROCK phosphorylates zipper-interacting protein kinase (ZIPK) which also phosphorylates MYPT1 thereby hampering binding of MLCP to MLC and preventing de-phosphorylation of the MLC S20 subunit (MacDonald et al., 2001).

Following contraction, Ca^{2+} dissociates from calmodulin triggering inactivation of MLCK and SMC relaxation (Touyz et al., 2018). Increased sarcoplasmic/endoplasmic reticulum Ca^{2+} ATPase (SERCA) activity induces Ca^{2+} re-uptake into the SR resulting in a decrease in cytosolic [Ca^{2+}] (Touyz et al., 2018). In addition, the transmembrane Na^{+}/Ca^{2+} exchanger ATP-dependently moves Ca^{2+} to the extracellular space (Touyz et al., 2018). Moreover, endothelium-derived NO signals via the cyclic guanosine monophosphate (cGMP)/protein kinase G (PKG) pathway which stimulates MLCP activity thereby promoting vSMC relaxation (Lee et al., 1997; Sauzeau et al., 2000; Sauzeau et al., 2003).

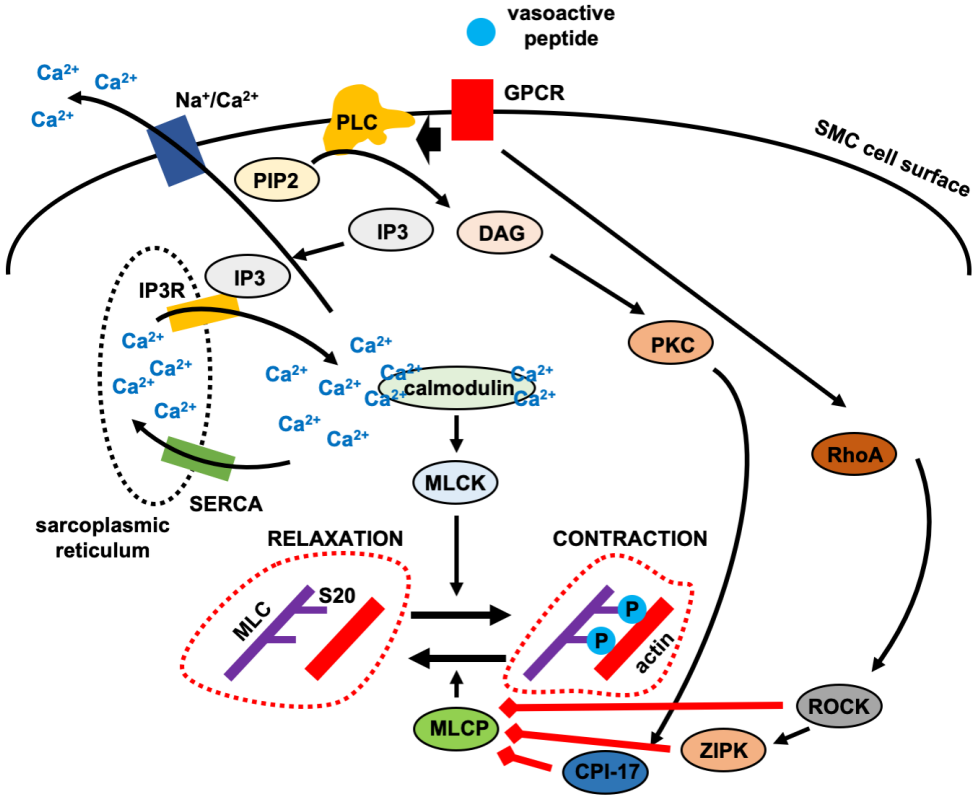

Figure 5-1 Regulation of vascular SMC contraction and relaxation. Vasoactive peptides bind to transmembrane G protein-coupled receptors (GPCR) thereby recruiting phospholipase C (PLC) which breaks down phosphatidylinositol 4,5-bisphosphate (PIP2) into inositol triphosphate (IP3) and diacylglycerol (DAG). IP3 binds to IP3 receptor (IP3R) triggering sarcoplasmic reticulum (SR) Ca^{2+} release. Increased cytosolic Ca^{2+} complexes with calmodulin activating MLCK triggering myosin light chain (MLC) S20 subunit phosphorylation which enables MLC/actin interaction triggering force build-up and contraction. DAG activates PKC triggering PKC-potentiated protein phosphatase 1 inhibitor (CPI-17) phosphorylation which blunts myosin light chain phosphatase (MLCP) activity. Activated GPCRs signal via RhoA to activate Rho kinase (ROCK). Active ROCK either directly de-activates MLCP or phosphorylates zipper-interacting protein kinase (ZIPK) which attenuates MLCP activity. Decreased MLCP activity decreases MLC S20 de-phosphorylation which dampens relaxation. Sarcoplasmic/endoplasmic reticulum Ca^{2+} (SERCA) and transmembrane Na^{+}/Ca^{2+} exchanger ATP-dependently move cytosolic Ca^{2+} to the SR and extracellular space respectively. Taken and modified from Touyz *et al.* (Touyz et al., 2018).

5.1.2 TGF-β_1-dependent regulation of Ca^{2+} handling in vSMCs

The TGF-β_1/ALK5 and AngII/AT_1R systems interact in the vasculature (Rodríguez-Vita et al., 2005). Ford *et al*. demonstrated that AngII drove *TGFB1* (encodes TGF-β_1) and *COL1A1* (alpha-1 type I collagen) mRNA expression levels in primary human IMASMCs (Ford et al., 1999). Both pharmacological AT_1R blockade with losartan and neutralising TGF-β_1 antibodies attenuated this effect demonstrating pathway synergism in the context of vascular fibrosis.

With regard to AngII-dependent Ca^{2+} handling in vSMC Zhu *et al*. found that 30-min TGF-β_1 stimulation reduced AngII-driven increases in cytosolic [Ca^{2+}] in primary aortic SMCs from normotensive Wistar Kyoto (WKY) and spontaneously hypertensive rats (SHR) compared to untreated controls when external Ca^{2+} was present (Zhu et al., 1995). In contrast, TGF-β_1 had no effect on AngII-dependent increases in cytosolic [Ca^{2+}] when no external Ca^{2+} was present indicating that TGF-β_1 negatively regulated Ca^{2+} influx from the extracellular space. In line with findings from this study, primary aortic SMCs from diabetic rats displayed impaired AngII-dependent cytosolic Ca^{2+} transients compared to normo-glycaemic controls when extracellular Ca^{2+} was present (Sharma et al., 2003). The addition of neutralising TGF-β_1 antibodies completely restored AngII-dependent Ca^{2+} responses in diabetic rat aortic SMCs (RASMCs) suggesting that TGF-β_1 suppressed AngII-mediated Ca^{2+} influx from the extracellular space in a hyperglycaemic environment. Contrasting these findings, a further study demonstrated that 24-h TGF-β_1 treatment triggered an increase in AngII-induced intracellular Ca^{2+} mobilisation in primary aortic SMCs from SHRs compared to untreated controls (Bouillier et al., 2000). Opposed to these findings, TGF-β_1 did not influence the AngII response in aortic SMCs from normotensive WKY controls potentially suggesting that TGF-β_1 may chronically potentiate AngII-driven vascular contractility in hypertension. Taken together, these studies demonstrate that TGF-β_1 has different effects on AngII-dependent Ca^{2+} responses in primary RASMCs. It appears that these TGF-β_1-mediated differences may depend on length of TGF-β_1 stimulation, AngII concentration, extracellular [Ca^{2+}] and whether primary aortic SMCs derive from normotensive, hypertensive or diabetic rats.

5.2 Aims

- To develop and validate a protocol for assessing AngII-driven intracellular Ca^{2+} mobilisation in primary HSVSMCs and HCASMCs.

- To determine intracellular Ca^{2+} release in response to BMP-9 and TGF-β_1 stimulation.

- To characterise primary HSVSMC homogeneity versus heterogeneity in the context of intracellular Ca^{2+} mobilisation.

- To investigate the effect of pharmacological AT_1R and ROCK blockade on AngII-driven intracellular Ca^{2+} release.

- To explore potential interaction of TGF-β superfamily and AngII signalling.

5.3 Results

5.3.1 Development and validation of a protocol for assessing AngII-driven intracellular Ca^{2+} release in primary human vascular SMCs

This protocol was partly based on a previously published study investigating crosstalk between vascular redox and calcium signalling in systemic hypertension (Alves-Lopes et al., 2020). All steps leading up to cell imaging are described in section 2.7.

Primary HSVSMCs which had been fluorescently labelled with the Cal-520™ calcium-sensitive dye were incubated in Ca^{2+}-free EGTA HEPES solution to ensure that no extracellular Ca^{2+} was present during measurements (Brock et al., 1985). The total fluorescent trace length was 6 min. At 2 min, 1 μM AngII final/Ca^{2+}-free EGTA HEPES solution was added to induce intracellular Ca^{2+} mobilisation and a subsequent increase in fluorescence intensity mediated by Cal520/Ca^{2+} ion interaction (Figure 5-2 A, B middle image). At 4 min, 1 μM ionomycin (IM)/Ca^{2+}-free EGTA HEPES solution was added to the well to induce maximum intracellular Ca^{2+} release by puncturing all cellular membranes (Figure 5-2 A, B right most image) (Beeler et al., 1979). Following live-cell recordings all whole frame fluorescent traces were background corrected using the Zeiss Zen software (Zeiss; Germany) and plotted using the Prism 5.0 software. Trace normalisation to background fluorescence enabled calculation of AngII- ($AngII_{max}$ fluorescence – baseline $fluorescence_{average}$) and IM-induced fluorescence amplitudes (IM_{max} - baseline $fluorescence_{average}$) (Figure 5-2 D).

AngII triggered a rapid increase in whole frame fluorescence intensity reflecting intracellular Ca^{2+} release in primary HSVSMCs quiesced for 72-h (Figure 5-2 C). Fluorescence intensity peaked approximately 30 s following AngII stimulation and normalised to baseline levels after 1 min. IM stimulation triggered a more rapid increase in fluorescence intensity peaking at approximately 5 s following stimulation and returning to baseline levels after 1 min (Figure 5-2 C). In contrast, 15% FCS-treated HSVSMCs displayed little to no intracellular Ca^{2+} release in response to AngII stimulation compared to quiesced HSVSMCs (mean AngII-induced fluorescence intensity amplitude ± S.E.M., 15% FCS: 1.822 ± 1.113,

0.2% FCS: 6.199 ± 0.7025, $p<0.05$) (Figure 5-3 A-C and E). In addition, preliminary findings showed that 15% FCS-treated HSVSMCs elicited enhanced IM-induced intracellular Ca^{2+} release compared to the low serum-treated group (15% FCS: 109.8 ± 2.825, 0.2% FCS: 56.69 ± 2.649, $p<0.001$) (Figure 5-3 A-C and D).

In conclusion, AngII and IM triggered an increase in Cal520/Ca^{2+}-mediated fluorescence intensity reflecting intracellular Ca^{2+} release in primary HSVSMCs. HSVSMCs quiesced for 72-h displayed increased AngII Ca^{2+} responses compared to the high serum-treated group indicating a contractile phenotype. Alongside these observations, 15% serum cultured HSVSMCs displayed enhanced IM Ca^{2+} responses compared to quiesced controls. Together with data from section 4.3.14 showing increased BrdU incorporation in 15% serum cultured HSVSMCs, these results potentially indicate that there is an unresponsive SR Ca^{2+} storage in proliferating HSVSMCs.

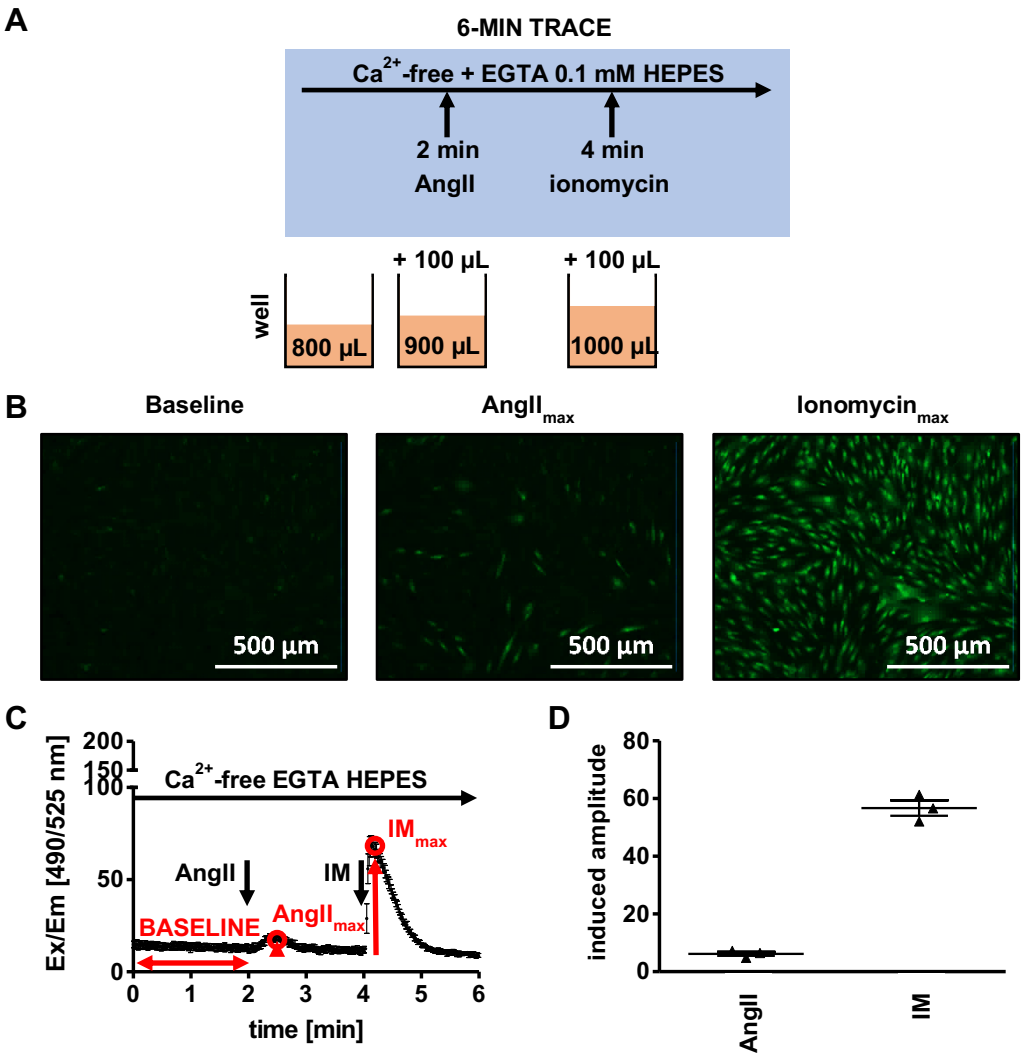

Figure 5-2 Protocol for assessing AngII mediated intracellular Ca^{2+} release in primary HSVSMCs. Primary human SMCs were seeded into 12-well plates ($1*10^5$ cells/well, technical n=3/condition). Upon achieving 80% confluence, HSVSMCs were quiesced in 0.2% FCS media (MEDIA1) for 72-h. Quiescence media was replaced with 400 µL 0.5% FCS HEPES medium containing 2 µM single wave Ca^{2+} indicator Cal-520. Cells were left to incubate at 37°C and 5% CO_2 protected from light for 75 min. Cal-520-containing medium was removed and cells were gently washed once with Ca^{2+}-free 0.1 mM EGTA HEPES solution. Cells were incubated in 800 µl Ca^{2+}-free 0.1 mM EGTA HEPES solution and left to equilibrate at room temperature protected from light for 25 min. Following equilibration, 12-well plates were imaged (Excitation/Emission (Ex/Em) 490/525 nm) on a live-cell microscope (Zeiss, Germany) at 10× magnification. **(A)** Each well was imaged on a live-cell fluorescence microscope (Zeiss, Germany; Excitation (Ex) 490 nm, Emission (Em) 525 nm) at 10× magnification and subjected to a 6-min trace. At 2 min 100 µL AngII (1 µM in HEPES solution) was added to 72-h quiesced HSVSMCs triggering an increase in fluorescence intensity (AngII-dependent intracellular Ca^{2+} release). At 4 min 100 µL ionomycin (IM) (1 µM in HEPES solution) was added to the well triggering maximum fluorescence increase (IM-dependent intracellular Ca^{2+} release). (**B**) Representative images display baseline fluorescence, maximum fluorescence following AngII stimulation and maximum fluorescence following IM stimulation. (**C**) Representative background-corrected 6-min fluorescence trace (whole region of interest). (**D**) Graph represents AngII- and IM-induced amplitudes. Data are presented as mean ± S.E.M. (biological n=1, technical n=3).

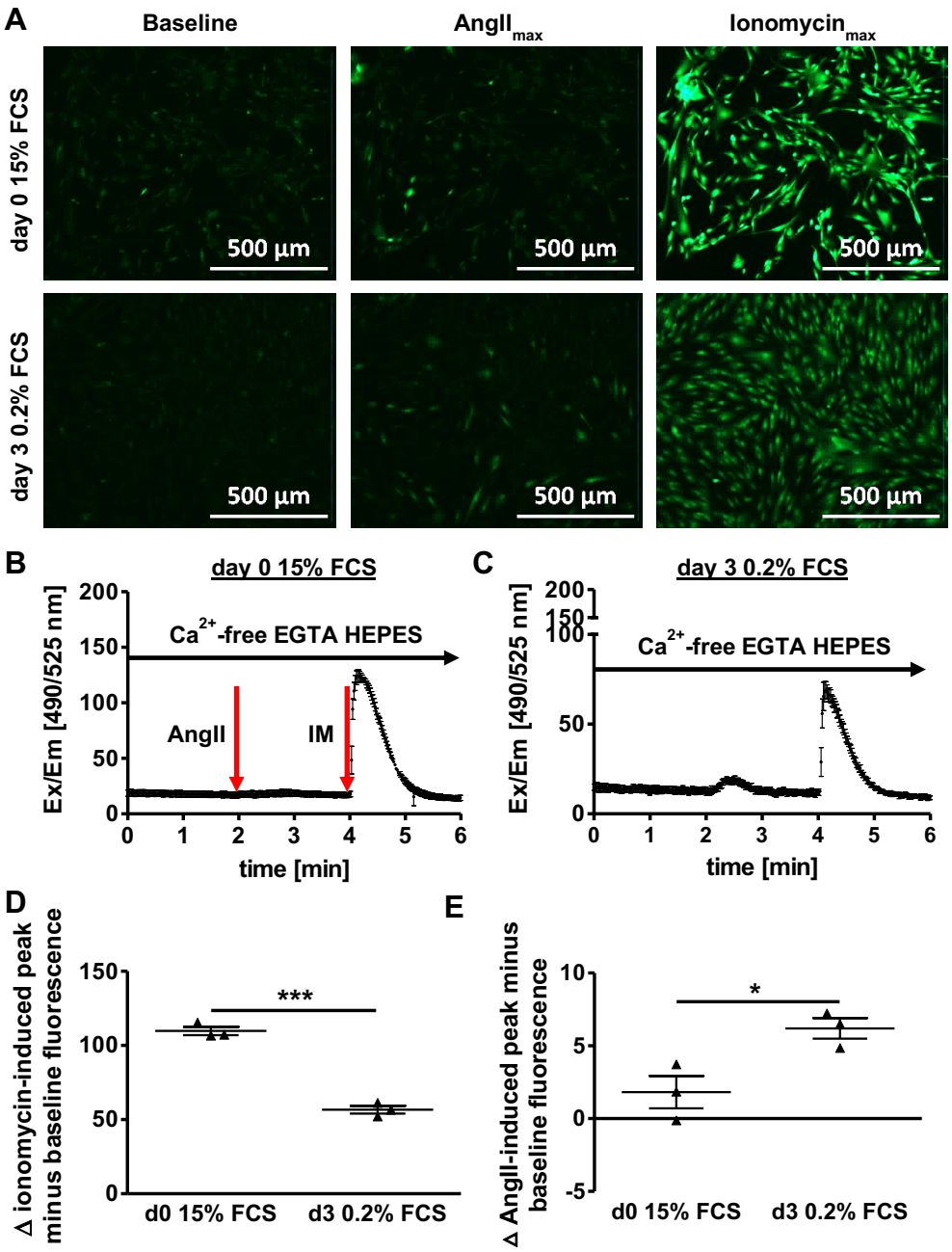

Figure 5-3 15% serum suppresses AngII-mediated intracellular Ca^{2+} release in primary HSVSMC. Upon achieving 80% confluency 15% FCS-treated cells were subjected to previously described protocol (**A**, top panel). A second set of cells was starved in 0.2% FCS media for 72-h and subjected to the same protocol (**B**, bottom panel). (**A**) Images show representative baseline, $AngII_{max}$-induced and IM_{max}-induced fluorescence. Graphs show representative 6-min fluorescent traces from 15% FCS-treated (**B**) and quiesced HSVSMCs (**C**). (**D**) Graph shows IM-induced amplitudes. (**E**) Graph shows AngII-induced amplitudes. (**D** and **E**) Data are presented as mean ± S.E.M. (biological n=1). A Student's t-test was performed to compare means between both groups. P-value <0.05 was considered statistically significant (* p-value<0.05, *** p-value<0.001).

5.3.2 BMP-9 attenuates TGF-β_1/ALK5 pathway-driven contractile responses in primary HSVSMCs

Following protocol validation, the next aim was to evaluate the impact of BMP-9 and/or TGF-β_1 treatment on AngII-induced intracellular Ca^{2+} mobilisation. Primary HSVSMCs quiesced for 72-h were treated with respective ligands in absence and presence of the pharmacological ALK5 inhibitor SB525334 (Thomas et al., 2009) and subjected to the previously described protocol.

TGF-β_1-treated HSVSMCs demonstrated enhanced AngII-induced intracellular Ca^{2+} release compared to vehicle-treated controls (mean AngII-induced fluorescence intensity amplitude ± S.E.M., TGF-β_1: 21.04 ± 6.098, vehicle control: 12.71 ± 1.761 [$p<0.05$]) (Figure 5-4 A, B and E). BMP-9 and SB525334 attenuated TGF-β_1-driven increases in AngII-dependent Ca^{2+} release (TGF-β_1: 21.04 ± 6.098, TGF-β_1 + BMP-9: 6.805 ± 2.593 [$p<0.001$], SB525334/TGF-β_1: 8.676 ± 2.586 [$p<0.01$]) (Figure 5-4 A, B, C and E). BMP-9-treatment alone did not significantly affect AngII-triggered Ca^{2+} release compared to vehicle-treated controls (Figure 5-4 A, B and E). However, there was a slight trend towards a decrease in fluorescence intensity (BMP-9: 8.584 ± 2.983, vehicle control: 12.71 ± 1.761, p 0.40). Neither ligand, SB525334 nor DMSO vehicle treatment affected IM-induced maximum Ca^{2+} release indicating that investigated cells were viable during fluorescent imaging (Figure 5-4 B-D). In two sets of patient cells, the TGF-β_1 treatment group displayed a trend towards a decrease in IM-induced Ca^{2+} mobilisation compared to vehicle-treated controls suggesting that increased cytosolic Ca^{2+} following AngII stimulation is removed to extracellular space where it is directly bound by EGTA and, therefore, cannot re-enter the cell.

In summary, TGF-β_1 enhanced AngII-induced intracellular Ca^{2+} release in an ALK5-dependent manner indicating that this pathway has the potential to positively regulate HSVSMC contractility. In contrast, BMP-9 blunted this effect suggesting ALK5 antagonism and/or differential regulation of Ca^{2+} handling in this cell type.

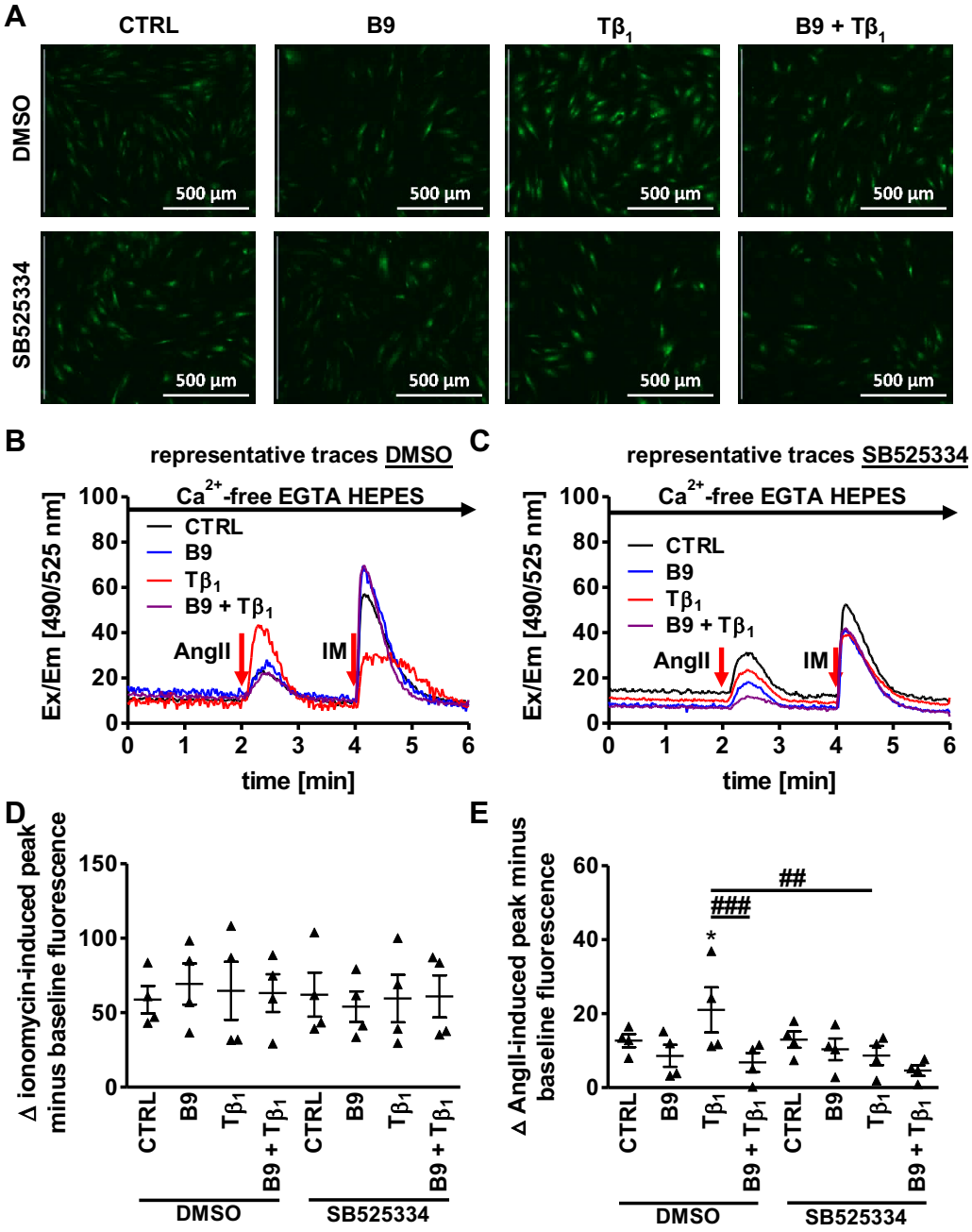

Figure 5-4 BMP-9 and pharmacological ALK5 inhibition prevent TGF-β1-driven enhanced intracellular Ca^{2+} release in primary HSVSMCs. 80% confluent primary HSVSMCs were quiesced in 0.2% FCS media for 72-h. Media was removed and cells were divided into two groups. Whereas one group of cells was incubated in 0.2% FCS media containing the ALK5 inhibitor SB525334 (10 µM) the other group was incubated in 0.2% FCS media containing vehicle control (DMSO). Following a 30-min incubation period media was removed and both sets of cells were subdivided into 4 groups. Both sets of 4 were stimulated with BMP-9 (10 ng/ml, B9), TGF-β1 (10 ng/ml, Tβ1), both ligands and vehicle control in the presence of DMSO or SB525334 respectively. Cells were analysed at 24-h following the previously described protocol. (**A**, top and bottom panel) Images show AngII-induced maximum fluorescence for respective treatment groups. Representative 6-min fluorescent traces are shown in **B** (DMSO controls) and in **C** (SB525334). (**D**) Graph shows IM-induced amplitudes. € Graph shows AngII-induced amplitudes. (**D** and **E**) Data are presented as mean ± S.E.M. (biological n=4). A One-way repeated ANOVA with a Bonferroni correction on selected columns was performed to compare means between groups. P-value<0.05 was considered significant (* p-value<0.05, target group versus DMSO vehicle control, ## p-value<0.01, ### p-value<0.001).

5.3.3 Evidence for distinct Ca^{2+} handling in primary HCASMCs

Primary HSVSMCs demonstrated an ALK5-dependent increase in AngII-driven intracellular Ca^{2+} mobilisation following TGF-β_1 stimulation. Since SMC phenotype and regulation of contractility differs between distinct vascular beds, the next goal was to determine AngII responses in BMP-9 and/or TGF-β_1-treated primary HCASMCs (Turner et al., 2007). HCASMCs serum-starved for 72-h were treated with respective ligands in absence and presence of SB525334 and subjected to the previously described protocol.

Although cells were viable evidenced by enhanced IM-induced intracellular Ca^{2+} release primary HCASMCs showed negligible response to AngII stimulation (mean AngII-induced fluorescence intensity ± S.E.M., vehicle control: 15.32 ± 9.382) (Figure 5-5 A and C). Paralleling findings from HSVSMCs, BMP-9 did not significantly affect AngII-driven Ca^{2+} release compared to vehicle-treated controls (Figure 5-5 A and B). However, there was a visible trend towards a reduction in Ca^{2+} responses (BMP-9: 4.773 ± 1.928, DMSO/vehicle control: 15.32 ± 9.382, p=0.50). TGF-β_1 and SB525334 treatment alone had no significant effect on AngII-mediated Ca^{2+} release (Figure 5-5 A and B). Nevertheless, SB525334-treated cells tended to elicit slightly higher fluorescence intensity responses compared to DMSO/vehicle-treated controls (SB525334: 32.52 ± 15.86, DMSO/vehicle control 15.32 ± 9.382, p=0.37) (Figure 5-5 A and B). In contrast, in the presence of SB525334, BMP-9 and TGF-β_1 co-stimulation significantly suppressed AngII Ca^{2+} responses compared to vehicle-treated controls (SB525334/BMP-9 + TGF-β_1 9.423 ± 5.211 versus SB525334/vehicle control 32.52 ± 15.86, $p<0.05$) (Figure 5-5 A and B).

Taken together, primary HCASMCs displayed higher IM-driven intracellular Ca^{2+} mobilisation than primary HSVSMCs potentially indicating increased intracellular Ca^{2+} storage which remained unresponsive to AngII treatment. In contrast to HSVSMCs, ALK5 inhibition in HCASMCs showed a non-significant trend towards an increase in AngII Ca^{2+} responses potentially suggesting that the ALK5 receptor negatively regulates arterial SMC contractility. Finally, BMP-9 alone or in combination with TGF-β_1 suppressed AngII responses indicating that SMAD1, and potentially SMAD5, pathway agonism may also negatively regulate arterial SMC contractility.

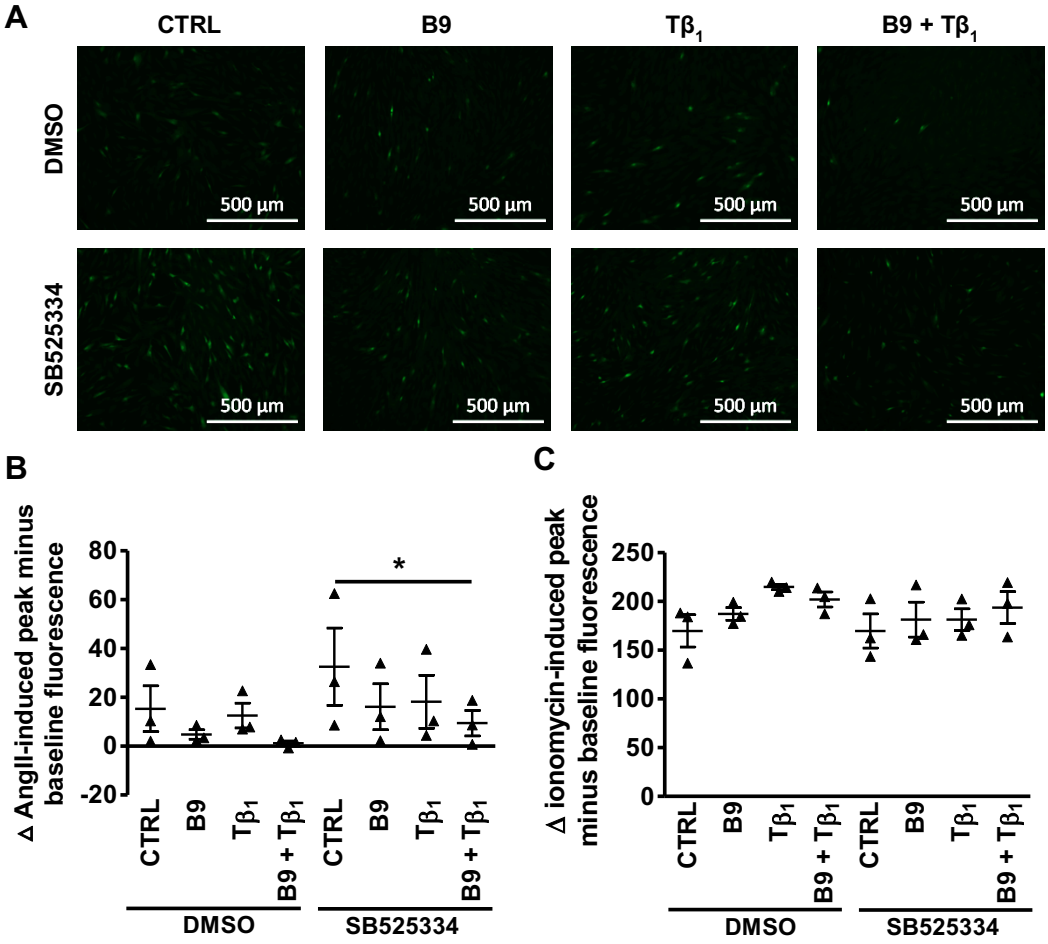

Figure 5-5 Evidence for distinct Ca^{2+} handling in primary HCASMCs. 80% confluent primary HCASMCs were quiesced in 0.2% FCS media for 72-h. Media was removed and cells were divided into two groups. Whereas one group of cells was incubated in 0.2% FCS media containing the ALK5 inhibitor SB525334 (10 μM) the other group was incubated in 0.2% FCS media containing vehicle control (DMSO). Following a 30-min incubation period media was removed and both sets of cells were subdivided into 4 groups. Both sets of 4 were stimulated with BMP-9 (10 ng/ml), TGF-β_1 (10 ng/ml), both ligands and vehicle control in the presence of DMSO or SB525334 respectively. Cells were analysed at 24-h following the previously described protocol (Figure 5-2). (**A**, top and bottom panel) Images show AngII-induced maximum fluorescence for respective treatment groups. (**B**) Graph shows IM-induced amplitudes. (**C**) Graph shows AngII-induced amplitudes. (**D** and **E**) Data are presented as mean ± S.E.M. (biological n=2, technical n=3). A One-way repeated ANOVA with a Bonferroni correction on selected columns was performed to compare means between groups. P-value<0.05 was considered statistically significant (* p-value<0.05).

5.3.4 Single cell resolution uncovers HSVSMC population heterogeneity

Whole frame fluorescence intensity analysis revealed enhanced TGF-β_1/ALK5-driven AngII Ca^{2+} responses in primary HSVSMCs. On closer inspection, fluorescence intensity changed over time and appeared to be different for every cell captured within one frame. Furthermore, this phenomenon appeared to be independent of the treatment group. Taken together, these observations prompted development of a protocol for analysing and presenting AngII-driven mobilisation of intracellular Ca^{2+} stores on a single cell basis.

Using live cell recordings and drawing single regions of interest around cells as described in section 2.7.2, Ca^{2+} mobilisation by AngII was analysed in individual cells (Figure 5-6 A). The aim was to calculate the geometric mean for all AngII-driven responses in each individual well (1 patient, technical n=3/condition, Figure 5-6 C). Since some AngII-induced amplitudes displayed negative values the constant 4.926025 was added to each value to prevent negative values following $\log_{10}$-transformation. Values from each well were averaged and this average was exponentiated to the basis of 10 ($10^{\wedge(average)}$). The constant 4.926025 was subtracted from each exponentiated value to generate the geometric mean.

The histogram for the first set of patient cells displayed a bimodal distribution of AngII-driven Ca^{2+} responses for all treatment groups (Figure 5-6 B). Subsequent analysis of two additional sets of patient cells confirmed these preliminary findings (Figure 5-8 A). Although cell populations displayed heterogeneity in a ligand-independent manner, TGF-β_1-treated SMC populations displayed a trend towards less non-responsive cells (bin 0, red bar versus black, blue and purple bars) and more cells displaying medium and higher AngII-driven responses compared to the other treatment groups (bin 10, 20 and 30 → red bar versus black, blue and purple bars). In line with this finding, TGF-β_1-treated HSVSMCs demonstrated an increased geometric mean compared to vehicle-treated controls paralleling findings following whole frame fluorescence analysis (geometric mean AngII-induced fluorescence intensity amplitude ± S.E.M., TGF-β_1 17.55 $\pm$ 6.411, vehicle control 5.641 $\pm$ 1.699, $p<0.05$) (Figure 5-7 B). Furthermore, BMP-9 attenuated the ability of TGF-β_1 to increase AngII-driven

intracellular Ca^{2+} release in single cells (BMP-9 + TGF-β_1 7.613 $\pm$ 3.065 versus vehicle control 5.641 $\pm$ 1.699, $p>0.05$). Finally, a Lowess curve fit was generated from 3 histograms derived from 3 individual sets of patient cells to highlight the ability of TGF-β_1 to induce a more homogeneous cell population (Figure 5-8 B, red line versus black, blue and purple lines).

In conclusion, single cell fluorescence analysis paralleled findings following whole frame fluorescence analysis and uncovered a heterogeneous distribution of AngII-driven Ca^{2+} responses within each treatment group. Moreover, BMP-9 blunted the ability of TGF-β_1 to induce a more homogeneous AngII response pattern.

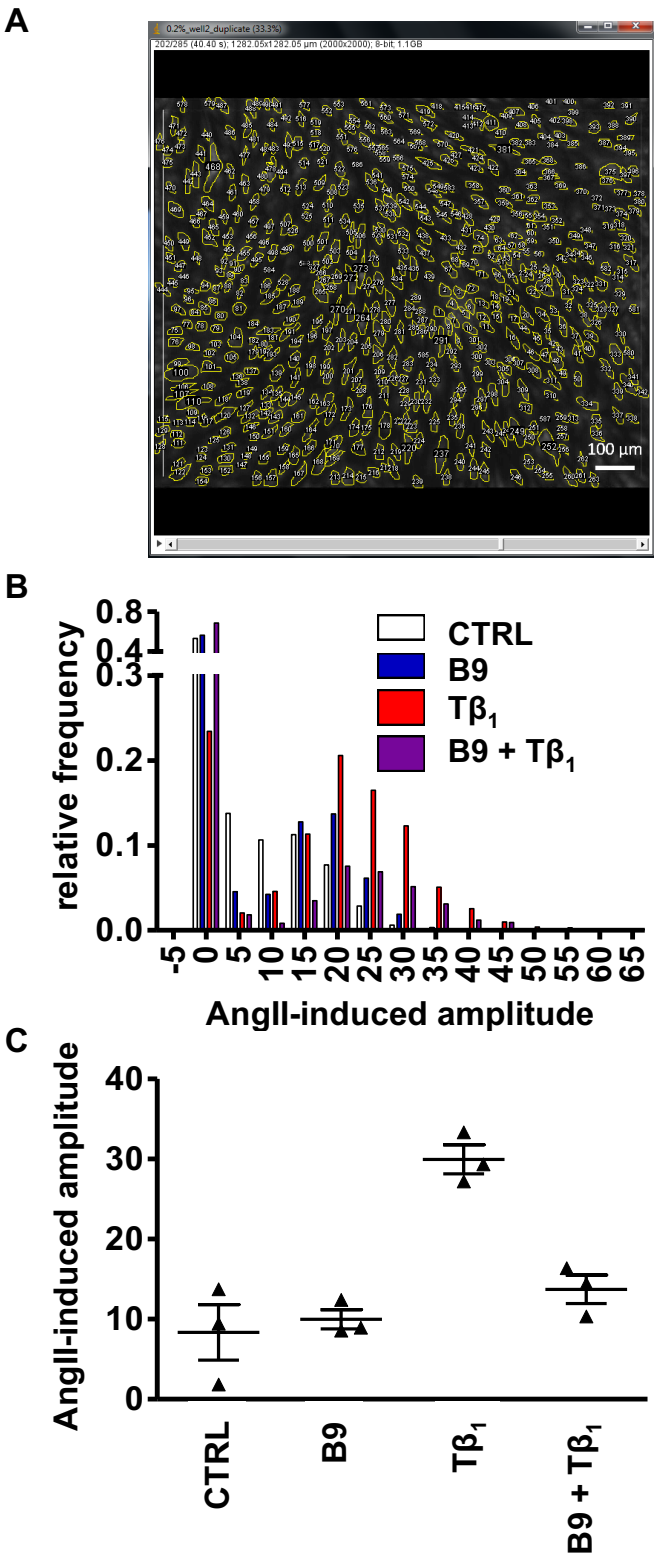

Figure 5-6 Protocol for assessing intracellular Ca^{2+} release in single primary HSVSMCs. 80% confluent primary HSVSMCs were quiesced in 0.2% FCS media for 72-h. Media was replaced with fresh 0.2% FCS stimulation media containing BMP-9 (10 ng/ml, B9), TGF-β_1 (10 ng/ml, Tβ_1), both ligands and vehicle control. Calcium handling was determined following the previously described protocol. (**A**) Video files of 6-min trace recordings were imported into the ImageJ software to determine intracellular Ca^{2+} release in single primary HSVSMCs. (**B**) Graph represents distribution of AngII-induced amplitudes for each cell from each treatment group captured within one frame (biological n=1, technical n=3). (**C**) Graph shows the geometric mean of all AngII-induced amplitudes for each treatment group. Data are presented as mean ± S.E.M. (biological n=1, technical n=3).

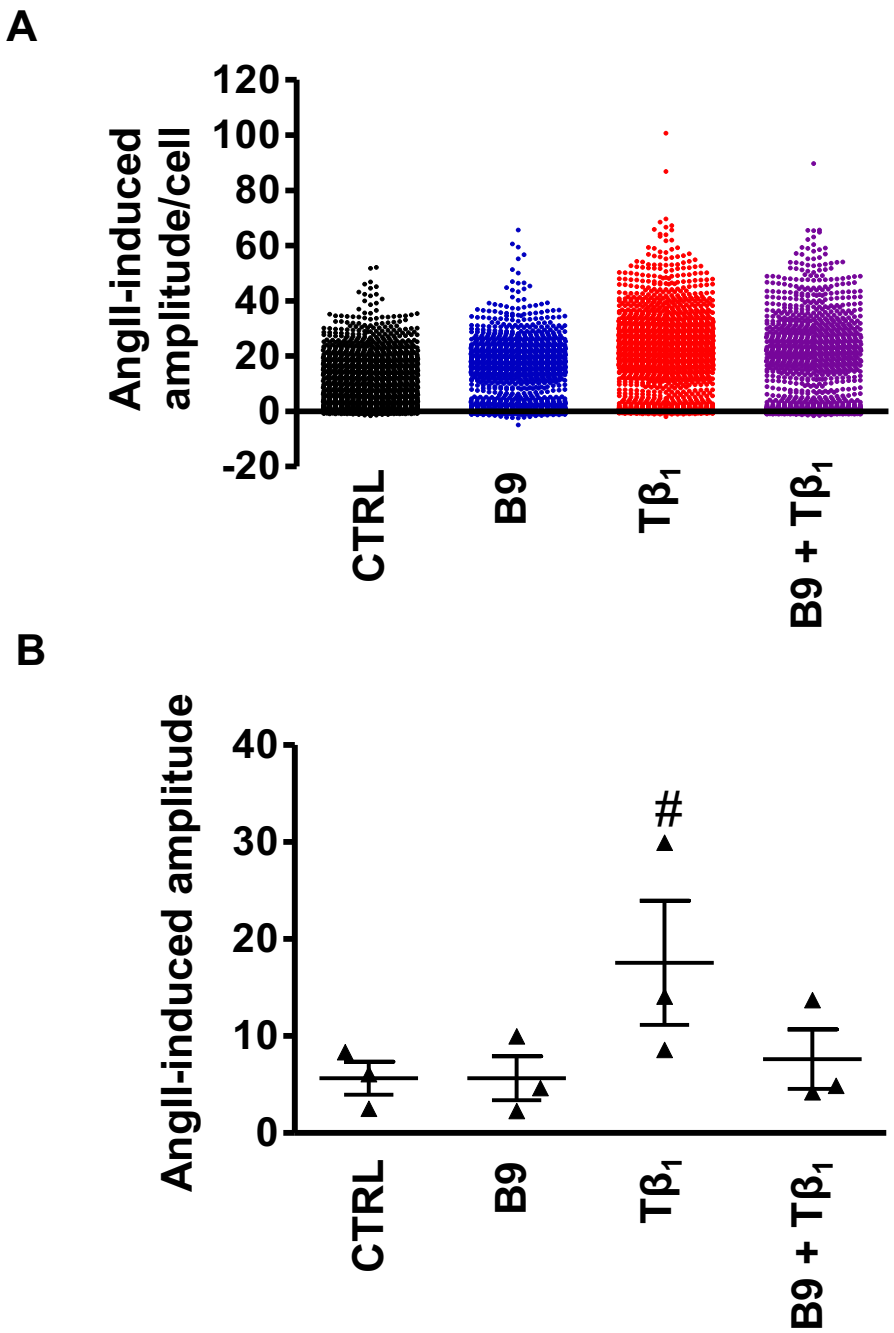

Figure 5-7 Single cell resolution reveals HSVSMC population heterogeneity (A). 80% confluent primary HSVSMCs were quiesced in 0.2% FCS media for 72-h. Media was replaced with fresh 0.2% FCS stimulation media containing BMP-9 (10 ng/ml, B9), TGF-β_1 (10 ng/ml, Tβ_1), both ligands and vehicle control. Calcium handling was determined following the previously described protocol. Video files of 6-min trace recordings were imported into the ImageJ software to determine intracellular Ca^{2+} release in single primary HSVSMCs. (**A**) Each dot represents one AngII-induced amplitude from each cell per treatment group (biological n=3). (**B**) Graph shows the geometric mean of all AngII-induced amplitudes for each treatment group. Data are presented as mean ± S.E.M. (biological n=3). A One-way repeated ANOVA with Tukey's correction was performed to compare means between groups. P-value<0.05 was considered statistically significant (# p-value<0.05, target group versus vehicle control).

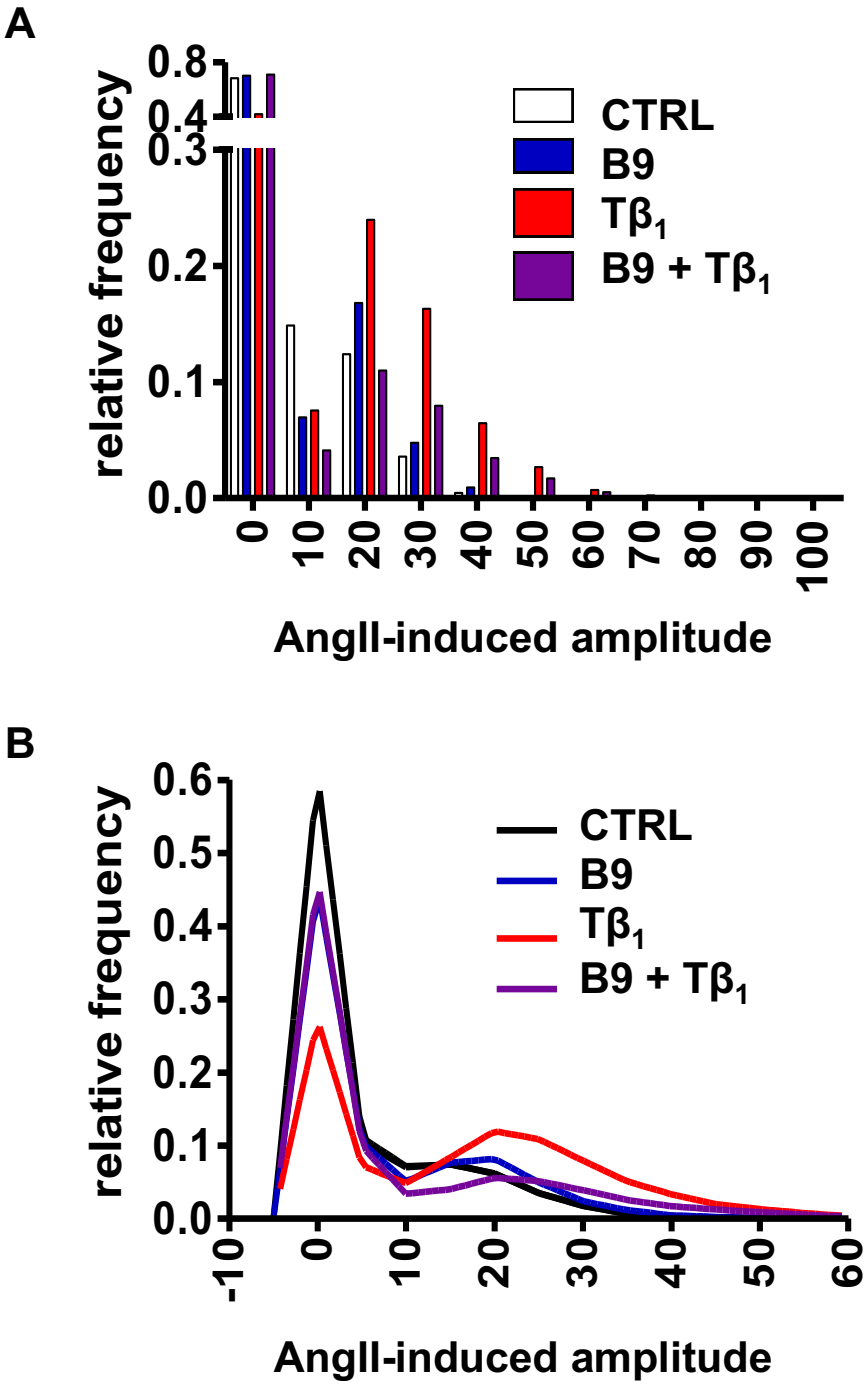

Figure 5-8 Single cell resolution reveals HSVSMC population heterogeneity (B). 80% confluent primary HSVSMCs were quiesced in 0.2% FCS media for 72-h. Media was replaced with fresh 0.2% FCS stimulation media containing BMP-9 (10 ng/ml, B9), TGF-β_1 (10 ng/ml, Tβ_1), both ligands and vehicle control. Calcium handling was determined following the previously described protocol. Video files of 6-min trace recordings were imported into the ImageJ software to determine intracellular Ca^{2+} release in single primary HSVSMCs. (**A**) Graph demonstrates distribution of AngII-induced amplitudes for each cell from each treatment group captured within one frame (biological n=3). (**B**) A Lowess curve fit was generated from AngII-induced amplitude distribution histograms from 3 patients.

5.3.5 AngII-induced intracellular Ca^{2+} mobilisation is mediated via AT_1R in primary HSVSMCs

The next experiment aimed to establish whether AngII signalled via the AT_1R or the AT_2R in primary HSVSMCs. To address this question, the pharmacological AT_1R inhibitor losartan was utilised to determine AngII-dependent Ca^{2+} mobilisation in the absence and presence of TGF-β_1. Losartan is a non-peptide-based AT_1R antagonist which prevents AngII-dependent AT_1R activation (Chiu et al., 1991; Rhaleb et al., 1991). In vSMCs losartan attenuated AngII-dependent intracellular/extracellular Ca^{2+} influx and subsequent vSMC and vessel contraction (Chiu et al., 1991).

Most group comparisons did not reach statistical significance in this set of experiments. Nevertheless, AT_1R blockade with losartan appeared to blunt AngII-induced Ca^{2+} release as evidenced by absence of fluorescence intensity following stimulation (mean AngII-induced fluorescence intensity amplitude ±S.E.M., losartan: -1.218 ± 1.064, vehicle control: 16.11 ± 5.813, $p>0.05$) (Figure 5-9 A and B). Opposed to previous findings, TGF-β_1-treated HSVSMCs did not display a significant increase in Ca^{2+} release in response to AngII. However, TGF-β_1-treated cells tended to display slightly higher AngII-induced fluorescence intensity amplitudes (TGF-β_1: 31.06 ± 13.53, vehicle control: 16.11 ± 5.813, $p>0.05$). Losartan significantly attenuated AngII-induced Ca^{2+} mobilisation in TGF-β_1- versus TGF-β_1/vehicle-treated HSVSMCs (losartan/TGF-β_1: -0.5906 ± 0.2766, TGF-β_1: 31.06 ± 13.53, $p<0.05$).

Although most differences between groups did not achieve statistical significance due to enhanced inter-patient variability, losartan consistently blunted AngII-induced Ca^{2+} mobilisation in primary HSVSMCs. Furthermore, it may be speculated that TGF-β_1/ALK5 signalling may sensitise the AngII/AT_1R/IP3 system potentially suggesting synergism between these two pathways.

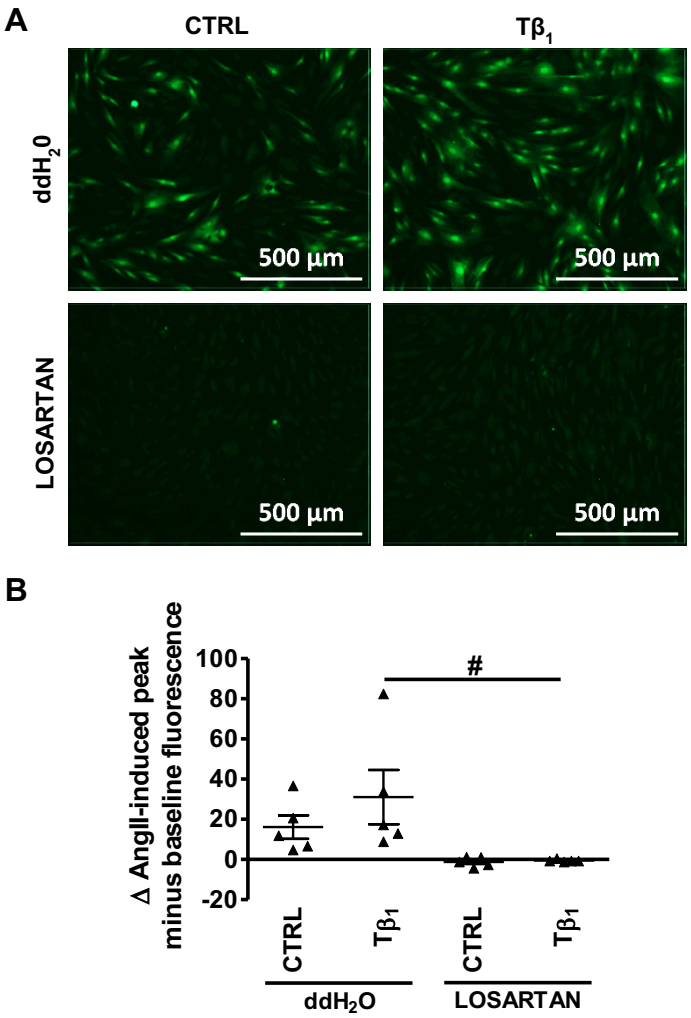

Figure 5-9 AngII triggers intracellular Ca^{2+} release via AT_1R in primary HSVSMCs. 80% confluent cells were quiesced in 0.2% FCS media for 72-h. Cells were analysed at 24-h following the previously described protocol (Figure 5-2) with the following addition. (**A**) Following incubation with Cal520 cells were either subjected to 25-min incubation in losartan (10 μM)/HEPES solution (bottom panel) or vehicle control (ddH_20)/ HEPES solution (top panel). Images show AngII-induced maximum fluorescence for respective treatment groups. (**B**) Graph shows AngII-induced amplitudes. Data are presented as mean ± S.E.M. (biological n=5). A One-way repeated ANOVA with a Bonferroni correction on selected columns was performed to compare means between groups. P-value<0.05 was considered statistically significant (# p-value<0.05).

5.3.6 Pharmacological ROCK blockade does not prevent AngII-mediated intracellular Ca^{2+} mobilisation in primary HSVSMCs

Fasudil is a drug which inhibits ROCK and PKC activity thereby promoting vSMC relaxation and subsequent vasorelaxation (Asano et al., 1998; Seto et al., 1991). This experiment was performed to evaluate whether AngII-mediated Ca^{2+} mobilisation and potential cell contraction triggered Ca^{2+} indicator (Cal520™) quenching and a subsequent false increase in fluorescence intensity.

Compared to untreated controls, fasudil-treated HSVSMCs displayed a similar amount of AngII-driven Ca^{2+} release (mean AngII-induced fluorescence intensity, fasudil ± S.E.M.:18.27 ± 8.895, vehicle control 23.17 ± 5.018, $p>0.05$) (Figure 5-10 A and B). In line with previous findings, TGF-β_1-stimulated cells demonstrated an increase in AngII-mediated Ca^{2+} mobilisation versus vehicle-treated controls (TGF-β_1: 55.16 ± 15.53, vehicle control: 23.17 ± 5.018, $p<0.05$). In the presence of fasudil, TGF-β_1-treated cells did not elicit a significant increase in AngII-dependent Ca^{2+} responses compared to vehicle-treated controls although cells tended to display higher fluorescence intensities in the presence of TGF-β_1 (fasudil/TGF-β_1: 42.7 ± 14.64, fasudil/vehicle control: 18.27 ± 8.895, $p>0.05$).

Taken together, ROCK/PKC inhibition with fasudil did not affect AngII-dependent Ca^{2+} responses in primary HSVSMCs. Hence, potential Ca^{2+}-dependent cell contraction did not appear to induce Cal520 quenching-and a subsequent false increase in fluorescence intensity.

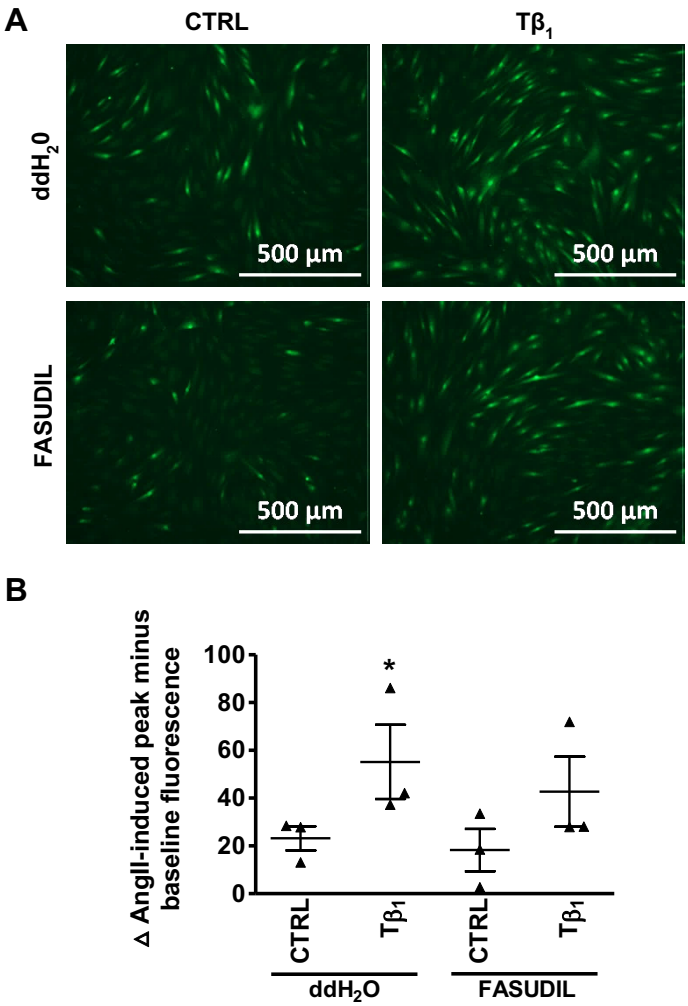

Figure 5-10 Pharmacological Rho-kinase blockade does not prevent AngII-induced intracellular Ca^{2+} release in primary HSVSMCs. 80% confluent cells were quiesced in 0.2% FCS media for 72-h. Cells were analysed at 24-h following the previously described protocol (Figure 5-2) with the following addition. (**A**) Following incubation with Cal520 cells were either subjected to 25-min incubation in fasudil (10 μM)/HEPES solution (bottom panel) or vehicle control (ddH_20)/HEPES solution (top panel). Images show AngII-induced maximum fluorescence for respective treatment groups. (**B**) Graph shows AngII-induced amplitudes. Data are presented as mean ± S.E.M. (biological n=3). A One-way repeated ANOVA with a Bonferroni correction on selected columns was performed to compare means between groups. P-value<0.05 was considered statistically significant (* p-value<0.05, target group versus ddH_20 vehicle control).

5.3.7 TGF-β_1 represses *MAS1* mRNA expression levels in HSVSMCs

Data presented in sections 4.3.7 and 4.3.12 demonstrated that TGF-β_1 drove contractile gene expression via ALK5 in primary HSVSMCs. Moreover, TGF-β_1 ALK5-dependently increased AngII-dependent intracellular Ca^{2+} mobilisation in HSVSMCs which was prevented in the presence of BMP-9. The next aim was to assess *AGTR1* (encodes AT_1R) and *MAS1* (encodes MAS proto-oncogene receptor) mRNA expression levels to determine whether changes in receptor expression levels in response to ligand treatment might explain TGF-β_1/AT_1R agonism and BMP-9/AT_1R antagonism. MAS1 is the alternative receptor for angiotensin peptide Ang-(1-7) (Santos et al., 2003) and antagonises AngII/AT_1R signalling (Kostenis et al., 2005).

BMP-9-treated HSVSMCs displayed a reduction in *AGTR1* mRNA expression levels compared to vehicle-treated controls (RQ_{mean} + error, BMP-9: 0.146 + 0.128, vehicle control: 1 + 0.406, $p<0.05$) (Figure 5-11 A). In contrast, TGF-β_1 ALK5-dependently prevented BMP-9-mediated downregulation of *AGTR1* mRNA levels (BMP-9 + TGF-β_1: 0.99 + 0.465, BMP-9: 0.146 + 0.128, $p<0.05$). Moreover, TGF-β_1 suppressed *MAS1* mRNA levels via ALK5 (TGF-β_1: 0.043 + 0.017, vehicle control: 1 + 0.624 [$p<0.001$] and SB525334/TGF-β_1: 2.876 + 0.4 [$p<0.001$]) (Figure 5-11 B). BMP-9 had no effect on *MAS1* mRNA levels compared to vehicle-treated controls. Finally, qRT-PCR did not detect *AGTR2* (encodes AT_2R) mRNA expression levels in HSVSMCs (data not shown).

Overall, BMP-9 suppressed *AGTR1* receptor mRNA expression levels. TGF-β_1 ALK5-dependently suppressed *MAS1* receptor expression levels indicating potential AT_1R agonism since the MAS1 receptor antagonises AT_1R function (Kostenis et al., 2005).

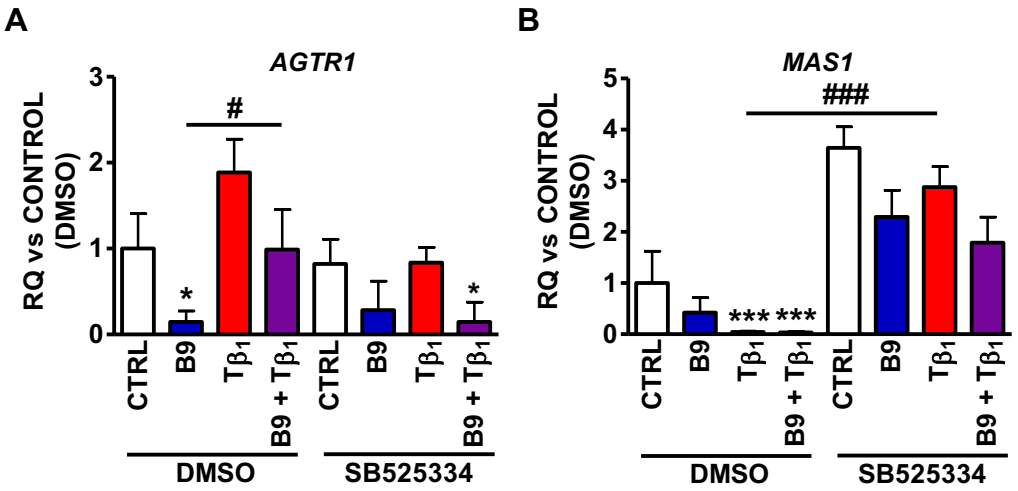

Figure 5-11 TGF-β_1 suppresses *MAS1* gene expression via ALK5. 80% confluent primary HSVSMCs were quiesced in 0.2% FCS media (MEDIA1) for 72-h. To achieve pharmacological ALK5 inhibition prior to ligand stimulation, the first 4 groups were incubated in MEDIA1 containing 10 μM SB525334 for 30 min. In parallel, the second 4 groups were incubated in MEDIA1 containing DMSO vehicle (1:1,000) for 30 mins. Media was replaced with fresh MEDIA1 containing recombinant human BMP-9 (10 ng/mL), TGF-β_1 (10 ng/mL) ± DMSO (1:1,000) or SB525334 (10 μM). After 24-h stimulation, primary HSVSMCs were lysed and subjected to RNA extraction. Reverse transcription was performed to generate cDNA. Quantitative RT-PCR was performed to determine relative *AGTR1* (**A**) and *MAS1* (**B**) mRNA expression levels. Relative target gene expression was normalised to *UBC* expression to determine δCT values, which were used to calculate relative quantification (RQ) values (target group versus DMSO vehicle control). Data are presented as RQ mean + RQ_{max} mean (biological n=3). A One-way repeated ANOVA with a Tukey's correction was performed to compare groups on the basis of δCT values. P-value<0.05 was considered statistically significant (* p-value<0.05 and *** p-value<0.001, target group versus DMSO vehicle control, ### p-value<0.001).

5.4 Discussion

The first aim of this chapter was to establish a robust protocol for assessing AngII-mediated intracellular Ca^{2+} mobilisation in primary human vSMCs. Following 72-h quiescence HSVSMCs labelled with Cal520™, a fluorogenic, calcium-sensitive dye, demonstrated an increase in fluorescence intensity (Ca^{2+} ions binding to Cal520™ probe) following AngII stimulation indicating intracellular mobilisation of Ca^{2+} stores in the absence of extracellular Ca^{2+}. Within 30 s following AngII stimulation fluorescence intensity reached its peak and subsequently returned to baseline levels at 60s. Trace morphology was similar to traces obtained from Fura-2-loaded primary RASMCs following AngII stimulation in the absence of extracellular Ca^{2+} (Bouillier et al., 2000). AngII-induced amplitudes were subsequently calculated and served as a surrogate marker of SMC contractility. Ionomycin stimulation induced a rapid maximum increase in fluorescence intensity reflecting maximum release of intracellular Ca^{2+} stores. Firstly, IM-induced fluorescence intensity confirmed cell viability during fluorescence trace imaging and, secondly, IM-induced amplitudes gave a rough estimation of the amount of intracellular Ca^{2+} stores since experiments were performed in a Ca^{2+}-free environment. Fluorescence intensity levels returned to baseline at 60 s following IM stimulation. Previous research showed that this drop in cytosolic [Ca^{2+}] in primary RASMCs following IM stimulation was mediated by the cell membrane-based Na^{+}/Ca^{2+} exchanger (Smith et al., 1989). Taken together, this Ca^{2+} handling protocol enabled robust investigation of AngII-dependent mobilisation of intracellular Ca^{2+} stores in primary human vSMCs.

Interestingly, initial findings also showed that serum treated HSVSMCs did not respond to AngII stimulation suggesting differential regulation of Ca^{2+} handling in proliferating SMCs. Indeed, studies investigating Ca^{2+} signalling remodelling during vSMC phenotype switching revealed a decrease in voltage-dependent membrane-bound L-type Ca^{2+} channel, SR-bound ryanodine type 3 Ca^{2+} release channel and SR-bound SERCA2A expression levels in proliferating vSMCs (Gollasch et al., 1998; Lipskaia et al., 2005; Vallot et al., 2000). Corriu *et al.* demonstrated that AngII triggered IP3 production and subsequent increase in cytosolic [Ca^{2+}] via AT_1R in quiesced primary RASMCs indicating functional AT_1R/PLC/IP3/SR Ca^{2+} release coupling (Corriu et al., 1994). The authors went on to show that AngII also bound to AT_1R on proliferating RASMCs triggering an

increase in cytosolic IP3 levels. However, the increase in IP3 did not induce SR Ca^{2+} release as opposed to findings in quiesced controls. This suggests that proliferating vSMCs are resistant to AngII-dependent SR Ca^{2+} release and subsequent contraction although AngII induces IP3 production. Hence, it may be speculated that SR-bound IP3R density is modulated in proliferating HSVSMCs. It must also be noted that serum-driven suppression of AngII-mediated Ca^{2+} release may potentially reflect an increase in serum-derived BMP-9 concentrations given the fact that serum displays biological BMP-9 activity (David et al., 2008). A future experiment should investigate the effect of neutralising BMP-9 antibodies on AngII-dependent Ca^{2+} release in 15% FCS-cultured primary HSVSMCs. In conclusion, it may be speculated that proliferating/de-differentiated vSMCs are resistant to AngII-induced Ca^{2+} release and contraction. Preliminary findings from this study warrant further experiments comparing AngII-induced Ca^{2+} transients and underlying mechanisms in proliferating versus quiesced primary HSVSMCs in the future.

After establishing a reproducible and robust Ca^{2+} handling protocol the next step was to investigate the effect of long-term BMP-9 and/or TGF-β_1 stimulation on AngII-dependent Ca^{2+} transients in primary HSVSMCs and HCASMCs. 24-h TGF-β_1 stimulation of primary HSVSMCs triggered an increase in AngII-dependent Ca^{2+} mobilisation compared to untreated controls, potentially indicating increased SMC contractility. This effect was attenuated in the presence of the ALK5 inhibitor SB525334 and BMP-9 demonstrating that TGF-β_1-driven effects were ALK5-dependent and that BMP-9 demonstrated TGF-β_1/ALK5 antagonism. These findings are partially in line with previously presented data from this study which showed that ligand-independent and -dependent ALK5 activation positively regulated contractile marker expression in primary HSVSMCs. In contrast to findings in HSVSMCs, TGF-β_1 treatment had no effect on AngII-regulated SR Ca^{2+} release in primary HCASMCs. Most differences between HCASMC treatment groups were not statistically significant because of inter-patient variability. However, there was a slight trend towards an increase in AngII-dependent Ca^{2+} responses in SB525334-treated cells versus vehicle-treated controls potentially suggesting ALK5 as a negative regulator of Ca^{2+} release in this cell type. In addition, there was a slight trend towards a suppression of Ca^{2+} transients in BMP-9-treated cells compared to vehicle-treated controls partially

paralleling trends in HSVSMCs. Moreover, IM-induced total SR Ca^{2+} release was higher in untreated HCASMCs than HSVSMCs indicating differential regulation of total intracellular Ca^{2+} storage in these two cell types. More n numbers should be added to these sets of experiments to overcome inter-patient variability in the future. Nevertheless, these findings raise several questions. Firstly, which mechanisms might explain why TGF-β_1/ALK5 signalling positively regulates AngII-triggered Ca^{2+} transients in HSVSMCs and what does this mean in the context of a contractile SMC phenotype and SVG disease? Secondly, how does BMP-9 antagonise this effect? Thirdly, why do HCASMCs display differential regulation of Ca^{2+} handling compared to HSVSMCs?

To address the first question AngII-driven Ca^{2+} responses were assessed in TGF-β_1 and vehicle-treated cells in the absence and presence of the AT_1R blocker losartan to establish whether AngII transduced its signal via the AT_1R or AT_2R. In TGF-β_1-treated cells, losartan significantly prevented AngII-mediated Ca^{2+} transients. In contrast to previous findings and in the absence of losartan, TGF-β_1-treated HSVSMCs did not display an increase in AngII-mediated Ca^{2+} release compared to untreated controls. The lack of significance between these two groups may be explained by enhanced inter-patient variability. To overcome this limitation more n numbers should be added to this experiment in the future. Although most differences between groups were not statistically significant, losartan-treated cells did not respond to AngII stimulation as evidenced by absence of increase in fluorescence intensity. These results show that AngII mediates intracellular Ca^{2+} mobilisation via AT_1R in HSVSMCs.

These findings prompted evaluation of Ang receptor mRNA expression levels following 24-h TGF-β_1 stimulation in absence and presence of SB525334. Whereas *AGTR1* mRNA levels were not affected, TGF-β_1 ALK5-dependently suppressed *MAS1* mRNA levels. Kostenis *et al*. found that the GPCR Mas1 receptor formed a hetero-oligomeric complex with AT_1R in CHO-K1 cells and that Mas1 overexpression dampened AngII-induced IP3 production and subsequent intracellular Ca^{2+} mobilisation (Kostenis et al., 2005). The same study demonstrated that genetic ablation of *Mas1* in mice resulted in an increase in AngII-induced vasoconstriction in mesenteric microvessels compared to wild-type controls indicating that the Mas receptor negatively regulates AngII/AT_1R-driven

vasoconstriction. Hence, it may be speculated that TGF-β_1/ALK5-dependent *MAS1* suppression may potentiate AngII/AT_1R signalling by blunting Mas-dependent AT_1R inhibition. To address this hypothesis, a future experiment should assess AngII-mediated Ca^{2+} transients in the presence of siRNA-mediated *MAS1* suppression to determine whether cells demonstrate an increase in AngII Ca^{2+} responses in HSVSMCs. A second experiment should assess whether *MAS1* overexpression rescues TGF-β_1-dependent downregulation of *MAS1* and subsequently dampens AngII-driven Ca^{2+} mobilisation. A third experiment should investigate the antagonistic interaction between Ang (1-7) and TGF-β_1/ALK5 signalling in the context of AngII-driven Ca^{2+} responses in HSVSMCs. In addition, it may be speculated that TGF-β_1/ALK5 signalling modulates downstream components of Ca^{2+} handling such as IP3R expression levels, SERCA2A expression levels/activity and total SR Ca^{2+} content in HSVSMCs. Furthermore, it is conceivable that TGF-β_1/ALK5 signalling may also affect contraction-sensitising pathways such PKC or RhoA/ROCK signalling in this cell type.

In line with presented findings from primary HSVSMCs, Bouillier *et al.* found that primary aortic SMCs from hypertensive rats treated with TGF-β_1 for 24-h displayed enhanced intracellular Ca^{2+} mobilisation in response to AngII stimulation compared to normotensive controls (Bouillier et al., 2000). Interestingly, pharmacological inhibition of PKC with calphostin inhibited long-term stimulatory effects of TGF-β_1 on AngII-driven Ca^{2+} release indicating that TGF-β_1 signalling may synergise with PKC. Furthermore, pharmacological inhibition of tyrosine kinase with genistein and global protein synthesis with cycloheximide also attenuated TGF-β_1-driven increases in AngII-dependent Ca^{2+} transients in hypertensive RASMCs, suggesting complex interaction of regulatory signalling pathways. Gao *et al.* investigated the role of TGF-β_1 in airway SMC hypercontractility in the context of asthma (Gao et al., 2013). Pharmacological SERCA inhibition with thapsigargin was utilised to determine total SR Ca^{2+} content in TGF-β_1-treated and untreated primary rat airway SMCs. Results demonstrated that TGF-β_1-treated SMCs released more Ca^{2+} from SR in response to thapsigargin than vehicle-treated controls indicating that TGF-β_1 induced an increase in total SR Ca^{2+} content. Corroborating Gao's findings, Kim *et al.* demonstrated that TGF-β_1-stimulated murine airway SMCs displayed enhanced intracellular Ca^{2+} mobilisation in response to bradykinin treatment indicating

hypercontractility (Kim et al., 2005). Based on these findings, it may be speculated that TGF-β_1 drives SERCA expression levels and/or activity thereby modulating SR Ca^{2+} content in SMCs. Future experiments should address the effect of TGF-β_1 on SR Ca^{2+} content and SERCA expression and activity levels in primary HSVSMCs.

Opposing these findings, Sharma *et al.* showed that TGF-β_1 dose-dependently attenuated AngII-dependent Ca^{2+} mobilisation in primary RASMCs (Sharma et al., 2003). The study also found that neutralising TGF-β_1 antibodies reversed hyperglycaemia-induced impairment of AngII-mediated Ca^{2+} release indicating TGF-β_1 as a pathological driver of vascular impairment in the context of diabetes. Moreover, aortas from diabetic rats displayed a reduction in IP3R expression levels which was reversed by systemic administration of neutralising TGF-β_1 antibodies suggesting that TGF-β_1 may impair AngII-driven Ca^{2+} release by suppressing IP3R expression in the context of diabetes. Partially in line with this finding, Zhu's study showed that 30-min TGF-β_1-treated primary RASMCs from normotensive and hypertensive rats displayed a reduction in AngII-induced increase in cytosolic [Ca^{2+}] in the presence of extracellular Ca^{2+} (Zhu et al., 1995). However, no difference was reported in the absence of extracellular Ca^{2+} contrasting findings by Sharma *et al.*.

Both Bouillier's and Zhu's study showed that TGF-β_1-treated primary aortic SMCs from normotensive rats did not display altered AngII-dependent Ca^{2+} responses compared to untreated controls (Bouillier et al., 2000; Zhu et al., 1995). These findings are in line with presented results from primary HCASMCs which show that TGF-β_1 does not affect AngII-mediated Ca^{2+} responses contrasting results from HSVSMCs. Moreover, there was a trend towards an increase in AngII-driven Ca^{2+} release in the presence of pharmacological ALK5 inhibition. A study investigating functional aortic changes in the context of LDS found that SMC-specific genetic ablation of *Tgfbr2* in mice triggered aortic hypercontractility in response to noradrenaline indicating that functional vSMC TGF-β signalling may negatively regulate contractile responses in the systemic arterial system (abstract) (Zhu et al., 2017). Distinct effects of TGF-β_1 on Ca^{2+} handling in HCASMCs and HSVSMCs may also be explained based on differential embryonic and post-natal development. Thakali *et al.* investigated mechanisms in venous

SMCs underlying venous SMC resistance to calcium channel blocker treatment (Thakali et al., 2010). The authors demonstrated that intracellular Ca^{2+} stores silenced L-type Ca^{2+} channels in venous SMCs, a mechanism absent in arterial SMCs. Differential mechanisms underlying Ca^{2+} handling in HSVSMCs and HCASMCs have not been studied before. However, Turner *et al.* established that HSVSMCs displayed an elevated capacity to de-differentiate compared to matched IMAG SMC controls (Turner et al., 2007). Hence, it appears conceivable that Ca^{2+} handling may also underlie differential regulation in venous versus arterial beds.

Taken together these studies demonstrate that TGF-β_1 regulates Ca^{2+} mobilisation in primary human vSMCs in distinct ways. TGF-β_1-dependent modulation of agonist-driven increase in Ca^{2+} mobilisation appears to depend on many factors including SMC type (venous, arterial or airway), species (human, rat or mouse), the length of TGF-β_1 stimulation and whether vSMCs derive from healthy normotensive/normo-glycaemic or diseased hypertensive/hyperglycaemic animals. Primary HSVSMCs utilised for Ca^{2+} handling experiments were not matched to donor patient phenotypes. Since many CABG patients suffer from additional co-morbidities including systemic hypertension and T2DM, which have been shown to influence experimental SMC Ca^{2+} handling, it is conceivable that primary HSVSMCs may also react differently to external stimuli depending on the patient's co-morbidities. This may also partially explain enhanced inter-patient variability in performed Ca^{2+} handling experiments presented in this chapter. This potential bias may be addressed by phenotyping CABG patients in more detail in the future and then link these phenotypical characteristics such as hypertension or T2DM to AngII-dependent Ca^{2+} responses in isolated HSVSMCs.

In addition to attenuating long-term stimulatory effects of TGF-β_1 on AngII-driven intracellular Ca^{2+} release, PKC inhibition with calphostin also dampened AngII-dependent Ca^{2+} mobilisation in untreated control rat vSMCs, indicating that PKC directly regulated AngII/AT_1R-dependent SR Ca^{2+} release (Bouillier et al., 2000). Nagumo *et al.* demonstrated that fasudil inhibited ROCK thereby preventing MLCP inhibition and promoting SMC relaxation (Nagumo et al., 2000). Moreover, the same study showed that fasudil also inhibited PKC, however to a lesser extent. These findings prompted evaluation of fasudil-mediated

ROCK/PKC blockade on acute AngII-induced intracellular Ca^{2+} mobilisation in TGF-β_1-treated and untreated primary HSVSMCs. Furthermore, this experiment aimed to establish whether potential SMC contraction induced Cal520™ probe quenching which would then yield false increases in fluorescence intensity in response to AngII stimulation. Firstly, fasudil treatment in the absence of TGF-β_1-did not appear to affect AngII-dependent increase in fluorescence intensity compared to untreated vehicle controls. This indicated that (i) SMC contraction did not appear to trigger Cal520 probe quenching and subsequent false increase in fluorescence intensity and (ii) combined ROCK/PKC inhibition did not attenuate acute AngII-driven SR Ca^{2+} release. In the absence of fasudil TGF-β_1 treatment triggered an increase in AngII-dependent Ca^{2+} transients compared to untreated vehicle controls. In the presence of fasudil TGF-β_1-treated cells did not display a significant increase in AngII-mediated Ca^{2+} release compared to vehicle controls. Although the difference between these two groups was not statistically significant there was a trend towards an increase in Ca^{2+} transients in the absence of fasudil. More n numbers should be added to this set of experiments to consolidate these findings in the future. Nevertheless, it is likely that short-term ROCK/PKC inhibition has little effect on TGF-β_1-driven AngII-mediated Ca^{2+} mobilisation. This stands in contrast to Bouillier's study which demonstrated that PKC inhibition with calphostin blunted AngII-driven SR Ca^{2+} release. The difference in cell type/species (primary HSVSMC vs primary hypertensive RASMC) and different pharmacological inhibitors (fasudil vs calphostin) may explain this discrepancy.

Ligand-dependent and -independent ALK5 activation drove contractile marker expression in primary HSVSMCs indicating the presence of a contractile phenotype. Furthermore, 24-h TGF-β_1 stimulation drove MLC S20 phosphorylation in HSVSMCs in an ALK5-dependent manner suggesting Ca^{2+}-independent modulation of SMC contractility (unpublished data) (Low et al., 2019). It may be speculated that TGF-β_1 synergises with RhoA/ROCK signalling to (i) induce a contractile SMC phenotype and to (ii) promote MLC S20 phosphorylation/SMC hypercontractility. In line with this hypothesis, Chen *et al*. showed that pharmacological inhibition of ROCK with Y27632 inhibited TGF-β_1-mediated differentiation of neural crest stem cells into SMCs and reversed TGF-β_1-dependent SMC morphology and contractility (Chen et al., 2006). The same study

also demonstrated that TGF-β_1 directly drove RhoA activation and that dominant negative RhoA prevented TGF-β_1-dependent pSMAD2/3 translocation to the nucleus highlighting the importance of functional RhoA in TGF-β_1-dependent regulation of contractile gene expression and SMC differentiation. This may be of clinical relevance in the context of SVG disease.

Another main finding within this study was that BMP-9 prevented TGF-β_1-dependent sensitisation of AngII/AT_1R-dependent SR Ca^{2+} release in primary HSVSMCs. Furthermore, the presence of BMP-9 appeared to trigger a trend towards a decrease in AngII-dependent Ca^{2+} transients in primary HCASMCs. Since results presented in 4.3.9 showed that BMP-9 binds to ALK1 and ALK2 in HSVSMC, it is likely that this inhibitory downstream effect is ALK1 and/or ALK2 dependent (David et al., 2007). One limitation of this study is that BMP-9-dependent negative regulation of Ca^{2+} handling was not investigated in more detail. Limited primary cell availability coupled with an extensive experimental set-up made it difficult to study more mechanisms in addition to experiments investigating the effect of pharmacological inhibition of ALK5, AT_1R and ROCK/PKC on ligand dependent Ca^{2+} handling. Future experiments are warranted to investigate BMP-9-dependent inhibitory effects in the presence of pharmacological ALK1 inhibition or siRNA-mediated *ALK1* ablation in primary vSMCs to establish whether this effect is ALK1 dependent.

One underlying BMP-9 dependent inhibitory downstream mechanism in HSVSMCs might have been explained by differential regulation of angiotensin receptor mRNA expression levels. Although single BMP-9 treatment significantly suppressed AT_1R mRNA levels versus vehicle treated controls, this effect was attenuated in the presence of TGF-β_1. Furthermore, BMP-9 did not affect *MAS1* mRNA levels which were suppressed by TGF-β_1. Hence, it is likely that BMP-9-driven inhibition of TGF-β_1-dependent sensitisation of the AngII/AT_1R system is not mediated via changes in angiotensin receptor levels. Furthermore, BMP-9 did not prevent TGF-β_1/ALK5-mediated increase in contractile gene expression in HSVSMCs suggesting that BMP-9 was unable to counter downstream ALK5/SMAD2/3 signalling. Since TGF-β_1 did not prevent BMP-9-dependent SMAD1 phosphorylation it is likely that inhibitory actions of BMP-9 are mediated via activation of SMAD1, and potentially SMAD5. Therefore, it may be speculated

that BMP-9/ALK1/ALK2 signalling axis modulates the PLC/IP3 system, total SR Ca^{2+} content and/or redirects Ca^{2+} for calcium phosphate formation.

A future *in vitro* experiment should assess AngII-induced IP3 production in BMP-9 and/or TGF-β_1-treated HSVSMCs utilising a radiometric inositol phosphate accumulation assay. Results would then show whether ligands influenced AngII/AT_1R-triggered and PLC-dependent catalysation of PIP2 to IP3 and DAG. As previously proposed, thapsigargin should be utilised to assess total SR Ca^{2+} content in ligand-treated HSVSMCs to determine potential changes which would then explain enhanced AngII-dependent Ca^{2+} release in TGF-β_1-treated cells and decreased Ca^{2+} release in cells treated with TGF-β_1 in the presence of BMP-9.

Importantly, BMP-9 may redirect intracellular Ca^{2+} to promote calcification and osteoblastic differentiation of primary HSVSMCs and HCASMCs (Zhu et al., 2015). BMP-9 drives alkaline phosphatase (ALP) activity and subsequent bone formation in a SMAD1/5/8-dependent manner (Chen et al., 2010). Quantitative RT-PCR data from this study demonstrated that BMP-9 attenuated TGF-β_1/ALK5-dependent suppression of *ALPL* mRNA levels in primary HSVSMCs. Guerrero *et al.* studied TGF-β_1-driven vSMC differentiation from mesenchymal stem cells in the presence of high phosphate a known to inducer of osteoblastic differentiation (Guerrero et al., 2014). The authors showed that TGF-β_1 prevented phosphate-induced osteoblastic differentiation by suppressing ALP activity and subsequent Ca^{2+} deposition. These findings suggest that TGF-β_1 negatively regulates osteoblastic vSMC differentiation. In contrast, Zhu *et al.* investigated the effect of BMP-9 on phosphate-induced osteoblastic differentiation of primary mouse aortic SMCs (Zhu et al., 2015). The investigators found that BMP-9/ALK1-dependently drove mRNA expression of osteoblastic markers, ALP activity and Ca^{2+} deposition indicating BMP-9 as a positive regulator of osteoblastic vSMC differentiation. In conclusion, it may be speculated that the potential TGF-β_1-dependent decrease in ALP activity in HSVSMCs may provide more Ca^{2+} for AngII-operated SR Ca^{2+} release. In contrast, although BMP-9 did not induce *ALPL* mRNA levels in HSVSMC it is conceivable that this ligand may stimulate ALP activity thereby redirecting free Ca^{2+} to calcification and reducing SR Ca^{2+} availability. It is important to stress that these are highly speculative statements. Hence, these findings warrant future experiments aimed at (i) determining ALP activity and

calcium deposition in ligand treated primary human vSMCs in absence and presence of high phosphate and (ii) assessing the impact of pharmacological ALP inhibition with DNB on AngII-induced intracellular Ca^{2+} mobilisation in ligand-treated primary human vSMCs.

In addition to findings based on whole region of interest fluorescence analysis, single cell fluorescence trace analysis revealed SMC population heterogeneity based on AngII-driven SR Ca^{2+} release. Independent of treatment, each group displayed a bimodal distribution of AngII-dependent Ca^{2+} transients. However, the presence of TGF-β_1 triggered a trend towards a reduction in non-responding HSVSMCs and instead an increase in the number of cells displaying medium and higher AngII-mediated Ca^{2+} responses. The presence of BMP-9 attenuated this TGF-β_1-driven effect. TGF-β_1 appeared to promote homogeneity based on AngII-induced release of intracellular Ca^{2+} stores. Subsequently one may hypothesise that saphenous vein media is made up of diverse SMC phenotypes reflecting local vessel wall heterogeneity.

These findings are in line with previous studies reporting distinct SMC phenotypes residing within healthy media of pulmonary, coronary and internal thoracic arteries (Frid et al., 1994; Hao et al., 2002; Li et al., 2001a). It is important to stress that these studies investigated large arteries and, hence, these findings may not directly reflect on SVG media composition. Nevertheless, scRNAseq data shown in section 6.3.4 supports the hypothesis of local SMC diversity within SVG media. Li and colleagues isolated 12 distinct SMC phenotypes from one fragment of the human internal thoracic artery (Li et al., 2001a). In the context of Ca^{2+} handling, the authors showed that spindle-shaped (contractile) SMCs displayed higher AngII-induced Ca^{2+} transients compared to epithelioid (synthetic) SMCs. Furthermore, the study showed that only spindle-shaped SMCs contracted in response to AngII stimulation. Although both clone subtypes expressed αSMA, MYH11 and calponin, epithelioid-shaped SMCs displayed greater proliferative and migratory capacities in response to treatment with 10% serum and PDGF-BB compared to spindle-shaped SMCs. This study revealed two important aspects. Firstly, it showed that contractile and synthetic SMCs resided side by side in healthy arterial media in the absence of a pathophysiologic stimuli. Hence, it may be speculated that even in the absence

of vascular disease/injury SMCs undergo phenotype switching to maintain vascular wall structure and function. Secondly, distinct SMC phenotypes reacted differently to pro-proliferative/-migratory stimuli. Based on this finding, it may be hypothesised that vSMCs react heterogeneously in certain vascular disease settings.

It is important to point out some limitations in this single cell analysis. Several cells within one set of patient cells did not respond to AngII stimulation although all experiments were performed at P5. It may be possible that examined SMC populations were made up of different SMC phenotypes reacting differently to BMP-9, TGF-β_1 and/or AngII stimuli (Li et al., 2001a). These phenomena may also contribute to inter-patient variability. Furthermore, all examined 6-min traces displayed a slight decline in baseline fluorescence intensity which may be explained by (i) photo-bleaching during fluorescence imaging or (ii) probe leaching into extracellular space. Although this caused negative amplitudes in some non-responding HSVSMCs this effect was only small. To prevent negative values following $\log_{10}$-transformation the constant 4.926025 was added to each amplitude from each cell to ensure that every amplitude was treated in the same way. Moreover, this study did not directly investigate fractional SMC shortening following AngII stimulation. Therefore, future experiments should be aimed at directly assessing SMC contraction to gain more insight into excitation-contraction coupling in primary HSVSMCS and HCASMCs. In the context of single cell resolution this may be achieved by high magnification phase contrast microscopy of single SMCs as described by Li *et al.* (Li et al., 2001a). However, this would only allow examination of a limited number of SMCs as opposed to examining a whole SMC population since the authors used trypsin-EGTA to loosen SMCs from the culture surface. In collaboration with Dr F. Burton and Prof G. Smith (University of Glasgow) an attempt was made to determine fractional SMC shortening in fluorescence imaging videos using a software designed to detect cell movement. However, this attempt did not yield any valid results since (i) the resolution (10× magnification for 6-min fluorescence trace imaging) was not sufficient to detect SMC movement and (ii) SMCs might not have displayed any movement in response to AngII stimulation since SMC shortening might have been hampered by SMC adherence to plastic substrate. This limitation may be overcome by seeding primary HSVSMCs onto Matrigel-coated wells. Li *et al.*

compared culturing of primary RASMCs in plastic versus Matrigel-coated wells (Li et al., 1994). The study showed that SMCs cultured on Matrigel displayed a morphological phenotype which more closely resembled a contractile SMC phenotype compared to SMCs cultured on plastic dishes. Furthermore, the authors determined SMC contraction by phase-contrast microscopy. Results showed that the number of contracting cells (shape change > 10%) in response to arginine vasopressin (AVP) was greater on Matrigel compared to plastic. In addition, the investigators examined intracellular Ca^{2+} release in Fura-2-loaded SMCs. AVP triggered increases in cytosolic [Ca^{2+}] in SMCs were similar between cells cultured on Matrigel and plastic. Based on this study, a future experiment should determine excitation-contraction coupling in primary HSVSMCs plated on Matrigel dishes. Loading SMCs with the Ca^{2+} indicator Cal520™ and performing high resolution fluorescence trace analysis in combination with phase-contrast imaging on a live-cell microscope may enable simultaneous visualisation of AngII-induced intracellular Ca^{2+} release and downstream contraction. This experiment could then be complemented by determining SVG contraction intensity and velocity *ex vivo* using myography.

5.5 Summary

HSVSMCs quiesced for 72-h and Cal520-loaded displayed a rapid and reproducible increase in fluorescence intensity in response to AngII and IM stimulation indicating release of intracellular Ca^{2+} stores. In contrast, preliminary results showed that serum treated HSVSMCs did not respond to AngII stimulation potentially suggesting that SR Ca^{2+} stores were unresponsive in proliferating HSVSMCs.

Having established a robust Ca^{2+} handling protocol the next aim was to investigate intracellular Ca^{2+} release in BMP-9 and/or TGF-β_1-treated primary HSVSMCs and HCASMCs in the absence and presence of SB525334. TGF-β_1-treated HSVSMCs displayed an increase in AngII-driven intracellular Ca^{2+} mobilisation in an ALK5-dependent manner, potentially suggesting increased contractility. In contrast, BMP-9 blunted this effect indicating ALK5 antagonism and/or differential utilisation of intracellular Ca^{2+}. Opposed to findings in primary HSVSMCs, TGF-β_1 did not affect AngII-dependent Ca^{2+} release in primary HCASMCs indicating differential regulation of Ca^{2+} handling in this cell type.

The next aims were to determine whether AngII signalled via the AT_1R or AT_2R and which mechanisms might explain why TGF-β_1 sensitised the AngII Ca^{2+} response in primary HSVSMCs. Pharmacological AT_1R inhibition with losartan blunted AngII-driven intracellular Ca^{2+} mobilisation in both untreated and TGF-β_1-treated HSVSMCs indicating AT_1R-dependency. Furthermore, TGF-β_1 ALK5-dependently suppressed *MAS1* receptor mRNA expression levels but did not affect *AGTR1* expression. Since MAS1 has been shown to counter-regulate AT_1R it may be hypothesised that reduced MAS1 levels in the presence of TGF-β_1 triggers an increased AngII/AT_1R excitation/contraction response.

Furthermore, the ROCK/PKC/contraction inhibitor fasudil did not affect AngII-induced Ca^{2+} release in untreated and TGF-β_1-treated HSVSMCs indicating that potential Ca^{2+}-dependent cell contraction did not trigger quenching of the Ca^{2+} indicator probe Cal520 and a subsequent false increase in fluorescence intensity. It may be speculated that although it is likely that fasudil dampens HSVSMC contraction in response to AngII, this drug does not prevent SR Ca^{2+} release

triggering potential downstream activation of Ca^{2+}-sensitive signalling pathways such as the NFAT/calcineurin system.

Single cell region of interest analysis revealed heterogeneous HSVSMC populations independent of ligand treatment. However, TGF-β_1-treated HSVSMC populations displayed a trend towards a reduction in non-responding cells and instead an increase in cells responding with higher fluorescence intensities indicating a more homogeneous population based on intracellular Ca^{2+} release. TGF-β_1-induced homogeneity was reversed in the presence of BMP-9 paralleling whole region of interest findings. It may be hypothesised that SMC population heterogeneity reflects SMC diversity within pre-implantation SVG media and that these diverse SMC populations react differently in SVG injury.

Chapter 6 Characterising primary HSVSMC transcriptome heterogeneity using single cell RNA sequencing

6.1 Introduction

Data presented in section 5.3.4 revealed HSVSMC population heterogeneity in each treatment group except for TGF-β_1-treated SMC populations which elicited a more homogeneous AngII-dependent Ca^{2+} response. This prompted evaluation of potential transcriptome heterogeneity in BMP-9 and/or TGF-β_1-treated HSVSMCs using the 10x Chromium microfluidics-based scRNAseq platform.

6.1.1 Single cell RNA sequencing as a technique to investigate vSMC heterogeneity

It has previously been postulated that arterial vSMC heterogeneity may play a role in vascular disease development and progression. Single cell RNA sequencing enables identification of distinct vascular cells and distinct SMC phenotypes in whole vessel homogenates, and as such constitutes a powerful tool for the evaluation of cellular heterogeneity (Dobnikar et al., 2018; Wirka et al., 2019).

Using scRNAseq analysis Dobnikar and colleagues uncovered 7 distinct SMC phenotypes within one region of healthy murine aortic media. Moreover, this study found that some SMCs within each of these 7 clusters expressed the mesenchymal stem cell marker *Sca1* (encodes stem cells antigen 1) and that these $Sca1^+$ SMCs displayed lower contractile gene expression levels. The authors went on to investigate Sca1 in the context of vascular injury and found that lineage-labelled *Myh11-CreERt2/EYFP* mice displayed *Sca1* up-regulation in 10-45% of $EYFP^+$ vSMCs in dispersed ligation-injured carotid arteries (Dobnikar et al., 2018). This potentially indicates expansion of a rare SMC sub-population following vascular injury. Yao *et al*. used scRNAseq to investigate vSMC de-differentiation in the context of NF following carotid balloon injury in rats (Yao et al., 2018). The study identified the histone variant *H2az* as a protective factor against vSMC de-differentiation and NF following vascular injury. The authors also demonstrated that H2az drove Smad3 recruitment thereby enabling activation of contractile gene expression. Wirka *et al*. investigated vSMC heterogeneity in hyperlipidaemic $ApoE^{-/-}$ SMC-lineage tracing mice (Wirka et al., 2019). With the help of scRNAseq the authors showed that hyperlipidaemic $ApoE^{-/-}$ SMC-lineage tracing mice displayed transformation of vSMCs into fibroblast-like cells, termed fibromyocytes. Furthermore, scRNAseq facilitated

identification of *TCF21* (encodes transcription factor of the basic helix-loop-helix family) as an athero-protective gene in human CAD.

In summary, these studies highlight that scRNAseq is a powerful technology to study rare SMC phenotypes/SMC heterogeneity and identify novel disease relevant genes in the context of vascular injury and atherosclerosis. Furthermore, the combination of scRNAseq and lineage tracing mice has further broadened the understanding of pathophysiological processes underlying NF and atherosclerosis development and progression. Hence, scRNAseq may help to identify novel pathophysiological mechanisms underlying NF in SVG disease.

6.2 Aims

- To characterise transcriptional heterogeneity versus homogeneity in response to BMP-9 and/or TGF-β_1 treatment.

- To identify potential SMC sub-lineages in untreated control and ligand treated HSVSMCs.

6.3 Results

6.3.1 Quality control filtering reveals high percentage of mitochondrial genes in primary HSVSMCs

All steps leading up to AnnData matrix file import into the existing Python computational TGF-β pipeline are described in 2.10.4. In brief, the CellRanger v.3.1.0 and STAR aligner softwares were used to perform nucleotide sequence alignment against the GRCh38 reference genome. This left 1,843 untreated (vehicle 4 mM HCl/1% BSA, 24-h), 1,372 BMP-9-treated (10 ng/ml, 24-h), 2,038 TGF-β_1 (10 ng/ml, 24-h)and 1,938 BMP-9 (10 ng/ml)/TGF-β_1 (10 ng/ml) co-treated (24-h) HSVSMCs for analysis using an existing Python pipeline (cells generated from one CABG patient) (unpublished data) (Low et al., 2019).

Preliminary quality control (QC) filtering included discarding cells expressing <2000 genes and genes with <100 corresponding cells. Following filtering, the total number of RNA molecules per cell (Figure 6-1 A), the mitochondrial gene percentage per cell (Figure 6-1 B) and total RNA count versus mitochondrial gene percentage (Figure 6-1 C) were computed. The read depth was approximately 30,000 reads/cell. The mitochondrial gene percentage/cell average was >5%. Based on these findings, cut offs were defined to prevent skewing of data analysis. Cells containing <10,000 and >45,000 RNA molecules as well as displaying a mitochondrial gene percentage >12.5% were filtered out (Figure 6-2 A). RNA molecule count versus corresponding mitochondrial gene percentage per cell did not demonstrate a correlation (Figure 6-2 B). Finally, the relationship between RNA molecule count and corresponding number of expressed genes per cell did not appear to behave in a linear fashion (Figure 6-2 C).

In summary, QC filtering revealed an increase in mitochondrial gene percentage average of >5% for all cells.

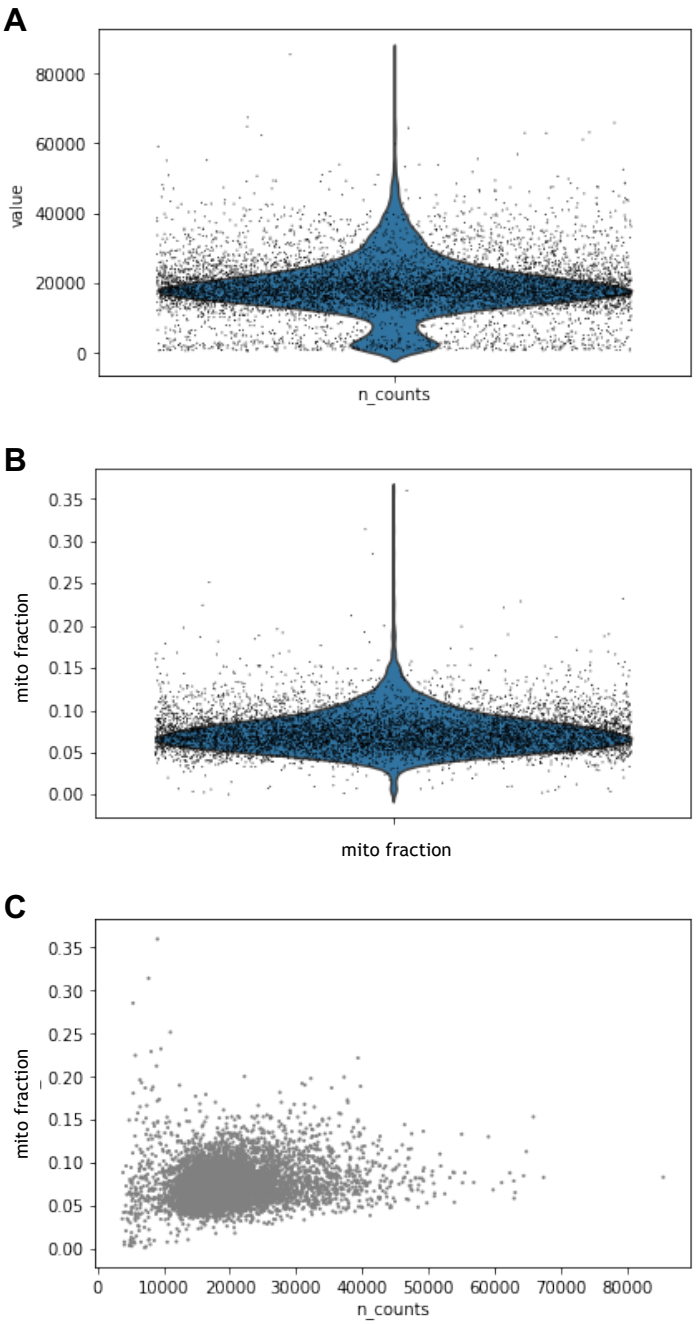

Figure 6-1 Preliminary quality control filtering identifies high percentage of mitochondrial genes in primary HSVSMCs. 80% confluent primary HSVSMCs were quiesced in 0.2% FCS media (MEDIA1) for 72-h. Quiescence media was replaced with stimulation media containing BMP-9 (10 ng/ml), TGF-β_1 (10 ng/ml), BMP-9 and TGF-β_1 (10 ng/ml) and vehicle control (4 mM HCl/1% BSA). Following 24-h, stimulation media was removed. Cells were prepared as described in section 2.10.1 and subjected to scRNAseq (biological n=1 CABG patient). Cells containing 10x barcodes which were not recognised by the CellRanger software were discarded. In addition, cells expressing <2000 genes and genes with <100 corresponding cells were also excluded from the analysis. (**A**) Plot displays distribution of RNA molecule counts per cell. (**B**) Plot displays distribution of mitochondrial gene fraction per cell. (**C**) Plot demonstrates RNA molecule counts versus mitochondrial gene fraction per cell.

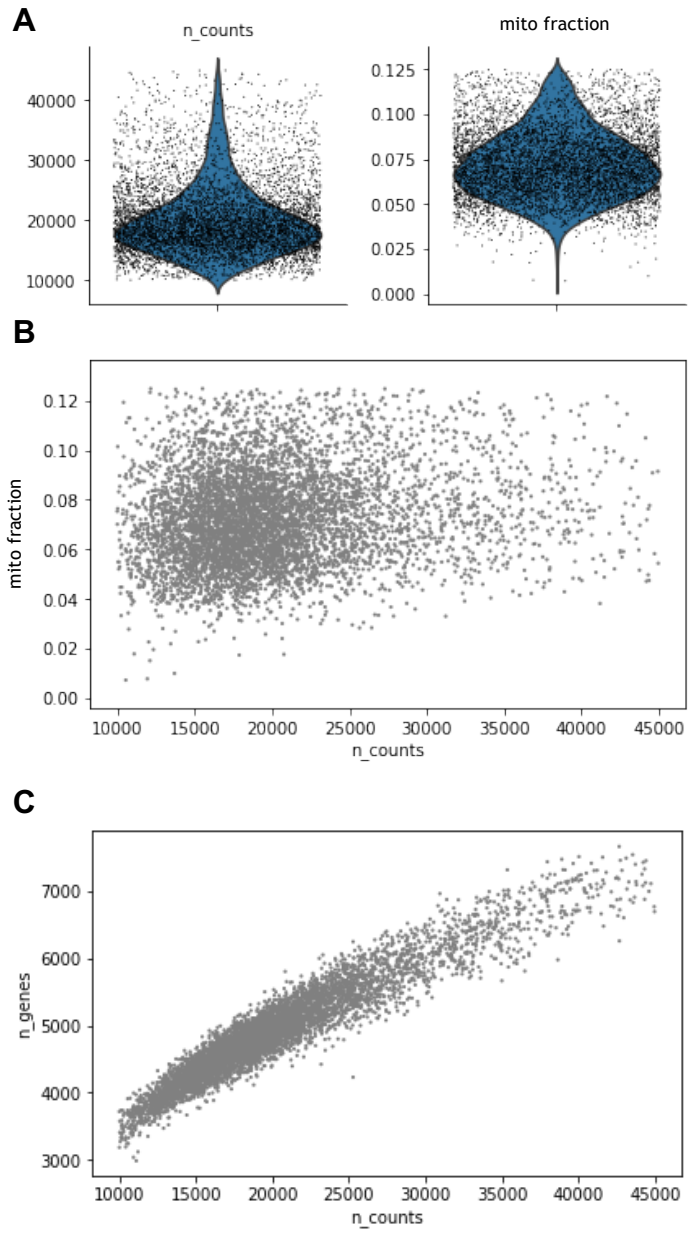

Figure 6-2 Final quality control filtering confirms high percentage of mitochondrial gene percentage. 80% confluent primary HSVSMCs were quiesced in 0.2% FCS media (MEDIA1) for 72-h. Quiescence media was replaced with stimulation media containing BMP-9 (10 ng/ml), TGF-β_1 (10 ng/ml), BMP-9 and TGF-β_1 (10 ng/ml) and vehicle control (4 mM HCl/1% BSA). Following 24-h, stimulation media was removed. Cells were prepared as described in section 2.10.1 and subjected to scRNAseq (biological n=1 CABG patient). To avoid skewing of data analysis, cells containing <10,000 and >45,000 RNA molecule counts as well as a mitochondrial gene percentage >12.5% were excluded from the analysis. (**A**) Plots demonstrate distribution of RNA molecule counts (left) and mitochondrial gene fraction (right) per cell. (**B**) Plot displays RNA molecule counts versus mitochondrial gene fraction per cell. (**C**) Plot displays RNA molecule counts versus number of expressed genes per cell.

6.3.2 Initial principal component analysis reveals distinct transcriptomes for each treatment group

Previous scRNAseq results from our group demonstrated that untreated control and TGF-β_1-treated primary HSVSMCs displayed transcriptional differences following principal component analysis (PCA) (unpublished data) (Low et al., 2019). To identify transcriptional differences between treatment groups, PCA was performed on all remaining cells following QC-filtering.

Dimensionality reduction using PCA uncovered transcriptional differences between all treatment groups (Figure 6-3 A). Transcriptional alterations appeared to be larger in TGF-β_1- versus BMP-9-treated HSVSMCs compared to untreated controls. In line with previous findings from our group, TGF-β_1-treated HSVSMCs displayed a visible reduction in mitochondrial gene expression (unpublished data) (Low et al., 2019). Paralleling previously presented bulk qRT-PCR findings from this study, BMP-9 and TGF-β_1 drove relative *ID1* and *SERPINE1* mRNA expression levels respectively (Figure 6-4 B and C).

In conclusion, BMP-9 and TGF-β_1 induced target gene expression demonstrating successful ligand stimulation. Moreover, PCA uncovered greater transcriptional alterations in TGF-β_1- versus BMP-9-treated HSVSMCs potentially suggesting that TGF-β_1 triggers greater transcriptional changes compared to control cells than BMP-9.

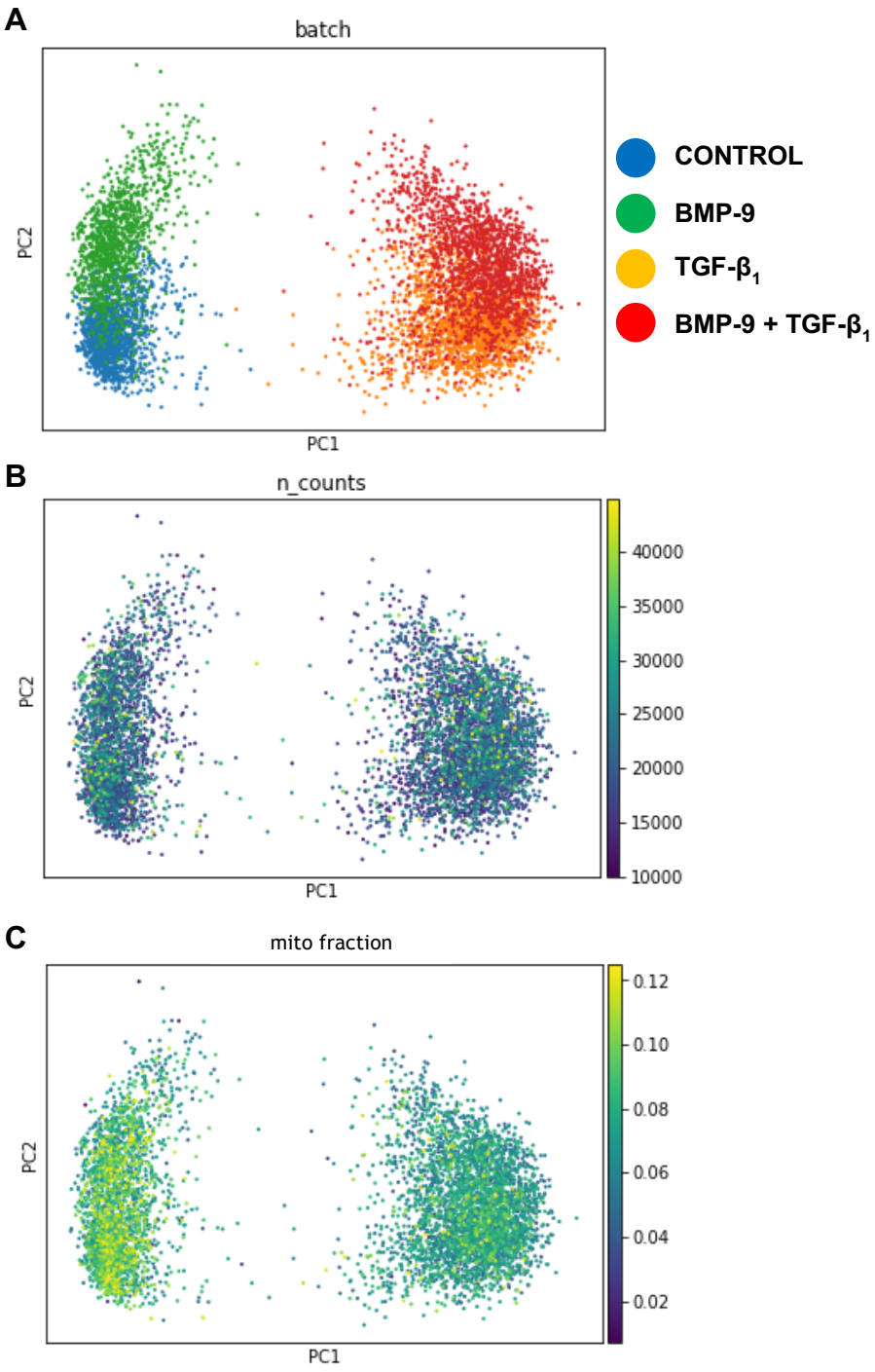

Figure 6-3 Principal component analysis reveals distinct transcriptomes within each treatment group. 80% confluent primary HSVSMCs were quiesced in 0.2% FCS media (MEDIA1) for 72-h. Quiescence media was replaced with stimulation media containing BMP-9 (10 ng/ml), TGF-β_1 (10 ng/ml), BMP-9 and TGF-β_1 (10 ng/ml) and vehicle control (4 mM HCl/1% BSA). Following 24-h, stimulation media was removed. Cells were prepared as described in section 2.10.1 and subjected to scRNAseq (biological n=1 CABG patient). Following QC filtering UMI counts were re-scaled to 10,000 in order to correct for library size (total number of UMIs). The constant 1 was added to each re-scaled UMI count prior to $\log_{10}$-transformation. Based on dispersion, highly variable genes were excluded from the analysis. Principal component analysis (PCA) was performed on all remaining cells to highlight differences between treatment groups and identify potential confounders. Finally, variations in cell count were regressed out. (**A)** Graph displays cells from each treatment group. (**B**) Graph displays distribution of RNA molecule counts per cell. The right-hand y-axis indicates RNA molecule counts. (**C**) Graph displays mitochondrial gene fraction. The right-hand y-axis indicates mitochondrial gene fraction.

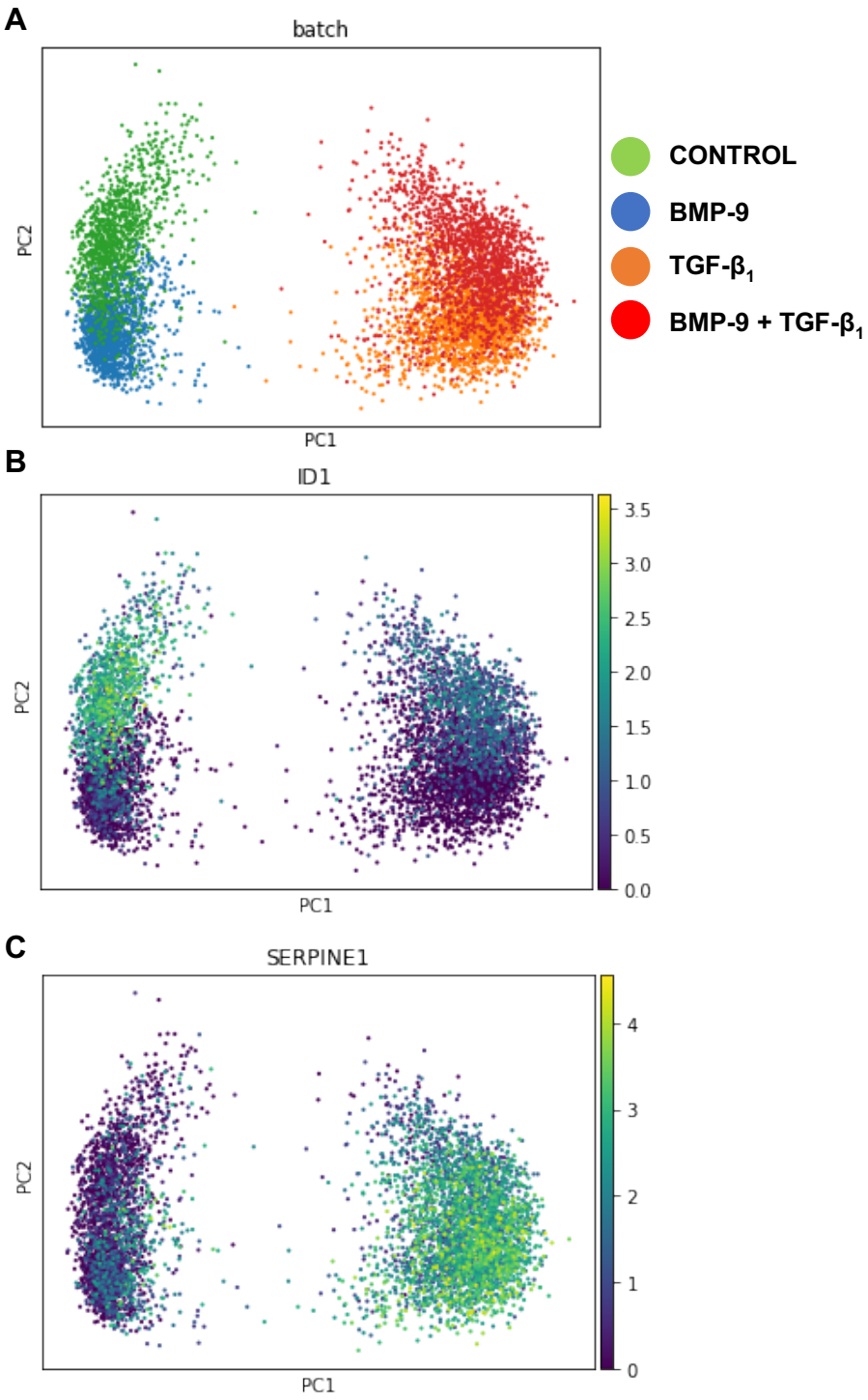

Figure 6-4 BMP-9 and TGF-β_1 drive target gene expression in primary HSVSMCs. 80% confluent primary HSVSMCs were quiesced in 0.2% FCS media (MEDIA1) for 72-h. Quiescence media was replaced with stimulation media containing BMP-9 (10 ng/ml), TGF-β_1 (10 ng/ml), BMP-9 and TGF-β_1 (10 ng/ml) and vehicle control (4 mM HCl/1% BSA). Following 24-h, stimulation media was removed. Cells were prepared as described in section 2.10.1 and subjected to scRNAseq (biological n=1 CABG patient). **(A)** Graph displays cells from each treatment group. (**B**) PCA plot displays rescaled *ID1* mRNA molecule counts for each treatment group (right-hand y-axis indicates rescaled RNA molecule counts). (**C**) PCA plot displays rescaled *SERPINE1* mRNA molecule counts for each treatment group (right-hand y-axis indicates rescaled RNA molecule counts).

6.3.3 Combined UMAP and Louvain clustering reveals transcriptome heterogeneity in primary HSVSMCs

The previous scRNAseq study from our group revealed 11 distinct clusters within TGF-β_1-treated HSVSMCs demonstrating transcriptome heterogeneity following ligand treatment (unpublished data) (Low et al., 2019). Based on this finding, uniform manifold approximation and projection (UMAP) non-linear dimensionality reduction alongside Louvain clustering were utilised to identify cell clusters based on transcriptome differences within untreated and 24-h ligand treated primary HSVSMCs.

UMAP plots revealed 7 distinct Louvain clusters within the untreated control group (Figure 6-5 A), 7 clusters within the BMP-9 treatment group (Figure 6-5 B), 8 clusters within the TGF-β_1 treatment group (Figure 6-5 C) and 9 clusters within the combined BMP-9/TGF-β_1 treatment group (Figure 6-5 D). Taken together, these data demonstrate transcriptional heterogeneity within each treatment group.

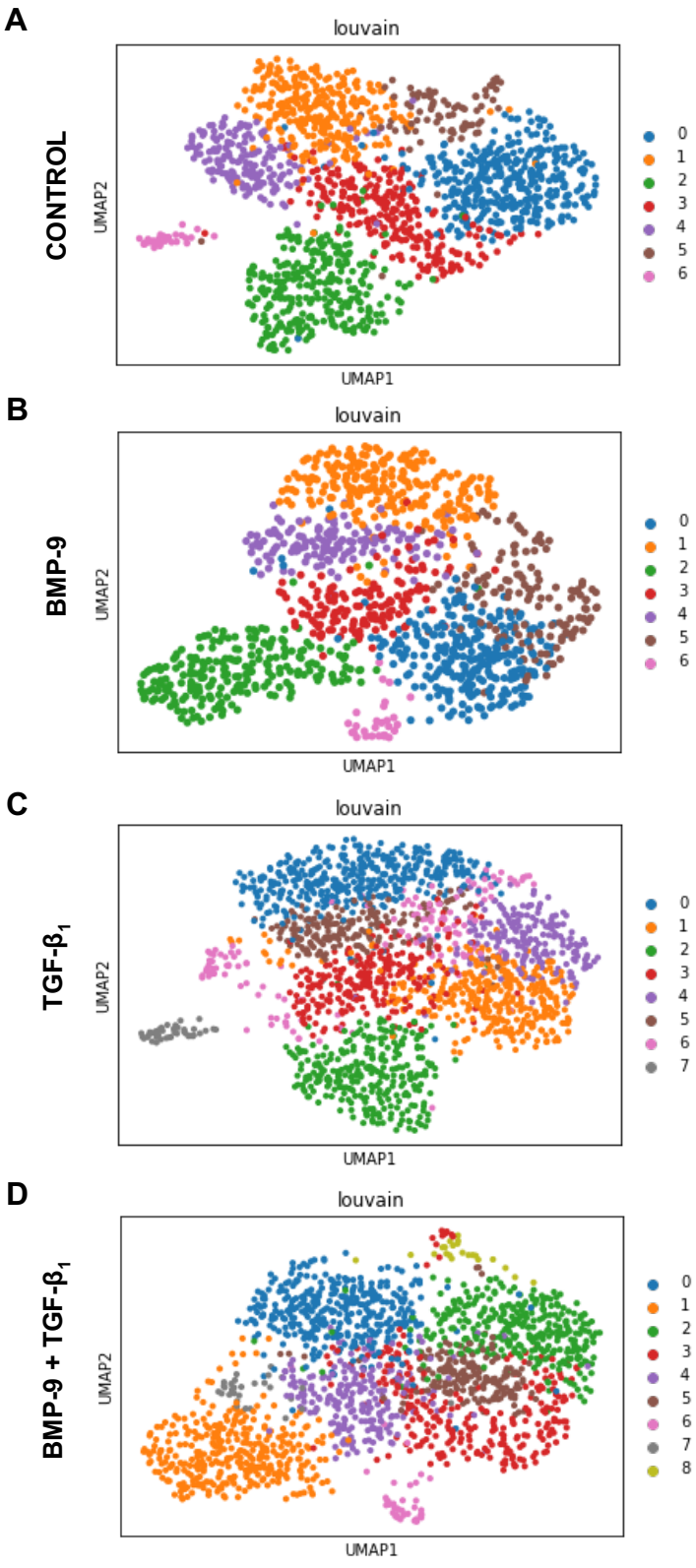

Figure 6-5 ScRNAseq uncovers transcriptional heterogeneity in each treatment group. 80% confluent primary HSVSMCs were quiesced in 0.2% FCS media (MEDIA1) for 72-h. Quiescence media was replaced with stimulation media containing BMP-9 (10 ng/ml) (**B**), TGF-β_1 (10 ng/ml) (**C**), BMP-9 and TGF-β_1 (10 ng/ml) (**D**) and vehicle control (4 mM HCl/1% BSA) (**A**). Following 24-h, stimulation media was removed. Cells were prepared as described in section 2.10.1 and subjected to scRNAseq (biological n=1 CABG patient). Following initial PCA, the 4 treatment groups were separated into 4 individual samples. PCA was performed on the Z scores of normalised expression values within each treatment group. Neighbourhood graphs were computed based on the top 40 principal components and the 10 nearest neighbours. UMAP was utilised as a non-linear dimensionality-reduction technique alongside Louvain community detection to cluster cells based on gene expression.

6.3.4 Serum-starved HSVSMC control population displays 7 distinct clusters

UMAP non-linear dimensionality reduction in combination with Louvain clustering identified 7 clusters based on transcriptome differences within untreated control primary HSVSMCs. Established RNA velocity and gene ontology (GO) analysis were performed to obtain more detailed information on transcriptome dynamics and underlying biological processes within each cluster (unpublished data) (Low et al., 2019). Figure 6-7 displays the top 30 most differentially expressed genes for each cluster. Relative *SERPINE1* and *ID1* mRNA expression was overlaid with RNA velocity analysis to determine dynamic ALK5 and ALK1/ALK2 pathway activation. RNA velocity is a high dimensional vector which predicts the future state of individual cells and is estimated by distinguishing between un-spliced and spliced mRNAs in scRNAseq protocols (La Manno et al., 2018).

RNA velocity vectors indicated that control HSVSMCs were differentiating along separate lineages (Figure 6-6 A). GO analysis revealed that clusters 0 (blue), 2 (green), 3 (red) and 5 (brown) displayed the highest fold enrichment scores, a measure of whether a term is over-represented in the dataset.

RNA velocity analyses showed that most clusters appeared to be moving away from cluster 3 (red) which displayed enrichment terms for ascending aorta morphogenesis (enriched cluster genes: *SOX4*, encodes transcription factor SOX-4; *TGFB2*), negative regulation of extracellular matrix disassembly (*DPP4*, encodes dipeptidyl peptidase 4; *FAP*, encodes prolyl endopeptidase FAP), atrial septum primum morphogenesis (*SOX4*; *TGFB2*), regulation of macrophage cytokine production (*CD74*, encodes HLA class II histocompatibility antigen gamma chain; *TGFB2*; *SPON2*, encodes spondin-2) and wound healing/spreading of cells (*PDPN*, encodes podoplanin; *MME*, encodes macrophage metalloelastase; *CD44*, encodes CD44 antigen; *ARHGAP24*, encodes Rho GTPase-activating protein 24) (Table 6-1).

Cluster 0 (blue) showed enrichment for regulation of high voltage-gated calcium channel activity (*CACNB2*, encodes voltage-dependent L-type calcium channel subunit beta-2; *PDE4B*, encodes cAMP-specific 3′,5′-cyclic phosphodiesterase 4B; *FGF14*, encodes fibroblast growth factor 14) (Figure 6-8 A-C) and coronary

vasculature development (*ADAMTS6*, encodes a disintegrin and metalloproteinase with thrombospondin motifs 6; *LTBP1*, encodes latent TGF-β-binding protein 1; *BMP4*; *HAND2*, encodes heart- and neural crest derivatives-expressed protein 2). In contrast, cluster 2 (green) demonstrated enrichment for Wnt signalling (*SFRP1*, encodes secreted frizzled-related protein 1; *DKK1*, encodes Dickkopf-related protein 1) and negative regulation of osteoblast proliferation (*NRP1*, encodes PKC-binding protein NELL1; *GREM1*, encodes gremlin 1; *SFRP1*). Cluster 5 (brown) displayed enrichment for oncogene-induced cell senescence (*HMGA1*, encodes high mobility group protein HMG-I/HMG-Y; *HMGA2*, encodes high mobility group protein HMG-C) and chronological cell ageing (*SERPINE1*; *ENG*). Both clusters 2 and 5 demonstrated visually higher relative *SERPINE1* mRNA levels compared to all other clusters indicating ALK5 pathway activation (Figure 6-6 B and C). Relative *ID1* mRNA levels were low throughout all clusters suggesting absence of ALK1/ALK2 pathway activation. Lower fold enrichment scored terms for clusters 1, 4 and 6 are listed in Table 6-1.

Taken together, these findings demonstrate transcriptional heterogeneity within untreated control primary HSVSMCs which may reflect SMC diversity within pre-implantation SVG media. Interestingly, cluster 0 (blue) displayed enrichment for regulation of high voltage-gated calcium channel activity which may be linked to pro-contractile Ca^{2+} system remodelling (Gollasch et al., 1998).

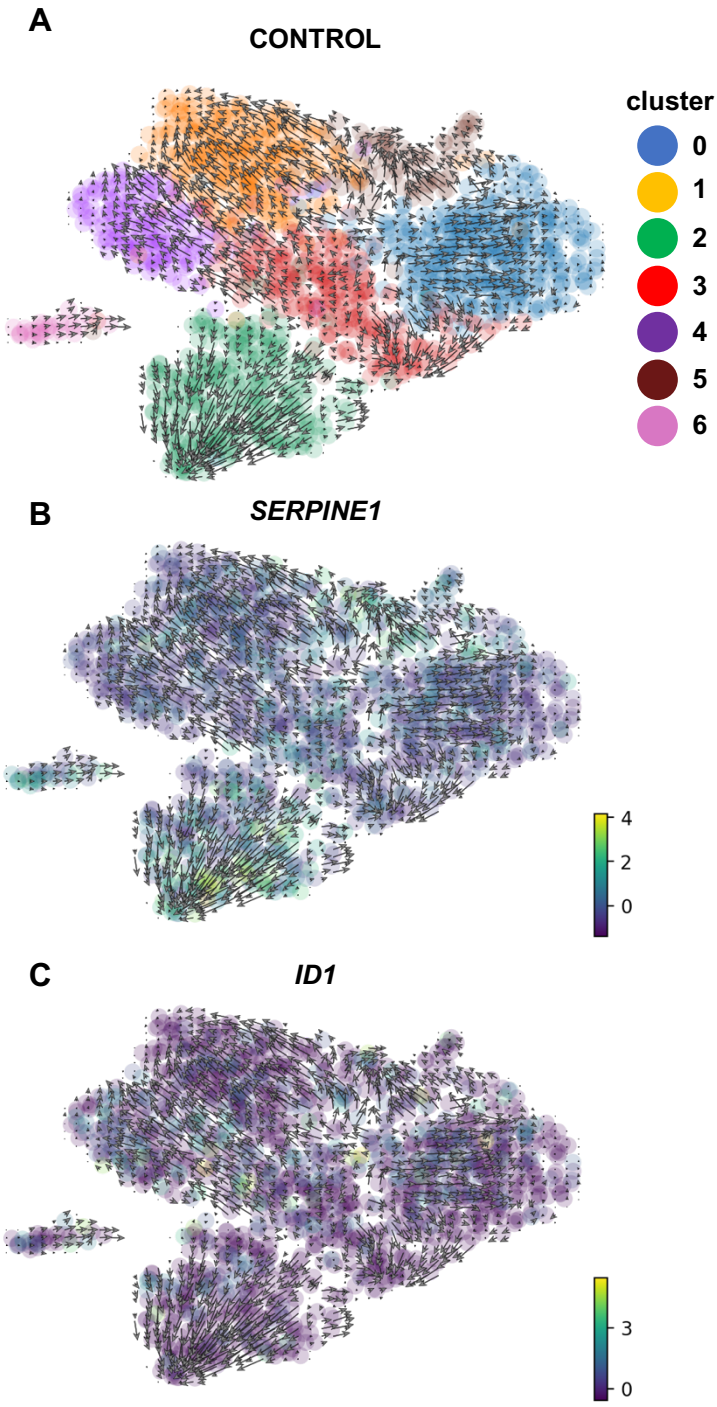

Figure 6-6 UMAP/Louvain clustering and RNA velocity in untreated control primary HSVSMCs. 80% confluent primary HSVSMCs were quiesced in 0.2% FCS media (MEDIA1) for 72-h. Quiescence media was replaced with media containing vehicle control (4 mM HCl/1% BSA). Following 24-h, media was removed. Cells were prepared as described in section 2.10.1 and subjected to scRNAseq (biological n=1 CABG patient). (**A-C**) Following identification of distinct clusters within untreated control HSVSMCs by UMAP dimensionality reduction alongside Louvain community detection, RNA velocity and partition-based graph abstraction were generated utilising the scvelo package. Arrows indicate directionality of RNA velocity vectors. (**A**) Louvain UMAP graph displays RNA velocity vectors within clusters. (**B**) Louvain UMAP graph displays relative *SERPINE1* mRNA expression with RNA velocity overlay. (**C**) Louvain UMAP graph displays relative *ID1* mRNA expression with RNA velocity overlay.

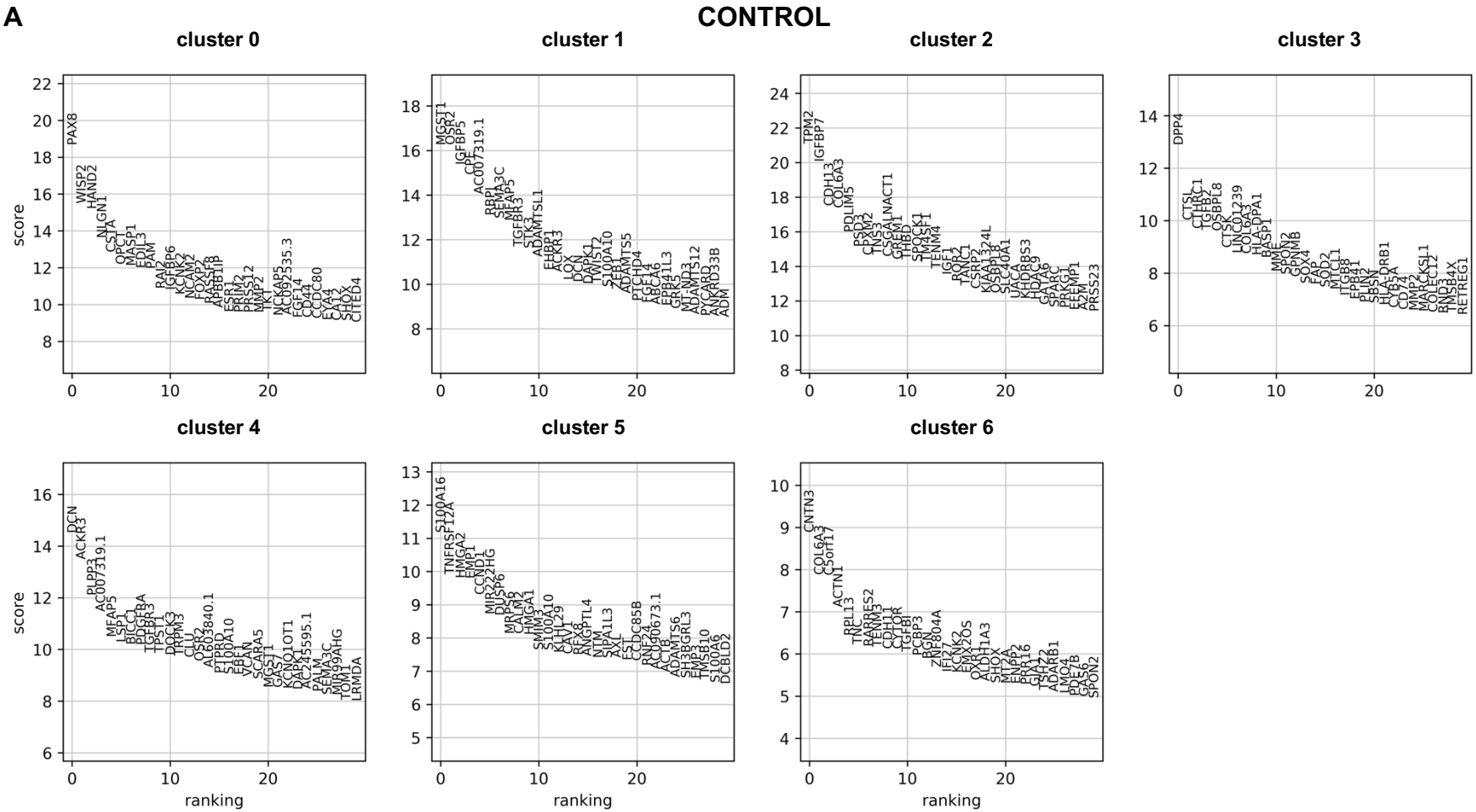

Figure 6-7 Top 30 most differentially regulated genes (DEGs) per cluster in untreated control primary HSVSMCs. (**A**) Clusters within untreated control HSVSMCs were identified by UMAP dimensionality reduction alongside Louvain community detection. The top 100 most DEGs were identified by using the Mann-Whitney-Wilcoxon test in combination with Benjamini-Hochberg correction. Graphs display the top 30 most DEGs for each cluster.

Cluster	GO biological process	No. of genes	Expected	Fold enrichment	Raw p value	FDR
0	regulation of high voltage-gated calcium channel activity	3	0.07	43.9	7.02E-05	4.67E-02
	negative regulation of animal organ morphogenesis	4	0.16	25.08	2.89E-05	3.08E-02
	coronary vasculature development	4	0.21	19.09	7.79E-05	4.79E-02
	cartilage development	7	0.71	9.85	9.45E-06	1.51E-02
	inner ear development	7	0.93	7.53	4.97E-05	3.78E-02
1	regulation of cellular response to growth factor stimulus	9	1.38	6.51	1.25E-05	5.01E-02
	heart development	12	2.47	4.86	7.81E-06	4.16E-02
	regulation of cell migration	15	4.12	3.64	1.64E-05	5.23E-02
	anatomical structure morphogenesis	26	10.29	2.53	7.10E-06	5.67E-02
	regulation of developmental process	30	12.52	2.4	4.53E-06	7.23E-02
2	Wnt signaling pathway involved in somitogenesis	2	0.02	80.97	4.94E-04	2.85E-02
	response to cortisol	2	0.02	80.97	4.94E-04	2.84E-02
	regulation of midbrain dopaminergic neuron differentiation	2	0.02	80.97	4.94E-04	2.83E-02
	axon extension involved in axon guidance	3	0.04	75.91	1.85E-05	2.04E-03
	negative regulation of osteoblast proliferation	3	0.04	67.48	2.46E-05	2.58E-03
3	ascending aorta morphogenesis	2	0.02	> 100	3.41E-04	3.58E-02
	negative regulation of extracellular matrix disassembly	2	0.02	> 100	3.41E-04	3.56E-02
	atrial septum primum morphogenesis	2	0.02	82.58	4.76E-04	4.63E-02
	regulation of macrophage cytokine production	3	0.07	41.29	8.42E-05	1.20E-02
	wound healing, spreading of cells	4	0.13	31.76	1.27E-05	2.81E-03
4	odontogenesis	6	0.58	10.32	3.34E-05	3.80E-02
	extracellular matrix organisation	12	1.75	6.86	2.44E-07	9.74E-04
	negative regulation of cell population proliferation	13	3.4	3.83	3.88E-05	4.13E-02
	positive regulation of developmental process	19	6.79	2.8	4.30E-05	4.29E-02
	regulation of multicellular organismal process	33	15.68	2.1	2.19E-05	2.91E-02
5	oncogene-induced cell senescence	2	0.01	> 100	1.24E-04	2.57E-02
	chronological cell aging	2	0.01	> 100	1.24E-04	2.54E-02
	senescence-associated heterochromatin focus assembly	2	0.01	> 100	2.06E-04	3.65E-02
	regulation of cytokine activity	2	0.02	> 100	3.08E-04	4.97E-02
	positive regulation of cell aging	3	0.07	43.44	7.24E-05	1.81E-02
6	bone development	7	0.86	8.13	3.12E-05	2.49E-02
	extracellular matrix organization	13	1.66	7.82	1.61E-08	2.58E-04
	wound healing	10	2	4.99	3.74E-05	2.85E-02
	regulation of cell migration	16	4.04	3.96	2.81E-06	3.45E-03
	circulatory system development	15	4.05	3.7	1.32E-05	1.32E-02

Table 6-1 GO enrichment terms for top 100 most DEGs within each cluster in untreated control primary HSVSMCs. GO enrichment analysis was performed based on the top 100 DEGs for each cluster. The top 5 biological processes are displayed for each cluster and are ranked by fold enrichment score with a false discovery rate (FDR) cut-off of $p<0.05$.

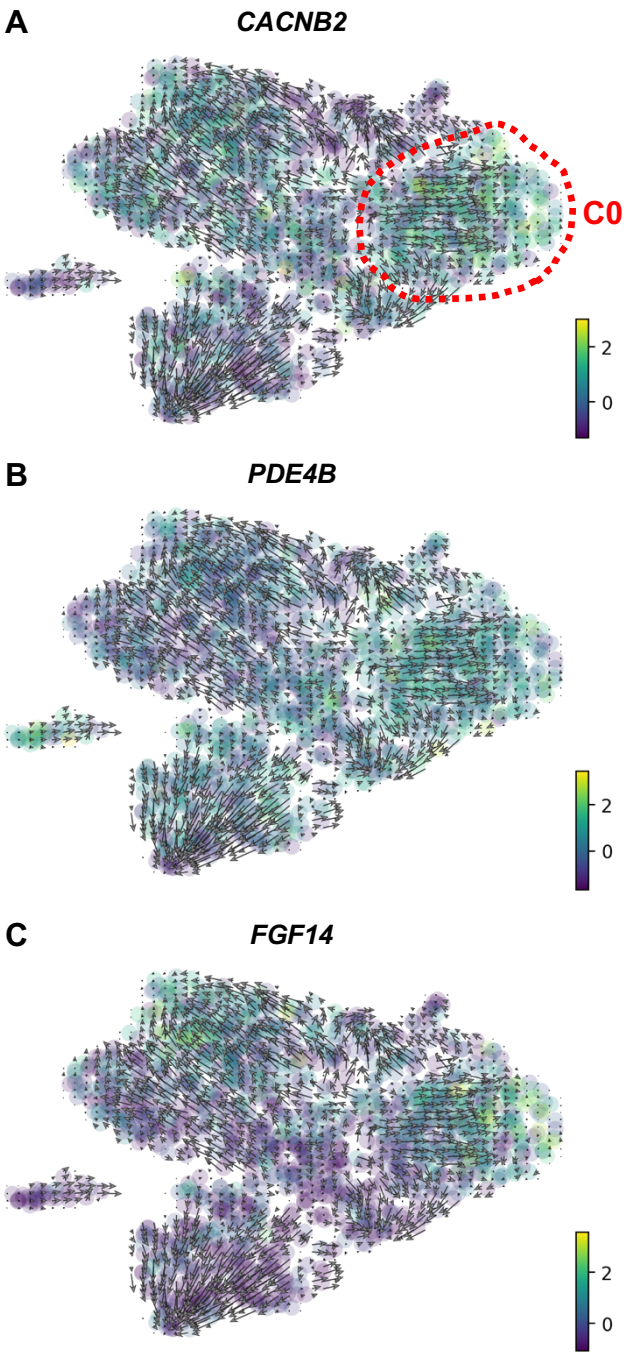

Figure 6-8 GO identifies enrichment for regulation of high voltage-gated calcium channel activity in cluster 0 in untreated control primary HSVSMCs. 80% confluent primary HSVSMCs were quiesced in 0.2% FCS media (MEDIA1) for 72-h. Quiescence media was replaced with media containing vehicle control (4 mM HCl/1% BSA). Following 24-h, media was removed. Cells were prepared as described in section 2.10.1 and subjected to scRNAseq (biological n=1 CABG patient). Following identification of distinct clusters within untreated control HSVSMCs by UMAP dimensionality reduction alongside Louvain community detection, RNA velocity and partition-based graph abstraction were generated utilising the scvelo package. Arrows indicate directionality of RNA velocity vectors. Louvain UMAP graphs display relative (**A**) *CACNB2*, (**B**) *PDE4B* and (**C**) *FGF14* mRNA expression with RNA velocity overlay.

6.3.5 ScRNA-seq analysis reveals a potentially osteogenic HSVSMC lineage following BMP-9 treatment

Previously presented immunoblot and qRT-PCR data in sections 4.3.10 and 4.3.11 demonstrated that BMP-9 induced SMAD1 phosphorylation and subsequent *ID1* mRNA expression in primary HSVSMCs. Combined UMAP/Louvain clustering alongside RNA velocity and GO analysis was performed to identify single cell transcriptional differences within BMP-9-treated primary HSVSMCs. Figure 6-10 displays the top 30 most differentially expressed genes for each cluster.

RNA velocity vectors indicated that BMP-9 treated HSVSMCs appeared to differentiate along 4 separate lineages starting from cluster 0 (blue) which displayed enrichment for white fat cell differentiation (enriched cluster genes: *AC092535*, encodes c-terminal-binding protein 1; *PPARG*, encodes peroxisome proliferator-activated receptor gamma; *SNAI2*, encodes zinc finger protein SNAI2) (Figure 6-11) and negative regulation of oxidative stress-induced cell death (*HSPB1*, encodes heat shock protein beta-1; *HGF*, encodes hepatocyte growth factor; *OXR1*, oxidation resistant protein 1; *FZD1*, encodes frizzled-1 (Figure 6-9 A) (Table 6-2).

Clusters 2 (green), 5 (brown) and 6 (pink) originated from clusters 0 (blue) and 3 (red). Whereas cluster 2 (green) showed enrichment for skeletal muscle cell maintenance (*IGF1*, encodes insulin-like growth factor-1; *FZD7*, encodes frizzled-7) and determination of dorsal identity (*GREM1*; *GREM2*) (Figure 6-11), the smaller cluster 5 (brown) displayed enrichment for coronary vasculature development (*ADAMTS6*; *LTBP1*; *TGFBR3*; *SGCD*, encodes delta-sarcoglycan) and response to calcium ion (*KCNMA1*, encodes calcium-activated potassium channel subunit alpha-1; *CALM2*, encodes calmodulin 2; *MEF2A*, encodes myocyte-specific enhancer factor 2A; *CAV1*, encodes caveolin 1; *S100A16*, encodes protein S100-A16; *CCND1*; *NLGN1*, encodes neuroligin-1).

In contrast, the smaller cluster 6 (pink) demonstrated enrichment for response to laminar fluid shear stress (*SREBF2*, encodes sterol regulatory element-binding protein 2; *ASS1*, encodes argininosuccinate synthase; *SMAD7*), chondrocyte development (*BMPR1B*, encodes bone morphogenetic protein receptor type-1B; *SULF1*, encodes extracellular sulfatase Sulf-1; *RUNX2*, encodes runt-related

transcription factor 2; *COL11A1*, encodes collagen alpha-1 11 chain) and bone morphogenesis (*INSIG1*, encodes insulin-induced gene 1 protein; *DHRS3*, encodes short-chain dehydrogenase/reductase 3; *BMPR1B*; *MMP16*, encodes matrix metalloproteinase-16; *SCX*, encodes basic helix-loop-helix transcription factor scleraxis; *RUNX2*).

Cluster 3 (red) also appeared to originate from cluster 0 (blue) and displayed enrichment for intramembranous ossification (*COL1A1*; *CTSK*, encodes cathepsin K; *MMP2*), regulation of macrophage cytokine production (*CD74*; *TGFB2*; *SPON2*) and regulation of ECM disassembly (*DPP4*; *FAP*; *PDPN*). Enrichment terms (and associated genes) in cluster 3 showed similarities to cluster 3 in untreated control HSVSMCs although relative *ID1* mRNA levels were higher indicating BMP-9/ALK1 or ALK2 pathway activation. Velocity vectors connected cluster 3 (red) to 4 (purple) and cluster 4 to 1 (orange). The 3 highest ranked biological processes were cellular response to prostaglandin D stimulus (*TNC*, encodes tenascin c; *AKR1C2*, encodes aldo-keto reductase family 1 member C2; *AKR1C3*), cellular response to hydroperoxide (*PRKD1*, encodes serine/threonine-protein kinase D1; *DAPK1*, encodes death-associated protein kinase 1; *MGST1*, microsomal glutathione S-transferase 1) and positive regulation of TGF-β production (*THBS1*, encodes thrombospondin-1; *CD34*, encodes hematopoietic progenitor cell antigen CD34; *LUM*, encodes lumican). Cluster 1 only displayed lowly ranked enrichment terms compared to all other examined clusters. Relative *SERPINE1* mRNA expression levels were low throughout all clusters suggesting absence of ALK5 pathway activation (Figure 6-9 A). In contrast, all clusters except for clusters 1 (orange) and 2 (green) displayed an increase in *ID1* mRNA levels indicating BMP-9-induced downstream SMAD1 pathway activation (Figure 6-9 B).

In summary BMP-9 drove 3 distinct HSVSMC lineages (clusters 2, 5 and 6) originating in cluster 0 (blue) which displayed an increase in *PPARG* and *SNAI2* mRNA expression levels. Of interest, cluster 2 displayed an increase in *IGF1* mRNA levels shown to potentiate BMP-9-induced osteogenic differentiation (Chen et al., 2016a). In addition, cluster 2 demonstrated an increase in *GREM1* and *GREM2* mRNA levels shown to negatively regulate BMP signalling within an inhibitory feedback loop (reviewed in) (Nolan and Thompson, 2014). Cluster 3

(red) showed enrichment term overlap with cluster 3 (red) in untreated control HSVSMCs suggesting the presence of a similar HSVSMC population. Finally, cluster 4 (purple) displayed an increase in *PRKD1*, *DAPK1* and *MGST* mRNA expression levels potentially reflecting transcriptional activation in response to oxidative stress (Eisenberg-Lerner and Kimchi, 2007; Kelner et al., 2000; Storz et al., 2005).

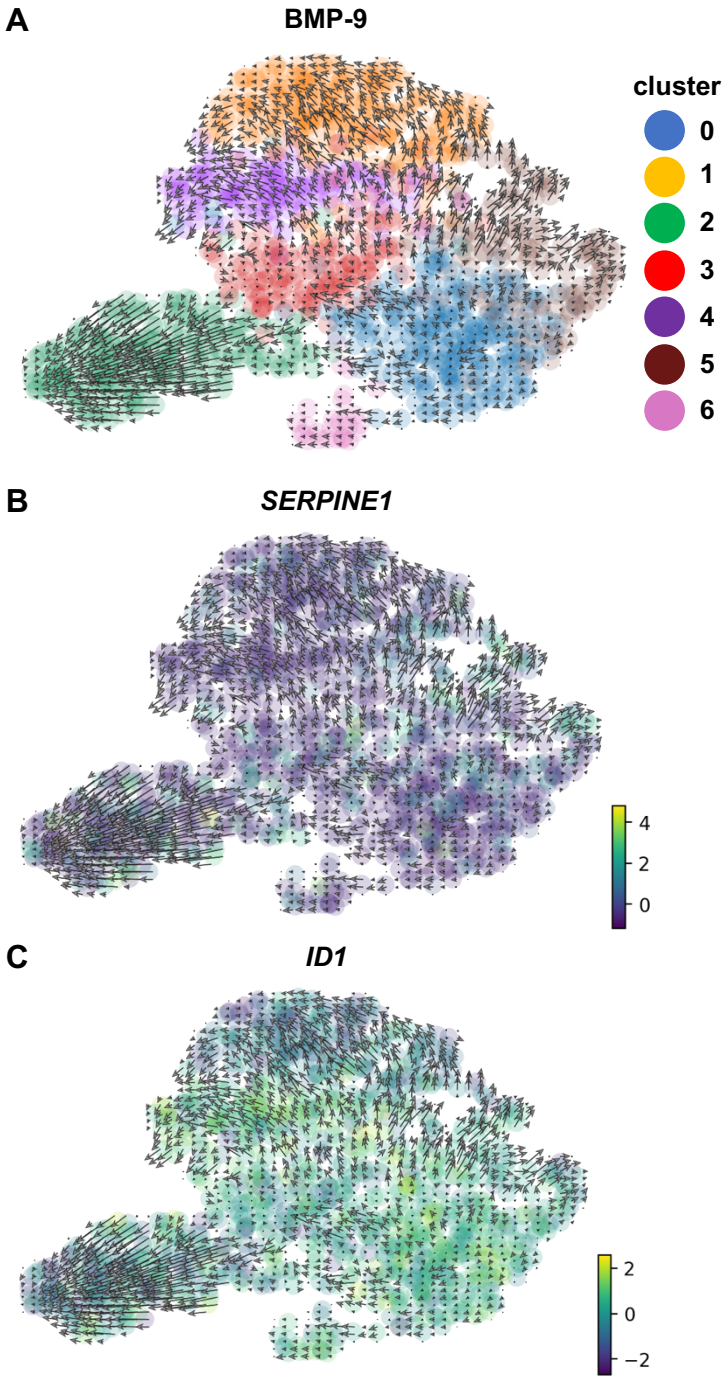

Figure 6-9 UMAP/Louvain clustering and RNA velocity in BMP-9-treated primary HSVSMCs. 80% confluent primary HSVSMCs were quiesced in 0.2% FCS media (MEDIA1) for 72-h. Quiescence media was replaced with stimulation media containing BMP-9 (10 ng/ml). Following 24-h, stimulation media was removed. Cells were prepared as described in section 2.10.1 and subjected to scRNAseq (biological n=1 CABG patient). (**A-C**) Following identification of distinct clusters within untreated control HSVSMCs by UMAP dimensionality reduction alongside Louvain community detection, RNA velocity and partition-based graph abstraction were generated utilising the scvelo package. Arrows indicate directionality of RNA velocity vectors. (**A**) Louvain UMAP graph displays RNA velocity vectors within clusters. (**B**) Louvain UMAP graph displays relative *SERPINE1* mRNA expression with RNA velocity overlay. (**C**) Louvain UMAP graph displays relative *ID1* mRNA expression with RNA velocity overlay.

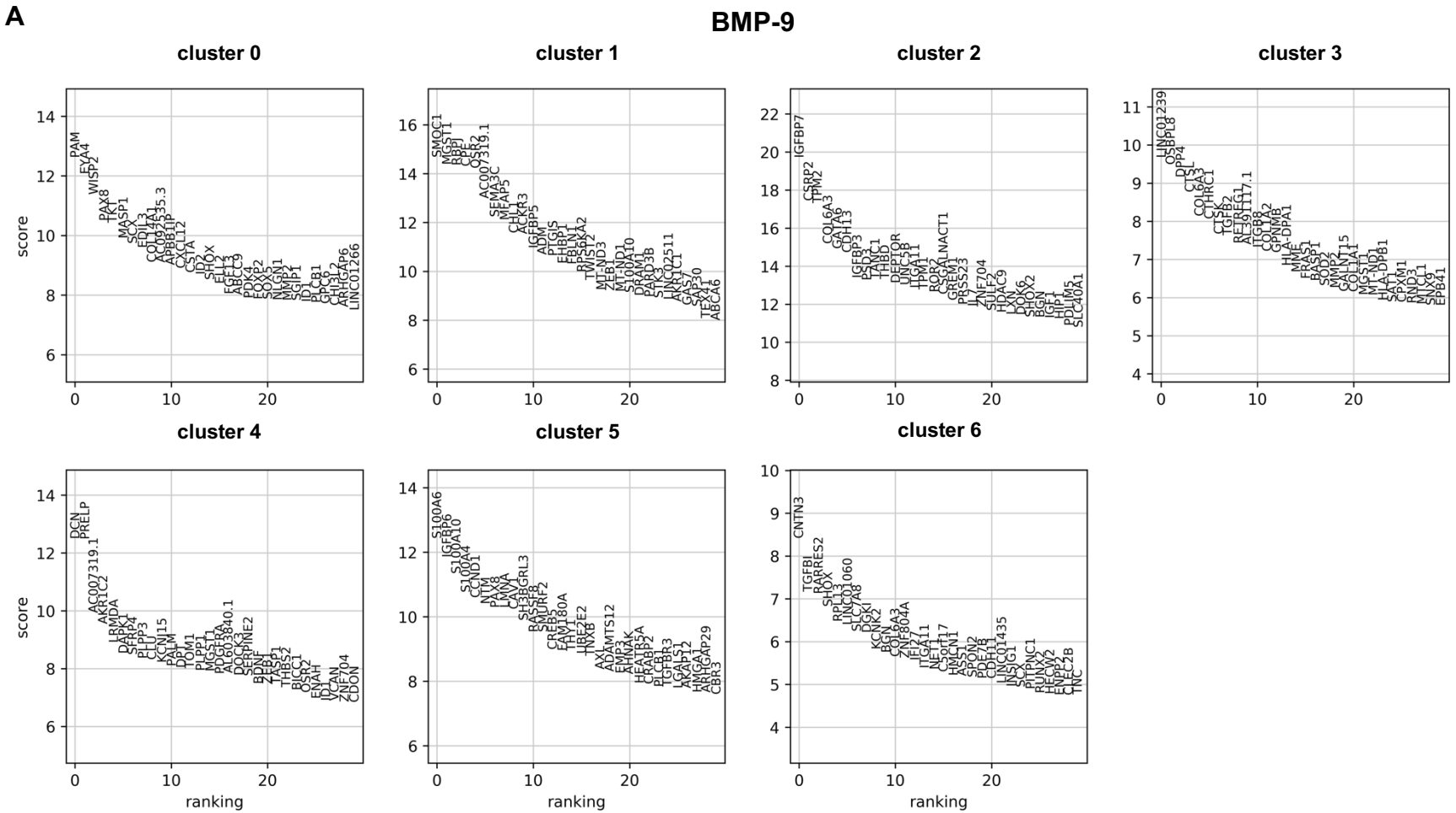

Figure 6-10 Top 30 most differentially regulated genes per cluster in BMP-9-treated primary HSVSMCs. (**A**) Clusters within BMP-9-treated HSVSMCs were identified by UMAP dimensionality reduction alongside Louvain community detection. The top 100 most DEGs were identified by using the Mann-Whitney-Wilcoxon test in combination with Benjamini-Hochberg correction. Graphs display the top 30 most DEGs for each cluster.

Cluster	GO biological process	No. of genes	Expected	Fold enrichment	Raw p value	FDR
0	white fat cell differentiation	3	0.07	46.06	6.24E-05	2.32E-02
	negative regulation of oxidative stress-induced cell death	4	0.22	18.29	9.14E-05	2.98E-02
	collagen fibril organization	4	0.22	17.91	9.86E-05	2.97E-02
	positive regulation of smooth muscle cell proliferation	5	0.41	12.08	7.60E-05	2.76E-02
	negative regulation of extrinsic apoptotic signaling pathway	5	0.49	10.14	1.67E-04	3.86E-02
1	regulation of cellular response to growth factor stimulus	8	1.42	5.62	1.08E-04	4.91E-02
	extracellular matrix organization	9	1.75	5.15	7.58E-05	4.84E-02
	eye development	9	1.81	4.98	9.67E-05	5.14E-02
	regulation of binding	9	1.82	4.95	1.01E-04	4.86E-02
	heart development	12	2.54	4.72	1.07E-05	1.22E-02
2	skeletal muscle satellite cell maintenance involved in skeletal muscle regeneration	2	0.02	> 100	3.21E-04	3.01E-02
	response to L-ascorbic acid	2	0.02	85.11	4.48E-04	3.85E-02
	determination of dorsal identity	2	0.02	85.11	4.48E-04	3.82E-02
	negative regulation of vascular associated smooth muscle cell migration	2	0.03	70.92	5.96E-04	4.68E-02
	gastro-intestinal system smooth muscle contraction	2	0.03	70.92	5.96E-04	4.66E-02
3	intramembranous ossification	3	0.03	> 100	9.21E-06	4.20E-03
	regulation of macrophage cytokine production	3	0.07	40.88	8.67E-05	2.10E-02
	regulation of extracellular matrix disassembly	3	0.08	38.33	1.03E-04	2.31E-02
	response to hydroperoxide	3	0.09	32.28	1.61E-04	3.26E-02
	collagen catabolic process	4	0.21	19.02	8.04E-05	2.04E-02
4	cellular response to prostaglandin D stimulus	3	0.02	> 100	5.30E-06	6.04E-03
	cellular response to hydroperoxide	3	0.04	80.61	1.55E-05	9.14E-03
	positive regulation of transforming growth factor beta production	3	0.09	33.94	1.39E-04	4.19E-02
	negative regulation of blood coagulation	5	0.24	21.07	6.08E-06	5.71E-03
	extracellular matrix organization	13	1.68	7.74	1.83E-08	1.46E-04
5	membrane assembly	4	0.16	24.91	2.95E-05	3.92E-02
	coronary vasculature development	4	0.21	19.5	7.18E-05	5.21E-02
	cardiac septum development	6	0.5	12.12	1.37E-05	2.74E-02
	cardiac ventricle development	6	0.58	10.43	3.09E-05	3.79E-02
	response to calcium ion	7	0.68	10.33	6.98E-06	2.23E-02
6	response to laminar fluid shear stress	3	0.07	40.1	9.18E-05	3.86E-02
	chondrocyte development	4	0.12	32.08	1.24E-05	8.58E-03
	positive regulation of cartilage development	4	0.16	25.06	2.98E-05	1.70E-02
	bone morphogenesis	6	0.48	12.53	1.18E-05	8.59E-03
	cardiac ventricle development	7	0.64	10.88	5.23E-06	4.17E-03

Table 6-2 GO enrichment terms for top 100 most DEGs within each cluster in BMP-9-treated primary HSVSMCs. GO enrichment analysis was performed based on the top 100 DEGs for each cluster. The top 5 biological processes are displayed for each cluster and are ranked by fold enrichment score with a false discovery rate (FDR) cut-off of $p<0.05$.

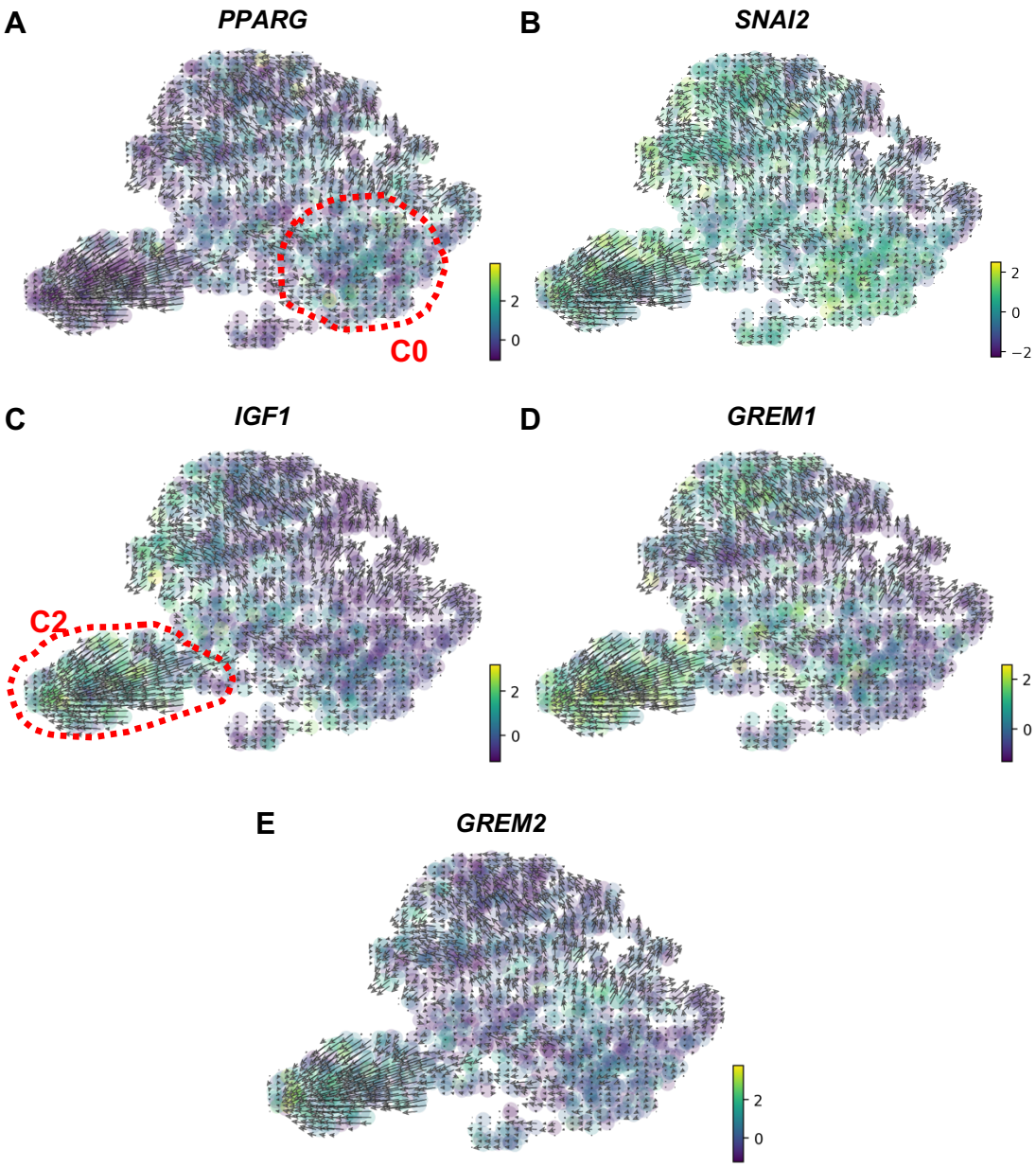

Figure 6-11 GO analysis identifies a potential osteogenic sub-lineage in BMP-9-treated primary HSVSMCs. 80% confluent primary HSVSMCs were quiesced in 0.2% FCS media (MEDIA1) for 72-h. Quiescence media was replaced with stimulation media containing BMP-9 (10 ng/ml). Following 24-h, stimulation media was removed. Cells were prepared as described in section 2.10.1 and subjected to scRNAseq (biological n=1 CABG patient). Following identification of distinct clusters within untreated control HSVSMCs by UMAP dimensionality reduction alongside Louvain community detection, RNA velocity and partition-based graph abstraction were generated utilising the scvelo package. Arrows indicate directionality of RNA velocity vectors. Louvain UMAP graphs display relative (**A**) *PPARG*, (**B**) *SNAI2*, (**C**) *IGF1*, (**D**) *GREM1* and (**E**) *GREM2* mRNA expression with RNA velocity overlay.

6.3.6 TGF-β_1-treated primary HSVSMC lineages express contractile, fibrotic and chemotactic genes

This study has so far comprehensively shown that TGF-β_1-drives contractile gene expression and AngII-dependent Ca^{2+} transients in primary HSVSMCs implicating the TGF-β_1/ALK5 pathway as a positive regulator of the contractile SMC phenotype. In addition, previous scRNAseq experiments from our group discovered simultaneous transcriptional activation of ALK1 and ALK5 target genes in HSVSMCs in response to TGF-β_1 treatment demonstrating non-overlapping ALK1- and ALK5-dominant SMC lineages within the same treatment group (unpublished data) (Low et al., 2019). Based on these findings, the next aim was to analyse scRNAseq data from TGF-β_1-treated HSVSMCs to identify potentially contractile SMC phenotypes and ALK1/ALK5-dominant lineages.

Single cell transcriptomics identified 8 distinct clusters within TGF-β_1-treated cells (Figure 6-12 A) (Table 6-3). Figure 6-13 displays the top 30 most differentially expressed genes for each cluster. Relative *SERPINE1* mRNA expression levels were elevated throughout all examined clusters indicating ALK5 pathway activation in all clusters (Figure 6-12 B). In contrast *ID1* mRNA levels were low indicating ALK1 or ALK2 pathway inactivation (Figure 6-12 C). Cluster 0 (blue) did not display any and cluster 4 (purple) only displayed 2 lowly ranked GO enrichment terms (Table 6-3).

RNA velocity vectors within cluster 1 (orange) indicated trans-differentiation towards clusters 2 (green), 3 (red) and 6 (pink) (Figure 6-12 A). The 3 highest ranked enrichment terms for cluster 1 (orange) were positive regulation of EMT (enriched cluster genes: *PAX8*, encodes paired box protein Pax-8; *LIF*, encodes leukaemia inhibitory factor), regulation of transepithelial transport (*ACTB*, encodes actin cytoplasmic 1; *ACTG1*, encodes actin cytoplasmic 2) and regulation of lymphangiogenesis (*VEGFC*, encodes vascular endothelial growth factor c; *FOXC1*, encodes forkhead box protein C1). In addition, cluster 1 showed enrichment for regulation of stress fibre formation (*ACTG1*; *CTGF*; *ALK5*; *TPM1*, encodes tropomyosin alpha-1 chain; *DLC1*, Rho GTPase-activating protein 7; expected 0.44; fold enrichment 11.47, raw p value 9.68E-05; FDR 1.61E-02; data not shown in table) (Figure 6-14 A-E).

Cluster 2 (green) originated from cluster 1 (orange) and showed enrichment terms for negative regulation of B-cell differentiation (*INHBA*, encodes inhibin beta A chain; *SFRP1*), response to heparin (*EGR1*, encodes early growth response protein 1; *SFRP1*), response to cortisol (*SLIT3*, encodes slit homolog 3 protein; *IGFBP7*, IGF-binding protein 7), intramembranous ossification (*COL1A1*; *MN1*, encodes transcriptional activator MN1) and collagen-activated tyrosine kinase receptor signalling pathway (*COL1A1*; *COL4A1*; *COL4A2*) (Figure 6-15 A-C) (Table 6-3). Within cluster 2 (green) velocity vectors indicated a split into two potential SMC sub-lineages (Figure 6-12 A).

Cluster 3 (red) also originated from cluster 1 (orange) (Figure 6-12 A). Cluster 3 demonstrated enrichment for regulation of chemokine-mediated signalling pathway (*HIF1A*, encodes hypoxia-inducible factor 1-alpha; *ROBO1*, roundabout homolog 1; *AL049569*, protein-arginine deiminase type-2), induction of positive chemotaxis (*SCG2*, encodes secretogranin-2; *VEGFA*; *CXCL12*, stromal cell-derived factor 1) (Figure 6-16 A-C), post-embryonic animal organ development (*EFEMP1*, encodes EGF-containing fibulin-like extracellular matrix protein 1; *VEGFA*; *AL049569*, encodes microfibrillar-associated protein 2), positive regulation of neuroblast proliferation (*HIF1A*; *VEGFA*; *GLI3*, encodes transcriptional activator GLI3) and collagen fibril organisation (*SERPINH1*, encodes serpin H1; *COL1A1*; *COL1A2*; *COL3A1*; *ADAMTS2*; *COL5A2*) (Table 6-3).

Moreover, velocity vectors indicated that cluster 5 (brown) originated from cluster 3 (red) (Figure 6-12 A). The 3 highest ranked enrichment terms were negative regulation of neuron migration (*NRG1*, encodes pro-neuregulin-1 membrane-bound isoform; *ERBB4*, encodes receptor tyrosine-protein kinase erbB-4; *COL3A1*), negative regulation of pathway-restricted SMAD protein phosphorylation (*PMEPA1*, encodes protein TMEPAI; *ENG*; *LDLRAD4*, encodes low-density lipoprotein receptor class A domain-containing protein 4) (Figure 6-17 A-C) and collagen fibril organisation (*LOXL1*, encodes lysyl oxidase homolog 1; *DPT*, dermatopontin; *CYP1B1*, encodes cytochrome P450 1B1; *LOXL1*; *COL3A1*) (Table 6-3).

The smaller cluster 6 (pink) originated from cluster 1 (orange) and in part from clusters 3 (red) and 5 (brown) as indicated by RNA velocity vectors (Figure 6-12 A). The top 2 enrichment terms were oncogene-induced cell senescence

(*HMGA1*; *HMGA2*) and positive regulation of cellular senescence (*HMGA1*; *HMGA2*; *B2M*, encodes beta-2-microglobulin) (Table 6-3). Finally, cluster 7 (olive) appeared to be separated from the other clusters (Figure 6-12 A). The highest ranked enrichment term was negative regulation of smooth muscle contraction (*KCNMA1*; *PRKG1*, encodes cGMP-dependent protein kinase 1; *AC007319*, encodes calcitonin gene-related peptide type 1 receptor) (Table 6-3).

In summary, TGF-β_1 drove 3 to 4 main HSVSMC lineages. Whereas ALK5 pathway activity was enhanced throughout all examined clusters the ALK1/ALK2 pathway appeared inactive contrasting results from our previous study (unpublished data) (Low et al., 2019). Cluster 1 (orange) demonstrated enrichment for stress fiber formation. In addition, this cluster showed an increase in *DLC1* mRNA levels shown to drive intracellular Ca^{2+} release in response to acetylcholine and coronary vasospasm (Kinjo et al., 2015; Murakami et al., 2010), potentially indicating a contractile SMC phenotype. In contrast, cluster 2 (green) appeared to be enriched for pro-fibrotic genes, such as collagen and *EGR1*. Cluster 3 demonstrated enrichment for the pro-inflammatory genes *VEGFA* and *CXCL12* mRNA levels. Finally, cluster 5 (brown) displayed enrichment *LDLRAD4* and *PMEPA1* potentially indicating negative regulation of TGF-β signalling (Clement et al., 2007; Fournier et al., 2015; Liu et al., 2017).

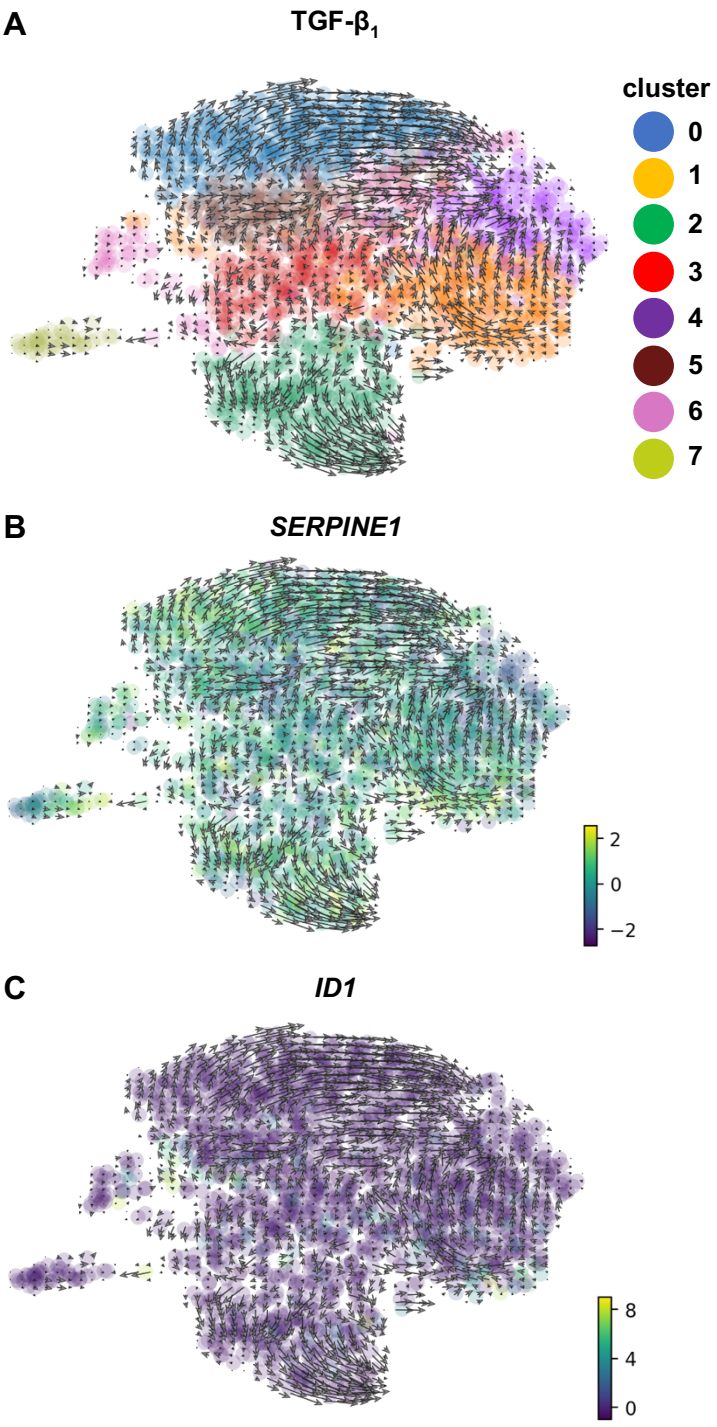

Figure 6-12 UMAP/Louvain clustering and RNA velocity in TGF-β_1-treated primary HSVSMCs. 80% confluent primary HSVSMCs were quiesced in 0.2% FCS media (MEDIA1) for 72-h. Quiescence media was replaced with stimulation media containing TGF-β_1 (10 ng/ml). Following 24-h, stimulation media was removed. Cells were prepared as described in section 2.10.1 and subjected to scRNAseq (biological n=1 CABG patient). (**A-C**) Following identification of distinct clusters within untreated control HSVSMCs by UMAP dimensionality reduction alongside Louvain community detection, RNA velocity and partition-based graph abstraction were generated utilising the scvelo package. Arrows indicate directionality of RNA velocity vectors. (**A**) Louvain UMAP graph displays RNA velocity vectors within clusters. (**B**) Louvain UMAP graph displays relative *SERPINE1* mRNA expression with RNA velocity overlay. (**C**) Louvain UMAP graph displays relative *ID1* mRNA expression with RNA velocity overlay.

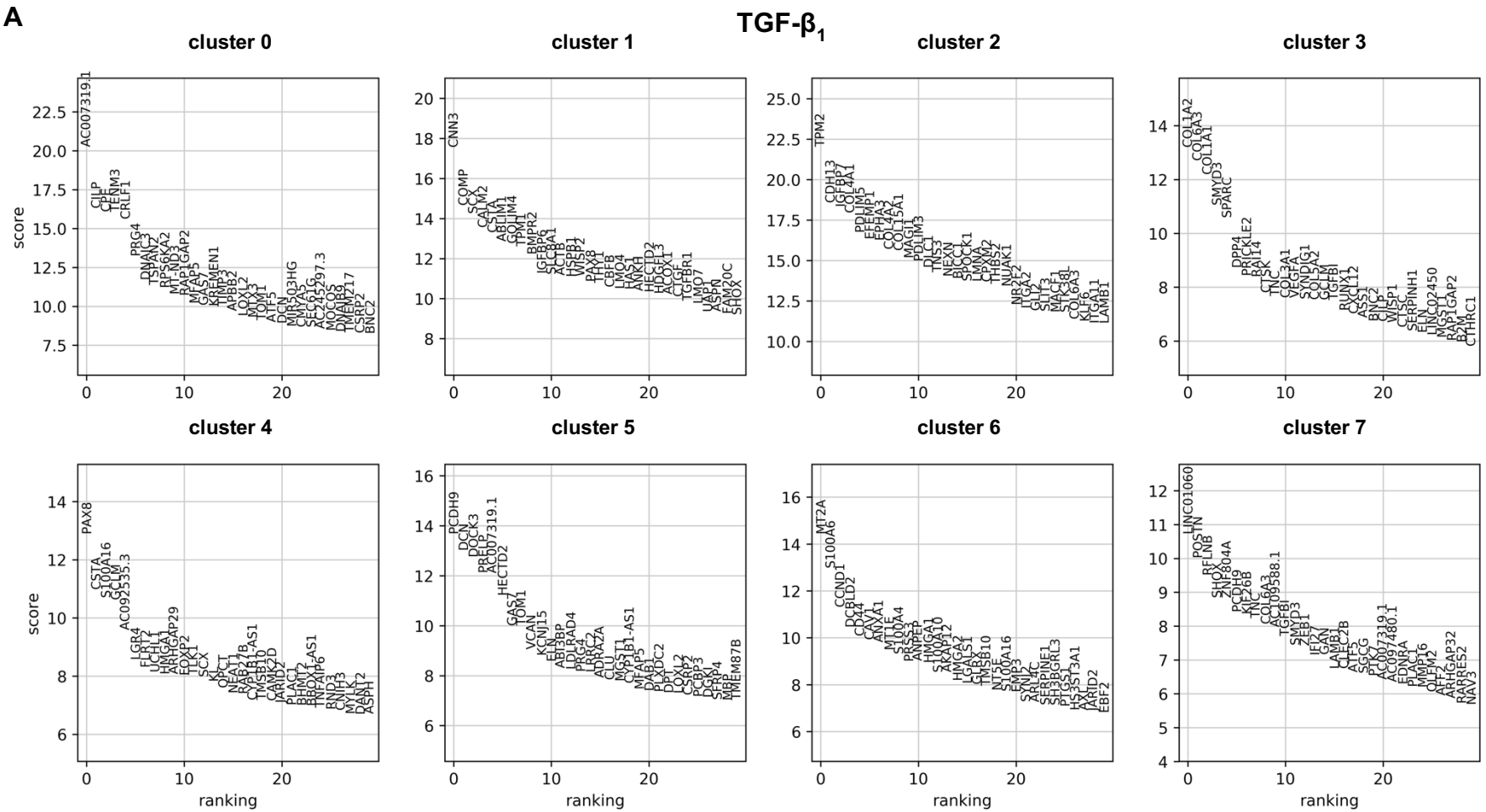

Figure 6-13 Top 30 most DEGs per cluster in TGF-β_1-treated primary HSVSMCs. (**A**) Clusters within TGF-β_1-treated HSVSMCs were identified by UMAP dimensionality reduction alongside Louvain community detection. The top 100 most DEGs were identified by using the Mann-Whitney-Wilcoxon test in combination with Benjamini-Hochberg correction. Graphs display the top 30 most DEGs for each cluster.

Cluster	GO biological process	No. of genes	Expected	Fold enrichment	Raw p value	FDR
1	positive regulation of mesenchymal to epithelial transition involved in metanephros morphogenesis	2	0.02	> 100	3.41E-04	3.97E-02
	regulation of transepithelial transport	2	0.02	> 100	3.41E-04	3.94E-02
	regulation of lymphangiogenesis	2	0.02	82.58	4.76E-04	4.93E-02
	regulation of endothelial cell chemotaxis	3	0.1	29.49	2.04E-04	2.91E-02
	vascular endothelial growth factor signaling pathway	3	0.11	28.15	2.32E-04	3.11E-02
2	negative regulation of B cell differentiation	2	0.02	85.11	4.48E-04	3.08E-02
	cellular response to heparin	2	0.02	85.11	4.48E-04	3.07E-02
	response to cortisol	2	0.02	85.11	4.48E-04	3.06E-02
	intramembranous ossification	2	0.03	70.92	5.96E-04	3.82E-02
	collagen-activated tyrosine kinase receptor signaling pathway	3	0.05	58.03	3.48E-05	4.56E-03
3	regulation of chemokine-mediated signaling pathway	3	0.05	60.15	3.28E-05	6.54E-03
	induction of positive chemotaxis	3	0.07	40.1	9.18E-05	1.42E-02
	post-embryonic animal organ development	3	0.08	35.38	1.27E-04	1.81E-02
	positive regulation of neuroblast proliferation	3	0.11	26.15	2.84E-04	3.34E-02
	collagen fibril organization	6	0.24	25.06	2.75E-07	1.37E-04
4	head development	15	3.72	4.03	4.86E-06	3.88E-02
	animal organ development	35	14.77	2.37	4.68E-07	7.47E-03
5	negative regulation of neuron migration	3	0.06	52.13	4.60E-05	2.72E-02
	negative regulation of pathway-restricted SMAD protein phosphorylation	3	0.06	48.12	5.65E-05	3.22E-02
	collagen fibril organization	5	0.23	21.72	5.36E-06	6.11E-03
	myelination	6	0.53	11.37	1.97E-05	1.50E-02
	striated muscle tissue development	9	1.37	6.56	1.19E-05	1.19E-02
6	oncogene-induced cell senescence	2	0.01	> 100	1.24E-04	4.71E-02
	positive regulation of cellular senescence	3	0.06	50.12	5.00E-05	3.99E-02
	response to progesterone	4	0.21	18.89	8.12E-05	4.32E-02
	endothelial cell migration	5	0.32	15.74	2.28E-05	2.60E-02
	tissue remodeling	5	0.46	10.97	1.17E-04	4.56E-02
7	negative regulation of smooth muscle contraction	3	0.07	42.12	7.93E-05	4.52E-02
	extracellular matrix organization	9	1.71	5.25	6.49E-05	3.98E-02
	tube morphogenesis	16	3.17	5.05	1.25E-07	3.99E-04
	cell-cell adhesion	11	2.43	4.53	3.61E-05	2.62E-02
	anatomical structure formation involved in morphogenesis	18	4.26	4.23	2.52E-07	5.04E-04

Table 6-3 GO enrichment terms for top 100 most DEGs within each cluster in TGF-β_1-treated primary HSVSMCs. GO enrichment analysis was performed based on the top 100 DEGs for each cluster. The top 5 biological processes are displayed for each cluster and are ranked by fold enrichment score with a false discovery rate (FDR) cut-off of $p<0.05$.

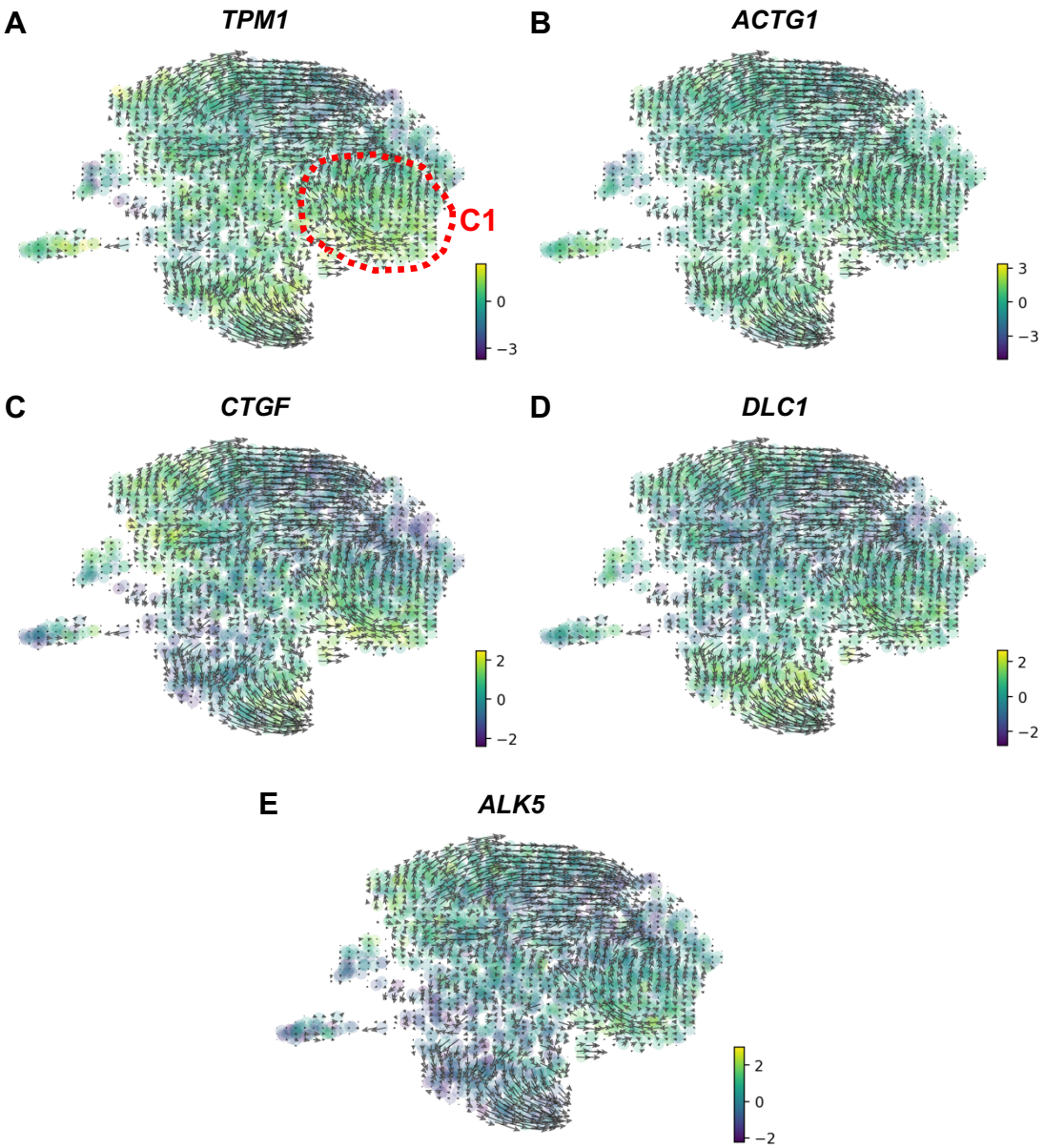

Figure 6-14 Cluster 1 displays enrichment for genes associated with stress fibre formation in primary HSVSMCs following TGF-β_1 treatment. 80% confluent primary HSVSMCs were quiesced in 0.2% FCS media (MEDIA1) for 72-h. Quiescence media was replaced with stimulation media containing TGF-β_1 (10 ng/ml). Following 24-h, stimulation media was removed. Cells were prepared as described in section 2.10.1 and subjected to scRNAseq (biological n=1 CABG patient). Following identification of distinct clusters within untreated control HSVSMCs by UMAP dimensionality reduction alongside Louvain community detection, RNA velocity and partition-based graph abstraction were generated utilising the scvelo package. Arrows indicate directionality of RNA velocity vectors. Louvain UMAP graph displays relative (**A**) *TPM1*, (**B**) *ACTG1*, (**C**) *CTGF*, (**D**) *DLC1* and (**E**) *ALK5* mRNA expression with RNA velocity overlay.

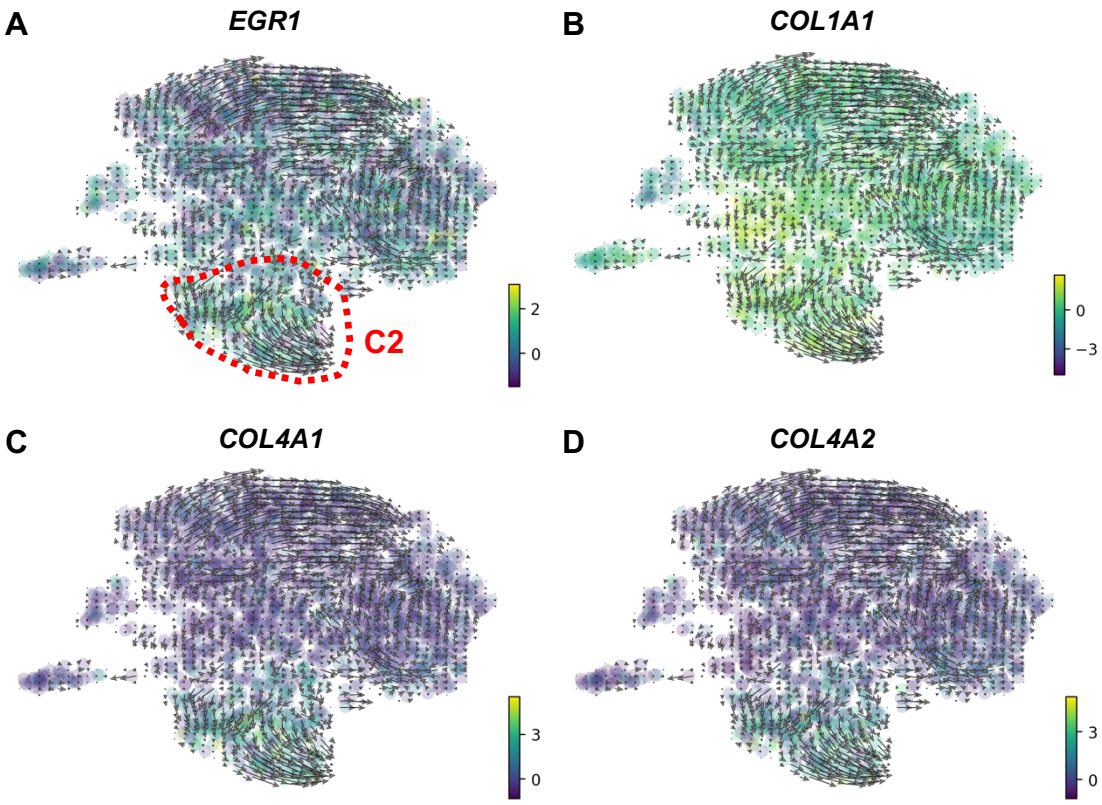

Figure 6-15 Cluster 2 displays enrichment for pro-fibrotic genes in primary HSVSMCs following TGF-β_1 treatment. 80% confluent primary HSVSMCs were quiesced in 0.2% FCS media (MEDIA1) for 72-h. Quiescence media was replaced with stimulation media containing TGF-β_1 (10 ng/ml). Following 24-h, stimulation media was removed. Cells were prepared as described in section 2.10.1 and subjected to scRNAseq (biological n=1 CABG patient). Following identification of distinct clusters within untreated control HSVSMCs by UMAP dimensionality reduction alongside Louvain community detection, RNA velocity and partition-based graph abstraction were generated utilising the scvelo package. Arrows indicate directionality of RNA velocity vectors. Louvain UMAP graph displays relative (**A**) *EGR1*, (**B**) *COL1A1*, (**C**) *COL4A1* and (**D**) *COL4A2* mRNA expression with RNA velocity overlay.

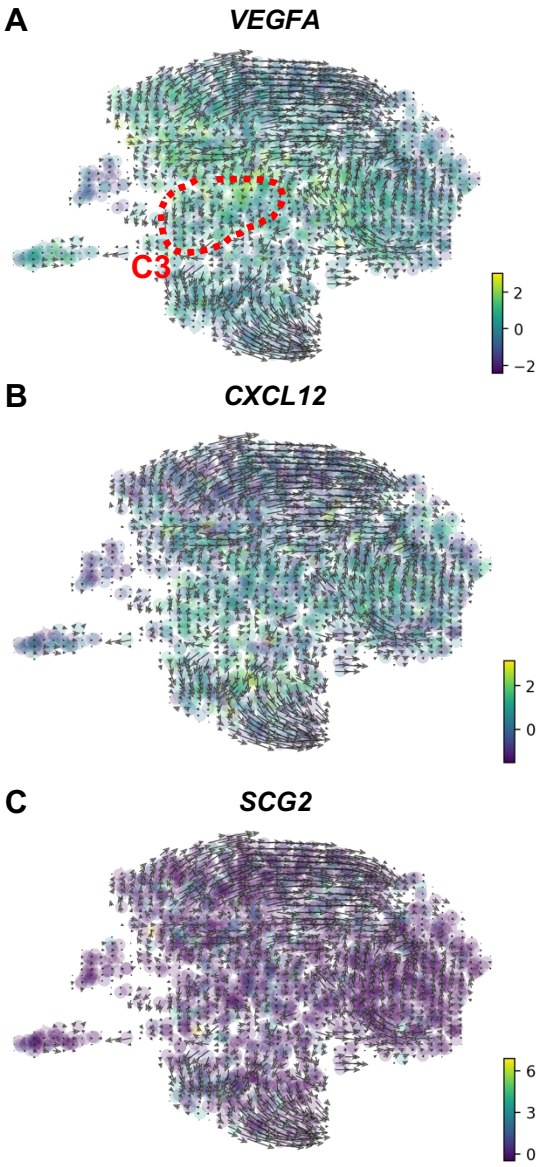

Figure 6-16 Cluster 3 demonstrates overlap of genes associated with induction of positive chemotaxis in primary HSVSMCs following TGF-β_1 treatment. 80% confluent primary HSVSMCs were quiesced in 0.2% FCS media (MEDIA1) for 72-h. Quiescence media was replaced with stimulation media containing TGF-β_1 (10 ng/ml). Following 24-h, stimulation media was removed. Cells were prepared as described in section 2.10.1 and subjected to scRNAseq (biological n=1 CABG patient). Following identification of distinct clusters within untreated control HSVSMCs by UMAP dimensionality reduction alongside Louvain community detection, RNA velocity and partition-based graph abstraction were generated utilising the scvelo package. Arrows indicate directionality of RNA velocity vectors. Louvain UMAP graph displays relative (**A**) *VEGFA*, (**B**) *CXCL12* and (**C**) *SCG2* mRNA expression with RNA velocity overlay.

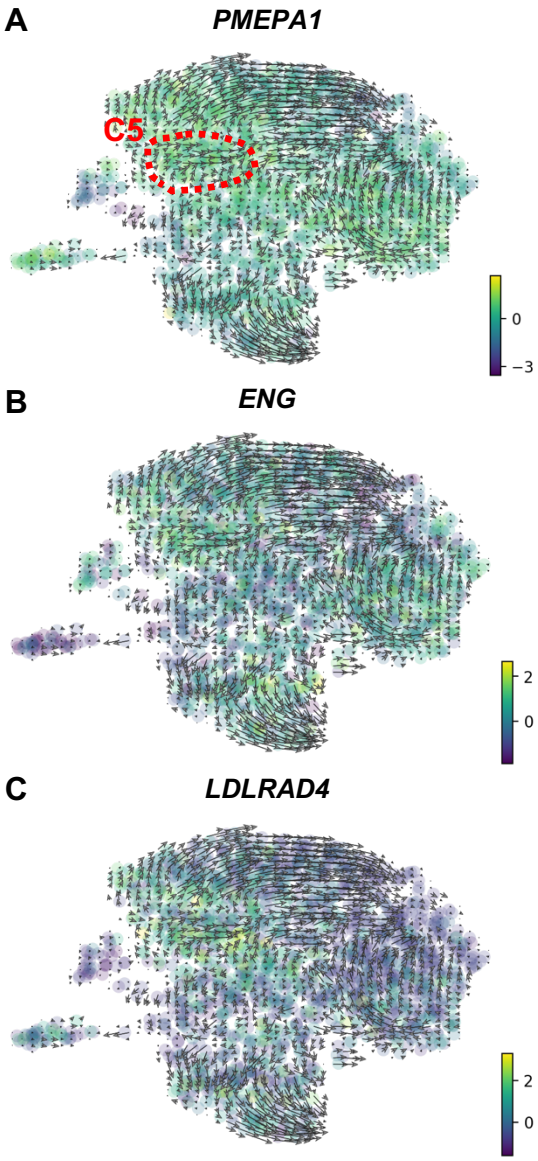

Figure 6-17 Cluster 5 displays overlap of genes associated with negative regulation of pathway-restricted SMAD protein phosphorylation in primary HSVSMCs following TGF-β_1 treatment. 80% confluent primary HSVSMCs were quiesced in 0.2% FCS media (MEDIA1) for 72-h. Quiescence media was replaced with stimulation media containing TGF-β_1 (10 ng/ml). Following 24-h, stimulation media was removed. Cells were prepared as described in section 2.10.1 and subjected to scRNAseq (biological n=1 CABG patient). Following identification of distinct clusters within untreated control HSVSMCs by UMAP dimensionality reduction alongside Louvain community detection, RNA velocity and partition-based graph abstraction were generated utilising the scvelo package. Arrows indicate directionality of RNA velocity vectors. Louvain UMAP graph displays relative (**A**) *PMEPA1*, (**B**) *ENG* and (**C**) *LDLRAD4* mRNA expression with RNA velocity overlay.

6.3.7 Single cell transcriptomics uncover potential mechanisms for negative regulation of contractility in BMP-9/TGF-β_1-co-treated primary HSVSMCs

Previously presented data showed that BMP-9 prevented TGF-β_1-induced increase in AngII-driven intracellular Ca^{2+} mobilisation (section 5.3.2) but did not prevent TGF-β_1-driven *SERPINE1* and contractile gene expression in primary HSVSMCs (4.3.11). Single cell transcriptional analysis was performed to (i) identify a potential underlying mechanism for the inhibitory BMP-9-mediated effect on TGF-β_1-dependent Ca^{2+} handling and to (ii) investigate potential BMP-9/TGF-β_1 signalling agonism and/or antagonism in primary HSVSMCs.

Combined UMAP/Louvain clustering identified 9 clusters within BMP-9/TGF-β_1-co-treated HSVSMCs (Figure 6-18 A, Table 6-4, Table 6-5). Figure 6-19 and Figure 6-20 display the top 30 most differentially expressed genes for each cluster. Cluster 3 (red) did not yield any GO enrichment terms. Relative *SERPINE1* mRNA levels appeared visually enhanced in all clusters except cluster 4 indicating ALK5 pathway activation (Figure 6-18 B). In contrast, only clusters 0 (blue), 4 (purple), 6 (pink) and 7 (grey) displayed an increase in relative *ID1* mRNA levels indicating ALK1/ALK2 pathway activation (Figure 6-18 C). In contrast to BMP-9 and TGF-β_1 stimulation alone, RNA velocity vector analysis did not show clear lineage differentiation paths within this treatment group.

Cluster 0 (blue) partially originated from cluster 1 (orange). GO enrichment terms for cluster 0 included inorganic diphosphate transport (enriched cluster genes: *ANKH*, encodes progressive ankylosis protein homolog; *ENPP1*, encodes ectonucleotide pyrophosphatase/phosphodiesterase family member 1) (Figure 6-21 A and B), germ cell migration (*TGFB1*; *TGFBR1*; *FOXC1*), positive regulation of hematopoietic progenitor cell differentiation (*ZBTB1*, encodes zinc finger and BTB domain-containing protein 1; *FOXC1*), regulation of lymphangiogenesis (*VEGFC*; *FOXC1*) and VEGF signalling pathway (*HSPB1*, encodes heat shock protein beta-1; *VEGFC*; *FOXC1*) (Table 6-4). Although not listed within the 5 highest ranking enrichment terms, cluster 0 showed enrichment for negative regulation of Ca^{2+}-mediated signalling (*CALM2*, encodes calmodulin-2; *FHL2*, encodes four and a half LIM domains protein 2; *RCAN1*, encodes calcipressin-1; expected 0.15; fold enrichment 19.67, raw p value 6.14E-04; FDR 4.61E-02; data

not shown in table) (Figure 6-21 C). In line with an increase in *ID1* mRNA levels this cluster also displayed enrichment for BMP signalling pathway (*TGFB1*; SMURF2, encodes E3 ubiquitin-protein ligase SMURF2; *SKI*, encodes Ski oncogene; *FST*, encodes follistatin; *BMPR2*; *SCX*; *ID1*; *COMP*, encodes cartilage oligomeric matrix protein; expected 0.45; fold enrichment 17.88, raw p value 3.01E-08; FDR 3.00E-05; data not shown in table).

Cluster 1 (orange) mainly originated from cluster 4 (purple) and displayed similarities with cluster 2 (green) in the TGF-β_1 treatment group (Figure 6-18 A). The top 5 enrichment terms were neural crest cell fate commitment (*SOX9*; *SFRP1*), negative regulation of B cell differentiation (*INHBA*, *SFRP1*), cellular response to heparin (*SOX9*; *SFRP1*), response to cortisol (*SLIT3*; *IGFBP7*) and determination of dorsal identity (*GREM1*; *GREM2*) (Table 6-4). In addition, this cluster enriched for collagen-activated signalling pathway (*ITGA2*, encodes integrin alpha-2; *ITGA11*, encodes integrin alpha-11; *COL4A1*; *COL4A2*; expected 0.07; fold enrichment 60.18; raw p value 1.36E-06; FDR 3.30E-04; data not shown in table) (Figure 6-22 B and C).

Cluster 4 (purple) demonstrated an increase in *ID1* mRNA levels indicating ALK1/ALK2 pathway activation (Figure 6-18 A, C). RNA velocity vectors suggested trans-differentiation towards clusters 0 (blue) and 1 (orange). Highest ranked biological processes included negative regulation of cell proliferation involved in contact inhibition (*SRPX*; encodes sushi repeat-containing protein SRPX; *FAP*), response to human chorionic gonadotropin (*GCLM*; encodes glutamate-cysteine ligase regulatory subunit; *MYC*, encodes Myc proto-oncogene protein), positive regulation of CD8-positive/alpha-beta T cell differentiation (*CBFB*, encodes core-binding factor subunit beta; *RUNX1*), negative regulation of ECM disassembly (*DPP4*; *FAP*) and negative regulation of endothelial cell differentiation (*ZEB1*, encodes zinc finger E-box-binding homeobox 1; *VEGFA*; *ID1*) (Table 6-4).

Velocity vectors within cluster 2 (green) indicated that cells originated from within the same cluster (Figure 6-18 A). The 3 highest ranking biological processes were arginine metabolic process (*DOK1*, encodes ecto-ADP-ribosyltransferase 4; *DDAH1*; encodes N(G),N(G)-dimethylarginine dimethylaminohydrolase 1; *ASS1*) (Figure 6-23 A-C), negative regulation of smooth muscle cell migration (*SERPINE1*; *PPARGC1A*, peroxisome proliferator-

activated receptor gamma coactivator 1-alpha; *IGFBP5*) and glycosaminoglycan biosynthetic process (*HAS1*, encodes hyaluronan synthase 1; *DCN*, encodes decorin; *UGDH*, UDP-glucose 6-dehydrogenase; *SDC1*, encodes syndecan-1; *ST3GAL1*, encodes CMP-N-acetylneuraminate-beta-galactosamide-alpha-2,3-sialyltransferase 1; *B4GALT1*, encodes beta-1,4-galactosyltransferase 1) (Table 6-4).

Cluster 5 (brown) mainly originated from cluster 2 (green) and partially from cluster 0 (blue) (Figure 6-18 A). This cluster displayed biological processes relating to re-entry into mitotic cell cycle (*CCND1*; *MYC*), response to human chorionic gonadotropin (*GLCM*; *MYC*), epithelial to mesenchymal transition involved in endocardial cushion formation (*MSX2*, encodes homeobox protein MSX-2; *ENG*; *TMEM100*, encodes transmembrane protein 100), venous blood vessel development (*VEGFA*; *BMPR2*; *ENG*) and regulation of blood vessel endothelial cell proliferation involved in sprouting angiogenesis (*NGFR*, encodes tumor necrosis factor receptor superfamily member 16; *VEGFA*; *HMOX1*, encodes heme oxygenase 1) (Table 6-4). From cluster 5 (brown) velocity vectors indicated trans-differentiation towards cluster 3 (red) which did not yield any biological processes (Figure 6-18 A).

Cluster 6 (pink) was small and appeared to originate from cluster 3 (red) (Figure 6-18 A). Biological processes identified by GO comparatively yielded lower fold enrichment scores (Table 6-5). The top 3 identified biological processes were chondrocyte development (*SULF2*; *SCX*; *SULF1*; *TGFB1*; *RUNX2*), embryonic skeletal system development (*SULF2*; *ZEB1*; *MMP16*; *SCX*; *SULF1*; *DLX2*, encodes Homeobox protein DLX-2; *RUNX2*) and developmental growth involved in morphogenesis (*TNC*; *PTK7*, encodes inactive tyrosine-protein kinase 7; *NRP2*, encodes neuropilin-2; *POSTN*, encodes periostin; *KIF26B*, encodes kinesin-like protein KIF26B). Together with an increase in *ID1* mRNA levels, this cluster showed some overlap with cluster 6 (pink) in BMP-9-treated HSVSMCs.

Cluster 7 (olive) was also small and was situated between clusters 1 (orange) and 4 (purple) (Figure 6-18 A). Velocity vectors did not allow to determine a clear origin for this cluster. The 5 highest ranking biological processes were glutamine catabolic process (*GLS*; glutaminase liver isoform, mitochondrial), regulation of transepithelial transport (*ACTB*; *ACTG1*), postsynaptic actin cytoskeleton

organisation (*ACTB*; *ACTG1*; *MYH10*, encodes myosin-10), ventricular cardiac muscle cell differentiation (*NRG1*; *MYH10*; *FHL2*) and relaxation of muscle (*KCNMA1*; *SLC8A1*, encodes sodium/calcium exchanger 1; *PLN*, encodes cardiac phospholamban) (Table 6-5).

Finally, the smallest cluster 8 (turquoise) originated from cluster 2 (green) (Figure 6-18 A). The top 3 biological processes were negative regulation of smooth muscle cell migration (*IGFBP3*; *SERPINE1*; *IBFBP5*), regulation of insulin-like growth factor receptor signalling pathway (*IGFBP3*; *IGFBP6*; *IGFBP7*) and positive regulation of G1/S transition of mitotic cell cycle (*EGFR*, encodes epidermal growth factor receptor; *CCND1*; *ADAMTS1*; *ANXA1*, encodes annexin A1) (Table 6-5).

In conclusion, UMAP/Louvain clustering identified 9 clusters within BMP-9/TGF-β_1-co-treated HSVSMCs. In contrast to single ligand-treated cells, RNA velocity vectors did not indicate clear lineage differentiation. Cluster 0 (blue) displayed an increase in *ANKH* and *ENPP1* mRNA levels, two known negative regulators of vascular calcification (Chen et al., 2019; Lomashvili et al., 2014). Furthermore, this cluster demonstrated an increase in *RCAN1* mRNA levels shown to negatively regulate vascular contractility (García-Redondo et al., 2018; Villahoz et al., 2018). Cluster 1 (orange) demonstrated some overlap with cluster 2 (green) within the TGF-β_1-treatment group potentially indicating the presence of a pro-fibrotic SMC sub-lineage. In addition, this cluster demonstrated an increase in *GREM1* and *GREM2* mRNA levels suggesting negative regulation of BMP-9 signalling. Moreover, cluster 2 (green) displayed enrichment for *DDAH1* and *ASS1* mRNA levels indicating potential positive regulation of the citrulline/NO cycle (Ghose and Raushel, 1985; Leiper et al., 2007). Finally, cluster 5 demonstrated enrichment for several genes involved in the regulation of blood vessel development.

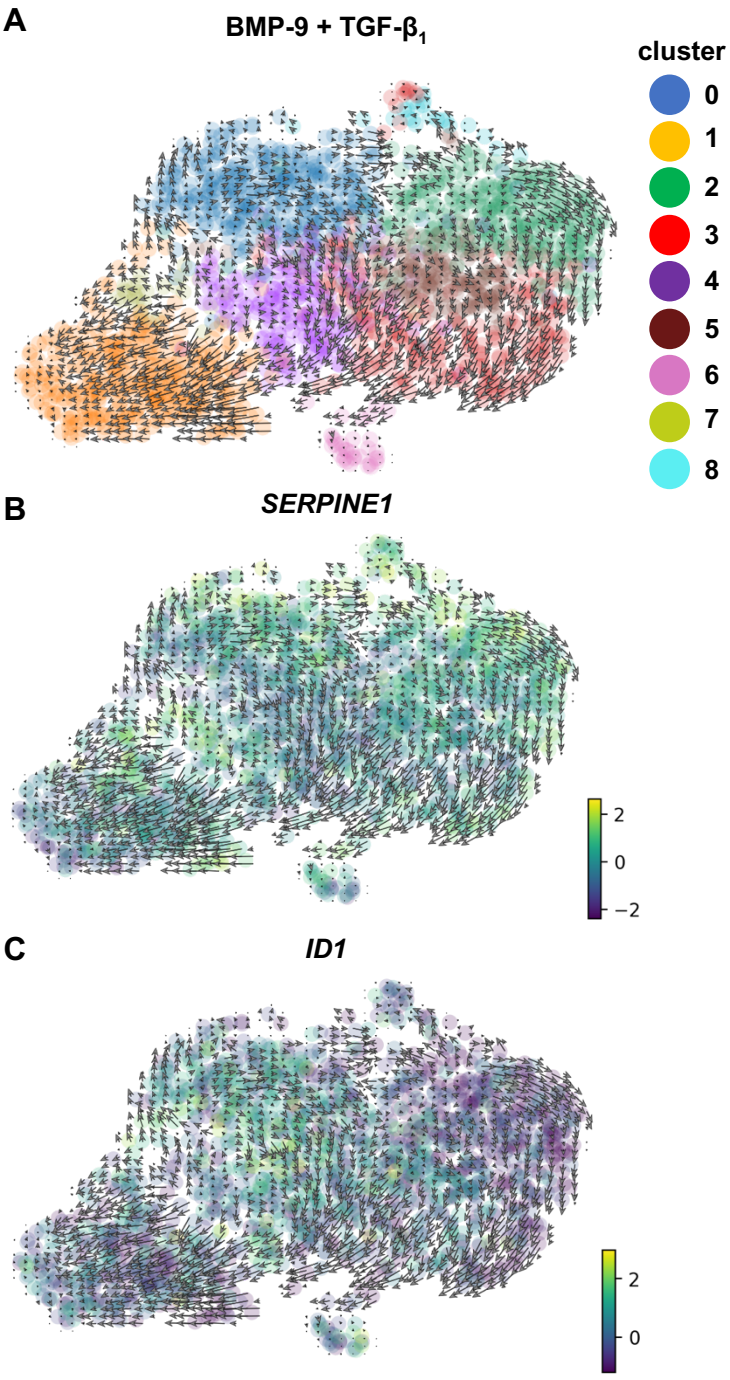

Figure 6-18 UMAP/Louvain clustering and RNA velocity in BMP-9/TGF-β$_1$-co-treated primary HSVSMCs. 80% confluent primary HSVSMCs were quiesced in 0.2% FCS media (MEDIA1) for 72-h. Quiescence media was replaced with stimulation media containing BMP-9 (10 ng/ml) and TGF-β$_1$ (10 ng/ml). Following 24-h, stimulation media was removed. Cells were prepared as described in section 2.10.1 and subjected to scRNAseq (biological n=1 CABG patient). (**A-C**) Following identification of distinct clusters within untreated control HSVSMCs by UMAP dimensionality reduction alongside Louvain community detection, RNA velocity and partition-based graph abstraction were generated utilising the scvelo package. Arrows indicate directionality of RNA velocity vectors. (**A**) Louvain UMAP graph displays RNA velocity vectors within clusters. (**B**) Louvain UMAP graph displays relative *SERPINE1* mRNA expression with RNA velocity overlay. (**C**) Louvain UMAP graph displays relative *ID1* mRNA expression with RNA velocity overlay.

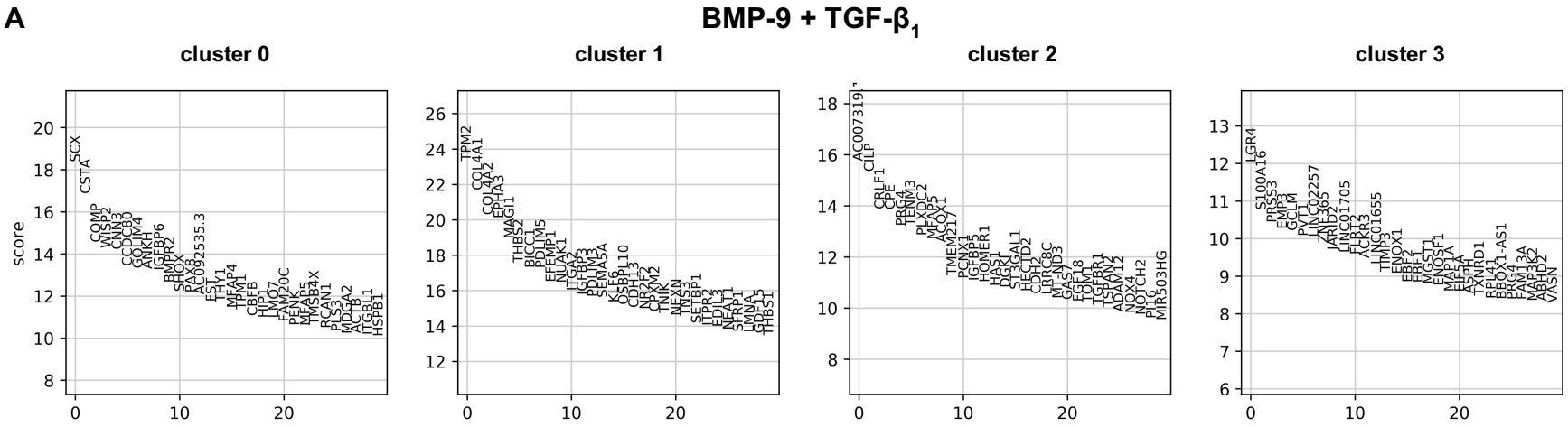

Figure 6-19 Top 30 most differentially regulated genes per cluster in BMP-9 and TGF-β_1 co-treated primary HSVSMCs (part 1). (**A**) Clusters within BMP-9/TGF-β_1-co-treated HSVSMCs were identified by UMAP dimensionality reduction alongside Louvain community detection. The top 100 most DEGs were identified by using the Mann-Whitney-Wilcoxon test in combination with Benjamini-Hochberg correction. Graphs display the top 30 most DEGs for clusters 0 to 3.

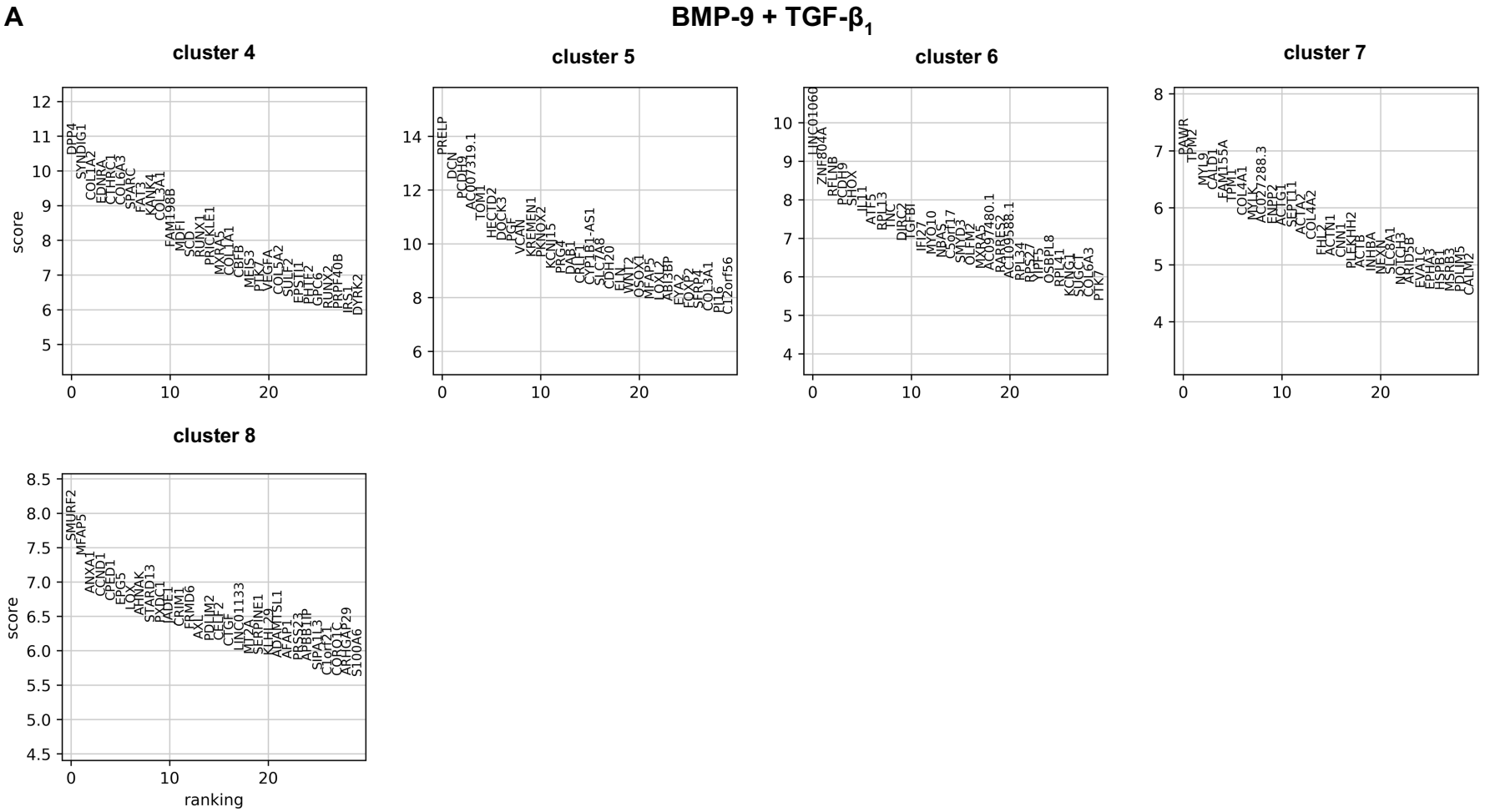

Figure 6-20 Top 30 most differentially regulated genes per cluster in BMP-9 and TGF-β_1 co-treated primary HSVSMCs (part 2). (**A**) Clusters within BMP-9/TGF-β_1-co-treated HSVSMCs were identified by UMAP dimensionality reduction alongside Louvain community detection. The top 100 most DEGs were identified by using the Mann-Whitney-Wilcoxon test in combination with Benjamini-Hochberg correction. Graphs display the top 30 most DEGs for clusters 4 to 8

Cluster	GO biological process	No. of genes	Expected	Fold enrichment	Raw p value	FDR
0	inorganic diphosphate transport	2	0.01	> 100	1.51E-04	1.75E-02
	germ cell migration	3	0.04	84.3	1.47E-05	3.17E-03
	positive regulation of hematopoietic progenitor cell differentiation	2	0.03	78.68	5.23E-04	4.12E-02
	regulation of lymphangiogenesis	2	0.03	78.68	5.23E-04	4.10E-02
	vascular endothelial growth factor signaling pathway	3	0.11	26.82	2.67E-04	2.54E-02
1	neural crest cell fate commitment	2	0.02	> 100	3.28E-04	3.15E-02
	negative regulation of B cell differentiation	2	0.02	84.25	4.57E-04	4.17E-02
	cellular response to heparin	2	0.02	84.25	4.57E-04	4.15E-02
	response to cortisol	2	0.02	84.25	4.57E-04	4.12E-02
	determination of dorsal identity	2	0.02	84.25	4.57E-04	4.10E-02
2	arginine metabolic process	3	0.08	36.43	1.17E-04	3.16E-02
	negative regulation of smooth muscle cell migration	3	0.11	28.15	2.32E-04	4.68E-02
	glycosaminoglycan biosynthetic process	6	0.49	12.26	1.32E-05	5.01E-03
	epithelial cell proliferation	5	0.43	11.6	9.21E-05	2.67E-02
	tissue remodeling	5	0.48	10.43	1.48E-04	3.76E-02
4	negative regulation of cell proliferation involved in contact inhibition	2	0.02	> 100	3.54E-04	4.25E-02
	response to human chorionic gonadotropin	2	0.02	> 100	3.54E-04	4.22E-02
	positive regulation of CD8-positive, alpha-beta T cell differentiation	2	0.02	> 100	3.54E-04	4.19E-02
	negative regulation of extracellular matrix disassembly	2	0.02	> 100	3.54E-04	4.16E-02
	negative regulation of endothelial cell differentiation	3	0.04	67.48	2.46E-05	6.13E-03
5	re-entry into mitotic cell cycle	2	0.01	> 100	2.32E-04	3.28E-02
	response to human chorionic gonadotropin	2	0.02	> 100	3.48E-04	4.44E-02
	epithelial to mesenchymal transition involved in endocardial cushion formation	3	0.06	51.11	4.88E-05	1.05E-02
	venous blood vessel development	3	0.07	40.88	8.67E-05	1.55E-02
	regulation of blood vessel endothelial cell proliferation involved in sprouting angiogenesis	3	0.08	38.33	1.03E-04	1.74E-02

Table 6-4 GO enrichment terms for top 100 most DEGs for clusters 0 to 5 in BMP-9 and TGF-β_1-co-treated primary HSVSMCs. GO enrichment analysis was performed based on the top 100 DEGs for clusters 0 to 5. The top 5 biological processes are displayed for each cluster and are ranked by fold enrichment score with a false discovery rate (FDR) cut-off of $p<0.05$.

Cluster	GO biological process	No. of genes	Expected	Fold enrichment	Raw p value	FDR
6	chondrocyte differentiation	5	0.34	14.74	3.14E-05	1.93E-02
	embryonic skeletal system development	7	0.65	10.71	5.75E-06	7.07E-03
	developmental growth involved in morphogenesis	6	0.6	10.02	3.93E-05	2.16E-02
	extracellular matrix organization	10	1.8	5.55	1.60E-05	1.42E-02
	tissue morphogenesis	11	2.74	4.01	1.08E-04	4.79E-02
7	glutamine catabolic process	2	0.01	> 100	2.15E-04	3.06E-02
	regulation of transepithelial transport	2	0.02	> 100	3.21E-04	4.03E-02
	postsynaptic actin cytoskeleton organization	3	0.07	42.55	7.70E-05	1.45E-02
	ventricular cardiac muscle cell differentiation	3	0.08	35.46	1.24E-04	2.11E-02
	relaxation of muscle	3	0.1	30.4	1.87E-04	2.84E-02
8	negative regulation of smooth muscle cell migration	3	0.1	29.93	1.93E-04	3.59E-02
	regulation of insulin-like growth factor receptor signaling pathway	3	0.1	28.63	2.18E-04	3.86E-02
	positive regulation of G1/S transition of mitotic cell cycle	4	0.16	24.39	3.20E-05	1.00E-02
	epithelial cell morphogenesis	4	0.16	24.39	3.20E-05	9.83E-03
	animal organ regeneration	5	0.35	14.44	3.37E-05	1.01E-02

Table 6-5 GO enrichment terms for top 100 most DEGs for clusters 6-8 in BMP-9 and TGF-β_1 co-treated primary HSVSMCs. GO enrichment analysis was performed based on the top 100 DEGs for clusters 6 to 8. The top 5 biological processes are displayed for each cluster and are ranked by fold enrichment score with a false discovery rate (FDR) cut-off of $p<0.05$.

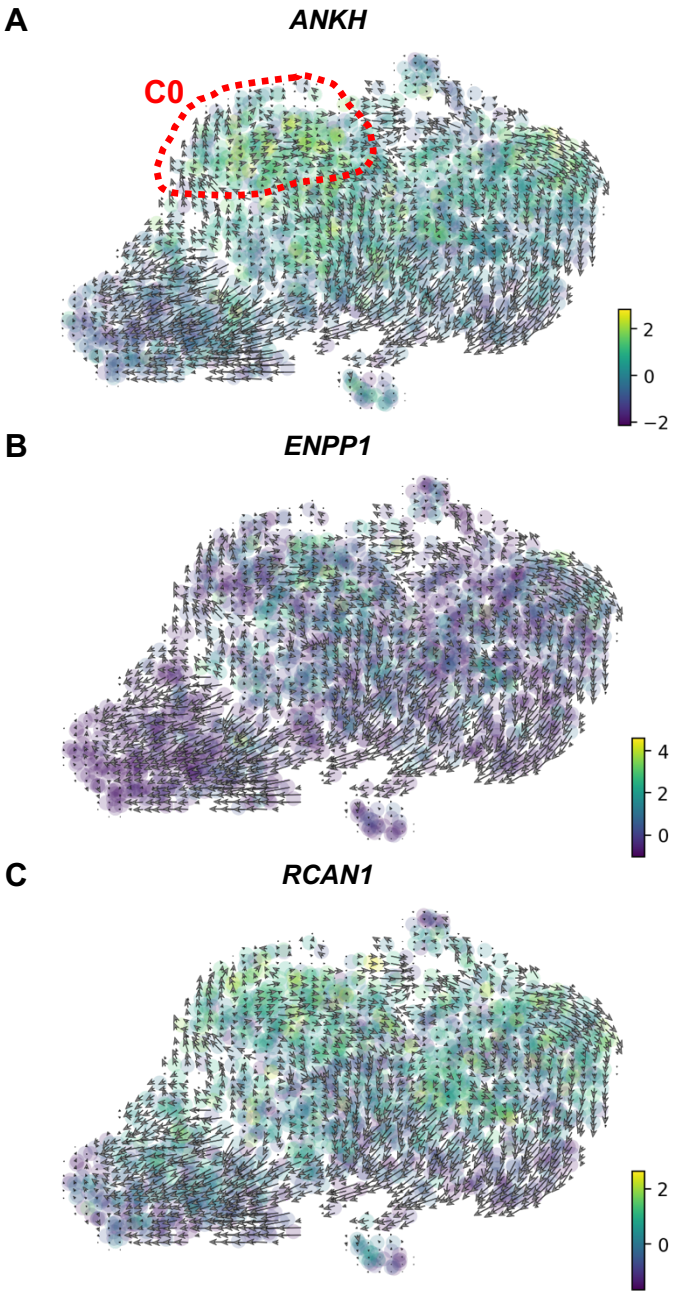

Figure 6-21 GO analysis reveals a sub-lineage in cluster 0 enriching for genes associated with negative regulation of vascular calcification and contraction in BMP-9/TGF-β_1-co-treated primary HSVSMCs. 80% confluent primary HSVSMCs were quiesced in 0.2% FCS media (MEDIA1) for 72-h. Quiescence media was replaced with stimulation media containing BMP-9 (10 ng/ml) and TGF-β_1 (10 ng/ml). Following 24-h, stimulation media was removed. Cells were prepared as described in section 2.10.1 and subjected to scRNAseq (biological n=1 CABG patient). Following identification of distinct clusters within untreated control HSVSMCs by UMAP dimensionality reduction alongside Louvain community detection, RNA velocity and partition-based graph abstraction were generated utilising the scvelo package. Arrows indicate directionality of RNA velocity vectors. Louvain UMAP graph displays relative (**A**) *ANKH*, (**B**) *ENPP1* and (**C**) *RCAN1* mRNA expression with RNA velocity overlay.

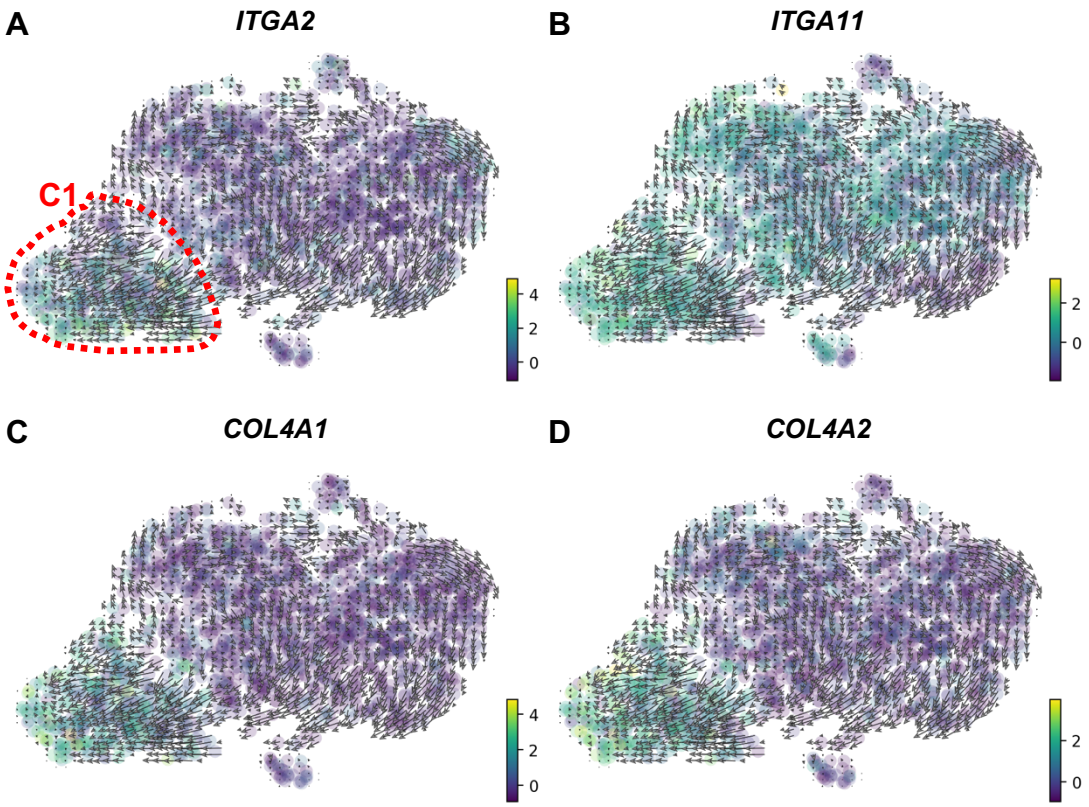

Figure 6-22 Cluster 1 displays overlap of pro-fibrotic genes in BMP-9/TGF-β_1-co-treated primary HSVSMCs. 80% confluent primary HSVSMCs were quiesced in 0.2% FCS media (MEDIA1) for 72-h. Quiescence media was replaced with stimulation media containing BMP-9 (10 ng/ml) and TGF-β_1 (10 ng/ml). Following 24-h, stimulation media was removed. Cells were prepared as described in section 2.10.1 and subjected to scRNAseq (biological n=1 CABG patient). Following identification of distinct clusters within untreated control HSVSMCs by UMAP dimensionality reduction alongside Louvain community detection, RNA velocity and partition-based graph abstraction were generated utilising the scvelo package. Arrows indicate directionality of RNA velocity vectors. Louvain UMAP graph displays relative (**A**) *ITGA2*, (**B**) *ITGA11*, (**C**) *COL4A1* and (**D**) *COL4A2* mRNA expression with RNA velocity overlay.

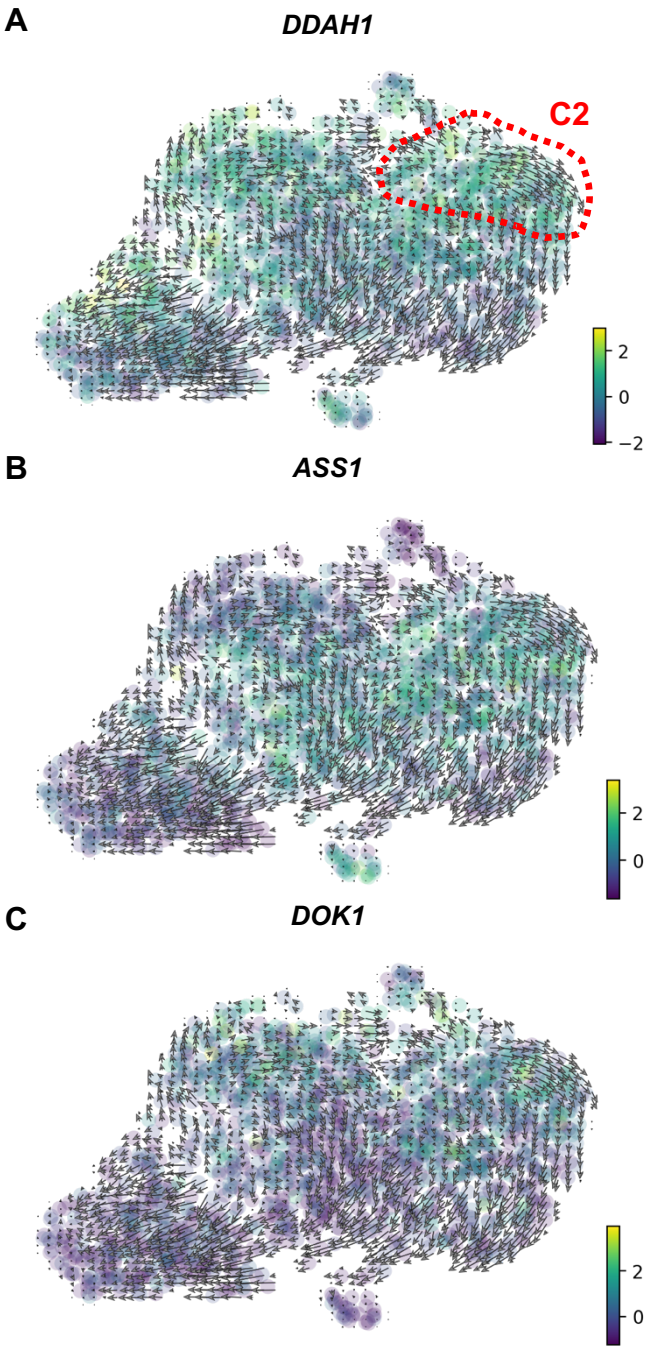

Figure 6-23 Cluster 2 demonstrates overlap of genes associated with regulation of the citrulline/NO cycle in BMP-9/TGF-β_1-co-treated primary HSVSMCs. 80% confluent primary HSVSMCs were quiesced in 0.2% FCS media (MEDIA1) for 72-h. Quiescence media was replaced with stimulation media containing BMP-9 (10 ng/ml) and TGF-β_1 (10 ng/ml). Following 24-h, stimulation media was removed. Cells were prepared as described in section 2.10.1 and subjected to scRNAseq (biological n=1 CABG patient). Following identification of distinct clusters within untreated control HSVSMCs by UMAP dimensionality reduction alongside Louvain community detection, RNA velocity and partition-based graph abstraction were generated utilising the scvelo package. Arrows indicate directionality of RNA velocity vectors. Louvain UMAP graph displays relative (**A**) *DDAH1*, (**B**) *ASS1* and (**C**) *DOK1* mRNA expression with RNA velocity overlay.

6.4 Discussion

The main aims of this chapter were to investigate potential transcriptional heterogeneity and to identify potential SMC sub-lineages within each treatment group.

Untreated control HSVSMCs displayed 7 clusters indicating transcriptional heterogeneity. RNA velocity vectors indicated that 5 clusters originated from the central cluster 3 (red) and transdifferentiated along distinct trajectories. GO analysis based on the top 100 most DEGs within cluster 2 (blue) identified enrichment for the regulation of high voltage-gated calcium channel activity which included the genes *CACNB2*, *PDE4B* and *FGF14*. In line with this finding, Gollasch *et al*. demonstrated that differentiated RASMCs expressing contractile genes displayed higher CACNB2 protein expression levels and greater L-type Ca^{2+} currents compared to 10% serum-treated controls indicating positive Ca^{2+} system remodelling and subsequent increase in contractile function (Gollasch et al., 1998). Partially in line with these findings, initial Ca^{2+} handling data demonstrated that AngII induced greater intracellular Ca^{2+} transients in serum-starved primary HSVSMCs compared to 15% serum-treated controls potentially suggesting the presence of a contractile HSVSMC phenotype (section 5.3.1). However, it must be pointed out that no extracellular Ca^{2+} was present during these measurements and, hence, it is not clear whether serum-starved HSVSMCs also display higher L-type Ca^{2+} channel activity. Nevertheless, these findings warrant additional experiments investigating CACNB2 expression and activity in quiesced versus proliferating HSVSMCs in the future.

Within untreated control HSVSMCs cluster 3 (red) displayed enrichment for cardiovascular development which included the gene *TGFB2*. Quiesced HSVSMCs demonstrated an increase in contractile protein expression indicating the presence of a contractile HSVSMC phenotype (Figure 4-22). Paralleling TGF-β_1-driven effects, previous work by Low *et al*. 2019 showed that TGF-β_2 induced SMAD1 and SMAD2 phosphorylation and drove relative *SERPINE1*, *CTGF*, *ID1* and *ID3* mRNA expression levels in primary HSVSMCs (unpublished data) (Low et al., 2019). Hence, it may be speculated that the TGF-β_2 isoform may also induce contractile gene expression in this cell type.

In summary, combined computational UMAP/Louvain clustering identified 7 distinct clusters in quiesced control primary HSVSMCs indicating transcriptional heterogeneity and potential SMC sub-lineages. Taken together with previous Ca^{2+} handling findings, these results may reflect a heterogeneous composition of vSMC phenotypes in pre-implantation SVG media.

Bulk Western Blotting and qRT-PCR analysis revealed that BMP-9 drove SMAD1 phosphorylation and subsequent downstream relative *ID1* mRNA expression levels in primary HSVSMCs (sections 4.3.10 and 4.3.11). Paralleling these findings, scRNAseq analysis demonstrated that BMP-9 induced *ID1* mRNA levels throughout most clusters within the BMP-9 treatment group confirming ALK1 or ALK2 pathway activation. In depth analysis revealed 7 clusters reflecting transcriptional heterogeneity following BMP-9 stimulation.

RNA velocity analysis within BMP-9-treated HSVSMCs indicated lineage trans-differentiation originating from clusters 0 (blue) and 3 (red) and terminating in cluster 2 (green). Of interest, cluster 2 (green) displayed enrichment for relative *IGF1*, *GREM1* and *GREM2* mRNA expression levels. In the context of osteogenesis, Chen and colleagues demonstrated that adenovirus-mediated *BMP-9* delivery to pluripotent murine C3H10T1/2 stem cells induced IGF1 protein expression (Chen et al., 2016a). Furthermore, exogenous *IGF1* expression potentiated BMP-9-dependent SMAD1 phosphorylation, alkaline phosphatase activity, matrix mineralisation and ectopic bone formation demonstrating that IGF1 synergised with BMP-9 signalling to drive osteogenesis. On the other hand, the BMP signalling antagonists GREM1 and GREM2 were shown to inhibit osteogenesis (Liu et al., 2020a; Wang et al., 2017). Based on these findings, it may be speculated that HSVSMCs identified in cluster 2 (green) were in the process of transdifferentiating towards an osteoblastic phenotype as evidenced by an increase in *IGF1* mRNA levels. The increase in *GREM1* and *GREM2* mRNA levels might have reflected auto-inhibition of BMP signalling following BMP-9 stimulation. Previous studies exploring BMP-9 in the context of osteogenesis and osteoblastic vSMC differentiation investigated late time-points (7-20 days) in *in vitro* experiments (Chen et al., 2016a; Zhu et al., 2015). Hence, 24-h BMP-9 stimulation may not have been sufficient to induce more substantial osteoblastic differentiation. Nevertheless, findings from this scRNAseq study warrant a

combined *in vitro*/scRNAseq experiment investigating long-term BMP-9-driven effects in primary HSVSMCs in the future.

The potential osteoblastic HSVSMC sub-lineage (cluster 2, green) partially originated from cluster 0 (blue) which displayed enrichment for white fat cell differentiation including the genes *AC092535*, *PPARG* and *SNAI2*. *PPARG* is a master-regulator of adipocyte and adipose tissue development (Rosen et al., 1999). In line with this finding, Akune *et al*. showed that homozygous *pparg*-deficient murine embryonic stem (ES) cells failed to differentiate into adipocytes (Akune et al., 2004). Instead, ES spontaneously underwent osteoblastic differentiation, while heterozygous *pparg*-deficient mice displayed an increase in bone mass and osteoblastogenesis. A study by Sun *et al*. confirmed these findings by demonstrating that targeted suppression of PPAR-γ increased osteogenesis (Sun et al., 2013). In addition, Pérez-Mancera and colleagues showed that the zinc-finger transcription factor *SNAI2* (SLUG) also positively regulated adipogenesis (Pérez-Mancera et al., 2007). Opposing anti-osteogenic effects of PPAR-γ, however, SNAI2 also acted as a positive regulator of osteogenesis (Tang et al., 2016). Furthermore, it was shown that BMP-9 drove relative *SNAI2* mRNA expression in primary human pulmonary artery ECs (Levet et al., 2015). Together, these studies may suggest that (i) PPAR-γ acts as a switch between adipo- and osteogenesis, (ii) SNAI2 positively regulates adipo- and osteogenesis and (iii) BMP-9 induces SNAI2 expression. Hence, it may be speculated that an increase in BMP-9-driven *SNAI2* mRNA levels in HSVSMCs within cluster 0 facilitated potential osteoblastic trans-differentiation towards cluster 2 (green). In contrast, like an increase in *GREM1* and *GREM2* expression, an increase in *PPARG* expression may reflect auto-inhibition of potential osteoblastic differentiation. However, it must be pointed out that these hypotheses are highly speculative and should be addressed in future *in vitro* experiments.

Transcriptional analysis identified 8 clusters within TGF-β_1-treated primary HSVSMCs. Relative *SERPINE1* mRNA expression levels were increased throughout most clusters indicating ALK5 pathway activation and paralleling bulk qRT-PCR analysis (section 4.3.11).

GO identified *ALK5* as a regulator of stress fibre formation within cluster 1 (orange). Crosas-Molist and colleagues showed that HASMCs from patients with Marfan syndrome (MFS), a genetic condition linked to excessive TGF-β_1/ALK5/SMAD2/3 signalling and aortic aneurysm formation, displayed an increase in contractile protein expression alongside more complex stress fibre formation (Crosas-Molist et al., 2015). The same study demonstrated that pharmacological ALK5 inhibition with LY364947 suppressed contractile protein expression and stress fibre formation. In line with these findings, data presented in sections 4.3.7 and 4.3.11 comprehensively demonstrated that functional ALK5 positively regulated contractile protein expression in primary HSVSMCs. It may be speculated, that ALK5 also positively regulates stress fibre formation in primary HSVSMCs and, hence, a future experiment should determine cytoskeletal structures in 24-h TGF-β_1-treated HSVSMCs to confirm this hypothesis. Moreover, cluster 1 displayed an increase in relative *CTGF* mRNA expression levels. CTGF is a key mediator of tissue fibrosis (reviewed in) (Lipson et al., 2012) and a validated downstream target gene of the ALK5/SMAD2/3 pathway (unpublished data) (Low et al., 2019). Interestingly, Chowdhury *et al*. showed that RhoA-dependent CTGF expression was paralleled by an increase in actin polymerisation in SMCs (Chowdhury and Chaqour, 2004). The authors went on to show that the pharmacological actin polymerisation inhibitor latrunculin B inhibited stress fibre formation and *CTGF* expression mechanistically linking cytoskeletal re-arrangement with *CTGF* expression. Hence, the observed increase in relative *CTGF* mRNA levels within cluster 1 (orange) in TGF-β_1-treated HSVSMCs may potentially be mediated via stress fibre formation. Finally, cluster 1 (orange) demonstrated an increase in relative *TPM1* mRNA expression levels. *TPM1* encodes for the cytoskeletal protein tropomyosin 1-α which is a late marker of differentiated SMCs (Vrhovski et al., 2005). Bakin *et al*. showed that TGF-β_1 induced expression of tropomyosins (TPMs) and stress fibre formation in epithelial cells (Bakin et al., 2004). The same study revealed that TGF-β_1-induced stress fibre formation was attenuated following siRNA-mediated ablation of TPMs indicating that TPMs are crucial components of intracellular contractile filaments. In line with this study, Wang *et al*. revealed that overexpression of TPM1 dampened PDGF-induced primary HASMC migration and proliferation (Wang et al., 2011). Taken together, these findings mechanistically link *ALK5*, *CTGF* and *TPM1* with pro-contractile cellular functions. Hence, it may

be speculated that cluster 1 displays a potentially contractile HSVSMC sub-lineage.

GO analysis uncovered overlap of *EGR1*, *COL1A1*, *COL4A1* and *COL4A2* in cluster 2 (green) within TGF-β_1-treated HSVSMCs. The transcription factor EGR-1 is a mediator of experimental renal fibrosis in mice and partially mediates TGF-β_1-driven *Col1a1* expression (Ho et al., 2016). Moreover, adenoviral-mediated overexpression of *EGR1* drives *COL4A1* and *COL4A2* expression in human skin fibroblasts (Bhattacharyya et al., 2011). Type 4 collagen deposition is increased in experimental hepatic fibrosis in rats indicating a pro-fibrotic role for type 4 collagen (Ala-Kokko et al., 1987). In the context of vSMCs, Turner *et al*. showed that TGF-β_1 drove *COL4A1* and *COL4A2* expression in primary HASMCs. Taken together, these studies outline a potential pro-fibrotic mechanism by which the TGF-β_1/ALK5 pathway activates EGR1 which in turn drives pro-fibrotic *COL1A1*, *COL4A1* and *COL4A2* gene expression in primary HSVSMCs. This hypothesis may be confirmed by bulk qRT-PCR or immunoblot analysis. Based on these findings, it may be speculated that SMCs within cluster 1 (green) represent a pro-fibrotic HSVSMC sub-lineage.

Within BMP-9/TGF-β_1-co-treated HSVSMCs UMAP/Louvain clustering revealed 9 clusters indicating transcriptional heterogeneity following combined ligand treatment. Compared to BMP-9 and TGF-β_1-treated HSVSMCs, RNA velocity analysis did not indicate clear lineage trans-differentiation paths.

Relative *SERPINE1* expression was increased throughout most clusters hinting at ALK5 pathway activation. In contrast, only clusters 0 (blue) and 4 (purple) displayed an increase in relative *ID1* expression suggesting BMP-9-driven ALK1/ALK2 pathway activation. Cluster 0 (blue) displayed simultaneous ALK5 and ALK1/ALK2 pathway activation. Within this cluster GO analysis identified enrichment for negative regulation of Ca^{2+}-mediated signalling which included the genes *CALM2*, *FHL2* and *RCAN1*. Both FHL2 and RCAN1 inhibit calcineurin activity, subsequent NFAT translocation to the nucleus and NFAT-dependent transcriptional regulation of target genes (Fuentes et al., 2000; Hojayev et al., 2012). The calcineurin inhibitor and immunosuppressant cyclosporin a augments AngII-induced intracellular Ca^{2+} mobilisation in primary RASMCs (Pfeilschifter and

Rüegg, 1987) and triggers systemic hypertension (reviewed in) (Taler et al., 1999). Since pharmacological calcineurin inhibition promotes intracellular Ca^{2+} release it may be speculated that an increase in RCAN1 and FHL2 expression may support this pro-contractile mechanism in primary HSVSMCs. Paradoxically, Villahoz and colleagues demonstrated that lentiviral-mediated overexpression of Rcan-1 in murine aortic SMCs triggered a reduction in MLC phosphorylation (Villahoz et al., 2018). In line with this finding, García-Redondo *et al*. showed that phenylephrine-induced aortic constriction was greater in homozygous *Rcan1*-deficient mice (García-Redondo et al., 2018). Both presented studies did not investigate the effect of Rcan-1 on intracellular Ca^{2+} release in vSMCs. Nevertheless, these two studies suggest that RCAN1 may also act as a negative regulator of vascular contractility and, hence, it may be speculated that BMP-9/TGF-β_1-co-treated HSVSMCs expressing higher levels of *RCAN1* may display reduced intracellular Ca^{2+} transients following AngII stimulation. This warrants a future experiment investigating AngII-driven Ca^{2+} release in ligand-treated HSVSMCs following siRNA-mediated *RCAN1* knockdown and plasmid-mediated overexpression of *RCAN1*. In summary, GO analysis identified a potential mechanism for negative regulation of AngII-driven intracellular Ca^{2+} release and HSVSMC calcification.

PCA-dependent comparison of whole treatment groups revealed that TGF-β_1 visually suppressed mitochondrial gene expression compared to BMP-9-treated and/or control HSVSMCs, indicating potential mitochondrial protection (Shi et al., 2014) and paralleling previous results from our group (unpublished data) (Low et al., 2019). Furthermore, TGF-β_1 induced relative *SERPINE1* mRNA levels paralleling previous findings and demonstrating that cells responded to TGF-β_1 treatment. In contrast, there was no clear divide between ALK1 and ALK5 HSVSMC sub-lineages following TGF-β_1 treatment in the present study. This may partially be explained by below mentioned technical and biological differences between these two scRNAseq studies. Another possible explanation could be that this set of HSVSMCs might have expressed lower ALK1 levels and, hence, might not have been able to transdifferentiate into an ALK1-dominant sub-lineage. Indeed, relative *ACVRL1* mRNA levels were not detectable in all examined HSVSMCs.

Since only one set of patient cells (n=1 CABG patient) was investigated, it is important to emphasise that conclusions/hypotheses drawn from presented findings in Chapter 6 require careful interpretation. Furthermore, it is important to address technical and biological limitations of this study. Presented results reflect relative mRNA expression changes which do not necessarily translate into biological relevance. Hence, any conclusions drawn from these results would have to be confirmed with at least 2 additional scRNAseq experiments and additional *in vitro* analysis to determine biological relevance in the future. Although UMAP/Louvain clustering enables identification of gene groups within one cluster, some of these identified genes are also expressed in other clusters of the same treatment group. Hence, in some instances this change in gene expression reflects a common ligand-dependent effect within all clusters within one entire treatment group rather than a singular effect within the investigated sub-cluster.

Moreover, the sequencing depth was ~30,000 read pairs per cell in the presented study compared to ~50,000 read pairs per cell obtained from this group's first scRNAseq experiment (unpublished data) (Low et al., 2019). However, the manufacturer recommends a minimum of 20,000 read pairs per cell (Chromium Single Cell 3' Reagent Kits v3 User Guide) and, hence, the number of read pairs is within a recommended range. In addition, the number of investigated cells within this chapter's study ranged from 1,372 (BMP-9) to 2,038 (TGF-β_1) cells per treatment group compared to 5,245 (vehicle control) and 7,073 (TGF-β_1) cells examined in the first scRNAseq study (unpublished data) (Low et al., 2019). The more sensitive v3 chemistry kit (10x Genomics) was utilised to generate the cDNA library for the current study whereas the less sensitive v2 chemistry kit was used for the previous study (unpublished data) (Low et al., 2019). Furthermore, the average mitochondrial gene percentage per cell was >5% in the present study compared to <5% in the previous study (unpublished data) (Low et al., 2019). A higher mitochondrial gene percentage is frequently observed in cells with a high metabolic turnover such as cardiomyocytes (Mercer et al., 2011). Since primary HSVSMCs were quiesced for 72-h before 24-h ligand treatment, it is unlikely that a higher metabolic rate would explain this increase in mitochondrial gene percentage. In this case, a higher mitochondrial gene percentage most likely means that mitochondrial genes were present in the

cytoplasm during Gel Bead loading potentially indicating mitochondrial damage. This may be explained by exposure to oxidative stress during culturing or the GEM lysis step which may have damaged the mitochondrial membrane. Cell viability was assessed during automated cell counting and was >95% confirming that viable cells were loaded onto the chip. Compared to the first scRNAseq study which utilised freshly isolated and passaged primary HSVSMCs, this study used cryo-preserved primary HSVSMCs. However, cells showed good outgrowth prior to study initiation at P5. Furthermore, primary HSVSMCs for this scRNAseq experiment derived from a 72-year-old male CABG patient with a BMI of 32. Although the pre-implantation SVG I/M ratio was not known for this study participant, it may be hypothesised that HSVSMC biology was impacted by age and/or obesity and, hence, might have been more susceptible to oxidative stress during culturing. Taken together, these differences may partially explain why some results from the first scRNAseq experiment could not be reproduced in the present study.

6.5 Summary

This study demonstrates that scRNAseq is a valid technique to determine transcriptional changes in single HSVSMCs following ligand treatment. Combined UMAP/Louvain clustering uncovered transcriptome heterogeneity in untreated and ligand-treated HSVSMCs potentially reflecting a heterogeneous composition of SMC sub-lineages within pre-implantation SVG media.

In contrast to Low *et al.*'s study, QC filtering revealed a mitochondrial gene percentage of >5% per cell potentially indicating mitochondrial damage (unpublished data) (Low et al., 2019). Paralleling previous findings by Low *et al.*, TGF-β_1-treated HSVSMCs displayed a reduction in mitochondrial gene expression hinting at mitochondrial protection. Despite an increase in mitochondrial gene percentage, both BMP-9 and TGF-β_1 drove target gene expression demonstrating functional ALK5 and ALK1/ALK2 pathway activation. Initial PCA revealed greater spatial distances between TGF-β_1 and BMP-9-treated HSVSMCs suggesting that TGF-β_1 triggered greater transcriptional activation compared to BMP-9.

In untreated control HSVSMCs, GO identified overlap of genes known to regulate high voltage-gated calcium channel activity potentially hinting at pro-contractile Ca^{2+} system remodelling. Within BMP-9 treated HSVSMCs, combined RNA velocity and GO analysis uncovered a potential osteogenic HSVSMC sub-lineage. Within TGF-β_1-treated HSVSMCs GO identified potentially contractile and pro-fibrotic sub-lineages as well as HSVSMCs expressing increased levels of pro-chemotactic genes. Finally, GO helped to uncover potential mechanisms for negative regulation of vascular contraction and calcification in BMP-9/TGF-β_1-co-treated HSVSMCs.

Chapter 7 General discussion

7.1 Overall Summary

TGF-β_1 may either signal via the ALK1 or ALK5 signalling pathways in primary HSVSMCs (unpublished data) (Low et al., 2019). The contribution of ALK5 signalling to vascular injury-driven NF is controversial with some studies implicating this pathway as a positive regulator of NF (Cooley et al., 2014; Friedl et al., 2004; Jiang et al., 2009; Liao et al., 2016; Tsai et al., 2009; Wolff et al., 2006) and other studies demonstrating protection from vSMC phenotype switching and NF (Chen et al., 2016b; Kobayashi et al., 2005; Martin-Garrido et al., 2013; Mii et al., 1993). With regards to ALK1, Garrido-Martín and colleagues reported an increase in neointimal ALK1 presence following vascular injury (Garrido-Martín et al., 2013). In line with this finding, Low *et al*. showed that (i) ALK1 co-localised with αSMA$^+$ SMCs within SVG neointima and (ii) systemic and heterozygous genetic ablation of *Smad1* dampened NF following experimental vascular injury in mice (unpublished data) (Low et al., 2019). The same study demonstrated that TGF-β_1 induced HSVSMC migration via ALK1 implicating this signalling axis as a driver of NF in SVG disease. BMP-9 circulates in the blood and signals via ALK1 in vascular ECs and SMCs (David et al., 2008; David et al., 2007; Zhu et al., 2015). Next to cancer neoangiogenesis and HHT, BMP-9 is being investigated in the context of NF-driven PAH (Brand et al., 2016; Hodgson et al., 2020; Wang et al., 2019; Wooderchak-Donahue et al., 2013). However, the role of BMP-9 is still controversial with one study implicating a protective function (Long et al., 2015) and an opposing study indicating BMP-9 as a driver of PAH (Tu et al., 2019). To date, no study has investigated the role of BMP-9 in SVG NF. Since BMP-9 is an ALK1 ligand and the ALK1 pathway drives HSVSMC migration and experimental NF it may be speculated that BMP-9 positively regulates NF via ALK1. Based on these findings, the first aim of this thesis was to evaluate BMP-9 presence in pre-implantation SVGs from CABG patients and experimentally injured murine carotid arteries.

IHC revealed BMP-9 presence in pre-implantation SVGs and uninjured/injured murine carotid arteries. Within SVGs, BMP-9 was present in all layers of the vessel and co-localised with αSMA$^+$ SMCs. In uninjured murine carotid arteries BMP-9 mainly localised to the adventitia along with some punctate staining in the media. Initial data generated from wire injured murine carotid arteries

demonstrated that total vessel BMP-9 presence was increased at day 14 compared to day 0 uninjured controls with brighter adventitial staining and some punctate staining within the forming neointima. This increase was paralleled by a reduction in total vessel αSMA presence suggesting vSMC phenotype switching (Lindner et al., 1993). In 3-week-old lesions, total BMP-9 presence dropped back to baseline levels.

A previous radioligand cross-linking study showed that BMP-9 bound to ALK1, ALK2, BMPR2, ACVR2A/B and endoglin on isolated primary HSVSMCs. Based on this finding and BMP-9 presence in pre-implantation SVGs and murine arterial vasculature, the next aim was to determine potential crosstalk between BMP-9/ALK1/2 and TGF-β_1/ALK1 signalling by assessing SMAD1 phosphorylation in isolated primary HSVSMCs. Recombinant BMP-9 induced sustained phosphorylation of SMAD1 and potentially SMAD5. TGF-β_1 also induced SMAD1 phosphorylation. However, TGF-β_1-driven SMAD1 phosphorylation was delayed and weaker compared to BMP-9 stimulation. The presence of TGF-β_1 did not potentiate BMP-9-driven SMAD1 phosphorylation thereby indicating absence of ALK1 pathway synergy. Bulk qRT-PCR analysis confirmed up-regulation of relative *ID1* mRNA expression levels following BMP-9 stimulation. In contrast to SMAD1 phosphorylation, the presence of TGF-β_1 attenuated BMP-9-driven *ID1* expression demonstrating lateral ALK5-mediated ALK1 pathway inhibition (Goumans et al., 2002). Further mechanistic studies revealed that BMP-9 did not affect proliferation of quiesced HSVSMCs and did not modulate serum-induced HSVSMC proliferation and migration.

Further IHC analysis revealed that the contractile vSMC marker MYH11 was reduced in the intima compared to the media of pre-implantation SVGs from CABG patients. In addition, calponin staining demonstrated a trend towards a reduction in intimal versus medial staining suggesting *in vivo* HSVSMC phenotype switching. This is in line with findings from Low *et al*. which demonstrated that pre-implantation SVGs from 75 CABG patients displayed pre-existing intimal thickening evidenced by a mean I/M ratio >0.15 (unpublished data) (Low et al., 2019). This is of clinical relevance since pre-existing intimal thickening is a known risk factor for early and late SVG failure (Panetta et al., 1992). Part of section 7.2 outlines a proposed clinical trial in CABG patients investigating

potential *in vivo* vSMC phenotype switching in pre-implantation SVGs in more detail.

These findings prompted development and validation of an *in vitro* model to mimic phenotype switching and contractile differentiation of isolated primary HSVSMCs. The differentiation protocol was based on a study by Chen *et al*. and enabled investigation of dynamic changes in ALK1 and ALK5 pathway activity during these two opposing processes (Chen et al., 2016b). Paralleling findings in primary HASMCs by Chen *et al*. (Chen et al., 2016b), SMDS-cultured HSVSMC demonstrated a time-dependent increase in contractile gene and protein expression along with a decrease in proliferation indicating contractile differentiation. Accumulation of contractile gene and protein expression was paralleled by a decrease in *ID1* expression suggesting ALK1 pathway suppression during contractile differentiation. Moreover, SMDS dynamically upregulated *ACVR2A* expression suggesting a role for this receptor during contractile HSVSMC differentiation. This finding prompted generation of an HAdV-5 expressing *ACVR2A*. Preliminary qRT-PCR data confirmed successful delivery of *ACVR2A* to primary HSVSMCs (n=1 CABG patient). However, the increase in *ACVR2A* did not affect α*SMA* expression in SMDS and 15% serum cultured HSVSMCs at the day 2 time point. Although overexpression of *ACVR2A* had no effect during early stages of contractile HSVSMC differentiation, more experiments investigating changes in contractile gene/protein expression and proliferation at later time points are warranted.

Data obtained during this PhD demonstrated that pharmacological ALK1 inhibition did not affect SMDS-mediated accumulation of contractile gene expression in HSVSMCs (unpublished data) (Low et al., 2019). In contrast, pharmacological ALK5 inhibition prevented SMDS-induced increase in contractile gene and protein expression. To confirm these findings, 72-h quiesced HSVSMCs were stimulated with recombinant TGF-β_1 and/or BMP-9 in absence and presence of pharmacological ALK5 inhibition. Bulk qRT-PCR analysis revealed that TGF-β_1 drove contractile gene expression in an ALK5-dependent manner. BMP-9 did not counter TGF-β_1-driven contractile gene expression. However, BMP-9 ALK5-dependently and mildly induced α*SMA* expression. In addition to bulk qRT-PCR, immunoblot data demonstrated that TGF-β_1 induced MLC S20 subunit

phosphorylation via ALK5, a known marker of SMC contractility (Montezano et al., 2018). In line with previous studies, these data indicate that both ligand-dependent and -independent ALK5 signalling positively regulated the contractile HSVSMC phenotype (Chen et al., 2016b; Tang et al., 2010). Partially paralleling previous findings by Garrido-Martín *et al.* and Mii *et al.*, further mechanistic studies revealed that TGF-β_1 attenuated serum-induced HSVSMC proliferation and HSVSMC-driven scratch closure indicating protection against phenotype switching (Martin-Garrido et al., 2013; Mii et al., 1993). Additional qRT-PCR analysis demonstrated that TGF-β_1 suppressed *ALPL* and *CD68* expression via ALK5 suggesting negative regulation of osteoblastic and macrophage-like HSVSMC trans-differentiation (Guerrero et al., 2014; Mallat et al., 2001).

Based on these results, the next aim was to assess HSVSMC contraction, using agonist driven intracellular Ca^{2+} release as a surrogate marker. 24-h TGF-β_1 stimulation of quiesced HSVSMCs triggered an increase in AngII-driven intracellular Ca^{2+} transients compared to untreated controls suggesting that TGF-β_1 drives an increase in contractile capacity. BMP-9 and pharmacological ALK5 inhibition blocked this TGF-β_1-dependent increase in intracellular Ca^{2+} release. In contrast, TGF-β_1 did not affect AngII-dependent Ca^{2+} release in primary HCASMCs suggesting differential regulation of Ca^{2+} handling in this cell type. Further mechanistic studies aimed to identify via which receptor AngII mediated Ca^{2+} responses and whether AngII/Ca^{2+}-dependent SMC contraction triggered Cal520™ quenching and, hence, false positive increase in fluorescence intensity. AngII drove Ca^{2+} transients via AT_1R and pharmacological ROCK/PKC (contraction) inhibition with fasudil did not prevent AngII-driven Ca^{2+} release. Bulk qRT-PCR analysis revealed that TGF-β_1 ALK5-dependently suppressed *MAS1* expression, a receptor known to negatively regulate AngII/AT_1R signalling, suggesting synergism between TGF-β_1/ALK5 and AngII/AT_1R signalling in HSVSMCs (Ford et al., 1999; Kostenis et al., 2005; Rodríguez-Vita et al., 2005). The potential clinical relevance of these findings is outlined in 7.2. In addition, single cell resolution uncovered heterogeneous distribution of AngII-driven Ca^{2+} transients in untreated and ligand treated HSVSMC populations potentially reflecting vSMC heterogeneity. TGF-β_1-stimulation of HSVSMC triggered a more homogenous Ca^{2+} response and this was blunted in the presence of BMP-9. Previous research showed that distinct vSMC phenotypes resided within the

media of large arteries (Frid et al., 1994; Hao et al., 2002; Li et al., 2001a). More recently, the combination of vSMC lineage tracing in transgenic mice and scRNAseq confirmed medial SMC heterogeneity and enabled identification of a potentially disease-relevant rare SMC sub-lineage in aortic media (Dobnikar et al., 2018). Low *et al.*'s study already demonstrated that TGF-β_1 stimulation of HSVSMCs drove ALK5- and ALK1-dominant SMC sub-lineages suggesting simultaneous ALK5 and ALK1 pathway activation within the same SMC population. Taken together, these findings prompted a scRNAseq study in HSVSMCs following BMP-9 and/or TGF-β_1 treatment to assess vSMC heterogeneity at a transcriptional level and identify that could explain ligand-dependent effects on AngII-driven Ca^{2+} transients.

Computational analysis of scRNAseq data uncovered heterogeneous transcriptomes in all treatment groups. BMP-9 and TGF-β_1 induced the expression of ALK1 and ALK5 target genes, respectively, and initial PCA analysis revealed greater transcriptional changes within the TGF-β_1-treated HSVSMC population. Contrasting previous findings by Low and colleagues, RNA velocity analysis did not show a clear distinction between ALK1- and ALK5-dominant sub-lineages within the TGF-β_1 treatment group. Nevertheless, combined RNA velocity and GO analysis of BMP-9-treated HSVSMCs identified a potentially osteoblastic SMC sub-lineage as evidenced by an increase in cluster-dependent pro-osteogenic *SNAI2* and *IGF1* expression levels (Chen et al., 2016a; Tang et al., 2016). With regards to BMP-9-driven inhibition of TGF-β_1-driven Ca^{2+} transients, it may be speculated that BMP-9 redirects intracellular Ca^{2+} towards mineralisation by activating pro-osteoblastic alkaline phosphatase activity (Zhu et al., 2015). The clinical relevance of potential BMP-9-driven osteoblastic differentiation in the context of SVG occlusion is discussed in section 7.2. Combined RNA velocity and GO analysis of TGF-β_1-treated HSVSMCs uncovered SMC sub-lineages with contractile and fibrotic gene expression patterns. In addition, a cluster of HSVSMCs expressed increased levels of pro-chemotactic *VEGFA* and *CXCL12*, two known positive regulators of monocyte/progenitor cell recruitment and subsequent NF in the context of acute vascular injury (Ohtani et al., 2004; Zernecke et al., 2005). Within, BMP-9/TGF-β_1-co-treated HSVSMCs, ALK5 pathway activation was more prevalent compared to ALK1 as evidenced by a more pronounced increase in *SERPINE1* compared to *ID1* expression throughout

all investigated clusters. GO analysis of co-treated HSVSMCs revealed potential mechanisms for negative regulation of vascular contractility (García-Redondo et al., 2018; Villahoz et al., 2018) and calcification (Lomashvili et al., 2004; Lomashvili et al., 2014; Zhao et al., 2012). As outlined in section 6.4, scRNAseq findings should be interpreted with caution and require validation experiments addressing generated hypotheses in the future. Nevertheless, taken together with Ca^{2+} handling findings uncovering heterogeneous AngII-driven Ca^{2+} responses in HSVSMCs, scRNAseq analysis revealed transcriptional heterogeneity in HSVSMCs that may reflect a heterogeneous composition of diverse SMC phenotypes within pre-implantation SVG media. Based on a study by Dobnikar *et al.*, it may be speculated that diverse SMC sub-populations react differently to SVG injury following implantation and this may be of clinical relevance in the context of SVG occlusion (Dobnikar et al., 2018).

In summary, TGF-β_1 drives contractile/fibrotic gene expression, drives MLC S20 phosphorylation and enhances AngII-driven intracellular Ca^{2+} transients via ALK5 in primary HSVSMCs (Figure 7-1). This indicates that ALK5 agonism positively regulates the contractile HSVSMC phenotype. In contrast, BMP-9 drives SMAD1 phosphorylation (and potentially SMAD5), *ID1* expression and blunts TGF-β_1/ALK5-driven AngII-dependent Ca^{2+} responses via ALK1 and/or ALK2 indicating partial ALK5 antagonism.

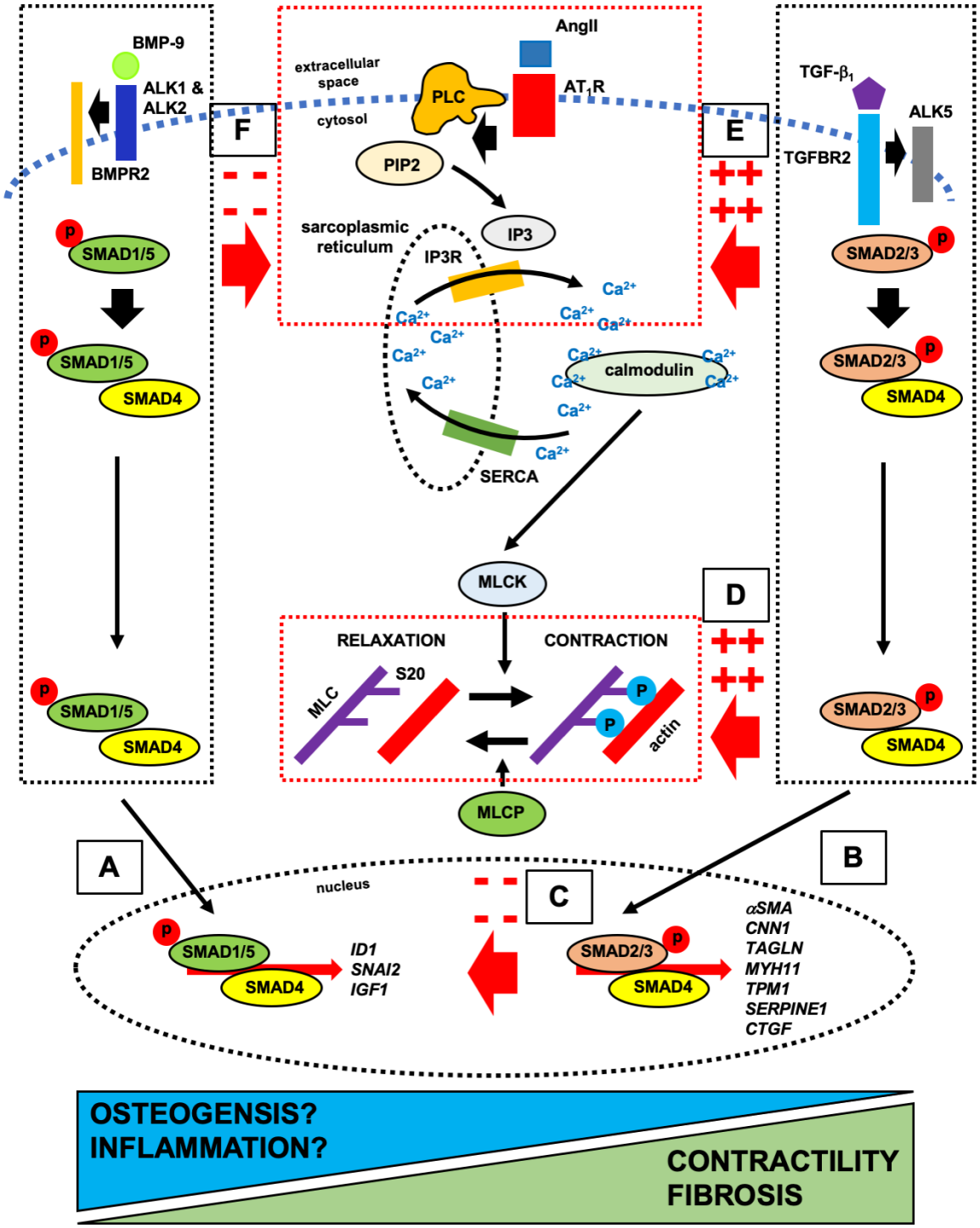

Figure 7-1 Proposed model of BMP-9/ALK1/2- and TGF-β_1/ALK5-driven regulation of HSVSMC phenotypes. (**A**) BMP-9 drives SMAD1/5 phosphorylation via ALK1 and/or ALK2/BMPR2 complex formation. The SMAD1/5/SMAD4 complex translocates to the nucleus and drives *ID1* and pro-osteogenic *SNAI2* and *IGF1* expression. Under disease conditions, the BMP-9/SMAD1/5 system may synergise with pro-osteogenic and pro-inflammatory signalling pathways. (**B**) TGF-β_1 drives SMAD2/3 phosphorylation via TGFBR2/ALK5 complex formation. The SMAD2/3/SMAD4 complex trans-locates to the nucleus and drives pro-contractile *αSMA*, *CNN1*, *TAGLN*, *MYH11* and *TPM1* and pro-fibrotic *SERPINE1* and *CTGF* gene expression. (**C**) TGF-β_1 attenuates BMP-9-driven *ID1* expression via ALK5. (**D**) TGF-β_1 directly drives MLC S20 phosphorylation via ALK5 (unknown underlying mechanism). (**E**) TGF-β_1 augments AngII-induced SR Ca^{2+} release via ALK5 (unknown underlying mechanism). (**F**) The BMP-9/SMAD1/5 system attenuates TGF-β_1-driven AngII-dependent intracellular Ca^{2+} transients (unknown underlying mechanism). In summary, TGF-β_1 promotes the contractile and fibrotic HSVSMC phenotypes via ALK5. BMP-9 partially antagonises TGF-β_1 /ALK5-driven contractile properties and potentially facilitates osteoblastic HSVSMC differentiation.

7.2 Future perspectives

Data generated during this PhD may be of relevance to CABG patient care in the future. The next paragraphs aim to highlight the most clinically relevant findings and bring them into disease context.

IHC analysis of pre-implantation SVGs from CABG patients revealed the presence of *in vivo* SMC phenotype switching along with BMP-9 which functionally drove ALK1/2 signalling and pro-osteoblastic gene expression in isolated primary HSVSMCs, although additional *in vitro* studies are required to strengthen the evidence supporting these investigations. The BMP-9/ALK1 axis induces osteoblastic vSMC differentiation and ALK1 positively regulates vascular LDL deposition thereby promoting vascular calcification and atherosclerosis respectively (Kraehling et al., 2016; Zhu et al., 2015). Pre-implantation SVGs display calcification (Pedigo et al., 2017), circulating BMP-9 levels are elevated in paediatric CKD patients (Zhu et al., 2015) and CKD is a risk factor for SVG occlusion (Wellenius et al., 2007). Moreover, SVGs are prone to accelerated atherosclerosis impeding long-term graft patency (Neitzel et al., 1986). Hence, it may be hypothesised that circulating BMP-9 drives SVG calcification and atherosclerotic plaque formation via the ALK1 pathway and serves as a biomarker for identifying CABG patients at risk of developing SVG failure.

Taken together, these findings warrant a translational study investigating the association of circulating BMP-9 levels with SVG patency and calcification in CABG patients. This may be complemented with an *in vivo* murine vein graft study. Lardenoye and colleagues demonstrated accelerated atherosclerosis and calcification of vena cava grafts following inter-positioning into common carotid arteries in hyperlipidaemic APOE*3 Leiden mice (Lardenoye et al., 2002). Alternatively, Zhang *et al.* demonstrated exacerbated NF in vena cava grafts inter-positioned into common carotid arteries in mice with 5/6ths nephrectomy, a validated murine model of CKD (Zhang et al., 2017). Based on both these models it may be hypothesised that systemic administration of neutralising BMP-9 antibodies attenuates vein graft NF, lipid retention and calcification. In addition, *in vitro* studies would investigate the effect of BMP-9 stimulation on (i) high-phosphate-induced osteoblastic differentiation (Zhu et al., 2015) and on (ii)

LDL-driven macrophage-like differentiation of isolated primary HSVSMCs (Beyea et al., 2012).

Another main finding of this PhD was that the TGF-β_1/ALK5 pathway augmented AngII/AT_1R-driven intracellular Ca^{2+} mobilisation, drove contractile gene expression and attenuated serum-induced proliferation in HSVSMCs. Hence, it is conceivable that transient, selective ALK5 agonism within SVGs may induce AngII-driven intracellular Ca^{2+} release, RhoA/ROCK activation (Chen et al., 2006), MLC S20 phosphorylation and contractile gene expression. This would be favourable in the context of SVG injury since this pathway would then protect the contractile HSVSMC phenotype thereby potentially improving graft contractility and preventing SMC phenotype switching and subsequent neointimal expansion. This warrants a pre-clinical study investigating the effect of systemic TGF-β_1 delivery prior to and at early time points following carotid injury in mice. Alternatively, this hypothesis may be tested by transducing murine vein grafts *ex vivo* with a recombinant HAdV-5 expressing ALK5 prior to carotid inter-positioning.

In contrast, long-term TGF-β_1-mediated sensitisation of AngII/AT_1R-driven SR Ca^{2+} release in HSVSMCs may accelerate SVG occlusion. Jiang *et al.* demonstrated that internal jugular vein grafts inter-positioned into the common carotid arteries in rabbits displayed progressive neointimal expansion over a period of 6 months (Jiang et al., 2009). This was paralleled by an increase in TGF-β_1 activity, ALK5/TGFBR2 ratio, SMAD2/3 phosphorylation and downstream *CTGF* expression suggesting that TGF-β_1 drove fibrotic neointimal remodelling. Hence, it is crucial to point out that the TGF-β_1/ALK5 signalling axis also drives ECM production thereby promoting neointimal expansion and subsequent vein graft occlusion. It may be hypothesised that late ALK5 antagonism may prevent neointimal expansion following vascular injury. This may be addressed in a pre-clinical study investigating the effect of late systemic pharmacological blockade of ALK5 following carotid injury in mice.

In summary, the work presented in this thesis shows that TGF-β_1 positively regulates the contractile HSVSMC phenotype via ALK5 and that BMP-9 partially antagonises TGF-β_1/ALK5-driven pro-contractile properties via ALK1 and/or

ALK2. Above-proposed studies will facilitate the understanding of how these key signalling pathways interact in HSVSMC biology and NF in the context of SVG disease.

List of references

Adelstein, R. S., and C. B. Klee, 1981, Purification and characterization of smooth muscle myosin light chain kinase: J Biol Chem, v. 256, p. 7501-9.

Adelstein, R. S., J. R. Sellers, M. A. Conti, M. D. Pato, and P. de Lanerolle, 1982, Regulation of smooth muscle contractile proteins by calmodulin and cyclic AMP: Fed Proc, v. 41, p. 2873-8.

Afewerki, T., S. Ahmed, and D. Warren, 2019, Emerging regulators of vascular smooth muscle cell migration: J Muscle Res Cell Motil, v. 40, p. 185-196.

Akune, T., S. Ohba, S. Kamekura, M. Yamaguchi, U. I. Chung, N. Kubota, Y. Terauchi, Y. Harada, Y. Azuma, K. Nakamura, T. Kadowaki, and H. Kawaguchi, 2004, PPARgamma insufficiency enhances osteogenesis through osteoblast formation from bone marrow progenitors: J Clin Invest, v. 113, p. 846-55.

Ala-Kokko, L., T. Pihlajaniemi, J. C. Myers, K. I. Kivirikko, and E. R. Savolainen, 1987, Gene expression of type I, III and IV collagens in hepatic fibrosis induced by dimethylnitrosamine in the rat: Biochem J, v. 244, p. 75-9.

Alba, R., A. H. Baker, and S. A. Nicklin, 2012, Vector systems for prenatal gene therapy: principles of adenovirus design and production: Methods Mol Biol, v. 891, p. 55-84.

Albini, P. T., A. M. Segura, G. Liu, C. G. Minard, J. S. Coselli, D. M. Milewicz, Y. H. Shen, and S. A. LeMaire, 2014, Advanced atherosclerosis is associated with increased medial degeneration in sporadic ascending aortic aneurysms: Atherosclerosis, v. 232, p. 361-8.

Alemany, R., Y. Dai, Y. C. Lou, E. Sethi, E. Prokopenko, S. F. Josephs, and W. W. Zhang, 1997, Complementation of helper-dependent adenoviral vectors: size effects and titer fluctuations: J Virol Methods, v. 68, p. 147-59.

Alexander, J. H., G. Hafley, R. A. Harrington, E. D. Peterson, T. B. Ferguson, Jr., T. J. Lorenz, A. Goyal, M. Gibson, M. J. Mack, D. Gennevois, R. M. Califf, N. T. Kouchoukos, and P. I. Investigators, 2005, Efficacy and safety of edifoligide, an E2F transcription factor decoy, for prevention of vein graft failure following coronary artery bypass graft surgery: PREVENT IV: a randomized controlled trial: JAMA, v. 294, p. 2446-54.

Alexander, R. W., T. A. Brock, M. A. Gimbrone, and S. E. Rittenhouse, 1985, Angiotensin increases inositol trisphosphate and calcium in vascular smooth muscle: Hypertension, v. 7, p. 447-51.

Allahverdian, S., A. C. Chehroudi, B. M. McManus, T. Abraham, and G. A. Francis, 2014, Contribution of intimal smooth muscle cells to cholesterol accumulation and macrophage-like cells in human atherosclerosis: Circulation, v. 129, p. 1551-9.

Alonso-Padilla, J., T. Papp, G. L. Kajan, M. Benko, M. Havenga, A. Lemckert, B. Harrach, and A. H. Baker, 2016, Development of Novel Adenoviral Vectors to Overcome Challenges Observed With HAdV-5-based Constructs: Mol Ther, v. 24, p. 6-16.

Alves-Lopes, R., K. B. Neves, A. Anagnostopoulou, F. J. Rios, S. Lacchini, A. C. Montezano, and R. M. Touyz, 2020, Crosstalk Between Vascular Redox and Calcium Signaling in Hypertension Involves TRPM2 (Transient Receptor Potential Melastatin 2) Cation Channel: Hypertension, v. 75, p. 139-149.

Andersson, O., E. Reissmann, and C. F. Ibáñez, 2006, Growth differentiation factor 11 signals through the transforming growth factor-beta receptor ALK5 to regionalize the anterior-posterior axis: EMBO Rep, v. 7, p. 831-7.

Andrews, B., and V. Measday, 1998, The cyclin family of budding yeast: abundant use of a good idea: Trends Genet, v. 14, p. 66-72.
Anyanwu, A. C., and D. H. Adams, 2018, Total Arterial Revascularization for Coronary Artery Bypass: Journal of the American College of Cardiology, v. 72, p. 1341-1345.
Anywaine, Z., H. Whitworth, P. Kaleebu, G. Praygod, G. Shukarev, D. Manno, S. Kapiga, H. Grosskurth, S. Kalluvya, V. Bockstal, D. Anumendem, K. Luhn, C. Robinson, M. Douoguih, and D. Watson-Jones, 2019, Safety and Immunogenicity of a 2-Dose Heterologous Vaccination Regimen With Ad26.ZEBOV and MVA-BN-Filo Ebola Vaccines: 12-Month Data From a Phase 1 Randomized Clinical Trial in Uganda and Tanzania: J Infect Dis, v. 220, p. 46-56.
Appleby, S. L., C. G. Mitrofan, A. Crosby, K. Hoenderdos, K. Lodge, P. D. Upton, C. M. Yates, G. B. Nash, E. R. Chilvers, and N. W. Morrell, 2016, Bone morphogenetic protein 9 enhances lipopolysaccharide-induced leukocyte recruitment to the vascular endothelium: J Immunol, v. 197, p. 3302-14.
Areström, I., B. Zuber, T. Bengtsson, and N. Ahlborg, 2012, Measurement of human latent Transforming Growth Factor-ß1 using a latency associated protein-reactive ELISA: J Immunol Methods, v. 379, p. 23-9.
Arthur, H. M., J. Ure, A. J. Smith, G. Renforth, D. I. Wilson, E. Torsney, R. Charlton, D. V. Parums, T. Jowett, D. A. Marchuk, J. Burn, and A. G. Diamond, 2000, Endoglin, an ancillary TGFbeta receptor, is required for extraembryonic angiogenesis and plays a key role in heart development: Dev Biol, v. 217, p. 42-53.
Asano, T., I. Ikegaki, S. Satoh, M. Seto, and Y. Sasaki, 1998, A Protein Kinase Inhibitor, Fasudil (AT-877): A Novel Approach to Signal Transduction Therapy: Cardiovascular Drug Review, v. 16, p. 76-87.
Attisano, L., J. L. Wrana, S. Cheifetz, and J. Massagué, 1992, Novel activin receptors: distinct genes and alternative mRNA splicing generate a repertoire of serine/threonine kinase receptors: Cell, v. 68, p. 97-108.
Babaev, V. R., Y. V. Bobryshev, G. K. Sukhova, and I. A. Kasantseva, 1993, Monocyte/macrophage accumulation and smooth muscle cell phenotypes in early atherosclerotic lesions of human aorta: Atherosclerosis, v. 100, p. 237-48.
Baden, L. R., D. J. Stieh, M. Sarnecki, S. R. Walsh, G. D. Tomaras, J. G. Kublin, M. J. McElrath, G. Alter, G. Ferrari, D. Montefiori, P. Mann, S. Nijs, K. Callewaert, P. Goepfert, S. Edupuganti, E. Karita, J. P. Langedijk, F. Wegmann, L. Corey, M. G. Pau, D. H. Barouch, H. Schuitemaker, F. Tomaka, and T. H. H. S. Team, 2020, Safety and immunogenicity of two heterologous HIV vaccine regimens in healthy, HIV-uninfected adults (TRAVERSE): a randomised, parallel-group, placebo-controlled, double-blind, phase 1/2a study: Lancet HIV, v. 7, p. e688-e698.
Bakin, A. V., A. Safina, C. Rinehart, C. Daroqui, H. Darbary, and D. M. Helfman, 2004, A critical role of tropomyosins in TGF-beta regulation of the actin cytoskeleton and cell motility in epithelial cells: Mol Biol Cell, v. 15, p. 4682-94.
Barbara, N. P., J. L. Wrana, and M. Letarte, 1999, Endoglin is an accessory protein that interacts with the signaling receptor complex of multiple members of the transforming growth factor-beta superfamily: J Biol Chem, v. 274, p. 584-94.
Barcellos-Hoff, M. H., and T. A. Dix, 1996, Redox-mediated activation of latent transforming growth factor-beta 1: Mol Endocrinol, v. 10, p. 1077-83.

Beeler, T. J., I. Jona, and A. Martonosi, 1979, The effect of ionomycin on calcium fluxes in sarcoplasmic reticulum vesicles and liposomes: J Biol Chem, v. 254, p. 6229-31.

Benihoud, K., P. Yeh, and M. Perricaudet, 1999, Adenovirus vectors for gene delivery: Curr Opin Biotechnol, v. 10, p. 440-7.

Beppu, H., M. Kawabata, T. Hamamoto, A. Chytil, O. Minowa, T. Noda, and K. Miyazono, 2000, BMP type II receptor is required for gastrulation and early development of mouse embryos: Dev Biol, v. 221, p. 249-58.

Bernard, D. J., 2004, Both SMAD2 and SMAD3 mediate activin-stimulated expression of the follicle-stimulating hormone beta subunit in mouse gonadotrope cells: Mol Endocrinol, v. 18, p. 606-23.

Bertoli-Avella, A. M., E. Gillis, H. Morisaki, J. M. A. Verhagen, B. M. de Graaf, G. van de Beek, E. Gallo, B. P. T. Kruithof, H. Venselaar, L. A. Myers, S. Laga, A. J. Doyle, G. Oswald, G. W. A. van Cappellen, I. Yamanaka, R. M. van der Helm, B. Beverloo, A. de Klein, L. Pardo, M. Lammens, C. Evers, K. Devriendt, M. Dumoulein, J. Timmermans, H. T. Bruggenwirth, F. Verheijen, I. Rodrigus, G. Baynam, M. Kempers, J. Saenen, E. M. Van Craenenbroeck, K. Minatoya, R. Matsukawa, T. Tsukube, N. Kubo, R. Hofstra, M. J. Goumans, J. A. Bekkers, J. W. Roos-Hesselink, I. M. B. H. van de Laar, H. C. Dietz, L. Van Laer, T. Morisaki, M. W. Wessels, and B. L. Loeys, 2015, Mutations in a TGF-ß ligand, TGFB3, cause syndromic aortic aneurysms and dissections: J Am Coll Cardiol, v. 65, p. 1324-1336.

Beyea, M. M., S. Reaume, C. G. Sawyez, J. Y. Edwards, C. O'Neil, R. A. Hegele, J. G. Pickering, and M. W. Huff, 2012, The oxysterol 24(s),25-epoxycholesterol attenuates human smooth muscle-derived foam cell formation via reduced low-density lipoprotein uptake and enhanced cholesterol efflux: J Am Heart Assoc, v. 1, p. e000810.

Bhatnagar, P., K. Wickramasinghe, J. Williams, M. Rayner, and N. Townsend, 2015, The epidemiology of cardiovascular disease in the UK 2014: Heart, v. 101, p. 1182-9.

Bhattacharyya, S., J. L. Sargent, P. Du, S. Lin, W. G. Tourtellotte, K. Takehara, M. L. Whitfield, and J. Varga, 2011, Egr-1 induces a profibrotic injury/repair gene program associated with systemic sclerosis: PLoS One, v. 6, p. e23082.

Bidart, M., N. Ricard, S. Levet, M. Samson, C. Mallet, L. David, M. Subileau, E. Tillet, J. J. Feige, and S. Bailly, 2012, BMP9 is produced by hepatocytes and circulates mainly in an active mature form complexed to its prodomain: Cell Mol Life Sci, v. 69, p. 313-24.

Bischoff, J. R., D. H. Kirn, A. Williams, C. Heise, S. Horn, M. Muna, L. Ng, J. A. Nye, A. Sampson-Johannes, A. Fattaey, and F. McCormick, 1996, An adenovirus mutant that replicates selectively in p53-deficient human tumor cells: Science, v. 274, p. 373-6.

Björkerud, S., 1991, Effects of transforming growth factor-beta 1 on human arterial smooth muscle cells in vitro: Arterioscler Thromb, v. 11, p. 892-902.

Blakytny, R., A. Ludlow, G. E. Martin, G. Ireland, L. R. Lund, M. W. Ferguson, and G. Brunner, 2004, Latent TGF-beta1 activation by platelets: J Cell Physiol, v. 199, p. 67-76.

Blanco, F. J., J. F. Santibanez, M. Guerrero-Esteo, C. Langa, C. P. Vary, and C. Bernabeu, 2005, Interaction and functional interplay between endoglin and ALK-1, two components of the endothelial transforming growth factor-beta receptor complex: J Cell Physiol, v. 204, p. 574-84.

Bobik, A., 2006, Transforming growth factor-betas and vascular disorders: Arterioscler Thromb Vasc Biol, v. 26, p. 1712-20.
Boileau, C., D. C. Guo, N. Hanna, E. S. Regalado, D. Detaint, L. Gong, M. Varret, S. K. Prakash, A. H. Li, H. d'Indy, A. C. Braverman, B. Grandchamp, C. S. Kwartler, L. Gouya, R. L. Santos-Cortez, M. Abifadel, S. M. Leal, C. Muti, J. Shendure, M. S. Gross, M. J. Rieder, A. Vahanian, D. A. Nickerson, J. B. Michel, G. Jondeau, D. M. Milewicz, and L. n. National Heart, and Blood Institute (NHLBI) Go Exome Sequencing Project, 2012, TGFB2 mutations cause familial thoracic aortic aneurysms and dissections associated with mild systemic features of Marfan syndrome: Nat Genet, v. 44, p. 916-21.
Borkenhagen, L. K., J. K. Fieldhouse, D. Seto, and G. C. Gray, 2019, Are adenoviruses zoonotic? A systematic review of the evidence: Emerg Microbes Infect, v. 8, p. 1679-1687.
Bossler, A. D., J. Richards, C. George, L. Godmilow, and A. Ganguly, 2006, Novel mutations in ENG and ACVRL1 identified in a series of 200 individuals undergoing clinical genetic testing for hereditary hemorrhagic telangiectasia (HHT): correlation of genotype with phenotype: Hum Mutat, v. 27, p. 667-75.
Bouillier, H., E. Samain, S. Miserey, C. Perret, J. F. Renaud, M. Safar, and G. Dagher, 2000, Transforming growth factor-beta1 modulates angiotensin II-induced calcium release in vascular smooth muscle cells from spontaneously hypertensive rats: J Hypertens, v. 18, p. 733-42.
Brand, V., C. Lehmann, C. Umkehrer, S. Bissinger, M. Thier, M. de Wouters, R. Raemsch, U. Jucknischke, A. Haas, S. Breuer, F. Birzele, T. Racek, M. Reis, E. Lorenzon, F. Herting, M. Stürzl, S. Lorenz, and Y. Kienast, 2016, Impact of selective anti-BMP9 treatment on tumor cells and tumor angiogenesis: Mol Oncol, v. 10, p. 1603-1620.
Bregeon, J., G. Loirand, P. Pacaud, and M. Rolli-Derkinderen, 2009, Angiotensin II induces RhoA activation through SHP2-dependent dephosphorylation of the RhoGAP p190A in vascular smooth muscle cells: Am J Physiol Cell Physiol, v. 297, p. C1062-70.
Brock, T. A., R. W. Alexander, L. S. Ekstein, W. J. Atkinson, and M. A. Gimbrone, 1985, Angiotensin increases cytosolic free calcium in cultured vascular smooth muscle cells: Hypertension, v. 7, p. I105-9.
Bulkley, B. H., and G. M. Hutchins, 1977, Accelerated "atherosclerosis". A morphologic study of 97 saphenous vein coronary artery bypass grafts: Circulation, v. 55, p. 163-9.
Cai, J., H. Yuan, Q. Wang, H. Yang, Y. Al-Abed, Z. Hua, J. Wang, D. Chen, J. Wu, B. Lu, J. P. Pribis, W. Jiang, K. Yang, D. J. Hackam, K. J. Tracey, T. R. Billiar, and A. F. Chen, 2015, HMGB1-Driven Inflammation and Intimal Hyperplasia After Arterial Injury Involves Cell-Specific Actions Mediated by TLR4: Arterioscler Thromb Vasc Biol, v. 35, p. 2579-93.
Caliskan, E., D. R. de Souza, A. Boning, O. J. Liakopoulos, Y. H. Choi, J. Pepper, C. M. Gibson, L. P. Perrault, R. K. Wolf, K. B. Kim, and M. Y. Emmert, 2020, Saphenous vein grafts in contemporary coronary artery bypass graft surgery: Nat Rev Cardiol, v. 17, p. 155-169.
Campeau, L., M. Enjalbert, J. Lesperance, C. Vaislic, C. M. Grondin, and M. G. Bourassa, 1983, Atherosclerosis and late closure of aortocoronary saphenous vein grafts: sequential angiographic studies at 2 weeks, 1 year, 5 to 7 years, and 10 to 12 years after surgery: Circulation, v. 68, p. Ii1-7.
Canham, P. B., H. M. Finlay, and D. R. Boughner, 1997, Contrasting structure of the saphenous vein and internal mammary artery used as coronary bypass vessels: Cardiovasc Res, v. 34, p. 557-67.

Capasso, C., M. Garofalo, M. Hirvinen, and V. Cerullo, 2014, The evolution of adenoviral vectors through genetic and chemical surface modifications: Viruses, v. 6, p. 832-55.
Caplice, N. M., C. N. Aroney, J. H. Bett, J. Cameron, J. H. Campbell, N. Hoffmann, P. T. McEniery, and M. J. West, 1997, Growth factors released into the coronary circulation after vascular injury promote proliferation of human vascular smooth muscle cells in culture: J Am Coll Cardiol, v. 29, p. 1536-41.
Carmeliet, P., L. Moons, J. M. Stassen, M. De Mol, A. Bouche, J. J. van den Oord, M. Kockx, and D. Collen, 1997, Vascular wound healing and neointima formation induced by perivascular electric injury in mice: Am J Pathol, v. 150, p. 761-76.
Cassar, A., D. R. Holmes, Jr., C. S. Rihal, and B. J. Gersh, 2009, Chronic coronary artery disease: diagnosis and management: Mayo Clin Proc, v. 84, p. 1130-46.
Chai, N., W. X. Li, J. Wang, Z. X. Wang, S. M. Yang, and J. W. Wu, 2015, Structural basis for the Smad5 MH1 domain to recognize different DNA sequences: Nucleic Acids Res, v. 43, p. 9051-64.
Chakrabarti, M., N. Al-Sammarraie, M. G. Gebere, A. Bhattacharya, S. Chopra, J. Johnson, E. A. Peña, J. F. Eberth, R. E. Poelmann, A. C. Gittenberger-de Groot, and M. Azhar, 2020, Transforming Growth Factor Beta3 is Required for Cardiovascular Development: J Cardiovasc Dev Dis, v. 7.
Chang, C. J., C. C. Chen, L. A. Hsu, G. J. Chang, Y. H. Ko, C. F. Chen, M. Y. Chen, S. H. Yang, and J. H. Pang, 2009, Degradation of the internal elastic laminae in vein grafts of rats with aortocaval fistulae: potential impact on graft vasculopathy: Am J Pathol, v. 174, p. 1837-46.
Chang, H., D. Huylebroeck, K. Verschueren, Q. Guo, M. M. Matzuk, and A. Zwijsen, 1999, Smad5 knockout mice die at mid-gestation due to multiple embryonic and extraembryonic defects: Development, v. 126, p. 1631-42.
Chang, Z., C. Huangfu, A. T. Grainger, J. Zhang, Q. Guo, and W. Shi, 2017, Accelerated atherogenesis in completely ligated common carotid artery of apolipoprotein E-deficient mice, Oncotarget, v. 8, p. 110289-99.
Chappell, J., J. L. Harman, V. M. Narasimhan, H. Yu, K. Foote, B. D. Simons, M. R. Bennett, and H. F. Jørgensen, 2016, Extensive Proliferation of a Subset of Differentiated, yet Plastic, Medial Vascular Smooth Muscle Cells Contributes to Neointimal Formation in Mouse Injury and Atherosclerosis Models: Circ Res, v. 119, p. 1313-1323.
Cheifetz, S., T. Bellón, C. Calés, S. Vera, C. Bernabeu, J. Massagué, and M. Letarte, 1992, Endoglin is a component of the transforming growth factor-beta receptor system in human endothelial cells: J Biol Chem, v. 267, p. 19027-30.
Cheifetz, S., H. Hernandez, M. Laiho, P. ten Dijke, K. K. Iwata, and J. Massagué, 1990, Distinct transforming growth factor-beta (TGF-beta) receptor subsets as determinants of cellular responsiveness to three TGF-beta isoforms: J Biol Chem, v. 265, p. 20533-8.
Chen, B., Y. Zhao, D. Han, B. Zhao, Y. Mao, Z. K. Cui, Y. C. Chu, L. Feng, S. Yin, C. Y. Wang, X. Wang, M. J. Xu, and G. Zhao, 2019, Wnt1 inhibits vascular smooth muscle cell calcification by promoting ANKH expression: J Mol Cell Cardiol, v. 135, p. 10-21.
Chen, L., W. Jiang, J. Huang, B. C. He, G. W. Zuo, W. Zhang, Q. Luo, Q. Shi, B. Q. Zhang, E. R. Wagner, J. Luo, M. Tang, C. Wietholt, X. Luo, Y. Bi, Y. Su, B. Liu, S. H. Kim, C. J. He, Y. Hu, J. Shen, F. Rastegar, E. Huang, Y. Gao, J. L. Gao, J. Z. Zhou, R. R. Reid, H. H. Luu, R. C. Haydon, T. C. He, and

Z. L. Deng, 2010, Insulin-like growth factor 2 (IGF-2) potentiates BMP-9-induced osteogenic differentiation and bone formation: J Bone Miner Res, v. 25, p. 2447-59.
Chen, L., X. Zou, R. X. Zhang, C. J. Pi, N. Wu, L. J. Yin, and Z. L. Deng, 2016a, IGF1 potentiates BMP9-induced osteogenic differentiation in mesenchymal stem cells through the enhancement of BMP/Smad signaling: BMB Rep, v. 49, p. 122-7.
Chen, P.-Y., L. Qin, G. Li, G. Tellides, and M. Simons, 2016b, Fibroblast growth factor (FGF) signaling regulates transforming growth factor beta (TGF ß)-dependent smooth muscle cell phenotype modulation: Scientific Reports, v. 6, p. 1-11.
Chen, Q., H. Chen, D. Zheng, C. Kuang, H. Fang, B. Zou, W. Zhu, G. Bu, T. Jin, Z. Wang, X. Zhang, J. Chen, L. J. Field, M. Rubart, W. Shou, and Y. Chen, 2009, Smad7 is required for the development and function of the heart: J Biol Chem, v. 284, p. 292-300.
Chen, S., M. Crawford, R. M. Day, V. R. Briones, J. E. Leader, P. A. Jose, and R. J. Lechleider, 2006, RhoA modulates Smad signaling during transforming growth factor-beta-induced smooth muscle differentiation: J Biol Chem, v. 281, p. 1765-70.
Chen, S., M. Kulik, and R. J. Lechleider, 2003, Smad proteins regulate transcriptional induction of the SM22alpha gene by TGF-beta: Nucleic Acids Res, v. 31, p. 1302-10.
Cheng, W. S., H. Dzojic, B. Nilsson, T. H. Tötterman, and M. Essand, 2006, An oncolytic conditionally replicating adenovirus for hormone-dependent and hormone-independent prostate cancer: Cancer Gene Ther, v. 13, p. 13-20.
Chida, A., M. Shintani, T. Nakayama, Y. Furutani, E. Hayama, K. Inai, T. Saji, S. Nonoyama, and T. Nakanishi, 2012, Missense mutations of the BMPR1B (ALK6) gene in childhood idiopathic pulmonary arterial hypertension: Circ J, v. 76, p. 1501-8.
Chiu, A. T., D. E. McCall, W. A. Price, P. C. Wong, D. J. Carini, J. V. Duncia, R. R. Wexler, S. E. Yoo, A. L. Johnson, and P. B. Timmermans, 1991, In vitro pharmacology of DuP 753: Am J Hypertens, v. 4, p. 282S-287S.
Choi, K. J., J. K. Nam, J. H. Kim, S. H. Choi, and Y. J. Lee, 2020, Endothelial-to-mesenchymal transition in anticancer therapy and normal tissue damage: Exp Mol Med, v. 52, p. 781-792.
Chowdhury, I., and B. Chaqour, 2004, Regulation of connective tissue growth factor (CTGF/CCN2) gene transcription and mRNA stability in smooth muscle cells. Involvement of RhoA GTPase and p38 MAP kinase and sensitivity to actin dynamics: Eur J Biochem, v. 271, p. 4436-50.
Chu, Y., D. Heistad, M. I. Cybulsky, and B. L. Davidson, 2001, Vascular cell adhesion molecule-1 augments adenovirus-mediated gene transfer: Arterioscler Thromb Vasc Biol, v. 21, p. 238-42.
Chung, J. K., T. Lee, I. M. Jung, Y. K. Kim, S. K. Min, J. W. Suh, and S. J. Kim, 2004, Expression of cell cycle regulators during smooth muscle cell proliferation after balloon catheter injury of rat artery: J Korean Med Sci, v. 19, p. 327-32.
Cleary, R. A., R. Wang, O. Waqar, H. A. Singer, and D. D. Tang, 2014, Role of c-Abl tyrosine kinase in smooth muscle cell migration: Am J Physiol Cell Physiol, v. 306, p. C753-61.
Clement, C. M., L. K. Thomas, Y. Mou, D. R. Croslan, G. H. Gibbons, and B. D. Ford, 2007, Neuregulin-1 attenuates neointimal formation following

vascular injury and inhibits the proliferation of vascular smooth muscle cells: J Vasc Res, v. 44, p. 303-12.

Collaborators, G. M. a. C. o. D., 2015, Global, regional, and national age-sex specific all-cause and cause-specific mortality for 240 causes of death, 1990-2013: a systematic analysis for the Global Burden of Disease Study 2013: Lancet, v. 385, p. 117-71.

Communal, C., F. Huq, D. Lebeche, C. Mestel, J. K. Gwathmey, and R. J. Hajjar, 2003, Decreased efficiency of adenovirus-mediated gene transfer in aging cardiomyocytes: Circulation, v. 107, p. 1170-5.

Compton, L. A., D. A. Potash, C. B. Brown, and J. V. Barnett, 2007, Coronary vessel development is dependent on the type III transforming growth factor beta receptor: Circ Res, v. 101, p. 784-91.

Cooley, B. C., J. Nevado, J. Mellad, D. Yang, C. St Hilaire, A. Negro, F. Fang, G. Chen, H. San, A. D. Walts, R. L. Schwartzbeck, B. Taylor, J. D. Lanzer, A. Wragg, A. Elagha, L. E. Beltran, C. Berry, R. Feil, R. Virmani, E. Ladich, J. C. Kovacic, and M. Boehm, 2014, TGF-ß signaling mediates endothelial-to-mesenchymal transition (EndMT) during vein graft remodeling: Sci Transl Med, v. 6, p. 227ra34.

Corriu, C., P. André, C. Schott, M. Michel, and J. C. Stoclet, 1994, ANG II receptor expression and function during phenotypic modulation of rat aortic smooth muscle cells: Am J Physiol, v. 266, p. H631-6.

Costa, M. A., and D. I. Simon, 2005, Molecular basis of restenosis and drug-eluting stents: Circulation, v. 111, p. 2257-73.

Crosas-Molist, E., T. Meirelles, J. López-Luque, C. Serra-Peinado, J. Selva, L. Caja, D. Gorbenko Del Blanco, J. J. Uriarte, E. Bertran, Y. Mendizábal, V. Hernández, C. García-Calero, O. Busnadiego, E. Condom, D. Toral, M. Castellà, A. Forteza, D. Navajas, E. Sarri, F. Rodríguez-Pascual, H. C. Dietz, I. Fabregat, and G. Egea, 2015, Vascular smooth muscle cell phenotypic changes in patients with Marfan syndrome: Arterioscler Thromb Vasc Biol, v. 35, p. 960-72.

Dai, G., M. R. Kaazempur-Mofrad, S. Natarajan, Y. Zhang, S. Vaughn, B. R. Blackman, R. D. Kamm, G. Garcia-Cardena, and M. A. Gimbrone, Jr., 2004, Distinct endothelial phenotypes evoked by arterial waveforms derived from atherosclerosis-susceptible and -resistant regions of human vasculature: Proc Natl Acad Sci U S A, v. 101, p. 14871-6.

Dai, Y., and S. Grant, 2003, Cyclin-dependent kinase inhibitors: Curr Opin Pharmacol, v. 3, p. 362-70.

Dakin, R. S., A. L. Parker, C. Delles, S. A. Nicklin, and A. H. Baker, 2015, Efficient transduction of primary vascular cells by the rare adenovirus serotype 49 vector: Hum Gene Ther, v. 26, p. 312-9.

Danthinne, X., and M. J. Imperiale, 2000, Production of first generation adenovirus vectors: a review: Gene Ther, v. 7, p. 1707-14.

David, C. J., and J. Massagué, 2018, Contextual determinants of TGFß action in development, immunity and cancer: Nature Reviews Molecular Cell Biology.

David, L., C. Mallet, M. Keramidas, N. Lamande, J. M. Gasc, S. Dupuis-Girod, H. Plauchu, J. J. Feige, and S. Bailly, 2008, Bone morphogenetic protein-9 is a circulating vascular quiescence factor: Circ Res, v. 102, p. 914-22.

David, L., C. Mallet, S. Mazerbourg, J. J. Feige, and S. Bailly, 2007, Identification of BMP9 and BMP10 as functional activators of the orphan activin receptor-like kinase 1 (ALK1) in endothelial cells: Blood, v. 109, p. 1953-61.

Davignon, J., and P. Ganz, 2004, Role of endothelial dysfunction in atherosclerosis: Circulation, v. 109, p. III27-32.
de Vries, M. R., K. H. Simons, J. W. Jukema, J. Braun, and P. H. Quax, 2016, Vein graft failure: from pathophysiology to clinical outcomes: Nat Rev Cardiol, v. 13, p. 451-70.
De Vries, M. R., K. H. Simons, J. W. Jukema, J. Braun, and P. H. A. Quax, 2016, Vein graft failure: from pathophysiology to clinical outcomes, v. 13, p. 451-470.
Deguchi, J., T. Namba, H. Hamada, T. Nakaoka, J. Abe, O. Sato, T. Miyata, M. Makuuchi, K. Kurokawa, and Y. Takuwa, 1999, Targeting endogenous platelet-derived growth factor B-chain by adenovirus-mediated gene transfer potently inhibits in vivo smooth muscle proliferation after arterial injury: Gene Ther, v. 6, p. 956-65.
dela Paz, N. G., and P. A. D'Amore, 2009, Arterial versus venous endothelial cells: Cell Tissue Res, v. 335, p. 5-16.
Deng, D. X., J. M. Spin, A. Tsalenko, A. Vailaya, A. Ben-Dor, Z. Yakhini, P. Tsao, L. Bruhn, and T. Quertermous, 2006, Molecular signatures determining coronary artery and saphenous vein smooth muscle cell phenotypes: distinct responses to stimuli: Arterioscler Thromb Vasc Biol, v. 26, p. 1058-65.
Dennler, S., S. Itoh, D. Vivien, P. ten Dijke, S. Huet, and J. M. Gauthier, 1998, Direct binding of Smad3 and Smad4 to critical TGF beta-inducible elements in the promoter of human plasminogen activator inhibitor-type 1 gene: EMBO J, v. 17, p. 3091-100.
Deo, S. V., S. M. Dunlay, I. K. Shah, S. E. Altarabsheh, P. J. Erwin, B. A. Boilson, S. J. Park, and L. D. Joyce, 2013, Dual anti-platelet therapy after coronary artery bypass grafting: is there any benefit? A systematic review and meta-analysis: J Card Surg, v. 28, p. 109-16.
Deraët, M., L. Rihakova, A. Boucard, J. Pèrodin, S. Sauvé, A. P. Mathieu, G. Guillemette, R. Leduc, P. Lavigne, and E. Escher, 2002, Angiotensin II is bound to both receptors AT1 and AT2, parallel to the transmembrane domains and in an extended form: Can J Physiol Pharmacol, v. 80, p. 418-25.
Di Guglielmo, G. M., C. Le Roy, A. F. Goodfellow, and J. L. Wrana, 2003, Distinct endocytic pathways regulate TGF-beta receptor signalling and turnover: Nat Cell Biol, v. 5, p. 410-21.
Dickson, M. C., J. S. Martin, F. M. Cousins, A. B. Kulkarni, S. Karlsson, and R. J. Akhurst, 1995, Defective haematopoiesis and vasculogenesis in transforming growth factor-beta 1 knock out mice: Development, v. 121, p. 1845-54.
Ding, L., J. Cao, W. Lin, H. Chen, X. Xiong, H. Ao, M. Yu, J. Lin, and Q. Cui, 2020, The Roles of Cyclin-Dependent Kinases in Cell-Cycle Progression and Therapeutic Strategies in Human Breast Cancer: Int J Mol Sci, v. 21.
Dobin, A., C. A. Davis, F. Schlesinger, J. Drenkow, C. Zaleski, S. Jha, P. Batut, M. Chaisson, and T. R. Gingeras, 2013, STAR: ultrafast universal RNA-seq aligner: Bioinformatics, v. 29, p. 15-21.
Dobnikar, L., A. L. Taylor, J. Chappell, P. Oldach, J. L. Harman, E. Oerton, E. Dzierzak, M. R. Bennett, M. Spivakov, and H. F. Jørgensen, 2018, Disease-relevant transcriptional signatures identified in individual smooth muscle cells from healthy mouse vessels: Nat Commun, v. 9, p. 4567.
Dol-Gleizes, F., N. Delesque-Touchard, A. M. Marès, A. L. Nestor, P. Schaeffer, and F. Bono, 2013, A new synthetic FGF receptor antagonist inhibits

arteriosclerosis in a mouse vein graft model and atherosclerosis in apolipoprotein E-deficient mice: PLoS One, v. 8, p. e80027.
Dormond, E., M. Perrier, and A. Kamen, 2009, From the first to the third generation adenoviral vector: what parameters are governing the production yield?: Biotechnol Adv, v. 27, p. 133-44.
Doyle, A. J., J. J. Doyle, S. L. Bessling, S. Maragh, M. E. Lindsay, D. Schepers, E. Gillis, G. Mortier, T. Homfray, K. Sauls, R. A. Norris, N. D. Huso, D. Leahy, D. W. Mohr, M. J. Caulfield, A. F. Scott, A. Destrée, R. C. Hennekam, P. H. Arn, C. J. Curry, L. Van Laer, A. S. McCallion, B. L. Loeys, and H. C. Dietz, 2012, Mutations in the TGF-ß repressor SKI cause Shprintzen-Goldberg syndrome with aortic aneurysm: Nat Genet, v. 44, p. 1249-54.
Du, K. L., H. S. Ip, J. Li, M. Chen, F. Dandre, W. Yu, M. M. Lu, G. K. Owens, and M. S. Parmacek, 2003, Myocardin is a critical serum response factor cofactor in the transcriptional program regulating smooth muscle cell differentiation: Mol Cell Biol, v. 23, p. 2425-37.
Dubois, C. M., M. H. Laprise, F. Blanchette, L. E. Gentry, and R. Leduc, 1995, Processing of transforming growth factor beta 1 precursor by human furin convertase: J Biol Chem, v. 270, p. 10618-24.
Ebisawa, T., K. Tada, I. Kitajima, K. Tojo, T. K. Sampath, M. Kawabata, K. Miyazono, and T. Imamura, 1999, Characterization of bone morphogenetic protein-6 signaling pathways in osteoblast differentiation: J Cell Sci, v. 112 (Pt 20), p. 3519-27.
Ehrhardt, A., and M. A. Kay, 2002, A new adenoviral helper-dependent vector results in long-term therapeutic levels of human coagulation factor IX at low doses in vivo: Blood, v. 99, p. 3923-30.
Ehsan, A., M. J. Mann, G. Dell'Acqua, and V. J. Dzau, 2001, Long-term stabilization of vein graft wall architecture and prolonged resistance to experimental atherosclerosis after E2F decoy oligonucleotide gene therapy: J Thorac Cardiovasc Surg, v. 121, p. 714-22.
Eisenberg-Lerner, A., and A. Kimchi, 2007, DAP kinase regulates JNK signaling by binding and activating protein kinase D under oxidative stress: Cell Death Differ, v. 14, p. 1908-15.
Elsharawy, M. A., M. M. Naim, E. M. Abdelmaguid, and A. A. Al-Mulhim, 2007, Role of saphenous vein wall in the pathogenesis of primary varicose veins: Interact Cardiovasc Thorac Surg, v. 6, p. 219-24.
Engelse, M. A., J. H. Lardenoye, J. M. Neele, J. M. Grimbergen, M. R. De Vries, M. L. Lamfers, H. Pannekoek, P. H. Quax, and C. J. De Vries, 2002, Adenoviral activin a expression prevents intimal hyperplasia in human and murine blood vessels by maintaining the contractile smooth muscle cell phenotype: Circ Res, v. 90, p. 1128-34.
Eto, M., T. Ohmori, M. Suzuki, K. Furuya, and F. Morita, 1995, A novel protein phosphatase-1 inhibitory protein potentiated by protein kinase C. Isolation from porcine aorta media and characterization: J Biochem, v. 118, p. 1104-7.
Evans, J. D., B. Girerd, D. Montani, X. J. Wang, N. Galiè, E. D. Austin, G. Elliott, K. Asano, E. Grünig, Y. Yan, Z. C. Jing, A. Manes, M. Palazzini, L. A. Wheeler, I. Nakayama, T. Satoh, C. Eichstaedt, K. Hinderhofer, M. Wolf, E. B. Rosenzweig, W. K. Chung, F. Soubrier, G. Simonneau, O. Sitbon, S. Gräf, S. Kaptoge, E. Di Angelantonio, M. Humbert, and N. W. Morrell, 2016, BMPR2 mutations and survival in pulmonary arterial hypertension: an individual participant data meta-analysis: Lancet Respir Med, v. 4, p. 129-37.

Farb, A., G. Sangiorgi, A. J. Carter, V. M. Walley, W. D. Edwards, R. S. Schwartz, and R. Virmani, 1999, Pathology of acute and chronic coronary stenting in humans: Circulation, v. 99, p. 44-52.

Fechner, H., A. Haack, H. Wang, X. Wang, K. Eizema, M. Pauschinger, R. Schoemaker, R. Veghel, A. Houtsmuller, H. P. Schultheiss, J. Lamers, and W. Poller, 1999, Expression of coxsackie adenovirus receptor and alphav-integrin does not correlate with adenovector targeting in vivo indicating anatomical vector barriers: Gene Ther, v. 6, p. 1520-35.

Feng, J., M. Ito, K. Ichikawa, N. Isaka, M. Nishikawa, D. J. Hartshorne, and T. Nakano, 1999, Inhibitory phosphorylation site for Rho-associated kinase on smooth muscle myosin phosphatase: J Biol Chem, v. 274, p. 37385-90.

Fernandes, P., A. C. Silva, A. S. Coroadinha, and P. M. Alves, 2016, Upstream Bioprocess for Adenovirus Vectors, Adenoviral Vectors for Gene Therapy, p. 139-161.

Ferns, G. A., E. W. Raines, K. H. Sprugel, A. S. Motani, M. A. Reidy, and R. Ross, 1991, Inhibition of neointimal smooth muscle accumulation after angioplasty by an antibody to PDGF: Science, v. 253, p. 1129-32.

Fihn, S. D., J. C. Blankenship, K. P. Alexander, J. A. Bittl, J. G. Byrne, B. J. Fletcher, G. C. Fonarow, R. A. Lange, G. N. Levine, T. M. Maddox, S. S. Naidu, E. M. Ohman, and P. K. Smith, 2014, 2014 ACC/AHA/AATS/PCNA/SCAI/STS focused update of the guideline for the diagnosis and management of patients with stable ischemic heart disease: a report of the American College of Cardiology/American Heart Association Task Force on Practice Guidelines, and the American Association for Thoracic Surgery, Preventive Cardiovascular Nurses Association, Society for Cardiovascular Angiography and Interventions, and Society of Thoracic Surgeons: J Am Coll Cardiol, v. 64, p. 1929-49.

Fisher, K. J., H. Choi, J. Burda, S. J. Chen, and J. M. Wilson, 1996, Recombinant adenovirus deleted of all viral genes for gene therapy of cystic fibrosis: Virology, v. 217, p. 11-22.

Folegatti, P. M., K. J. Ewer, P. K. Aley, B. Angus, S. Becker, S. Belij-Rammerstorfer, D. Bellamy, S. Bibi, M. Bittaye, E. A. Clutterbuck, C. Dold, S. N. Faust, A. Finn, A. L. Flaxman, B. Hallis, P. Heath, D. Jenkin, R. Lazarus, R. Makinson, A. M. Minassian, K. M. Pollock, M. Ramasamy, H. Robinson, M. Snape, R. Tarrant, M. Voysey, C. Green, A. D. Douglas, A. V. S. Hill, T. Lambe, S. C. Gilbert, A. J. Pollard, and O. C. V. T. Group, 2020, Safety and immunogenicity of the ChAdOx1 nCoV-19 vaccine against SARS-CoV-2: a preliminary report of a phase 1/2, single-blind, randomised controlled trial: Lancet, v. 396, p. 467-478.

Ford, C. M., S. Li, and J. G. Pickering, 1999, Angiotensin II stimulates collagen synthesis in human vascular smooth muscle cells. Involvement of the AT(1) receptor, transforming growth factor-beta, and tyrosine phosphorylation: Arterioscler Thromb Vasc Biol, v. 19, p. 1843-51.

Fournier, P. G., P. Juárez, G. Jiang, G. A. Clines, M. Niewolna, H. S. Kim, H. W. Walton, X. H. Peng, Y. Liu, K. S. Mohammad, C. D. Wells, J. M. Chirgwin, and T. A. Guise, 2015, The TGF-β Signaling Regulator PMEPA1 Suppresses Prostate Cancer Metastases to Bone: Cancer Cell, v. 27, p. 809-21.

Francis, S. E., S. Hunter, C. M. Holt, P. A. Gadsdon, S. Rogers, G. W. Duff, A. C. Newby, and G. D. Angelini, 1994, Release of platelet-derived growth factor activity from pig venous arterial grafts: J Thorac Cardiovasc Surg, v. 108, p. 540-8.

Frid, M. G., E. P. Moiseeva, and K. R. Stenmark, 1994, Multiple phenotypically distinct smooth muscle cell populations exist in the adult and developing bovine pulmonary arterial media in vivo: Circ Res, v. 75, p. 669-81.
Friedl, R., J. Li, B. Schumacher, H. Hanke, J. Waltenberger, A. Hannekum, and S. Stracke, 2004, Intimal hyperplasia and expression of transforming growth factor-beta1 in saphenous veins and internal mammary arteries before coronary artery surgery: Ann Thorac Surg, v. 78, p. 1312-8.
Frismantiene, A., M. Philippova, P. Erne, and T. J. Resink, 2018, Smooth muscle cell-driven vascular diseases and molecular mechanisms of VSMC plasticity: Cell Signal, v. 52, p. 48-64.
Fu, J., L. Li, and M. Bouvier, 2011, Adenovirus E3-19K proteins of different serotypes and subgroups have similar, yet distinct, immunomodulatory functions toward major histocompatibility class I molecules: J Biol Chem, v. 286, p. 17631-9.
Fuentes, J. J., L. Genescà, T. J. Kingsbury, K. W. Cunningham, M. Pérez-Riba, X. Estivill, and S. de la Luna, 2000, DSCR1, overexpressed in Down syndrome, is an inhibitor of calcineurin-mediated signaling pathways: Hum Mol Genet, v. 9, p. 1681-90.
Fukui, R., M. Amakawa, M. Hoshiga, N. Shibata, E. Kohbayashi, M. Seto, Y. Sasaki, T. Ueno, N. Negoro, T. Nakakoji, M. Ii, F. Nishiguchi, T. Ishihara, and N. Ohsawa, 2000, Increased migration in late G(1) phase in cultured smooth muscle cells: Am J Physiol Cell Physiol, v. 279, p. C999-1007.
Furukawa, Y., Y. Terui, K. Sakoe, M. Ohta, and M. Saito, 1994, The role of cellular transcription factor E2F in the regulation of cdc2 mRNA expression and cell cycle control of human hematopoietic cells: J Biol Chem, v. 269, p. 26249-58.
Galili, O., J. Herrmann, J. Woodrum, K. J. Sattler, L. O. Lerman, and A. Lerman, 2004, Adventitial vasa vasorum heterogeneity among different vascular beds: J Vasc Surg, v. 40, p. 529-35.
Gao, Y. D., J. W. Zheng, P. Li, M. Cheng, and J. Yang, 2013, Store-operated Ca2+ entry is involved in transforming growth factor-ß1 facilitated proliferation of rat airway smooth muscle cells: J Asthma, v. 50, p. 439-48.
García-Redondo, A. B., V. Esteban, A. M. Briones, L. S. Díaz Del Campo, M. González-Amor, N. Méndez-Barbero, M. R. Campanero, J. M. Redondo, and M. Salaices, 2018, Regulator of calcineurin 1 modulates vascular contractility and stiffness through the upregulation of COX-2-derived prostanoids: Pharmacol Res, v. 133, p. 236-249.
Garrido-Martín, E. M., F. J. Blanco, M. Roquè, L. Novensà, M. Tarocchi, U. E. Lang, T. Suzuki, S. L. Friedman, L. M. Botella, and C. Bernabéu, 2013, Vascular injury triggers Krüppel-like factor 6 mobilization and cooperation with specificity protein 1 to promote endothelial activation through upregulation of the activin receptor-like kinase 1 gene: Circ Res, v. 112, p. 113-27.
Gaudino, M., R. Lorusso, M. Rahouma, A. Abouarab, D. Y. Tam, C. Spadaccio, G. Saint-Hilary, J. Leonard, M. Iannaccone, F. D'Ascenzo, A. Di Franco, G. Soletti, M. K. Kamel, C. Lau, L. N. Girardi, T. A. Schwann, U. Benedetto, D. P. Taggart, and S. E. Fremes, 2019, Radial Artery Versus Right Internal Thoracic Artery Versus Saphenous Vein as the Second Conduit for Coronary Artery Bypass Surgery: A Network Meta-Analysis of Clinical Outcomes: J Am Heart Assoc, v. 8, p. e010839.
Gentry, L. E., M. N. Lioubin, A. F. Purchio, and H. Marquardt, 1988, Molecular events in the processing of recombinant type 1 pre-pro-transforming

growth factor beta to the mature polypeptide: Mol Cell Biol, v. 8, p. 4162-8.
Gentry, L. E., and B. W. Nash, 1990, The pro domain of pre-pro-transforming growth factor beta 1 when independently expressed is a functional binding protein for the mature growth factor: Biochemistry, v. 29, p. 6851-7.
George, S. J., C. T. Lloyd, G. D. Angelini, A. C. Newby, and A. H. Baker, 2000, Inhibition of late vein graft neointima formation in human and porcine models by adenovirus-mediated overexpression of tissue inhibitor of metalloproteinase-3: Circulation, v. 101, p. 296-304.
George, S. J., S. Wan, J. Hu, R. MacDonald, J. L. Johnson, and A. H. Baker, 2011, Sustained reduction of vein graft neointima formation by ex vivo TIMP-3 gene therapy: Circulation, v. 124, p. S135-42.
Gerthoffer, W. T., 2007, Mechanisms of vascular smooth muscle cell migration: Circ Res, v. 100, p. 607-21.
Ghose, C., and F. M. Raushel, 1985, Determination of the mechanism of the argininosuccinate synthetase reaction by static and dynamic quench experiments: Biochemistry, v. 24, p. 5894-8.
Goldman, S., J. Copeland, T. Moritz, W. Henderson, K. Zadina, T. Ovitt, J. Doherty, R. Read, E. Chesler, and Y. Sako, 1989, Saphenous vein graft patency 1 year after coronary artery bypass surgery and effects of antiplatelet therapy. Results of a Veterans Administration Cooperative Study: Circulation, v. 80, p. 1190-7.
Gollasch, M., H. Haase, C. Ried, C. Lindschau, I. Morano, F. C. Luft, and H. Haller, 1998, L-type calcium channel expression depends on the differentiated state of vascular smooth muscle cells: FASEB J, v. 12, p. 593-601.
Gomez-Puerto, M. C., I. van Zuijen, C. J. Huang, R. Szulcek, X. Pan, M. A. van Dinther, K. Kurakula, C. C. Wiesmeijer, M. J. Goumans, H. J. Bogaard, N. W. Morrell, A. A. Rana, and P. Ten Dijke, 2019, Autophagy contributes to BMP type 2 receptor degradation and development of pulmonary arterial hypertension: J Pathol, v. 249, p. 356-367.
Goumans, M. J., G. Valdimarsdottir, S. Itoh, F. Lebrin, J. Larsson, C. Mummery, S. Karlsson, and P. ten Dijke, 2003, Activin receptor-like kinase (ALK)1 is an antagonistic mediator of lateral TGFbeta/ALK5 signaling: Mol Cell, v. 12, p. 817-28.
Goumans, M. J., G. Valdimarsdottir, S. Itoh, A. Rosendahl, P. Sideras, and P. ten Dijke, 2002, Balancing the activation state of the endothelium via two distinct TGF-beta type I receptors: Embo j, v. 21, p. 1743-53.
Graham, F. L., J. Smiley, W. C. Russell, and R. Nairn, 1977, Characteristics of a human cell line transformed by DNA from human adenovirus type 5: J Gen Virol, v. 36, p. 59-74.
Grainger, D., J. Metcalfe, A. Grace, and D. Mosedale, 1998, Transforming Growth Factor-Beta Dynamically Regulates Vascular Smooth Muscle Differentiation in Vivo: Journal of cell science, v. 111 (Pt 19).
Greber, U. F., M. Willetts, P. Webster, and A. Helenius, 1993, Stepwise dismantling of adenovirus 2 during entry into cells: Cell, v. 75, p. 477-86.
Grewe, P. H., T. Deneke, A. Machraoui, J. Barmeyer, and K. M. Muller, 2000, Acute and chronic tissue response to coronary stent implantation: pathologic findings in human specimen: J Am Coll Cardiol, v. 35, p. 157-63.
Groenendijk, B. C., G. F. Benus, A. Klous, Y. M. Pacheco, O. L. Volger, J. O. Fledderus, V. Ferreira, M. A. Engelse, H. Pannekoek, P. ten Dijke, A. J.

Horrevoets, and C. J. de Vries, 2011, Activin A induces a non-fibrotic phenotype in smooth muscle cells in contrast to TGF-ß: Exp Cell Res, v. 317, p. 131-42.

Grondin, C. M., J. Lespérance, M. G. Bourassa, A. Pasternac, L. Campneau, and P. Grondin, 1974, Serial angiograpic evaluation in 60 consecutive patients with aorto-coronary artery vein grafts 2 weeks, 1 year, and 3 years after operation: J Thorac Cardiovasc Surg, v. 67, p. 1-6.

Grosskreutz, C. L., B. Anand-Apte, C. Dupláa, T. P. Quinn, B. I. Terman, B. Zetter, and P. A. D'Amore, 1999, Vascular endothelial growth factor-induced migration of vascular smooth muscle cells in vitro: Microvasc Res, v. 58, p. 128-36.

Guerrero, F., C. Herencia, Y. Almadén, J. M. Martínez-Moreno, A. Montes de Oca, M. E. Rodriguez-Ortiz, J. M. Diaz-Tocados, A. Canalejo, M. Florio, I. López, W. G. Richards, M. Rodriguez, E. Aguilera-Tejero, and J. R. Muñoz-Castañeda, 2014, TGF-ß prevents phosphate-induced osteogenesis through inhibition of BMP and Wnt/ß-catenin pathways: PLoS One, v. 9, p. e89179.

Hamamoto, T., H. Beppu, H. Okada, M. Kawabata, T. Kitamura, K. Miyazono, and M. Kato, 2002, Compound disruption of smad2 accelerates malignant progression of intestinal tumors in apc knockout mice: Cancer Res, v. 62, p. 5955-61.

Han, M., L. H. Dong, B. Zheng, J. H. Shi, J. K. Wen, and Y. Cheng, 2009, Smooth muscle 22 alpha maintains the differentiated phenotype of vascular smooth muscle cells by inducing filamentous actin bundling: Life Sci, v. 84, p. 394-401.

Han, M., J. K. Wen, B. Zheng, Y. Cheng, and C. Zhang, 2006, Serum deprivation results in redifferentiation of human umbilical vascular smooth muscle cells: Am J Physiol Cell Physiol, v. 291, p. C50-8.

Hao, H., P. Ropraz, V. Verin, E. Camenzind, A. Geinoz, M. S. Pepper, G. Gabbiani, and M. L. Bochaton-Piallat, 2002, Heterogeneity of smooth muscle cell populations cultured from pig coronary artery: Arterioscler Thromb Vasc Biol, v. 22, p. 1093-9.

Harmon, K. J., L. L. Couper, and V. Lindner, 2000, Strain-dependent vascular remodeling phenotypes in inbred mice: Am J Pathol, v. 156, p. 1741-8.

Harrach, B., M. Benkö, G. Both, M. Brown, A. Davison, M. Echavarría, M. Hess, Jones MS., A. Kajon, H. Lehmkuhl, V. Mautner, S. Mittal, and G. Wadell, 2011, The double stranded DNA viruses: adenoviridae. In: Virus taxonomy: ninth report of the international committee of viruses., Academic Press: Elsevier.

Harrach, B., Z. L. Tarján, and M. Benkő, 2019, Adenoviruses across the animal kingdom: a walk in the zoo: FEBS Lett, v. 593, p. 3660-3673.

Harris, R., B. Croce, and D. H. Tian, 2013, Coronary artery bypass grafting: Ann Cardiothorac Surg, v. 2, p. 579.

Harskamp, R. E., R. D. Lopes, C. E. Baisden, R. J. de Winter, and J. H. Alexander, 2013, Saphenous vein graft failure after coronary artery bypass surgery: pathophysiology, management, and future directions: Ann Surg, v. 257, p. 824-33.

Hasegawa, K., H. Tamai, E. Kyo, K. Kosuga, S. Ikeguchi, T. Hata, M. Okada, S. Fujita, T. Tsuji, S. Takeda, R. Fukuhara, Y. Kikuta, S. Motohara, K. Ono, and E. Takeuchi, 2006, Histopathological findings of new in-stent lesions developed beyond five years: Catheter Cardiovasc Interv, v. 68, p. 554-8.

Hata, A., G. Lagna, J. Massagué, and A. Hemmati-Brivanlou, 1998, Smad6 inhibits BMP/Smad1 signaling by specifically competing with the Smad4 tumor suppressor: Genes Dev, v. 12, p. 186-97.

Hautmann, M. B., C. S. Madsen, and G. K. Owens, 1997, A transforming growth factor beta (TGFbeta) control element drives TGFbeta-induced stimulation of smooth muscle alpha-actin gene expression in concert with two CArG elements: J Biol Chem, v. 272, p. 10948-56.

Heinecke, J. W., H. Rosen, and A. Chait, 1984, Iron and copper promote modification of low density lipoprotein by human arterial smooth muscle cells in culture: J Clin Invest, v. 74, p. 1890-4.

Heldman, A. W., L. Cheng, G. M. Jenkins, P. F. Heller, D. W. Kim, M. Ware, Jr., C. Nater, R. H. Hruban, B. Rezai, B. S. Abella, K. E. Bunge, J. L. Kinsella, S. J. Sollott, E. G. Lakatta, J. A. Brinker, W. L. Hunter, and J. P. Froehlich, 2001, Paclitaxel stent coating inhibits neointimal hyperplasia at 4 weeks in a porcine model of coronary restenosis: Circulation, v. 103, p. 2289-95.

Hering, S., C. Jost, H. Schulz, B. Hellmich, H. Schatz, and H. Pfeiffer, 2002, Circulating transforming growth factor beta1 (TGFbeta1) is elevated by extensive exercise: Eur J Appl Physiol, v. 86, p. 406-10.

Herring, B. P., A. M. Hoggatt, C. Burlak, and S. Offermanns, 2014, Previously differentiated medial vascular smooth muscle cells contribute to neointima formation following vascular injury: Vasc Cell, v. 6, p. 21.

Ho, L. C., J. M. Sung, Y. T. Shen, H. F. Jheng, S. H. Chen, P. J. Tsai, and Y. S. Tsai, 2016, Egr-1 deficiency protects from renal inflammation and fibrosis: J Mol Med (Berl), v. 94, p. 933-42.

Hoch, J. R., V. K. Stark, D. A. Hullett, and W. D. Turnipseed, 1994, Vein graft intimal hyperplasia: leukocytes and cytokine gene expression: Surgery, v. 116, p. 463-70; discussion 470-1.

Hodgson, J., E. M. Swietlik, R. M. Salmon, C. Hadinnapola, I. Nikolic, J. Wharton, J. Guo, J. Liley, M. Haimel, M. Bleda, L. Southgate, R. D. Machado, J. M. Martin, C. M. Treacy, K. Yates, L. C. Daugherty, O. Shamardina, D. Whitehorn, S. Holden, H. J. Bogaard, C. Church, G. Coghlan, R. Condliffe, P. A. Corris, C. Danesino, M. Eyries, H. Gall, S. Ghio, H. A. Ghofrani, J. S. R. Gibbs, B. Girerd, A. C. Houweling, L. Howard, M. Humbert, D. G. Kiely, G. Kovacs, A. Lawrie, R. V. MacKenzie Ross, S. Moledina, D. Montani, A. Olschewski, H. Olschewski, W. H. Ouwehand, A. J. Peacock, J. Pepke-Zaba, I. Prokopenko, C. J. Rhodes, L. Scelsi, W. Seeger, F. Soubrier, J. Suntharalingam, M. R. Toshner, R. C. Trembath, A. Vonk Noordegraaf, S. J. Wort, M. R. Wilkins, P. B. Yu, W. Li, S. Gräf, P. D. Upton, and N. W. Morrell, 2020, Characterization of *GDF2* Mutations and Levels of BMP9 and BMP10 in Pulmonary Arterial Hypertension: Am J Respir Crit Care Med, v. 201, p. 575-585.

Hojayev, B., B. A. Rothermel, T. G. Gillette, and J. A. Hill, 2012, FHL2 binds calcineurin and represses pathological cardiac growth: Mol Cell Biol, v. 32, p. 4025-34.

Holmes, D. R., M. Savage, J. M. LaBlanche, L. Grip, P. W. Serruys, P. Fitzgerald, D. Fischman, S. Goldberg, J. A. Brinker, A. M. Zeiher, L. M. Shapiro, J. Willerson, B. R. Davis, J. J. Ferguson, J. Popma, S. B. King, A. M. Lincoff, J. E. Tcheng, R. Chan, J. R. Granett, and M. Poland, 2002, Results of Prevention of REStenosis with Tranilast and its Outcomes (PRESTO) trial: Circulation, v. 106, p. 1243-50.

Hong, F., B. D. Haldeman, O. A. John, P. D. Brewer, Y. Y. Wu, S. Ni, D. P. Wilson, M. P. Walsh, J. E. Baker, and C. R. Cremo, 2009, Characterization of tightly associated smooth muscle myosin-myosin light-chain kinase-calmodulin complexes: J Mol Biol, v. 390, p. 879-92.

Hong, S. S., L. Karayan, J. Tournier, D. T. Curiel, and P. A. Boulanger, 1997, Adenovirus type 5 fiber knob binds to MHC class I alpha2 domain at the surface of human epithelial and B lymphoblastoid cells: EMBO J, v. 16, p. 2294-306.
Hu, Y., Y. Zou, H. Dietrich, G. Wick, and Q. Xu, 1999, Inhibition of neointima hyperplasia of mouse vein grafts by locally applied suramin: Circulation, v. 100, p. 861-8.
Insull, W., 2009, The pathology of atherosclerosis: plaque development and plaque responses to medical treatment: Am J Med, v. 122, p. S3-S14.
Ishikawa, M., T. Sasajima, and Y. Kubo, 1996, Re-endothelialisation in autogenous vein grafts: Eur J Vasc Endovasc Surg, v. 11, p. 105-11.
Izzard, T. D., C. Taylor, S. D. Birkett, C. L. Jackson, and A. C. Newby, 2002, Mechanisms underlying maintenance of smooth muscle cell quiescence in rat aorta: role of the cyclin dependent kinases and their inhibitors: Cardiovasc Res, v. 53, p. 242-52.
Jelsig, A. M., P. M. Tørring, A. D. Kjeldsen, N. Qvist, A. Bojesen, U. B. Jensen, M. K. Andersen, A. M. Gerdes, K. Brusgaard, and L. B. Ousager, 2016, JP-HHT phenotype in Danish patients with SMAD4 mutations: Clin Genet, v. 90, p. 55-62.
Jiang, Z., M. Tao, K. A. Omalley, D. Wang, C. K. Ozaki, and S. A. Berceli, 2009, Established neointimal hyperplasia in vein grafts expands via TGF-beta-mediated progressive fibrosis: Am J Physiol Heart Circ Physiol, v. 297, p. H1200-7.
Jullien, P., T. M. Berg, and D. A. Lawrence, 1989, Acidic cellular environments: activation of latent TGF-beta and sensitization of cellular responses to TGF-beta and EGF: Int J Cancer, v. 43, p. 886-91.
Kalra, M., and V. M. Miller, 2000, Early remodeling of saphenous vein grafts: proliferation, migration and apoptosis of adventitial and medial cells occur simultaneously with changes in graft diameter and blood flow: J Vasc Res, v. 37, p. 576-84.
Karper, J. C., M. R. de Vries, B. T. van den Brand, I. E. Hoefer, J. W. Fischer, J. W. Jukema, H. W. Niessen, and P. H. Quax, 2011, Toll-like receptor 4 is involved in human and mouse vein graft remodeling, and local gene silencing reduces vein graft disease in hypercholesterolemic APOE*3Leiden mice: Arterioscler Thromb Vasc Biol, v. 31, p. 1033-40.
Katagiri, T., M. Imada, T. Yanai, T. Suda, N. Takahashi, and R. Kamijo, 2002, Identification of a BMP-responsive element in Id1, the gene for inhibition of myogenesis: Genes Cells, v. 7, p. 949-60.
Kauhanen, P., V. Sirén, O. Carpén, A. Vaheri, M. Lepäntalo, and R. Lassila, 1997, Plasminogen activator inhibitor-1 in neointima of vein grafts: its role in reduced fibrinolytic potential and graft failure: Circulation, v. 96, p. 1783-9.
Kavsak, P., R. K. Rasmussen, C. G. Causing, S. Bonni, H. Zhu, G. H. Thomsen, and J. L. Wrana, 2000, Smad7 binds to Smurf2 to form an E3 ubiquitin ligase that targets the TGF beta receptor for degradation: Mol Cell, v. 6, p. 1365-75.
Kelner, M. J., R. D. Bagnell, M. A. Montoya, L. A. Estes, L. Forsberg, and R. Morgenstern, 2000, Structural organization of the microsomal glutathione S-transferase gene (MGST1) on chromosome 12p13.1-13.2. Identification of the correct promoter region and demonstration of transcriptional regulation in response to oxidative stress: J Biol Chem, v. 275, p. 13000-6.

Kern, W. H., W. J. Wells, and B. W. Meyer, 1981, The pathology of surgically excised aortocoronary saphenous vein bypass grafts: Am J Surg Pathol, v. 5, p. 491-6.
Kim, C. W., H. Song, S. Kumar, D. Nam, H. S. Kwon, K. H. Chang, D. J. Son, D. W. Kang, S. A. Brodie, D. Weiss, J. D. Vega, N. Alberts-Grill, K. Griendling, W. R. Taylor, and H. Jo, 2013, Anti-inflammatory and anti-atherogenic role of BMP Receptor II in endothelial cells: Arterioscler Thromb Vasc Biol, v. 33, p. 1350-9.
Kim, J. H., D. Jain, O. Tliba, B. Yang, W. F. Jester, R. A. Panettieri, Y. Amrani, and E. Puré, 2005, TGF-beta potentiates airway smooth muscle responsiveness to bradykinin: Am J Physiol Lung Cell Mol Physiol, v. 289, p. L511-20.
Kinjo, T., M. Tanaka, T. Osanai, S. Shibutani, I. Narita, T. Tanno, K. Nishizaki, H. Ichikawa, Y. Kimura, Y. Ishida, T. Yokota, M. Shimada, Y. Homma, H. Tomita, and K. Okumura, 2015, Enhanced p122RhoGAP/DLC-1 Expression Can Be a Cause of Coronary Spasm: PLoS One, v. 10, p. e0143884.
Kishimoto, A., Y. Takai, T. Mori, U. Kikkawa, and Y. Nishizuka, 1980, Activation of calcium and phospholipid-dependent protein kinase by diacylglycerol, its possible relation to phosphatidylinositol turnover: J Biol Chem, v. 255, p. 2273-6.
Kloppenburg, G. T., G. E. Grauls, C. A. Bruggeman, and F. R. Stassen, 2009, Adenoviral activin A expression prevents vein graft intimal hyperplasia in a rat model: Interact Cardiovasc Thorac Surg, v. 8, p. 31-4.
Kobayashi, K., K. Yokote, M. Fujimoto, K. Yamashita, A. Sakamoto, M. Kitahara, H. Kawamura, Y. Maezawa, S. Asaumi, T. Tokuhisa, S. Mori, and Y. Saito, 2005, Targeted disruption of TGF-beta-Smad3 signaling leads to enhanced neointimal hyperplasia with diminished matrix deposition in response to vascular injury: Circ Res, v. 96, p. 904-12.
Kockx, M. M., B. A. Cambier, H. E. Bortier, G. R. De Meyer, S. C. Declercq, P. A. van Cauwelaert, and J. Bultinck, 1994, Foam cell replication and smooth muscle cell apoptosis in human saphenous vein grafts: Histopathology, v. 25, p. 365-71.
Kockx, M. M., B. A. Cambier, H. E. Bortier, G. R. De Meyer, and P. A. Van Cauwelaert, 1992, The modulation of smooth muscle cell phenotype is an early event in human aorto-coronary saphenous vein grafts: Virchows Arch A Pathol Anat Histopathol, v. 420, p. 155-62.
Kockx, M. M., G. R. De Meyer, H. Bortier, N. de Meyere, J. Muhring, A. Bakker, W. Jacob, L. Van Vaeck, and A. Herman, 1996, Luminal foam cell accumulation is associated with smooth muscle cell death in the intimal thickening of human saphenous vein grafts: Circulation, v. 94, p. 1255-62.
Kohno, T., N. Urao, T. Ashino, V. Sudhahar, H. Inomata, M. Yamaoka-Tojo, R. D. McKinney, T. Fukai, and M. Ushio-Fukai, 2013, IQGAP1 links PDGF receptor-ß signal to focal adhesions involved in vascular smooth muscle cell migration: role in neointimal formation after vascular injury: Am J Physiol Cell Physiol, v. 305, p. C591-600.
Komatsu, R., M. Ueda, T. Naruko, A. Kojima, and A. E. Becker, 1998, Neointimal tissue response at sites of coronary stenting in humans: macroscopic, histological, and immunohistochemical analyses: Circulation, v. 98, p. 224-33.
Kostenis, E., G. Milligan, A. Christopoulos, C. F. Sanchez-Ferrer, S. Heringer-Walther, P. M. Sexton, F. Gembardt, E. Kellett, L. Martini, P. Vanderheyden, H. P. Schultheiss, and T. Walther, 2005, G-protein-coupled

receptor Mas is a physiological antagonist of the angiotensin II type 1 receptor: Circulation, v. 111, p. 1806-13.

Kraehling, J. R., J. H. Chidlow, C. Rajagopal, M. G. Sugiyama, J. W. Fowler, M. Y. Lee, X. Zhang, C. M. Ramirez, E. J. Park, B. Tao, K. Chen, L. Kuruvilla, B. Larrivee, E. Folta-Stogniew, R. Ola, N. Rotllan, W. Zhou, M. W. Nagle, J. Herz, K. J. Williams, A. Eichmann, W. L. Lee, C. Fernandez-Hernando, and W. C. Sessa, 2016, Genome-wide RNAi screen reveals ALK1 mediates LDL uptake and transcytosis in endothelial cells: Nat Commun, v. 7, p. 13516.

Kruth, H. S., W. Huang, I. Ishii, and W. Y. Zhang, 2002, Macrophage foam cell formation with native low density lipoprotein: J Biol Chem, v. 277, p. 34573-80.

Ku, D. N., D. P. Giddens, C. K. Zarins, and S. Glagov, 1985, Pulsatile flow and atherosclerosis in the human carotid bifurcation. Positive correlation between plaque location and low oscillating shear stress: Arteriosclerosis, v. 5, p. 293-302.

Kulik, A., P. Voisine, P. Mathieu, R. G. Masters, T. G. Mesana, M. R. Le May, and M. Ruel, 2011, Statin therapy and saphenous vein graft disease after coronary bypass surgery: analysis from the CASCADE randomized trial: Ann Thorac Surg, v. 92, p. 1284-90; discussion 1290-1.

Kumar, A., and V. Lindner, 1997, Remodeling with neointima formation in the mouse carotid artery after cessation of blood flow: Arterioscler Thromb Vasc Biol, v. 17, p. 2238-44.

Kumar, V., A. Abbas, N. Fausto, and R. Mitchell, 2007, The Blood Vessels, *in* V. Kumar, A. Abbas, N. Fausto, and R. Mitchell, eds., Robbins Basic Pathology, Saunders Elsevier, p. 343-353.

Kuntz, R. E., D. S. Baim, D. J. Cohen, J. J. Popma, J. P. Carrozza, S. Sharma, D. J. McCormick, D. A. Schmidt, A. J. Lansky, K. K. Ho, K. J. Dandreo, C. M. Setum, and S. R. Ramee, 2002, A trial comparing rheolytic thrombectomy with intracoronary urokinase for coronary and vein graft thrombus (the Vein Graft AngioJet Study [VeGAS 2]): Am J Cardiol, v. 89, p. 326-30.

La Manno, G., R. Soldatov, A. Zeisel, E. Braun, H. Hochgerner, V. Petukhov, K. Lidschreiber, M. E. Kastriti, P. Lönnerberg, A. Furlan, J. Fan, L. E. Borm, Z. Liu, D. van Bruggen, J. Guo, X. He, R. Barker, E. Sundström, G. Castelo-Branco, P. Cramer, I. Adameyko, S. Linnarsson, and P. V. Kharchenko, 2018, RNA velocity of single cells: Nature, v. 560, p. 494-498.

Lai, N. C., D. M. Roth, M. H. Gao, S. Fine, B. P. Head, J. Zhu, M. D. McKirnan, C. Kwong, N. Dalton, K. Urasawa, D. A. Roth, and H. K. Hammond, 2000, Intracoronary delivery of adenovirus encoding adenylyl cyclase VI increases left ventricular function and cAMP-generating capacity: Circulation, v. 102, p. 2396-401.

Lamfers, M. L., J. Grill, C. M. Dirven, V. W. Van Beusechem, B. Geoerger, J. Van Den Berg, R. Alemany, J. Fueyo, D. T. Curiel, G. Vassal, H. M. Pinedo, W. P. Vandertop, and W. R. Gerritsen, 2002, Potential of the conditionally replicative adenovirus Ad5-Delta24RGD in the treatment of malignant gliomas and its enhanced effect with radiotherapy: Cancer Res, v. 62, p. 5736-42.

Lan, T. H., X. Q. Huang, and H. M. Tan, 2013, Vascular fibrosis in atherosclerosis: Cardiovasc Pathol, v. 22, p. 401-7.

Lardenoye, J. H., M. R. de Vries, C. W. Löwik, Q. Xu, C. R. Dhore, J. P. Cleutjens, V. W. van Hinsbergh, J. H. van Bockel, and P. H. Quax, 2002, Accelerated atherosclerosis and calcification in vein grafts: a study in APOE*3 Leiden transgenic mice: Circ Res, v. 91, p. 577-84.

Larsson, J., M. J. Goumans, L. J. Sjöstrand, M. A. van Rooijen, D. Ward, P. Levéen, X. Xu, P. ten Dijke, C. L. Mummery, and S. Karlsson, 2001, Abnormal angiogenesis but intact hematopoietic potential in TGF-beta type I receptor-deficient mice: EMBO J, v. 20, p. 1663-73.

Latif, F., L. Uyeda, R. Edson, D. L. Bhatt, S. Goldman, D. R. Holmes, S. V. Rao, K. Shunk, K. Aggarwal, B. Uretsky, I. Bolad, K. Ziada, E. McFalls, A. Irimpen, H. T. Truong, S. Kinlay, V. Papademetriou, R. S. Velagaleti, B. V. Rangan, K. Mavromatis, M. C. Shih, S. Banerjee, and E. S. Brilakis, 2020, Stent-Only Versus Adjunctive Balloon Angioplasty Approach for Saphenous Vein Graft Percutaneous Coronary Intervention: Insights From DIVA Trial: Circ Cardiovasc Interv, v. 13, p. e008494.

Lebrin, F., M. J. Goumans, L. Jonker, R. L. Carvalho, G. Valdimarsdottir, M. Thorikay, C. Mummery, H. M. Arthur, and P. ten Dijke, 2004, Endoglin promotes endothelial cell proliferation and TGF-beta/ALK1 signal transduction: Embo j, v. 23, p. 4018-28.

Lee, C. S., E. S. Bishop, R. Zhang, X. Yu, E. M. Farina, S. Yan, C. Zhao, Z. Zheng, Y. Shu, X. Wu, J. Lei, Y. Li, W. Zhang, C. Yang, K. Wu, Y. Wu, S. Ho, A. Athiviraham, M. J. Lee, J. M. Wolf, R. R. Reid, and T. C. He, 2017, Adenovirus-Mediated Gene Delivery: Potential Applications for Gene and Cell-Based Therapies in the New Era of Personalized Medicine: Genes Dis, v. 4, p. 43-63.

Lee, D., J. Liu, H. J. Junn, E. J. Lee, K. S. Jeong, and D. W. Seol, 2019, No more helper adenovirus: production of gutless adenovirus (GLAd) free of adenovirus and replication-competent adenovirus (RCA) contaminants: Exp Mol Med, v. 51, p. 1-18.

Lee, J., and H. Kang, 2019, Hypoxia Promotes Vascular Smooth Muscle Cell Proliferation through microRNA-Mediated Suppression of Cyclin-Dependent Kinase Inhibitors: Cells, v. 8.

Lee, M. K., C. Pardoux, M. C. Hall, P. S. Lee, D. Warburton, J. Qing, S. M. Smith, and R. Derynck, 2007, TGF-beta activates Erk MAP kinase signalling through direct phosphorylation of ShcA: EMBO J, v. 26, p. 3957-67.

Lee, M. R., L. Li, and T. Kitazawa, 1997, Cyclic GMP causes Ca2+ desensitization in vascular smooth muscle by activating the myosin light chain phosphatase: J Biol Chem, v. 272, p. 5063-8.

Lee, S. J., L. A. Reed, M. V. Davies, S. Girgenrath, M. E. Goad, K. N. Tomkinson, J. F. Wright, C. Barker, G. Ehrmantraut, J. Holmstrom, B. Trowell, B. Gertz, M. S. Jiang, S. M. Sebald, M. Matzuk, E. Li, L. F. Liang, E. Quattlebaum, R. L. Stotish, and N. M. Wolfman, 2005, Regulation of muscle growth by multiple ligands signaling through activin type II receptors: Proc Natl Acad Sci U S A, v. 102, p. 18117-22.

Leiper, J., M. Nandi, B. Torondel, J. Murray-Rust, M. Malaki, B. O'Hara, S. Rossiter, S. Anthony, M. Madhani, D. Selwood, C. Smith, B. Wojciak-Stothard, A. Rudiger, R. Stidwill, N. Q. McDonald, and P. Vallance, 2007, Disruption of methylarginine metabolism impairs vascular homeostasis: Nat Med, v. 13, p. 198-203.

Levet, S., D. Ciais, G. Merdzhanova, C. Mallet, T. A. Zimmers, S. J. Lee, F. P. Navarro, I. Texier, J. J. Feige, S. Bailly, and D. Vittet, 2013, Bone morphogenetic protein 9 (BMP9) controls lymphatic vessel maturation and valve formation: Blood, v. 122, p. 598-607.

Levet, S., M. Ouarné, D. Ciais, C. Coutton, M. Subileau, C. Mallet, N. Ricard, M. Bidart, T. Debillon, F. Faravelli, C. Rooryck, J. J. Feige, E. Tillet, and S. Bailly, 2015, BMP9 and BMP10 are necessary for proper closure of the ductus arteriosus: Proc Natl Acad Sci U S A, v. 112, p. E3207-15.

Lewis, T. C., and R. Prywes, 2013, Serum regulation of Id1 expression by a BMP pathway and BMP responsive element: Biochim Biophys Acta, v. 1829, p. 1147-59.
Li, H., J. Liang, D. H. Castrillon, R. A. DePinho, E. N. Olson, and Z. P. Liu, 2007, FoxO4 regulates tumor necrosis factor alpha-directed smooth muscle cell migration by activating matrix metalloproteinase 9 gene transcription: Mol Cell Biol, v. 27, p. 2676-86.
Li, P., Y. L. Li, Z. Y. Li, Y. N. Wu, C. C. Zhang, X. A, C. X. Wang, H. T. Shi, M. Z. Hui, B. Xie, M. Ahmed, and J. Du, 2014, Cross talk between vascular smooth muscle cells and monocytes through interleukin-1beta/interleukin-18 signaling promotes vein graft thickening: Arterioscler Thromb Vasc Biol, v. 34, p. 2001-11.
Li, S., Y. S. Fan, L. H. Chow, C. Van Den Diepstraten, E. van Der Veer, S. M. Sims, and J. G. Pickering, 2001a, Innate diversity of adult human arterial smooth muscle cells: cloning of distinct subtypes from the internal thoracic artery: Circ Res, v. 89, p. 517-25.
Li, X., P. Tsai, E. D. Wieder, A. Kribben, V. Van Putten, R. W. Schrier, and R. A. Nemenoff, 1994, Vascular smooth muscle cells grown on Matrigel. A model of the contractile phenotype with decreased activation of mitogen-activated protein kinase: J Biol Chem, v. 269, p. 19653-8.
Li, Y., D. C. Yu, Y. Chen, P. Amin, H. Zhang, N. Nguyen, and D. R. Henderson, 2001b, A hepatocellular carcinoma-specific adenovirus variant, CV890, eliminates distant human liver tumors in combination with doxorubicin: Cancer Res, v. 61, p. 6428-36.
Liang, M., 2018, Oncorine, the World First Oncolytic Virus Medicine and its Update in China: Curr Cancer Drug Targets, v. 18, p. 171-176.
Liao, J., Q. Wei, Y. Zou, J. Fan, D. Song, J. Cui, W. Zhang, Y. Zhu, C. Ma, X. Hu, X. Qu, L. Chen, X. Yu, Z. Zhang, C. Wang, C. Zhao, Z. Zeng, R. Zhang, S. Yan, T. Wu, X. Wu, Y. Shu, J. Lei, Y. Li, H. H. Luu, M. J. Lee, R. R. Reid, G. A. Ameer, J. M. Wolf, T. C. He, and W. Huang, 2017, Notch Signaling Augments BMP9-Induced Bone Formation by Promoting the Osteogenesis-Angiogenesis Coupling Process in Mesenchymal Stem Cells (MSCs): Cell Physiol Biochem, v. 41, p. 1905-1923.
Liao, M., P. Yang, F. Wang, S. A. Berceli, Y. H. Ali, K. L. Chan, and Z. Jiang, 2016, Smooth muscle cell-specific Tgfbr1 deficiency attenuates neointimal hyperplasia but promotes an undesired vascular phenotype for injured arteries: Physiol Rep, v. 4.
Lim, S., and P. Kaldis, 2013, Cdks, cyclins and CKIs: roles beyond cell cycle regulation: Development, v. 140, p. 3079-93.
Lin, X., M. Liang, and X. H. Feng, 2000, Smurf2 is a ubiquitin E3 ligase mediating proteasome-dependent degradation of Smad2 in transforming growth factor-beta signaling: J Biol Chem, v. 275, p. 36818-22.
Lindner, V., J. Fingerle, and M. A. Reidy, 1993, Mouse model of arterial injury: Circ Res, v. 73, p. 792-6.
Lindsay, M. E., D. Schepers, N. A. Bolar, J. J. Doyle, E. Gallo, J. Fert-Bober, M. J. Kempers, E. K. Fishman, Y. Chen, L. Myers, D. Bjeda, G. Oswald, A. F. Elias, H. P. Levy, B. M. Anderlid, M. H. Yang, E. M. Bongers, J. Timmermans, A. C. Braverman, N. Canham, G. R. Mortier, H. G. Brunner, P. H. Byers, J. Van Eyk, L. Van Laer, H. C. Dietz, and B. L. Loeys, 2012, Loss-of-function mutations in TGFB2 cause a syndromic presentation of thoracic aortic aneurysm: Nat Genet, v. 44, p. 922-7.
Lipskaia, L., F. del Monte, T. Capiod, S. Yacoubi, L. Hadri, M. Hours, R. J. Hajjar, and A. M. Lompré, 2005, Sarco/endoplasmic reticulum Ca2+-

ATPase gene transfer reduces vascular smooth muscle cell proliferation and neointima formation in the rat: Circ Res, v. 97, p. 488-95.

Lipson, K. E., C. Wong, Y. Teng, and S. Spong, 2012, CTGF is a central mediator of tissue remodeling and fibrosis and its inhibition can reverse the process of fibrosis: Fibrogenesis Tissue Repair, v. 5, p. S24.

Liu, H., X. Han, H. Yang, Y. Cao, C. Zhang, J. Du, S. Diao, and Z. Fan, 2020a, GREM1 inhibits osteogenic differentiation, senescence and BMP transcription of adipose-derived stem cells: Connect Tissue Res, p. 1-12.

Liu, R., W. Hu, X. Li, D. Pu, G. Yang, H. Liu, M. Tan, and D. Zhu, 2019, Association of circulating BMP9 with coronary heart disease and hypertension in Chinese populations: BMC Cardiovasc Disord, v. 19, p. 131.

Liu, W., Z. Deng, Z. Zeng, J. Fan, Y. Feng, X. Wang, D. Cao, B. Zhang, L. Yang, B. Liu, M. Pakvasa, W. Wagstaff, X. Wu, H. Luo, J. Zhang, M. Zhang, F. He, Y. Mao, H. Ding, Y. Zhang, C. Niu, R. C. Haydon, H. H. Luu, J. M. Wolf, M. J. Lee, W. Huang, T. C. He, and Y. Zou, 2020b, Highly expressed BMP9/GDF2 in postnatal mouse liver and lungs may account for its pleiotropic effects on stem cell differentiation, angiogenesis, tumor growth and metabolism: Genes Dis, v. 7, p. 235-244.

Liu, X., Y. Sun, S. N. Constantinescu, E. Karam, R. A. Weinberg, and H. F. Lodish, 1997, Transforming growth factor beta-induced phosphorylation of Smad3 is required for growth inhibition and transcriptional induction in epithelial cells: Proc Natl Acad Sci U S A, v. 94, p. 10669-74.

Liu, Y., S. Sinha, O. McDonald, Y. Shang, M. Hoofnagle, and G. Owens, 2005a, Kruppel-like Factor 4 Abrogates Myocardin-Induced Activation of Smooth Muscle Gene Expression: The Journal of biological chemistry, v. 280.

Liu, Z., X. Huo, S. Zhao, J. Yang, W. Shi, L. Jing, W. Li, Y. Li, L. Ma, Y. Gao, and A. Diao, 2017, Low density lipoprotein receptor class A domain containing 4 (LDLRAD4) promotes tumorigenesis of hepatic cancer cells: Exp Cell Res, v. 360, p. 189-198.

Liu, Z. P., Z. Wang, H. Yanagisawa, and E. N. Olson, 2005b, Phenotypic modulation of smooth muscle cells through interaction of Foxo4 and myocardin: Dev Cell, v. 9, p. 261-70.

Locker, C., L. E. Greiten, M. R. Bell, R. L. Frye, A. Lerman, R. C. Daly, K. L. Greason, S. M. Said, B. D. Lahr, J. M. Stulak, J. A. Dearani, and H. V. Schaff, 2019, Repeat Coronary Bypass Surgery or Percutaneous Coronary Intervention After Previous Surgical Revascularization: Mayo Clin Proc, v. 94, p. 1743-1752.

Loeys, B. L., J. Chen, E. R. Neptune, D. P. Judge, M. Podowski, T. Holm, J. Meyers, C. C. Leitch, N. Katsanis, N. Sharifi, F. L. Xu, L. A. Myers, P. J. Spevak, D. E. Cameron, J. De Backer, J. Hellemans, Y. Chen, E. C. Davis, C. L. Webb, W. Kress, P. Coucke, D. B. Rifkin, A. M. De Paepe, and H. C. Dietz, 2005, A syndrome of altered cardiovascular, craniofacial, neurocognitive and skeletal development caused by mutations in TGFBR1 or TGFBR2: Nat Genet, v. 37, p. 275-81.

Lomashvili, K. A., S. Cobbs, R. A. Hennigar, K. I. Hardcastle, and W. C. O'Neill, 2004, Phosphate-induced vascular calcification: role of pyrophosphate and osteopontin: J Am Soc Nephrol, v. 15, p. 1392-401.

Lomashvili, K. A., S. Narisawa, J. L. Millán, and W. C. O'Neill, 2014, Vascular calcification is dependent on plasma levels of pyrophosphate: Kidney Int, v. 85, p. 1351-6.

Long, L., M. L. Ormiston, X. Yang, M. Southwood, S. Gräf, R. D. Machado, M. Mueller, B. Kinzel, L. M. Yung, J. M. Wilkinson, S. D. Moore, K. M. Drake,

M. A. Aldred, P. B. Yu, P. D. Upton, and N. W. Morrell, 2015, Selective enhancement of endothelial BMPR-II with BMP9 reverses pulmonary arterial hypertension: Nature Medicine, v. 21, p. 777-785.

Lopes, R. D., J. B. Williams, R. H. Mehta, E. M. Reyes, G. E. Hafley, K. B. Allen, M. J. Mack, E. D. Peterson, R. A. Harrington, C. M. Gibson, R. M. Califf, N. T. Kouchoukos, T. B. Ferguson, T. J. Lorenz, and J. H. Alexander, 2012, Edifoligide and long-term outcomes after coronary artery bypass grafting: PRoject of Ex-vivo Vein graft ENgineering via Transfection IV (PREVENT IV) 5-year results: Am Heart J, v. 164, p. 379-386 e1.

Low, E., J. Schwartze, A. Kurkiewicz, M. Pek, D. Kelly, A. Shaw, M. Thorikay, J. McClure, M. McBride, S. Arias-Rivas, S. Francis, N. Morrell, C. Delles, P. Herzyk, M. Havenga, S. Nicklin, P. T. Dijke, A. Baker, and A. Bradshaw, 2019, Transforming growth factor-beta signaling via ALK1 and ALK5 regulates distinct functional pathways in vein graft intimal hyperplasia. bioRxiv https://doi.org/10.1101/860320

Luo, Y., L. Li, X. Xu, T. Wu, M. Yang, C. Zhang, H. Mou, T. Zhou, Y. Jia, C. Cai, H. Liu, G. Yang, and X. Zhang, 2017, Decreased circulating BMP-9 levels in patients with Type 2 diabetes is a signature of insulin resistance: Clin Sci (Lond), v. 131, p. 239-246.

Lusis, A. J., 2000, Atherosclerosis: Nature, v. 407, p. 233-41.

López-Casillas, F., H. M. Payne, J. L. Andres, and J. Massagué, 1994, Betaglycan can act as a dual modulator of TGF-beta access to signaling receptors: mapping of ligand binding and GAG attachment sites: J Cell Biol, v. 124, p. 557-68.

López-Casillas, F., J. L. Wrana, and J. Massagué, 1993, Betaglycan presents ligand to the TGF beta signaling receptor: Cell, v. 73, p. 1435-44.

MacDonald, J. A., M. A. Borman, A. Murányi, A. V. Somlyo, D. J. Hartshorne, and T. A. Haystead, 2001, Identification of the endogenous smooth muscle myosin phosphatase-associated kinase: Proc Natl Acad Sci U S A, v. 98, p. 2419-24.

Mache, C. J., A. Gamillscheg, H. H. Popper, and S. G. Haworth, 2008, Early-life pulmonary arterial hypertension with subsequent development of diffuse pulmonary arteriovenous malformations in hereditary haemorrhagic telangiectasia type 1: Thorax, v. 63, p. 85-6.

Macías-Silva, M., S. Abdollah, P. A. Hoodless, R. Pirone, L. Attisano, and J. L. Wrana, 1996, MADR2 is a substrate of the TGFbeta receptor and its phosphorylation is required for nuclear accumulation and signaling: Cell, v. 87, p. 1215-24.

Majesky, M. W., 2007, Developmental basis of vascular smooth muscle diversity: Arterioscler Thromb Vasc Biol, v. 27, p. 1248-58.

Mallat, Z., A. Gojova, C. Marchiol-Fournigault, B. Esposito, C. Kamaté, R. Merval, D. Fradelizi, and A. Tedgui, 2001, Inhibition of transforming growth factor-beta signaling accelerates atherosclerosis and induces an unstable plaque phenotype in mice: Circ Res, v. 89, p. 930-4.

Martin-Garrido, A., H. C. Williams, M. Lee, B. Seidel-Rogol, X. Ci, J. T. Dong, B. Lassègue, A. S. Martín, and K. K. Griendling, 2013, Transforming growth factor ß inhibits platelet derived growth factor-induced vascular smooth muscle cell proliferation via Akt-independent, Smad-mediated cyclin D1 downregulation: PLoS One, v. 8, p. e79657.

Mast, T. C., L. Kierstead, S. B. Gupta, A. A. Nikas, E. G. Kallas, V. Novitsky, B. Mbewe, P. Pitisuttithum, M. Schechter, E. Vardas, N. D. Wolfe, M. Aste-Amezaga, D. R. Casimiro, P. Coplan, W. L. Straus, and J. W. Shiver, 2010, International epidemiology of human pre-existing adenovirus (Ad) type-5,

type-6, type-26 and type-36 neutralizing antibodies: correlates of high Ad5 titers and implications for potential HIV vaccine trials: Vaccine, v. 28, p. 950-7.
Mathews, L. S., and W. W. Vale, 1991, Expression cloning of an activin receptor, a predicted transmembrane serine kinase: Cell, v. 65, p. 973-82.
Matt, P., F. Schoenhoff, J. Habashi, T. Holm, C. Van Erp, D. Loch, O. D. Carlson, B. F. Griswold, Q. Fu, J. De Backer, B. Loeys, D. L. Huso, N. B. McDonnell, J. E. Van Eyk, H. C. Dietz, and G. Consortium, 2009, Circulating transforming growth factor-beta in Marfan syndrome: Circulation, v. 120, p. 526-32.
Matzuk, M. M., T. R. Kumar, and A. Bradley, 1995, Different phenotypes for mice deficient in either activins or activin receptor type II: Nature, v. 374, p. 356-60.
McDonald, O. G., B. R. Wamhoff, M. H. Hoofnagle, and G. K. Owens, 2006, Control of SRF binding to CArG box chromatin regulates smooth muscle gene expression in vivo: J Clin Invest, v. 116, p. 36-48.
Mercado, N. B., R. Zahn, F. Wegmann, C. Loos, A. Chandrashekar, J. Yu, J. Liu, L. Peter, K. McMahan, L. H. Tostanoski, X. He, D. R. Martinez, L. Rutten, R. Bos, D. van Manen, J. Vellinga, J. Custers, J. P. Langedijk, T. Kwaks, M. J. G. Bakkers, D. Zuijdgeest, S. K. Rosendahl Huber, C. Atyeo, S. Fischinger, J. S. Burke, J. Feldman, B. M. Hauser, T. M. Caradonna, E. A. Bondzie, G. Dagotto, M. S. Gebre, E. Hoffman, C. Jacob-Dolan, M. Kirilova, Z. Li, Z. Lin, S. H. Mahrokhian, L. F. Maxfield, F. Nampanya, R. Nityanandam, J. P. Nkolola, S. Patel, J. D. Ventura, K. Verrington, H. Wan, L. Pessaint, A. Van Ry, K. Blade, A. Strasbaugh, M. Cabus, R. Brown, A. Cook, S. Zouantchangadou, E. Teow, H. Andersen, M. G. Lewis, Y. Cai, B. Chen, A. G. Schmidt, R. K. Reeves, R. S. Baric, D. A. Lauffenburger, G. Alter, P. Stoffels, M. Mammen, J. Van Hoof, H. Schuitemaker, and D. H. Barouch, 2020, Single-shot Ad26 vaccine protects against SARS-CoV-2 in rhesus macaques: Nature, v. 586, p. 583-588.
Mercer, T. R., S. Neph, M. E. Dinger, J. Crawford, M. A. Smith, A. M. Shearwood, E. Haugen, C. P. Bracken, O. Rackham, J. A. Stamatoyannopoulos, A. Filipovska, and J. S. Mattick, 2011, The human mitochondrial transcriptome: Cell, v. 146, p. 645-58.
Mignery, G. A., and T. C. Südhof, 1990, The ligand binding site and transduction mechanism in the inositol-1,4,5-triphosphate receptor: EMBO J, v. 9, p. 3893-8.
Mii, S., J. A. Ware, and K. C. Kent, 1993, Transforming growth factor-beta inhibits human vascular smooth muscle cell growth and migration: Surgery, v. 114, p. 464-70.
Mikoshiba, K., T. Furuichi, A. Miyawaki, S. Yoshikawa, T. Nakagawa, N. Yamada, Y. Hamanaka, I. Fujino, T. Michikawa, and Y. Ryo, 1993, Inositol trisphosphate receptor and Ca2+ signalling: Philos Trans R Soc Lond B Biol Sci, v. 340, p. 345-9.
Miller, A. F., S. A. Harvey, R. S. Thies, and M. S. Olson, 2000, Bone morphogenetic protein-9. An autocrine/paracrine cytokine in the liver: J Biol Chem, v. 275, p. 17937-45.
Minty, A., and L. Kedes, 1986, Upstream regions of the human cardiac actin gene that modulate its transcription in muscle cells: presence of an evolutionarily conserved repeated motif: Mol Cell Biol, v. 6, p. 2125-36.
Mitrofan, C. G., S. L. Appleby, G. B. Nash, Z. Mallat, E. R. Chilvers, P. D. Upton, and N. W. Morrell, 2017, Bone morphogenetic protein 9 (BMP9) and BMP10 enhance tumor necrosis factor-α-induced monocyte recruitment to the

vascular endothelium mainly via activin receptor-like kinase 2, J Biol Chem, v. 292, p. 13714-26.

Mittal, S., Y. Ahi, and S. Vemula, 2016, Xenogenic Adenoviral Vectors, *in* D. Curiel, ed., Adenoviral Vectors for Gene Therapy (Second Edition), Academic Press, p. 495-528.

Miura, S., and S. S. Karnik, 1999, Angiotensin II type 1 and type 2 receptors bind angiotensin II through different types of epitope recognition: J Hypertens, v. 17, p. 397-404.

Miyazono, K., A. Olofsson, P. Colosetti, and C. H. Heldin, 1991, A role of the latent TGF-beta 1-binding protein in the assembly and secretion of TGF-beta 1: EMBO J, v. 10, p. 1091-101.

Molin, D. G., M. C. DeRuiter, L. J. Wisse, M. Azhar, T. Doetschman, R. E. Poelmann, and A. C. Gittenberger-de Groot, 2002, Altered apoptosis pattern during pharyngeal arch artery remodelling is associated with aortic arch malformations in Tgfbeta2 knock-out mice: Cardiovasc Res, v. 56, p. 312-22.

Montezano, A. C., L. De Lucca Camargo, P. Persson, F. J. Rios, A. P. Harvey, A. Anagnostopoulou, R. Palacios, A. C. P. Gandara, R. Alves-Lopes, K. B. Neves, M. Dulak-Lis, C. E. Holterman, P. L. de Oliveira, D. Graham, C. Kennedy, and R. M. Touyz, 2018, NADPH Oxidase 5 Is a Pro-Contractile Nox Isoform and a Point of Cross-Talk for Calcium and Redox Signaling-Implications in Vascular Function: J Am Heart Assoc, v. 7.

Moreno, P. R., V. H. Bernardi, J. López-Cuéllar, A. M. Murcia, I. F. Palacios, H. K. Gold, R. Mehran, S. K. Sharma, Y. Nemerson, V. Fuster, and J. T. Fallon, 1996, Macrophages, smooth muscle cells, and tissue factor in unstable angina. Implications for cell-mediated thrombogenicity in acute coronary syndromes: Circulation, v. 94, p. 3090-7.

Mori, T., Y. Takai, B. Yu, J. Takahashi, Y. Nishizuka, and T. Fujikura, 1982, Specificity of the fatty acyl moieties of diacylglycerol for the activation of calcium-activated, phospholipid-dependent protein kinase: J Biochem, v. 91, p. 427-31.

Morinaga, K., K. Okadome, M. Kuroki, T. Miyazaki, Y. Muto, and K. Inokuchi, 1985, Effect of wall shear stress on intimal thickening of arterially transplanted autogenous veins in dogs: J Vasc Surg, v. 2, p. 430-3.

Morishita, R., G. H. Gibbons, M. Horiuchi, K. E. Ellison, M. Nakama, L. Zhang, Y. Kaneda, T. Ogihara, and V. J. Dzau, 1995, A gene therapy strategy using a transcription factor decoy of the E2F binding site inhibits smooth muscle proliferation in vivo: Proc Natl Acad Sci U S A, v. 92, p. 5855-9.

Moroi, M., L. Zhang, T. Yasuda, R. Virmani, H. K. Gold, M. C. Fishman, and P. L. Huang, 1998, Interaction of genetic deficiency of endothelial nitric oxide, gender, and pregnancy in vascular response to injury in mice: J Clin Invest, v. 101, p. 1225-32.

Munger, J. S., X. Huang, H. Kawakatsu, M. J. Griffiths, S. L. Dalton, J. Wu, J. F. Pittet, N. Kaminski, C. Garat, M. A. Matthay, D. B. Rifkin, and D. Sheppard, 1999, The integrin alpha v beta 6 binds and activates latent TGF beta 1: a mechanism for regulating pulmonary inflammation and fibrosis: Cell, v. 96, p. 319-28.

Murakami, R., T. Osanai, H. Tomita, S. Sasaki, A. Maruyama, K. Itoh, Y. Homma, and K. Okumura, 2010, p122 protein enhances intracellular calcium increase to acetylcholine: its possible role in the pathogenesis of coronary spastic angina: Arterioscler Thromb Vasc Biol, v. 30, p. 1968-75.

Nagumo, H., Y. Sasaki, Y. Ono, H. Okamoto, M. Seto, and Y. Takuwa, 2000, Rho kinase inhibitor HA-1077 prevents Rho-mediated myosin phosphatase

inhibition in smooth muscle cells: Am J Physiol Cell Physiol, v. 278, p. C57-65.
Nakashima, Y., H. Fujii, S. Sumiyoshi, T. N. Wight, and K. Sueishi, 2007, Early human atherosclerosis: accumulation of lipid and proteoglycans in intimal thickenings followed by macrophage infiltration: Arterioscler Thromb Vasc Biol, v. 27, p. 1159-65.
Nasim, M. T., T. Ogo, M. Ahmed, R. Randall, H. M. Chowdhury, K. M. Snape, T. Y. Bradshaw, L. Southgate, G. J. Lee, I. Jackson, G. M. Lord, J. S. Gibbs, M. R. Wilkins, K. Ohta-Ogo, K. Nakamura, B. Girerd, F. Coulet, F. Soubrier, M. Humbert, N. W. Morrell, R. C. Trembath, and R. D. Machado, 2011, Molecular genetic characterization of SMAD signaling molecules in pulmonary arterial hypertension: Hum Mutat, v. 32, p. 1385-9.
Neitzel, G. F., J. J. Barboriak, K. Pintar, and I. Qureshi, 1986, Atherosclerosis in aortocoronary bypass grafts. Morphologic study and risk factor analysis 6 to 12 years after surgery: Arteriosclerosis, v. 6, p. 594-600.
Neumann, F. J., M. Sousa-Uva, A. Ahlsson, F. Alfonso, A. P. Banning, U. Benedetto, R. A. Byrne, J. P. Collet, V. Falk, S. J. Head, P. Juni, A. Kastrati, A. Koller, S. D. Kristensen, J. Niebauer, D. J. Richter, P. M. Seferovic, D. Sibbing, G. G. Stefanini, S. Windecker, R. Yadav, and M. O. Zembala, 2019, 2018 ESC/EACTS Guidelines on myocardial revascularization: Eur Heart J, v. 40, p. 87-165.
Nicklin, S. A., D. J. Von Seggern, L. M. Work, D. C. Pek, A. F. Dominiczak, G. R. Nemerow, and A. H. Baker, 2001, Ablating adenovirus type 5 fiber-CAR binding and HI loop insertion of the SIGYPLP peptide generate an endothelial cell-selective adenovirus: Mol Ther, v. 4, p. 534-42.
NICOR, 2019, National Adult Cardiac Surgery Audit, The National Institute For Cardiovascular Outcomes Research (NICOR).
Nikol, S., J. M. Isner, J. G. Pickering, M. Kearney, G. Leclerc, and L. Weir, 1992, Expression of transforming growth factor-beta 1 is increased in human vascular restenosis lesions: J Clin Invest, v. 90, p. 1582-92.
Nishimura, G., I. Manabe, K. Tsushima, K. Fujiu, Y. Oishi, Y. Imai, K. Maemura, M. Miyagishi, Y. Higashi, H. Kondoh, and R. Nagai, 2006, DeltaEF1 mediates TGF-beta signaling in vascular smooth muscle cell differentiation: Dev Cell, v. 11, p. 93-104.
Nolan, K., and T. B. Thompson, 2014, The DAN family: modulators of TGF-ß signaling and beyond: Protein Sci, v. 23, p. 999-1012.
Oh, S. P., and E. Li, 1997, The signaling pathway mediated by the type IIB activin receptor controls axial patterning and lateral asymmetry in the mouse: Genes Dev, v. 11, p. 1812-26.
Ohtani, K., K. Egashira, K. Hiasa, Q. Zhao, S. Kitamoto, M. Ishibashi, M. Usui, S. Inoue, Y. Yonemitsu, K. Sueishi, M. Sata, M. Shibuya, and K. Sunagawa, 2004, Blockade of vascular endothelial growth factor suppresses experimental restenosis after intraluminal injury by inhibiting recruitment of monocyte lineage cells: Circulation, v. 110, p. 2444-52.
Okamoto, E., T. Couse, H. De Leon, J. Vinten-Johansen, R. B. Goodman, N. A. Scott, and J. N. Wilcox, 2001, Perivascular inflammation after balloon angioplasty of porcine coronary arteries: Circulation, v. 104, p. 2228-35.
Olsen, O. E., K. F. Wader, H. Hella, A. K. Mylin, I. Turesson, I. Nesthus, A. Waage, A. Sundan, and T. Holien, 2015, Activin A inhibits BMP-signaling by binding ACVR2A and ACVR2B: Cell Commun Signal, v. 13, p. 27.
Olsen, O. E., K. F. Wader, K. Misund, T. K. Våtsveen, T. B. Rø, A. K. Mylin, I. Turesson, B. F. Størdal, S. H. Moen, T. Standal, A. Waage, A. Sundan, and T. Holien, 2014, Bone morphogenetic protein-9 suppresses growth of

myeloma cells by signaling through ALK2 but is inhibited by endoglin: Blood Cancer J, v. 4, p. e196.

Oshima, M., H. Oshima, and M. M. Taketo, 1996, TGF-beta receptor type II deficiency results in defects of yolk sac hematopoiesis and vasculogenesis: Dev Biol, v. 179, p. 297-302.

Owen, N. E., G. J. Alexander, S. Sen, K. Bunclark, G. Polwarth, J. Pepke-Zaba, A. P. Davenport, N. W. Morrell, and P. D. Upton, 2020, Reduced circulating BMP10 and BMP9 and elevated endoglin are associated with disease severity, decompensation and pulmonary vascular syndromes in patients with cirrhosis: EBioMedicine, v. 56, p. 102794.

Palecek, S. P., A. Huttenlocher, A. F. Horwitz, and D. A. Lauffenburger, 1998, Physical and biochemical regulation of integrin release during rear detachment of migrating cells: J Cell Sci, v. 111 (Pt 7), p. 929-40.

Panetta, T. F., M. L. Marin, F. J. Veith, J. Goldsmith, R. E. Gordon, A. M. Jones, M. L. Schwartz, S. K. Gupta, and K. R. Wengerter, 1992, Unsuspected preexisting saphenous vein disease: an unrecognized cause of vein bypass failure: J Vasc Surg, v. 15, p. 102-10.

Pardali, E., M. J. Goumans, and P. ten Dijke, 2010, Signaling by members of the TGF-beta family in vascular morphogenesis and disease: Trends Cell Biol, v. 20, p. 556-67.

Parker, A. L., K. M. White, C. A. Lavery, J. Custers, S. N. Waddington, and A. H. Baker, 2013, Pseudotyping the adenovirus serotype 5 capsid with both the fibre and penton of serotype 35 enhances vascular smooth muscle cell transduction: Gene Ther, v. 20, p. 1158-64.

Parks, R. J., L. Chen, M. Anton, U. Sankar, M. A. Rudnicki, and F. L. Graham, 1996, A helper-dependent adenovirus vector system: removal of helper virus by Cre-mediated excision of the viral packaging signal: Proc Natl Acad Sci U S A, v. 93, p. 13565-70.

Pato, M. D., and E. Kerc, 1985, Purification and characterization of a smooth muscle myosin phosphatase from turkey gizzards: J Biol Chem, v. 260, p. 12359-66.

Pearson, S., H. Jia, and K. Kandachi, 2004, China approves first gene therapy: Nat Biotechnol, v. 22, p. 3-4.

Pedigo, S., C. Guth, K. Hocking, A. Banathy, F. Li, J. Cheung-Flynn, C. Brophy, R. Guzman, and P. Komalavilas, 2017, Calcification of Human Saphenous Vein Associated With Endothelial Dysfunction: A Pilot Histopathophysiological and Demographical Study: Frontiers in surgery, v. 4.

Perek, B., A. Malinska, D. Ostalska-Nowicka, M. Puslecki, M. Ligowski, M. Misterski, M. Zabel, M. Jemielity, and M. Nowicki, 2013, Cytokeratin 8 in venous grafts: a factor of unfavorable long-term prognosis in coronary artery bypass grafting patients: Cardiol J, v. 20, p. 583-91.

Petukhov, V., J. Guo, N. Baryawno, N. Severe, D. T. Scadden, M. G. Samsonova, and P. V. Kharchenko, 2018, dropEst: pipeline for accurate estimation of molecular counts in droplet-based single-cell RNA-seq experiments: Genome Biol, v. 19, p. 78.

Pfeilschifter, J., and U. T. Rüegg, 1987, Cyclosporin A augments angiotensin II-stimulated rise in intracellular free calcium in vascular smooth muscle cells: Biochem J, v. 248, p. 883-7.

Pickering, J. G., S. Uniyal, C. M. Ford, T. Chau, M. A. Laurin, L. H. Chow, C. G. Ellis, J. Fish, and B. M. Chan, 1997, Fibroblast growth factor-2 potentiates vascular smooth muscle cell migration to platelet-derived growth factor:

upregulation of alpha2beta1 integrin and disassembly of actin filaments: Circ Res, v. 80, p. 627-37.
Priddy, F. H., D. Brown, J. Kublin, K. Monahan, D. P. Wright, J. Lalezari, S. Santiago, M. Marmor, M. Lally, R. M. Novak, S. J. Brown, P. Kulkarni, S. A. Dubey, L. S. Kierstead, D. R. Casimiro, R. Mogg, M. J. DiNubile, J. W. Shiver, R. Y. Leavitt, M. N. Robertson, D. V. Mehrotra, E. Quirk, and M. V.-S. Group, 2008, Safety and immunogenicity of a replication-incompetent adenovirus type 5 HIV-1 clade B gag/pol/nef vaccine in healthy adults: Clin Infect Dis, v. 46, p. 1769-81.
Pérez-Mancera, P. A., C. Bermejo-Rodríguez, I. González-Herrero, M. Herranz, T. Flores, R. Jiménez, and I. Sánchez-García, 2007, Adipose tissue mass is modulated by SLUG (SNAI2): Hum Mol Genet, v. 16, p. 2972-86.
Qin, L., Y. B. Yang, Y. X. Yang, Y. Z. Gong, X. L. Li, G. Y. Li, H. D. Luo, X. J. Xie, X. L. Zheng, and D. F. Liao, 2014, Inhibition of smooth muscle cell proliferation by ezetimibe via the cyclin D1-MAPK pathway: J Pharmacol Sci, v. 125, p. 283-91.
Qiu, P., R. P. Ritchie, Z. Fu, D. Cao, J. Cumming, J. M. Miano, D. Z. Wang, H. J. Li, and L. Li, 2005, Myocardin enhances Smad3-mediated transforming growth factor-beta1 signaling in a CArG box-independent manner: Smad-binding element is an important cis element for SM22alpha transcription in vivo: Circ Res, v. 97, p. 983-91.
Ramachandran, A., P. Vizán, D. Das, P. Chakravarty, J. Vogt, K. W. Rogers, P. Müller, A. P. Hinck, G. P. Sapkota, and C. S. Hill, 2018, TGF-ß uses a novel mode of receptor activation to phosphorylate SMAD1/5 and induce epithelial-to-mesenchymal transition: Elife, v. 7.
Raper, S. E., N. Chirmule, F. S. Lee, N. A. Wivel, A. Bagg, G. P. Gao, J. M. Wilson, and M. L. Batshaw, 2003, Fatal systemic inflammatory response syndrome in a ornithine transcarbamylase deficient patient following adenoviral gene transfer: Mol Genet Metab, v. 80, p. 148-58.
Rebbapragada, A., H. Benchabane, J. L. Wrana, A. J. Celeste, and L. Attisano, 2003, Myostatin signals through a transforming growth factor beta-like signaling pathway to block adipogenesis: Mol Cell Biol, v. 23, p. 7230-42.
Rensen, S. S., P. A. Doevendans, and G. J. van Eys, 2007, Regulation and characteristics of vascular smooth muscle cell phenotypic diversity: Neth Heart J, v. 15, p. 100-8.
Rensen, S. S., P. M. Niessen, X. Long, P. A. Doevendans, J. M. Miano, and G. J. van Eys, 2006, Contribution of serum response factor and myocardin to transcriptional regulation of smoothelins: Cardiovasc Res, v. 70, p. 136-45.
Rhaleb, N. E., N. Rouissi, F. Nantel, P. D'Orléans-Juste, and D. Regoli, 1991, DuP 753 is a specific antagonist for the angiotensin receptor: Hypertension, v. 17, p. 480-4.
Ricard, N., D. Ciais, S. Levet, M. Subileau, C. Mallet, T. A. Zimmers, S. J. Lee, M. Bidart, J. J. Feige, and S. Bailly, 2012, BMP9 and BMP10 are critical for postnatal retinal vascular remodeling: Blood, v. 119, p. 6162-71.
Robinson, C. M., D. Seto, M. S. Jones, D. W. Dyer, and J. Chodosh, 2011, Molecular evolution of human species D adenoviruses: Infect Genet Evol, v. 11, p. 1208-17.
Rodriguez, E., E. H. Lambert, M. G. Magno, and J. D. Mannion, 2000, Contractile smooth muscle cell apoptosis early after saphenous vein grafting: Ann Thorac Surg, v. 70, p. 1145-53.
Rodríguez-Vita, J., E. Sánchez-López, V. Esteban, M. Rupérez, J. Egido, and M. Ruiz-Ortega, 2005, Angiotensin II activates the Smad pathway in vascular

smooth muscle cells by a transforming growth factor-beta-independent mechanism: Circulation, v. 111, p. 2509-17.

Rosen, E. D., P. Sarraf, A. E. Troy, G. Bradwin, K. Moore, D. S. Milstone, B. M. Spiegelman, and R. M. Mortensen, 1999, PPAR gamma is required for the differentiation of adipose tissue in vivo and in vitro: Mol Cell, v. 4, p. 611-7.

Russell, W. C., 2000, Update on adenovirus and its vectors: J Gen Virol, v. 81, p. 2573-2604.

Saharinen, J., J. Taipale, and J. Keski-Oja, 1996, Association of the small latent transforming growth factor-beta with an eight cysteine repeat of its binding protein LTBP-1: EMBO J, v. 15, p. 245-53.

Salmon, M., D. Gomez, E. Greene, L. Shankman, and G. K. Owens, 2012, Cooperative binding of KLF4, pELK-1, and HDAC2 to a G/C repressor element in the SM22α promoter mediates transcriptional silencing during SMC phenotypic switching in vivo: Circ Res, v. 111, p. 685-96.

Salmon, R. M., J. Guo, J. H. Wood, Z. Tong, J. S. Beech, A. Lawera, M. Yu, D. J. Grainger, J. Reckless, N. W. Morrell, and W. Li, 2020, Molecular basis of ALK1-mediated signalling by BMP9/BMP10 and their prodomain-bound forms: Nat Commun, v. 11, p. 1621.

Samano, N., H. Geijer, M. Liden, S. Fremes, L. Bodin, and D. Souza, 2015, The no-touch saphenous vein for coronary artery bypass grafting maintains a patency, after 16 years, comparable to the left internal thoracic artery: A randomized trial: The Journal of Thoracic and Cardiovascular Surgery, v. 150, p. 880-888.

Santos, R. A., A. C. Simoes e Silva, C. Maric, D. M. Silva, R. P. Machado, I. de Buhr, S. Heringer-Walther, S. V. Pinheiro, M. T. Lopes, M. Bader, E. P. Mendes, V. S. Lemos, M. J. Campagnole-Santos, H. P. Schultheiss, R. Speth, and T. Walther, 2003, Angiotensin-(1-7) is an endogenous ligand for the G protein-coupled receptor Mas: Proc Natl Acad Sci U S A, v. 100, p. 8258-63.

Sasaki, Y., S. Suehiro, A. E. Becker, H. Kinoshita, and M. Ueda, 2000, Role of endothelial cell denudation and smooth muscle cell dedifferentiation in neointimal formation of human vein grafts after coronary artery bypass grafting: therapeutic implications: Heart, v. 83, p. 69-75.

Sata, M., Y. Maejima, F. Adachi, K. Fukino, A. Saiura, S. Sugiura, T. Aoyagi, Y. Imai, H. Kurihara, K. Kimura, M. Omata, M. Makuuchi, Y. Hirata, and R. Nagai, 2000, A mouse model of vascular injury that induces rapid onset of medial cell apoptosis followed by reproducible neointimal hyperplasia: J Mol Cell Cardiol, v. 32, p. 2097-104.

Sauzeau, V., H. Le Jeune, C. Cario-Toumaniantz, A. Smolenski, S. M. Lohmann, J. Bertoglio, P. Chardin, P. Pacaud, and G. Loirand, 2000, Cyclic GMP-dependent protein kinase signaling pathway inhibits RhoA-induced Ca2+ sensitization of contraction in vascular smooth muscle: J Biol Chem, v. 275, p. 21722-9.

Sauzeau, V., M. Rolli-Derkinderen, C. Marionneau, G. Loirand, and P. Pacaud, 2003, RhoA expression is controlled by nitric oxide through cGMP-dependent protein kinase activation: J Biol Chem, v. 278, p. 9472-80.

Saxena, U., E. Ferguson, and C. L. Bisgaier, 1993, Apolipoprotein E modulates low density lipoprotein retention by lipoprotein lipase anchored to the subendothelial matrix: J Biol Chem, v. 268, p. 14812-9.

Saxena, U., M. G. Klein, T. M. Vanni, and I. J. Goldberg, 1992, Lipoprotein lipase increases low density lipoprotein retention by subendothelial cell matrix: J Clin Invest, v. 89, p. 373-80.

Scharpfenecker, M., M. van Dinther, Z. Liu, R. L. van Bezooijen, Q. Zhao, L. Pukac, C. W. Löwik, and P. ten Dijke, 2007, BMP-9 signals via ALK1 and inhibits bFGF-induced endothelial cell proliferation and VEGF-stimulated angiogenesis: J Cell Sci, v. 120, p. 964-72.
Scheller, E. L., and P. H. Krebsbach, 2009, Gene therapy: design and prospects for craniofacial regeneration: J Dent Res, v. 88, p. 585-96.
Schnell, M. A., Y. Zhang, J. Tazelaar, G. P. Gao, Q. C. Yu, R. Qian, S. J. Chen, A. N. Varnavski, C. LeClair, S. E. Raper, and J. M. Wilson, 2001, Activation of innate immunity in nonhuman primates following intraportal administration of adenoviral vectors: Mol Ther, v. 3, p. 708-22.
Schober, A., J. Bernhagen, M. Thiele, U. Zeiffer, S. Knarren, M. Roller, R. Bucala, and C. Weber, 2004, Stabilization of atherosclerotic plaques by blockade of macrophage migration inhibitory factor after vascular injury in apolipoprotein E-deficient mice: Circulation, v. 109, p. 380-5.
Schwartze, J. T., S. Becker, E. Sakkas, L. A. Wujak, G. Niess, J. Usemann, F. Reichenberger, S. Herold, I. Vadasz, K. Mayer, W. Seeger, and R. E. Morty, 2014, Glucocorticoids recruit Tgfbr3 and Smad1 to shift transforming growth factor-beta signaling from the Tgfbr1/Smad2/3 axis to the Acvrl1/Smad1 axis in lung fibroblasts: J Biol Chem, v. 289, p. 3262-75.
Schwartze, J. T., E. L. Low, and A. C. Bradshaw, 2019, TGF-ß in vascular pathobiology, *in* R. M. Touyz, and C. Delles, eds., Textbook of Vascular Medicine, Springer, p. 137-148.
Sellers, J. R., and M. D. Pato, 1984, The binding of smooth muscle myosin light chain kinase and phosphatases to actin and myosin: J Biol Chem, v. 259, p. 7740-6.
Seto, M., Y. Sasaki, and H. Hidaka, 1991, Effects of HA1077, a protein kinase inhibitor, on myosin phosphorylation and tension in smooth muscle: Eur J Pharmacol, v. 195, p. 267-72.
Shah, N. M., A. K. Groves, and D. J. Anderson, 1996, Alternative neural crest cell fates are instructively promoted by TGFbeta superfamily members: Cell, v. 85, p. 331-43.
Sharma, A., X. Li, D. S. Bangari, and S. K. Mittal, 2009, Adenovirus receptors and their implications in gene delivery: Virus Res, v. 143, p. 184-94.
Sharma, K., L. Deelman, M. Madesh, B. Kurz, E. Ciccone, S. Siva, T. Hu, Y. Zhu, L. Wang, R. Henning, X. Ma, and G. Hajnoczky, 2003, Involvement of transforming growth factor-beta in regulation of calcium transients in diabetic vascular smooth muscle cells: Am J Physiol Renal Physiol, v. 285, p. F1258-70.
Shayakhmetov, D. M., A. Gaggar, S. Ni, Z. Y. Li, and A. Lieber, 2005, Adenovirus binding to blood factors results in liver cell infection and hepatotoxicity: J Virol, v. 79, p. 7478-91.
Shi, W., C. Sun, B. He, W. Xiong, X. Shi, D. Yao, and X. Cao, 2004, GADD34-PP1c recruited by Smad7 dephosphorylates TGFbeta type I receptor: J Cell Biol, v. 164, p. 291-300.
Shi, X., L. W. Guo, S. M. Seedial, Y. Si, B. Wang, T. Takayama, P. A. Suwanabol, S. Ghosh, D. DiRenzo, B. Liu, and K. C. Kent, 2014, TGF-ß/Smad3 inhibit vascular smooth muscle cell apoptosis through an autocrine signaling mechanism involving VEGF-A: Cell Death Dis, v. 5, p. e1317.
Shi, Y., J. E. O'Brien, A. Fard, J. D. Mannion, D. Wang, and A. Zalewski, 1996a, Adventitial myofibroblasts contribute to neointimal formation in injured porcine coronary arteries: Circulation, v. 94, p. 1655-64.

Shi, Y., J. E. O'Brien, Jr., J. D. Mannion, R. C. Morrison, W. Chung, A. Fard, and A. Zalewski, 1997, Remodeling of autologous saphenous vein grafts. The role of perivascular myofibroblasts: Circulation, v. 95, p. 2684-93.
Shi, Y., S. Patel, K. L. Davenpeck, R. Niculescu, E. Rodriguez, M. G. Magno, M. L. Ormont, J. D. Mannion, and A. Zalewski, 2001, Oxidative stress and lipid retention in vascular grafts: comparison between venous and arterial conduits: Circulation, v. 103, p. 2408-13.
Shi, Y., M. Pieniek, A. Fard, J. O'Brien, J. D. Mannion, and A. Zalewski, 1996b, Adventitial remodeling after coronary arterial injury: Circulation, v. 93, p. 340-8.
Shi-Wen, X., F. Rodríguez-Pascual, S. Lamas, A. Holmes, S. Howat, J. D. Pearson, M. R. Dashwood, R. M. du Bois, C. P. Denton, C. M. Black, D. J. Abraham, and A. Leask, 2006, Constitutive ALK5-independent c-Jun N-terminal kinase activation contributes to endothelin-1 overexpression in pulmonary fibrosis: evidence of an autocrine endothelin loop operating through the endothelin A and B receptors: Mol Cell Biol, v. 26, p. 5518-27.
Shiokawa, Y., M. F. Rahman, Y. Ishii, and K. Sueishi, 1989, The rate of re-endothelialization correlates inversely with the degree of the following intimal thickening in vein grafts. Electron microscopic and immunohistochemical studies: Virchows Arch A Pathol Anat Histopathol, v. 415, p. 225-35.
Singh, S., R. Kumar, and B. Agrawal, 2018, Adenoviral Vector-Based Vaccines and Gene Therapies: Current Status and Future Prospects, Adenoviruses, IntechOpen, p. 1-38.
Sisto, T., S. Ylä-Herttuala, J. Luoma, H. Riekkinen, and T. Nikkari, 1990, Biochemical composition of human internal mammary artery and saphenous vein: J Vasc Surg, v. 11, p. 418-22.
Skålén, K., M. Gustafsson, E. K. Rydberg, L. M. Hultén, O. Wiklund, T. L. Innerarity, and J. Borén, 2002, Subendothelial retention of atherogenic lipoproteins in early atherosclerosis: Nature, v. 417, p. 750-4.
Smith, J. B., T. Zheng, and R. M. Lyu, 1989, Ionomycin releases calcium from the sarcoplasmic reticulum and activates Na+/Ca2+ exchange in vascular smooth muscle cells: Cell Calcium, v. 10, p. 125-34.
Song, C. Z., T. E. Siok, and T. D. Gelehrter, 1998, Smad4/DPC4 and Smad3 mediate transforming growth factor-beta (TGF-beta) signaling through direct binding to a novel TGF-beta-responsive element in the human plasminogen activator inhibitor-1 promoter: J Biol Chem, v. 273, p. 29287-90.
Song, J. J., A. J. Celeste, F. M. Kong, R. L. Jirtle, V. Rosen, and R. S. Thies, 1995, Bone morphogenetic protein-9 binds to liver cells and stimulates proliferation: Endocrinology, v. 136, p. 4293-7.
Souza, D. S., R. H. Christofferson, V. Bomfim, and D. Filbey, 1999, "No-touch" technique using saphenous vein harvested with its surrounding tissue for coronary artery bypass grafting maintains an intact endothelium: Scand Cardiovasc J, v. 33, p. 323-9.
Squadrito, F., B. Deodato, A. Bova, H. Marini, F. Saporito, M. Calo, M. Giacca, L. Minutoli, F. S. Venuti, A. P. Caputi, and D. Altavilla, 2003, Crucial role of nuclear factor-kappaB in neointimal hyperplasia of the mouse carotid artery after interruption of blood flow: Atherosclerosis, v. 166, p. 233-42.
Steegenga, W. T., A. Shvarts, N. Riteco, J. L. Bos, and A. G. Jochemsen, 1999, Distinct regulation of p53 and p73 activity by adenovirus E1A, E1B, and E4orf6 proteins: Mol Cell Biol, v. 19, p. 3885-94.

Steele, P. M., J. H. Chesebro, A. W. Stanson, D. R. Holmes, Jr., M. K. Dewanjee, L. Badimon, and V. Fuster, 1985, Balloon angioplasty. Natural history of the pathophysiological response to injury in a pig model: Circ Res, v. 57, p. 105-12.

Steinbrecher, U. P., S. Parthasarathy, D. S. Leake, J. L. Witztum, and D. Steinberg, 1984, Modification of low density lipoprotein by endothelial cells involves lipid peroxidation and degradation of low density lipoprotein phospholipids: Proc Natl Acad Sci U S A, v. 81, p. 3883-7.

Sterpetti, A. V., A. Cucina, S. Lepidi, B. Randone, V. Corvino, L. S. D'Angelo, and A. Cavallaro, 1998, Formation of myointimal hyperplasia and cytokine production in experimental vein grafts: Surgery, v. 123, p. 461-9.

Storz, P., H. Döppler, and A. Toker, 2005, Protein kinase D mediates mitochondrion-to-nucleus signaling and detoxification from mitochondrial reactive oxygen species: Mol Cell Biol, v. 25, p. 8520-30.

Strobeck, M., S. Kim, J. C. Zhang, C. Clendenin, K. L. Du, and M. S. Parmacek, 2001, Binding of serum response factor to CArG box sequences is necessary but not sufficient to restrict gene expression to arterial smooth muscle cells: J Biol Chem, v. 276, p. 16418-24.

Strong, J. P., G. T. Malcom, C. A. McMahan, R. E. Tracy, W. P. Newman, E. E. Herderick, and J. F. Cornhill, 1999, Prevalence and extent of atherosclerosis in adolescents and young adults: implications for prevention from the Pathobiological Determinants of Atherosclerosis in Youth Study: JAMA, v. 281, p. 727-35.

Sun, H., J. K. Kim, R. Mortensen, L. P. Mutyaba, K. D. Hankenson, and P. H. Krebsbach, 2013, Osteoblast-targeted suppression of PPARγ increases osteogenesis through activation of mTOR signaling: Stem Cells, v. 31, p. 2183-92.

Suwanabol, P. A., S. M. Seedial, X. Shi, F. Zhang, D. Yamanouchi, D. Roenneburg, B. Liu, and K. C. Kent, 2012, Transforming growth factor-ß increases vascular smooth muscle cell proliferation through the Smad3 and extracellular signal-regulated kinase mitogen-activated protein kinases pathways: J Vasc Surg, v. 56, p. 446-54.

Suzuki, Y., N. Ohga, Y. Morishita, K. Hida, K. Miyazono, and T. Watabe, 2010, BMP-9 induces proliferation of multiple types of endothelial cells in vitro and in vivo: J Cell Sci, v. 123, p. 1684-92.

Takaku, K., M. Oshima, H. Miyoshi, M. Matsui, M. F. Seldin, and M. M. Taketo, 1998, Intestinal tumorigenesis in compound mutant mice of both Dpc4 (Smad4) and Apc genes: Cell, v. 92, p. 645-56.

Talasila, A., H. Yu, M. Ackers-Johnson, M. Bot, T. van Berkel, M. R. Bennett, I. Bot, and S. Sinha, 2013, Myocardin regulates vascular response to injury through miR-24/-29a and platelet-derived growth factor receptor-ß: Arterioscler Thromb Vasc Biol, v. 33, p. 2355-65.

Taler, S. J., S. C. Textor, V. J. Canzanello, and L. Schwartz, 1999, Cyclosporin-induced hypertension: incidence, pathogenesis and management: Drug Saf, v. 20, p. 437-49.

Tamai, H., K. Katoh, T. Yamaguchi, H. Hayakawa, K. Kanmatsuse, K. Haze, T. Aizawa, S. Nakanishi, S. Suzuki, T. Suzuki, S. Takase, H. Nishikawa, and O. Katoh, 2002, The impact of tranilast on restenosis after coronary angioplasty: the Second Tranilast Restenosis Following Angioplasty Trial (TREAT-2): Am Heart J, v. 143, p. 506-13.

Tan, E. P., F. E. Duncan, and C. Slawson, 2017, The sweet side of the cell cycle: Biochem Soc Trans, v. 45, p. 313-322.

Tang, Y., T. Feinberg, E. T. Keller, X. Y. Li, and S. J. Weiss, 2016, Snail/Slug binding interactions with YAP/TAZ control skeletal stem cell self-renewal and differentiation: Nat Cell Biol, v. 18, p. 917-29.
Tang, Y., S. Urs, J. Boucher, T. Bernaiche, D. Venkatesh, D. B. Spicer, C. P. Vary, and L. Liaw, 2010, Notch and transforming growth factor-beta (TGFbeta) signaling pathways cooperatively regulate vascular smooth muscle cell differentiation: J Biol Chem, v. 285, p. 17556-63.
Tao, B., J. R. Kraehling, S. Ghaffari, C. M. Ramirez, S. Lee, J. W. Fowler, W. L. Lee, C. Fernandez-Hernando, A. Eichmann, and W. C. Sessa, 2020, BMP-9 and LDL crosstalk regulates ALK-1 endocytosis and LDL transcytosis in endothelial cells: J Biol Chem, v. 295, p. 18179-18188.
Tatsis, N., and H. C. Ertl, 2004, Adenoviruses as vaccine vectors: Mol Ther, v. 10, p. 616-29.
ten Dijke, P., H. Yamashita, H. Ichijo, P. Franzén, M. Laiho, K. Miyazono, and C. H. Heldin, 1994, Characterization of type I receptors for transforming growth factor-beta and activin: Science, v. 264, p. 101-4.
Thakali, K. M., S. V. Kharade, S. K. Sonkusare, S. W. Rhee, J. R. Stimers, and N. J. Rusch, 2010, Intracellular Ca2+ silences L-type Ca2+ channels in mesenteric veins: mechanism of venous smooth muscle resistance to calcium channel blockers: Circ Res, v. 106, p. 739-47.
Thomas, M., C. Docx, A. M. Holmes, S. Beach, N. Duggan, K. England, C. Leblanc, C. Lebret, F. Schindler, F. Raza, C. Walker, A. Crosby, R. J. Davies, N. W. Morrell, and D. C. Budd, 2009, Activin-like kinase 5 (ALK5) mediates abnormal proliferation of vascular smooth muscle cells from patients with familial pulmonary arterial hypertension and is involved in the progression of experimental pulmonary arterial hypertension induced by monocrotaline: Am J Pathol, v. 174, p. 380-9.
Tillet, E., and S. Bailly, 2014, Emerging roles of BMP9 and BMP10 in hereditary hemorrhagic telangiectasia: Front Genet, v. 5, p. 456.
Tillet, E., M. Ouarne, A. Desroches-Castan, C. Mallet, M. Subileau, R. Didier, A. Lioutsko, G. Belthier, J. J. Feige, and S. Bailly, 2018, A heterodimer formed by bone morphogenetic protein 9 (BMP9) and BMP10 provides most BMP biological activity in plasma: J Biol Chem, v. 293, p. 10963-10974.
Tomko, R. P., R. Xu, and L. Philipson, 1997, HCAR and MCAR: the human and mouse cellular receptors for subgroup C adenoviruses and group B coxsackieviruses: Proc Natl Acad Sci U S A, v. 94, p. 3352-6.
Touyz, R. M., R. Alves-Lopes, F. J. Rios, L. L. Camargo, A. Anagnostopoulou, A. Arner, and A. C. Montezano, 2018, Vascular smooth muscle contraction in hypertension: Cardiovasc Res, v. 114, p. 529-539.
Trembath, R. C., J. R. Thomson, R. D. Machado, N. V. Morgan, C. Atkinson, I. Winship, G. Simonneau, N. Galie, J. E. Loyd, M. Humbert, W. C. Nichols, N. W. Morrell, J. Berg, A. Manes, J. McGaughran, M. Pauciulo, and L. Wheeler, 2001, Clinical and molecular genetic features of pulmonary hypertension in patients with hereditary hemorrhagic telangiectasia: N Engl J Med, v. 345, p. 325-34.
Tremblay, K. D., N. R. Dunn, and E. J. Robertson, 2001, Mouse embryos lacking Smad1 signals display defects in extra-embryonic tissues and germ cell formation: Development, v. 128, p. 3609-21.
Tsai, S., S. T. Hollenbeck, E. J. Ryer, R. Edlin, D. Yamanouchi, R. Kundi, C. Wang, B. Liu, and K. C. Kent, 2009, TGF-β through Smad3 signaling stimulates vascular smooth muscle cell proliferation and neointimal formation, Am J Physiol Heart Circ Physiol, v. 297, p. H540-9.

Tsuchida, K., M. Nakatani, A. Uezumi, T. Murakami, and X. Cui, 2008, Signal transduction pathway through activin receptors as a therapeutic target of musculoskeletal diseases and cancer: Endocr J, v. 55, p. 11-21.
Tu, L., A. Desroches-Castan, C. Mallet, L. Guyon, A. Cumont, C. Phan, F. Robert, R. Thuillet, J. Bordenave, A. Sekine, A. Huertas, O. Ritvos, L. Savale, J. J. Feige, M. Humbert, S. Bailly, and C. Guignabert, 2019, Selective BMP-9 Inhibition Partially Protects Against Experimental Pulmonary Hypertension: Circ Res, v. 124, p. 846-855.
Turner, N. A., S. Ho, P. Warburton, D. J. O'Regan, and K. E. Porter, 2007, Smooth muscle cells cultured from human saphenous vein exhibit increased proliferation, invasion, and mitogen-activated protein kinase activation in vitro compared with paired internal mammary artery cells: J Vasc Surg, v. 45, p. 1022-8.
Unni, K. K., B. A. Kottke, J. L. Titus, R. L. Frye, R. B. Wallace, and A. L. Brown, 1974, Pathologic changes in aortocoronary saphenous vein grafts: Am J Cardiol, v. 34, p. 526-32.
Unsöld, C., M. Hyytiäinen, L. Bruckner-Tuderman, and J. Keski-Oja, 2001, Latent TGF-beta binding protein LTBP-1 contains three potential extracellular matrix interacting domains: J Cell Sci, v. 114, p. 187-197.
Upton, P. D., R. J. Davies, R. C. Trembath, and N. W. Morrell, 2009, Bone morphogenetic protein (BMP) and activin type II receptors balance BMP9 signals mediated by activin receptor-like kinase-1 in human pulmonary artery endothelial cells: J Biol Chem, v. 284, p. 15794-804.
Urness, L. D., L. K. Sorensen, and D. Y. Li, 2000, Arteriovenous malformations in mice lacking activin receptor-like kinase-1: Nat Genet, v. 26, p. 328-31.
Vallot, O., L. Combettes, P. Jourdon, J. Inamo, I. Marty, M. Claret, and A. M. Lompré, 2000, Intracellular Ca(2+) handling in vascular smooth muscle cells is affected by proliferation: Arterioscler Thromb Vasc Biol, v. 20, p. 1225-35.
van de Laar, I. M., D. van der Linde, E. H. Oei, P. K. Bos, J. H. Bessems, S. M. Bierma-Zeinstra, B. L. van Meer, G. Pals, R. A. Oldenburg, J. A. Bekkers, A. Moelker, B. M. de Graaf, G. Matyas, I. M. Frohn-Mulder, J. Timmermans, Y. Hilhorst-Hofstee, J. M. Cobben, H. T. Bruggenwirth, L. van Laer, B. Loeys, J. De Backer, P. J. Coucke, H. C. Dietz, P. J. Willems, B. A. Oostra, A. De Paepe, J. W. Roos-Hesselink, A. M. Bertoli-Avella, and M. W. Wessels, 2012, Phenotypic spectrum of the SMAD3-related aneurysms-osteoarthritis syndrome: J Med Genet, v. 49, p. 47-57.
van der Pluijm, I., N. van Vliet, J. H. von der Thusen, J. L. Robertus, Y. Ridwan, P. M. van Heijningen, B. S. van Thiel, M. Vermeij, S. E. Hoeks, R. M. G. B. Buijs-Offerman, H. J. M. Verhagen, R. Kanaar, A. M. Bertoli-Avella, and J. Essers, 2016, Defective Connective Tissue Remodeling in Smad3 Mice Leads to Accelerated Aneurysmal Growth Through Disturbed Downstream TGF-ß Signaling: EBioMedicine, v. 12, p. 280-294.
van Son, J. A., F. Smedts, P. C. de Wilde, N. H. Pijls, L. Wong-Alcala, K. Kubat, G. Tavilla, and L. K. Lacquet, 1993, Histological study of the internal mammary artery with emphasis on its suitability as a coronary artery bypass graft: Ann Thorac Surg, v. 55, p. 106-13.
van Son, J. A., F. Smedts, J. G. Vincent, H. J. van Lier, and K. Kubat, 1990, Comparative anatomic studies of various arterial conduits for myocardial revascularization: J Thorac Cardiovasc Surg, v. 99, p. 703-7.
Vassalli, G., R. Agah, R. Qiao, C. Aguilar, and D. A. Dichek, 1999, A mouse model of arterial gene transfer: antigen-specific immunity is a minor

determinant of the early loss of adenovirus-mediated transgene expression: Circ Res, v. 85, p. e25-32.
Vengrenyuk, Y., H. Nishi, X. Long, M. Ouimet, N. Savji, F. O. Martinez, C. P. Cassella, K. J. Moore, S. A. Ramsey, J. M. Miano, and E. A. Fisher, 2015, Cholesterol loading reprograms the microRNA-143/145-myocardin axis to convert aortic smooth muscle cells to a dysfunctional macrophage-like phenotype: Arterioscler Thromb Vasc Biol, v. 35, p. 535-46.
Vestergaard, L. P., L. Benhassen, I. S. Modrau, F. de Paoli, and E. Boedtkjer, 2017, Increased Contractile Function of Human Saphenous Vein Grafts Harvested by "No-Touch" Technique: Front Physiol, v. 8, p. 1135.
Villahoz, S., P. S. Yunes-Leites, N. Méndez-Barbero, K. Urso, E. Bonzon-Kulichenko, S. Ortega, J. F. Nistal, J. Vazquez, S. Offermanns, J. M. Redondo, and M. R. Campanero, 2018, Conditional deletion of Rcan1 predisposes to hypertension-mediated intramural hematoma and subsequent aneurysm and aortic rupture: Nat Commun, v. 9, p. 4795.
Virmani, R., A. P. Burke, F. D. Kolodgie, and A. Farb, 2002, Vulnerable plaque: the pathology of unstable coronary lesions: J Interv Cardiol, v. 15, p. 439-46.
Virmani, R., F. D. Kolodgie, A. P. Burke, A. Farb, and S. M. Schwartz, 2000, Lessons from sudden coronary death: a comprehensive morphological classification scheme for atherosclerotic lesions: Arterioscler Thromb Vasc Biol, v. 20, p. 1262-75.
Vlodaver, Z., and J. E. Edwards, 1971, Pathologic changes in aortic-coronary arterial saphenous vein grafts: Circulation, v. 44, p. 719-28.
Von Seggern, D. J., J. Kehler, R. I. Endo, and G. R. Nemerow, 1998, Complementation of a fibre mutant adenovirus by packaging cell lines stably expressing the adenovirus type 5 fibre protein: J Gen Virol, v. 79 (Pt 6), p. 1461-8.
Vrhovski, B., K. McKay, G. Schevzov, P. W. Gunning, and R. P. Weinberger, 2005, Smooth muscle-specific alpha tropomyosin is a marker of fully differentiated smooth muscle in lung: J Histochem Cytochem, v. 53, p. 875-83.
Wakefield, L. M., D. M. Smith, K. C. Flanders, and M. B. Sporn, 1988, Latent transforming growth factor-beta from human platelets. A high molecular weight complex containing precursor sequences: J Biol Chem, v. 263, p. 7646-54.
Walts, A. E., M. C. Fishbein, H. Sustaita, and J. M. Matloff, 1982, Ruptured atheromatous plaques in saphenous vein coronary artery bypass grafts: a mechanism of acute, thrombotic, late graft occlusion: Circulation, v. 65, p. 197-201.
Wang, C. L., F. Xiao, C. D. Wang, J. F. Zhu, C. Shen, B. Zuo, H. Wang, Li, X. Y. Wang, W. J. Feng, Z. K. Li, G. L. Hu, X. Zhang, and X. D. Chen, 2017, Gremlin2 Suppression Increases the BMP-2-Induced Osteogenesis of Human Bone Marrow-Derived Mesenchymal Stem Cells Via the BMP-2/Smad/Runx2 Signaling Pathway: J Cell Biochem, v. 118, p. 286-297.
Wang, H. H., A. Nakamura, A. Matsumoto, S. Yoshiyama, X. Qin, L. H. Ye, C. Xie, Y. Zhang, Y. Gao, R. Ishikawa, and K. Kohama, 2009, Nonkinase activity of MLCK in elongated filopodia formation and chemotaxis of vascular smooth muscle cells toward sphingosylphosphorylcholine: Am J Physiol Heart Circ Physiol, v. 296, p. H1683-93.
Wang, M., W. Li, G. Q. Chang, C. S. Ye, J. S. Ou, X. X. Li, Y. Liu, T. Y. Cheang, X. L. Huang, and S. M. Wang, 2011, MicroRNA-21 regulates vascular smooth muscle cell function via targeting tropomyosin 1 in arteriosclerosis

obliterans of lower extremities: Arterioscler Thromb Vasc Biol, v. 31, p. 2044-53.

Wang, X. J., T. Y. Lian, X. Jiang, S. F. Liu, S. Q. Li, R. Jiang, W. H. Wu, J. Ye, C. Y. Cheng, Y. Du, X. Q. Xu, Y. Wu, F. H. Peng, K. Sun, Y. M. Mao, H. Yu, C. Liang, J. Y. Shyy, S. Y. Zhang, X. Zhang, and Z. C. Jing, 2019, Germline BMP9 mutation causes idiopathic pulmonary arterial hypertension: Eur Respir J, v. 53.

Wang, Z., D. Z. Wang, D. Hockemeyer, J. McAnally, A. Nordheim, and E. N. Olson, 2004, Myocardin and ternary complex factors compete for SRF to control smooth muscle gene expression: Nature, v. 428, p. 185-9.

Ward, M. R., T. Sasahara, A. Agrotis, R. J. Dilley, G. L. Jennings, and A. Bobik, 1998, Inhibitory effects of tranilast on expression of transforming growth factor-beta isoforms and receptors in injured arteries: Atherosclerosis, v. 137, p. 267-75.

Weber, J. D., D. M. Raben, P. J. Phillips, and J. J. Baldassare, 1997, Sustained activation of extracellular-signal-regulated kinase 1 (ERK1) is required for the continued expression of cyclin D1 in G1 phase: Biochem J, v. 326 (Pt 1), p. 61-8.

Wellenius, G. A., K. J. Mukamal, W. C. Winkelmayer, and M. A. Mittleman, 2007, Renal dysfunction increases the risk of saphenous vein graft occlusion: results from the Post-CABG trial: Atherosclerosis, v. 193, p. 414-20.

Wickham, T. J., P. Mathias, D. A. Cheresh, and G. R. Nemerow, 1993, Integrins alpha v beta 3 and alpha v beta 5 promote adenovirus internalization but not virus attachment: Cell, v. 73, p. 309-19.

Wirka, R. C., D. Wagh, D. T. Paik, M. Pjanic, T. Nguyen, C. L. Miller, R. Kundu, M. Nagao, J. Coller, T. K. Koyano, R. Fong, Y. J. Woo, B. Liu, S. B. Montgomery, J. C. Wu, K. Zhu, R. Chang, M. Alamprese, M. D. Tallquist, J. B. Kim, and T. Quertermous, 2019, Atheroprotective roles of smooth muscle cell phenotypic modulation and the TCF21 disease gene as revealed by single-cell analysis: Nat Med, v. 25, p. 1280-1289.

Wolff, R. A., R. L. Malinowski, N. S. Heaton, D. A. Hullett, and J. R. Hoch, 2006, Transforming growth factor-beta1 antisense treatment of rat vein grafts reduces the accumulation of collagen and increases the accumulation of h-caldesmon: J Vasc Surg, v. 43, p. 1028-36.

Wong, A. P., N. Nili, and B. H. Strauss, 2005, In vitro differences between venous and arterial-derived smooth muscle cells: potential modulatory role of decorin: Cardiovasc Res, v. 65, p. 702-10.

Wooderchak-Donahue, W. L., J. McDonald, B. O'Fallon, P. D. Upton, W. Li, B. L. Roman, S. Young, P. Plant, G. T. Fülöp, C. Langa, N. W. Morrell, L. M. Botella, C. Bernabeu, D. A. Stevenson, J. R. Runo, and P. Bayrak-Toydemir, 2013, BMP9 mutations cause a vascular-anomaly syndrome with phenotypic overlap with hereditary hemorrhagic telangiectasia: Am J Hum Genet, v. 93, p. 530-7.

Worgall, S., G. Wolff, E. Falck-Pedersen, and R. G. Crystal, 1997, Innate immune mechanisms dominate elimination of adenoviral vectors following in vivo administration: Hum Gene Ther, v. 8, p. 37-44.

Work, L. M., P. N. Reynolds, and A. H. Baker, 2004, Improved gene delivery to human saphenous vein cells and tissue using a peptide-modified adenoviral vector: Genet Vaccines Ther, v. 2, p. 14.

Wrana, J. L., L. Attisano, J. Cárcamo, A. Zentella, J. Doody, M. Laiho, X. F. Wang, and J. Massagué, 1992, TGF beta signals through a heteromeric protein kinase receptor complex: Cell, v. 71, p. 1003-14.

Wu, W., C. Wang, H. Zang, L. Qi, M. Azhar, M. Nagarkatti, P. Nagarkatti, G. Cai, M. C. M. Weiser-Evans, and T. Cui, 2020, Mature Vascular Smooth Muscle Cells, but Not Endothelial Cells, Serve as the Major Cellular Source of Intimal Hyperplasia in Vein Grafts: Arterioscler Thromb Vasc Biol, v. 40, p. 1870-1890.

Wu, W., W. Zhang, M. Choi, J. Zhao, P. Gao, M. Xue, H. A. Singer, D. Jourd'heuil, and X. Long, 2019, Vascular smooth muscle-MAPK14 is required for neointimal hyperplasia by suppressing VSMC differentiation and inducing proliferation and inflammation: Redox Biol, v. 22, p. 101137.

Wylie, L. A., K. P. Mouillesseaux, D. C. Chong, and V. L. Bautch, 2018, Developmental SMAD6 loss leads to blood vessel hemorrhage and disrupted endothelial cell junctions: Dev Biol, v. 442, p. 199-209.

Yahagi, K., F. D. Kolodgie, F. Otsuka, A. V. Finn, H. R. Davis, M. Joner, and R. Virmani, 2016, Pathophysiology of native coronary, vein graft, and in-stent atherosclerosis: Nat Rev Cardiol, v. 13, p. 79-98.

Yamaguchi, M., Y. Hayashi, and A. Matsukage, 1995, Essential role of E2F recognition sites in regulation of the proliferating cell nuclear antigen gene promoter during Drosophila development: J Biol Chem, v. 270, p. 25159-65.

Yamashita, H., P. ten Dijke, D. Huylebroeck, T. K. Sampath, M. Andries, J. C. Smith, C. H. Heldin, and K. Miyazono, 1995, Osteogenic protein-1 binds to activin type II receptors and induces certain activin-like effects: J Cell Biol, v. 130, p. 217-26.

Yamashita, T., S. Kawashima, M. Ozaki, Y. Rikitake, T. Hirase, N. Inoue, K. Hirata, and M. Yokoyama, 2001, A calcium channel blocker, benidipine, inhibits intimal thickening in the carotid artery of mice by increasing nitric oxide production: J Hypertens, v. 19, p. 451-8.

Yan, X., H. Liao, M. Cheng, X. Shi, X. Lin, X. H. Feng, and Y. G. Chen, 2016, Smad7 Protein Interacts with Receptor-regulated Smads (R-Smads) to Inhibit Transforming Growth Factor-β (TGF-β)/Smad Signaling: J Biol Chem, v. 291, p. 382-92.

Yang, H., L. Zhang, S. M. Weakley, P. H. Lin, Q. Yao, and C. Chen, 2011, Transforming growth factor-beta increases the expression of vascular smooth muscle cell markers in human multi-lineage progenitor cells: Med Sci Monit, v. 17, p. BR55-61.

Yang, J., X. Li, Y. Li, M. Southwood, L. Ye, L. Long, R. S. Al-Lamki, and N. W. Morrell, 2013, Id proteins are critical downstream effectors of BMP signaling in human pulmonary arterial smooth muscle cells: Am J Physiol Lung Cell Mol Physiol, v. 305, p. L312-21.

Yang, M., Z. Liang, Y. Jia, G. Yang, Y. He, X. Li, H. F. Gu, H. Zheng, Z. Zhu, and L. Li, 2019, Role of bone morphogenetic protein-9 in the regulation of glucose and lipid metabolism: Faseb j, v. 33, p. 10077-10088.

Yang, Y., F. A. Nunes, K. Berencsi, E. E. Furth, E. Gönczöl, and J. M. Wilson, 1994, Cellular immunity to viral antigens limits E1-deleted adenoviruses for gene therapy: Proc Natl Acad Sci U S A, v. 91, p. 4407-11.

Yao, F., P. Yu, Y. Li, X. Yuan, Z. Li, T. Zhang, F. Liu, Y. Wang, D. Li, B. Ma, C. Shu, W. Kong, B. Zhou, and L. Wang, 2018, Histone Variant H2A.Z Is Required for the Maintenance of Smooth Muscle Cell Identity as Revealed by Single-Cell Transcriptomics: Circulation, v. 138, p. 2274-2288.

Yao, Y., A. F. Zebboudj, A. Torres, E. Shao, and K. Bostrom, 2007, Activin-like kinase receptor 1 (ALK1) in atherosclerotic lesions and vascular mesenchymal cells: Cardiovasc Res, v. 74, p. 279-89.

Yi, J. Y., I. Shin, and C. L. Arteaga, 2005, Type I transforming growth factor beta receptor binds to and activates phosphatidylinositol 3-kinase: J Biol Chem, v. 280, p. 10870-6.

Yndestad, A., K. O. Larsen, E. Oie, T. Ueland, C. Smith, B. Halvorsen, I. Sjaastad, O. H. Skjønsberg, T. M. Pedersen, O. G. Anfinsen, J. K. Damås, G. Christensen, P. Aukrust, and A. K. Andreassen, 2009, Elevated levels of activin A in clinical and experimental pulmonary hypertension: J Appl Physiol (1985), v. 106, p. 1356-64.

Yoshida, T., S. Sinha, F. Dandré, B. R. Wamhoff, M. H. Hoofnagle, B. E. Kremer, D. Z. Wang, E. N. Olson, and G. K. Owens, 2003, Myocardin is a key regulator of CArG-dependent transcription of multiple smooth muscle marker genes: Circ Res, v. 92, p. 856-64.

Yoshida, T., M. Yamashita, C. Horimai, and M. Hayashi, 2013, Smooth muscle-selective inhibition of nuclear factor-kappaB attenuates smooth muscle phenotypic switching and neointima formation following vascular injury: J Am Heart Assoc, v. 2, p. e000230.

Yu, B., Y. Zhou, H. Wu, Z. Wang, Y. Zhan, X. Feng, R. Geng, Y. Wu, W. Kong, and X. Yu, 2012, Seroprevalence of neutralizing antibodies to human adenovirus type 5 in healthy adults in China: J Med Virol, v. 84, p. 1408-14.

Yu, H., M. C. Clarke, N. Figg, T. D. Littlewood, and M. R. Bennett, 2011, Smooth muscle cell apoptosis promotes vessel remodeling and repair via activation of cell migration, proliferation, and collagen synthesis: Arterioscler Thromb Vasc Biol, v. 31, p. 2402-9.

Yu, L., M. C. Hébert, and Y. E. Zhang, 2002, TGF-beta receptor-activated p38 MAP kinase mediates Smad-independent TGF-beta responses: EMBO J, v. 21, p. 3749-59.

Yu, Q., and I. Stamenkovic, 2000, Cell surface-localized matrix metalloproteinase-9 proteolytically activates TGF-beta and promotes tumor invasion and angiogenesis: Genes Dev, v. 14, p. 163-76.

Yung, L. M., P. Yang, S. Joshi, Z. M. Augur, S. S. J. Kim, G. A. Bocobo, T. Dinter, L. Troncone, P. S. Chen, M. E. McNeil, M. Southwood, S. Poli de Frias, J. Knopf, I. O. Rosas, D. Sako, R. S. Pearsall, J. D. Quisel, G. Li, R. Kumar, and P. B. Yu, 2020, ACTRIIA-Fc rebalances activin/GDF versus BMP signaling in pulmonary hypertension: Sci Transl Med, v. 12.

Zamanian, M., and N. B. La Thangue, 1992, Adenovirus E1a prevents the retinoblastoma gene product from repressing the activity of a cellular transcription factor: EMBO J, v. 11, p. 2603-10.

Zawel, L., J. L. Dai, P. Buckhaults, S. Zhou, K. W. Kinzler, B. Vogelstein, and S. E. Kern, 1998, Human Smad3 and Smad4 are sequence-specific transcription activators: Mol Cell, v. 1, p. 611-7.

Zent, J., and L. W. Guo, 2018, Signaling Mechanisms of Myofibroblastic Activation: Outside-in and Inside-Out: Cell Physiol Biochem, v. 49, p. 848-868.

Zernecke, A., A. Schober, I. Bot, P. von Hundelshausen, E. A. Liehn, B. Möpps, M. Mericskay, P. Gierschik, E. A. Biessen, and C. Weber, 2005, SDF-1alpha/CXCR4 axis is instrumental in neointimal hyperplasia and recruitment of smooth muscle progenitor cells: Circ Res, v. 96, p. 784-91.

Zhang, L., K. Peppel, L. Brian, L. Chien, and N. J. Freedman, 2004, Vein graft neointimal hyperplasia is exacerbated by tumor necrosis factor receptor-1 signaling in graft-intrinsic cells: Arterioscler Thromb Vasc Biol, v. 24, p. 2277-83.

Zhang, L., J. H. Wu, J. C. Otto, S. B. Gurley, E. R. Hauser, S. K. Shenoy, K. Nagi, L. Brian, V. Wertman, N. Mattocks, J. H. Lawson, and N. J. Freedman, 2017, Interleukin-9 mediates chronic kidney disease-dependent vein graft disease: a role for mast cells: Cardiovasc Res, v. 113, p. 1551-1559.

Zhang, L. N., U. o. C. a. Davis, V. D. Cunha, B. AG, B. Martin-McNulty, B. AG, D. W. Wilson, M. a. I. Pathology, dwwilson@ucdavis.edu, M. E. Sullivan, B. AG, R. Vergona, B. AG, J. C. Rutledge, C. Medicine, jcrutledge@ucdavis.edu, Y. X. Wang, and B. AG, 2020, Endothelial nitric oxide synthase deficiency enhanced carotid artery ligation-induced remodeling by promoting vascular inflammation: Journal of Applied Research, v. 6, p. 100-114.

Zhang, Y., N. Chirmule, G. P. Gao, R. Qian, M. Croyle, B. Joshi, J. Tazelaar, and J. M. Wilson, 2001, Acute cytokine response to systemic adenoviral vectors in mice is mediated by dendritic cells and macrophages: Mol Ther, v. 3, p. 697-707.

Zhang, Y., T. Musci, and R. Derynck, 1997, The tumor suppressor Smad4/DPC 4 as a central mediator of Smad function: Curr Biol, v. 7, p. 270-6.

Zhao, G., M. J. Xu, M. M. Zhao, X. Y. Dai, W. Kong, G. M. Wilson, Y. Guan, C. Y. Wang, and X. Wang, 2012, Activation of nuclear factor-kappa B accelerates vascular calcification by inhibiting ankylosis protein homolog expression: Kidney Int, v. 82, p. 34-44.

Zhao, Y., S. Biswas, P. McNulty, M. Kozak, J. Jun, and L. Segar, 2011, PDGF-induced Vascular Smooth Muscle Cell Proliferation Is Associated With Dysregulation of Insulin Receptor Substrates: American journal of physiology. Cell physiology, v. 300.

Zheng, G. X., J. M. Terry, P. Belgrader, P. Ryvkin, Z. W. Bent, R. Wilson, S. B. Ziraldo, T. D. Wheeler, G. P. McDermott, J. Zhu, M. T. Gregory, J. Shuga, L. Montesclaros, J. G. Underwood, D. A. Masquelier, S. Y. Nishimura, M. Schnall-Levin, P. W. Wyatt, C. M. Hindson, R. Bharadwaj, A. Wong, K. D. Ness, L. W. Beppu, H. J. Deeg, C. McFarland, K. R. Loeb, W. J. Valente, N. G. Ericson, E. A. Stevens, J. P. Radich, T. S. Mikkelsen, B. J. Hindson, and J. H. Bielas, 2017, Massively parallel digital transcriptional profiling of single cells: Nat Commun, v. 8, p. 14049.

Zhu, D., N. C. Mackenzie, C. M. Shanahan, R. C. Shroff, C. Farquharson, and V. E. MacRae, 2015, BMP-9 regulates the osteoblastic differentiation and calcification of vascular smooth muscle cells through an ALK1 mediated pathway: J Cell Mol Med, v. 19, p. 165-74.

Zhu, F. C., Y. H. Li, X. H. Guan, L. H. Hou, W. J. Wang, J. X. Li, S. P. Wu, B. S. Wang, Z. Wang, L. Wang, S. Y. Jia, H. D. Jiang, T. Jiang, Y. Hu, J. B. Gou, S. B. Xu, J. J. Xu, X. W. Wang, W. Wang, and W. Chen, 2020, Safety, tolerability, and immunogenicity of a recombinant adenovirus type-5 vectored COVID-19 vaccine: a dose-escalation, open-label, non-randomised, first-in-human trial: Lancet, v. 395, p. 1845-1854.

Zhu, H., P. Kavsak, S. Abdollah, J. L. Wrana, and G. H. Thomsen, 1999, A SMAD ubiquitin ligase targets the BMP pathway and affects embryonic pattern formation: Nature, v. 400, p. 687-693.

Zhu, J., F. I. A. Yildrim, S. N. Angeloc, H. Wei, and D. Dichek, 2017, Smooth Muscle Cell Tgfbr2 Deletion in Mice Causes Aortic Hypercontractility and Impaired Endothelium-Dependent Relaxation: Arteriosclerosis, Thrombosis, and Vascular Biology, v. 37, p. A9.

Zhu, Z., M. Tepel, M. Neusser, and W. Zidek, 1995, Transforming growth factor beta 1 modulates angiotensin II-induced calcium influx in vascular smooth muscle: Eur J Clin Invest, v. 25, p. 317-21.

Zou, Y., H. Dietrich, Y. Hu, B. Metzler, G. Wick, and Q. Xu, 1998, Mouse model of venous bypass graft arteriosclerosis: Am J Pathol, v. 153, p. 1301-10.